

Modeling Microstructural Effects on Deformation Resistance and Thermal Conductivity

by

Ju Li

Submitted to the Department of Nuclear Engineering
in partial fulfillment of the requirements for the degree of

Doctor of Philosophy

at the

MASSACHUSETTS INSTITUTE OF TECHNOLOGY

August 2000

© Massachusetts Institute of Technology 2000. All rights reserved.

Author
Department of Nuclear Engineering
August 2, 2000

Certified by
Sidney Yip
Professor, Department of Nuclear Engineering
Thesis Supervisor

Accepted by
Sow-Hsin Chen
Chairman, Departmental Committee on Graduate Students

Modeling Microstructural Effects on Deformation Resistance and Thermal Conductivity

by

Ju Li

Submitted to the Department of Nuclear Engineering
on August 2, 2000, in partial fulfillment of the
requirements for the degree of
Doctor of Philosophy

Abstract

This is a study of the microstructural influences on thermo-mechanical behavior of selected metals and ceramics using computer simulation, with original contributions in both theoretical and applied aspects. There are three major thrusts.

First, by constructing a many-body empirical potential for ZrC_x and then carrying out MD simulations to calculate its lattice thermal conductivity, I obtain the first quantitative evidence ever that the vibrational contribution is only a small part of the total thermal conductivity of refractory carbides at realistic carbon vacancy concentrations. This is a long-standing problem which even the most recent review article on the subject gives what I now believe is the wrong estimate.

Second, ideal strengths are calculated for Ar, Cu, SiC crystals using both lattice and molecular dynamics methods. A set of homogeneous instability criteria are derived. Tension tests are performed on amorphous and nanocrystalline SiC at room temperature, based on which a grain size cutoff of ~ 20 nm is extrapolated for the Hall-Petch effect. Nano-indentation is performed on single-crystal and nanocrystalline Cu, and bursts of dislocation loops are observed at a local stress level consistent with recent experiments on Cu thin films.

Third, an invariant loop summation similar to the J -integral is derived for the driving force on defect motion, but with the loop size now down to nanometers, and the summation now expressed in terms of interatomic forces instead of stress, a field concept which is hard to use in atomistic calculations and becomes ill-defined when defect separations approach the nanometer scale. It is shown first that the change in a system's total Helmholtz free energy due to a defect's move can be approximated by a local quantity involving only scores of atoms immediately surrounding the defect. Then, perturbation expansion is used to evaluate this local invariant for defect translation using only the current configuration. This driving force measure is tested on a) self-interstitial diffusion near free surface in α -iron, b) crack-tip extension near a void in Si, c) screw dislocation translation in Si, all with convincing results down to literally $r = 1$ nm, at a fraction of the cost of a full relaxation or free energy calculation for the whole system. This means that defect mobility can now be characterized

by a universal and invariant standard, computable from a tiny atomistic calculation without relying on elasticity formulas or image summations. This standard is used to determine the true Peierls-Nabarro stress in Si-like materials.

Thesis Supervisor: Sidney Yip

Title: Professor, Department of Nuclear Engineering

Acknowledgments

I would like to thank Prof. Ali Argon and Prof. John Joannopoulos for serving on my thesis committee. The three courses I took under Prof. Argon on mechanical behavior and the two courses I took under Prof. Joannopoulos on theory of solids are the best I have taken at M.I.T., which not only account for a major part of my knowledge but also strongly fuel my interest in these directions as this thesis shows. I would also like to thank Prof. Sow-Hsin Chen for serving as the Chairman of the thesis committee.

I am grateful to M.I.T., especially Nuclear Engineering Department, for admitting me as a graduate student in 1994. To me, M.I.T. is a very special place, and I thank all those who contribute to and are in stewardship of this unique and wonderful environment.

I acknowledge the Manson Benedict Fellowship award from Nuclear Engineering Department for providing financial support during 1996-1997. My research has also been funded by the American Chemical Society, Air Force Office of Scientific Research, Sandia National Laboratory, and Knolls Atomic Power Laboratory. I would like to thank Honda R & D North America for the valuable gift to our group, the Origin2000 computer, on which most of my computation was performed.

I would like to thank Dr. Cai-Zhuang Wang and Prof. Kai-Ming Ho for their hospitality during my summer visits to the Ames Laboratory, where I learned the techniques of electronic structure calculation and potential fitting. I would like to thank Dr. Joshua Fujiwara for his support and camaraderie, and Dr. Hideo Kaburaki, Dr. Channy Wong, Dr. Reza Najafabadi and Dr. Bill Hamm for close collaborations and support.

I would like to thank Dr. Lisa Porter and Dr. Vasily Bulatov for their exemplar roles in our group and their strong support both in research and in life. Same to Dr. Joao Justo who was like a big brother to me and helped me in many ways. You all occur to me whenever I recall Santa Barbara, which was such a nice experience. Dr. Meijie Tang, Dr. Maurice de Koning and Dr. Genrich Krasko were also constant

sources of strength to me.

One cannot do without buddies. Dongyi Liao, Wei Cai and Jinpeng Chang, you are all wonderful friends. I will always remember the many happy occasions and what I learned from you.

I must thank my dear daughter Clara who is now 5-month-old for not crying that much and for the heavenly and frequent all-gum grin, and Qing and her mother for taking care of everything. I thank my mother for her fortitude and encouragements that helped build my character and stimulated my interest in science since childhood. I love you all.

Lastly, Prof. Sidney Yip has been my mentor for six years, without whose wisdom, guidance and support this work and my other achievements would have been impossible.

Contents

1	Introduction	23
1.1	Motivation	23
1.2	Problem Statement	24
2	Fundamental Concepts and Simulation Determination	29
2.1	Stress, Strain and Elastic Constants	29
2.1.1	Atomistic Local Strain	34
2.2	Thermodynamic Ensembles and Fluctuations	36
2.2.1	Canonical Ensemble	39
2.2.2	Micro-canonical Ensemble	47
2.3	Lattice Vibrational Formalisms	61
2.3.1	Order- N Method to Calculate the Local Density of States . .	73
2.4	Mechanical Deformation at Finite Strain	73
2.4.1	Elastic Instabilities	73
2.4.2	Deformation of a Periodic Simulation Cell	87
3	Case Studies: Ar and SiC	100
3.1	Ideal Strength of Ar	100
3.1.1	General Properties	101
3.1.2	Lattice Dynamical Calculation of Ideal Strength	104
3.1.3	MD Simulation of Ideal Strength	106
3.2	Thermal Conductivity of Ar	110
3.3	Strength of SiC	114

3.3.1	General Properties	114
3.3.2	Lattice Dynamical Calculation of Ideal Strength	117
3.3.3	MD Simulation of Ideal Strength	117
3.3.4	MD Simulation of Amorphous Strength	120
3.3.5	MD Simulation of Nanocrystal Strength	123
3.4	Thermal Conductivity of Crystalline and Irradiated SiC	128
4	Thermal Conductivities of Refractory Carbides	130
4.1	Problem Statement	130
4.2	Nature of Chemical Bonds in ZrC	138
4.3	The Potential Model	144
4.3.1	Introduction	144
4.3.2	Second-moment approximation and WF potential for pure Zr	146
4.3.3	New Empirical Potential for Zr/C	152
4.4	Fitted Properties	157
4.5	Predicted Properties	164
4.6	MD Calculation of Lattice Thermal Conductivity	173
4.6.1	MD Heating Experiment	174
4.6.2	Thermal Conductivity Calculation	174
5	Nano-Indentation of Cu	178
5.1	Calculation of General Properties	178
5.2	Ideal Strength	181
5.3	Nano-Indentation Simulation	185
5.4	Experimental Result	188
6	Atomistic Measure of Thermodynamic Driving Force	190
6.1	Motivation	190
6.2	Derivation	193
6.3	Microscopic Free Energies	201
6.4	Connection to Atomistic Local Stress	207

6.5	Self-Interstitial near Surface in α -Iron	210
6.6	Crack-Tip Extension near Void in Si	212
6.7	Peierls-Nabarro Stress of Perfect Screw Dislocation in Si	214
6.7.1	Slip Systems	214
6.7.2	Low- T Plastic Deformation	215
6.7.3	Status of Atomistic Calculations	219
6.7.4	Results	220
6.8	Conclusion and Insights	224
7	Summary	226
A	Nodal Dynamics Study of Precipitation Hardening	229
B	Linear Response Theory of Transport	245
C	N-body Microscopic Heat Current Expression	265
D	Lattice Thermal Conductivity	270
D.1	Phonon Boltzmann Equation	271
D.2	3-Phonon Process	278
D.3	Debye Function for Temperature Rescaling	280
D.4	Connection between Classical and Quantum Phonon Scattering	283
E	Spectral Method in Thermal Conductivity Calculation	309
F	Four Heat Currents in a Crystal	333
G	Truncation Schemes for Pair Potential	349
H	Improving the Efficiency of Stillinger-Weber Potential	353
	Bibliography	358

List of Figures

3-1	Comparison of Ar phonon dispersion at $P = 0$ of the Lennard-Jones potential (solid line) with experimental measurements [75] (^{36}Ar result (circles) is rescaled for $m = 39.948$ amu). The plot on left is $r_c = 2.5\sigma$, right is $r_c = 5\sigma$	102
3-2	Phonon density of states of Ar at $P = 0$, using the Lennard-Jones potential with $r_c = 5\sigma$	103
3-3	Thermal expansion coefficient of Ar predicted using the 0K phonon spectrum and Gruneisen parameter, assuming $\gamma_k = d \log \omega_k / d \log \Omega$ stay constant with T , but $B(T)$ linearly drops to $B(T = 0)/2$ at $T = T_M$.103	
3-4	Phonon heat capacities predicted under the same assumptions as Fig. 3-3.	104
3-5	$g(r)$ of amorphous Ar at $T = 10\text{K}$	105
3-6	Phonon dispersion of Ar crystal under shear strain $\epsilon_{xy} = 0.087$, with $\sigma_{xy} = 562$ MPa, $\sigma_{xx} = \sigma_{yy} = -391$ MPa. A label tracks only one of the original high-symmetry \mathbf{k} -points. Notice the Γ' -point soft mode in the $[111]$ direction.	105
3-7	Phonon dispersion of Ar crystal under uniaxial tensile strain $\epsilon_{xx} = 0.138$, with $\sigma_{xx} = 266$ MPa, $\sigma_{yy} = \sigma_{zz} = 119$ MPa. A label tracks only one of the original high-symmetry \mathbf{k} -points. Notice the Γ' -point soft mode in the $[011]$ direction.	106
3-8	Phonon dispersion of Ar crystal under hydrostatic tensile strain $\epsilon_{xx} = \epsilon_{yy} = \epsilon_{zz} = 0.113$, with $\sigma_{xx} = \sigma_{yy} = \sigma_{zz} = 234$ MPa. Notice the Γ -point soft mode in the $[100]$ direction.	107

3-9	Stress-strain curve in the uniaxial deformation of Ar perfect crystal at $T = 0.3\epsilon/k_B = 35.9$ K.	107
3-10	Configurations corresponding to (a), (b), (c) arrows in Fig. 3-9.	108
3-11	Comparison of stress-strain curves in the hydrostatic deformation of Ar perfect crystal (star) and an 8 nm volume element with a void of 3 nm in diameter (circle).	109
3-12	Configurations corresponding to (a) and (b) arrows in Fig. 3-11. Atomistic local strain is color-encoded.	110
3-13	Comparison of the NEMD method result [64], with the equilibrium fluctuation method, for Ar fluid near triple point: $T_R = 0.69, \rho_R = 0.84$. The number of particles is 256.	111
3-14	Comparison of the NEMD method result [64], with the equilibrium fluctuation method, for solid Ar at $T_R = 0.2983, \rho_R = 0.90$. The left is result with 256 particles, the right is result with 108 particles.	112
3-15	Comparison of calculated Ar crystalline thermal conductivity with experiments.	113
3-16	log-log plot of the heat flux autocorrelation function in Ar crystal at $T = 20$ K, illustrating the two stages and their sharp transition at $\tau \sim 1$ ps.	114
3-17	Calculated crystalline and amorphous SiC elastic constants as a function of T	115
3-18	Left: Mean Squared Displacements in amorphous SiC as a function of simulation time. Right: experimental Si/C phase diagram.	116
3-19	Left: calculated (100) surface energy of crystalline β -SiC as a function of T . Right: calculated surface energy of amorphous SiC.	116
3-20	Phonon dispersion curve of β -SiC crystal under hydrostatic strain $\epsilon_{xx} = \epsilon_{yy} = \epsilon_{zz} = 0.24$, with $\sigma_{xx} = \sigma_{yy} = \sigma_{zz} = 39$ GPa. Notice the Γ' -point soft mode in the [111] direction.	117

3-21	Phonon dispersion curve of β -SiC crystal under shear strain $\epsilon_{xy} = 0.20$, with $\sigma_{xy} = 62$ GPa. A label tracks only one of the original high-symmetry \mathbf{k} -points. Notice the L -point soft mode.	118
3-22	Critical hydrostatic strain and stress as a function of T for β -SiC crystal.	118
3-23	Critical tension strain and stress under plane strain condition as a function of T for β -SiC crystal.	119
3-24	Critical shear strain and stress as a function of T for β -SiC crystal. .	119
3-25	Configuration after pure shear instability of β -SiC crystal at $T = 1300\text{K}$ and $\sigma_{xy} = 43$ GPa, compared to a moment ago just prior to the catastrophe. An elliptical microcrack and an accompanying deformation band have formed.	120
3-26	Critical hydrostatic strain and stress as a function of T for amorphous-SiC.	121
3-27	Critical tension strain and stress under plane strain condition as a function of T for amorphous-SiC.	121
3-28	Critical shear strain and stress as a function of T for amorphous-SiC.	122
3-29	Configuration after hydrostatic decohesion of amorphous-SiC crystal at $T = 300\text{K}$ and $\sigma_{xx} = \sigma_{yy} = \sigma_{zz} = 22$ GPa, compared to the undeformed amorphous-SiC.	122
3-30	Stress-strain curve during hydrostatic deformation of SiC nanocrystal at 300K. The stress-strain curves of β -SiC crystal and amorphous-SiC under identical conditions are also shown for comparison.	124
3-31	Configurations corresponding to (a) and (b) arrows in Fig. 3-30. The atoms are color-encoded by their atomistic local shear strain.	125
3-32	Cutoff to the Hall-Petch relation in SiC.	126
4-1	A collection of experimental measurements of ZrC thermal conductivity as a function of temperature. <i>CRC Handbook</i> [146] recommended values are plotted in solid line.	132

4-2	Comparison of experimental and simulation results for the thermal conductivities of SiC, for both perfect crystal (experiment a: circles with solid line to guide the eye; experiment b: squares; simulation: stars), and crystal with defects (experiment on radiation damaged SiC: diamond; simulation with 0.5% point defects: pluses, crosses, triangles).	132
4-3	Experimental thermal conductivity of amorphous SiO ₂	133
4-4	Experimental thermal conductivity of Au,Al,Na,Nb.	134
4-5	Reproduced Fig. 3 of a most recent review article [148]. Notice that the proposed crossover in dominance occurs at $T = 1000\text{K}$. At $T = 2000\text{K}$, the vibrational contribution is still thought to be non-negligible. . . .	136
4-6	Bond types in fcc pure Zr and NaCl-ZrC.	138
4-7	Electron density of states of Ti and Zr, reproduced from Fig. 6 of [152]. The dash line is the Fermi level.	139
4-8	An intuitive view of NaCl-ZrC _x	140
4-9	Phase diagram of Zr-C system, reproduced from Fig. 2 of [210]. . . .	140
4-10	Total and representation decomposed electron density of states in NaCl TiC, reproduced from Fig. 4 of [207]. The Fermi level is at 0.	142
4-11	An illustration of the Zr-C bond screening.	155
4-12	(a) Should screening loss be a geometrical series? (b) “Random” screening loss approximation.	155
4-13	Illustration of the screening decay factor $\exp(-\sqrt{s_{ij}})$ (assuming all h ’s are equal).	157
4-14	Radial functions for bare interaction strengths. The <i>1st</i> arrow is at the nearest neighbor distance (Zr-C) in equilibrium ZrC; the <i>2nd</i> arrow is at the second-nearest neighbor distance (Zr-Zr) in equilibrium ZrC. The <i>hcp Zr</i> arrow is at the nearest neighbor distance (Zr-Zr) in equilibrium hcp Zr.	158
4-15	Cohesive energy curves of three cubic phases of ZrC: NaCl-ZrC, ZnS-ZrC, CsCl-ZrC. Solid lines are from LDA calculations (rigidly shifted to match in $E_{\min}^{\text{NaCl-ZrC}}$), dash lines are from my empirical potential. .	158

4-16	C atom force constants in ZrC in unit of N/m. Jochym <i>et al</i> 's GGA calculation results [201] are the numbers above, my results are the numbers below. Only the atoms that contribute significantly to the total “resistance” are shown, and some are omitted by symmetry. . .	160
4-17	Zr atom force constants in ZrC in unit of N/m. Jochym <i>et al</i> 's GGA calculation results [201] are the numbers above, my results are the numbers below. Only the atoms that contribute significantly to the total “resistance” are shown, and some are omitted by symmetry. . .	161
4-18	Phonon dispersion curve of ZrC: comparing my result (solid line) with experiment [209] (circles), and recent GGA calculations [201] (dots). .	163
4-19	Phonon DOS (full line) and LDOS (dotted lines) in ZrC. Zr atom LDOS almost completely fills the acoustic band, while the C atom LDOS almost completely fills the optical band.	163
4-20	Illustration of the shrinkage of the nearest C-M bond pointing to a carbon vacancy.	169
4-21	Average Grüneisen parameter of ZrC as a function of T using phonon frequencies at 0K.	170
4-22	Thermal expansion coefficient derived from the overall 0K Grüneisen parameter.	171
4-23	Calculated heat capacities of ZrC using phonon frequencies at 0K. The circles are experimentally measured C_P for $\text{ZrC}_{0.96}$ [145].	171
4-24	Vibrational amplitudes of Zr and C atoms in NaCl-ZrC (dash line is the average $\sqrt{0.5[\langle \Delta \mathbf{r}_{\text{Zr}} ^2 \rangle + \langle \Delta \mathbf{r}_{\text{C}} ^2 \rangle]}$), and Lindemann’s law’s prediction of the melting point. One experimental measurement of carbon atom’s vibrational amplitude at room temperature is shown in triangle, and five “averaged” experimental points at other temperatures are shown in circles [222].	172
4-25	(a) Cluster configuration at 3500K. (b) Cluster configuration at 3650K.	173
4-26	Thermal strain measured in experiment [222] and in a direct MD simulation.	174

4-27	Short-term behavior of the heat current correlation function of crystalline ZrC at 1000K	175
4-28	Time-convergence of the heat current correlation function integral of crystalline ZrC at 1000K.	175
5-1	Comparison of Cu phonon dispersion at $P = 0$ using BAJ and EMT-96-NN potentials (solid line) with experimental measurements (triangles) [225].	180
5-2	Phonon dispersion relation of Cu crystal under uniaxial tensile strain $\epsilon_{xx} = 0.16$, with $\sigma_{xx} = 17.3$ and $\sigma_{yy} = \sigma_{zz} = 12.2$ GPa, using the BAJ potential [174]. A label tracks only one of the original high-symmetry k -points. Notice the Γ -point soft mode in the $[011]$ direction.	181
5-3	Phonon dispersion relation of Cu crystal under shear strain $\epsilon_{xy} = 0.082$, with $\sigma_{xy} = 17.1$, $\sigma_{xx} = \sigma_{yy} = -10.9$ and $\sigma_{zz} = -9.35$ GPa, using the BAJ potential [174]. A label tracks only one of the original high-symmetry k -points. Notice the Γ -point soft mode in the $[1\bar{1}0]$ direction.	182
5-4	Phonon dispersion relation of Cu crystal under hydrostatic strain $\epsilon_{xx} = \epsilon_{yy} = \epsilon_{zz} = 0.121$, with $\sigma_{xx} = \sigma_{yy} = \sigma_{zz} = 20.3$ GPa, using the BAJ potential [174]. Notice the L-point finite k soft mode.	183
5-5	Phonon dispersion relation of Cu crystal under uniaxial tensile strain $\epsilon_{xx} = 0.235$, with $\sigma_{xx} = 21.4$ and $\sigma_{yy} = \sigma_{zz} = 11.4$ GPa, using the EMT-96-NN potential [191]. Notice the X-point finite k soft mode.	184
5-6	Phonon dispersion relation of Cu crystal under shear strain $\epsilon_{xy} = 0.104$, with $\sigma_{xy} = 23.6$, $\sigma_{xx} = \sigma_{yy} = -16.0$ and $\sigma_{zz} = -11.4$ GPa, using the EMT-96-NN potential [191]. Notice the Γ -point soft mode in the $[1\bar{1}0]$ direction.	184
5-7	Phonon dispersion relation of Cu crystal under hydrostatic strain $\epsilon_{xx} = \epsilon_{yy} = \epsilon_{zz} = 0.0905$, with $\sigma_{xx} = \sigma_{yy} = \sigma_{zz} = 19.4$ GPa, using the the EMT-96-NN potential [191]. Notice the L-point finite k soft mode.	185
5-8	Nano-indentation simulation setup.	186

5-9	Indenter nominal pressure versus indentation depth at $T = 0\text{K}$ and 300K	186
5-10	Configuration immediately after the first cusp (labeled as b) in Fig. 5-9, color-encoded by the atom coordination number, at $T = 0\text{K}$	187
5-11	Configuration color-encoded by the atom coordination number after several cusps in Fig. 5-9 (labeled as c), at $T = 0\text{K}$	188
5-12	Brief summary of recent nano-indentation experiment on Cu thin films by Gouldstone <i>et al</i> [142, 143].	189
6-1	Illustration of how the validity of a theoretical description influences the applicable range of the corresponding invariant measure.	192
6-2	Illustration of reversal versus dissipative deformations.	194
6-3	Illustration of free energy change as defect motion driving force, reflected by kinetic transition rates.	196
6-4	Illustration of virtual work by atomistic summation.	198
6-5	Illustration of further simplifications for defect translation.	199
6-6	Illustration of the true meaning of free energy.	201
6-7	Domain decomposition that de-couples defect core with the outside environment by an atom layer of finite thickness.	202
6-8	Illustration of what happens to the free energies when a defect moves.	204
6-9	Diffusion near surface: invariant loop summation for $\langle 110 \rangle$ dumbbell self-interstitial in α -iron.	210
6-10	Crack-tip extension near a void: atoms are color-encoded by the atomistic local shear strain. The invariant loop of $r = 1\text{ nm}$ is also labeled.	213
6-11	Crack-tip extension near a void: the entire loading curve.	215
6-12	Slip system in Si-like materials.	216
6-13	Recent experimental results by Suzuki <i>et al</i> [239, 240, 241].	217
6-14	Proposed plastic deformation mechanisms for Si-like materials.	218
6-15	Environment (a): screw-screw configuration.	221
6-16	Environment (b): screw-notch configuration.	221

6-17	Comparison of results from environments (a) and (b).	223
A-1	Dislocation impeded by the obstacle, forming a cusp.	232
A-2	Numerical solution of cusp evolution using finite difference scheme (A.9) with $r = 0.9$	234
A-3	Overall view of a simulation: dash rectangle shows the PBC cell; small green dots are the obstacles, which turns red/big if in contact with dislocation.	241
A-4	Blowup of a tiny region: the white points are dislocation mesh points linked by blue lines to guide the eye. The green and red dots are obstacles.	241
A-5	Average dislocation velocity at $T = 300\text{K}$, $a = 10b$, $c = 0.001$, $K/2\epsilon =$ 0.1	242
A-6	Average separation of nearest obstacles impeding the dislocation λ , divided by theoretical threshold (A.4), λ_c	243
A-7	Verification of the $\sigma_c \propto (K/2\epsilon)^{3/2}$ scaling law.	243
A-8	Verification of the $\sigma_c \propto c^{1/2}$ scaling law.	244
B-1	Illustration of entropy increase.	249
B-2	Illustration of transport.	251
D-1	Possible three-phonon processes.	279
D-2	Phase space trajectories of an harmonic oscillator and its quantization	285
D-3	Occupation number of a quantum oscillator as compared to a classical one (dash line).	286
D-4	Comparison of heat capacity between a quantum oscillator and a clas- sical one (dash line).	287

D-5	Two scenarios in the activation of phonons. When $k_B T \gg \hbar \omega_D$, the thermal energy (large) circle encloses the entire BZ; so the classical equi-partition theorem is good for all phonons and thermal (representative) phonons are those on the BZ boundary. On the other hand, when $k_B T < \hbar \omega_D$, the activation circle is in BZ: inside the occupation is still classical, but outside the Bose-Einstein distribution must be used, which is exponentially small. The thermal phonons are those on the circle.	288
D-6	Character of the streaming, Normal and Umklapp-collisional terms. .	290
D-7	Schematics of a collective deformation mode (D.73) in phonon occupation. \pm means increase or decrease from its global equilibrium distribution.	294
D-8	Schematics of quantum \leftrightarrow classical partial equivalence transformation.	299
E-1	Flowchart of the spectral method to calculate the thermal conductivity.	311
E-2	Discrete power spectrum summation.	316
E-3	Power spectrum (plotted in circles and properly normalized to the unit of W/m/K) versus frequency number n , of the heat current data from a 747 ps MD simulation of β -SiC crystal at $T = 1500\text{K}$ in a 512-particle cell. The stars are results after 4-point smoothing, with solid line to guide the eye.	318
E-4	Normalized heat current correlation function $g(\tau)/g(0)$ from a single MD run ($g(0) = 17.3 \text{ W/m/K/ps}$), for perfect β -SiC at 1500K. The dashed line is the fit to exponential decay in the range 1 to 9 ps. . . .	319
E-5	Well converged normalized heat current correlation function $g(\tau)/g(0)$ for perfect β -SiC at 1700K ($g(0) = 22.0 \text{ W/m/K/ps}$). The dashed line is the fit to exponential decay in the range 1 to 9 ps.	320
E-6	Well converged normalized heat current correlation function $g(\tau)/g(0)$ for perfect β -SiC at 760K ($g(0) = 15.5 \text{ W/m/K/ps}$). The dashed line is the fit to exponential decay in the range 5 to 25 ps.	321

E-7	Well converged normalized heat current correlation function $g(\tau)/g(0)$ for perfect β -SiC at 284K ($g(0) = 7.8 \text{ W/m/K/ps}$). The dashed line is the fit to exponential decay in the range 5 to 35 ps	321
E-8	A small portion of the random signal a_i in case A, with $N = 2^{21}$ and $N/L = 1000$	325
E-9	Power spectrum $ F_n ^2/2N$ versus frequency number n in case A. The empty circles are the raw data, while the stars (with solid line to guide the eye) are the smoothed results after passing through a zero-phase filter of nearby 10 points. The inset graph shows the raw data on a larger scale.	326
E-10	Correlation function g_k versus k/L in case A. The solid line is the numerical result; the dashed line is the theoretical prediction of Eq. (E.34). The dotted line (indistinguishable from the theoretical curve in this case) is the EF fit to numerical result in the region $0.5 \leq k/L \leq 1.5$, indicated by the two stars. The inset graph shows the numerical result on a larger scale.	327
E-11	Power spectrum $ F_n ^2/2N$ versus frequency number n in case B. The empty circles are the raw data, while the stars (with solid line to guide the eye) are the smoothed results after passing through a zero-phase filter of nearby 5 points. The inset graph shows the raw data on a larger scale.	328
E-12	Correlation function g_k versus k/L in case B. The solid line is the numerical result; the dashed line is the theoretical prediction of Eq. (E.34). The dotted line is the EF fit to numerical result in the region $0.5 \leq k/L \leq 1.5$, indicated by the two stars. The inset graph shows the numerical result on a larger scale.	329

E-13	Power spectrum $ F_n ^2/2N$ versus frequency number n in case C. The empty circles are the raw data, while the stars (with solid line to guide the eye) are the smoothed results after passing through a zero-phase filter of nearby 5 points. The inset graph shows the raw data on a larger scale.	330
E-14	Correlation function g_k versus k/L in case C. The solid line is the numerical result; the dashed line is the theoretical prediction of Eq. (E.34). The dotted line is the EF fit to numerical result in the region $0.5 \leq k/L \leq 1.5$, indicated by the two stars. The inset graph shows the numerical result on a larger scale.	331
F-1	Normalized $\langle \mathbf{J}_1(\tau) \cdot \mathbf{J}_1(0) \rangle$ of solid Ar (500 particles) at 20K, using Woon's pair potential[71]. The calculated $\kappa = 1.56$ W/M/K.	342
F-2	Normalized $\langle \mathbf{J}_1(\tau) \cdot \mathbf{J}_1(0) \rangle$ of solid Ar (500 particles) at 60K, using Woon's pair potential. The calculated $\kappa = 0.334$ W/M/K.	342
F-3	A length of J_{1x} heat current in an atomistic simulation of solid Ar at 20K using Woon's pair potential. The smoothed curve will be shown to mainly come from the phonon heat current \mathbf{J}_4 , while the high-frequency "fluctuations" mainly come from \mathbf{J}_3^- and \mathbf{J}_3^F	344
G-1	Lennard Jones potential and its modified forms with cutoff $r_c = 2.37343\sigma$. Black lines indicate positions of neighbors in a single-element fcc crystal at 0K.	350
G-2	fcc neighboring shells. For example, label "6 ₈ ; 8 ₆ " means there are eight 6th-nearest neighbors of the type shown in figure, which adds up to 86 neighbors in all if included. The ABC stacking planes are also shown in the figure.	351

List of Tables

3.1	Comparison of crystalline Ar equilibrium properties at 0K.	102
4.1	Comparison of elastic constants of hcp Zr, ZrC and TiC. The first three columns are from experiment and recent <i>ab initio</i> calculations. The 4th column is of a recent tight-binding potential for TiC [205] that has been used on surface [204] and dislocation slip-system [206] problems. The last column is from my empirical potential for ZrC. . .	141
4.2	Parameters of WM potential in (4.27) form	151
4.3	Parameters of massaged WM potential (4.28) in the eV-Å unit system	152
4.4	Optimized parameters of (4.34,4.36) in the eV-Å unit system	156
4.5	Heat of formation of ZrC.	164
4.6	Comparison of equilibrium structure and lattice stability for the hexagonal WC phase. The FPLMTO results are believed to be the most accurate.	165
4.7	Carbon vacancy formation and migration energies in ZrC/TiC.	166
4.8	Metal vacancy formation and migration energies in ZrC/TiC.	167
4.9	Rumpled relaxation of ZrC/TiC(001) surface.	168
4.10	Shrinkage of the nearest C-Zr bond pointing to a carbon vacancy. . .	168
4.11	MD Simulation Results for the Lattice Thermal Conductivity of ZrC _X	176
5.1	Comparison of calculated and experimental crystalline Cu equilibrium properties at 0K.	180
5.2	Comparison of the average Gruneisen parameter, Debye temperature, vacancy formation energy and formation volume in crystalline Cu. . .	180

6.1	Convergence of 2- and 1-evaluation invariant loop summations for the $\langle 110 \rangle$ dumbbell self-interstitial diffusion near (100) surface in α -iron. The exact energy change is -0.00013921 eV.	211
6.2	Convergence of 2- and 1-evaluation invariant loop summations for crack tip extension near a void in Si at $\varepsilon_{yy} = 0.04$. The exact energy change is 3.15602 eV.	214
6.3	Summary of the simulation results for τ_{PN} in Si.	219
6.4	Convergence of the 2- and 1-evaluation invariant loop summations for the Si screw-dipole configuration (7560 atoms, supercell $(139.6821 \times 141.1002 \times 7.6805 \text{ \AA})$ has $21 \times 15 \times 2$ unit cells, $\epsilon_{yz} = 0$, dipole separation is 6 out of 21, or 39.91 \AA). The exact energy change is 1.052396 eV.	222
E.1	Recommended Parameters for Perfect Crystal β -SiC Thermal Conductivity Calculation	322
G.1	FCC neighboring shells included in Eqn (G.4)	352

Chapter 1

Introduction

1.1 Motivation

Materials research is widely recognized for its relevance to technological innovation and competitiveness. With the advent of high performance computing, this field, which traditionally has relied on experiment and theory, now embraces a third approach: computer simulation. Increasingly materials modeling has taken on the meaning of theory and simulation of materials properties and behavior across length and time scales from the atomistic to the macroscopic.

As materials research expands in both breadth and depth, molecular engineering of materials becomes more of a reality. This is the long-held dream of every materials scientist and engineer where new materials can be created with such benefits as enhanced performance, extended service life, and acceptable environmental impact, not to mention cost reduction. Even though computer-aided materials design has yet to achieve the success of computer-aided molecular (drug) design, there is impressive progress being made, especially in the area of functional materials for microelectronics, optical and magnetic applications. In contrast, for structural materials the complexities of mechanical, thermal, chemical (alloying, corrosion, etc.) phenomena continue to pose formidable challenges to reliable and predictive modeling. As a result, it is believed that the most promising approach to understanding and controlling of these phenomena is to effectively combine several modeling techniques, each one

being suited for a particular length and time scale. This is another way of seeing the relevance of multiscale materials modeling.

The overall theme of my research has been to develop an approach to materials modeling which combines contemporary theoretical concepts with the simulation and sampling techniques of molecular dynamics and Monte Carlo. Since particle simulations are well suited to deal with highly nonlinear, inhomogeneous, or nonequilibrium processes, a variety of physical phenomena in crystalline, amorphous, and liquid states of matter can be investigated to provide information on local molecular environments, interatomic bonding and forces, and various microscopic details pertaining to structure and dynamics.

In this thesis my focus is directed at the mechanistic understanding and analysis of materials phenomena as manifested in stress-driven or thermally activated structural instabilities, thermal transport in crystalline and defected systems, and atomic modes of defect mobility and microstructural evolution.

1.2 Problem Statement

This is an investigation of the deformation response and thermal conduction of solids through theoretical formulations and atomistic simulations, with emphasis on correctly handling the property-controlling microstructures so as to make quantitative predictions.

Both the simulations and the analyses are based on fundamental concepts in solid mechanics, lattice dynamics, and statistical thermodynamics, and which are integrated with visualization tools for the specific purpose of extracting intrinsic physical properties and gaining mechanistic insights from atomistic modeling.

1. Determination of lattice thermal conductivity of a technologically important ceramic material, ZrC, for which an empirical interatomic potential model of any kind did not exist.

A many-body empirical potential, with six parameters, has been successfully constructed using the heat of formation, cohesive energies of three cubic phases,

and the interatomic force constants generated from *ab initio* calculations. This is possible only by thoroughly understanding the nature of chemical bonds in ZrC, revealed by its electronic structure. The model is validated by comparing predicted hexagonal phase properties, point-defect formation and migration energies, and finite-temperature vibrational behavior including melting with available experiments and with recent electronic-structure calculations for TiC. Using the model developed, thermal conductivities of a single crystal as well as the effects of various point defects at concentrations appropriate to realistic off-stoichiometry are computed through the Green-Kubo expression in linear response theory. The results show a temperature dependence that is similar to the experimental behavior observed of SiC, which we have previously studied using a bond-order potential model. The implication of this finding is that the observed temperature variation of ZrC, anomalous in the sense of total thermal conductivity rising with increasing temperature, should be attributed to direct electronic contributions for which a mechanism of ambipolar diffusion had been previously suggested.

2. Ideal strengths are calculated for Ar, Cu, and SiC crystals and amorphous SiC under uniaxial, hydrostatic, and shear modes of loading, using both lattice dynamical and molecular dynamics methods. Finite- \mathbf{k} lattice instabilities are found in both Cu and SiC, previous unaccounted for by elastic instabilities.

Materials with existent microstructures such as void and nano-grains are deformed in simulations and are observed to result in a significant reduction in strength, combined with a softening of the transition abruptness. This is explained by a “condensation” model of point-defect-like inhomogeneities caused by soft vibrational modes. In the tension test of Ar perfect crystal the coalescence of these uniformly distributed inhomogeneities results in the abrupt slip of an entire plane, creating of a stacking fault; but if a void exists, such inhomogeneities become unstable prematurely near the void, resulting in the arrest of its propagation and a partial release of the strain energy before the

main transition occurs.

Failure of nanocrystalline SiC is found to occur by intra-granular fracture at a critical stress value of 20 GPa at which the amorphous SiC also fails, and that agrees with the observation that the grain boundary (GB) of SiC is largely amorphous. This means that the strength of a SiC nanocrystal is upper-bounded by the strength of amorphous SiC which “glues” the grains together. On the other hand, if one assumes the controlling flaw size to be proportional to the grain size, then inter-granular fracture stress versus grain size relation similar to the Hall-Petch relation can be derived, and my computed SiC surface energy leads to a Griffith fracture toughness value that agrees with an experimental measurement of SiC fiber strength. Combining the two considerations we arrive at a maximal strength prediction for SiC nano-crystals at grain size 20 nm, beyond which further grain refinements would have no impact.

Molecular dynamics simulation of nano-indentation in a thin film model of crystalline Cu showing successive events of stress reliefs in variation with indenter depth, thus providing an atomistic link between heterogeneous deformation response and the theoretical strength of the bulk material.

MD simulations and data analyses enable the direct correlation between the variation of nominal indenter pressure with indenter depth on the one hand and visualizations of dislocation nucleation and punch out also as a function of indenter depth. The results, quite preliminary at this stage, suggest that the first instability observed occurs at a critical stress approaching the theoretical strength of the bulk material, and this phenomenon is associated with the nucleation and motion of dislocation loops. Sample temperature plays a significant role, lowering the critical stress threshold by as much as a factor of two from zero to room temperature. Further work is clearly indicated.

3. A method of invariant cluster is formulated for determining the thermodynamic driving force for defect mobility through atomistic simulation, and its utility in the determination of the Peierls-Nabarro stress for moving a screw dislocation

in Si is demonstrated.

We propose a definition of microscopic (local) free energy by introducing a buffer layer in the domain decomposition of an atomistic region surrounding the defect of interest from a surrounding which is less perturbed when the defect undergoes a unit displacement. In effect, the buffer layer decouples the atomistic region from the surrounding and enables the development of efficient ways of computing the relevant free energies. Implementation of the method is first demonstrated in the illustrative example of calculating the driving force for an interstitial in the bulk moving toward a free surface, and further elaborated in the problem of crack-tip extension in Si in the vicinity of a void. In the most revealing application to date, we show that an invariant result for the Peierls-Nabarro stress can be obtained for a screw dislocation in Si, a quantity which can be compared with recent determinations in the literature. There are several significant and far-reaching implications of this study which will be discussed later in this thesis.

In addition to the above, there are important theoretical developments such as the rigorous connection between classical and quantum phonon scattering, the possible existence of nonlinear diffusive heat carriers as revealed by the Ar heat current correlation function, and methodology developments such as a definition of atomistic local strain, improved Parrinello-Rahman method, $\mathcal{O}(N)$ MD simulation with deformable box, $\mathcal{O}(N)$ method to calculate the local density of states, spectral method to compute time-correlation function integrals, and fast rendering methods for the computer visualization of atom configurations.

The thesis is organized as follows. In Chap 2 we discuss the basic concepts needed to describe the mechanical and thermal behavior of interest in the present study, and the atomistic simulation methodologies that will be used throughout the thesis. The concepts were originally developed in the classical disciplines of solid mechanics (Sec. 2.1), thermodynamics and statistical mechanics (Sec. 2.2), and lattice dynamics (Sec. 2.3), which existed before the field of materials science came into being. As we will

see they are also fundamental to the materials modeling investigations that will be discussed in the chapters to follow. Similarly, a set of simulation techniques has been developed to specifically treat the problems of large-strain deformation and lattice thermal conductivity calculation, the two phenomena being studied in this work; they are described in Secs. 2.4 and 2.5 respectively. Application of the concepts and tools collected in Chap 2 is immediately taken up in Chap 3 which contains results for argon, perhaps the simplest elemental solid, and for SiC, a relatively more complicated covalent binary compound. Chap 4 follows with an in-depth investigation of the thermal conductivity of ZrC, a refractory ceramic for which a suitable interatomic potential model had to be constructed. We then return to the theme of mechanical deformation and present results relevant to the understanding of strength, deformation and toughness through atomistic simulations. In Chap 5 we discuss a molecular dynamics study of nano-indentation in Cu and show that experimental observations of dislocation bursts can provide a strength measure approaching the theoretical limit. In Chap 6 we describe a new method of determining the thermodynamic driving force for defect mobility which involves the concept of microscopic (and local) free energy and that of invariant loop summation, in a way reminiscent of the J-integral in fracture mechanics. Usefulness of the method is illustrated by considering the driving force for interstitial motion near a surface in Fe, crack-tip extension in Si near a void, and the Peierls-Nabarro stress for a screw dislocation in Si. A summary of the results and their implications is given in Chap 7, along with comments on future work. A number of detailed calculations and developments of simulation techniques and visualization, undertaken during the course of the thesis research, are collected in the appendices for the benefit of future workers.

Chapter 2

Fundamental Concepts and Simulation Determination

2.1 Stress, Strain and Elastic Constants

Stress and strain have many definitions, which although do not change the physics, differ in efficiency representing it.

Strain is *relative*. To define strain, one must first declare the reference state. That is reasonable because strain describes deformation. Strain should be frame-covariant like any true second-rank tensor [1], since how an object is deformed does not really depend on the angle one looks at it. Here on I denote the geometrical configuration of an object by X, Y or Z , which describes its shape, i.e., surface constraints.

Affine transformation of an object from one shape to the other is specified by the tensor J , expressed as $Y = JX$, which is homogeneous in the sense that surface constraints of the object change uniformly according to J . But it does not have to be a *microscopically* homogeneous transformation, as different kinds of atoms may have different atomic-scale relaxations.

The Lagrangian strain is defined to be,

$$\eta_X^Y \equiv \frac{1}{2}(J^T J - 1). \quad (2.1)$$

X in η_X^Y denotes the reference state and Y denotes the final state. If the final state is apparent in the current context we may omit the superscript and simply write as η_X .

The Polar Decomposition Theorem [2] states that every matrix can be uniquely expressed as the left or right product of a symmetric matrix and a rotational matrix,

$$\begin{cases} J = RM = ML \\ M^T = M, \quad R^T R = L^T L = 1 \end{cases} \quad (2.2)$$

Therefore,

$$\eta_X = \frac{1}{2}(J^T J - 1) = \frac{1}{2}(M^2 - 1). \quad (2.3)$$

There is one-to-one correspondence between η_X and M , as,

$$M = \sqrt{1 + 2\eta_X} = 1 + \eta_X - \frac{1}{2}\eta_X^2 + \dots \quad (2.4)$$

Let $Y = JX$, $Z = KY = KJX$. There is

$$\begin{aligned} \eta_Y^Z &= \frac{1}{2}(K^T K - 1), \\ \eta_X^Z &= \frac{1}{2}(J^T K^T K J - 1) \\ &= \frac{1}{2}(J^T (1 + 2\eta_Y^Z) J - 1) \\ &= J^T \eta_Y^Z J + \eta_X^Y, \end{aligned} \quad (2.5)$$

which is the law of η -conversion between reference systems.

Contrary to strain, stress should be *absolute*, meaning it should not depend on any reference besides the current state of the object. We use two definitions of stress in this thesis: the first is the external stress τ_{ij} , which is the usual “force per area” definition used by engineers and mathematicians,

$$dT_i = \tau_{ij} n_j dS, \quad (2.6)$$

where dT_i is the external traction force, n_j is the outward surface normal and dS is the surface area. τ_{ij} is what the outside environment exerts on the object. To prevent rotation, it must satisfy $\tau_{ij} = \tau_{ji}$.

The second kind of stress is the thermodynamic stress t_{ij} , also called the *intrinsic stress*, whose definition is based on the Helmholtz free energy $F(N, T, X)$ of the object: [3, 4]

$$F(N, T, X) = E - TS \equiv -k_B T \ln Z(N, T, X) \quad (2.7)$$

where $Z(N, T, X)$ is the partition function,

$$Z(N, T, X) \equiv \int_X \exp(-\beta \mathcal{H}(q^N, p^N)) \frac{dq^N dp^N}{N! h^{3N}}. \quad (2.8)$$

Here F is a function of the particle number N , temperature T , and geometrical constraint X . Since the Hamiltonian $\mathcal{H}(q^N, p^N)$ is usually rotationally invariant, F is also rotationally invariant. Thus,

$$\begin{aligned} F(N, T, Y) &= F(N, T, JX) \\ &= F(N, T, RMX) \\ &= F(N, T, MX) \\ &= F(N, T, \sqrt{1 + 2\eta_X} X) \\ &= F(N, T, \eta_X, X), \end{aligned} \quad (2.9)$$

i.e., F is a *function* of η_X , once X is chosen.

A function can always be expanded into Taylor series:

$$F(\eta_X, X) = F(0, X) + \left(\frac{\partial F}{\partial \eta_{ij}} \bigg|_{\eta_X=0} \right) \eta_{ij} + \frac{1}{2} \left(\frac{\partial^2 F}{\partial \eta_{ij} \partial \eta_{kl}} \bigg|_{\eta_X=0} \right) \eta_{ij} \eta_{kl} + \dots \quad (2.10)$$

Because η_{ij} is symmetric, the expansion should only involve 6 independent variables: η_{11} , η_{22} , η_{33} , η_{12} , η_{13} , η_{23} . But that is often inconvenient for index contraction, so what people do is to symmetrize the expansion coefficients over η_{ij} and η_{ji} whenever possible, but pretending η_{ij} , η_{ji} to be different summation variables. Let me define

second and 4th rank symmetrization operators:

$$\hat{S}_2(G_{ij}) = \frac{1}{2}(G_{ij} + G_{ji}), \quad (2.11)$$

$$\hat{S}_4(H_{ijkl}) = \frac{1}{4}(H_{ijkl} + H_{ijlk} + H_{jikl} + H_{jilk}). \quad (2.12)$$

The thermodynamic stress at configuration X is defined to be,

$$t_{ij}(X) = \frac{1}{\Omega(X)} \hat{S}_2 \left(\left. \frac{\partial F(\eta_X, X)}{\partial \eta_{ij}} \right|_{\eta_X=0} \right), \quad (2.13)$$

and the elastic constant:

$$C_{ijkl}(X) = \frac{1}{\Omega(X)} \hat{S}_4 \left(\left. \frac{\partial^2 F(\eta_X, X)}{\partial \eta_{ij} \partial \eta_{kl}} \right|_{\eta_X=0} \right), \quad (2.14)$$

where $\Omega(X)$ is the volume of the object at X , so t_{ij} and C_{ijkl} are made intensive quantities. By definition,

$$\begin{aligned} F(\eta_X, X) &= F_0 + \Omega(X) \left\{ t_{ij}(X) \eta_{ij} + \frac{1}{2} C_{ijkl}(X) \eta_{ij} \eta_{kl} \right\} \dots \\ t_{ij} &= t_{ji}, \quad C_{ijkl} = C_{ijlk} = C_{jikl} = C_{jilk}. \end{aligned} \quad (2.15)$$

Notice that since t_{ij} and C_{ijkl} are expansion coefficients of η_X in $F(\eta_X, X)$ at $\eta_X = 0$, they themselves are not functions of η_X , but only of X . That means the definitions of thermodynamic stress and elastic constant do not require a reference state, since to evaluate them the object uses *itself* at the moment as the reference state. This “co-moving frame” in defining stress and elastic constant has some “weird” properties, as generalized in differential geometry [1]. For instance, in general,

$$t_{ij}(Y) \neq t_{ij}(X) + C_{ijkl}(X)(\eta_X^Y)_{kl} + \dots, \quad (2.16)$$

which is not what one may expect for the Taylor expansion of the “first-order derivative” in terms of the “second-order derivative”, which people use in *fixed frames*.

In fact, in light of (2.5),

$$\begin{aligned} F(Z) &= F(\eta_Y^Z, Y) \\ &= F(Y) + \Omega(Y) \text{Tr} \left(t(Y) \eta_Y^Z \right) + \mathcal{O} \left((\eta_Y^Z)^2 \right) \end{aligned} \quad (2.17)$$

$$\begin{aligned} &= F(\eta_X^Z, X) \\ &= F(X) + \Omega(X) \text{Tr} \left(t(X) \eta_X^Z \right) + \frac{\Omega(X)}{2} \text{Tr} \left(\eta_X^Z \mathbf{C}(X) \eta_X^Z \right) \\ &\quad + \mathcal{O} \left((\eta_X^Z)^3 \right) \\ &= F(X) + \Omega(X) \text{Tr} \left(t(X) \eta_X^Z \right) + \frac{\Omega(X)}{2} \text{Tr} \left(\eta_X^Z \mathbf{C}(X) \eta_X^Z \right) \\ &\quad + \mathcal{O} \left((\eta_X^Y)^2 \right) \eta_Y^Z + \mathcal{O} \left((\eta_Y^Z)^2 \right). \end{aligned} \quad (2.18)$$

The linear coefficient of η_Y^Z in (2.17) and (2.18) must be equal. Plugging in (2.5) to (2.18), we have,

$$\begin{aligned} F(Z) &= \text{const} + \Omega(X) \text{Tr} \left(J t(X) J^T \eta_Y^Z \right) + \Omega(X) \text{Tr} \left(J \eta_X^Y \mathbf{C}(X) J^T \eta_Y^Z \right) \\ &\quad + \mathcal{O} \left((\eta_X^Y)^2 \right) \eta_Y^Z + \mathcal{O} \left((\eta_Y^Z)^2 \right). \end{aligned} \quad (2.19)$$

Therefore matching the linear coefficient of η_Y^Z to that of (2.17), we have,

$$t(Y) = \frac{J t(X) J^T}{\det |J|} + \frac{J (\mathbf{C}(X) \eta_X^Y) J^T}{\det |J|} + \mathcal{O} \left((\eta_X^Y)^2 \right). \quad (2.20)$$

It will be shown in section 2.4.1 that if J is constrained to be symmetric, then

$$t_{ij}(Y) = t_{ij}(X) + B_{ijkl}(X) (\eta_X^Y)_{kl} + \mathcal{O} \left((\eta_X^Y)^2 \right), \quad (2.21)$$

where $B_{ijkl}(X)$ is the *elastic stiffness coefficient* (equation 2.240). $B_{ijkl}(X)$ is equal to $C_{ijkl}(X)$ only when $t_{ij}(X) = 0$, therefore the use of elastic constant as the linear expansion coefficient of stress versus strain is only a valid practice for objects under zero loading.

2.1.1 Atomistic Local Strain

It is not too difficult to define local strain when the reference state is known: one may carry out a least-square fitting procedure outlined in (6.34) to get a best fit of the affine transformation matrix \mathbf{J} to the relative positions of atoms nearby. The problem is harder when there is no given reference system, for example a dislocation would cause lattice mis-registry that makes the original reference hard to keep track of. What we need is a *geometrical* characterization of the local atomic environments that works in much the same way as the coordination number, but provides strain information when the measure is applied to a piece of deformed yet perfect lattice. Because there is no reference frame, it can at best output the *matrix invariants* of the strain tensor, e.g., the dilatational component

$$\eta_m \equiv \frac{1}{3} \text{Tr} \eta, \quad (2.22)$$

and the shear component,

$$\eta_s \equiv \sqrt{\frac{1}{2} \text{Tr}(\eta - \eta_m \mathbf{I})^2}, \quad (2.23)$$

calibrated to the cases of hydrostatic dilatation $\eta_{xx} = \eta_{yy} = \eta_{zz} = \eta_m$, and pure shear $\eta_{xy} = \eta_{yx} = \eta_s$.

Consider 3×3 matrix,

$$\mathbf{M}_i \equiv \sum_{j \in N_i} \mathbf{q}_{ij} \mathbf{q}_{ij}^T, \quad (2.24)$$

defined at each atom i , where \mathbf{q}_{ij} is the relative position between atom j and i ,

$$\mathbf{q}_{ij} \equiv \mathbf{q}_j - \mathbf{q}_i, \quad (2.25)$$

and $j \in N_i$ is the set of i 's neighbors, whose definition is to be chosen. Two possible choices are,

$$N_i^R : \{j \in N_i^R \mid |\mathbf{q}_{ij}| \leq R\}, \quad (2.26)$$

where R is a cutoff distance, usually picked to be between the first and second nearest

neighbors at the material's perfect crystalline state; or,

$$N_i^C \equiv N_i^{R_i}, \text{ with } |N_i^{R_i}| = C, \quad (2.27)$$

i.e., we sort j according to $|\mathbf{q}_{ij}|$ and pick only the nearest C atoms, where C is the ordinary coordination number of the crystal, like 12 for fcc, etc. Anyway, N_i must be chosen such that,

$$\mathbf{M}_i^0 = d_0 \mathbf{I}, \quad (2.28)$$

at the material's perfect crystalline equilibrium. Satisfying (2.28) may seem quite impossible at the first glance, but actually materials with cubic or T_d symmetry automatically do, including fcc, bcc, hcp (perfect c/a ratio), diamond cubic, and NaCl, ZnS, CsCl binary structures.

Consider how local strain and rotation influences (2.24) of a perfect crystal. For a given local affine transformation \mathbf{J} ,

$$\mathbf{q}_{ij} \rightarrow \mathbf{q}'_{ij} = \mathbf{J} \mathbf{q}_{ij}. \quad (2.29)$$

Therefore, if *neighbors do not enter or leave* N_i ,

$$\mathbf{M}_i = \sum_{j \in N_i} \mathbf{q}'_{ij} \mathbf{q}_{ij}^T = \mathbf{J} \left(\sum_{j \in N_i} \mathbf{q}_{ij} \mathbf{q}_{ij}^T \right) \mathbf{J}^T = \mathbf{J} \mathbf{M}_i^0 \mathbf{J}^T. \quad (2.30)$$

But if requirement (2.28) is satisfied, there would be

$$\mathbf{M}_i = \mathbf{J} (d_0 \mathbf{I}) \mathbf{J}^T = d_0 \mathbf{J} \mathbf{J}^T. \quad (2.31)$$

As the local Lagrangian strain at atom i is defined to be,

$$\eta = \frac{1}{2} (\mathbf{J}^T \mathbf{J} - \mathbf{I}), \quad (2.32)$$

the local strain hydrostatic invariant is,

$$\eta_m = \frac{1}{3}\text{Tr}\eta = \frac{1}{6}(\text{Tr}\mathbf{J}^T\mathbf{J} - 3) = \frac{1}{6}(\text{Tr}\mathbf{J}\mathbf{J}^T - 3) = \frac{1}{6}(d_0^{-1}\text{Tr}\mathbf{M}_i - 3), \quad (2.33)$$

and the local strain shear invariant is,

$$\begin{aligned} \eta_s &= \sqrt{\frac{1}{2}\text{Tr}(\eta - \eta_m\mathbf{I})^2} \\ &= \sqrt{\frac{1}{2}\text{Tr}\eta^2 - \frac{3}{2}\eta_m^2} \\ &= \sqrt{\frac{1}{8}\text{Tr}(\mathbf{J}^T\mathbf{J} - \mathbf{I})^2 - \frac{3}{2}\eta_m^2} \\ &= \sqrt{\frac{1}{8}\text{Tr}\mathbf{J}^T\mathbf{J}\mathbf{J}^T\mathbf{J} - \frac{1}{4}\text{Tr}\mathbf{J}^T\mathbf{J} + \frac{\text{Tr}\mathbf{I}}{8} - \frac{3}{2}\eta_m^2} \\ &= \sqrt{\frac{1}{8}\text{Tr}\mathbf{J}\mathbf{J}^T\mathbf{J}\mathbf{J}^T - \frac{1}{4}\text{Tr}\mathbf{J}\mathbf{J}^T + \frac{\text{Tr}\mathbf{I}}{8} - \frac{3}{2}\eta_m^2} \\ &= \sqrt{\frac{1}{8}\text{Tr}(\mathbf{J}\mathbf{J}^T - \mathbf{I})^2 - \frac{3}{2}\eta_m^2} \\ &= \sqrt{\frac{1}{8}\text{Tr}(d_0^{-1}\mathbf{M}_i - \mathbf{I})^2 - \frac{3}{2}\eta_m^2} \\ &= \sqrt{\frac{1}{8}\text{Tr}(d_0^{-1}\mathbf{M}_i - \mathbf{I})^2 - \frac{1}{24}(d_0^{-1}\text{Tr}\mathbf{M}_i - \text{Tr}\mathbf{I})^2} \\ &= d_0^{-1}\sqrt{\frac{1}{8}\text{Tr}(\mathbf{M}_i - \frac{\text{Tr}\mathbf{M}_i}{3}\mathbf{I})^2}. \end{aligned} \quad (2.34)$$

After obtaining $\{\mathbf{M}_i\}$ for all atoms, one may also compute system average $\langle\mathbf{M}\rangle$ and evaluate local deviations from $\langle\mathbf{M}\rangle$. The above scheme (2.24) to (2.34) works extremely well in practice, allowing one to directly visualize microstructures and their strain fields with color-encoding. Successful examples include point defects, dislocations, cracks, grain boundaries, stacking faults and even kinks.

2.2 Thermodynamic Ensembles and Fluctuations

This section deals with the thermodynamic state of an atomistic simulation which can either be molecular dynamics (MD) or Monte Carlo (MC) [7]. In MD, one numerically

integrates the time trajectory (preferably smooth) governed by a certain dynamics. The choice of the integration algorithm is not very important for the thermodynamics, but it *is* very important for calculating transport coefficients and time-correlation functions. To save effort, here when I introduce MD implementations of thermodynamic ensembles, I will also introduce integration algorithms, which together may serve as a pointer to some recent developments in MD methodology.

Given an ordinary Hamiltonian $\mathcal{H}(q^N, p^N) = T(p^N) + V(q^N)$, if we pick an initial condition and rigorously follow its Hamiltonian dynamics, by the ergodic hypothesis [5] we generate a phase space probability distribution $\delta(\mathcal{H}(q^N, p^N) - E)$ ¹, which is defined to be the micro-canonical ensemble.

There exist two competing families of numerical integrators for integrating Hamiltonian dynamics. The first family is the predictor-corrector algorithm, explained in [7], which can be extended to order ~ 14 following Gear's original derivation [12] for double-precision floating-point architecture. The other family is the so-called symplectic integrators which preserve the property of phase space volume conservation (Liouville's theorem) of Hamiltonian dynamics. The well-known Verlet leap-frog algorithm [13], after slight modification [14], is shown to be symplectic, followed by higher-order extensions by Yoshida [15, 16] and Sanz-Serna [17]. As with the predictor-corrector algorithm, symplectic integrators tend to perform better at higher order, even on a per cost basis [18, 19].

I have benchmarked the two families of integrators by numerically solving the Kepler's problem (eccentricity 0.5) which is nonlinear and periodic, to compare with the exact analytical solution. The two families have different numerical error versus time characteristics: non-symplectic integrators all have linear energy error ($\Delta E \propto t$) and quadratic phase point error ($|\Delta \Gamma| \propto t^2$) with time, while symplectic integrators have constant (fluctuating) energy error ($\Delta E \propto t^0$) and linear phase point error

¹This is not exactly true since there are other conserved quantities like the total momentum. For the most up-to-date treatment see [11], and also [9, 10]. Because the micro-canonical ensemble $\delta(\mathcal{H}(q^N, p^N) - E)$ is more widely used, I take it to be the object of study, and simply assume that certain dynamics, which should not be too far from the Hamiltonian dynamics, is able to generate that phase space probability distribution.

($|\Delta\Gamma| \propto t$) with time. Therefore the asymptotic long-term performance of a symplectic integrator is always superior to that of a non-symplectic integrator. But, it is found that for a reasonable integration duration, say 100 Kepler periods, high-order predictor-corrector integrators can have a significantly better performance than the best of the symplectic integrators published at *large integration timesteps*, or small number of force evaluations per period. That is important, because it says that if one does not care about the correlation of a mode beyond 100 oscillation periods (say, the natural decay time of the mode is only 50 oscillation periods due to mode-scattering, so there is no point ensuring numerical fidelity much beyond that), then the high-order predictor-corrector algorithm may preserve the physics at a significantly smaller computational cost.

On the other hand, via modified Langevin-type dynamics [21, 22, 23, 24, 25, 26] such as the Nose-Hoover thermostat, one can generate canonical ensemble phase space probability distribution $\exp(-\beta\mathcal{H}(q^N, p^N))$. For such dynamics, phase space volume is not conserved in the normal sense, but one may still in specific cases construct symplectic integrators for the extended system [27, 28, 29]. The predictor-corrector algorithm is also widely used here, but sometimes with curious differences in the coefficients. For example, in the 5th-order (a misnomer, better called 6-value) Gear predictor-corrector algorithm, $F_{02} = 3/20$ is used in Gear's own paper and book [12], but $F_{02} = 3/16$ is used by Haile in his MD primer, his Fortran code, and his book [8], by Rahman in his early paper on MD and Fortran code, and is apparently quite widespread. I find that $F_{02} = 3/20$ gives better accuracy than $F_{02} = 3/16$ by 1 or 2 magnitudes for the Kepler's problem.

Returning to the main topic: we see that a system can be simulated either with Hamiltonian-like dynamics in the micro-canonical ensemble, or with Langevin dynamics in the canonical ensemble. How do that influence the results? As one will see in the following discussions: for the *first-order* derivatives of thermodynamic potentials, such as T , P , t_{ij} etc. which I call the *thermodynamic variables*, it matters little, meaning that the atomistic expressions one derives for the variables in one ensemble can be directly used in another ensemble, with negligible $\mathcal{O}(1/N)$ error. Examples

include the expression for T in terms of particle kinetic energies. People often do not switch expression for T when they switch ensembles, which is fine.

Nothing can be further from the truth for the *second-order* derivatives, also called the *static susceptibilities*, where I am going to list a collection of atomistic expressions classified as *fluctuation formulas*, following the derivations by Pearson *et al* [9], Ray [30], and Lutsko [31, 32]. They all have the same feature of evaluating the averaged products of *fluctuations*, which by themselves are small (meaning not intensive, $\propto \sqrt{N}$ in an N -particle system), and then divide by N . Here, if one switches ensembles without switching the expressions, one would get $\mathcal{O}(1)$ error, which makes the practice useless. An example is $\langle \Delta E^2 \rangle / N$: in canonical ensemble one can show that it is proportional to c_V^{-1} and therefore is a route to compute c_V . But taking the same expression to the micro-canonical ensemble, one would get 0, which is clearly wrong.

2.2.1 Canonical Ensemble

Atomistic expressions for the thermodynamic stress and elastic constants can be derived for the canonical ensemble. [30, 31] The partition function for a deformed system is,

$$Z(X, M) = \int_{MX} \exp(-\beta \mathcal{H}(\tilde{\mathbf{q}}^N, \tilde{\mathbf{p}}^N)) \frac{d\tilde{\mathbf{q}}^N d\tilde{\mathbf{p}}^N}{N! h^{3N}}, \quad (2.35)$$

where we assume,

$$\mathcal{H}(\tilde{\mathbf{q}}^N, \tilde{\mathbf{p}}^N) = \sum_{n=1}^N \frac{\tilde{\mathbf{p}}_n^T \cdot \tilde{\mathbf{p}}_n}{2m_n} + V(\tilde{\mathbf{q}}_1, \tilde{\mathbf{q}}_2, \dots, \tilde{\mathbf{q}}_N). \quad (2.36)$$

Under a change of variables $\tilde{\mathbf{q}}_n \rightarrow \mathbf{q}_n, \tilde{\mathbf{p}}_n \rightarrow \mathbf{p}_n$:

$$\tilde{\mathbf{q}}_n \equiv M \mathbf{q}_n, \quad \tilde{\mathbf{p}}_n \equiv M^{-1} \mathbf{p}_n, \quad n = 1..N, \quad (2.37)$$

the Hamiltonian can be written as,

$$\mathcal{H}(\mathbf{q}^N, \mathbf{p}^N) = \sum_{n=1}^N \frac{\mathbf{p}_n^T M^{-2} \mathbf{p}_n}{2m_n} + V(M \mathbf{q}_1, M \mathbf{q}_2, \dots, M \mathbf{q}_N). \quad (2.38)$$

Using (2.4) and also,

$$M^{-2} = \frac{1}{1 + 2\eta_X} = 1 - 2\eta_X + 4\eta_X^2 + \dots \quad (2.39)$$

the partition function can be written as:

$$Z(X, \eta_X) = \int_X \exp[-\beta \{ \sum_{n=1}^N \frac{\mathbf{p}_n^T (1 - 2\eta_X + 4\eta_X^2) \mathbf{p}_n}{2m_n} + V((1 + \eta_X - \frac{1}{2}\eta_X^2)q^N) \}] dq^N dp^N, \quad (2.40)$$

where I threw away the $N!h^{3N}$ constant. Using index notation η_{ij} for matrix η_X :

$$\frac{\partial F}{\partial \eta_{ij}} = -\frac{1}{\beta Z} \cdot \frac{\partial Z}{\partial \eta_{ij}} = \frac{1}{Z} \int_X T_{ij} \exp(-\beta \mathcal{H}) dq^N dp^N \quad (2.41)$$

where,

$$\mathcal{H}(q^N, p^N) \approx \sum_{n=1}^N \frac{\mathbf{p}_n^T (1 - 2\eta_X + 4\eta_X^2) \mathbf{p}_n}{2m_n} + V((1 + \eta_X - \frac{1}{2}\eta_X^2)q^N), \quad (2.42)$$

and

$$T_{ij} = \frac{\partial \mathcal{H}}{\partial \eta_{ij}} = \sum_{n=1}^N \frac{p_i^n (-\delta_{jk} + 4\eta_{jk}) p_k^n}{m_n} + (\delta_{ik} - \eta_{ik}) q_k^n \nabla_j^n V((1 + \eta_X)q^N). \quad (2.43)$$

Setting η_X to zero, we get the atomistic formula for the thermodynamic stress:

$$t_{ij} = \left\langle \frac{1}{\Omega(X)} \hat{S}_2 \left(\sum_{n=1}^N \frac{-p_i^n p_j^n}{m_n} + q_i^n \nabla_j^n V(q^N) \right) \right\rangle. \quad (2.44)$$

The $\langle \rangle$ means canonical ensemble average in the original configuration X .

One may wonder why the sum (2.44) does not always give 0 at $T = 0$, since $\nabla_j^n V(q^N) \equiv 0$ for bulk atoms at equilibrium. The answer is that if we were to compute the stress using (2.44) *directly*, we must count those atoms on the surface, whose equilibrium conditions $F_j^n = \nabla_j^n V(q^N)$ in general require the presence of external

force F_j^n , which is the force the wall exerts on the atom to keep it within X . Since those F^n 's are weighted by q^n 's in (2.44), this surface contribution does not vanish in the thermodynamic limit as the surface energy.

On the other hand, it appeals to one's intuition that stress originates from the bulk, not from the surface, and is an intensive quantity. This can be validated in the following way: because $V(q^N)$ in general is the *sum of local interactions*, for instance $V(q^N) = \sum_{\{lmn\}} W(q_l, q_m, q_n)$, where W is a three-body interatomic potential. Due to translational symmetry: $W(q_l + \delta, q_m + \delta, q_n + \delta) = W(q_l, q_m, q_n)$, one must have $\nabla^l W + \nabla^m W + \nabla^n W \equiv 0$, and the contribution of this specific interaction to the total (2.44) sum is $(q_i^l - q_i^n) \nabla_j^l W + (q_i^m - q_i^n) \nabla_j^m W$, conceptualized as $\Delta F \cdot \Delta q$, i.e., force contribution weighted by the relative distance between action and counter-action. Through this *localization* procedure, one can convert all q^n weighting factors to Δq 's which are no longer than the interatomic distance. In this localized form, which should be constructed from (2.44) as soon as the potential model is known, the surface contribution would vanish in the thermodynamic limit like the surface energy. Thus, for local interactions, we can prove that the stress is intensive and indeed originates from the bulk.

To get the atomistic formula for elastic constants, we need to further differentiate (2.41):

$$\begin{aligned} \frac{\partial^2 F}{\partial \eta_{ij} \partial \eta_{kl}} &= \frac{1}{Z} \int_X \left(\frac{\partial T_{ij}}{\partial \eta_{kl}} - \beta T_{ij} T_{kl} \right) \exp(-\beta \mathcal{H}) dq^N dp^N \\ &\quad + \frac{\beta}{Z} \left(\int_X T_{kl} \exp(-\beta \mathcal{H}) dq^N dp^N \right) \langle T_{ij} \rangle \\ &= \beta \{ \langle T_{ij} \rangle \langle T_{kl} \rangle - \langle T_{ij} T_{kl} \rangle \} + \left\langle \frac{\partial T_{ij}}{\partial \eta_{kl}} \right\rangle. \end{aligned} \quad (2.45)$$

From (2.43) we can get:

$$\left. \frac{\partial T_{ij}}{\partial \eta_{kl}} \right|_{\eta_X=0} = \sum_{n=1}^N \frac{4p_i^n p_k^n}{m_n} \delta_{jl} + \sum_{m,n=1}^N \{ q_k^m q_i^n \nabla_l^m \nabla_j^n V(q^N) - \delta_{il} q_k^n \nabla_j^n V(q^N) \}. \quad (2.46)$$

So we get the unsymmetrized form of elastic constants:

$$D_{ijkl} = \beta\Omega(X) (\langle t_{ij} \rangle \langle t_{kl} \rangle - \langle t_{ij} t_{kl} \rangle) + \frac{1}{\Omega(X)} \left\langle \sum_{n=1}^N \frac{4p_i^n p_k^n}{m_n} \delta_{jl} \right\rangle + \frac{1}{\Omega(X)} \left\langle \sum_{m,n=1}^N q_k^m q_i^n \nabla_l^m \nabla_j^n V(q^N) - \sum_{n=1}^N q_k^n \nabla_j^n V(q^N) \delta_{il} \right\rangle. \quad (2.47)$$

The first term is defined to be the fluctuation term. The last term is defined to be the Born term, usually written as C_{ijkl}^B . The elastic constant is therefore

$$C_{ijkl} = \hat{S}_4(D_{ijkl}), \quad (2.48)$$

which is valid at finite temperature and stress.

It is interesting to study the zero temperature limit of the first term in (2.47), because as we approach $T = 0$ the fluctuation $\rightarrow 0$, but $\beta \rightarrow \infty$. The school starting from Born [46] look at the $T = 0$ elastic constant from a different perspective: since $F = V$ at $T = 0$, they directly evaluate the second-order derivative of V due to deformation, provided that V is always fully relaxed. After careful analysis a general formula was derived by Martin [47] where the $T = 0$ elastic constant can be computed by lattice methods. I give a new and more direct derivation in section 2.2.1 by separating the surface and bulk atoms. The equivalence of the static derivation with (2.47) will be shown in section 2.2.1 where I analytically take the $T \rightarrow 0$ limit of (2.47), following Lutsko [31, 32].

Static Derivation

Separate q^N (total) into q^S (surface) and q^B (bulk) atoms. We know from previous discussion that they play different roles in (2.44). For bulk atoms at equilibrium, there are $\nabla^B V(q^N)|_{\bar{q}^N} = 0$, but it is not the case for the surface atoms. Define force constant matrix \mathbf{D} at X to be,

$$D_{mi,nj} \equiv \left. \frac{\partial V(q^N)}{\partial q_i^m \partial q_j^n} \right|_{\bar{q}^N}. \quad (2.49)$$

One can do a quadratic expansion,

$$\begin{aligned} V(q^N) &= V(\bar{q}^N) + \nabla V(\bar{q}^N) \cdot (q^N - \bar{q}^N) \\ &\quad + \frac{1}{2}(q^N - \bar{q}^N)^T \mathbf{D} (q^N - \bar{q}^N) + \dots \end{aligned} \quad (2.50)$$

The free energy at $T = 0$ is the minimized potential energy:

$$F(M, X) = \min_{q^N \in M_X} V(q^N). \quad (2.51)$$

In order to study the M dependence of F , a very simple approach is to “stick” the surface atoms on walls, and minimize V with respect to the bulk coordinates q^B . We know from the previous discussion that the actual surface state does not affect bulk properties in the thermodynamic limit. Here although the surface atoms are not allowed to relax, the method will still give the correct bulk expression.

Denote η_X by matrix η . Since affine transformation is applied to the surface atoms,

$$\begin{cases} q^S = M\bar{q}^S = \bar{q}^S + \eta\bar{q}^S - \frac{1}{2}\eta^2\bar{q}^S + \mathcal{O}(\eta^3), \\ q^B = M\bar{q}^B + r^B = \bar{q}^B + \eta\bar{q}^B + r^B + \mathcal{O}(\eta^2), \end{cases} \quad (2.52)$$

where in addition to uniform affine transformation, the bulk atoms are allowed to relax by r^B . It will be shown later that $r^B \propto \eta$. There is,

$$\begin{aligned} F(M, X) &= \min_{\{r^B\}} \{V(q^S; q^B)\} \\ &= \min_{\{r^B\}} \{V(\bar{q}^S + \eta\bar{q}^S - \frac{1}{2}\eta^2\bar{q}^S; \bar{q}^B + \eta\bar{q}^B + r^B)\} \\ &= V(q^N) + \nabla^S V \cdot (\eta\bar{q}^S - \frac{1}{2}\eta^2\bar{q}^S) + \frac{1}{2}(\bar{q}^N)^T \eta \mathbf{D} \eta \bar{q}^N \\ &\quad + \min_{\{r^B\}} \{(\bar{q}^N)^T \eta \mathbf{D}^{tb} r^B + \frac{1}{2}(r^B)^T \mathbf{D}^{bb} r^B\} + \dots \end{aligned} \quad (2.53)$$

where we have used the fact that $\nabla^B V(\bar{q}^N) = 0$, and so first-order expansion for $M\bar{q}^B$ is enough. The minimum happens at,

$$(\bar{q}^N)^T \eta \mathbf{D}^{tb} + (r^B)^T \mathbf{D}^{bb} = 0, \quad (2.54)$$

and so,

$$r^B = -(\mathbf{D}^{bb})^{-1} \mathbf{D}^{bt} \eta \bar{q}^N \propto \eta. \quad (2.55)$$

Therefore to second order in η , the relaxed total energy is

$$\begin{aligned} F(\eta, X) &= V(q^N) + \nabla^S V \cdot \eta \bar{q}^S - \frac{1}{2} \nabla^S V \cdot \eta^2 \bar{q}^S \\ &+ \frac{1}{2} (\bar{q}^N)^T \eta \mathbf{D} \eta \bar{q}^N - \frac{1}{2} (\bar{q}^N)^T \eta \mathbf{D}^{tb} (\mathbf{D}^{bb})^{-1} \mathbf{D}^{bt} \eta \bar{q}^N, \end{aligned} \quad (2.56)$$

where the last term results from relaxation. We can evaluate the unsymmetrized $\mathbf{t}(X)$ and $\mathbf{C}(X)$ using definitions (2.13), (2.14):

$$\mathbf{t}(X) = \frac{\bar{q}^S \nabla^S V(\bar{q}^N)}{\Omega(X)} = \frac{1}{\Omega(X)} \mathbf{T}(q^N) \Big|_{\bar{q}^N}, \quad (2.57)$$

where we define the total stress functional $\mathbf{T}(q^N)$ to be

$$\mathbf{T}(q^N) = q^N \nabla V(q^N), \quad (2.58)$$

which is the same as (2.44) at $T = 0$. Then,

$$\mathbf{C}(X) = \frac{1}{\Omega(X)} \{ (\bar{q}^N)^T \mathbf{D} \bar{q}^N - \mathbf{T}(X) \mathbf{I} - (\bar{q}^N)^T \mathbf{D}^{tb} (\mathbf{D}^{bb})^{-1} \mathbf{D}^{bt} \bar{q}^N \}. \quad (2.59)$$

The first two terms are identified to be the $T = 0$ Born term, while the last one corresponds to relaxation. To eliminate the surface entirely from our derivation, we observe that,

$$\begin{aligned} \frac{\partial \mathbf{T}(q^N)}{\partial q^B} \Big|_{\bar{q}^N} &= \frac{\partial (q^N \nabla V(q^N))}{\partial q^B} \Big|_{\bar{q}^N} \\ &= \nabla^B(q^N) \Big|_{\bar{q}^N} + \bar{q}^N \mathbf{D}^{tb} \\ &= \mathbf{D}^{bt} \bar{q}^N, \end{aligned} \quad (2.60)$$

and thus if we define matrix constant

$$A_{ij,mc} = \left. \frac{\partial T_{ij}(q^N)}{\partial q_c^m} \right|_{\bar{q}^N}, \quad (2.61)$$

which can be evaluated for any localized model, we will have,

$$\begin{aligned} C_{ijkl}(X) &= C_{ijkl}^B(X) + C_{ijkl}^R(X) \\ &= \frac{1}{\Omega(X)} \{ \bar{q}_k^m \bar{q}_i^n D_{ml,nj} - T_{kj} \delta_{il} - A_{ij,mc} D_{mc,nd}^{-1} A_{kl,nd} \}, \end{aligned} \quad (2.62)$$

which yet needs to be symmetrized. This expression is the same as Martin's result [47].

The described relaxation does not occur in simple monoatomic crystals, as well as for crystals with inversion symmetry [48, 49] like NaCl. This can be shown by (2.55), since both \mathbf{D} and η are even under inversion, while \bar{q}^N is odd, so $r^B \equiv 0$. It would be useful to tabulate group-theoretical results for C_{ijkl}^R for other structures.

Zero Temperature Limit

I want to show that in the limit of $T \rightarrow 0$ the fluctuation formula (2.47) reduces to the same result as (2.62). This was first shown by Lutsko [32], here I put down more details.

As $T \rightarrow 0$, the second term in (2.47) vanishes because $\langle (p_i^n)^2 \rangle$ scales as T . The third term just gives C_{ijkl}^B , the unrelaxed elastic constant. The limit of the first line, the fluctuation term, is not yet clear: but if one inspects (2.44), it can be seen that the momentum part, $-p_i^n p_j^n / m_n$, gives zero contribution to the fluctuation limit because its magnitude scales as T , and it is also not correlated with the second term, $q_i^n \nabla_j^n V$, which is defined as $\mathbf{T}(q^N)$ in (2.58). So there must be

$$C_{ijkl}(X, T=0) = C_{ijkl}^F + C_{ijkl}^B, \quad (2.63)$$

where

$$C_{ijkl}^F = \lim_{\beta \rightarrow +\infty} \beta (\langle T_{ij} \rangle \langle T_{kl} \rangle - \langle T_{ij} T_{kl} \rangle) / \Omega(X). \quad (2.64)$$

When T is small, the atomic displacements

$$\Delta q_i^n = q_i^n - \bar{q}_i^n, \quad (2.65)$$

from equilibrium positions are small, and so one can expand

$$\Delta T_{ij} = \sum_{m=1}^N \sum_{c=1}^3 A_{ij,mc} \Delta q_c^m + \mathcal{O}(q^2), \quad (2.66)$$

following A 's definition in (2.61). Thus,

$$\begin{aligned} & \langle T_{ij} T_{kl} \rangle - \langle T_{ij} \rangle \langle T_{kl} \rangle \\ = & \langle \Delta T_{ij} \Delta T_{kl} \rangle \\ = & \sum_{m,n=1}^N \sum_{c,d=1}^3 A_{ij,mc} A_{kl,nd} \langle \Delta q_c^m \Delta q_d^n \rangle + \mathcal{O}(\langle q^4 \rangle). \end{aligned} \quad (2.67)$$

One can also expand the potential energy as (2.50) when Δq_i^n 's are small. Except for atoms near the wall, the probability distribution of atomic displacements approaches that of Gaussian, with

$$\begin{aligned} dP &= dq^N \exp(-\beta V(q^N)) / Z \\ &= dq^N \exp(-\beta D_{mc,nd} \Delta q_c^m \Delta q_d^n / 2 + \mathcal{O}(\Delta q^3)) / Z. \end{aligned} \quad (2.68)$$

What we have in mind is a saddle point expansion of the partition function in order to get the leading order fluctuation amplitudes. The wall atoms, though having the same problem of $\nabla_j^n V(q^N) \neq 0$ as which leads to the stress localization procedure in section 2.2.1, is not a big problem here because unlike q , $\langle \Delta q^2 \rangle$ is always finite. For the bulk atoms, one can show that

$$\langle \Delta q_c^m \Delta q_d^n \rangle = (\beta D)_{mc,nd}^{-1} + \mathcal{O}(\beta^{-2}), \quad (2.69)$$

which follows from the well-known identities

$$\int_{-\infty}^{+\infty} \prod_i d\alpha_i \exp(-\frac{1}{2}\alpha^T K \alpha) = \sqrt{\frac{(2\pi)^N}{\det |K|}} \quad (2.70)$$

and

$$\frac{\partial \ln(\det |K|)}{\partial K_{ij}} = \frac{K_{ij}^*}{\det |K|} = (K^{-1})_{ij}, \quad (2.71)$$

where α is a vector and K is a Hermitian matrix.

So following (2.64,2.67,2.69) there is,

$$C_{ijkl}^F = C_{ijkl}^R = - \sum_{m,n=1}^N \sum_{c,d=1}^3 A_{ij,mc} D_{mc,nd}^{-1} A_{kl,nd} / \Omega(X), \quad (2.72)$$

which is the same as (2.62).

There is a simple test, where the elastic constants of β -SiC are calculated using the fluctuation formula, with C_{ijkl}^R identified as the fluctuation term in (2.47). Long enough MD simulation is performed to ensure numerical convergence at $T = 2K$. What happens is that $C_{11}^R = C_{12}^R = 0$, but C_{44}^R has finite value, accounting for about 20% of the total C_{44} . The combined Born and relaxation term agrees very well with results from direct stress-strain simulations.

2.2.2 Micro-canonical Ensemble

Let us consider systems of N identical particles with mass m , contained in a volume described by geometrical configuration variable Y . Each system evolves according to the Hamiltonian

$$\mathcal{H}(\tilde{q}^N, p^N) = \sum_{n=1}^N \sum_{i=1}^3 \frac{(p_n^i)^2}{2m} + V(\tilde{q}^N). \quad (2.73)$$

If we consider all such systems with total energy E , we have a micro-canonical ensemble. From now on let us regard N as fixed. The appropriate thermodynamical potential for micro-canonical ensemble is system entropy, [5]

$$S(E, Y) = k_B \ln \int_Y d\tilde{q}^N dp^N \delta(E - \mathcal{H}(\tilde{q}^N, p^N)), \quad (2.74)$$

with fundamental relations

$$\frac{1}{T} = \left. \frac{\partial S}{\partial E} \right|_Y, \quad (2.75)$$

and

$$F(T, Y) = E - TS(E, Y). \quad (2.76)$$

One can integrate out the momentum degrees of freedom from (2.74) as follows: consider $\{p_n^i\}, n = 1..N, i = 1..3$ as a large vector \mathbf{p} with $3N$ components, then the total kinetic energy K is simply $p^2/2m$ with $p = |\mathbf{p}|$. Also, for a $3N$ -dimensional \mathbf{p} hypersphere,

$$dp^N = \prod_{n=1}^N \prod_{i=1}^3 dp_n^i = S_{3N} p^{3N-1} dp \quad (2.77)$$

if all angles are integrated over, with S_{3N} being a constant. Then,

$$\begin{aligned} & \int_Y d\tilde{q}^N dp^N \delta(E - \mathcal{H}(\tilde{q}^N, p^N)) \\ &= \int_Y d\tilde{q}^N S_{3N} p^{3N-1} dp \delta(E - p^2/2m - V(\tilde{q}^N)) \\ &= \int_Y d\tilde{q}^N m p^{3N-2} d(p^2/2m) \delta(E - p^2/2m - V(\tilde{q}^N)) \\ &= \text{const} \times \int_Y d\tilde{q}^N K^{3N/2-1}, \end{aligned} \quad (2.78)$$

where

$$K = E - V(\tilde{q}^N), \quad (2.79)$$

and it is implicitly understood that the $\int_Y d\tilde{q}^N$ integration is carried out in $\{K(\tilde{q}^N) > 0, \tilde{\mathbf{q}}_n \in Y\}$ regions.

Thus, it follows that for any symmetric homogeneous deformation $Y = MX$ (see (2.1) to (2.9)) from a certain reference configuration X ,

$$\begin{aligned} & S(E, Y = MX) \\ &= \text{const} + Nk_B \ln \det |M| + k_B \ln \Pi, \end{aligned} \quad (2.80)$$

where

$$\Pi = \int d\mathbf{q}^N (E - V(M\mathbf{q}^N))^{3N/2-1}, \quad (2.81)$$

and q^N are particle coordinates in “undeformed frame” whose bounds are independent of M .

To get some flavor, let us derive the heat capacity at constant volume, C_V (really should be C_Y), using microcanonical ensemble samples. If we vary E (and T) in (2.75),

$$-\frac{\delta T}{T^2} = \frac{\partial^2 S}{\partial E^2} \Big|_Y \delta E \quad (2.82)$$

and so

$$\begin{aligned} C_V &= \delta E / \delta T \\ &= -T^{-2} / \left(\frac{\partial^2 S}{\partial E^2} \Big|_Y \right) \\ &= -k_B \left(\frac{\partial \ln \Pi}{\partial E} \Big|_Y \right)^2 / \left(\frac{\partial^2 \ln \Pi}{\partial E^2} \Big|_Y \right). \end{aligned} \quad (2.83)$$

In order to get microscopic expressions, let us vary E in (2.81),

$$\begin{aligned} &\frac{\partial \Pi}{\partial E} \Big|_Y \\ &= (3N/2 - 1) \int dq^N (E - V(Mq^N))^{3N/2-2} \end{aligned} \quad (2.84)$$

for $3N/2 - 1 > 0$, because modifications of $\int dq^N$ integration bounds with E does not give contributions as long as the integrand vanishes there. Since N is usually much larger than unity, we will not mention this boundary term from now on. Then,

$$\frac{1}{k_B T} = \frac{\partial \ln \Pi}{\partial E} \Big|_Y = (3N/2 - 1) \langle K^{-1} \rangle, \quad (2.85)$$

where the $\langle \rangle$ average is taken over microcanonical ensemble samples (or a single evolution trajectory if the ergodic hypothesis holds). One can further differentiate (2.85), and it is straightforward to show that

$$\begin{aligned} \frac{\partial^2 \ln \Pi}{\partial E^2} \Big|_Y &= (3N/2 - 1)(3N/2 - 2) \langle K^{-2} \rangle \\ &\quad - (3N/2 - 1)^2 \langle K^{-1} \rangle^2. \end{aligned} \quad (2.86)$$

And so combining (2.85), (2.86) and (2.83), we arrive at a fluctuation formula for C_V that can be directly evaluated in a MD or MC simulation[7].

Now let me derive fluctuation formulas for the thermodynamic stress tensor $t_{ij}(X)$ and the *isothermal* elastic constants $C_{ijkl}(X)$, defined in (2.15), using micro-canonical ensemble samples. The reason is because $t_{ij}(X)$ and $C_{ijkl}(X)$ are the more useful quantities in various applications, although micro-canonical ensembles are easier to realize in MD. Except for the $S(E, Y) \rightarrow F(T, Y)$ translation, the procedure is similar to what we did in section 2.2.1 using canonical ensemble samples.

Imagine a homogeneous and symmetric deformation of the system $Y = MX$, which is also uniquely determined by the small Lagrangian strain $\eta = \eta_X^Y = (M^2 - 1)/2$. We are thus eligible to write $S(E, Y)$ as $S(E, \eta, X)$ and $F(T, Y)$ as $F(T, \eta, X)$, and the dependence on X is usually not explicitly stated. For finite η , there is a correspondent change of energy ΔE if the temperature is to stay constant, as in (2.15). To get ΔE , we can expand (2.75) around X ,

$$0 = \left. \frac{\partial^2 S}{\partial E^2} \right|_X \Delta E + \frac{\partial^2 S}{\partial E \partial \eta_{ij}} \eta_{ij} + \mathcal{O}(E^2, \eta^2, E\eta), \quad (2.87)$$

and thus

$$\Delta E = - \left(\frac{\partial^2 S}{\partial E \partial \eta_{ij}} \right) / \left(\left. \frac{\partial^2 S}{\partial E^2} \right|_X \right) \eta_{ij} + \mathcal{O}(\eta^2), \quad (2.88)$$

where we keep track of orders because we have to do a second order expansion later.

And so, if we expand (2.76), holding T fixed,

$$\begin{aligned} \Delta F &= \Delta E - T \left. \frac{\partial S}{\partial E} \right|_X \Delta E - T \left. \frac{\partial S}{\partial \eta_{ij}} \right|_E \eta_{ij} - \\ &\quad \frac{T}{2} \left[\left. \frac{\partial^2 S}{\partial \eta_{ij} \partial \eta_{kl}} \right|_E \eta_{ij} \eta_{kl} + 2 \frac{\partial^2 S}{\partial E \partial \eta_{ij}} (\Delta E) \eta_{ij} + \left. \frac{\partial^2 S}{\partial E^2} \right|_X (\Delta E)^2 \right] \\ &\quad + \mathcal{O}((\Delta E)^3, \eta^3, \text{etc.}) \\ &= -T \left. \frac{\partial S}{\partial \eta_{ij}} \right|_E \eta_{ij} - \frac{T}{2} \left[\left. \frac{\partial^2 S}{\partial \eta_{ij} \partial \eta_{kl}} \right|_E \eta_{ij} \eta_{kl} + 2 \frac{\partial^2 S}{\partial E \partial \eta_{ij}} (\Delta E) \eta_{ij} + \left. \frac{\partial^2 S}{\partial E^2} \right|_X (\Delta E)^2 \right] \\ &\quad + \mathcal{O}((\Delta E)^3, \eta^3, \text{etc.}), \end{aligned} \quad (2.89)$$

and plugging in (2.88), we obtain

$$\begin{aligned} \Delta F = & -T \frac{\partial S}{\partial \eta_{ij}} \Big|_E \eta_{ij} - \frac{T}{2} \left[\frac{\partial^2 S}{\partial \eta_{ij} \partial \eta_{kl}} \Big|_E - \left(\frac{\partial^2 S}{\partial E \partial \eta_{ij}} \cdot \frac{\partial^2 S}{\partial E \partial \eta_{kl}} \right) / \left(\frac{\partial^2 S}{\partial E^2} \Big|_X \right) \right] \eta_{ij} \eta_{kl} \\ & + \mathcal{O}(\eta^3). \end{aligned} \quad (2.90)$$

which, when compared with (2.15), suggests that

$$t_{ij}(X) = -\frac{T}{\Omega(X)} \hat{S}_2 \left(\frac{\partial S}{\partial \eta_{ij}} \Big|_E \right), \quad (2.91)$$

and

$$\begin{aligned} C_{ijkl}(X) = & \frac{T}{\Omega(X)} \hat{S}_4 \left[-\frac{\partial^2 S}{\partial \eta_{ij} \partial \eta_{kl}} \Big|_E + \right. \\ & \left. \left(\frac{\partial^2 S}{\partial E \partial \eta_{ij}} \cdot \frac{\partial^2 S}{\partial E \partial \eta_{kl}} \right) / \left(\frac{\partial^2 S}{\partial E^2} \Big|_X \right) \right]. \end{aligned} \quad (2.92)$$

In order to get microscopic expressions, we need to work with (2.80) and (2.81). First, because

$$\begin{aligned} \ln \det |M| &= \text{Tr} \ln M = \text{Tr} \ln \sqrt{1 + 2\eta} \\ &= \text{Tr} \eta - \text{Tr} \eta^2 + \mathcal{O}(\eta^3), \end{aligned} \quad (2.93)$$

it is easy to show that

$$\hat{S}_2 \left(\frac{\partial \ln \det |M|}{\partial \eta_{ij}} \Big|_{\eta=0} \right) = \delta_{ij}, \quad (2.94)$$

and

$$\hat{S}_4 \left(\frac{\partial^2 \ln \det |M|}{\partial \eta_{ij} \partial \eta_{kl}} \Big|_{\eta=0} \right) = -\delta_{ik} \delta_{jl} - \delta_{il} \delta_{jk}. \quad (2.95)$$

Second, because

$$K = E - V(\tilde{q}^N) = E - V(Mq^N)$$

in (2.81), where q^N are particle coordinates “before deformation”, and referring to (2.4), we have

$$\tilde{q}_i^n = q_i^n + \eta_{ij} q_j^n - \eta_{ij} \eta_{jk} q_k^n / 2 + \mathcal{O}(\eta^3). \quad (2.96)$$

It follows that

$$\frac{\partial K}{\partial \eta_{ij}} = -\frac{\partial V}{\partial \tilde{q}_i^n} q_j^n + \frac{\partial V}{\partial \tilde{q}_i^n} \eta_{jk} q_k^n + \mathcal{O}(\eta^2), \quad (2.97)$$

and so

$$\left. \frac{\partial K}{\partial \eta_{ij}} \right|_{\eta=0} = -\left. \frac{\partial V}{\partial \tilde{q}_i^n} \right|_X q_j^n \quad (2.98)$$

and

$$\left. \frac{\partial^2 K}{\partial \eta_{ij} \partial \eta_{kl}} \right|_{\eta=0} = -\left. \frac{\partial^2 V}{\partial \tilde{q}_i^n \partial \tilde{q}_k^m} \right|_X q_j^n q_l^m + \left. \frac{\partial V}{\partial \tilde{q}_i^n} \right|_X \delta_{jl} q_k^n, \quad (2.99)$$

where $|_X$ means taking derivatives in undeformed state X , and as before I treated η as if it has 9 independent components but will symmetrize the expressions in the end. Thus, following (2.80), (2.81) and (2.98),

$$\begin{aligned} \left. \frac{\partial S}{\partial \eta_{ij}} \right|_E &= N k_B \delta_{ij} + \\ & (3N/2 - 1) k_B \left\langle \left(-\left. \frac{\partial V}{\partial \tilde{q}_i^n} \right|_X q_j^n \right) / K \right\rangle, \end{aligned} \quad (2.100)$$

and so

$$\begin{aligned} & t_{ij}(X) \\ &= -\frac{k_B T}{\Omega(X)} \hat{S}_2 \left(N \delta_{ij} + (3N/2 - 1) \left\langle \sum_{n=1}^N F_i^n q_j^n / K \right\rangle \right), \end{aligned} \quad (2.101)$$

where the first term is clearly the “ideal gas” contribution and second term the Virial contribution. (2.101) is not very different from (2.44) formula for the canonical ensemble samples, beside that the Virial contribution is scaled by the total kinetic energy K , which is a persistent feature in micro-canonical ensemble expressions, reflecting the effect of constant total energy constraint on fluctuations. Because in the limit of large N the relative fluctuation of K is $\mathcal{O}(N^{-1/2})$, one only makes vanishingly small error in $t_{ij}(X)$ calculation even if (2.44) expression is used for microcanonical ensemble samples. However, as we will show next, it is not so for $C_{ijkl}(X)$ calculation, because (2.47) is a fluctuation formula, and the constant total energy constraint severely distort fluctuations.

Following (2.100), it is straightforward to show that

$$\begin{aligned}
& \left. \frac{\partial^2 S}{\partial E \partial \eta_{ij}} \right|_{\eta=0} \\
= & (3N/2 - 1)(3N/2 - 2)k_B \left\langle \left(-\frac{\partial V}{\partial q_i^n} \Big|_X q_j^n \right) / K^2 \right\rangle \\
& - (3N/2 - 1)^2 k_B \left\langle \left(-\frac{\partial V}{\partial q_i^n} \Big|_X q_j^n \right) / K \right\rangle \langle K^{-1} \rangle \\
= & (3N/2 - 1)k_B \hat{S}_2 \left[(3N/2 - 2) \left\langle \sum_{n=1}^N F_i^n q_j^n / K^2 \right\rangle - \right. \\
& \left. (3N/2 - 1) \left\langle \sum_{n=1}^N F_i^n q_j^n / K \right\rangle \langle K^{-1} \rangle \right]. \tag{2.102}
\end{aligned}$$

Lastly, combining (2.81), (2.98) and (2.99), it is not difficult to show that

$$\begin{aligned}
& \left. \frac{\partial^2 \ln \Pi}{\partial \eta_{ij} \partial \eta_{kl}} \right|_{\eta=0} \\
= & (3N/2 - 1) \left[(3N/2 - 2) \langle F_i^n q_j^n F_k^m q_l^m / K^2 \rangle \right. \\
& - (3N/2 - 1) \langle F_i^n q_j^n / K \rangle \langle F_k^m q_l^m / K \rangle \\
& \left. - \left\langle \left(\frac{\partial^2 V}{\partial q_i^n \partial q_k^m} \Big|_X q_j^n q_l^m + F_i^n q_k^n \delta_{jl} \right) / K \right\rangle \right], \tag{2.103}
\end{aligned}$$

and so, with (2.80), (2.85) and (2.92), we arrive at

$$\begin{aligned}
C_{ijkl}(X) = & \frac{N \langle K^{-1} \rangle^{-1}}{(3N/2 - 1)\Omega} (\delta_{ik} \delta_{jl} + \delta_{il} \delta_{jk}) + \langle K^{-1} \rangle^{-1} \cdot \hat{S}_4 \\
& \left[\left\langle \left(\sum_{n,m=1}^N \frac{\partial^2 V}{\partial q_i^n \partial q_k^m} \Big|_X q_j^n q_l^m + \sum_{n=1}^N F_i^n q_k^n \delta_{jl} \right) / K \Omega \right\rangle \right. \\
& + (3N/2 - 1) \left\langle \sum_{n=1}^N F_i^n q_j^n / K \sqrt{\Omega} \right\rangle \left\langle \sum_{m=1}^N F_k^m q_l^m / K \sqrt{\Omega} \right\rangle \\
& \left. - (3N/2 - 2) \left\langle \sum_{n,m=1}^N F_i^n q_j^n F_k^m q_l^m / K^2 \Omega \right\rangle \right] + \\
& \frac{\langle K^{-1} \rangle^{-1} \left(\frac{\partial^2 S}{\partial E \partial \eta_{ij}} \Big|_{\eta=0} / k_B \sqrt{\Omega} \right) \left(\frac{\partial^2 S}{\partial E \partial \eta_{kl}} \Big|_{\eta=0} / k_B \sqrt{\Omega} \right)}{(3N/2 - 1)^2 \left[(3N/2 - 2) \langle K^{-2} \rangle - (3N/2 - 1) \langle K^{-1} \rangle^2 \right]}. \tag{2.104}
\end{aligned}$$

Hydrostatic Response

Consider mainly a liquid or gaseous system which cannot sustain static shear loading,

$$t_{ij}(X) = -P\delta_{ij}, \quad (2.105)$$

and the pressure P is only a function of system volume

$$P = P(T, \Omega). \quad (2.106)$$

The discussions will also apply to any solid system that has cubic symmetry and is under hydrostatic loading. With that, one can define the isothermal bulk modulus

$$B_T = -\left. \frac{\partial P}{\partial \ln \Omega} \right|_T, \quad (2.107)$$

and the volumetric thermal expansion coefficient

$$\alpha = \left. \frac{\partial \ln \Omega}{\partial T} \right|_P. \quad (2.108)$$

We want to seek relations between B_T and $C_{ijkl}(X)$, such that we could use our fluctuation formulas (2.92) or (2.47). But before that, let us consider a seemingly irrelevant question: does ideal gas has finite C_{44} ?

The intuitive answer is no, because ideal gas cannot provide shear stress no matter how it is deformed. However, if one refers to (2.104),

$$C_{44} = C_{2323} = \frac{N \langle K^{-1} \rangle^{-1}}{(3N/2 - 1)\Omega} = \frac{Nk_B T}{\Omega}, \quad (2.109)$$

or work out the (2.47) expression for canonical ensembles using Gaussian variable contraction rules:

$$\langle p_i^n p_j^m / m \rangle = k_B T \delta_{nm} \delta_{ij}, \quad (2.110)$$

and thus

$$\begin{aligned}
& \langle t_{ij} t_{kl} \rangle - \langle t_{ij} \rangle \langle t_{kl} \rangle \\
= & \frac{1}{\Omega^2} \sum_{n,m=1}^N \left\langle (p_i^n p_j^n / m) (p_k^m p_l^m / m) \right\rangle - \left\langle p_i^n p_j^n / m \right\rangle \left\langle p_k^m p_l^m / m \right\rangle \\
= & \frac{1}{\Omega^2} \sum_{n,m=1}^N \left\langle p_i^n p_j^n p_k^m p_l^m / m^2 \right\rangle_{\text{linked}} \\
= & \frac{1}{\Omega^2} \sum_{n,m=1}^N k_B^2 T^2 (\delta_{nm} \delta_{ik} \cdot \delta_{nm} \delta_{jl} + \delta_{nm} \delta_{il} \cdot \delta_{nm} \delta_{jk}) \\
= & \frac{N k_B^2 T^2}{\Omega^2} (\delta_{ik} \delta_{jl} + \delta_{il} \delta_{jk}), \tag{2.111}
\end{aligned}$$

and

$$\hat{S}_4 \left(\left\langle \sum_{n=1}^N \frac{4 p_i^n p_k^n}{m_n} \delta_{jl} \right\rangle \right) = 2 N k_B T (\delta_{ik} \delta_{jl} + \delta_{il} \delta_{jk}), \tag{2.112}$$

so (2.47) turns out to be

$$C_{ijkl} = \frac{N k_B T}{\Omega} (\delta_{ik} \delta_{jl} + \delta_{il} \delta_{jk}) \tag{2.113}$$

for ideal gas, which can also be derived if one simply expands

$$F_{\text{i.g.}}(T, \Omega) = -k_B T \ln \left(\frac{\Omega}{(h/\sqrt{2\pi m k_B T})^3} \right)^N. \tag{2.114}$$

So, all analytical evidence indicate that ideal gas has non-zero C_{44} , in fact on the same order of magnitude as B_T and P . How can one compromise this with the intuition that ideal gas can never have shear stress? The answer lies in the fact that C_{ijkl} is not the “derivative” of t_{ij} with strain, so $t_{23} \equiv 0$ is *not* contradictory to $C_{44} \neq 0$. One should use the elastic stiffness coefficients, $B_{ijkl}(X)$, to relate stress with strain (see (2.21)).

Referring to (2.240), (2.105), (2.113) and ideal gas law

$$P(T, \Omega) = \frac{N k_B T}{\Omega}, \tag{2.115}$$

one has

$$\begin{aligned}
& B_{ijkl}(X) \\
= & C_{ijkl} + \frac{1}{2}(\delta_{ik}t_{jl} + \delta_{jk}t_{il} + \delta_{il}t_{jk} + \delta_{jl}t_{ik} - 2\delta_{kl}t_{ij}) \\
= & \frac{Nk_B T}{\Omega}[\delta_{ik}\delta_{jl} + \delta_{il}\delta_{jk} + \delta_{kl}\delta_{ij} - \\
& (\delta_{ik}\delta_{jl} + \delta_{jk}\delta_{il} + \delta_{il}\delta_{jk} + \delta_{jl}\delta_{ik})/2] \\
= & \frac{Nk_B T}{\Omega}\delta_{ij}\delta_{kl}, \tag{2.116}
\end{aligned}$$

in perfect agreement with our intuition and what would happen if one just plugs (2.115) into (2.105) and differentiate with respect to η_{ij} .

Since it is well established now that B_{ijkl} is the connection between stress and strain, let us study the pressure response of the system to volumetric expansion when (2.105) always holds. Then

$$t_{11} = -P = t_{22} = t_{33} \tag{2.117}$$

and

$$\eta_{11} = \eta_{22} = \eta_{33} \approx \frac{1}{3}\Delta \ln \Omega, \tag{2.118}$$

so

$$\begin{aligned}
B_T &= -\frac{\partial P}{\partial \ln \Omega} \Big|_T = \frac{\partial t_{11}}{\partial \ln \Omega} \Big|_T \\
&= (B_{1111} + B_{1122} + B_{1133})/3, \tag{2.119}
\end{aligned}$$

and since

$$B_{ijkl} = C_{ijkl} + P(\delta_{ij}\delta_{kl} - \delta_{ik}\delta_{jl} - \delta_{il}\delta_{jk}), \tag{2.120}$$

there is

$$B_T = (C_{11} + 2C_{12} + P)/3, \tag{2.121}$$

which can be directly evaluated using fluctuations formulas (2.104) or (2.47).

Let us study the thermal behavior of such systems. The geometrical condition is

now only specified by one variable, Ω ,

$$S(E, Y) = S(E, \Omega), \quad F(T, Y) = F(T, \Omega), \quad (2.122)$$

whether it is genuinely so as in liquids, or only appears to be for a solid with high symmetry under hydrostatic loading. In this case, one can recover from (2.91) the fundamental thermodynamical relation[5]

$$P = T \frac{\partial S}{\partial \Omega} \Big|_E, \quad (2.123)$$

and so

$$\begin{aligned} & \frac{\partial P}{\partial T} \Big|_\Omega \\ &= \frac{\partial S}{\partial \Omega} \Big|_E + T \frac{\partial \left(\frac{\partial S}{\partial \Omega} \Big|_E \right)}{\partial T} \Big|_\Omega \\ &= \frac{P}{T} + T \frac{\partial^2 S}{\partial \Omega \partial E} \cdot \frac{\partial E}{\partial T} \Big|_\Omega \\ &= \frac{P}{T} + C_V T \frac{\partial^2 S}{\partial E \partial \Omega}. \end{aligned} \quad (2.124)$$

Following (2.102), there is

$$\begin{aligned} \frac{\partial^2 S}{\partial E \partial \Omega} &= \frac{(3N/2 - 1)k_B}{3\Omega} \cdot \hat{S}_2 \left[\begin{aligned} & (3N/2 - 2) \left\langle \sum_{n=1}^N \mathbf{F}_n \cdot \mathbf{q}_n / K^2 \right\rangle \\ & - (3N/2 - 1) \left\langle \sum_{n=1}^N \mathbf{F}_n \cdot \mathbf{q}_n / K \right\rangle \left\langle K^{-1} \right\rangle \end{aligned} \right] \end{aligned} \quad (2.125)$$

and the fluctuation formula for C_V is already given in (2.83).

Because of the functional identity

$$\frac{\partial \Omega}{\partial T} \Big|_P \cdot \frac{\partial T}{\partial P} \Big|_\Omega \cdot \frac{\partial P}{\partial \Omega} \Big|_T = -1, \quad (2.126)$$

the volumetric thermal expansion coefficient is simply

$$\begin{aligned}
\alpha &= \frac{1}{\Omega} \frac{\partial \Omega}{\partial T} \Big|_P \\
&= - \frac{1}{\Omega} \frac{\partial P}{\partial T} \Big|_{\Omega} \frac{\partial \Omega}{\partial P} \Big|_T \\
&= \frac{\partial P}{\partial T} \Big|_{\Omega} / B_T,
\end{aligned} \tag{2.127}$$

and so α can be calculated by (2.107) and (2.124).

Lastly, let us find the representation for C_P , the constant pressure heat capacity, defined by

$$C_P = T \frac{\partial S}{\partial T} \Big|_P, \tag{2.128}$$

and so

$$\begin{aligned}
C_P &= T \frac{\partial S}{\partial T} \Big|_{\Omega} + T \frac{\partial S}{\partial \Omega} \Big|_T \frac{\partial \Omega}{\partial T} \Big|_P \\
&= C_V + \Omega T \frac{\partial P}{\partial T} \Big|_{\Omega} \alpha \\
&= C_V + \Omega T \alpha^2 B_T,
\end{aligned} \tag{2.129}$$

where we used the Maxwell's identity

$$\frac{\partial S}{\partial \Omega} \Big|_T = \frac{\partial P}{\partial T} \Big|_{\Omega}, \tag{2.130}$$

and (2.127). At this point we see that all thermodynamical derivatives are expressible in terms of microscopic fluctuation formulas that can be directly evaluated in a single MD simulation run.

Application to Pair Potential

Expressions such as

$$\lambda_{ijkl} = \Gamma_{ijkl} - \Pi_{ijkl} \tag{2.131}$$

$$= \sum_{m,n=1}^N q_k^m q_i^n \nabla_l^m \nabla_j^n V(q^N) - \sum_{n=1}^N q_k^n \nabla_j^n V(q^N) \delta_{il}$$

appearing in (2.47) and (2.104) can be localized (see discussion in section 2.2.1) through the following procedure: we first note that λ_{ijkl} is linear in V . That is, if $V = V_1 + V_2$, then λ_{ijkl} is the sum of contribution only due to V_1 and contribution only due to V_2 . So we only need to calculate each pair or triplet or n -let interaction, and in the end simply add their contributions together.

Secondly, we need to show that the quantity to evaluate is in fact translationally invariant, which means that if we make a rigid translation:

$$\hat{\mathbf{q}}_n = \mathbf{q}_n + \mathbf{a}, \quad (2.132)$$

where \mathbf{a} is the same for all particles, there is

$$\begin{aligned} & \hat{\Pi}_{ijkl} \\ = & \sum_{n=1}^N \hat{q}_k^n \hat{\nabla}_j^n V_1(\hat{q}^N) \delta_{il} \\ = & \sum_{n=1}^N (q_k^n + a_k) \nabla_j^n V_1(q^N) \delta_{il} \\ = & \sum_{n=1}^N q_k^n \nabla_j^n V_1(q^N) \delta_{il} + a_k \sum_{n=1}^N \nabla_j^n V_1(q^N) \\ = & \sum_{n=1}^N q_k^n \nabla_j^n V_1(q^N) \delta_{il} \\ = & \Pi_{ijkl}, \end{aligned} \quad (2.133)$$

since

$$\sum_{n=1}^N \nabla_j^n V_1(q^N) \equiv 0 \quad (2.134)$$

for any translationally invariant potential $V_1(q^N)$. We can prove the same thing for

$$\Gamma_{ijkl} = \sum_{m,n=1}^N q_k^m q_i^n \nabla_l^m \nabla_j^n V_1(q^N)$$

by plugging in (2.132) and grouping free indices. And so, it does not matter in which coordinate frame λ_{ijkl} is evaluated, and we can choose any frame that makes the evaluation simple, such as by letting the origin sit on one particle.

For instance, if the particles interact via pair potential

$$V(q^N) = \sum_{\alpha < \beta} W(\mathbf{q}_\alpha, \mathbf{q}_\beta) = \sum_{\alpha < \beta} W(|\mathbf{q}_\alpha - \mathbf{q}_\beta|), \quad (2.135)$$

then we can single out any interacting pair $W(|\mathbf{q}_\alpha - \mathbf{q}_\beta|)$, and choose our frame such that $\mathbf{q}_\beta = 0$. Then, all terms in

$$\Delta\lambda_{ijkl} = \sum_{m,n=\alpha,\beta} q_k^m q_i^n \nabla_l^m \nabla_j^n W - \sum_{n=\alpha,\beta} q_k^n \nabla_j^n W \delta_{il}$$

cease to contribute except for $m = n = \alpha$, and it is simply

$$\Delta\lambda_{ijkl} = q_k q_i \nabla_l \nabla_j W(q) - q_k \nabla_j W(q) \delta_{il} \quad (2.136)$$

where $q = |\mathbf{q}_\alpha|$, and we have simplified the two-body expression to a one-body expression. Since

$$\nabla_j W(q) = W' \frac{q_j}{q}, \quad (2.137)$$

and

$$\nabla_l \nabla_j W = W'' \frac{q_j q_l}{q^2} - W' \frac{q_j q_l}{q^3} + W' \frac{\delta_{jl}}{q}, \quad (2.138)$$

there is

$$\begin{aligned} \Delta\lambda_{ijkl} &= q_k q_i \left(W'' \frac{q_j q_l}{q^2} - W' \frac{q_j q_l}{q^3} + W' \frac{\delta_{jl}}{q} \right) - q_k W' \frac{q_j}{q} \delta_{il}, \end{aligned} \quad (2.139)$$

and so

$$\hat{S}_4(\Delta\lambda_{ijkl}) = q_i q_j q_k q_l \left(\frac{W''}{q^2} - \frac{W'}{q^3} \right), \quad (2.140)$$

which is just the contribution to Born elastic constant (see (2.47) from this single pair

of interaction. One should remember that in this special coordinate frame $\mathbf{q}^\beta = 0$, so \mathbf{q} should be replaced by $\mathbf{q}_\alpha - \mathbf{q}_\beta$ in a general frame.

For instance, in the Lennard Jones pair potential[7] for rare gas solids,

$$W(q) = 4\epsilon \left[\left(\frac{\sigma}{q} \right)^{12} - \left(\frac{\sigma}{q} \right)^6 \right], \quad (2.141)$$

one can show from (2.140) that

$$\begin{aligned} & \hat{S}_4(\Delta\lambda_{ijkl}) \\ = & \epsilon \cdot \frac{q_i q_j q_k q_l}{\sigma^4} \left[672 \left(\frac{\sigma}{q} \right)^{16} - 192 \left(\frac{\sigma}{q} \right)^{10} \right]. \end{aligned} \quad (2.142)$$

In general, one can always simplify a n body expression into a $n-1$ body expression using the above coordinate frame invariant observation.

2.3 Lattice Vibrational Formalisms

Consider a 3D crystal with r atomic species. Denote the unit cells by L and atom type by S , $S = 1..r$. The position vector is \mathbf{R}_S^L , and the atomic displacement

$$u_\alpha \left(\begin{smallmatrix} L \\ S \end{smallmatrix} \right) = R_\alpha \left(\begin{smallmatrix} L \\ S \end{smallmatrix} \right) - R_\alpha^0 \left(\begin{smallmatrix} L \\ S \end{smallmatrix} \right) \quad (2.143)$$

where α denotes Cartesian components. For convenience's sake, sometime we contract (α, L, S) into a single index m , $u_m = u_\alpha \left(\begin{smallmatrix} L \\ S \end{smallmatrix} \right)$.

Near equilibrium, the total crystalline potential energy $V(q^N)$ could be expanded into

$$V(q^N) = \frac{1}{2} \Phi_{mn} u_m u_n + \frac{1}{6} \Phi_{mm'm''} u_m u_{m'} u_{m''} + \dots \quad (2.144)$$

where

$$\Phi_{mn} = \left. \frac{\partial^2 V(q^N)}{\partial u_\alpha \left(\begin{smallmatrix} L \\ S \end{smallmatrix} \right) \partial u_\beta \left(\begin{smallmatrix} L' \\ S' \end{smallmatrix} \right)} \right|_{q_0^N} \quad (2.145)$$

$$\Phi_{mm'm''} = \frac{\partial^3 V(q^N)}{\partial u_\alpha \binom{L}{S} \partial u_{\alpha'} \binom{L'}{S'} \partial u_{\alpha''} \binom{L''}{S''}} \bigg|_{q_0^N} \quad (2.146)$$

For a crystal, Φ 's will only depend on relative distances between unit cells:

$$\Phi_{\alpha\beta} \binom{LL'}{SS'} = \Phi_{\alpha\beta} \binom{L-L'}{SS'}, \Phi_{\alpha\beta\gamma} \binom{LL'L''}{SS'S''} = \Phi_{\alpha\beta\gamma} \binom{L-L'', L'-L''}{SS'S''}, \dots \quad (2.147)$$

and by exchanging the order of differentiation, there is

$$\Phi_{\alpha\beta} \binom{LL'}{SS'} = \Phi_{\beta\alpha} \binom{L'L}{S'S}, \quad \text{i.e.,} \quad \Phi_{mn} = \Phi_{nm} \quad (2.148)$$

and thus

$$\Phi_{\alpha\beta} \binom{L}{SS'} = \Phi_{\beta\alpha} \binom{-L}{S'S} \quad (2.149)$$

From the translational and rotational invariance of the interaction potential, there must be

$$\sum_{L', S'} \Phi_{\alpha\beta} \binom{LL'}{SS'} = 0 \quad (2.150)$$

$$\sum_{L', S'} \Phi_{\alpha\beta} \binom{LL'}{SS'} R_\gamma^0 \binom{L'}{S'} = \sum_{L', S'} \Phi_{\alpha\gamma} \binom{LL'}{SS'} R_\beta^0 \binom{L'}{S'} \quad (2.151)$$

For instance, Eq(2.151) could be proved by considering a virtual rotation in direction \mathbf{n} for small angle $\delta\theta$, so the displacement of each atom is $\mathbf{n} \times \mathbf{R}^0 \binom{L'}{S'} \delta\theta$. Consider the force on atom (L, S) , it's

$$\begin{aligned} F_\alpha \binom{L}{S} &= - \sum_{L', S', \beta} \Phi_{\alpha\beta} \binom{LL'}{SS'} (\epsilon_{\beta\sigma\gamma} n_\sigma R_\gamma^0 \binom{L'}{S'}) \delta\theta \\ &= - \frac{1}{2} \sum_{L', S', \beta} [\Phi_{\alpha\beta} \binom{LL'}{SS'} R_\gamma^0 \binom{L'}{S'} - \Phi_{\alpha\gamma} \binom{LL'}{SS'} R_\beta^0 \binom{L'}{S'}] \epsilon_{\beta\sigma\gamma} n_\sigma \delta\theta \end{aligned} \quad (2.152)$$

Since $F_\alpha \binom{L}{S}$ should be zero for any \mathbf{n} , it's obvious that Eq(2.151) must be satisfied.

Consider mass-scaled quantities

$$v_m = \sqrt{M_S} u_\alpha \binom{L}{S} \quad (2.153)$$

and

$$D_{mn} = \frac{\Phi_{mn}}{\sqrt{M_S M_{S'}}}, \quad D_{mm'm''} = \frac{\Phi_{mm'm''}}{\sqrt{M_S M_{S'} M_{S''}}}, \quad \dots \quad (2.154)$$

We are concerned with the diagonalization of D_{mn} , i.e., finding a unitary matrix that

$$D_{mn} = U_{mk}^\dagger \omega_k^2 U_{kn}, \quad \text{where} \quad U_{mk}^\dagger U_{kn} = \delta_{mn} \quad (2.155)$$

In doing this, we should know the fact that by using irreducible basis functions $\{\exp(i\mathbf{q} \cdot \mathbf{r})\}$ of the translational group we can easily block-diagonalize this $3rN \times 3rN$ matrix into N $3r \times 3r$ matrices (only functions with the same \mathbf{q} in the first B.Z. can couple to each other through the Hamiltonian). This means we can label our normal coordinates of the crystal by k , which is the contraction of two indices ($\mathbf{q}j$):

$$V_n^k = V_\alpha^{\mathbf{q}j} \binom{L}{S} = \frac{1}{\sqrt{N}} \exp(i\mathbf{q} \cdot \mathbf{R}(L)) e_\alpha^{\mathbf{q}j}(S) \quad (2.156)$$

such that

$$\sum_n V_n^{k*} V_n^{k'} = \sum_{\alpha, L, S} V_\alpha^k \binom{L}{S}^* V_\alpha^{k'} \binom{L}{S} = \delta_{kk'} \quad (2.157)$$

Here $j(1..3r)$ denote the phonon branch, by which polarization vector $e_\alpha^{\mathbf{q}j}(S)$ is specified. For Eq(2.157) to be correct, $e^{\mathbf{q}j}$'s for the same \mathbf{q} should be orthonormal to each other,

$$\sum_{\alpha, S} e_\alpha^{\mathbf{q}j}(S)^* e_\alpha^{\mathbf{q}j'}(S) = \delta_{jj'} \quad (2.158)$$

Also, since $\{k\}$ form a complete basis set, there should be completeness relation

$$\sum_k V_n^{k*} V_{n'}^k = \delta_{nn'} \quad (2.159)$$

To block diagonalize D_{mn} , there should be

$$D_{mn} V_n^k = \omega_k^2 V_m^k \quad (2.160)$$

so

$$\sum_{\beta, L', S'} \frac{\Phi_{\alpha\beta}^{(L-L')}(SS')}{\sqrt{M_S M_{S'}}} \exp(i\mathbf{q} \cdot \mathbf{R}(L')) e_{\beta}^k(S') = \omega_k^2 \exp(i\mathbf{q} \cdot \mathbf{R}(L)) e_{\alpha}^k(S) \quad (2.161)$$

$$\sum_{\beta, L', S'} \frac{\Phi_{\alpha\beta}^{(L-L')}(SS')}{\sqrt{M_S M_{S'}}} \exp(-i\mathbf{q} \cdot \mathbf{R}(L - L')) e_{\beta}^k(S') = \omega_k^2 e_{\alpha}^k(S) \quad (2.162)$$

Define the 3×3 *dynamical matrix* in \mathbf{q} space to be

$$\mathbf{D}_{(SS')}^{(\mathbf{q})} = \frac{1}{\sqrt{M_S M_{S'}}} \sum_L \Phi_{(SS')}^L \exp(-i\mathbf{q} \cdot \mathbf{R}(L)) \quad (2.163)$$

then there would be

$$\sum_{S'} \mathbf{D}_{(SS')}^{(\mathbf{q})} \mathbf{e}^k(S') = \omega_k^2 \mathbf{e}^k(S) \quad (2.164)$$

From time-reversal symmetry (conjugate invariance),

$$\mathbf{D}_{(SS')}^{(\mathbf{q})} = \mathbf{D}_{(SS')}^{*(-\mathbf{q})} \quad (2.165)$$

$$\omega_k^2 = \omega_{-k}^2 \quad (2.166)$$

$$\mathbf{e}^k(S) = \mathbf{e}^{-k}(S)^* \quad (2.167)$$

Explicitly written, the $3r \times 3r$ matrix equation is

$$\begin{pmatrix} \mathbf{D}_{(11)}^{(\mathbf{q})} & \mathbf{D}_{(12)}^{(\mathbf{q})} & \dots & \mathbf{D}_{(1r)}^{(\mathbf{q})} \\ \mathbf{D}_{(21)}^{(\mathbf{q})} & \mathbf{D}_{(22)}^{(\mathbf{q})} & \dots & \mathbf{D}_{(2r)}^{(\mathbf{q})} \\ \mathbf{D}_{(31)}^{(\mathbf{q})} & . & \dots & . \\ . & . & \dots & . \\ . & . & \dots & . \\ \mathbf{D}_{(r1)}^{(\mathbf{q})} & \mathbf{D}_{(r2)}^{(\mathbf{q})} & \dots & \mathbf{D}_{(rr)}^{(\mathbf{q})} \end{pmatrix} \begin{pmatrix} \mathbf{e}^{\mathbf{q}j}(1) \\ \mathbf{e}^{\mathbf{q}j}(2) \\ \mathbf{e}^{\mathbf{q}j}(3) \\ . \\ . \\ \mathbf{e}^{\mathbf{q}j}(r) \end{pmatrix} = \omega_{\mathbf{q}j}^2 \begin{pmatrix} \mathbf{e}^{\mathbf{q}j}(1) \\ \mathbf{e}^{\mathbf{q}j}(2) \\ \mathbf{e}^{\mathbf{q}j}(3) \\ . \\ . \\ \mathbf{e}^{\mathbf{q}j}(r) \end{pmatrix} \quad (2.168)$$

and with

$$\left(\mathbf{e}^{\mathfrak{q}j}(1)^*, \mathbf{e}^{\mathfrak{q}j}(2)^*, \mathbf{e}^{\mathfrak{q}j}(3)^*, \dots, \mathbf{e}^{\mathfrak{q}j}(r)^* \right) \begin{pmatrix} \mathbf{e}^{\mathfrak{q}j'}(1) \\ \mathbf{e}^{\mathfrak{q}j'}(2) \\ \mathbf{e}^{\mathfrak{q}j'}(3) \\ \vdots \\ \mathbf{e}^{\mathfrak{q}j'}(r) \end{pmatrix} = \delta_{jj'} \quad (2.169)$$

Diagonalization complete. We have $3rN$ unit vectors for the crystal now, and thus the unitary matrix $U_{mk}^\dagger = V_k^m$.

Lagrangian Formulation

Decompose

$$\sqrt{M_S} u_\alpha \binom{L}{S} = v_m = \sum_k Q_k V_m^k \quad (2.170)$$

Since $u_\alpha \binom{L}{S}$ is real, there is

$$Q_k = Q_{-k}^* \quad (2.171)$$

and

$$\dot{v}_\alpha \binom{L}{S} = \sum_k \dot{Q}_k V_m^k = \sum_k \dot{Q}_k^* V_m^{k*} \quad (2.172)$$

the Lagrangian of the crystal then become

$$\begin{aligned} \mathcal{L} &= \sum_m \frac{1}{2} M_S \dot{u}_m^2 - \sum_{mn} \frac{1}{2} u_m \Phi_{mn} u_n \\ &= \sum_m \frac{1}{2} \dot{v}_m^2 - \sum_{mn} \frac{1}{2} v_m D_{mn} v_n \\ &= \sum_{k,k'} \left\{ \sum_m \frac{1}{2} \dot{Q}_k^* V_m^{k*} \dot{Q}_{k'} V_m^{k'} - \sum_m \frac{1}{2} Q_k^* V_m^{k*} D_{mn} Q_{k'} V_n^{k'} \right\} \\ &= \sum_k \frac{1}{2} \dot{Q}_k^* \dot{Q}_k - \frac{1}{2} \omega_k^2 Q_k^* Q_k \end{aligned} \quad (2.173)$$

So

$$P_k = \frac{\partial \mathcal{L}}{\partial \dot{Q}_k} = \dot{Q}_k^* = \dot{Q}_{-k} \quad (2.174)$$

and

$$\begin{aligned} \mathcal{H} &= \sum_k P_k \dot{Q}_k - \mathcal{L} \\ &= \sum_k \frac{P_k^* P_k}{2} + \frac{\omega_k^2}{2} Q_k^* Q_k \\ &= \sum_k \frac{P_{-k} P_k}{2} + \frac{\omega_k^2}{2} Q_{-k} Q_k \end{aligned} \quad (2.175)$$

From here we can see that

$$u_\alpha \binom{L}{S} = \frac{1}{\sqrt{M_S}} \sum_k Q_k \cdot \frac{1}{\sqrt{N}} \exp(i\mathbf{q} \cdot \mathbf{R}(L)) e_\alpha^k(S) \quad (2.176)$$

$$\begin{aligned} p_\alpha \binom{L}{S} &= \sqrt{M_S} \sum_k \dot{Q}_k \cdot \frac{1}{\sqrt{N}} \exp(i\mathbf{q} \cdot \mathbf{R}(L)) e_\alpha^k(S) \\ &= \sqrt{M_S} \sum_k P_{-k} \cdot \frac{1}{\sqrt{N}} \exp(i\mathbf{q} \cdot \mathbf{R}(L)) e_\alpha^k(S) \end{aligned} \quad (2.177)$$

And so the inverse

$$Q_k = \sum_{\alpha, L, S} \sqrt{M_S} u_\alpha \binom{L}{S} \frac{1}{\sqrt{N}} \exp(-i\mathbf{q} \cdot \mathbf{R}(L)) e_\alpha^k(S)^* \quad (2.178)$$

$$P_{-k} = \sum_{\alpha, L, S} \frac{1}{\sqrt{M_S}} p_\alpha \binom{L}{S} \frac{1}{\sqrt{N}} \exp(-i\mathbf{q} \cdot \mathbf{R}(L)) e_\alpha^k(S)^* \quad (2.179)$$

Second Quantization

Second Quantization is to simply replace all the $u_\alpha \binom{L}{S}, p_\alpha \binom{L}{S}$ in the classical Hamiltonian

$$\mathcal{H} = \sum_{\alpha, L, S} \frac{p_\alpha^2 \binom{L}{S}}{2M_S} + \frac{1}{2} u_\alpha \binom{L}{S} \Phi_{\alpha\beta} \binom{LL'}{SS'} u_\beta \binom{L'}{S'} + \dots \quad (2.180)$$

by operators $\hat{p}_\alpha \binom{L}{S}, \hat{u}_\alpha \binom{L}{S}$. Starting from here is a bit cumbersome, but is much safer.

Define \hat{Q}_k, \hat{P}_{-k} through Eq(2.178),Eq(2.179), then

$$\hat{Q}_k = \sum_{\alpha,L,S} \sqrt{\frac{M_S}{N}} \hat{u}_\alpha^L(S) \exp(-i\mathbf{q} \cdot \mathbf{R}(L)) e_\alpha^k(S)^* \quad (2.181)$$

$$\hat{P}_{-k} = \sum_{\alpha,L,S} \frac{1}{\sqrt{NM_S}} \hat{p}_\alpha^L(S) \exp(-i\mathbf{q} \cdot \mathbf{R}(L)) e_\alpha^k(S)^* \quad (2.182)$$

If we also define

$$\hat{v}_n = \sqrt{M_S} \hat{u}_n, \quad \hat{w}_n = \frac{1}{\sqrt{M_S}} \hat{p}_n \quad (2.183)$$

then

$$\hat{Q}_k = U_{kn} \hat{v}_n, \quad \hat{P}_{-k} = U_{kn} \hat{w}_n \quad (2.184)$$

and

$$\hat{Q}_k^\dagger = U_{kn}^* \hat{v}_n = \hat{Q}_{-k}, \quad \hat{P}_{-k}^\dagger = U_{kn}^* \hat{w}_n = \hat{P}_k \quad (2.185)$$

Then

$$[\hat{Q}_k, \hat{P}_{k'}] = U_{kn} U_{k'm}^* [\hat{v}_n, \hat{w}_m] = i\hbar \delta_{kk'} \quad (2.186)$$

and obviously

$$[\hat{Q}_k, \hat{Q}_{k'}] = [\hat{P}_k, \hat{P}_{k'}] = 0 \quad (2.187)$$

That's good. However notice that \hat{Q}_k and \hat{P}_k are *not* Hermitian.

Define

$$\hat{a}_k = \frac{1}{\sqrt{2\hbar\omega_k}} (\omega_k \hat{Q}_k + i\hat{P}_{-k}) \quad \hat{a}_k^\dagger = \frac{1}{\sqrt{2\hbar\omega_k}} (\omega_k \hat{Q}_{-k} - i\hat{P}_k) \quad (2.188)$$

$$\hat{a}_{-k} = \frac{1}{\sqrt{2\hbar\omega_k}} (\omega_k \hat{Q}_{-k} + i\hat{P}_k) \quad \hat{a}_{-k}^\dagger = \frac{1}{\sqrt{2\hbar\omega_k}} (\omega_k \hat{Q}_k - i\hat{P}_{-k}) \quad (2.189)$$

Then

$$[\hat{a}_k, \hat{a}_{k'}^\dagger] = \frac{1}{2\hbar\sqrt{\omega_k\omega_{k'}}} (-i\omega_k [\hat{Q}_k, \hat{P}_{k'}] + i\omega_{k'} [\hat{P}_{-k}, \hat{Q}_{-k'}]) = \delta_{kk'} \quad (2.190)$$

$$[\hat{a}_k, \hat{a}_{k'}] = \frac{1}{2\hbar\sqrt{\omega_k\omega_{k'}}} (i\omega_k [\hat{Q}_k, \hat{P}_{-k'}] + i\omega_{k'} [\hat{P}_{-k}, \hat{Q}_{k'}]) = 0 \quad (2.191)$$

$$[\hat{a}_k^\dagger, \hat{a}_{k'}^\dagger] = \frac{1}{2\hbar\sqrt{\omega_k\omega_{k'}}} (-i\omega_k [\hat{Q}_{-k}, \hat{P}_{k'}] - i\omega_{k'} [\hat{P}_k, \hat{Q}_{-k'}]) = 0 \quad (2.192)$$

With this in mind and with Eq(2.184) we have

$$\hat{v}_n = U_{nk}^\dagger \hat{Q}_k, \quad \hat{w}_n = U_{nk}^\dagger \hat{P}_{-k} \quad (2.193)$$

So

$$\begin{aligned} \mathcal{H} &= \sum_n \frac{\hat{w}_n \hat{w}_n}{2} + \sum_{nm} \frac{1}{2} \hat{v}_m D_{mn} \hat{v}_n \\ &= \frac{1}{2} (\hat{P}_{-k}^\dagger (U_{nk}^\dagger)^* U_{nk}^\dagger \hat{P}_{-k} + \omega_k^2 \hat{Q}_k^\dagger \hat{Q}_k) \\ &= \sum_k \frac{1}{2} (\hat{P}_k^\dagger \hat{P}_k + \omega_k^2 \hat{Q}_k^\dagger \hat{Q}_k) \end{aligned} \quad (2.194)$$

But

$$\begin{aligned} &\sum_k \hbar \omega_k (\hat{a}_k^\dagger \hat{a}_k + \frac{1}{2}) \\ &= \sum_k \hbar \omega_k \left\{ \frac{1}{2\hbar \omega_k} (\omega_k^2 \hat{Q}_{-k} \hat{Q}_k + \hat{P}_k \hat{P}_{-k} - i\omega_k \hat{P}_k \hat{Q}_k + i\omega_k \hat{Q}_{-k} \hat{P}_{-k}) + \frac{1}{2} \right\} \\ &= \sum_k \frac{1}{2} [\hat{P}_{-k} \hat{P}_k + \omega_k^2 \hat{Q}_{-k} \hat{Q}_k] + \hbar \omega_k \left\{ \frac{i}{2\hbar} [\hat{Q}_k, \hat{P}_k] + \frac{1}{2} \right\} \\ &= \sum_k \frac{1}{2} [\hat{P}_k^\dagger \hat{P}_k + \omega_k^2 \hat{Q}_k^\dagger \hat{Q}_k] \end{aligned} \quad (2.195)$$

Compare with Eq(2.194), we see that

$$\mathcal{H} = \sum_k \hbar \omega_k (\hat{a}_k^\dagger \hat{a}_k + \frac{1}{2}) \quad (2.196)$$

Quantization complete. All conclusions of the algebra could be transported onto 3D crystal. Notice that k and $-k$ phonons are entirely decoupled, although they share the same frequency.

Important dynamical operators:

$$\hat{Q}_k = \sqrt{\frac{\hbar}{2\omega_k}} (\hat{a}_k + \hat{a}_{-k}^\dagger), \quad \hat{P}_{-k} = -i\sqrt{\frac{\hbar \omega_k}{2}} (\hat{a}_k - \hat{a}_{-k}^\dagger) \quad (2.197)$$

and

$$\begin{aligned}
\hat{u}_\alpha \binom{L}{S} &= \frac{1}{\sqrt{NM_S}} \sum_k e_\alpha^k(S) \exp(i\mathbf{q} \cdot \mathbf{R}(L)) \hat{Q}_k \\
&= \sum_k \sqrt{\frac{\hbar}{2NM_S\omega_k}} e_\alpha^k(S) \exp(i\mathbf{q} \cdot \mathbf{R}(L)) (\hat{a}_k + \hat{a}_{-k}^\dagger) \\
&= \sum_k \sqrt{\frac{\hbar}{2NM_S\omega_k}} \{e_\alpha^k(S) \exp(i\mathbf{q} \cdot \mathbf{R}(L)) \hat{a}_k + e_\alpha^k(S)^* \exp(-i\mathbf{q} \cdot \mathbf{R}(L)) \hat{a}_{-k}^\dagger\} \quad (2.198)
\end{aligned}$$

$$\begin{aligned}
\hat{p}_\alpha \binom{L}{S} &= \sqrt{\frac{M_S}{N}} \sum_k e_\alpha^k(S) \exp(i\mathbf{q} \cdot \mathbf{R}(L)) \hat{P}_{-k} \\
&= \sum_k -i \sqrt{\frac{\hbar M_S \omega_k}{2N}} e_\alpha^k(S) \exp(i\mathbf{q} \cdot \mathbf{R}(L)) (\hat{a}_k - \hat{a}_{-k}^\dagger) \\
&= \sum_k -i \sqrt{\frac{\hbar M_S \omega_k}{2N}} \{e_\alpha^k(S) \exp(i\mathbf{q} \cdot \mathbf{R}(L)) \hat{a}_k - e_\alpha^k(S)^* \exp(-i\mathbf{q} \cdot \mathbf{R}(L)) \hat{a}_{-k}^\dagger\} \quad (2.199)
\end{aligned}$$

Phonons will form bands, as all excitations in a periodic lattice. One important difference between phonon and electron band is that a pure phonon state $|n_k\rangle$ won't carry momentum, which is easily seen from Eq(2.199). A pure electron Bloch state $|\psi_k^n\rangle$ however, does carry the momentum $m_e \mathbf{v}_G$, where \mathbf{v}_G is the group velocity:

$$\mathbf{v}_G = \frac{\partial w_n(\mathbf{q})}{\partial \mathbf{q}} \quad (2.200)$$

Conservation Laws

We now consider general conservation laws for periodic systems, not only under harmonic approximation, but with arbitrary interactions, and with external probes inside the system, say, neutrons or photons. We know that conservation laws are linked closely with some invariance operators, like the conservation of energy with time-translational operator:

$$\hat{U}_\tau = \exp\left(\frac{\hat{\mathcal{H}}\tau}{i\hbar}\right) \quad (2.201)$$

Here the infinitesimal generator of \hat{U}_τ is $\hat{\mathcal{H}}$. Since obviously

$$[\hat{U}_\tau, \hat{\mathcal{H}}] = 0 \quad (2.202)$$

as physical laws doesn't depend on the time origin, there is

$$[\hat{\mathcal{H}}, \hat{\mathcal{H}}] = 0 \quad (2.203)$$

which we know directly otherwise. So the measurement of the generator of \hat{U}_τ is conserved, i.e.,

$$\langle \hat{\mathcal{H}} \rangle = \text{const} \quad (2.204)$$

Consider the Hamiltonian of a general crystal,

$$\hat{\mathcal{H}} = \sum_{\alpha, L, S} \frac{\hat{p}_\alpha \binom{L}{S}^2}{2M_S} + V(\{\hat{u}_\alpha \binom{L}{S}\}) + \frac{\hat{P}^2}{2m} + W(\hat{r}, \{\hat{u}_\alpha \binom{L}{S}\}) \quad (2.205)$$

Here \hat{P}, \hat{r} are operators for the external probe, W is its interaction with the crystal. From Eq(2.204) we can see that

$$E_i^{tot} = E_f^{tot}$$

in the case of a photon,

$$\hbar\omega_i + E_i^{xtal} = \hbar\omega_f + E_f^{xtal} \quad (2.206)$$

There are two kinds of spatial translations for a periodic system: one is the common real-space translations with arbitrary displacement,

$$\hat{U}_\delta = \exp\left(\frac{i}{\hbar}\left(\sum_{L, S} \hat{p} \binom{L}{S} + \hat{P}\right) \cdot \delta\right) \quad (2.207)$$

This means

$$\hat{r} \rightarrow \hat{r} + \delta, \quad \hat{u} \binom{L}{S} \rightarrow \hat{u} \binom{L}{S} + \delta$$

and obviously

$$[\hat{U}_\delta, \hat{\mathcal{H}}] = 0 \quad (2.208)$$

as the translation of the entire system in space for δ won't change the energy. So,

$$\langle \sum_{L,S} \hat{p}_S^{(L)} + \hat{P} \rangle = \text{const} \quad (2.209)$$

as the law of total momentum conservation. This law isn't so interesting since the recoil of a crystal in a scattering experiment is negligible.

The other one is more subtle, which involves only the translation of *labeling*. Consider the following operation

$$\hat{r} \rightarrow \hat{r} + \mathbf{R}, \quad \hat{u}_S^{(L)} \rightarrow \hat{u}_S^{(L-1)}, \quad \hat{p}_S^{(L)} \rightarrow \hat{p}_S^{(L-1)}$$

with \mathbf{R} being a lattice vector. Obviously, this will also leave the total Hamiltonian invariant, as the incident particle would find itself in the same environment as before. The operator for this translation is

$$\hat{U}_{\mathbf{R}} = \exp\left(\frac{i}{\hbar}(\hat{K} + \hat{P}) \cdot \mathbf{R}\right) \quad (2.210)$$

where

$$\hat{K} = \sum_k \hbar \mathbf{q} (\hat{a}_k^\dagger \hat{a}_k) \quad (2.211)$$

This can be proven in the following way. Since

$$[\hat{a}_k^\dagger \hat{a}_k, \hat{a}_k] = -\hat{a}_k, \quad [\hat{a}_k^\dagger \hat{a}_k, \hat{a}_k^\dagger] = \hat{a}_k^\dagger \quad (2.212)$$

if we define \hat{K} which operates on operators

$$\hat{K} \hat{A} = [\hat{K}, \hat{A}] \quad (2.213)$$

it's obvious that $\hat{a}_k, \hat{a}_k^\dagger$ are the eigenvectors of \hat{K} with eigenvalues $-\hbar \mathbf{q}$ and $\hbar \mathbf{q}$, and so

$$\hat{U}_{\mathbf{R}} \hat{a}_k \hat{U}_{\mathbf{R}}^\dagger$$

$$\begin{aligned}
&= \exp\left(\frac{i}{\hbar} \hat{K} \cdot \mathbf{R}\right) \hat{a}_k \exp\left(-\frac{i}{\hbar} \hat{K} \cdot \mathbf{R}\right) \\
&= \exp\left(\frac{i}{\hbar} \hat{K} \cdot \mathbf{R}\right) \hat{a}_k \\
&= \exp(-i\mathbf{q} \cdot \mathbf{R}) \hat{a}_k
\end{aligned} \tag{2.214}$$

also

$$\hat{U}_{\mathbf{R}} \hat{a}_k^\dagger \hat{U}_{\mathbf{R}}^\dagger = \exp(i\mathbf{q} \cdot \mathbf{R}) \hat{a}_k^\dagger \tag{2.215}$$

Then from Eq(2.198),Eq(2.199)

$$\hat{U}_{\mathbf{R}} \hat{u}_\alpha \binom{L}{S} \hat{U}_{\mathbf{R}}^\dagger = \hat{u}_\alpha \binom{L-1}{S} \tag{2.216}$$

$$\hat{U}_{\mathbf{R}} \hat{p}_\alpha \binom{L}{S} \hat{U}_{\mathbf{R}}^\dagger = \hat{p}_\alpha \binom{L-1}{S} \tag{2.217}$$

$$\hat{U}_{\mathbf{R}} \hat{r} \hat{U}_{\mathbf{R}}^\dagger = \hat{r} + \mathbf{R} \tag{2.218}$$

And so indeed we have proven $\hat{U}_{\mathbf{R}}$ to be the operator we described. This means the measurement of $\hat{U}_{\mathbf{R}}$ shall always be conserved. Note that although we used $\hat{a}_k, \hat{a}_k^\dagger$ in our derivation, we do not have to be in the harmonic approximation.

Suppose before and after the scattering the incident particle is free, and we are not far from a harmonic crystal such that the instantaneous configuration is represented by a number state. For $\langle E_q(2.210) \rangle$ to be invariant, also for any lattice vector \mathbf{R} , there must be

$$P_i + \sum_k n_k^i \hbar \mathbf{q} = P_f + \sum_k n_k^f \hbar \mathbf{q} + \mathbf{G} \tag{2.219}$$

where \mathbf{G} is a reciprocal lattice vector. Thus we can define the concept of *crystal momentum*, which is just $\sum_k n_k \hbar \mathbf{q}$. Crystal momentum isn't real momentum. It defines the vibrational phase relation between different labeling but identical atoms, and that, adding the phase factor of the incident particle, should be conserved.

2.3.1 Order- N Method to Calculate the Local Density of States

This part has been published [70]. Due to length limitation only the abstract is shown below. Please refer to the original paper for details.

“We present a rigorous and general method to extract the local density of states $\rho_i(\omega)$ of a system from its time response to a specified external perturbation. This method is order- N when the matrix is sparse. In a single run it gives $\rho_i(\omega)$, $\rho_i(2\omega)$, .. , $\rho_i(n\omega)$, .. concurrently, which enhances the total efficiency by two decades. Application to a lattice dynamics problem of 4096 SiC particles in a supercell with dynamical matrix generated from an appropriate interatomic potential shows excellent agreement with exact phonon dispersion calculations; the accelerated algorithm yields a full LDOS spectrum for each supercell \mathbf{k} -point in 15 minutes on a desktop workstation. Results showing the effects of an antisite-pair defect are given for which methods requiring lattice periodicity can not be used.”

2.4 Mechanical Deformation at Finite Strain

2.4.1 Elastic Instabilities

All homogeneous deformations can be described by the movement of a configurational variable in deformation space, in general a 9 dimensional space with origin at an arbitrarily chosen reference state X . In this space any configuration can be represented by the deformation gradient J (relative to X). Moreover, if there exists particular constraints which allow us to uniquely determine J from η_X , then deformation space becomes 6 dimensional, which we call *unique* to stress the fact that any configuration can be specified in terms of η_X instead of J . As an example, in the Parrinello-Rahman method [34] for performing atomistic simulation at constant stress, J is usually constrained to be symmetric. Because J in this case can then be uniquely determined

by η_X from the equation

$$J = \sqrt{1 + 2\eta_X} = 1 + \eta_X - \frac{1}{2}\eta_X^2 + \dots$$

it is unique and we will give it a special name: symmetric deformation space.

There can be other unique deformation spaces. For instance, we can constrain J to be always upper triangular: this case corresponds to deforming a cube while constraining one edge on the x axis and one face on the xy plane. Thus J has 6 non-zero elements which can also be uniquely determined by η_X . The opposite of unique is called *general*.

The classification of deformation space is necessary: because once we have some constraints on how J can be perturbed, there might be instability paths in general deformation space, but which is forbidden in unique spaces. So when the general case is already unstable, the unique case might still be stable in the same configuration.

Since every point in deformation space is either denoted by J or η_X , we can treat it as a 9 or 6 dimensional *vector* instead of a 3×3 matrix. Define the inner product between two vectors(matrices) in deformation space to be:

$$A \cdot B = \text{Tr}(A^T B) = \sum_{i,j}^3 A_{ij} B_{ij} \quad (2.220)$$

We have

$$\begin{aligned} A \cdot B &= B \cdot A \\ A \cdot (B + C) &= A \cdot B + A \cdot C \\ A \cdot A &\geq 0 \end{aligned} \quad (2.221)$$

thus it has the properties of Euclidean space and the measure of distance between vectors is well defined.

The purpose of this thesis is to study the stability behavior of materials under finite deformation. Obviously some kind of external loading must be present. It turns

out that the accurate description of this loading condition is crucial to our stability analysis because we rely on second-order expansions: thus the loading condition itself should be exactly determined to at least second order. A certain stability criteria is only for a certain loading condition.

From now on we focus our attention on the so called $(NT\tau)$ ensemble, meaning constant particle number N , constant temperature T , and constant *external stress* τ , which is defined in previous section and commonly used in engineering. Before going further, the authors want to make it clear that we choose this ensemble to be our model system not because we have impeccable justifications for it, nor do we insist on using it if a better description for a specific problem is available. Nevertheless, the approach we took here is universal and can be applied onto any system once the loading condition is known, so that the virtual work integral can be written down. The $(NT\tau)$ ensemble is considered to be the appropriate carrier for our discussion because it is the most commonly used scenario, and leads to analytical results quickly.

As a warning, we think that some researchers might be unsatisfied with the fact (as we will show later) that $(NT\tau)$ ensemble is a dissipative system and no valid thermodynamic potential exists: we want to say that (as far as in our knowledge) we are the ones to first point out this feature clearly, not because we like it. On the other hand, this situation enable us to set up an *ad hoc* theory based on thermodynamic driving force in deformation space in the absence of a potential, and stability criteria derived from this formalism will naturally lead to the symmetrization of the B matrix, which in turn can be understood as mapping a dissipative system onto an equivalent conservative system with a symmetric A . This justifies the practical applicability of the $(NT\tau)$ stability criteria, because in realistic situations when the second order feature of a certain loading condition is not known, we can use the $(NT\tau)$ criteria as a reasonable guess, which only requires input from the stress condition. Since constant τ does capture the main feature of many applications, we'd expect the criteria to be of some predictive value.

Let's start from the beginning: there is a direct analogy between the commonly used (NTP) ensemble and $(NT\tau)$ ensemble, in fact the former belongs to the latter.

The thermodynamic potential for (NTP) ensemble is the Gibbs free energy

$$G = F(N, T, V) + PV \quad (2.222)$$

The stability criteria for this system is the requirement of convexity of V under constant thermodynamic field (NTP). The term PV in (2.222) is just the virtual work integral. (The significance of thermodynamic potentials come from the second law of thermodynamics: $dS \geq 0$, and are generated by integrating the inequality under different constraint conditions.) We get the corresponding virtual work term for ($NT\tau$) ensemble.

Imagine a path l in deformation space which starts from X and ends at Z . We want to know the net work done by external stress τ when we reach Z if we deform the object along this path. To calculate this, let Y to be any point on the path: $Y = JX$, and make a small deformation: $J \rightarrow J + \delta J$. This would cause displacements on the surface area of this material by δu_i , and the work done by τ is then given by surface integral

$$\begin{aligned} \delta W &= \oint_S \tau_{ij} n_j \cdot \delta u_i dS \\ &= \int_Y \nabla \cdot (\tau \delta u) dV \\ &= \Omega(Y) \tau_{ij} \frac{\partial \delta u_i}{\partial Y_j} \\ &= \Omega(Y) \frac{\tau_{ij}}{2} \left(\frac{\partial \delta u_i}{\partial Y_j} + \frac{\partial \delta u_j}{\partial Y_i} \right) \end{aligned} \quad (2.223)$$

Here δu is the virtual displacement on the surface. Making use the fact that $\delta u = (\delta J)X = \delta J \cdot J^{-1}Y$, which leads to

$$\delta W = \Omega(Y) \frac{\tau_{ij}}{2} (\delta J \cdot J^{-1} + J^{-T} \cdot \delta J^T)_{ij} \quad (2.224)$$

and the fact that the differential of (2.1) is

$$\delta \eta_X = \frac{1}{2} [J^T \delta J + (\delta J^T) J] \quad (2.225)$$

or

$$J^{-T} \delta \eta_X J^{-1} = \frac{1}{2} [\delta J \cdot J^{-1} + J^{-T} \cdot \delta J^T]$$

we obtain for the incremental (differential) work,

$$\delta W = \Omega(Y) \text{Tr}(J^{-1} \tau J^{-T} \delta \eta_X) \quad (2.226)$$

The work done over the deformation path l is therefore

$$\Delta W(l) = \int_l \Omega(Y) \text{Tr}(J^{-1} \tau J^{-T} d\eta_X) \quad (2.227)$$

To examine system stability at configuration X we consider the difference between the increase in Helmholtz free energy and the work done by external stress,

$$\begin{aligned} \Delta G(Y, l) &= \Delta F(X, \eta_X) - \Delta W(l) \\ &= \int_l \text{Tr}(g(Y) d\eta_X) \\ &= \int_l \vec{g}(Y) \cdot d\vec{\eta}_X \end{aligned} \quad (2.228)$$

with

$$g(Y) = \frac{\partial F}{\partial \eta_X} - \Omega(Y) J^{-1} \tau J^{-T} \quad (2.229)$$

We define ΔG to be the *Gibbs integral* in analogy with the Gibbs free energy, and identify $-\vec{g}(Y)$ as the Gibbs driving force, a *vector* field spanning deformation space whose path integral has the meaning of work. However, we have to show that this “work” is path independent to establish it as a potential. If it is, then everything is fine. If it is not, and yet we want to do something about the problem, we can go to the lower level and study the properties of $-\vec{g}(Y)$ as a force field around equilibrium position, to formulate an *ad hoc* theory. In both cases the Gibbs driving force and its derivatives will play a central role.

Virtual work expression (2.227) is correct for general deformation spaces. However, when J is not a function of η_X it is not always convenient to use the form.

Sometimes we use another quantity

$$U = J - 1 \quad (2.230)$$

which fully describe the configuration and has 9 degrees of freedom, thus

$$\eta_X = \frac{1}{2} \{ (1 + U^T)(1 + U) - 1 \} \quad (2.231)$$

Differentiate (2.231) and take back into (2.228). Make use of the fact that g_{ij} is a symmetric matrix, we get the integral expression for general deformation space in U representation:

$$\begin{aligned} \Delta G(Y, l) &= \Delta F(X, \eta_X) - \Delta W(l) \\ &= \int_l \text{Tr} (g^*(Y) dU) \\ &= \int_l \vec{g}^*(Y) \cdot d\vec{U} \end{aligned} \quad (2.232)$$

with

$$\begin{aligned} g^*(Y) &= g(1 + U^T) \\ &= \left\{ \frac{\partial F}{\partial \eta_X} - \Omega(Y) J^{-1} \tau J^{-T} \right\} (1 + U^T) \end{aligned}$$

Symmetric Deformation Space

In this section and next we study stability behaviors in symmetric deformation space, which is often used in computer simulation. Since there is a one to one correspondence between η_X and J , the space is 6 dimensional and all related second-rank tensors(strain, stress) can be treated as *vectors* in space.

$-\vec{g}(Y)$ is defined as the Gibbs driving force in view of (2.228). Under the metrics of the space in which the forces are defined, $-\vec{g}(Y)$ points to the direction of *steepest descent* of the Gibbs integral, i.e, if a virtual move is made in the same direction as $-\vec{g}(Y)$, the system will have the most significant net loss combining the effect of de-

creasing its Helmholtz free energy and letting work done by the outside environment. So in a quasi-static process, the direction $-\vec{g}(Y)$ is pointing at should the be the most likely direction of action for system at Y , and its trajectory would be the flow line of this vector field. As an example, suppose we put a point charge into an electric field and make such that it moves quasi-statically, the trajectory will follow the flow line of the electric field, although in order to do this, the electric field does not need to have a potential: $\nabla \times \vec{E} = 0$.

The condition for equilibrium at X is simply the requirement of vanishing driving force:

$$\begin{aligned} g_{ij}(X) &= [\frac{\partial F}{\partial \eta_{ij}} - \Omega(Y)(J^{-1}\tau J^{-T})_{ij}]_{J=1} \\ &= \Omega(X)[t_{ij}(X) - \tau_{ij}] \\ &= 0 \end{aligned} \tag{2.233}$$

or

$$t_{ij}(X) = \tau_{ij} \tag{2.234}$$

which states the equality between thermodynamic stress and external stress means equilibrium.

Suppose the system, initially at equilibrium: $\vec{g}(X) = 0$, is perturbed to configuration Y with corresponding strain η_X . In view of (2.229) the first-order expansion for $\vec{g}(Y)$ becomes

$$\begin{aligned} g_{ij}(Y) &= g_{ij}(\eta_X^Y, X) \\ &= \Omega(X)B_{ijkl}\eta_{kl} + \dots \end{aligned} \tag{2.235}$$

where

$$B_{ijkl} = C_{ijkl} - \frac{\partial(\det |J| J_{im}^{-1} \tau_{mn} J_{nj}^{-1})}{\partial \eta_{kl}} \Big|_{\eta_X=0, J=1} \tag{2.236}$$

Since

$$J^{-1} = \frac{1}{\sqrt{1+2\eta_X}} = 1 - \eta_X + \dots \tag{2.237}$$

$$\det |J| = 1 + \text{Tr}(\eta_X) + \dots \quad (2.238)$$

(2.236) can be evaluated to give

$$B_{ijkl} = C_{ijkl} - \delta_{kl}\tau_{ij} + \delta_{ik}\tau_{jl} + \delta_{jl}\tau_{ik} \quad (2.239)$$

As η_{ij} and η_{ji} (η_{kl} and η_{lk}) are not separate variables, we need to symmetrize (2.239) with respect to the interchange of indices ($i \leftrightarrow j$) and ($k \leftrightarrow l$). Thus,

$$\begin{aligned} B_{ijkl} & \\ &= C_{ijkl} + \frac{1}{2}(\delta_{ik}\tau_{jl} + \delta_{jk}\tau_{il} + \delta_{il}\tau_{jk} + \delta_{jl}\tau_{ik} - 2\delta_{kl}\tau_{ij}). \end{aligned} \quad (2.240)$$

(2.240) is the expression defining the elastic stiffness coefficient [4] B . We can see that B does not possess $(ij) \leftrightarrow (kl)$ symmetry, so ΔG is path dependent in general, unless the applied load is hydrostatic, i.e., $\tau_{ij} \propto \delta_{ij}$.

The physical meaning of (2.235) is that in deformation space the shape of force field around the origin is described by the “second-rank tensor” B . Consider the following inner product between two vectors

$$\lambda = \vec{\eta}_X \cdot B \vec{\eta}_X \quad (2.241)$$

$\vec{\eta}_X$ is the displacement from the origin, $-B\vec{\eta}_X$ is the direction of driving force, thus the most likely direction for system evolution, at point Y . If we can show that $\lambda > 0$ for any $\vec{\eta}_X$, then in a quasi-static process the perturbed system will always be decreasing its distance with the origin. And thus the system is stable. On the other hand if there exists an $\vec{\eta}_X$ for which $\lambda < 0$, then a kinetic path could lead the system to instability.

Given that B is asymmetric in general, the stability of the system is governed by its symmetrized counterpart,

$$A = \frac{1}{2}(B^T + B) \quad (2.242)$$

because

$$\begin{aligned}\lambda &= \vec{\eta}_X \cdot B \vec{\eta}_X \\ &= \frac{1}{2} \vec{\eta}_X \cdot (B^T + B) \vec{\eta}_X\end{aligned}\tag{2.243}$$

for any vector $\vec{\eta}_X$. The stability criterion is then the requirement that all the eigenvalues of A be positive. Stated another way, the system becomes unstable when

$$\det |A| = 0\tag{2.244}$$

for the first time. We can also think of it as mapping a dissipative system unto its equivalent conservative system with a symmetric effective A , after some coarse-graining.

Implementations

In the actual implementation of the criterea, we use Voigt's notation:

$$\begin{array}{ll}\text{Original } ij \text{ (or } kl\text{):} & 11 \quad 22 \quad 33 \quad 23 \quad 13 \quad 12 \\ \text{Contracted notation:} & 1 \quad 2 \quad 3 \quad 4 \quad 5 \quad 6\end{array}$$

As said before, symmetric deformation space has only 6 independent variables, but since it is easier to sum over Cartesian indices, we had always treated it as if we had 9. Time has come to change back to explicitly 6 variables, because η_{ij} and η_{ji} are bound together and an instability eigen-mode which has $\eta_{ij} \neq \eta_{ji}$ is not possible. Please be reminded that when we use Voigt's notation the times of η_4 (or η_5, η_6) appearing should be doubled because it represent both η_{12} and η_{21} .

In general a 9×9 matrix (not necessarily $(ij) \leftrightarrow (kl)$ symmetric, but has $(i \leftrightarrow j)$ and $(k \leftrightarrow j)$ symmetry), with row and column index arraying as $\{11, 22, 33, 12, 13, 23, 21, 31, 32\}$, contracts into a 6×6 matrix in Voigt's notation in the following manner:

$$\begin{vmatrix} A & B & B \\ C & D & D \\ C & D & D \end{vmatrix} \Rightarrow \begin{vmatrix} A & 2B \\ 2C & 4D \end{vmatrix}\tag{2.245}$$

Following this contraction rule, we can write down:

$$B_{6 \times 6} = C_{6 \times 6} + W_{6 \times 6} \quad (2.246)$$

In view of (2.240), we get the general form of W :

$$W_{6 \times 6} = \begin{bmatrix} \tau_{11} & -\tau_{11} & -\tau_{11} & 2\tau_{12} & 2\tau_{13} & 0 \\ -\tau_{22} & \tau_{22} & -\tau_{22} & 2\tau_{12} & 0 & 2\tau_{23} \\ -\tau_{33} & -\tau_{33} & \tau_{33} & 0 & 2\tau_{13} & 2\tau_{23} \\ 0 & 0 & -2\tau_{12} & 2\tau_{11} + 2\tau_{22} & 2\tau_{23} & 2\tau_{13} \\ 0 & -2\tau_{13} & 0 & 2\tau_{23} & 2\tau_{11} + 2\tau_{33} & 2\tau_{12} \\ -2\tau_{23} & 0 & 0 & 2\tau_{13} & 2\tau_{12} & 2\tau_{22} + 2\tau_{33} \end{bmatrix} \quad (2.247)$$

Because $W_{6 \times 6}$ is asymmetric,

$$A = \frac{1}{2}(B + B^T) = C + \frac{1}{2}(W + W^T) \quad (2.248)$$

so,

$$A_{6 \times 6} = C_{6 \times 6} + \begin{bmatrix} \tau_{11} & \frac{\tau_{11} + \tau_{22}}{-2} & \frac{\tau_{11} + \tau_{33}}{-2} & \tau_{12} & \tau_{13} & -\tau_{23} \\ \frac{\tau_{11} + \tau_{22}}{-2} & \tau_{22} & \frac{\tau_{22} + \tau_{33}}{-2} & \tau_{12} & -\tau_{13} & \tau_{23} \\ \frac{\tau_{11} + \tau_{33}}{-2} & \frac{\tau_{22} + \tau_{33}}{-2} & \tau_{33} & -\tau_{12} & \tau_{13} & \tau_{23} \\ \tau_{12} & \tau_{12} & -\tau_{12} & 2\tau_{11} + 2\tau_{22} & 2\tau_{23} & 2\tau_{13} \\ \tau_{13} & -\tau_{13} & \tau_{13} & 2\tau_{23} & 2\tau_{11} + 2\tau_{33} & 2\tau_{12} \\ -\tau_{23} & \tau_{23} & \tau_{23} & 2\tau_{13} & 2\tau_{12} & 2\tau_{22} + 2\tau_{33} \end{bmatrix} \quad (2.249)$$

Example 1: Hydrostatic Tension

Hydrostatic tension [38, 41] is the only case which retains the original symmetry of the crystal, and has true Gibbs free energy. For crystals with cubic symmetry:

$$C_{6 \times 6} = \begin{bmatrix} C_{11} & C_{12} & C_{12} & & & \\ C_{12} & C_{11} & C_{12} & & & \\ C_{12} & C_{12} & C_{11} & & & \\ & & & 4C_{44} & & \\ & & & & 4C_{44} & \\ & & & & & 4C_{44} \end{bmatrix} \quad (2.250)$$

Let $\tau_{11} = \tau_{22} = \tau_{33} = T$ and refer to (2.247), we get

$$W_{6 \times 6} = \begin{bmatrix} T & -T & -T & & & \\ -T & T & -T & & & \\ -T & -T & T & & & \\ & & & 4T & & \\ & & & & 4T & \\ & & & & & 4T \end{bmatrix} \quad (2.251)$$

so

$$B_{6 \times 6} = \begin{bmatrix} C_{11} + T & C_{12} - T & C_{12} - T & & & \\ C_{12} - T & C_{11} + T & C_{12} - T & & & \\ C_{12} - T & C_{12} - T & C_{11} + T & & & \\ & & & 4(C_{44} + T) & & \\ & & & & 4(C_{44} + T) & \\ & & & & & 4(C_{44} + T) \end{bmatrix} \quad (2.252)$$

Just by inspection we can see that

$$C_{44} + T = 0 \quad (2.253)$$

$$C_{11} - C_{12} + 2T = 0 \quad (2.254)$$

$$C_{11} + 2C_{12} - T = 0 \quad (2.255)$$

are the three instability modes. The first one is 3-fold degenerate, and is called shear instability because the crystal tends to change shape without changing volume. The second one is 2-fold degenerate, and is defined as the Born instability: it shows that the material will automatically break the symmetry by elongating in one direction and shrinking in the other. The third one is defined as spinodal instability in the sense of weak bulk modulus, this is the case where the material is collapsing as a whole, which happens in solid state amorphization [39].

Example 2: Uniaxial Tension

Impose uniaxial tension $\tau_{11} = T$ on an originally cubic crystal. It will break the symmetry, with

$$C_{6 \times 6} = \begin{bmatrix} C_{11} & C_{12} & C_{12} & & & \\ C_{12} & C_{22} & C_{23} & & & \\ C_{12} & C_{23} & C_{22} & & & \\ & & & 4C_{44} & & \\ & & & & 4C_{44} & \\ & & & & & 4C_{66} \end{bmatrix} \quad (2.256)$$

and

$$W_{6 \times 6} = \begin{bmatrix} T & -T & -T & & & \\ 0 & 0 & 0 & & & \\ 0 & 0 & 0 & & & \\ & & & 2T & & \\ & & & & 2T & \\ & & & & & 0 \end{bmatrix} \quad (2.257)$$

so

$$A_{6 \times 6} = \begin{bmatrix} C_{11} + T & C_{12} - \frac{T}{2} & C_{12} - \frac{T}{2} & & & \\ C_{12} - \frac{T}{2} & C_{22} & C_{23} & & & \\ C_{12} - \frac{T}{2} & C_{23} & C_{22} & & & \\ & & & 4C_{44} + 2T & & \\ & & & & 4C_{44} + 2T & \\ & & & & & 4C_{66} \end{bmatrix} \quad (2.258)$$

From lower half of matrix we get two modes,

$$C_{66} = 0 \quad (2.259)$$

$$C_{44} + \frac{1}{2}T = 0 \quad (2.260)$$

corresponding to the shear instability.

From the upper half we get one obvious mode

$$C_{22} - C_{23} = 0 \quad (2.261)$$

corresponding to the Born instability.

The last two modes are not obvious, but has to rely on this quadratic equation:

$$2(C_{12} - \frac{T}{2})^2 - (C_{22} + C_{23})(C_{11} + T) = 0 \quad (2.262)$$

General Deformation Space

All arguments used in constructing the “ A criterea” for symmetric deformation space still hold for general deformation space, the only difference is that we have 9 degrees of freedom, so we should use the representation of (2.232),

$$\Delta G(Y, l) = \int_l \text{Tr} (g^*(Y) dU)$$

with

$$\begin{aligned} g^*(Y) &= g(1 + U^T) \\ &= \left\{ \frac{\partial F}{\partial \eta_X} - \Omega(Y) J^{-1} \tau J^{-T} \right\} (1 + U^T) \end{aligned}$$

It is easy to show that

$$J^{-1} = \frac{1}{1 + U} = 1 - U + \dots \quad (2.263)$$

$$J^{-T} = 1 - U^T + \dots \quad (2.264)$$

$$\det |J| = 1 + \text{Tr}(U) + \dots \quad (2.265)$$

and

$$\begin{aligned} \eta_X &= \frac{1}{2} (J^T J - 1) \\ &= \frac{1}{2} (U^T + U) + \dots \end{aligned} \quad (2.266)$$

The condition for equilibrium at X remains to be:

$$\begin{aligned} g_{ij}^*(X) &= g(1 + U^T) \Big|_{J=1, U=0} \\ &= \Omega(X) (t_{ij}(X) - \tau_{ij}) \\ &= 0 \end{aligned} \quad (2.267)$$

Suppose $g^*(X) = 0$ and we want to do first order expansion for $g^*(Y)$ near X . Since g is first order itself, we can ignore the $(1 + U^T)$ term behind it. Thus

$$g^* \simeq g \quad (2.268)$$

and

$$g_{ij} = \partial F / \partial \eta_X - \Omega(Y) J^{-1} \tau J^{-T}$$

$$\begin{aligned}
&\simeq \Omega(X)\{C_{ijkl}\eta_{kl} - U_{kk}\tau_{ij} + U_{ik}\tau_{kj} + \tau_{ik}U_{jk}\} \\
&\simeq \Omega(X)\{\frac{1}{2}C_{ijkl}(U_{kl} + U_{lk}) - U_{kk}\tau_{ij} + U_{ik}\tau_{kj} + \tau_{ik}U_{jk}\} \\
&= \Omega(X)\{C_{ijkl}U_{kl} - U_{kk}\tau_{ij} + U_{ik}\tau_{kj} + \tau_{ik}U_{jk}\}
\end{aligned} \tag{2.269}$$

So

$$g_{ij}^* = \Omega(X)B_{ijkl}^*U_{kl} + \dots \tag{2.270}$$

with

$$B_{ijkl}^* = C_{ijkl} - \tau_{ij}\delta_{kl} + \tau_{jl}\delta_{ik} + \tau_{il}\delta_{jk} \tag{2.271}$$

Similar to the arguments in symmetric deformation space, stability behavior in general deformation space is governed by

$$A^* = (B^* + (B^*)^T)/2 \tag{2.272}$$

When

$$\det |A^*| = 0 \tag{2.273}$$

for the first time, the system become unstable. Note that A^* is a 9×9 matrix.

As an observation, when a configuration is stable in general deformation space, i.e., none of the eigenvalues of A^* are negative, the configuration would be stable in all deformation spaces.

2.4.2 Deformation of a Periodic Simulation Cell

Basic setup

We will simulate particle systems that interact via short-ranged potentials of cutoff radius r_{cut} . Given any radial function $w(r)$, this can be done by redefining a $\tilde{w}(r)$,

$$\tilde{w}(r) \equiv \begin{cases} w(r) - w(r_{\text{cut}}) - w'(r_{\text{cut}})(r - r_{\text{cut}}), & 0 < r < r_{\text{cut}} \\ 0, & r \geq r_{\text{cut}} \end{cases}, \tag{2.274}$$

which² ensures continuity in both energy and forces as a particle crosses $r = r_{\text{cut}}$. In the case of multiple-component systems, r_{cut} is generalized to a matrix $r_{\text{cut}}^{\alpha\beta}$, where $\alpha \equiv c(i), \beta \equiv c(j)$ are the chemical types of atoms i, j . As a convention, i suggests a “host” atom at the “frame origin”, whereas j suggests a “client” atom. We then define

$$\mathbf{x}_{ij} \equiv \mathbf{x}_j - \mathbf{x}_i, \quad r_{ij} \equiv |\mathbf{x}_{ij}|, \quad \hat{\mathbf{x}}_{ij} \equiv \frac{\mathbf{x}_{ij}}{r_{ij}}. \quad (2.275)$$

Quantities such as the pair force $\mathbf{f}_{ij} \equiv \left(-\tilde{V}'(r_{ij})\right) \hat{\mathbf{x}}_{ij}$ are understood as the force on j due to i . \mathbf{f}_{ij} should be *parallel* to \mathbf{x}_{ij} when the potential is *repulsive*, a mnemonic device.

The supercell is a parallelepiped, which can be tiled in space indefinitely if desired. The three edges are row vectors

$$\mathbf{a}_1 = (H_{11}, H_{12}, H_{13}), \quad \mathbf{a}_2 = (H_{21}, H_{22}, H_{23}), \quad \mathbf{a}_3 = (H_{31}, H_{32}, H_{33}), \quad (2.276)$$

in Cartesian coordinates, with $H_{\mu\nu}$ forming a 3×3 matrix \mathbf{H} .³ The position of particle i is specified by a row vector, $\mathbf{s}_i = (s_{i1}, s_{i2}, s_{i3})$, with $s_{i\mu}$ ’s usually satisfying

$$0 \leq s_{i\mu} < 1, \quad \mu = 1..3, \quad (2.277)$$

and the Cartesian coordinate of this particle, \mathbf{x}_i , also a row vector, is

$$\mathbf{x}_i = s_{i1}\mathbf{a}_1 + s_{i2}\mathbf{a}_2 + s_{i3}\mathbf{a}_3 = \mathbf{s}_i\mathbf{H}, \quad (2.278)$$

where $s_{i\mu}$ has the geometrical interpretation of the fraction of the μ th edge to build

²An alternative is to define $\tilde{w}(r) \equiv w(r) \exp(r_s/(r - r_{\text{cut}}))$ which has all derivatives continuous at $r = r_{\text{cut}}$. Another efficient scheme for the LJ6-12 potential is $w(r) \equiv 4\epsilon[(\frac{\sigma}{r})^{12} - (\frac{\sigma}{r})^6 + (2(\frac{\sigma}{r_{\text{cut}}})^{18} - (\frac{\sigma}{r_{\text{cut}}})^{12})(\frac{r}{\sigma})^6 - 3(\frac{\sigma}{r_{\text{cut}}})^{12} + 2(\frac{\sigma}{r_{\text{cut}}})^6]$, which expands in r^6 instead of r , and avoids using `sqrt` or `exp`.

³This labelling scheme is literally followed in both my C (1–3 becomes 0–2) and Fortran source codes, irrespective of *internal storage arrangements*. That is, I may sacrifice efficiency for clarity in Fortran (where *columns* are stored contiguously), to achieve easy-to-read correspondence with C source codes, where this arrangement *is* computationally more efficient for edge vector operations.

\mathbf{x}_i .

The volume of the supercell is

$$\Omega = |\det H| = |\mathbf{a}_1 \cdot (\mathbf{a}_2 \times \mathbf{a}_3)| > 0. \quad (2.279)$$

The inverse of the \mathbf{H} matrix $\mathbf{B} \equiv \mathbf{H}^{-1}$ satisfies

$$\mathbf{I} = \mathbf{H}\mathbf{B} = \mathbf{B}\mathbf{H}. \quad (2.280)$$

If we define row vectors

$$\mathbf{b}_1 \equiv (B_{11}, B_{21}, B_{31}), \quad \mathbf{b}_2 \equiv (B_{12}, B_{22}, B_{32}), \quad \mathbf{b}_3 \equiv (B_{13}, B_{23}, B_{33}), \quad (2.281)$$

then (2.280) is equivalent to

$$\mathbf{a}_i \cdot \mathbf{b}_j \equiv \mathbf{a}_i \mathbf{b}_j^T = \delta_{ij}. \quad (2.282)$$

Since \mathbf{b}_1 is perpendicular to both \mathbf{a}_2 and \mathbf{a}_3 , it must be collinear with the normal direction \mathbf{n} of the $\mathbf{a}_2/\mathbf{a}_3$ plane: $\mathbf{b}_1 \equiv |\mathbf{b}_1|\mathbf{n}$. And so by (2.282),

$$1 = \mathbf{a}_1 \cdot \mathbf{b}_1 = \mathbf{a}_1 \cdot (|\mathbf{b}_1|\mathbf{n}) = |\mathbf{b}_1|(\mathbf{a}_1 \cdot \mathbf{n}). \quad (2.283)$$

But $|\mathbf{a}_1 \cdot \mathbf{n}|$ is nothing other than the *thickness* of the supercell along the \mathbf{a}_1 edge. Therefore, the thicknesses (distances between two parallel surfaces) of the supercell are,

$$d_1 = \frac{1}{|\mathbf{b}_1|}, \quad d_2 = \frac{1}{|\mathbf{b}_2|}, \quad d_3 = \frac{1}{|\mathbf{b}_3|}. \quad (2.284)$$

The general design of the simulation should allow for deformation of \mathbf{H} that includes rotational components, even though one may choose to impose the constraint of symmetric deformation later, whose dynamics is derived in section 2.4.2. In general one should use the Lagrangian strain $\underline{\underline{\eta}}$, a true rank-2 tensor under coordinate transformation, to measure the deformation of a MD supercell as it is unlikely to be

infinitesimal. To define $\underline{\underline{\eta}}$, one needs a reference \mathbf{H}_0 of a previous time, with $\mathbf{x}_0 = \mathbf{s}\mathbf{H}_0$ and $d\mathbf{x}_0 = (d\mathbf{s})\mathbf{H}_0$, and then imagine that with \mathbf{s} and $d\mathbf{s}$ fixed, $d\mathbf{x}_0$ is transformed to $d\mathbf{x} = (d\mathbf{s})\mathbf{H}$, under $\mathbf{H}_0 \rightarrow \mathbf{H} \equiv \mathbf{H}_0\mathbf{K}$.

The Lagrangian strain is defined by the change in the differential line length,

$$dl^2 = d\mathbf{x}d\mathbf{x}^T \equiv d\mathbf{x}_0(\mathbf{I} + 2\underline{\underline{\eta}})d\mathbf{x}_0^T, \quad (2.285)$$

where by plugging in $d\mathbf{x} = (d\mathbf{s})\mathbf{H} = (d\mathbf{x}_0)\mathbf{H}_0^{-1}\mathbf{H} = (d\mathbf{x}_0)\mathbf{K}$, $\underline{\underline{\eta}}$ is seen to be

$$\underline{\underline{\eta}} = \frac{1}{2} \left(\mathbf{H}_0^{-1}\mathbf{H}\mathbf{H}^T\mathbf{H}_0^{-T} - \mathbf{I} \right) = \frac{1}{2} \left(\mathbf{K}\mathbf{K}^T - \mathbf{I} \right). \quad (2.286)$$

Because $\underline{\underline{\eta}}$ is a symmetric matrix, it always has three mutually orthogonal eigen-directions $\mathbf{x}_1\underline{\underline{\eta}} = \mathbf{x}_1\eta_1$, $\mathbf{x}_2\underline{\underline{\eta}} = \mathbf{x}_2\eta_2$, $\mathbf{x}_3\underline{\underline{\eta}} = \mathbf{x}_3\eta_3$. Along those directions, the line lengths are changed by factors $\sqrt{1+2\eta_1}$, $\sqrt{1+2\eta_2}$, $\sqrt{1+2\eta_3}$, which achieve extrema among *all* line directions. Thus, as long as η_1 , η_2 and η_3 oscillate between $[-\eta_{\text{bound}}, \eta_{\text{bound}}]$ for some chosen η_{bound} , any line segment at \mathbf{H}_0 can be lengthened by no more than $\sqrt{1+2\eta_{\text{bound}}}$ and shortened by no less than $\sqrt{1-2\eta_{\text{bound}}}$. That is, if we define length measure

$$L(\Delta\mathbf{s}, \mathbf{H}) \equiv \sqrt{\Delta\mathbf{s}\mathbf{H}\mathbf{H}^T\Delta\mathbf{s}^T}, \quad (2.287)$$

then so long as η_1 , η_2 , η_3 oscillate between $[\eta_{\min}, \eta_{\max}]$, there is

$$\sqrt{1+2\eta_{\min}} L(\Delta\mathbf{s}, \mathbf{H}_0) \leq L(\Delta\mathbf{s}, \mathbf{H}) \leq \sqrt{1+2\eta_{\max}} L(\Delta\mathbf{s}, \mathbf{H}_0). \quad (2.288)$$

One can use the above result to define a *strain session*, which begins with $\mathbf{H}_0 \equiv \mathbf{H}$ and during which no line segment is allowed to *shrink by less than a threshold* $f_c \leq 1$, *compared to its length at* \mathbf{H}_0 . This is equivalent to requiring that,

$$f \equiv \sqrt{1+2(\min(\eta_1, \eta_2, \eta_3))} \leq f_c. \quad (2.289)$$

Whenever this condition is violated, the session terminates and a new session starts

with the current \mathbf{H} as the new \mathbf{H}_0 . In my implementation of the $\mathcal{O}(N)$ molecular dynamics program, this is associated with a repartitioning of the supercell into equal-size bins, and is called a strain-induced bin repartitioning.

The purpose of a bin partition and a strain session is the following: it can be a very demanding task to determine if atoms i, j are within r_{cut} or not, *for all possible ij combinations*.⁴ Formally, this requires checking

$$r_{ij} \equiv L(\Delta \mathbf{s}_{ij}, \mathbf{H}) \leq r_{\text{cut}}. \quad (2.290)$$

Because \mathbf{s}_i , \mathbf{s}_j and \mathbf{H} are *mobile* – they differ from step to step, it appears that we have to do this at each step. This $\mathcal{O}(N^2)$ complexity would indeed be the case but for the observation that, in most MD, MC and static minimization applications, \mathbf{s}_i ’s and \mathbf{H} often change *only a little* from the previous step. Therefore, once we ensured that (2.290) hold at some previous step, we can devise a *sufficient condition* to test whether (2.290) still must hold *now* or not, at a much smaller cost. Only when this sufficient condition breaks down, which is taken to be less frequent, do we resort to a more complicated search and check in the fashion of (2.290).

My implementation of the above idea is as follows: I associate each \mathbf{s}_i with a *semi-mobile* reduced coordinate \mathbf{s}_i^a called atom i ’s *anchor*. At each step, I check if $L(\mathbf{s}_i - \mathbf{s}_i^a, \mathbf{H})$, that is, the current distance between i and its anchor, is greater than a certain $r_{\text{drift}} \geq r_{\text{drift}}^0$ or not. If it is not, then \mathbf{s}_i^a does not change; if it is, then I redefine $\mathbf{s}_i^a \equiv \mathbf{s}_i$ at this step, which is called atom i ’s *flash* incident. At i ’s flash, atom

⁴It is often more efficient to count *pairs* if the potential function allows for easy use of such “half-lists”, such as pair- or EAM potentials. In these scenarios we pick a unique “caretaker” among i and j to store the information about the ij -pair, that is, a particle’s “personal list” only keeps possible pairs that are under its own care. For load-balancing it is best if the responsibilities are distributed evenly among particles. We use a pseudo-random choice of “if $i + j$ is odd and $i > j$, or if $i + j$ is even and $i < j$, then i is the caretaker; otherwise it is j .” As $i > j$ is “uncorrelated” with whether $i + j$ is even or odd, significant “load imbalance” is unlikely to occur even if the indices correlate strongly with the atoms’ positions.

i is required to update records ⁵ of all atoms whose anchors satisfy

$$L(\mathbf{s}_j^a - \mathbf{s}_i^a, \mathbf{H}_0) \leq r_{\text{list}} \equiv \frac{r_{\text{cut}} + 2r_{\text{drift}}^0}{f_c}. \quad (2.291)$$

Note that the distance is between *anchors* instead of *atoms* ⁶, and the length is measured by \mathbf{H}_0 , not the current \mathbf{H} . (2.291) nominally takes $\mathcal{O}(N)$ work per flash, but I accelerate it to $\mathcal{O}(1)$ per flash by partitioning the supercell into $m_1 \times m_2 \times m_3$ bins at the start of the session, whose thicknesses by \mathbf{H}_0 (see (2.284)) are required to be greater than or equal to r_{list} :

$$\frac{d_1(\mathbf{H}_0)}{m_1}, \frac{d_2(\mathbf{H}_0)}{m_2}, \frac{d_3(\mathbf{H}_0)}{m_3} \geq r_{\text{list}}. \quad (2.292)$$

The bins deform with \mathbf{H} and remains commensurate with it, that is, its \mathbf{s} -partition $1/m_1, 1/m_2, 1/m_3$ remains fixed during a strain session. Each bin keeps an updated list⁷ of all *anchors* inside. Then, if at the time of i 's flash two anchors are separated by more than one bin, there would be

$$L(\mathbf{s}_j^a - \mathbf{s}_i^a, \mathbf{H}_0) > \frac{d_1(\mathbf{H}_0)}{m_1}, \frac{d_2(\mathbf{H}_0)}{m_2}, \frac{d_3(\mathbf{H}_0)}{m_3} \geq r_{\text{list}}, \quad (2.293)$$

and they cannot possibly satisfy (2.291). Therefore we only need to test (2.291) for anchors within adjacent 27 bins. To synchronize, all atoms flash at the start of a strain session. From then on, atoms flash individually whenever $L(\mathbf{s}_i - \mathbf{s}_i^a, \mathbf{H}) > r_{\text{drift}}$.⁸ We see that to maintain anchor lists that captures all solutions to (2.291) among the latest anchors, it takes only $\mathcal{O}(N)$ work per step, and the pre-factor of which is also small because flash events happen quite infrequently for a tolerably large r_{drift}^0 .

The central claim of the scheme is that if j is not in i 's anchor records (suppose

⁵Parts of the records may be stored in j 's if pairs are counted and j happens to be the caretaker of the ij pair.

⁶ $\mathbf{s}_i^a = \mathbf{s}_i$, though.

⁷When atom i flashes, it also updates the bin-anchor list if necessary.

⁸If two anchors flash at the same step in a loop, the first flash may get it wrong – that is, missing the second anchor, but the second flash will correct the mistake. The important thing here is to *not* lose an interaction.

i 's last flash is more recent than j 's), which was created *some time ago* in the strain session, then $r_{ij} > r_{\text{cut}}$. The reason is that the *current* separation between the anchor i and anchor j , $L(\mathbf{s}_j^a - \mathbf{s}_i^a, \mathbf{H})$, is greater than $r_{\text{cut}} + 2r_{\text{drift}}^0$, since by (2.288), (2.289) and (2.291),

$$L(\mathbf{s}_j^a - \mathbf{s}_i^a, \mathbf{H}) \geq f \cdot L(\mathbf{s}_j^a - \mathbf{s}_i^a, \mathbf{H}_0) > f \cdot r_{\text{list}} \geq f_c \cdot r_{\text{list}} = f_c \cdot \frac{r_{\text{cut}} + 2r_{\text{drift}}^0}{f_c}. \quad (2.294)$$

In fact, we see that the $r_{ij} > r_{\text{cut}}$ conclusion maintains if neither i or j currently drifts more than

$$r_{\text{drift}} \equiv \frac{f \cdot r_{\text{list}} - r_{\text{cut}}}{2} \geq r_{\text{drift}}^0, \quad (2.295)$$

from respective anchors. Put it another way, when we design r_{list} in (2.291), we take into consideration both atom drifts and \mathbf{H} shrinkage which both may bring ij closer than r_{cut} , but since the current \mathbf{H} shrinkage has not yet reached the designed critical value, we can convert it to more leeway for the atom drifts.

For multi-component systems, we define

$$r_{\text{list}}^{\alpha\beta} \equiv \frac{r_{\text{cut}}^{\alpha\beta} + 2r_{\text{drift}}^0}{f_c}, \quad (2.296)$$

where both f_c and r_{drift}^0 are species-independent constants, and r_{drift}^0 can be thought of as putting a lower bound on r_{drift} , so flash events cannot occur too frequently – a self-protection mechanism. At each bin repartitioning, we would require

$$\frac{d_1(\mathbf{H}_0)}{m_1}, \frac{d_2(\mathbf{H}_0)}{m_2}, \frac{d_3(\mathbf{H}_0)}{m_3} \geq \max_{\alpha,\beta} r_{\text{list}}^{\alpha\beta}. \quad (2.297)$$

And during the strain session, $f \geq f_c$, we have

$$r_{\text{drift}}^\alpha \equiv \min \left[\min_{\beta} \left(\frac{f \cdot r_{\text{list}}^{\alpha\beta} - r_{\text{cut}}^{\alpha\beta}}{2} \right), \min_{\beta} \left(\frac{f \cdot r_{\text{list}}^{\beta\alpha} - r_{\text{cut}}^{\beta\alpha}}{2} \right) \right], \quad (2.298)$$

a time- and species-dependent atom drift bound that controls whether to flash.

Improved Parrinello-Rahman method

I will present an extension to the Invariant Molecular Dynamics method [35], which was an improvement over the Parrinello-Rahman method [34]. Given reference state \mathbf{H}_0 , a material point $\mathbf{x}_0 = \mathbf{s}\mathbf{H}_0$ is carried to $\mathbf{x} = \mathbf{s}\mathbf{H}$ under transformation $\mathbf{H}_0 \rightarrow \mathbf{H} \equiv \mathbf{H}_0\mathbf{K}$ as $\mathbf{x} = \mathbf{x}_0\mathbf{K}$, and the Lagrangian strain of \mathbf{H} with respect to \mathbf{H}_0 is $(\mathbf{K}\mathbf{K}^T - \mathbf{I})/2$.

My improvement will be on the term of work done by constant external stress \mathbf{S} , under a loading condition of *constant* “traction force per surface area” – the external stress’ standard engineering definition. In Wentzcovitch the work term is the correct but restricted $-P\Omega(\mathbf{H})$ where P is the constant external pressure. It turns out that the generalization of work done by constant external pressure to constant external stress is tricky, because as will be shown next, the work done is a path integral that is generally dependent not only on the end point of the path but also on the path itself, which is to say to work done by constant external stress is not a *potential function* in \mathbf{K} -space.

At our currently strained state \mathbf{H} , there is $\mathbf{x} = \mathbf{x}_0\mathbf{K}$. For an *additional* small change in shape $\delta\mathbf{K} : \mathbf{K} \rightarrow \mathbf{K} + \delta\mathbf{K}$, each \mathbf{x} point makes a small displacement $\delta\mathbf{u}(\mathbf{x}) = \mathbf{x}_0\delta\mathbf{K} = \mathbf{x}\mathbf{K}^{-1}\delta\mathbf{K}$. Since traction force per area \mathbf{S} is being applied to \mathbf{H} ’s surface, it means additional virtual work

$$\begin{aligned}
\delta W &= \int \int_A dA S_{\mu\nu} n_\nu \delta u_\mu \\
&= \int \int \int_{\mathbf{H}} d^3\mathbf{x} (S_{\mu\nu} \delta u_\mu)_{,\nu} \\
&= \int \int \int_{\mathbf{H}} d^3\mathbf{x} S_{\mu\nu} \delta u_{\mu,\nu} \\
&= \Omega(\mathbf{H}) S_{\mu\nu} (\mathbf{K}^{-1} \delta \mathbf{K})_{\nu\mu} \\
&= \Omega(\mathbf{H}) \text{Tr} (\mathbf{S} \mathbf{K}^{-1} \delta \mathbf{K}), \tag{2.299}
\end{aligned}$$

where the Gauss’ theorem was applied on the current body \mathbf{H} to convert a surface integral to a volume integral.

Now let us consider a deformation path that starts at $\mathbf{K} = \mathbf{I}$ ($\mathbf{H} = \mathbf{H}_0$) and ends

at $\mathbf{K} = \mathbf{K}_f$ ($\mathbf{H} = \mathbf{H}_f$). The total work done is then

$$\Delta W = \oint_{\mathbf{I}}^{\mathbf{K}_f} \Omega(\mathbf{H}) \text{Tr}(\mathbf{S} \mathbf{K}^{-1} \delta \mathbf{K}), \quad (2.300)$$

and by a bit of analysis of the integrand it can be shown that ΔW thus defined is in general *path-dependent*, meaning ΔW is not a simple function of the end state \mathbf{K}_f , except for when \mathbf{S} is hydrostatic pressure: $\mathbf{S} = -P\mathbf{I}$, in which case

$$\begin{aligned} \Delta W &= -P \oint_{\mathbf{I}}^{\mathbf{K}_f} \Omega(\mathbf{H}) \text{Tr}(\mathbf{K}^{-1} \delta \mathbf{K}) \\ &= -P \Omega(\mathbf{H}_0) \oint_{\mathbf{I}}^{\mathbf{K}_f} (\det \mathbf{K}) \text{Tr}(\mathbf{K}^{-1} \delta \mathbf{K}). \end{aligned} \quad (2.301)$$

It happens that $(\det \mathbf{K}) \text{Tr}(\mathbf{K}^{-1} \delta \mathbf{K})$ is the perfect differential $\delta(\det \mathbf{K})$, and therefore

$$\Delta W = -P \Omega(\mathbf{H}_0) (\det \mathbf{K}_f - 1) = -P (\Omega(\mathbf{H}_f) - \Omega(\mathbf{H}_0)), \quad (2.302)$$

as we recover a more well-known result that is the only true deformation potential in \mathbf{K} -space.

The above may sound like an academic point, since in the physical world there *is no ready example* of constant “traction force per surface area” loading condition with respect to non-infinitesimal shape changes, except for constant external pressure (an implement, say, in the deep sea). Nonetheless, if the goal of the molecular dynamics simulation is not to reproduce some quite specific real-world loading condition and dynamics, but to serve as a generic probe of the desired parts of the material’s phase space and its Helmholtz free energy, then the dynamics proposed next (which recovers to the Wentzcovitch method when $\mathbf{S} = -P\mathbf{I}$) would be superbly fit for the purpose. It guarantees that, *if the dynamics reaches equilibrium* at \mathbf{H} , then

$$\mathbf{t}(\mathbf{H}) + \mathbf{S} = 0, \quad (2.303)$$

where $\mathbf{t}(\mathbf{H})$ is the *thermodynamic* definition of the stress of system at \mathbf{H} :

$$\mathbf{t}(\mathbf{H}) \equiv -\frac{1}{\Omega(\mathbf{H})} \cdot \left. \frac{\partial F(N, T, \mathbf{H}')}{\partial \eta_{\mathbf{H}}^{\mathbf{H}'}} \right|_{\mathbf{H}'=\mathbf{H}}, \quad (2.304)$$

which can be shown to lead to the well-known Virial summation formula:

$$t_{\mu\nu}(\mathbf{H}) = \frac{1}{\Omega(\mathbf{H})} \left\langle \sum_{i=1}^N \frac{p_{\mu}^i p_{\nu}^i}{m_i} - \left(\nabla_{\mu}^i V(\mathbf{x}^N) \right) x_{\nu}^i \right\rangle, \quad (2.305)$$

where $\langle \rangle$ means ensemble average at \mathbf{H} . Because $V(\mathbf{x}^N)$ is rotationally invariant, it can be shown that $t_{\mu\nu} = t_{\nu\mu}$.

In comparison, the Parrinello-Rahman method does not guarantee (2.303) at equilibrium: if one imposes a nominal “100 MPa shear stress”, the system will relax to a \mathbf{H} at which the average internal shear stress from the Virial sum may be only 95 MPa. Were the system loaded to \mathbf{H} in reality, the external “traction force per surface area” would also be 95 MPa, since the thermodynamic and engineering definitions of stress agree at equilibrium. This arises out of the Parrinello-Rahman method because the “100 MPa shear stress” is meant for \mathbf{H}_0 and not for \mathbf{H} . It can be readily seen in their paper because the authors treated pressure and shear components of the external stress differently, and only the pressure component was guaranteed (2.303). One may also regard what they did for the shear component as a tradeoff between theoretical clarity and ease-of-useness, because although it does not provide (2.303), the work term they assigned to the shear component is a genuine deformation potential, and there is rigorous conservation of the Hamiltonian; whereas my dynamics cannot provide such rigorous conservation due to the fact my work term (2.300) is not a rigorous potential. However I can approximate (2.300) by a potential, which allows for rough conservation.⁹

⁹The conservation feature is not critically important in MD simulations, but *is* necessary for static “Gibbs free energy” minimizations under constant external stress condition, because most conjugate gradient minimizers require both energy and gradient inputs and would complain if large inconsistency exists between the two.

Let me define

$$\mathbf{U} \equiv \mathbf{K} - \mathbf{I}. \quad (2.306)$$

One can approximate (2.300) by a potential $W(\mathbf{U})$,

$$W(\mathbf{U}) = \int_0^1 \left[\Omega(\mathbf{H}_0(\mathbf{I} + \lambda \mathbf{U})) \operatorname{Tr}(\mathbf{S}(\mathbf{I} + \lambda \mathbf{U})^{-1} \mathbf{U}) \right] d\lambda. \quad (2.307)$$

which is nothing other than an evaluation of (2.300) along a *straight path* linking $\mathbf{0}$ and \mathbf{U} . (2.307) can be computed using one-dimensional numerical integration (Gaussian or Romberg quadrature). On the other hand, if one is asked to provide the gradient of $W(\mathbf{U})$, it should be taken to mean,

$$\frac{\partial W(\mathbf{U})}{\partial U_{\mu\nu}} \approx \frac{\partial \Delta W}{\partial U_{\mu\nu}} = \Omega(\mathbf{H}) (\mathbf{S} \mathbf{K}^{-1})_{\nu\mu} = \Omega(\mathbf{H}) (\mathbf{K}^{-1} \mathbf{S})_{\mu\nu}, \quad (2.308)$$

following (2.299), since it is hard and out of our original purpose to evaluate the actual numerical derivative of $W(\mathbf{U})$. Thus there is slight inconsistency between the “gradient” and the potential, but which often works out satisfactorily in practice.

If \mathbf{U} is constrained to be symmetric, we have only 6 degrees of freedom, which leads to,

$$\frac{\partial W(\mathbf{U})}{\partial U_{\mu\mu}} = \Omega(\mathbf{H}) (\mathbf{K}^{-1} \mathbf{S})_{\mu\mu}, \quad \mu = 1..3. \quad (2.309)$$

$$\frac{\partial W(\mathbf{U})}{\partial U_{\mu\nu}} = \Omega(\mathbf{H}) (\mathbf{K}^{-1} \mathbf{S} + \mathbf{S} \mathbf{K}^{-1})_{\mu\nu}, \quad \mu < \nu. \quad (2.310)$$

Or, we can still nominally think of it as having 9 degrees of freedom, but letting

$$\frac{\partial W(\mathbf{U})}{\partial U_{\mu\nu}} = \Omega(\mathbf{H}) \left[\hat{S}_2 (\mathbf{K}^{-1} \mathbf{S}) \right]_{\mu\nu} \quad (2.311)$$

where \hat{S}_2 is the rank-2 symmetrization operator.

The Lagrangian is proposed to be

$$\mathcal{L}(\mathbf{s}_i, \dot{\mathbf{s}}_i, \mathbf{U}, \dot{\mathbf{U}}) = \frac{1}{2} \left(\sum_{i=1}^N m_i \dot{\mathbf{s}}_i \mathbf{G} \dot{\mathbf{s}}_i^T + W \operatorname{Tr} \dot{\mathbf{U}}^2 \right) - V(\mathbf{x}^N) + W(\mathbf{U}), \quad (2.312)$$

where \mathbf{G} is the metric

$$\mathbf{G} \equiv \mathbf{H}\mathbf{H}^T = \mathbf{H}_0\mathbf{K}^2\mathbf{H}_0^T = \mathbf{H}_0(\mathbf{I} + \mathbf{U})^2\mathbf{H}_0^T, \quad (2.313)$$

and W is a constant of unit $[\text{mass}][\text{length}]^2$ to be determined later. Then,

$$\frac{\partial \mathcal{L}}{\partial \dot{\mathbf{s}}_i} = m_i \dot{\mathbf{s}}_i \mathbf{G}, \quad (2.314)$$

$$\frac{\partial \mathcal{L}}{\partial \mathbf{s}_i} = \mathbf{f}_i \mathbf{H}^T, \quad (2.315)$$

$$\frac{\partial \mathcal{L}}{\partial \dot{\mathbf{U}}} = W \dot{\mathbf{U}}, \quad (2.316)$$

$$\frac{\partial \mathcal{L}}{\partial \mathbf{U}} = \hat{S}_2 \left(\sum_{i=1}^N m_i \dot{\mathbf{v}}_i^T \dot{\mathbf{v}}_i \mathbf{K}^{-1} \right) + \hat{S}_2 \left(\sum_{i=1}^N \mathbf{f}_i^T \mathbf{x}_i \mathbf{K}^{-1} \right) + \Omega(\mathbf{H}) \hat{S}_2 (\mathbf{K}^{-1} \mathbf{S}), \quad (2.317)$$

where \mathbf{v}_i , the nominal velocity of particle i , is defined to be

$$\mathbf{v}_i \equiv \dot{\mathbf{s}}_i \mathbf{H} = \dot{\mathbf{s}}_i \mathbf{H}_0 \mathbf{K}. \quad (2.318)$$

Then the equation of motion for \mathbf{s}_i is

$$\ddot{\mathbf{s}}_i \mathbf{G} + \dot{\mathbf{s}}_i \dot{\mathbf{G}} = \frac{\mathbf{f}_i}{m_i} \mathbf{H}^T, \quad (2.319)$$

$$\ddot{\mathbf{s}}_i = \frac{\mathbf{f}_i}{m_i} \mathbf{H}^T \mathbf{G}^{-1} - \dot{\mathbf{s}}_i \dot{\mathbf{G}} \mathbf{G}^{-1} = \frac{\mathbf{f}_i}{m_i} \mathbf{H}^{-1} - \dot{\mathbf{s}}_i \dot{\mathbf{G}} \mathbf{G}^{-1}, \quad (2.320)$$

where by plugging in (2.313),

$$\ddot{\mathbf{s}}_i = \frac{\mathbf{f}_i}{m_i} \mathbf{H}^{-1} - \dot{\mathbf{s}}_i \mathbf{H} [\mathbf{K}^{-1} \dot{\mathbf{U}} + \dot{\mathbf{U}} \mathbf{K}^{-1}] \mathbf{H}^{-1}. \quad (2.321)$$

And,

$$\ddot{\mathbf{U}} = \frac{\Omega(\mathbf{H})}{W} \hat{S}_2 [(\tilde{\mathbf{t}} + \mathbf{S}) \mathbf{K}^{-1}]. \quad (2.322)$$

where $\tilde{\mathbf{t}}$ is the instantaneous internal stress, in the same form as (2.305) but without the $\langle \rangle$.

Let me estimate the timescale τ_U of \mathbf{U} 's relaxation, given $\langle \tilde{\mathbf{t}} \rangle + \mathbf{S} \neq 0$ initially. As \mathbf{U} is almost equivalent to strain, there is $|\Delta \mathbf{t}| \sim C|\Delta \mathbf{U}|$ where C is the scale of the material's elastic constant. It is then easy to see that $\tau_U^{-2} \sim C\Omega/W$, or conversely, $W \sim C\Omega\tau_U^2$. When C is not known, a rough estimate could be $W \sim 3.0Ne_{\text{coh}}\tau_U^2$ where e_{coh} is the cohesive energy per atom and N is the number of atoms in the supercell.

As heat is generated when this relaxation occurs, τ_U should be on the same order of magnitude as the temperature coupling time constant τ_T , so that no overheating happens during the stress relaxation which might damage the configuration, such as melting. Also, to prevent runaway decohesion due to inappropriate initial condition, one might limit the amount of energy that can be carried by $W\mathbf{Tr}\dot{\mathbf{U}}^2/2$.

Chapter 3

Case Studies: Ar and SiC

3.1 Ideal Strength of Ar

Introduction

The solid and liquid states of Ar are very well understood compared to those of most materials, principally because its closed-shell electron configuration does not allow it to participate in covalent bondings with neighbors which are in general strong and complex, but only to interact via weak van der Waals bonds that are perturbational in nature and therefore mainly additive, resulting in the well-known Lennard-Jones potential function description [7].

There exists large amount of experimental results [76] for solid Ar, and many theoretical models such as the self-consistent phonon theory [4] are quite successful here. This combined with the fact that Ar has a larger mass than He and Ne which puts its dynamics satisfactorily within the classical regime at $T > T_M/2$ (T_M is the melting-point, 83.8K for Ar), make solid Ar a good testing-ground for MD simulation.

There is not a lot of experimental information on the mechanical properties of solid Ar yet. So simulation plays a leading role here, whose purpose is not for real applications but rather for revealing deformation mechanisms for fcc metals. Although there are better potentials for such metals [179, 186, 174], the Lennard-Jones potential is the simplest one that allows for calculating dimensionless constants.

In practice, however, it is not as straightforward to implement the Lennard-Jones potential as what was just said because one must impose an interaction cutoff. As I will show soon, this has a rather significant impact on the results and efficiency of the simulation. There are so many different ways people truncate their Lennard-Jones potential that sometimes the results are entirely non-transferable. I list some truncation schemes in Appendix G, hoping that at least within a small working group people reach a consensus as to what to use so they can communicate. In this chapter I always use the (G.3) scheme, with the popular $r_c = 2.5\sigma$ cutoff. $r_c = 5\sigma$ is occasionally used to approximate the $r_c = \infty$ results for contrast. But be warned that it is quite demanding to use $r_c = 5\sigma$ in real simulations. For definiteness, I use $\sigma = 3.405\text{\AA}$ and $\epsilon = 119.8\text{K} = 0.01032362805932\text{eV}$ in the Lennard-Jones potential, the standard parameters for Ar [7]. The mass is taken to be 39.948 amu.

Woon [71] recently fitted a pair potential for Ar by highly accurate quantum chemistry computations of dimer energies. Since the fitting of the potential does not rely on *any* experimental information, such potential is sometimes called *ab initio* potential [174]. This approach to potential construction has gained great popularity recently ¹ since any result one gets from this empirical potential is actually a “100%” theoretical prediction. The Woon’s potential has been used to calculate the transport properties of Ar liquids [73] and its melting curve [74]. We have also used it to compute Ar’s lattice thermal conductivity. Its results are sometimes listed side by side with the Lennard-Jones potential results for comparison.

3.1.1 General Properties

Table 3.1 lists the equilibrium properties of Ar crystals at $T = 0$. We see that there is a large difference in the cohesive energy when we use $r_c = 2.5\sigma$ cutoff for the Lennard-Jones potential. Also notice that the experimental C_{12} is very close to C_{44} , suggesting that the actual interaction is very pair-potential like.

Fig. 3-1 shows the phonon dispersion curves of $P = 0$ Ar crystals for the Lennard-

¹The construction of the ZrC_X potential in section 4.3 basically follows this approach.

	a_0 [Å]	E_{coh} [eV/at.]	C_{11} [MPa]	C_{12} [MPa]	C_{44} [MPa]
LJ ($r_c = 2.5\sigma$)	5.304986	-0.068694	3616	2074	2074
LJ ($r_c = 5\sigma$)	5.256172	-0.086259	4311	2465	2465
Woon ($r_c = 2.5\sigma$)	5.289691	-0.077184	4257	2432	2432
Woon ($r_c = 5\sigma$)	5.282308	-0.080054	4372	2495	2495
exp't [76]	5.31108	N/A	4240	2390	2250

Table 3.1: Comparison of crystalline Ar equilibrium properties at 0K.

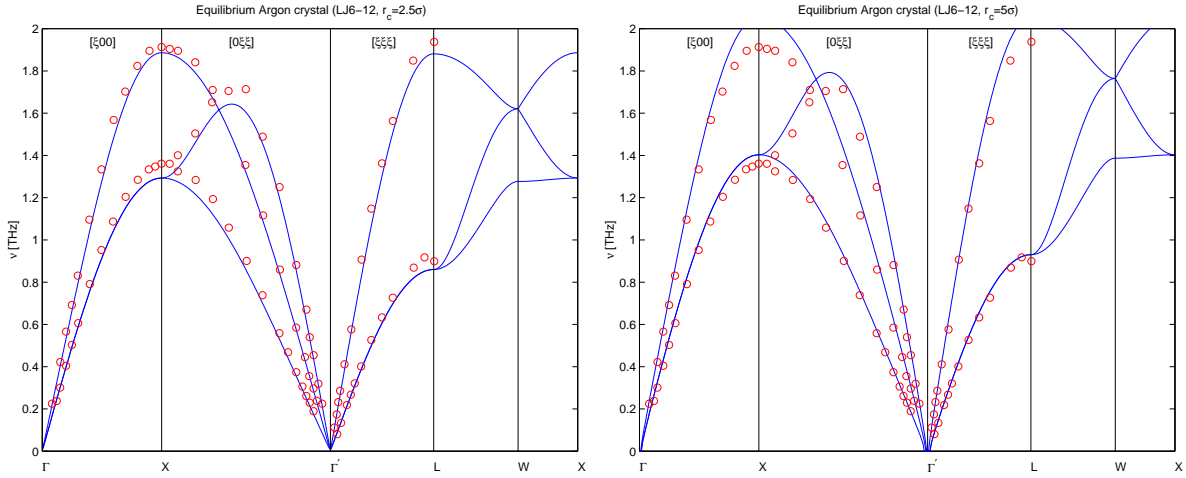


Figure 3-1: Comparison of Ar phonon dispersion at $P = 0$ of the Lennard-Jones potential (solid line) with experimental measurements [75] (^{36}Ar result (circles) is rescaled for $m = 39.948$ amu). The plot on left is $r_c = 2.5\sigma$, right is $r_c = 5\sigma$.

Jones potential at $r_c = 2.5\sigma$ and $r_c = 5\sigma$, in comparison with experiment [75], which was measured on ^{36}Ar but which is scaled to compare with $m = 39.948$ amu.

Fig. 3-2 shows the phonon density of states of Ar at $P = 0$.

The average Gruneisen parameter [223] is found to approach 2.9 at $T > 10\text{K}$ for $r_c = 5\sigma$, in fair agreement with the experimental result of 2.6. If we take the mode-specific Gruneisen parameters $\gamma_k = d \log \omega_k / d \log \Omega$ to be independent of T , but use the empirical rule that $B(T)$ linearly drop to $B(T = 0)/2$ at $T = T_M$ ², then one arrives at the thermal expansion coefficient prediction shown in Fig. 3-3, which agrees quite well with experiment.

²This rule is observed to hold well for Ar in both experiment and simulation, and also works well for most metals. However, it does not work for most ceramic materials.

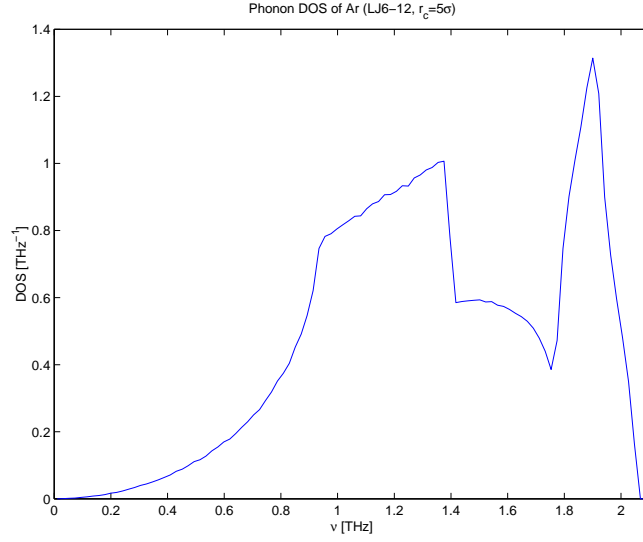


Figure 3-2: Phonon density of states of Ar at $P = 0$, using the Lennard-Jones potential with $r_c = 5\sigma$.

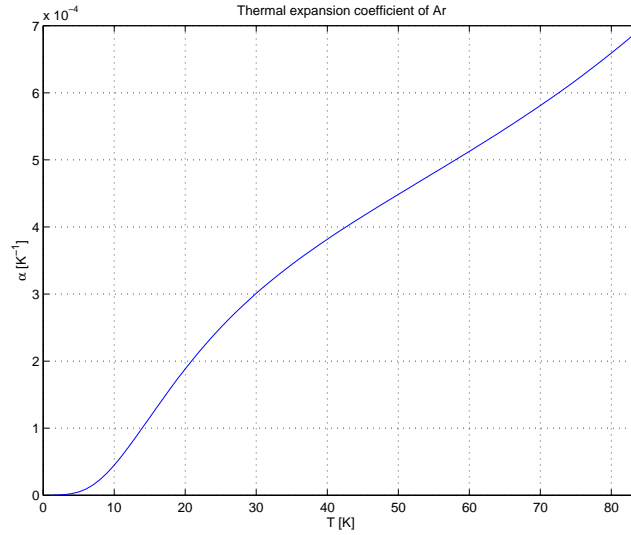


Figure 3-3: Thermal expansion coefficient of Ar predicted using the 0K phonon spectrum and Gruneisen parameter, assuming $\gamma_k = d \log \omega_k / d \log \Omega$ stay constant with T , but $B(T)$ linearly drops to $B(T = 0)/2$ at $T = T_M$.

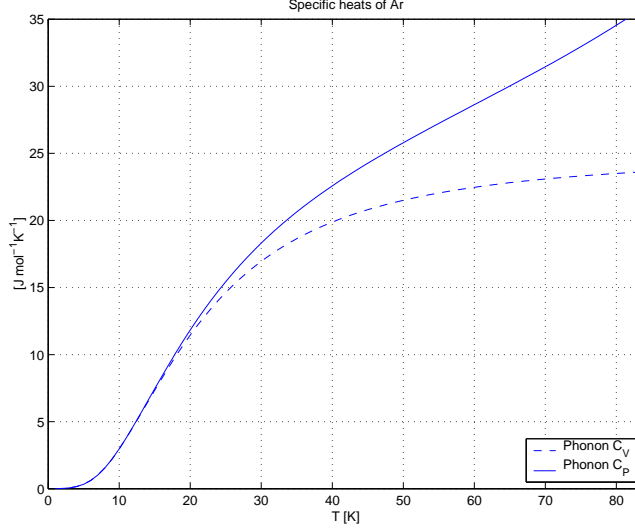


Figure 3-4: Phonon heat capacities predicted under the same assumptions as Fig. 3-3.

Under the same set of assumptions, one can predict the C_V and C_P for the system, shown in Fig. 3-4. They also agree well with experiments [76]. As I have checked by direct MD simulations, these lattice dynamical predictions are quite accurate.

I am able to generate amorphous Ar by quenching it down from a liquid while relaxing the total volume, but the configuration is found to be unstable at T above ~ 20 K, at which point one begins to observe infrequent annealing events in simulations of ~ 1 ns durations. Fig. 3-5 plots the $g(r)$ of the amorphous configuration at $T = 10$ K, showing the characteristic split second peak.

3.1.2 Lattice Dynamical Calculation of Ideal Strength

I impose shear, uniaxial, and hydrostatic strains on the $P = 0$ crystal. At a given strain magnitude, I first compute the crystal force constants, and then randomly sample the Brillouin zone 10,000 times. If none of those \mathbf{k} -points yield imaginary frequencies, then I consider the lattice system to be stable, and vice versa. Using binary search I can quickly locate the critical strain magnitude, at which point the phonon dispersions are shown in Fig. 3-6, 3-7, and 3-8.

I find that in all three cases the soft modes occur near $\mathbf{k} = 0$, and furthermore along the direction of an originally high-symmetry \mathbf{k} -point (as the Brillouin zone

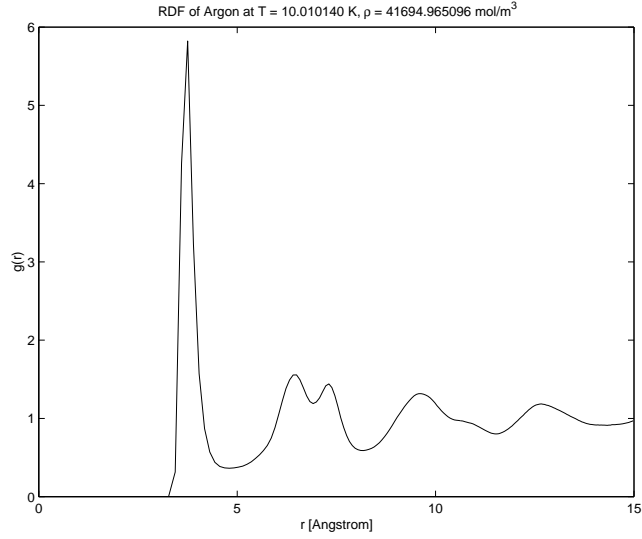


Figure 3-5: $g(r)$ of amorphous Ar at $T = 10\text{K}$.

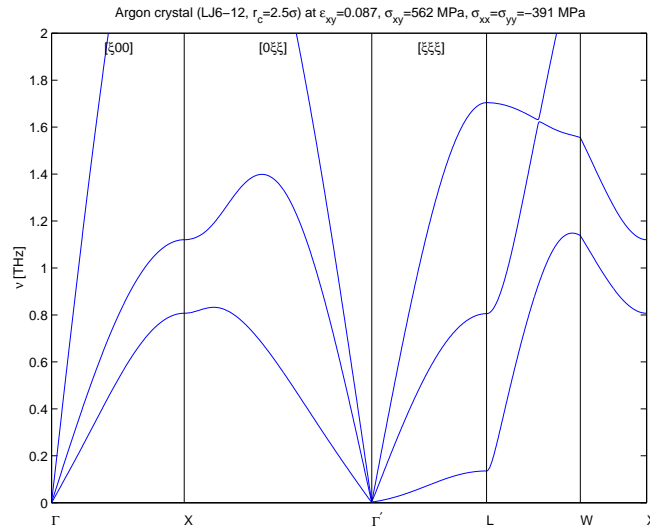


Figure 3-6: Phonon dispersion of Ar crystal under shear strain $\epsilon_{xy} = 0.087$, with $\sigma_{xy} = 562 \text{ MPa}$, $\sigma_{xx} = \sigma_{yy} = -391 \text{ MPa}$. A label tracks only one of the original high-symmetry \mathbf{k} -points. Notice the Γ' -point soft mode in the $[111]$ direction.

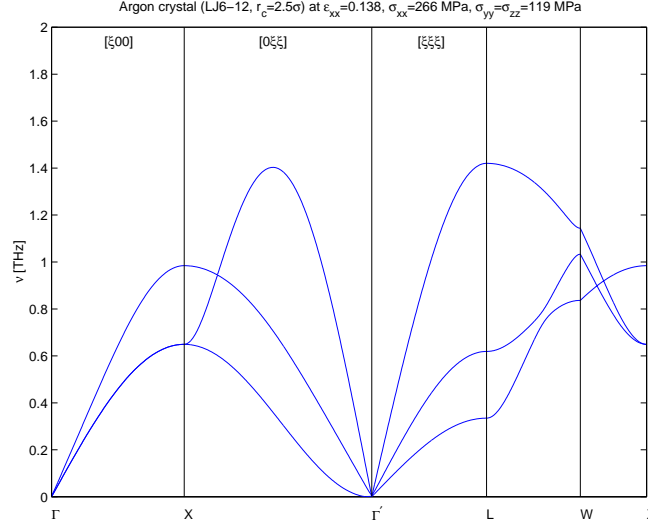


Figure 3-7: Phonon dispersion of Ar crystal under uniaxial tensile strain $\epsilon_{xx} = 0.138$, with $\sigma_{xx} = 266$ MPa, $\sigma_{yy} = \sigma_{zz} = 119$ MPa. A label tracks only one of the original high-symmetry \mathbf{k} -points. Notice the Γ' -point soft mode in the $[011]$ direction.

deforms with the lattice) which makes the task of illustration easier.

The value of the critical shear stress in Fig. 3-6 appears to be unreasonably large, but actually is not so because it is not the resolved shear stress in the $[11\bar{2}](111)$ slip system. A more careful stress analysis can be found in section 5.2 for Cu. More work still needs to be done before one can chart out the ideal strength behavior of the Lennard Jones system.

3.1.3 MD Simulation of Ideal Strength

Direct MD simulations of the uniaxial deformation on Ar perfect crystal are performed at finite temperatures. Fig. 3-9 shows the stress-strain curve at $T = 35.9$ K. The first cusp occurs at $\epsilon_{xx} \approx 0.1$, with $\sigma_{xx} \approx 130$ MPa, followed by a second, almost identical cusp at $\epsilon_{xx} \approx 0.15$ at nearly the same stresses.

The atomistic configurations corresponding to the (a), (b), (c) arrows in Fig. 3-9 are shown in Fig. 3-10. We see that in (a), several local inhomogeneities very much like point defects are formed. They have not yet relieve the stored strain energy, but will soon serve as nucleation sites for a bigger defect that will release the strain energy on a massive scale. In (b), which is immediately after the release, we can clearly see

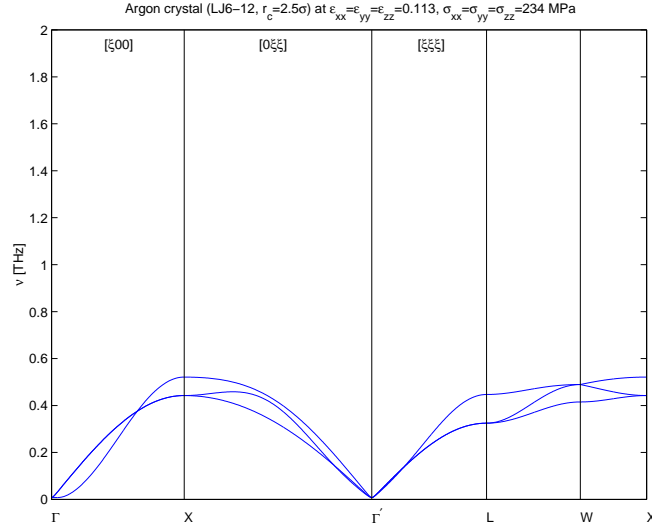


Figure 3-8: Phonon dispersion of Ar crystal under hydrostatic tensile strain $\epsilon_{xx} = \epsilon_{yy} = \epsilon_{zz} = 0.113$, with $\sigma_{xx} = \sigma_{yy} = \sigma_{zz} = 234$ MPa. Notice the Γ -point soft mode in the $[100]$ direction.

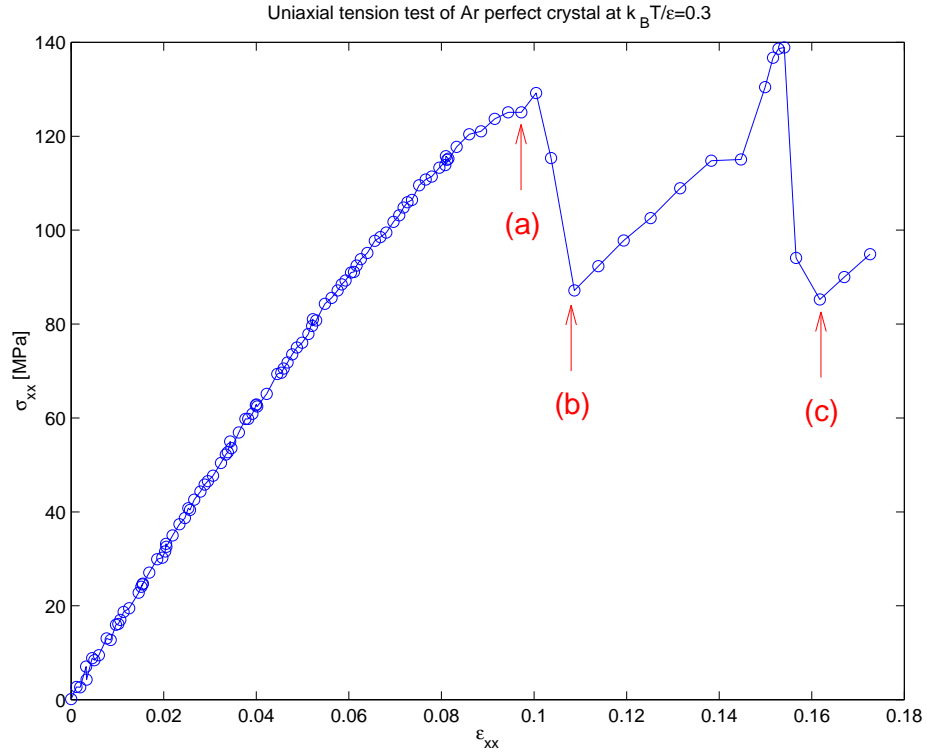


Figure 3-9: Stress-strain curve in the uniaxial deformation of Ar perfect crystal at $T = 0.3\epsilon/k_B = 35.9$ K.

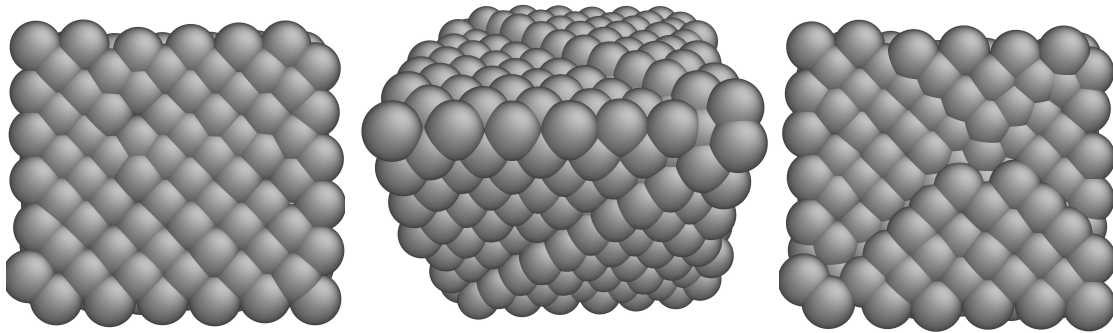


Figure 3-10: Configurations corresponding to (a), (b), (c) arrows in Fig. 3-9.

that an elementary slip has occurred on an entire (111) plane. This process happens so fast in the small system that it is hard to capture the intermediate configurations, but figuratively speaking the following must have happened: a dislocation loop is spontaneously created on the (111) plane, which enlarges at a very high speed, coalesces with other loops (or what I have called inhomogeneities), until in the end it annihilates with itself on the opposite side of PBC, and an entire (111) plane would have shifted, either by $\mathbf{b} = [\bar{1}01]/2$, or by $[11\bar{2}]/6$, creating a stacking fault (which is the case here).

It is found that after (b), the material rotated a bit in such a way that the resolved shear stress on the slipped plane becomes less than that on planes of other orientations which have not slipped. Therefore as I keep increasing the strain, it is more likely that the next slip would occur on a different plane, or slip system. And indeed the configuration (c) indicates such. This activation of several different slip systems to accommodate a single mode of deformation is related to the idea of geometrically necessary dislocations [116].

Let us extend the discussion a bit to inhomogeneous loading. In the case here, the loading is homogeneous, and so everywhere on the slip plane is equally driven, and the dislocation loop, once formed, would have no relief until it sweeps clean everything and annihilates. Suppose the stress is inhomogeneous, such as under an indenter, then the dislocation loop may nucleate and propagate very fast initially,

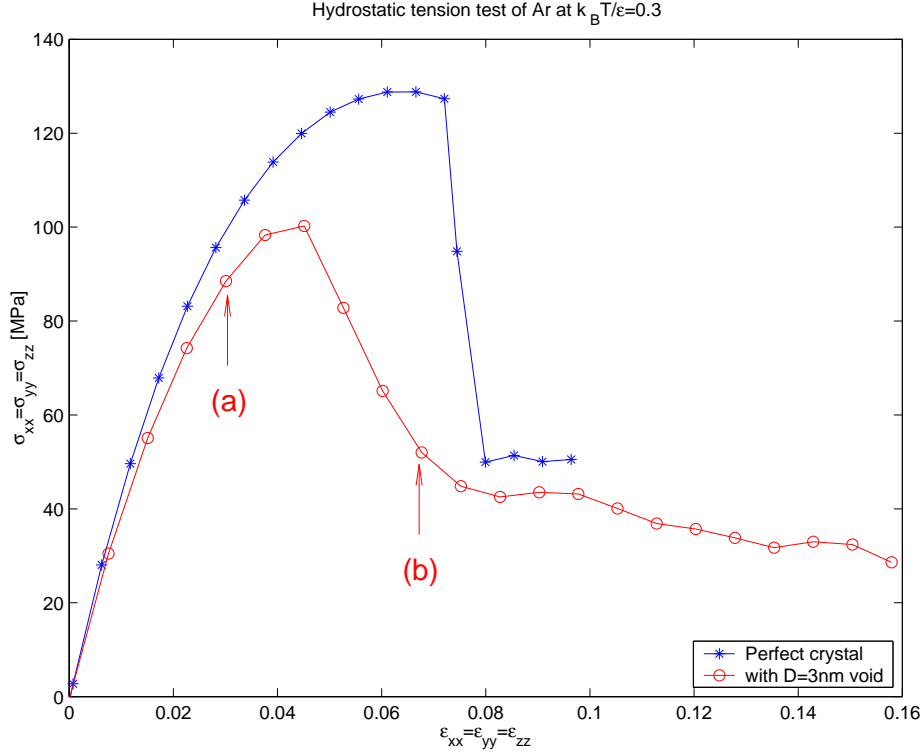


Figure 3-11: Comparison of stress-strain curves in the hydrostatic deformation of Ar perfect crystal (star) and an 8 nm volume element with a void of 3 nm in diameter (circle).

but as it travels to less and less driven regions it slows down and eventually stops by the Peierls barrier. Thus we would have generated a dislocation loop at the border of the instability region, which would not move unless, say, the indenter is pushed further. Therefore, there is an intimate relation between the simple example in Fig. 3-9, 3-10, and the dislocation nucleation problem [136, 144].

In the second example, I conducted hydrostatic deformation simulation on Ar perfect crystal, to compare with that on a volume element of 8 nm in width with a built-in void of diameter 3 nm. The stress-strain curves are shown in Fig. 3-11. While the instability cusp is sharp for the perfect crystal, it is rather soft for the volume element with the void.

A closer look at the configurations indicates that the perfect crystal remains largely defect-free ³ up to the cusp, while the voided configuration already has a lot of new

³The said “inhomogeneities” of course exist due to soft long waves, but at a much smaller

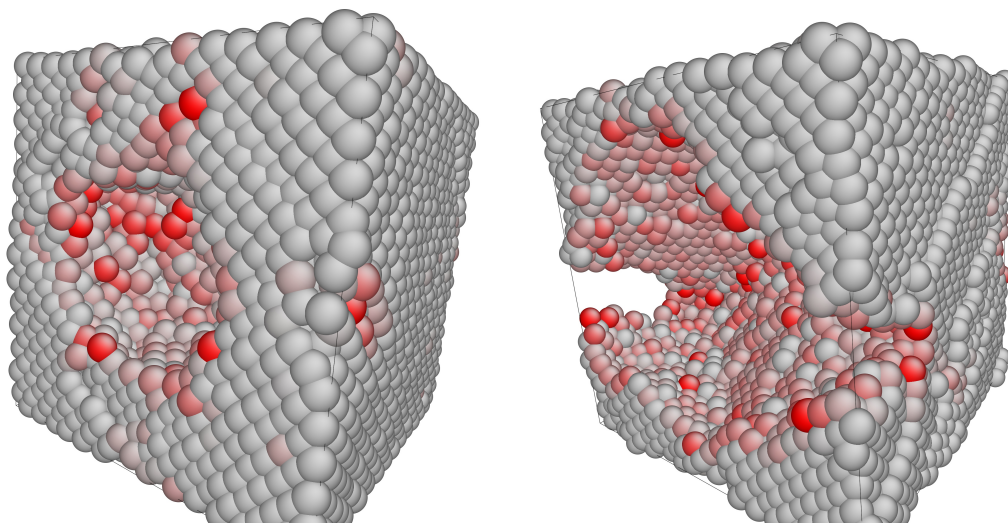


Figure 3-12: Configurations corresponding to (a) and (b) arrows in Fig. 3-11. Atomistic local strain is color-encoded.

defects long before its own main transition (Fig. 3-12). Those defects should already have released some of the strain energy, making the peak resistance somewhat softer.

To understand this behavior we should continue the discussion in the first example. After putting in microstructures, even an overall homogeneous strain would cause inhomogeneous local stresses. Especially, near the void, there should be a stress concentration factor, which makes the transition occur earlier in certain lattice regions near the void. However, as soon as the inhomogeneities run a little further, they cannot find enough local support and therefore are arrested. The main transition only happens when an inhomogeneity can run all the way across the cell, causing a catastrophe. In this case it can be postulated for (b) that the catastrophe is the creation of a link between two image voids, in the form of a crack.

3.2 Thermal Conductivity of Ar

There are three main approaches to calculating the thermal conductivity of condensed matter excluding the electron contribution: the first is the vibrational analysis approach, which in the case of a perfect crystal is exemplified by solving the phonon

concentration.

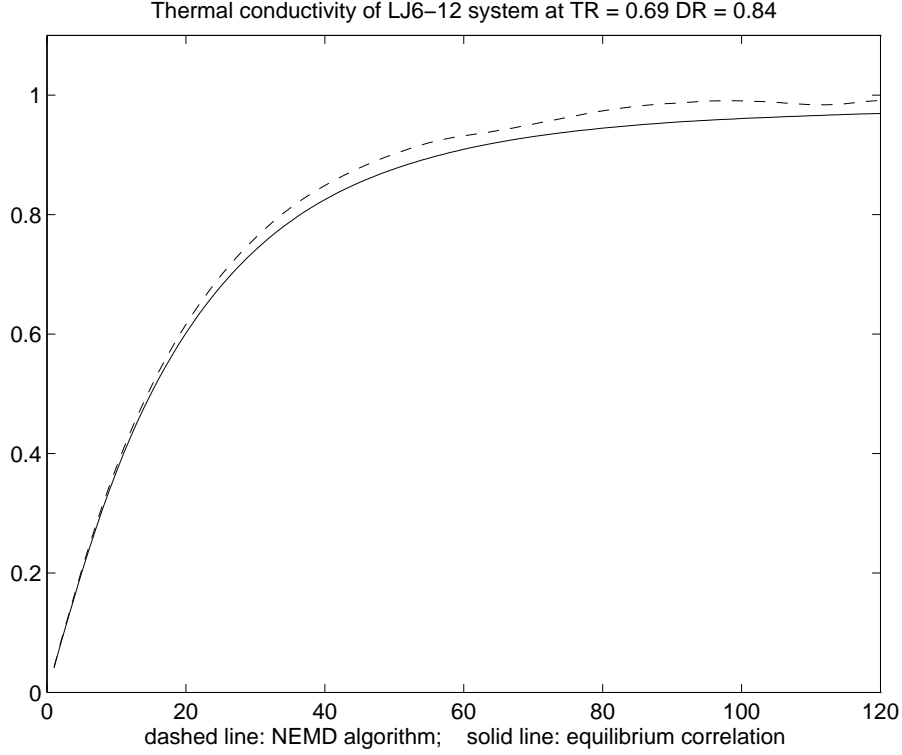


Figure 3-13: Comparison of the NEMD method result [64], with the equilibrium fluctuation method, for Ar fluid near triple point: $T_R = 0.69$, $\rho_R = 0.84$. The number of particles is 256.

Boltzmann equation [61, 62, 63], and in the case of amorphous solid by the analysis of vibrational lifetimes [83]. The second approach is the so-called non-equilibrium molecular dynamics (NEMD) method [64], mainly used in liquids. The third approach is the Green-Kubo equilibrium fluctuation method [50, 55, 56, 80]. Of the three approaches, only the Green-Kubo method is exact, and can be applied to all of the crystalline, amorphous, and liquid phases.

I have implemented both the NEMD scheme by Gillan and Dixon [64] and the equilibrium fluctuation method for the Lennard-Jones system. For general methodologies of using the spectral method to extract time-correlation functions, please refer to Appendix E.

Fig. 3-13 shows a comparison between the NEMD and the equilibrium fluctuation method results for Lennard-Jones fluid near triple point: $T_R = 0.69$, $\rho_R = 0.84$. The thermal conductivity is in reduced unit, the X axis showing the time steps, with

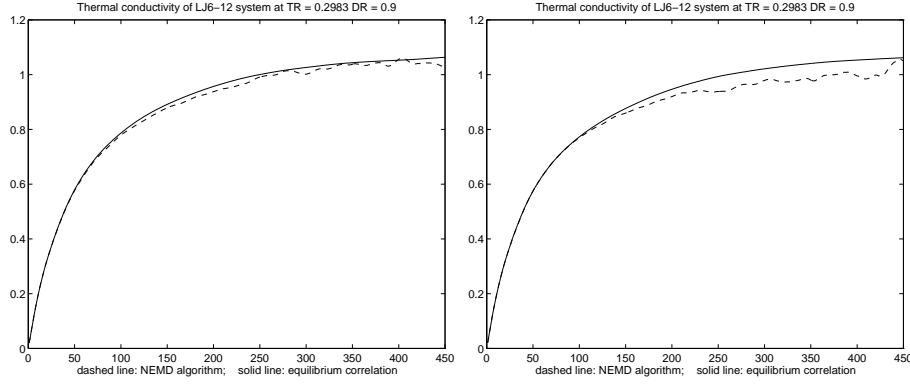


Figure 3-14: Comparison of the NEMD method result [64], with the equilibrium fluctuation method, for solid Ar at $T_R = 0.2983$, $\rho_R = 0.90$. The left is result with 256 particles, the right is result with 108 particles.

one step $\Delta t = 10ps$. A total number of 2745 NEMD runs had been taken within the range of 340000 running steps. For the equilibrium correlation method, 329380 different origins had been taken (each running step after equilibration as a new origin), with correlation length = 120 steps: the number of effective origins is much smaller than the number of 329380 as these origins are highly correlated, but since it's a long run we are quite sure that the phase space was fully sampled. The calculated κ for liquid argon at this condition is 0.99 ± 0.03 , close to the published results by Gillan and Dixon.

Fig. 3-14 shows the results for solid Ar at $T_R = 0.2983$, $\rho_R = 0.90$, with 256-particle cell result on the left, and 108-particle cell result on the right. A total number of 1887 NEMD runs had been taken within the range of one million steps, the correlation length being 450, which is almost 4 times the length needed for the liquid to converge.

Since thermal conductivity in a crystal mainly results from the aharmonicity of the lattice, i.e., inelastic phonon-phonon collisions, the size of the simulation cell is an important issue here, as it directly controls how many \mathbf{k} points we have. We can see that the equilibrium correlation curve changed little in Fig. 3-14, but the NEMD curve became shaky after about 150 steps. For overall considerations we decided that it does not make much difference between 108 and 256 particles if we use equilibrium correlation method.

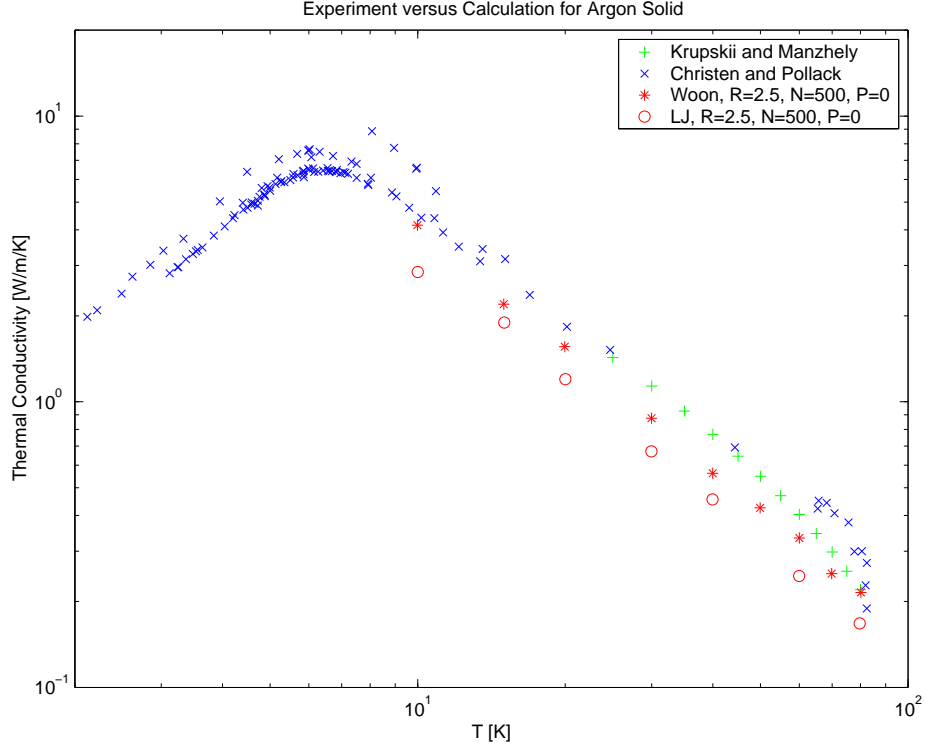


Figure 3-15: Comparison of calculated Ar crystalline thermal conductivity with experiments.

The thermal conductivities of solid Argon has been calculated [67] as a function of T by the equilibrium fluctuation method. The results for the temperature dependence of thermal conductivity for the free standing condition agree well with experiments [68, 69], shown in Fig. 3-15.

We find that the heat flux autocorrelation function consists of two stages in solid argon, both decaying exponentially, but the first stage decays much faster than the second at low T , and one can clearly see a sharp transition at $\tau \sim 1$ ps, as shown in Fig. 3-16. The first stage is identified to be the contribution from certain nonlinear diffusive heat carriers previously not accounted for by the phonon heat current expression proposed by Peierls [57], while the second stage comes from these canonical phonon heat carriers. At low T , the crystalline Ar thermal conductivity is dominated by the phonon carriers, but at high T or when the lattice becomes amorphous the diffusive heat carriers become important. Thus there is an *intrinsic* connection between crystalline and amorphous thermal conduction, revealed through the short-time behavior

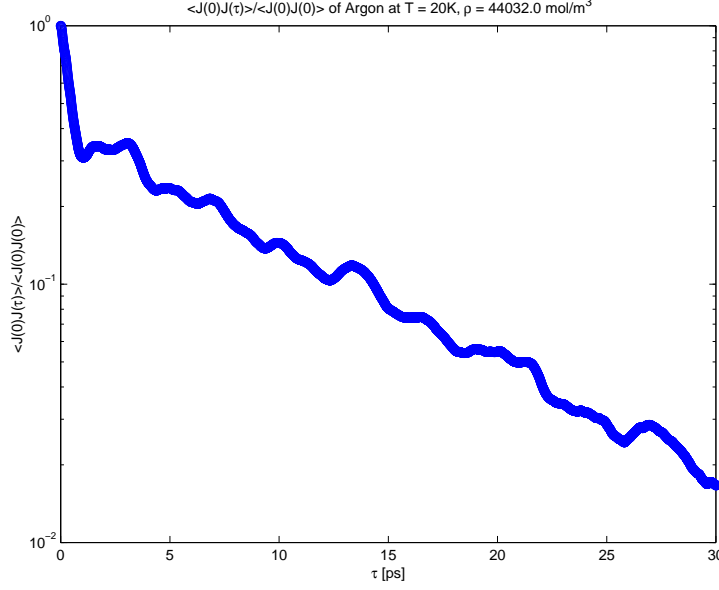


Figure 3-16: log-log plot of the heat flux autocorrelation function in Ar crystal at $T = 20\text{K}$, illustrating the two stages and their sharp transition at $\tau \sim 1\text{ ps}$.

of the heat flux autocorrelation function, which is not reflected in traditional phonon theories on lattice conduction. For a detailed analysis, please refer to Appendix F.

3.3 Strength of SiC

3.3.1 General Properties

Continuing the work of M. Tang [39, 40], we used the Tersoff potential [158, 159, 160, 161, 162, 163] to model the thermal and mechanical behavior of SiC in crystalline, amorphous and nano-crystalline forms. Detailed discussions about using the Tersoff potential can be found in references [79, 80], which due to length limitation will not be included here.

I use the amorphous SiC configuration produced by G. Galli [45] using first-principles molecular dynamics [154] (128 atoms), then periodically replicated and re-annealed using the Tersoff potential. Fig. 3-17 shows the calculated crystalline and amorphous SiC elastic constants as a function of T . We see that the amorphous SiC configuration obtained is almost 50% softer than the perfect crystal, and is quite

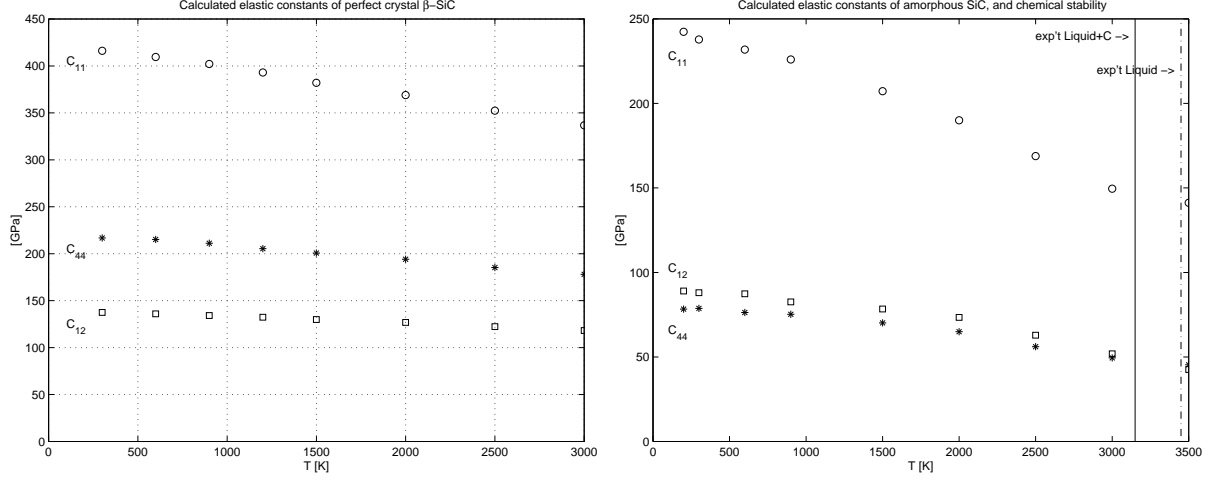


Figure 3-17: Calculated crystalline and amorphous SiC elastic constants as a function of T .

isotropic as $C_{12}(T) \approx C_{44}(T)$.

As I heat up the SiC perfect crystal, the lattice remains stable up to 5000K. The experimental Si/C phase diagram (right half of Fig. 3-18) indicates that SiC should thermally decompose at ~ 2900 K, and therefore the Tersoff potential does not capture the melting of SiC crystal very well, or at least some unrealistic super-heating is required. However, in a similar experiment on amorphous SiC, I find that the amorphous configuration melts near 3000K, shown by the atoms' mean squared displacements as a function of simulation time in Fig. 3-18.

Fig. 3-19 shows the calculated surface energies of crystalline and amorphous SiC as a function of T . In both cases two complementary surfaces are created by cutting and separating a bulk configuration to avoid unequal species count. In the case of the β -SiC crystal, the cutting direction is $\langle 100 \rangle$ and I obtain a C-terminated and a Si-terminated (100) surface. The surface energy shown in Fig. 3-19 can be considered as the average of the two types. In the case of the amorphous surface there is no such distinction. We see that the amorphous surface energy is about 50% of the perfect crystal surface energy, similar to the elastic constants.

Crystalline and amorphous SiC are known to be brittle at low T , so the computed surface energies can be directly converted to fracture toughness by the Griffith criterion [234]. For crystalline β -SiC, my computed $K_{C\langle 100 \rangle}^I = 2.45 \text{ MPa}\cdot\text{m}^{1/2}$, in fair

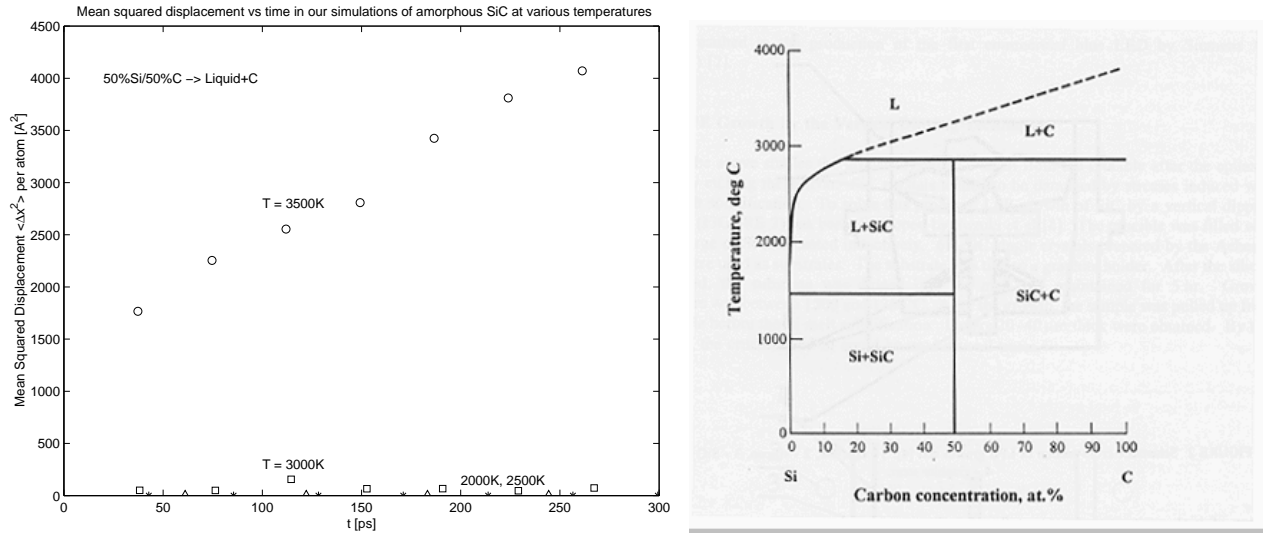


Figure 3-18: Left: Mean Squared Displacements in amorphous SiC as a function of simulation time. Right: experimental Si/C phase diagram.

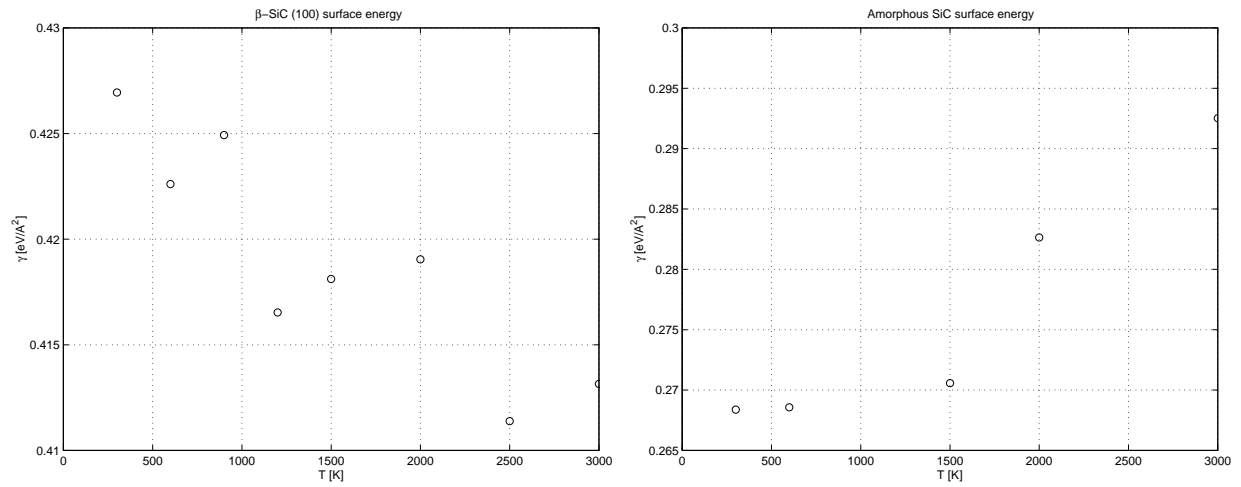


Figure 3-19: Left: calculated (100) surface energy of crystalline β -SiC as a function of T . Right: calculated surface energy of amorphous SiC.

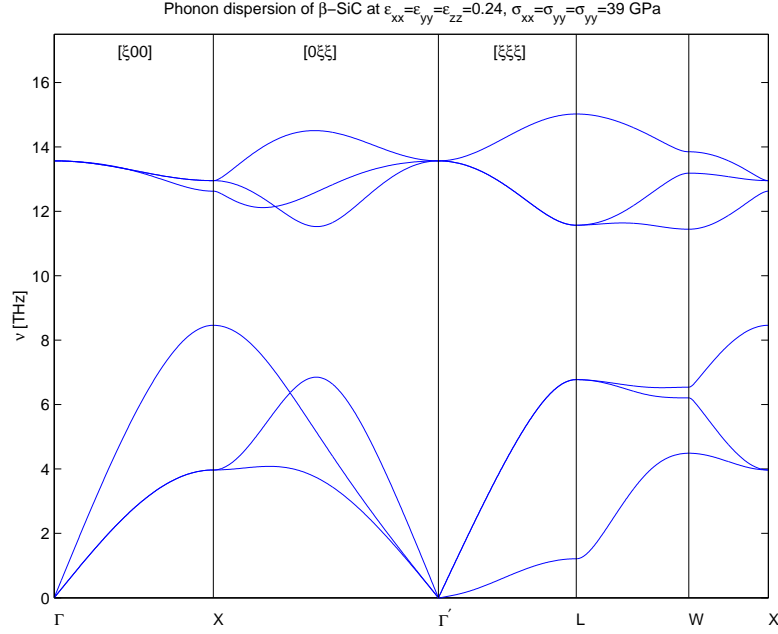


Figure 3-20: Phonon dispersion curve of β -SiC crystal under hydrostatic strain $\epsilon_{xx} = \epsilon_{yy} = \epsilon_{zz} = 0.24$, with $\sigma_{xx} = \sigma_{yy} = \sigma_{zz} = 39$ GPa. Notice the Γ' -point soft mode in the $[111]$ direction.

agreement with the experimental result of $2.8 \text{ MPa} \cdot \text{m}^{1/2}$ measured for sintered β -SiC polycrystal [122].

3.3.2 Lattice Dynamical Calculation of Ideal Strength

In Fig. 3-20 the phonon dispersion curve of β -SiC crystal under hydrostatic strain $\epsilon_{xx} = \epsilon_{yy} = \epsilon_{zz} = 0.24$ and $\sigma_{xx} = \sigma_{yy} = \sigma_{zz} = 39$ MPa is plotted. Here the instability is of the $\mathbf{k} = 0$ long-wave type, classified as the elastic instability. [39, 41]

In Fig. 3-21, the phonon dispersion curve of β -SiC crystal under shear strain $\epsilon_{xy} = 0.20$, $\sigma_{xy} = 62$ GPa is plotted. The L -point soft mode is *not* a long-wave, or elastic, instability, and must be tracked down by lattice dynamical calculations.

3.3.3 MD Simulation of Ideal Strength

I carry out direct MD simulations of deforming β -SiC perfect crystal. Fig. 3-22 shows the collected critical hydrostatic strain and stress as a function of T .

Fig. 3-23 shows the collected critical tension strain and stress as a function of

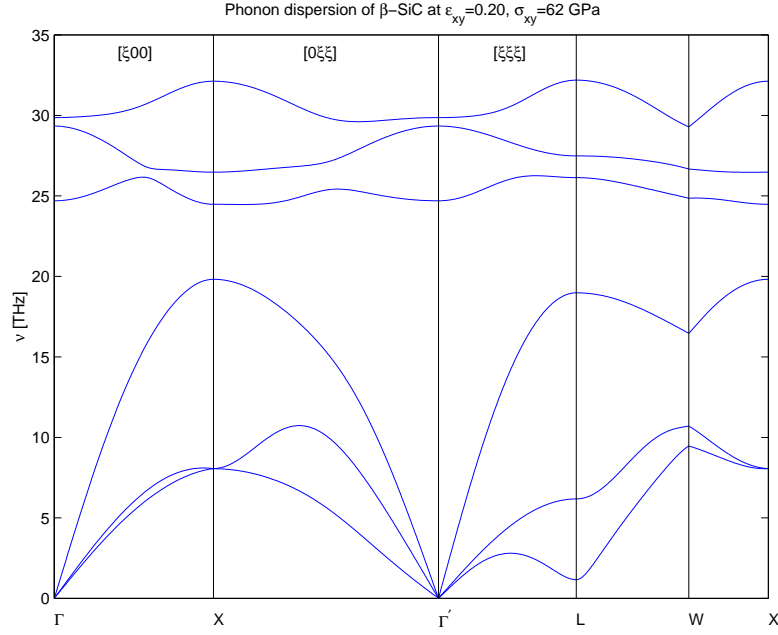


Figure 3-21: Phonon dispersion curve of β -SiC crystal under shear strain $\epsilon_{xy} = 0.20$, with $\sigma_{xy} = 62$ GPa. A label tracks only one of the original high-symmetry \mathbf{k} -points. Notice the L -point soft mode.

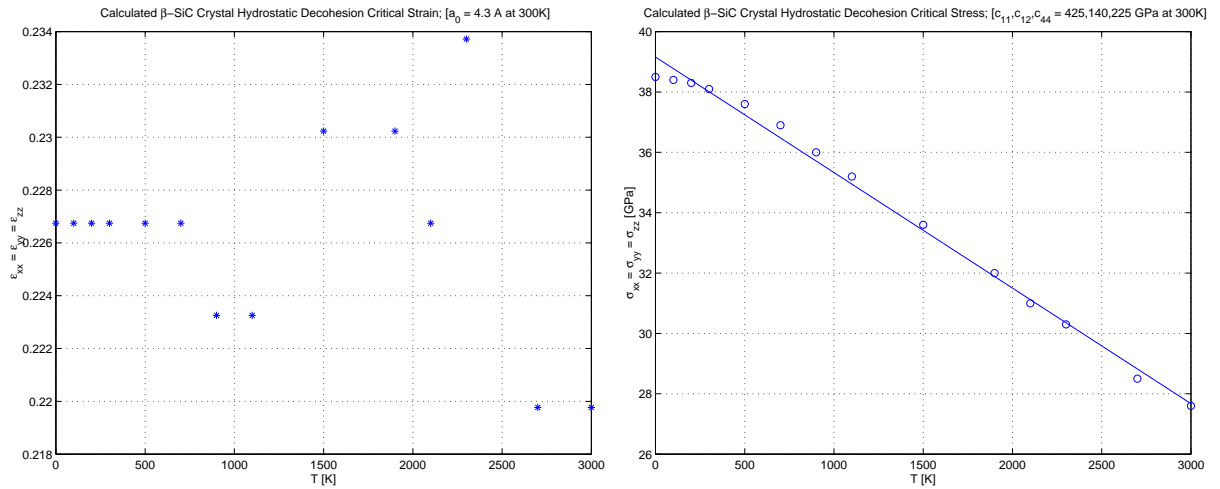


Figure 3-22: Critical hydrostatic strain and stress as a function of T for β -SiC crystal.

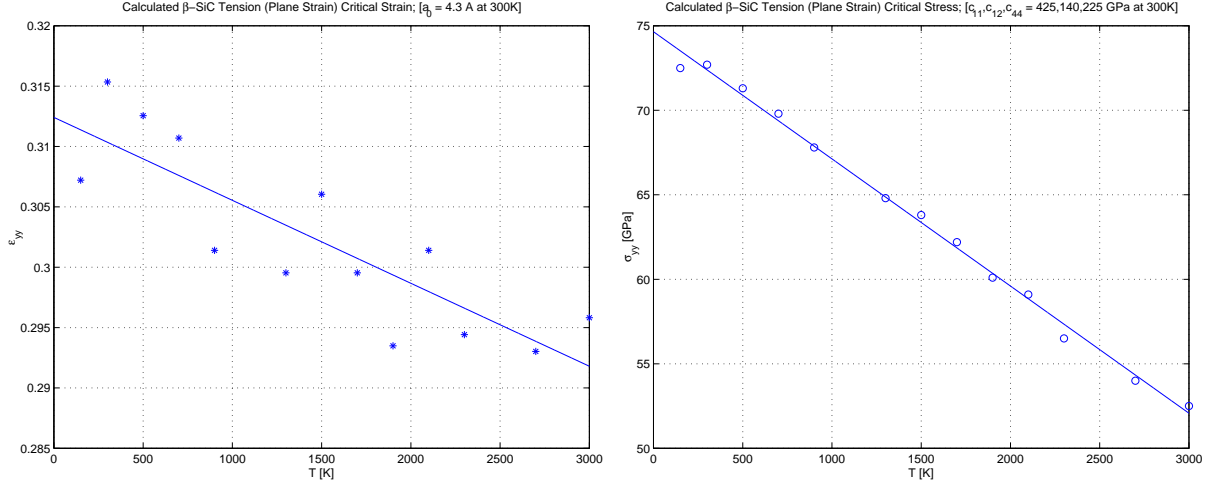


Figure 3-23: Critical tension strain and stress under plane strain condition as a function of T for β -SiC crystal.

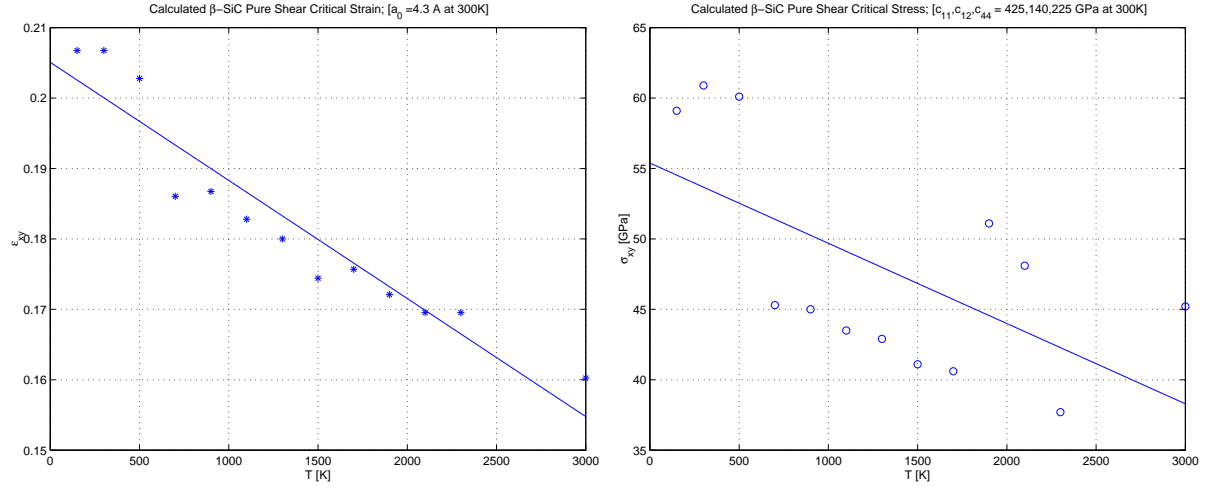


Figure 3-24: Critical shear strain and stress as a function of T for β -SiC crystal.

T . The simulations are performed under plane strain condition, meaning the lateral stresses σ_{xx} , σ_{zz} are not relaxed when σ_{yy} tension is applied. It mimics the loading condition of a bulk volume element in front of a long crack [234], and so I think the results are more representative of the real situation than the plane stress simulation, where σ_{xx} , σ_{zz} are relaxed. Usually, one expects higher critical stress under triaxial loading (plane strain) than uniaxial loading (plane stress).

Fig. 3-24 shows the collected critical shear strain and stress as a function of T . Fig. 3-25 shows the atomistic configuration after the shear instability, compared to

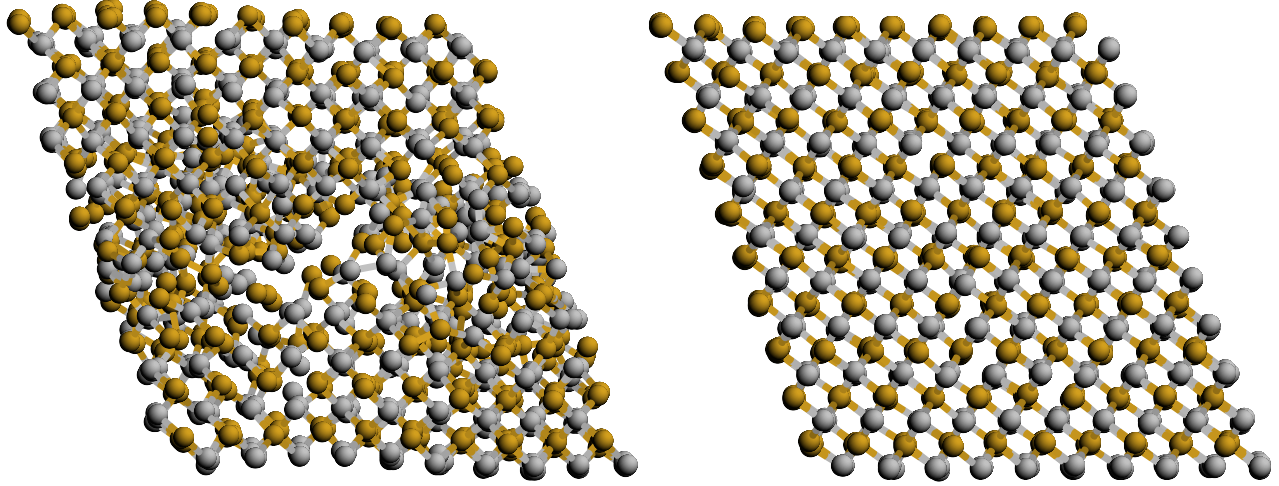


Figure 3-25: Configuration after pure shear instability of β -SiC crystal at $T = 1300\text{K}$ and $\sigma_{xy} = 43\text{ GPa}$, compared to a moment ago just prior to the catastrophe. An elliptical microcrack and an accompanying deformation band have formed.

just a moment ago prior to the instability. An elliptical microcrack has nucleated along the direction of maximum tension (45 degrees).

In all the three loading conditions I have performed simulations with: hydrostatic tension, plane strain tension, and pure shear, β -SiC crystal fails by cleavage fracture.

3.3.4 MD Simulation of Amorphous Strength

Fig. 3-26, 3-27, 3-28 show the hydrostatic, plane strain tension, and shear instability results for amorphous SiC as a function of T , under exactly the same setup as those for the perfect crystal.

Fig. 3-29 shows the atomistic configuration of amorphous-SiC after hydrostatic decohesion, compared to the undeformed amorphous-SiC. Two through cracks have formed.

An outstanding feature of the amorphous-SiC results is that all three deformation modes have nearly the same failure stress, at $\sim 22\text{ GPa}$, in contrast to the sensitive mode-dependence of the β -SiC perfect crystal ($\sim 40\text{ GPa}$ under hydrostatic, $\sim 70\text{ GPa}$ under plane strain tension, $\sim 55\text{ GPa}$ under shear).

My tension failure result ($\sim 25\text{ GPa}$) agrees very well with the recent *ab initio* MD simulation result of Galli *et al* [45], who obtained $\sim 24\text{ GPa}$ for the tensile

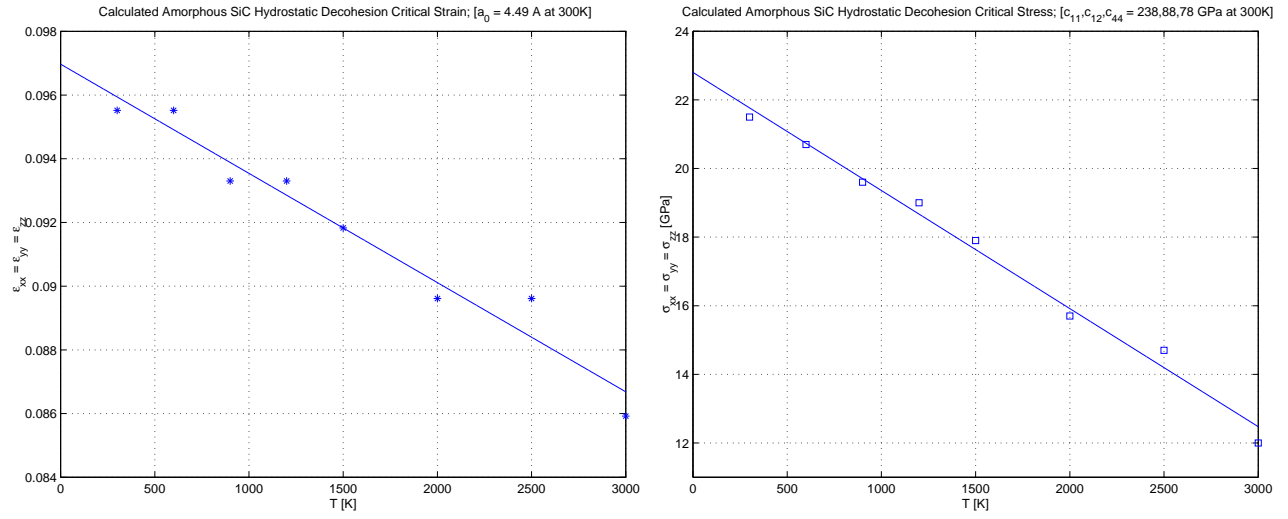


Figure 3-26: Critical hydrostatic strain and stress as a function of T for amorphous-SiC.

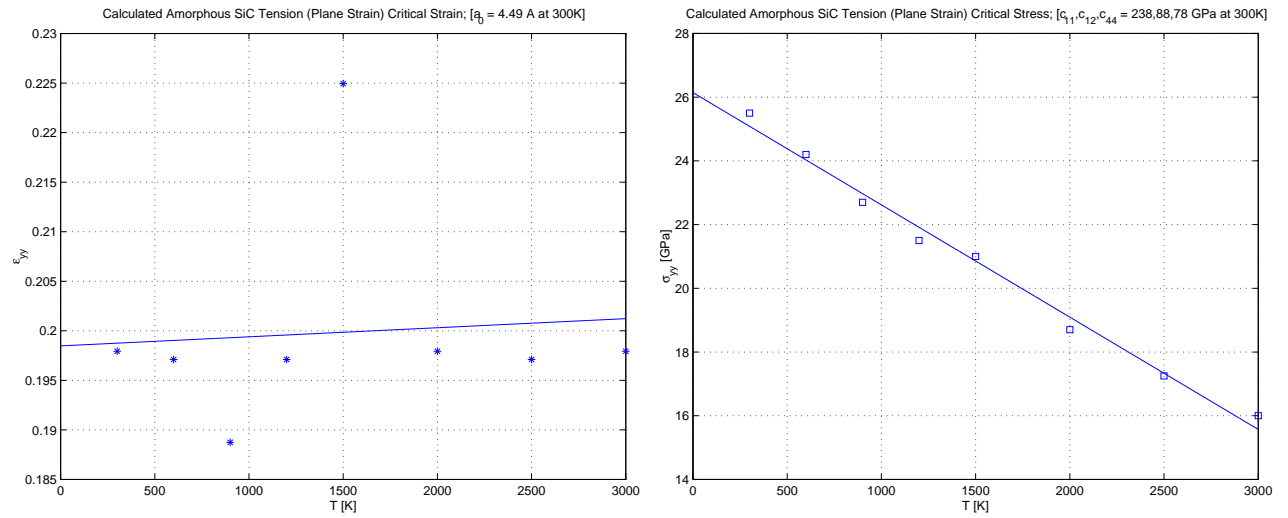


Figure 3-27: Critical tension strain and stress under plane strain condition as a function of T for amorphous-SiC.

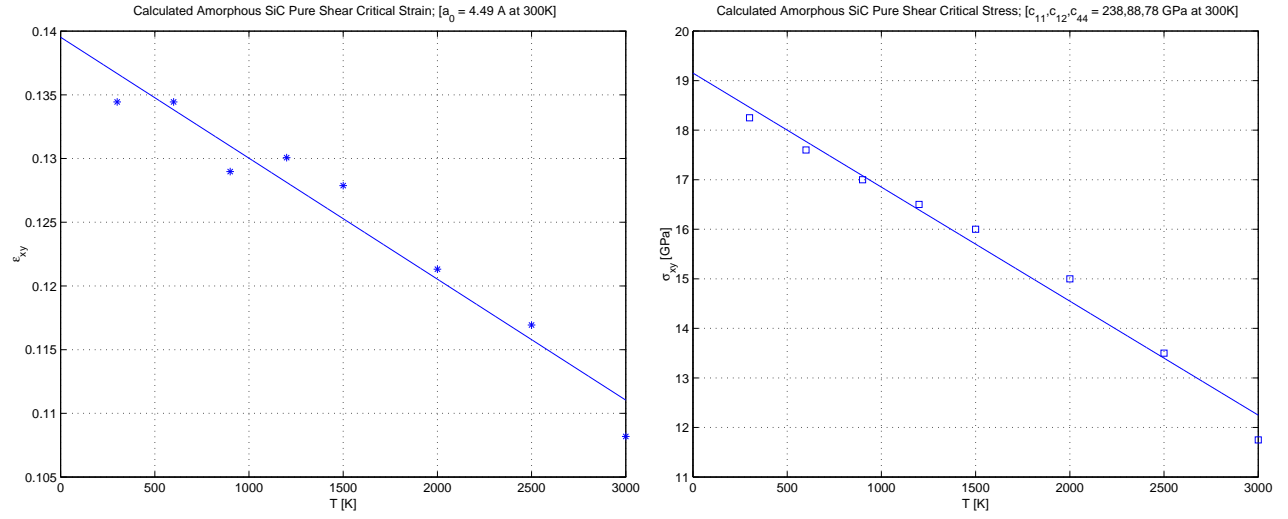


Figure 3-28: Critical shear strain and stress as a function of T for amorphous-SiC.

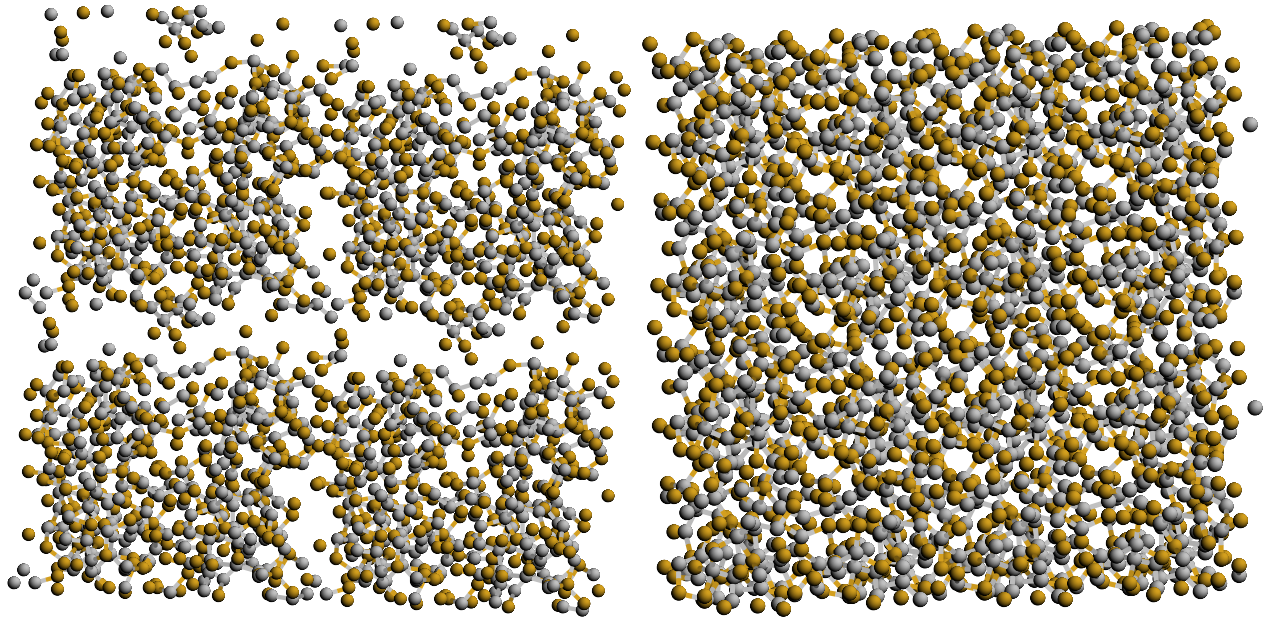


Figure 3-29: Configuration after hydrostatic decohesion of amorphous-SiC crystal at $T = 300\text{K}$ and $\sigma_{xx} = \sigma_{yy} = \sigma_{zz} = 22 \text{ GPa}$, compared to the undeformed amorphous-SiC.

failure of amorphous-SiC. It also agrees well with the measured 28 – 30 GPa by El Khakani *et al* [43] from nano-indentation experiments on amorphous-SiC thin films. This gives me confidence in the ensuing strength calculations for nanocrystal using the Tersoff potential. Nanocrystal is a relatively large inhomogeneous system which has significant amorphous content in its grain boundaries.

3.3.5 MD Simulation of Nanocrystal Strength

A nanocrystal configuration is created by the Voronoi construction, with 4 Voronoi sites arranged in fcc structure in an 8000 atom supercell, with a random orientation assigned to each grain. After the removal of too-close atoms, about 20% of the atoms are classified as grain boundary atoms (distance $< 1.4\text{\AA}$ from the Voronoi cut plane). I then compress and anneal the configuration. The relaxed nanocrystal has slightly larger equilibrium volume (edge length 4.32 nm compared to the crystalline 4.29 nm) and fewer (7810) atoms.

I then load the nanocrystal hydrostatically by slowly increasing the supercell size. The stress-strain curve at $T = 300\text{K}$ is shown in Fig. 3-30. At cell size 4.63 nm ($\epsilon = 0.0718$) it fails, at a critical stress of 20 GPa. In comparison, β -SiC crystal fails at $\epsilon = 0.1512$ and 38.1 GPa under identical conditions; thus both the critical stress and strain of the nanocrystal are halved compared to the perfect crystal. This is more likely to be an indication of the strength of the grain boundary, which is amorphous-like, than that of the crystalline grains.

The above viewpoint is further strengthened by plotting the stress-strain curve of amorphous-SiC in Fig. 3-30. We see that the nanocrystal fails at about the same stress as the amorphous-SiC. That there is a slight reduction in the failure strain compared to amorphous-SiC is easily explainable since we know (section 3.3.1) that amorphous-SiC is softer than the perfect crystal, thus at an *average* expansion 0.0718 of the entire nanocrystal system, the amorphous content in the grain boundary should have a larger local ϵ . So, one should rescale the nanocrystal stress-strain curve in the ϵ -axis to make a fair comparison with the amorphous-SiC stress-strain curve, and we see that indeed they are very similar in shape. For instance, the nanocrystal stress-

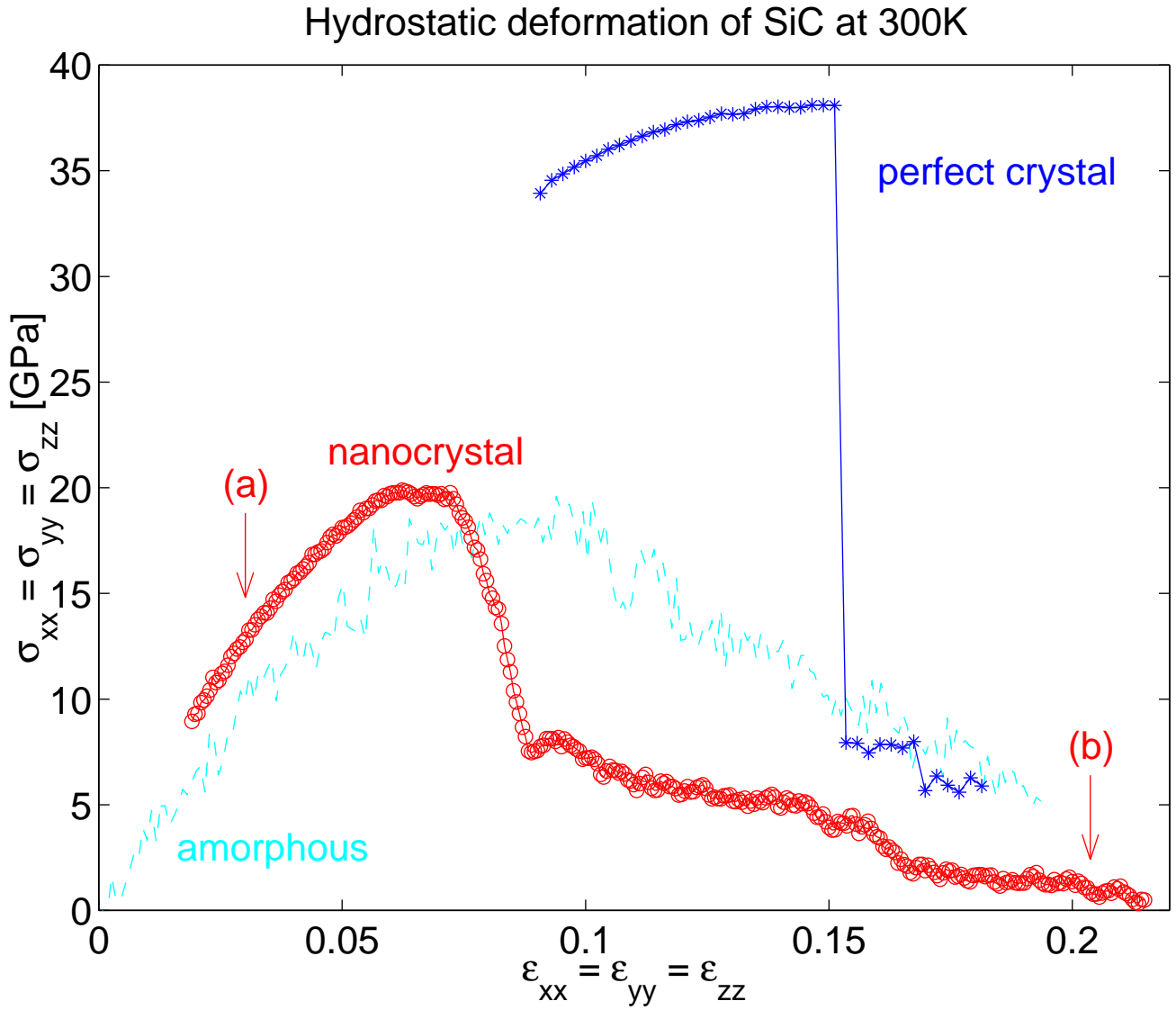


Figure 3-30: Stress-strain curve during hydrostatic deformation of SiC nanocrystal at 300K. The stress-strain curves of β -SiC crystal and amorphous-SiC under identical conditions are also shown for comparison.

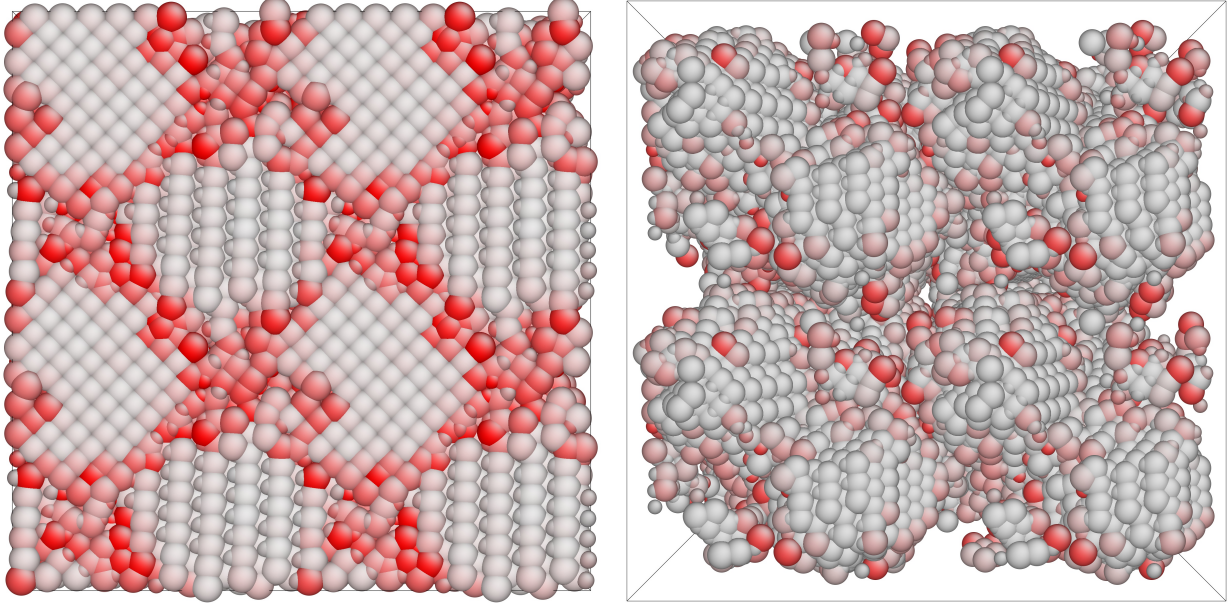


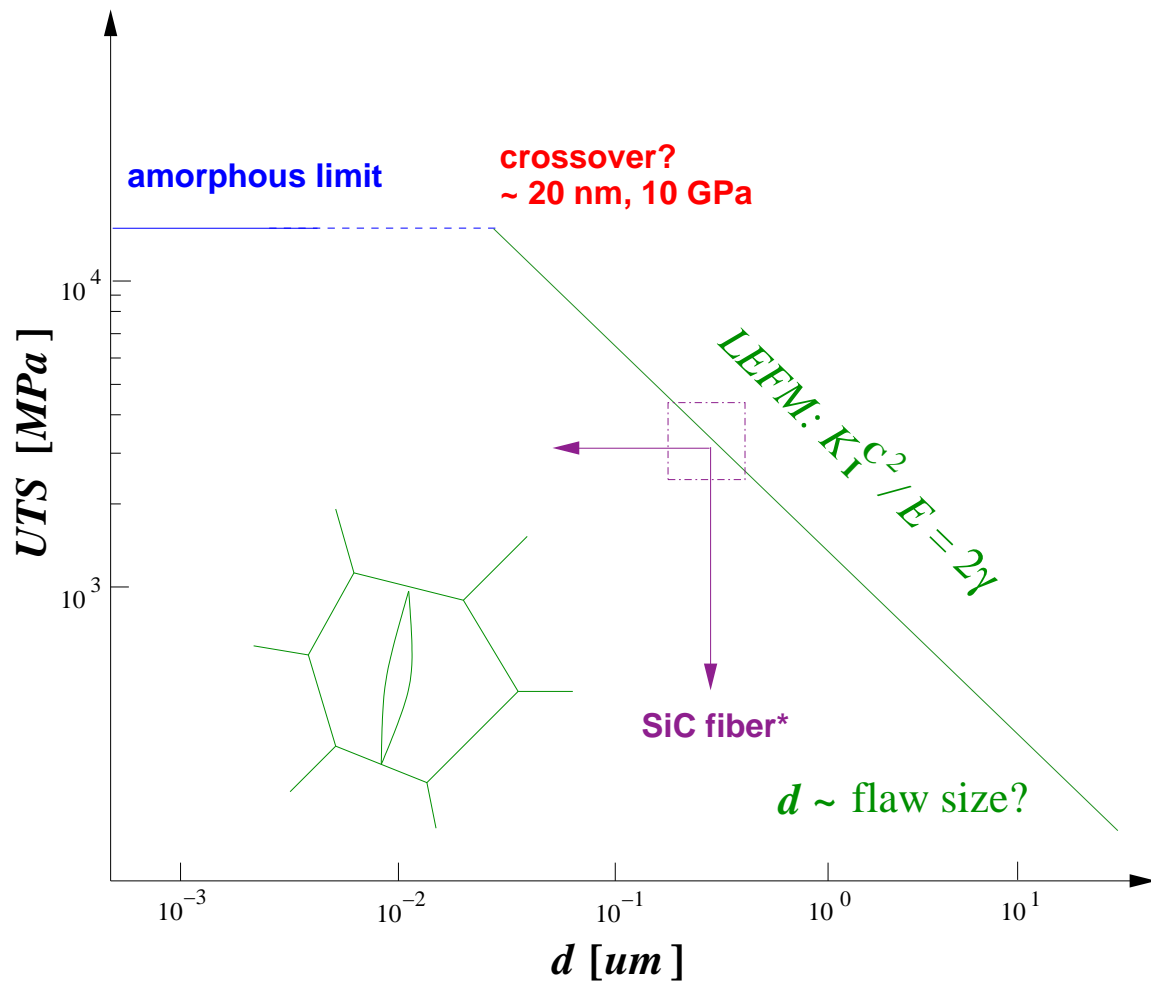
Figure 3-31: Configurations corresponding to (a) and (b) arrows in Fig. 3-30. The atoms are color-encoded by their atomistic local shear strain.

strain curve does not have a sharp cusp at failure, similar to the amorphous-SiC but unlike the perfect crystal.

The atomistic configurations corresponding to (a) and (b) arrows in Fig. 3-30 are shown in Fig. 3-31. In (a), one can clearly see regular, space-filling nano-grains of different orientations. In (b), we see that the nanocrystal has come apart, not by the breaking of any grain but by grain boundary decohesion. The nanocrystal fails by intragranular fracture, and the failure stress is closely related to the failure stress of bulk amorphous-SiC, with the interpretation that the grain-boundary content of the nanocrystal is largely amorphous.

The significance of this result in the broader context of the mechanical strength of SiC is as follows: there is a well-known scaling relation called the Hall-Petch law [88, 115], which states that the yield stress of a polycrystalline metal is inversely proportional to the square root of its grain size d . This relation can be derived from a model of dislocation pile-up at the grain boundary which can sustain certain maximal local stress, and the stress concentration from the dislocation pile-up is not unlike the problem of a crack that spans the whole grain.

Scaling Relation for UTS of SiC



* M.D. Sacks, J. Eur. Ceram. Soc. 19, 2305 (1999).

Fiber UTS: 3 GPa Dominant flaw size: 0.2–0.3 μm

Figure 3-32: Cutoff to the Hall-Petch relation in SiC.

The Hall-Petch relation suggests that by shrinking the grain size, one can increase the yield stress of a material, which is one reason for nano-materials research. But on the other hand, this law cannot hold forever in the limit of small d , since small grain sizes facilitate diffusional creep and other deformation mechanisms, which takes over the dislocation flow mechanism at $d < 100$ nm. This is supported by experimental evidences and has recently been reproduced by atomistic simulation [117, 118, 119, 120].

For brittle materials such as SiC, a scaling relation like the Hall-Petch law exists but takes on a different meaning. At low T , the yield stress of a ductile material is replaced by the ultimate tensile stress (UTS), under which a polycrystal fails by fracture. If we assume that the strength-controlling flaw (a microcrack, for example) has a size equal to the grain size, then using fracture mechanics one can easily derive a scaling relation like the Hall-Petch law. In fact, since I have computed the surface energies of SiC in both crystalline and amorphous phases (section 3.3.1), which ranges from 0.27 (amorphous) to 0.43 eV/Å², they convert to a fracture toughness $K_C \sim 2$ MPa·m^{1/2} by the Griffith law $K_C^2/E = J_C = 2\gamma$, which leads to the line in Fig. 3-32 that has slope 1/2. Sacks [123] measured the tensile strength of specially treated SiC fibers to be as high as 3 GPa. By independent means of characterization, the dominant flaw size is determined to be 0.2 to 0.3 μm, which falls right onto the calculated prediction.

But this is not the whole story. By common sense one cannot strengthen a material indefinitely by refining the grains. At one point, a crossover should happen. From our hydrostatic deformation simulation of SiC nanocrystal, we see that the (amorphous) grain boundary strength controls the strength of the system at nm-scale grain sizes. After taking into account the stress concentration factor under uniaxial tension in a polycrystal, which is usually ~ 2 , the UTS of SiC is predicted to be bounded above by ~ 10 GPa, and the crossover in mechanism should occur at a grain size ~ 20 nm. At smaller grain sizes, we predict that the mechanical strength of SiC would not improve and may deteriorate, especially at high temperatures.

3.4 Thermal Conductivity of Crystalline and Irradiated SiC

This part has been published [79, 80]. Due to length limitation only the abstracts are quoted below. Please refer to the original papers for details.

Paper I [79]. *“We present a two-part theoretical study of the thermal properties of crystalline β -SiC based on an empirical interatomic potential developed by Tersoff which emphasizes the bond-order nature of covalent solids. In part I we use this description of interatomic interactions in both lattice dynamical calculations and molecular dynamics simulations with a temperature-scaling procedure to obtain reasonably accurate predictions of the heat capacity and the thermal expansion coefficient. Our results notwithstanding, improvement of the potential to include ionic interactions for the description of vibrational properties, and extension of short-range forces beyond the nearest neighbors, would be quite useful.”*

Paper II [80]. *“In this the second part of a theoretical study of the thermal properties of crystalline β -SiC, the thermal conductivity is calculated by using molecular dynamics simulation to evaluate directly the heat current correlation function and thus obtain the conductivity through the Green-Kubo expression in linear response theory. Adopting the same empirical potential model and the temperature scaling method as in part one, we predict absolute conductivity values for a perfect crystal which are in satisfactory agreement with available data, except in the low-temperature region (below 400K) where quantum effects become important. The effects of carbon and silicon vacancies and antisite defects are studied by introducing a single defect into the simulation cell, allowing the atomic configuration to relax, and then performing heat capacity, thermal expansion and conductivity calculations. We find that the heat capacity and thermal expansion coefficient are affected very little by point defects even at a high concentration of 0.5%. On the other hand, the thermal conductivity is observed to degrade markedly as a result of the greatly enhanced decay of the heat current correlation, clearly attributable to the dominant mechanism of defect scattering of phonons. The defect simulations also reveal that the conductivity becomes essen-*

tially temperature independent. Both characteristics appear to have correspondence with observations on conductivity behavior in neutron-irradiated specimens.”

Chapter 4

Thermal Conductivities of Refractory Carbides

4.1 Problem Statement

ZrC is a typical transition metal carbide (nitride), which as a class of materials (also called refractory carbides) has the following unique properties [145]:

- Hardness (Vickers microhardness of ZrC: 25.5 GPa) - among the hardest compounds known.
- Very high melting temperature (ZrC: 3700 K). In fact, HfC, TaC, graphite (sublime), ZrC, NbC are the five highest melting point materials known.
- Ideal stoichiometry is generally not found in these materials, which contains at least a few atomic percent and high up to 50% carbon vacancies. The defects tend to form complex super-lattices.
- Chemically inert and resistant and nearly impervious to hydrogen to exceeding 3000K. At room temperature only very concentrated acid can attack it slowly.
- Extremely strong at high temperatures. Though brittle at room temperature, they undergo brittle-to-ductile transition at $< 1300\text{K}$. For example, at 2100K a

2-phase alloy of VC and TiC has the highest compressive yield strengths among any known material.

- They manifest *metallic* behaviors in their electrical, magnetic, and optical properties. Some are even superconductors.

Due to their hardness, wear resistance, chemical inertness and good thermal shock resistance, transition metal carbides are widely used as abrasives, machining tools, wear resistant parts, and coating materials. Some have attracted attention as potential chemical catalysts and high temperature electronic materials. ZrC, especially, has application in the nuclear industry: for instance, ZrC coated graphite matrix are used to embed nuclear fuel particles for advanced nuclear reactors.

Because their applications almost always involve heat generation at high temperatures, refractory carbides' thermal conductivities are of the utmost importance. It is therefore surprising that till present day no one has given a fixed answer to even the most elementary question: what dominates the thermal conductivity at high temperature, electrons or phonons (lattice vibrations)? Different answer to this question leads to very different directions of trying to modify the conductivity, which till now are carried out experimentally on a trial-and-error basis. If the electron contribution dominates, then one probably should focus on band structure and chemical means of modifying it. If the phonon contribution dominates - as in SiC, then one may focus on minimizing and annealing the lattice defects which are good phonon reflectors.

This is a challenging problem, both experimentally and theoretically. Fig. 4-1 shows a collection of ZrC thermal conductivity measurements done by different researchers. We see large scatter in the results, which is mostly probably due to the different specimens. None of the tested samples were stoichiometrical: the reported characterizations has $> 2\%$ and up to 10% carbon vacancies, and additional metal and oxide impurities. Despite this, it is clear that the overall trend of conductivity with temperature is *increasing*. This is puzzling. To put the problem in context, let us review three types of materials whose thermal conduction we believe we understand well, each representing a mechanism that might be dominant in ZrC.

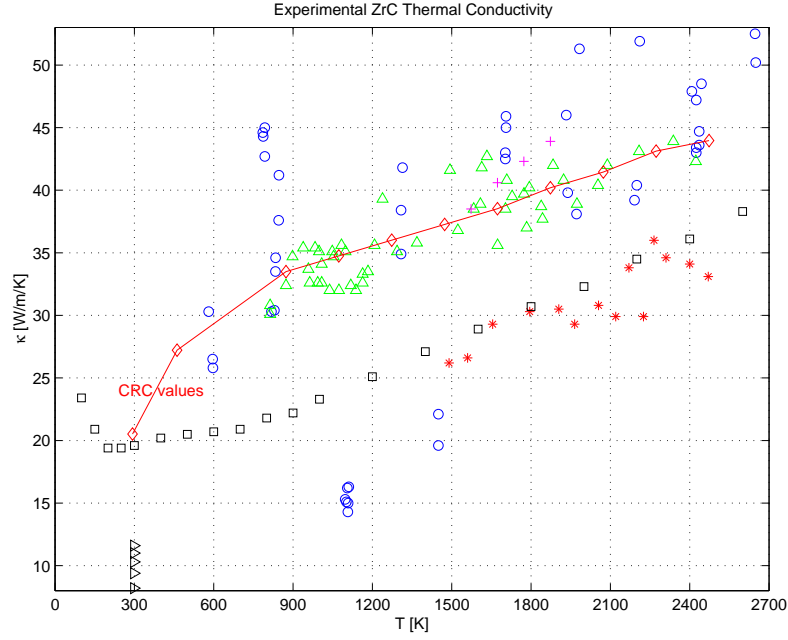


Figure 4-1: A collection of experimental measurements of ZrC thermal conductivity as a function of temperature. *CRC Handbook* [146] recommended values are plotted in solid line.

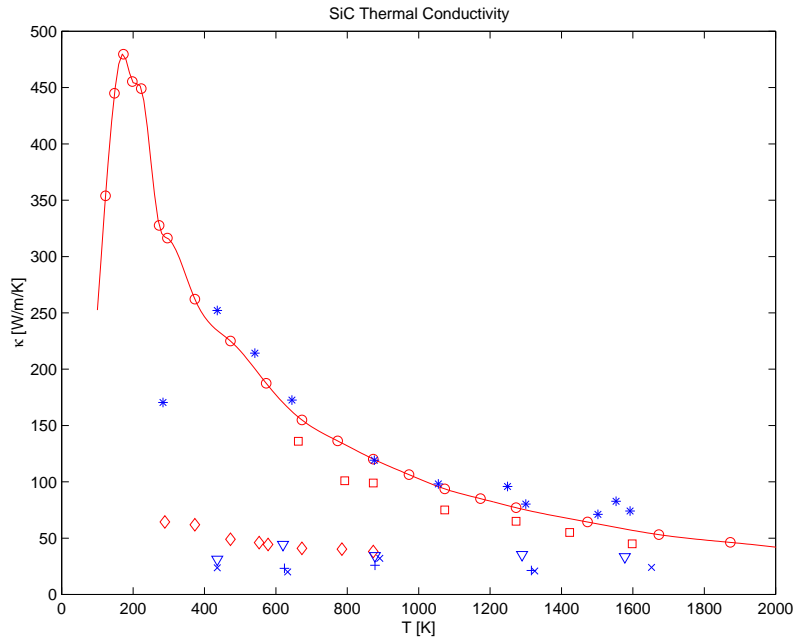


Figure 4-2: Comparison of experimental and simulation results for the thermal conductivities of SiC, for both perfect crystal (experiment a: circles with solid line to guide the eye; experiment b: squares; simulation: stars), and crystal with defects (experiment on radiation damaged SiC: diamond; simulation with 0.5% point defects: pluses, crosses, triangles).

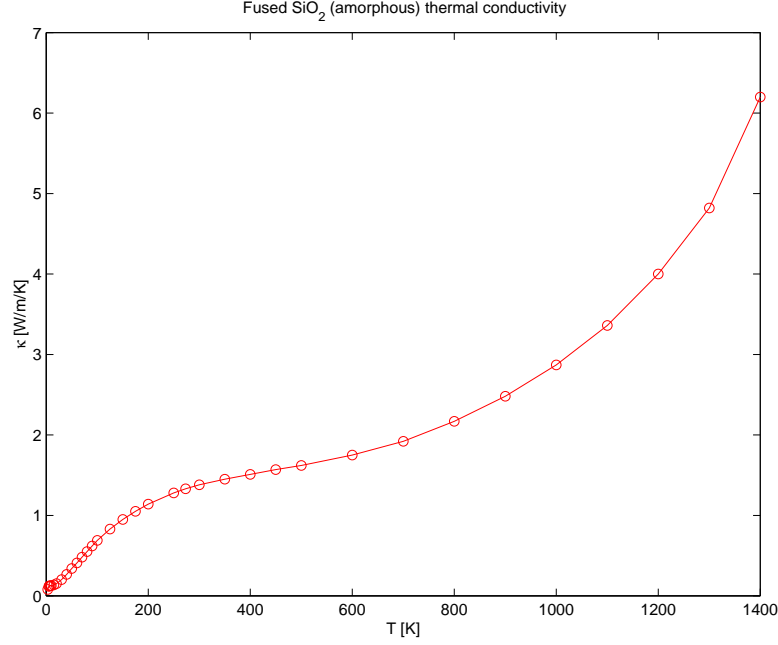


Figure 4-3: Experimental thermal conductivity of amorphous SiO_2 .

Fig. 4-2 shows the thermal conductivities of SiC by both experimental measurements and classical molecular dynamics simulation[80]. The higher values are those of perfect crystal; in contrast, the lower values are of those after radiation damage, which we simulate by putting in small concentrations ($< 0.5\%$) of point defects. It can be seen that the simulation is quite successful at intermediate and high temperatures (at room temperature the quantum effects set in and a different method has to be used, but that is irrelevant to the ZrC problem). Especially, it captures the dramatic effects - reduction on the order of a decade and an almost complete loss of temperature dependence - that a small amount of lattice defects can have on the thermal conductivity, in agreement with experimental observations of radiation damaged SiC. As a dielectric solid, SiC has no electron contribution to the conductivity. The conduction mechanism it represents (namely, phonon scattering) is relevant to ZrC because ZrC is also a binary, hard, ceramic carbide that has some similar applications. Furthermore, we see that under appropriate conditions, the lattice contribution alone is able to provide the magnitude of conductivity that is observed in ZrC. *However*, in SiC the lattice conductivity does not increase with temperature.

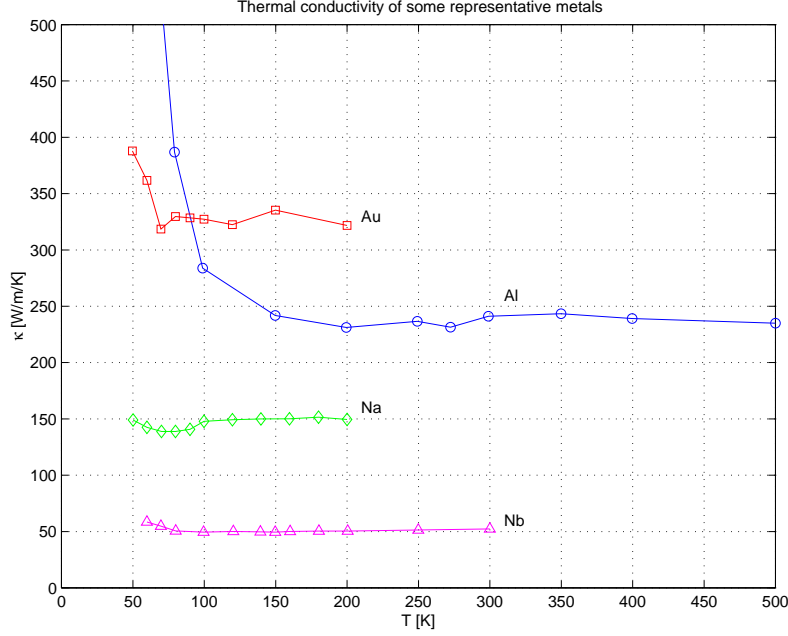


Figure 4-4: Experimental thermal conductivity of Au,Al,Na,Nb.

Fig. 4-3 plots the experimental thermal conductivity of amorphous SiO_2 , which is also a dielectric solid with no electron contribution to the conductivity. However, due to its amorphous lattice structure, the vibrational conductivity *increases* with temperature, such that although the magnitude of conductivity is quite low at room temperature, it rises to a quite significant value at 1400K. There are well-tested theories explaining this behavior, and they *could* be viable models for ZrC, because at such large defect concentrations, the mechanisms that explain the conductivity *increase* with T in amorphous glass might carry over to ZrC.

Lastly, Fig. 4-4 shows the experimental thermal conductivities of four quite distinct metals: Au,Al,Na,Nb. In metals the electron contribution are known to dominate over the lattice contribution. The most striking feature of Fig. 4-4 is that the conductivities are almost all constants with respect to T , except when T is very low. This is a consequence of the well-known Wiedemann-Franz law for metals, $\kappa = L\sigma T$, where κ is the thermal conductivity, σ is the electrical conductivity and L , known as the “Lorenz number”, is a universal constant ($2.45 \times 10^{-8} \text{ volt}^2/\text{K}^2$) that is material-independent. The WF law can be rigorously derived [150] in both strong and weak limits of electron coupling. Because σ is $\sim 1/T$ for metals above room temperature, κ

approaches a constant with respect to T . The metal model and WF law are relevant to ZrC because unlike other ceramic materials, refractory carbides are electrically conductive and are even sometimes called *semi-metals*. ZrC, for instance, has a electrical resistivity that is about twice as that of pure Zr. Therefore, it is highly probable that the electron contribution plays a dominant role in ZrC. But before reaching that conclusion for ZrC, one must first solve two puzzles:

- Why does κ increase with T , while κ of ordinary metals are constant with T ?
- ZrC, even with its large defect concentration, has a thermal conductivity that is *bigger* than pure Zr's. As we mentioned that ZrC has twice the electrical resistivity as pure Zr's, or $1/2$ the σ , this is inconsistent with the WF law.

Eventually, at a deeper level, one must answer what physical mechanisms are responsible for this unique electronic behavior, *if one is convinced that this is indeed caused by electrons*.

The above questions were posed in as early as the 1960's (see references in [148]). Indeed, several theoretical attempts were since made towards explaining Fig. 4-1. It was proposed that the increase of κ with T is due to *residual electrical resistivity*, namely, instead of $\sigma^{-1} \sim T$ as in normal metals, σ^{-1} is actually $\sim \sigma_0^{-1} + T$ for refractory carbides. Then, to resolve the inconsistency still between κ and σ , a different Lorenz number, 4×10^{-8} volt²/K², had been proposed for refractory carbides, that is significantly larger than the “universal number” among ordinary metals. One explanation for this is a so-called *ambipolar diffusion* mechanism, where it was proposed that instead of electrons migrating alone, an electron and a hole travel together so as to not carry net charges, but heat would still be transported when they recombine.

The above theories might be true or partially true, but the situation of published literature is confusing, to say the least, for actual practitioners. The proposed theories suffer critically from the fact that they are not *quantitative enough* as to resolve without doubt the dominance of electron and phonon contributions. Indeed, the latest review article on the subject [148] has a figure, reproduced in Fig. 4-5, that imparts the impression that the phonon contribution is on par with the electron

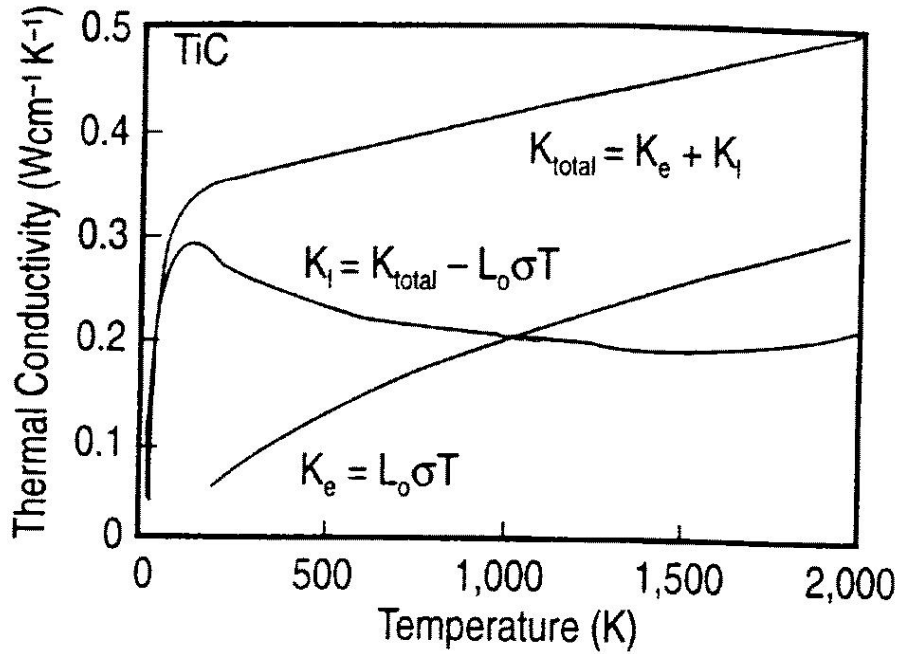


Figure 3. Measured and interpolated thermal conductivity K_{total} of TiC⁷ separated into electron thermal conductivity K_e from measured electrical resistivity via WF law and lattice (phonon) conductivity K_l calculated from the difference.^{2,9}

Figure 4-5: Reproduced Fig. 3 of a most recent review article [148]. Notice that the proposed crossover in dominance occurs at $T = 1000\text{K}$. At $T = 2000\text{K}$, the vibrational contribution is still thought to be non-negligible.

contribution up to $T = 2000\text{K}$, which, turned out to dramatically disagree with my MD simulation results - the main contribution of this work. Experiments cannot yet help to resolve this issue because only the means to measure the *total* conductivity are known, which are already quite costly. Furthermore, the fact that the material is not stoichiometrical and have complex defect microstructures poses a huge problem to experimentalists (see Fig. 4-1) and theoreticians alike.

We think that to accurately describe the effects of defects on either lattice or electron parts of the conductivity so as to *quantitatively* resolve their contributions, one cannot do without atomistic simulation. Pure theory, no matter how sound, cannot describe the effect of carbon vacancies without knowing its structural, energetic, and vibrational details with the help of numerical computation. It is therefore our strategy to do a clean job on calculating the lattice contribution to the ZrC thermal conductivity, which, as we have seen in the SiC case, *can* reach the quantitative accuracy required for the resolution.

This is the route I took, but not without its share of challenges and risks, the foremost being that there is no empirical potential published on ZrC or any other refractory carbides that is suitable for thermal conductivity calculation, itself being a rather difficult part in the MD methodology. In the case of SiC, the Tersoff potential[163] was already a well-known and well-tested potential (a Ph.D. thesis was based on it in our group) when I undertook the thermal conductivity calculation. Here, we must construct the potential from scratch, which entails the following steps,

- Understand the nature of bonding in ZrC, and propose an inspired functional form for the interaction.
- Collect or generate property database for the material.
- Fit parameters against the above database. Make sure you know what is fitted and what is not. It is very helpful to think about how many *really* independent properties there are in the database, and that should be at least a few times the number of free parameters in the potential. Make sure there is no “floating” parameter in the model which does not reflect in the database properties or

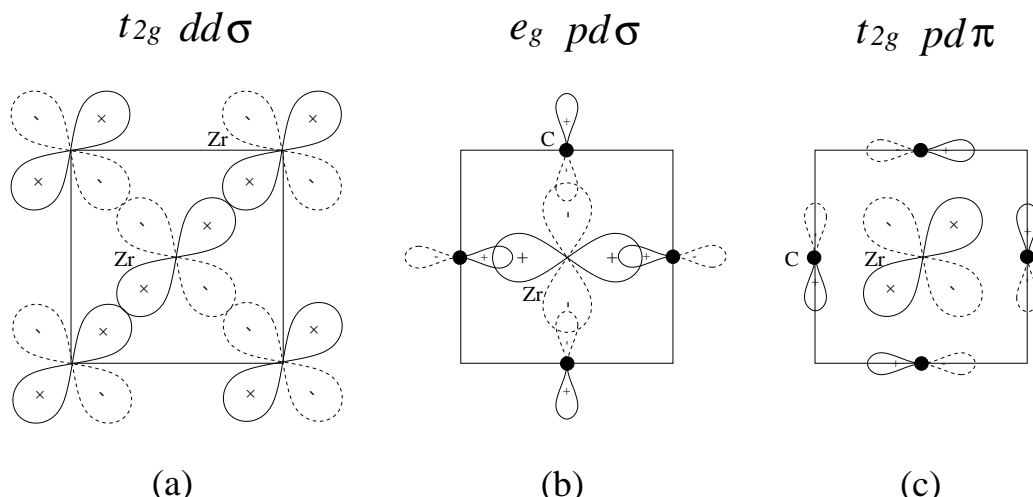


Figure 4-6: Bond types in fcc pure Zr and NaCl-ZrC.

very weakly, and keep in mind that this is a dangerous game that is prone to completely meaningless artifacts.

- Check the potential against properties that are *not* in the database. The more, the better.

Only when the potential is fully tested in almost all aspects, can we begin to trust the lattice conductivity it gives.

As it turned out, we did not use *any* experimental results in fitting this potential, as the experimental data are either too complex or contain too much noise to be suitable for fitting purposes. All of the property database are based on modern electronic structure calculations. Thus, whether I can correctly resolve the lattice conductivity of ZrC becomes a true test of the predictive power of the entire computational approach, as it will solve a problem of practical importance, and which has no known answer. One must proceed very carefully in each step.

4.2 Nature of Chemical Bonds in ZrC

Ti,Zr,Hf are group IV transition metals, whose zero-pressure ground-states are all hcp. The electron configuration of an isolated Zr atom is $5s^2 4d^2$. In condensed phases the s -electrons can be promoted to p - and d -orbitals to occupy bonding states

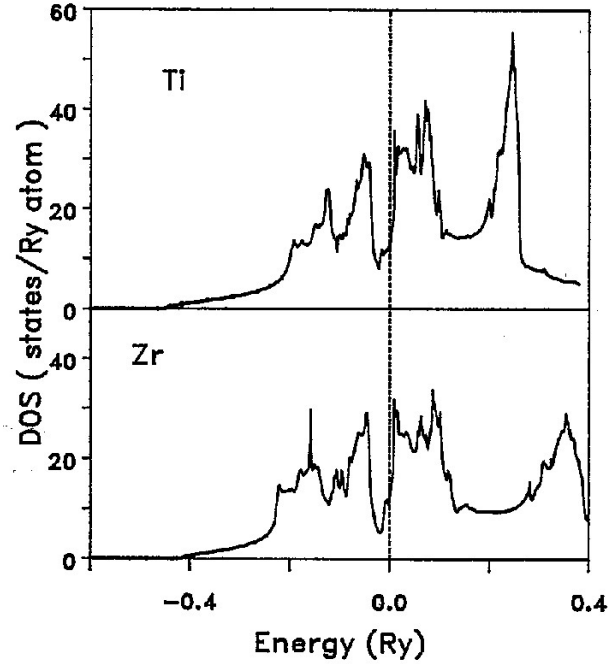


Figure 4-7: Electron density of states of Ti and Zr, reproduced from Fig. 6 of [152]. The dash line is the Fermi level.

with surrounding atoms. Exactly how that goes depends on the local environment. In fcc pure Zr and NaCl-ZrC, the point group of the crystal field surrounding a Zr atom is octahedral O_h group, under which the d -orbitals split into two irreducible representations: $t_{2g}:\{xy, yz, zx\}$, and $e_g:\{x^2 - y^2, 3z^2 - r^2\}$. In fcc Zr, the t_{2g} orbitals point to the nearest neighbor Zr atoms (bond type (a) in Fig. 4-6) and is lower in energy. To fully occupy them, each Zr atom needs 3 electrons, and so one s -electron is promoted to the d -band, leaving the other to the broader sp -band. Essentially the same thing happens in hcp Zr which is only a few hundredth of eV/atom lower in energy than fcc Zr [199]. The electron density of states of pure hcp Ti and Zr is reproduced in Fig. 4-7 [152]. Both are about 0.96 states/eV/atom at the Fermi level.

The reason fcc Zr is considered is because it serves as a reference state for NaCl-ZrC_X (see Fig. 4-8), which is a thermodynamically stable phase between $X = 0.5$ and $X = 1$ (Fig. 4-9). Because Zr is more than twice larger in Slater empirical radius (1.55Å) than C (0.7Å) [151], one can think of ZrC_X as carbon atoms filling in the octahedral interstitial sites of a fcc Zr lattice, which hardly changes the total

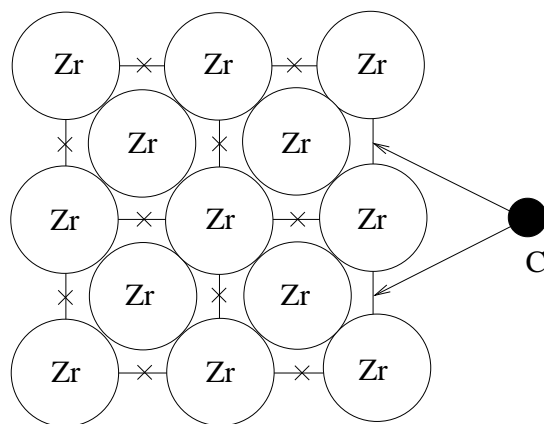


Figure 4-8: An intuitive view of NaCl-ZrC_x.

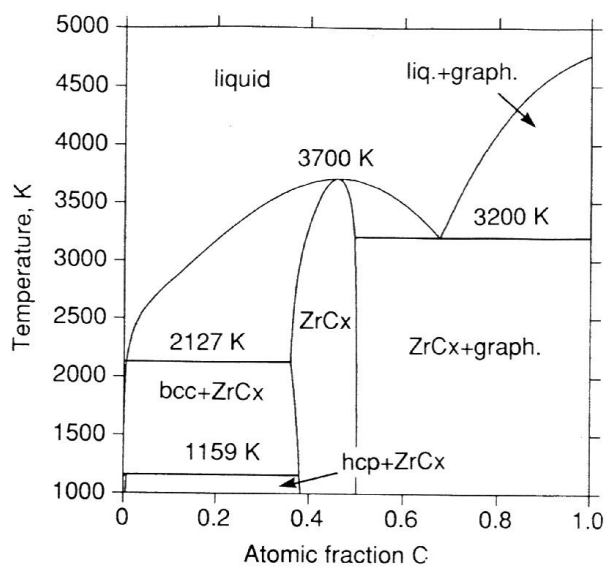


Figure 4-9: Phase diagram of Zr-C system, reproduced from Fig. 2 of [210].

volume. Even if all the interstices are filled, C only takes up 11.6% of the total mass. Nevertheless, it has a profound effect on the material’s properties, so much so that I think it is worthwhile to a quick look at a comparison of elastic constants in Table 4.1.

	hcp Zr[199]	ZrC[201]	TiC[205]	TiC (TB)[205]	ZrC (New)
C_{11} [GPa]	155.4	480.2	515	313	381.1
C_{12} [GPa]	67.2	101.8	106	207	121.0
C_{44} [GPa]	36.3	169.7	179	119	177.7

Table 4.1: Comparison of elastic constants of hcp Zr, ZrC and TiC. The first three columns are from experiment and recent *ab initio* calculations. The 4th column is of a recent tight-binding potential for TiC [205] that has been used on surface [204] and dislocation slip-system [206] problems. The last column is from my empirical potential for ZrC.

In the first column of Table 4.1, pure Zr shows the behavior of a typical metal, namely, a large C_{12} and a small C_{44} , therefore having a positive Cauchy discrepancy $(C_{12} - C_{44})/B$. However once the carbon atoms are added (second column in Table 4.1), the bulk modulus would be more than doubled. Even more dramatically, C_{44} would be nearly *quintupled*, such that its relative strength against C_{12} is now completely reversed, and we have a large negative Cauchy discrepancy, typical of ceramic materials. The fact that ZrC_X has an extremely high melting-point and is stable down to $X = 0.5$ (when C vacancies “percolate” and the fcc lattice collapses) can all be attributed to this extraordinary C_{44} . Something *different from metallic bonding* must have occurred in ZrC to strengthen the material by so much, in particular C_{44} .

The elastic constants of TiC are listed in the third column of Table 4.1, which are very close to those of ZrC. Because Ti/C and Zr/C are very similar in chemical properties, from now on I do not always distinguish them explicitly.

Another clue to what happens to the bonding is ZrC’s large heat of formation: 2.14 eV/pair, in its synthesis,



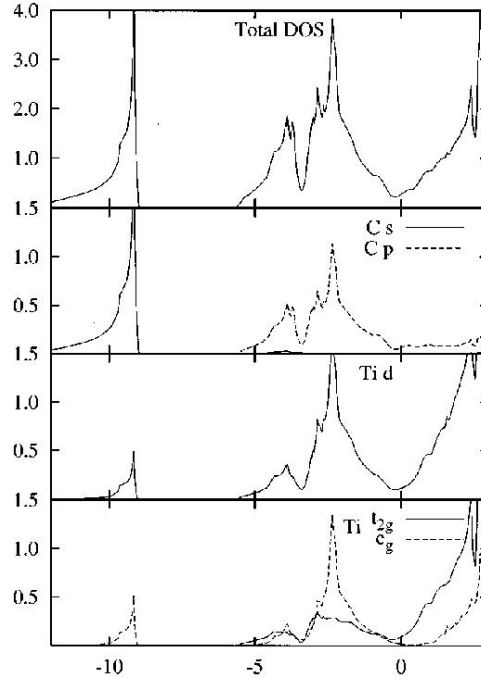


Figure 4-10: Total and representation decomposed electron density of states in NaCl TiC, reproduced from Fig. 4 of [207]. The Fermi level is at 0.

In comparison, SiC's heat of formation is only 0.64 eV/pair. This and above suggest that *strong bonds* of certain kind must be formed between metal and carbon, replacing the old metal-metal bonds. And those bonds must be highly *angular-dependent* in order to quintuple C_{44} .

What are those bonds? Structurally, the NaCl ground-state at first may suggest ionic bonding. There had been controversy about this [145, 212] historically, but the situation is now very clear that it is *not* the case. The properties of ZrC are dominated by the strong covalent bonds of $pd\sigma$ type illustrated in (b) of Fig. 4-6, assisted by weaker and slightly metallic $pd\pi$ bonds in (c) of Fig. 4-6. Though charge transfer occurs appreciably from Zr to C (0.42 electron) [205], it happens in an *isolated sd*-band 3.4 eV below the main band (see Fig. 4-10) and metallic screening neutralizes its apparent effects. In short, ionic bonding and the original metal-metal $dd\sigma$ bonds are weak in ZrC that they can be neglected in the first approximation. The story of ZrC is the story of how (b) and (c) bond types in Fig. 4-6 replaces the (a) bond type of pure Zr to receive the huge benefit of *chemical affinity* proportional to the heat of

formation, and what *prerequisites* that demands on the configuration.

To illustrate the above, consider the total and symmetry-decomposed electron density of states of TiC from a recent full potential LMTO calculation [207] in Fig. 4-10. At the Fermi level, the total DOS is 0.24 states/eV/atom, which is about 1/4 of that in hcp Ti. Below the Fermi level, C p - and Ti d - LDOS show a strong correlation, indicating the formation of substantial chemical bonding, in which the Ti d orbitals can be further decomposed into e_g and t_{2g} symmetry parts. We see that the e_g d -LDOS is in general larger than the t_{2g} d -LDOS, but it drops to zero at the Fermi level and is clearly split between occupied bonding and unoccupied anti-bonding states, which means that the $pd\sigma$ bond between C and Ti is purely covalent. On the other hand, the Ti t_{2g} d -LDOS, though weaker, is nonzero at the Fermi level, and it correlates with the non-zero C p -LDOS at the Fermi level. Thus, $pd\pi$ bonding between C and Ti is slightly metallic, which accounts for the fact that TiC is electrically conductive. The original Ti-Ti $dd\sigma$ bond plays little role in this electrical conductivity: it is tiny below the Fermi level that it can have little effect. Only when C is removed from the system does $dd\sigma$ bond begin to have a more significant influence, so we cannot ignore it completely.

If the main band is summed, one finds [205] that 3.01 electrons occupy the C p - and 2.99 electrons occupy the Ti d - orbitals, thereby confirming the rule of *local charge neutrality* in metallic alloys [155]. However, there is an isolated and narrow band 3.4 eV below the main band that has 1.41 electrons occupying C s -orbitals and 0.59 electrons occupying the Ti d -orbitals, which accounts for the total of 8 valence electrons of a Ti/C pair. As a side remark, we observe no sign of sp -hybridization on C of the types that occur in diamond or graphite.

Now comes the crucial question: why do $pd\sigma$ bonds and maybe to a lesser degree $pd\pi$ bonds, favor the octahedral arrangement and strongly resist its shear? This clearly has do with C, because pure Zr has a very small C_{44} (see Table 4.1). To put the question in perspective, let us consider the classical case of diamond. There, sp^3 hybridization favors the tetrahedral arrangement. It penalizes shear deformation relatively severely as compared to metals, because unlike volumetric deformation,

shear strain destroys the perfect *orthogonality* of hybridized orbitals in Hilbert space. Recall that sp^3 orbitals achieve orthogonality in Hilbert space without requiring them to be orthogonal in real space (bond angle 109.47°) *due to the participation of s-orbital*¹. Without hybridizing with the s -orbital, as the carbon p -LDOS in Fig. 4-10 clearly shows, the local orbitals on carbon pointing to the Zr neighbors composed of p -states only, necessarily have to be mutually orthogonal in real space in order to remain orthogonal in Hilbert space. Whenever that cannot be satisfied, the two $pd\sigma$ bonds involved should be both reduced in strength. Therefore, the octahedral arrangement with 6 Zr nearest neighbors is the maximum that a C atom can accommodate with the above criterion. If one adds in more neighbors, it would not receive nearly as much benefit in band energy as previous due to the *unavailability* of p -orbitals, whereas core repulsion would make this over-coordination attempt energetically unfavorable.

Thus the crucial points of a successful potential for ZrC_X must be the same as those of past potentials for Si or C, no matter whether it is formulated as empirical [157, 163, 164] or tight-binding model [168]. That is, how can one correctly describe the angular dependence of bonds, or *bond interference* effect.

4.3 The Potential Model

4.3.1 Introduction

The Finnis-Sinclair potential and its variants [169] based on the second-moment approximation [155] have been tremendously successful in modeling transition metals and their alloys during the past 15 years. Compared with similar approaches like the Embedded Atom Method [179, 182, 183] or the Effective Medium Theory [186, 191], its winning feature is simplicity. In 1989, Willaime and Massobrio [198] fitted such a second-moment potential for Zr with only 4 adjustable parameters. It has been shown to work rather well for defect formation and migration, thermal expansion and phonon properties in both hcp- and bcc-Zr; especially, it is able to capture the

¹ $|h_{[111]} \rangle = |s \rangle + |p_x \rangle + |p_y \rangle + |p_z \rangle$, $|h_{[1\bar{1}\bar{1}]} \rangle = |s \rangle + |p_x \rangle - |p_y \rangle - |p_z \rangle$, $|h_{[\bar{1}1\bar{1}]} \rangle = |s \rangle - |p_x \rangle + |p_y \rangle - |p_z \rangle$, $|h_{[\bar{1}\bar{1}1]} \rangle = |s \rangle - |p_x \rangle - |p_y \rangle + |p_z \rangle$.

temperature-dependent phonon anomalies in bcc-Zr that is related to the hcp \rightarrow bcc transition [199]. Recently the model has been used to study the fast diffusion of impurities in hcp Zr with additional parameterizations for Ni-Ni and Ni-Zr interactions [200].

We think that the WF potential is a good basis which the new empirical potential for Zr/C can use. True to its tradition, I decide that the number of additional parameters should be *minimized*. As shown in the last section, angular dependence (which is lacking in the WF potential) must now exist in the new potential to reflect the fundamental change in bonding nature from pure Zr to ZrC_x . The question is *what is the minimum number of parameters that is able to do that*. I have tried 11, 9, 7, and in the end settled down with 6 parameters to describe Zr-C bonding, in which 2 describe core repulsion and 2 describe hopping strength that are the same as the WF potential, and uses only 2 parameters to describe the angular dependence or *bond interference* effect. There is no explicit C-C term [202] because carbon separations in ZrC are well beyond their normal bond distance cutoffs, and attempting to fit them would subject the model to artifacts. Based on physical insights from the last section, a more plausible mechanism is proposed for the C-C force constants in ZrC, and my model indeed fits well to the results from a recent GGA calculation [201].

During the fitting it was observed that as the number of free parameters dropped from 11 to 9 to 7, and to 6, there is a gradual but appreciable increase in the fitting error. Nevertheless I stucked to the original plan of minimal-parameterization and keep reducing the description. Among several plausible mechanisms that can have similar effects, I only keep one that proves to be the most indispensable. In the long run, I think this approach would pay off. My database of fitting targets, though not small, is not wide and accurate enough that one can use to differentiate similar mechanisms. And *indeterminism*, that is, several mechanisms having identical effect, or one mechanism having *no* effect that reflects in the *current* database, is the most common trap in constructing a potential, as it is likely to generate “black holes” in the property space not fitted.

4.3.2 Second-moment approximation and WF potential for pure Zr

The moments theorem derived by Cyrot-Lackmann [203] is based on the Local Combination of Atomic Orbitals (LCAO) or Tight Binding (TB) picture of electronic structure. It formalizes the idea that the spread (and higher-order shape factors) of the valence electron LDOS at an atomic orbital is directly related to its “interactions”, or matrix elements, with neighboring orbitals, thus providing theoretical support for the *local interaction* approach that is used by almost all empirical potentials. To illustrate key concepts, let me briefly sketch its proof. For simplicity, allow me to pretend there is only one generic atomic orbital at each site, labelled by i or j .

Define

$$h_{ij} \equiv \langle i | \mathcal{H} | j \rangle, \quad e_i \equiv h_{ii}, \quad (4.1)$$

where \mathcal{H} is the self-consistent valence electron Hamiltonian. Assume also that the $|i\rangle$'s are Wannier function type orbitals [150] which are mutually orthogonal,

$$\langle i | j \rangle \equiv \delta_{ij}. \quad (4.2)$$

Let me label \mathcal{H} 's global eigenstate by k , with eigen-energy E_k ,

$$\mathcal{H} | k \rangle \equiv E_k | k \rangle. \quad (4.3)$$

The local density of states at i is,

$$\rho_i(E) \equiv \sum_k \delta(E - E_k) |\langle k | i \rangle|^2, \quad (4.4)$$

and the total density of states is

$$\rho(E) \equiv \sum_k \delta(E - E_k) = \sum_i \rho_i(E). \quad (4.5)$$

As a distribution, $\rho_i(E)$'s mean is,

$$\langle E \rangle_i \equiv \int dE \rho_i(E) E = \sum_k E_k |\langle k|i \rangle|^2 = \sum_k \langle i|\mathcal{H}|k \rangle \langle k|i \rangle = \langle i|\mathcal{H}|i \rangle = e_i. \quad (4.6)$$

This is quite intuitive. It says that when an atom is placed in condensed phase, its discrete electronic energy level spreads into band(s), but still *centers* around the old value².

Let me define the n th central moment of $\rho_i(E)$ to be,

$$\mu_i^{(n)} \equiv \int dE \rho_i(E) (E - e_i)^n = \sum_k (E_k - e_i)^n |\langle k|i \rangle|^2 = \langle i|(\mathcal{H} - e_i)^n|i \rangle, \quad (4.7)$$

which follows what happened before. But now comes the crucial step,

$$\mu_i^{(n)} = \langle i|(\mathcal{H} - e_i)^n|i \rangle = \sum_{j,j',\dots,j^{(n-2)}} \langle i|\mathcal{H} - e_i|j \rangle \langle j|\mathcal{H} - e_i|j' \rangle \dots |j^{(n-2)} \rangle \langle j^{(n-2)}|\mathcal{H} - e_i|i \rangle. \quad (4.8)$$

The product can be simplified using (4.1) and (4.2). j, j' etc. cannot be i , since

$$\langle i|\mathcal{H} - e_i|i \rangle = 0, \quad (4.9)$$

but when they are not i ,

$$\langle i|\mathcal{H} - e_i|j \rangle = \langle i|\mathcal{H}|j \rangle = h_{ij}. \quad (4.10)$$

Therefore,

$$\mu_i^{(n)} = \sum_{j,j',\dots,j^{(n-2)} \neq i} h_{ij} h_{jj'} \dots h_{j^{(n-2)}i}, \quad (4.11)$$

which sums over all real-space paths of n hops that both starts and ends at i . Specifically, for $n = 2$, there is

$$\mu_i^{(2)} = \sum_{j \neq i} |h_{ij}|^2. \quad (4.12)$$

²It is not quite exact because \mathcal{H} is now the self-consistent Hamiltonian, not the Hamiltonian of the isolated atom.

This remarkably clean result motivates the Finnis-Sinclair potential, which is based on the observation that although distributions $\rho_i(E)$ rigorously should be parametrized by $e_i, \mu_i^{(2)}, \mu_i^{(3)}, \dots$ up to $n = \infty$, a lot of times just e_i and $\mu_i^{(2)}$ would be good enough. Which is to say, one hypothesizes that there is an intrinsic character or shape to $\rho_i(E)$ that is relatively stable with respect to changes in the local configuration, *after being shifted by e_i and scaled by $\mu_i^{(2)}$* . That one may assume in the first approximation that $\rho_i(E)$ is parameterized by only e_i and $\mu_i^{(2)}$. Note that this does not require the shapes of $\rho_i(E)$ to be the same for all i 's. It can vary with the chemical species of i . Figuratively speaking, species A can have a block shape $\rho_i(E)$ whereas species B can have a Gaussian shape $\rho_i(E)$, within the same configuration. It only requires that $\rho_i(E) \approx \rho_A(E|e_i, \mu_i^{(2)})$ for A and $\rho_i(E) \approx \rho_B(E|e_i, \mu_i^{(2)})$ for B atoms.

Let us consider the system total energy E^{tot} , which is our object of fitting. Within the tight binding approximation, the total energy can be expressed as [153],

$$E^{\text{tot}} = E^{\text{rep}} + E^{\text{b}}, \quad (4.13)$$

where E^{rep} is the repulsive potential that comes from overlapping cores. The band structure energy,

$$E^{\text{b}} \equiv \int^{E_F} dE \rho(E) E, \quad (4.14)$$

is attractive and describes the valence electron bonding effect that holds the material together. We may define localized version of the bonding energy as,

$$E_i^{\text{b}} \equiv \int^{E_F} dE \rho_i(E) E, \quad \longrightarrow \quad E^{\text{b}} = \sum_i E_i^{\text{b}}. \quad (4.15)$$

The Fermi level E_F is determined by solving the implicit equation,

$$\int^{E_F} dE \rho(E) \equiv N, \quad (4.16)$$

where N is the total number of electrons. The above is true for the general system,

but in metals and alloys, a even stronger condition should hold,

$$\int^{E_F} dE \rho_i(E) \equiv 1, \quad (4.17)$$

which is the so-called *local charge neutrality* condition [155]. It is based on the observation that screening in metals is exceedingly efficient that there can be practically no net charge transfer. If we start with some unequal distribution in charge, Gauss' theorem would lead to a *long-ranged* electric field which simply cannot be tolerated in a metal: electrons from afar would flow in/out to the field source until the condition is corrected completely³.

Let us do a dimensional analysis on E_i^b by using $\sqrt{\mu_i^{(2)}}$, the spectrum spread, as the basic energy scale, and define the cumulative distribution,

$$\int^{E_F} dE \rho_i(E|e_i, \mu_i^{(2)}) \equiv P_{\alpha_i}(E_F, e_i, \sqrt{\mu_i^{(2)}}) = g_{\alpha_i} \left(\frac{E_F - e_i}{\sqrt{\mu_i^{(2)}}} \right), \quad (4.18)$$

where α_i is the chemical type of atom i , and the second equality is due to

$$\rho_i(E|e_i, \mu_i^{(2)}) = \frac{1}{\sqrt{\mu_i^{(2)}}} \rho_i \left(\frac{E - e_i}{\sqrt{\mu_i^{(2)}}} \right), \quad (4.19)$$

by dimensional argument. Therefore, the solution to (4.17) must be

$$\frac{E_F - e_i}{\sqrt{\mu_i^{(2)}}} = c_{\alpha_i} \equiv g_{\alpha_i}^{-1}(1), \quad (4.20)$$

where c_{α_i} is a configuration independent constant. Using the same dimensional argument one can show that,

$$\int^{E_F} dE \rho_i(E) E = E_i^b(E_F, e_i, \sqrt{\mu_i^{(2)}}) = -\sqrt{\mu_i^{(2)}} f \left(\frac{E_F - e_i}{\sqrt{\mu_i^{(2)}}} \right), \quad (4.21)$$

³Charge transfer occurs in insulators and semiconductors because even as the surrounding medium feels the electrostatic potential and does not like it, there is no way for their electrons to flow in/out to the source because *there is no extra states available at the source*. The medium can only put up incomplete screening - the dielectric response, by locally rearranging the charges.

and therefore,

$$E_i^b = \sqrt{\mu_i^{(2)}} f(c_{\alpha_i}) = -f_{\alpha_i} \sqrt{\mu_i^{(2)}}, \quad (4.22)$$

where f_{α_i} is again a *configuration independent* constant. And so,

$$E^b = \sum_i E_i^b = -\sum_i f_{\alpha_i} \sqrt{\mu_i^{(2)}} = -\sum_i f_{\alpha_i} \sqrt{\sum_{j \neq i} |h_{ij}|^2}, \quad (4.23)$$

which is the conclusion of the second-moment approximation.

(4.23) provides valuable insights into how one may fit empirical potentials for metals, especially for transition metals whose narrow d -band satisfies the (4.19) description very well. In practice, one may take h_{ij} to be $|h_{ij}|$, because the phase factor of the matrix element $\langle i|\mathcal{H}|j\rangle$ has no use in (4.23). For a monoatomic metal, the constant f_{α_i} can be absorbed into h_{ij} and need not to be fitted separately. For an alloy, f_{α_i} can also be absorbed, but we would then lose the symmetry $h_{ij} = h_{ji}$. However, many people would not bother with that subtlety [200], and continue to assume that $h_{ij} = h_{ji}$.

It is a common practice in tight-binding theory to assume that the core repulsion E^{rep} in (4.13) is the sum of pair interactions,

$$E^{\text{rep}} = \sum_i \left(\sum_{j \neq i} \phi_{\alpha_i \beta_j}(r_{ij}) \right), \quad (4.24)$$

for which the simple exponential form $a_{\alpha\beta} \exp(-b_{\alpha\beta} r)$ is widely used.

The main conceptual proposition of the Finnis-Sinclair potential is that h_{ij} in (4.23) can also be well-represented by a radial function $h_{\alpha_i \beta_j}(r_{ij})$. This is to a large degree a very good approximation in transition metals, for the following reason: there are *five* d -orbitals at every atom, and each d -orbital has *four* lobes (expect $3z^2 - r^2$) that can point to four neighbors simultaneously, so overall there is less shortage of empty orbitals that can bond with a new neighbor, and which still remains largely orthogonal to other occupied bond orbitals in Hilbert space. In contrast, in ZrC, the availability of C p -orbitals is a real issue: because there are only *three* p -orbital at each site and a p -orbital has only two lobes that can form σ -bond with neighbors. There-

fore, it should not be surprising that $h_{ij} = h(r_{ij})$ may be an excellent approximation for Zr-Zr, but not so for Zr-C bonds.

A properly parametrized second-moment empirical potential,

$$E^{\text{tot}} = \sum_i \left(\sum_{j \neq i} \phi_{\alpha_i \beta_j}(r_{ij}) - \sqrt{\sum_{j \neq i} h_{\alpha_i \beta_j}^2(r_{ij})} \right), \quad (4.25)$$

can be a great improvement over pair potentials like the Lennard-Jones or Morse potential, for metals. Foremost, the many-body effect of *saturation* is built in. If an atom has Z neighbors, the bonding energy is $\propto \sqrt{Z}$ instead of $\propto Z$ as a pair potential would give. This means lower coordination number structures like the bcc phase may now be stabilized against the fcc phase. The strength of an individual bond, that is, how much force a bond can convey when the other atom is displaced, is now $\propto 1/\sqrt{Z}$, which is the same for the energy benefit of adding a new neighbor. Secondly, the fact that (4.25) is based on more physics is reflected naturally in its elastic properties. A pair potential can only give $C_{12} = C_{44}$. Without much elaboration, most (4.25) parameterizations would give a C_{12} that is closer to twice of its C_{44} , which is what actually happens for most metals. Lastly, in terms of computational effort, (4.25) is on the same order as a pair potential, in fact no more than twice as expensive. The above features make (4.25) the method of choice for atomistic simulation of metals.

Willaime and Massobrio (WM) published their potential for Zr in 1989 [198]:

$$E^{\text{tot}} = \sum_i V_i, \quad (4.26)$$

$$V_i = \left\{ a \sum_{r_{ij} < r_c} \exp \left[-p \left(\frac{r_{ij}}{r_0} - 1 \right) \right] \right\} - \left\{ \sum_{r_{ij} < r_c} \xi^2 \exp \left[-2q \left(\frac{r_{ij}}{r_0} - 1 \right) \right] \right\}^{1/2} \quad (4.27)$$

with the parameters listed in Table 4.2.

Table 4.2: Parameters of WM potential in (4.27) form

$a[\text{eV}]$	$r_c[\text{\AA}]$	p	$r_0 [\text{\AA}]$	$\xi[\text{eV}]$	q
0.179364	6.8	9.3	3.1744	2.2014548	2.1

Within the eV-Å unit system, (4.27) can be massaged into a numerically simpler form,

$$V_i = \left\{ \sum_{r_{ij} < r_c} \exp[A(B - r_{ij})] \right\} - \left\{ \sum_{r_{ij} < r_c} \exp[C(D - r_{ij})] \right\}^{1/2} \quad [\text{eV}], \quad (4.28)$$

where

$$A \equiv \frac{p}{r_0}, \quad B \equiv r_0 \left(1 + \frac{\log(a)}{p} \right), \quad C \equiv \frac{2q}{r_0}, \quad D \equiv r_0 \left(1 + \frac{\log(\xi)}{q} \right). \quad (4.29)$$

Thus there are only four free parameters in the model if one exclude r_c , and they are listed in Table 4.3.

Table 4.3: Parameters of massaged WM potential (4.28) in the eV-Å unit system

$A_{\text{ZrZr}}[\text{\AA}^{-1}]$	$B_{\text{ZrZr}}[\text{\AA}]$	$C_{\text{ZrZr}}[\text{\AA}^{-1}]$	$D_{\text{ZrZr}}[\text{\AA}]$
2.9296875	2.58787395638939	1.32308467741935	4.3672464262563

4.3.3 New Empirical Potential for Zr/C

To continue from last section, it is a common practice to extend the second-moment potential to AB alloys,

$$\begin{aligned}
E^{\text{tot}} &= \sum_{i \in A} V_i + \sum_{i \in B} V_i, \\
\forall i \in A : \\
V_i &= \sum_{j \in A \neq i} \phi_{AA}(r_{ij}) + \sum_{j \in B} \phi_{AB}(r_{ij}) - X_i^{1/2} \\
X_i &= \sum_{j \in A \neq i} h_{AA}^2(r_{ij}) + \sum_{j \in B} h_{AB}^2(r_{ij}), \\
\forall i \in B : \\
V_i &= \sum_{j \in A} \phi_{BA}(r_{ij}) + \sum_{j \in B \neq i} \phi_{BB}(r_{ij}) - X_i^{1/2} \\
X_i &= \sum_{j \in A} h_{BA}^2(r_{ij}) + \sum_{j \in B \neq i} h_{BB}^2(r_{ij}), \quad (4.30)
\end{aligned}$$

where one certainly can have

$$\phi_{AB}(r_{ij}) = \phi_{BA}(r_{ij}). \quad (4.31)$$

And although it is *not* supported by theory, to save parameterization one may stipulate that,

$$h_{AB}(r_{ij}) = h_{BA}(r_{ij}). \quad (4.32)$$

The new Zr/C potential follows the expression of (4.30) with A=Zr and B=C, but with the following important modifications,

- Unlike $h_{\text{ZrZr}}(r)$, the so-called *bare strength* $h_{\text{ZrC}}(r)$ would not be used directly in (4.30). The so-called *screened strength* \tilde{h}_{ZrC} would take its place, whose value is h_{ZrC} scaled by an interference factor depending on nearby h_{ZrC} strengths and respective angular cosines.
- The bare strength is supposed to be the overlap matrix element when both atoms have *empty* bonding orbitals pointing to each other. For Zr-Zr this is not a big problem, but for Zr-C it is severely constrained by the availability of carbon *p*-orbitals, and its orthogonality preference in Hilbert space (thus in real space).
- h_{ZrC} must be stronger than h_{ZrZr} , but it must also be short-ranged. A cutoff distance of $r_c^{\text{ZrC}} = 3.5\text{\AA}$ is imposed arbitrarily, which is right in the middle of the first and third nearest neighbor (both Zr-C) distances in NaCl-ZrC.
- I have set $h_{\text{CC}} = \phi_{\text{CC}} = 0$, which differs from the cohesive energy model of [202]. There is no evidence of direct C-C bonding in ZrC. C-C distances in ZrC ($\sim 3.3\text{\AA}$) are well larger than their normal cutoff distances ($\sim 2.1\text{\AA}$) [161, 164, 167], and the size of Zr atom should provide excellent screening (see Fig. 4-8). The large energy gain of Zr-C bonding should make C's electrons concentrate on nearest neighbor bonds of mostly covalent character, in a Zr-rich environment.
- We will use simple exponential form for both $\phi_{\alpha\beta}(r)$ and $h_{\alpha\beta}(r)$ following the

WF potential. But the WF potential has no smooth cutoffs, which is problematic in atomistic simulations. We will impose smooth cutoff scheme on all functions by multiplying with $\exp(\frac{K}{r-r_c})$ with an arbitrarily picked $K = 0.1$ Å, which would make all derivatives continuous at $r = r_c$. The original $r_c^{\text{ZrZr}} = 6.8$ Å is now shifted to $r_c^{\text{ZrZr}} = 7$ Å to accommodate this change, and we have found no significant differences in the fitted pure Zr properties after this modification.

- I will take the shortcut $h_{\text{ZrC}}(r) = h_{\text{CZr}}(r)$ with the intent of saving one parameter. In the future, if the database is substantially enlarged and contains more off-stoichiometry targets, I may release this constraint.

To recapitulate, $\phi_{\text{CC}}(r) = h_{\text{CC}}(r) = 0$, and,

$$\begin{aligned} \phi_{\text{ZrZr}}(r) &= \exp\left(A_{\text{ZrZr}}(B_{\text{ZrZr}} - r) + \frac{K}{r - r_c^{\text{ZrZr}}}\right) \quad [\text{eV}], \\ h_{\text{ZrZr}}^2(r) &= \exp\left(C_{\text{ZrZr}}(D_{\text{ZrZr}} - r) + \frac{K}{r - r_c^{\text{ZrZr}}}\right) \quad [\text{eV}^2], \end{aligned} \quad (4.33)$$

where $K = 0.1$ Å, $r_c^{\text{ZrZr}} = 7$ Å, and A_{ZrZr} , B_{ZrZr} , C_{ZrZr} , D_{ZrZr} are listed in Table 4.3. And,

$$\begin{aligned} \phi_{\text{ZrC}}(r) &= \phi_{\text{CZr}}(r) = \exp\left(A_{\text{ZrC}}(B_{\text{ZrC}} - r) + \frac{K}{r - r_c^{\text{ZrC}}}\right) \quad [\text{eV}], \\ h_{\text{ZrC}}(r) &= h_{\text{CZr}}(r) = \exp\left(C_{\text{ZrC}}(D_{\text{ZrC}} - r) + \frac{K}{r - r_c^{\text{ZrC}}}\right) \quad [\text{eV}], \end{aligned} \quad (4.34)$$

with $r_c^{\text{ZrC}} = 3.5$ Å, and A_{ZrC} , B_{ZrC} , C_{ZrC} , D_{ZrC} are to be fitted.

After many iterations of selections and reductions, I decided that the screening of h_{ZrC} should take the following form:

$$\tilde{h}_{\text{ZrC}}(i = \text{Zr}, j = \text{C}) = h_{\text{ZrC}}(r_{ij}) \times \exp\left(-\frac{\sqrt{s_{ij}}}{h_{\text{ZrC}}(r_{ij})}\right), \quad (4.35)$$

where i is the Zr atom and j is the C atom of the Zr-C bond, and the screening

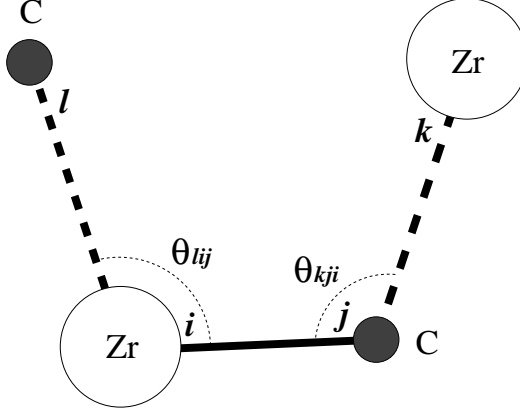


Figure 4-11: An illustration of the Zr-C bond screening.

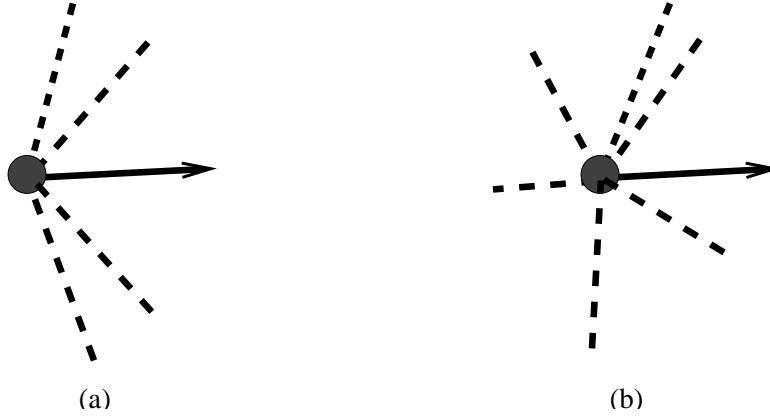


Figure 4-12: (a) Should screening loss be a geometrical series? (b) “Random” screening loss approximation.

strength s_{ij} is,

$$s_{ij} \equiv \sum_{l \in \text{C}} \left(\frac{1 + \cos \theta_{lij}}{\alpha_{\text{ZrC}}} \right)^{\beta_{\text{ZrC}}} h_{\text{ZrC}}^2(r_{il}) + \sum_{k \in \text{Zr}} \left(\frac{1 + \cos \theta_{kji}}{\alpha_{\text{CZr}}} \right)^{\beta_{\text{CZr}}} h_{\text{ZrC}}^2(r_{jk}), \quad (4.36)$$

where l 's are all the C atoms that interacts with i , and k 's are all the Zr atoms that interacts j (see Fig. 4-11). For the sake of reduction I have taken $\alpha_{\text{ZrC}} = \alpha_{\text{CZr}}$ and $\beta_{\text{ZrC}} = \beta_{\text{CZr}}$, so we have only two screening parameters to fit.

The meaning of (4.35,4.36) is the following:

1. How strongly ij matrix element is screened must depend on the bare strengths of the screener: il or jk . We cannot have a new neighbor just entering the cutoff to strongly screen other bonds which are much closer to i or j . Therefore

s_{ij} must depend on $h_{\text{ZrC}}(r_{il})$ and $h_{\text{ZrC}}(r_{jk})$ in some fashion. As normalization, $h_{\text{ZrC}}(r_{ij})$ ends up in the denominator.

2. $\sqrt{s_{ij}}$ is used instead of s_{ij} in (4.35) for the following reason. When ij bond is not perfectly orthogonal to the other bonds, the screening penalty might work a bit like the Gram-Schmidt procedure in linear algebra: one keeps subtracting off components that are aligned to the other vectors until finally ending up with a part that can be called its own. When we put s_{ij} in the exponential, it can be considered as the *loss rate* during that procedure. The question is, is geometrical series loss rate - meaning when ij is screened by the first bond it losses a certain ratio, and when it is screened by the second bond it losses another ratio of *what's left*, reasonable?

I consider it to be too drastic, since the vectors that inflict the loss have redundancy in themselves (see (a) of Fig. 4-12). In my opinion, the screening actions are not organized, so the total effect should be summed according to the rule of summing random numbers, and thus the rationale for using $h_{\text{ZrC}}^2(r_{il})$ and $h_{\text{ZrC}}^2(r_{jk})$ in (4.36), and $\sqrt{s_{ij}}$ is used instead of s_{ij} in (4.35).

3. As for the angular dependence, I chose the simplest form available. β_{ZrC} will be large, so the screening would be practically non-existent when $\theta \geq 2\pi/3$, but it rises dramatically when $\theta < \pi/2$.

The procedure and results of fitting (4.34,4.36) will be detailed in the next section. But the optimized parameters are listed in Table 4.4 here.

Table 4.4: Optimized parameters of (4.34,4.36) in the eV-Å unit system

$A_{\text{ZrC}}[\text{\AA}^{-1}]$	$B_{\text{ZrC}}[\text{\AA}]$	$C_{\text{ZrC}}[\text{\AA}^{-1}]$	$D_{\text{ZrC}}[\text{\AA}]$
3.24589393669854	2.05679804919117	0.82303818052368	4.15482225815134
α_{ZrC}	β_{ZrC}		
1.80853303846249	14.59345494373451		

With the optimized parameters in Table 4.4, the screening factor $\exp(-\sqrt{s_{ij}})$ is illustrated in Fig. 4-13, where we simplify by taking all h 's to be of equal strength.

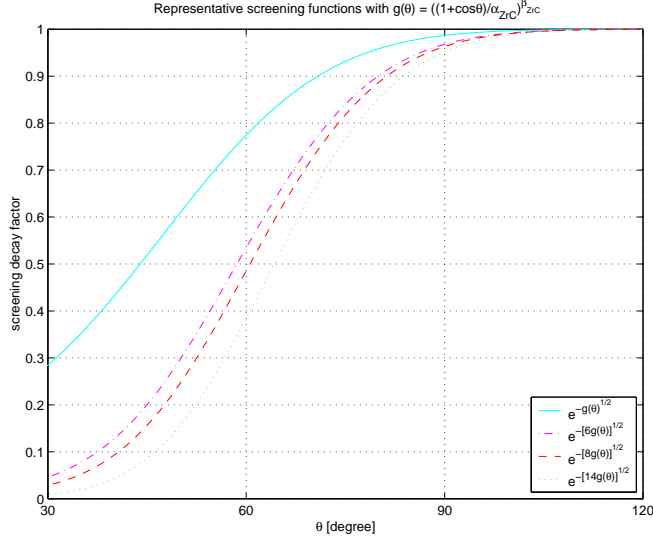


Figure 4-13: Illustration of the screening decay factor $\exp(-\sqrt{s_{ij}})$ (assuming all h 's are equal).

In NaCl ZrC, for each Zr-C bond there are $2 \times 4 = 8$ other Zr-C bonds attached, with bond angle $\sim \pi/2$ (2 other bonds with angle $\sim \pi$ have little effect), so $\exp(-\sqrt{8((1 + \cos \theta)/\alpha_{\text{ZrC}})^{\beta_{\text{ZrC}}}})$ is drawn for an illustration of the magnitude and stiffness of screening; and the same for $2 \times 3 = 6$ (ZnS structure) at $\theta \sim 109.47^\circ$ and $2 \times 7 = 14$ (CsCl structure).

Fig. 4-14 shows the bare strengths $2\phi_{\text{ZrZr}}(r)$, $-h_{\text{ZrZr}}(r)$, $2\phi_{\text{ZrC}}(r)$, $-h_{\text{ZrC}}(r)$. Note that ϕ and h are *not* directly comparable, because ϕ 's effect increases linearly with coordination Z , but h 's effect increases as $\propto \sqrt{Z}$. They are together in Fig. 4-14 only for illustration purposes.

4.4 Fitted Properties

Cohesive Energy Curves of Three Cubic Phases

Cohesive energy curves of ZrC in three cubic structures: NaCl, ZnS and CsCl, are shown in Fig. 4-15, corresponding to coordination numbers 6, 4 and 8. My results are shown in dash lines, the LDA results are shown in solid lines and are rigidly shifted to match in $E_{\text{min}}^{\text{NaCl-ZrC}}$, as the absolute value of the LDA total energy carries

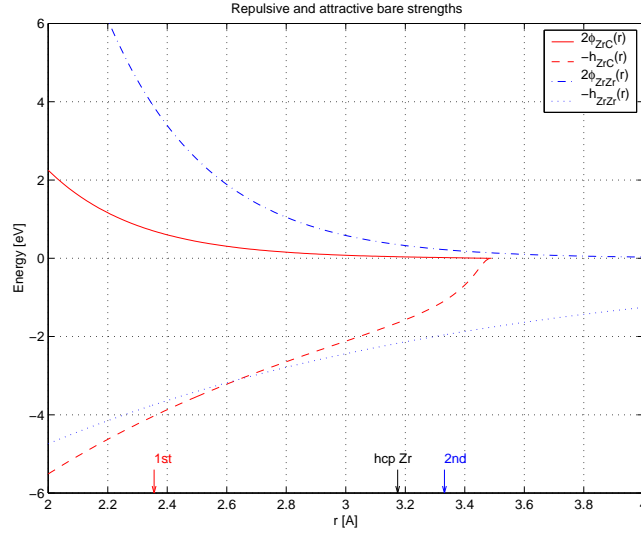


Figure 4-14: Radial functions for bare interaction strengths. The *1st* arrow is at the nearest neighbor distance (Zr-C) in equilibrium ZrC; the *2nd* arrow is at the second-nearest neighbor distance (Zr-Zr) in equilibrium ZrC. The *hcp Zr* arrow is at the nearest neighbor distance (Zr-Zr) in equilibrium hcp Zr.

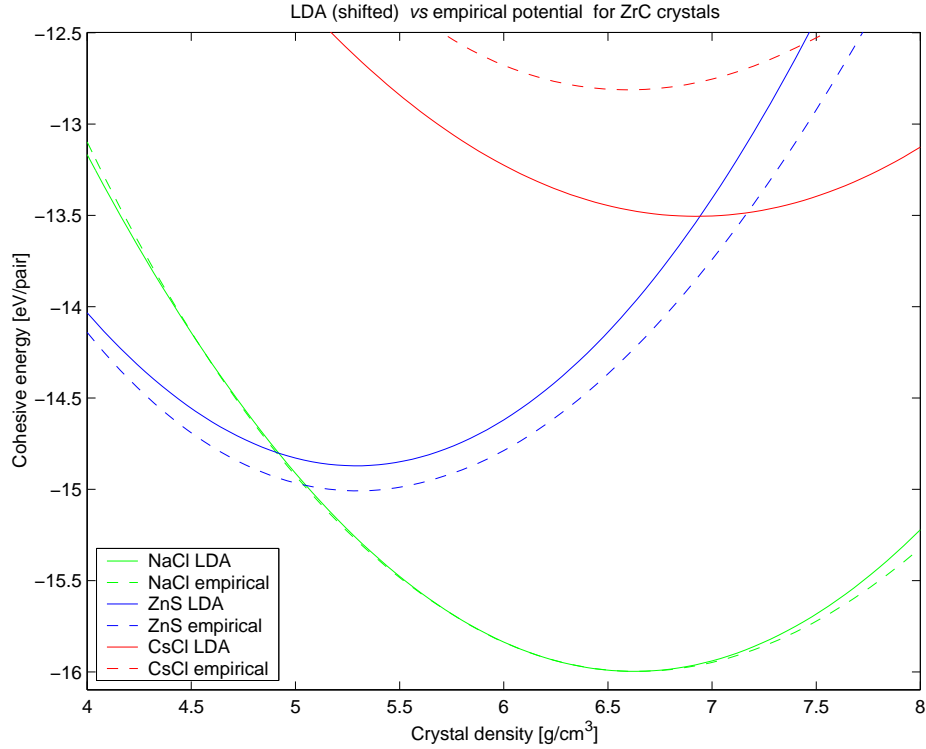


Figure 4-15: Cohesive energy curves of three cubic phases of ZrC: NaCl-ZrC, ZnS-ZrC, CsCl-ZrC. Solid lines are from LDA calculations (rigidly shifted to match in $E_{\min}^{\text{NaCl-ZrC}}$), dash lines are from my empirical potential.

no meaning, whereas my potential does.

Not many bond-order potentials for compounds nowadays are able to fit three different phases this well. The Tersoff potential for SiC, for example, behaves badly for structures other than the 4-coordinated, as the potential only ensures that they are pushed “up” in energy.

Elastic Constants of NaCl-ZrC

I then focus on NaCl-ZrC at $P = 0$. The elastic constants from my potential are given in the rightmost column of Table 4.1. They are significantly better than the results of the tight-binding potential of Tan *et al* [205] whose hopping integrals do not have angular dependence ($h_{\alpha\beta} = h_{\alpha\beta}(r)$). Specifically, my $C_{44} \gg C_{12}$, whereas their $C_{12} \gg C_{44}$, under the master constraint that both give the same bulk modulus. This comparison suggests that environment dependence is essential for correctly describing the largely covalent bonding in such systems, which offers more shear resistance than purely metallic systems. On the other hand, the natural complexities of environment dependence can easily make a researcher fall into the trap of over-parameterization (for a limited database), so I strive to obtain a minimal description, in the end getting a 6-parameter model with only 2 parameters for the angular dependence. Whether that works or not needs to be carefully tested.

Atomic Force Constants of NaCl-ZrC

A very recent work by Jochym and Parlinski [201] provides elastic constants and atomic force constants of NaCl-ZrC. After comparing experimental, LDA and GGA calculation results, they conclude that the GGA results are the most accurate. So I use their GGA calculation result as my fitting target. My force constants are obtained by setting up a large cell, moving the atom at origin (C or Zr) by a small amount, and seeing the forces on the surrounding atoms. Due to cubic symmetry, just one small displacement in the x -direction is sufficient.

C atom force constants are shown in Fig. 4-16. Zr atom force constants are shown

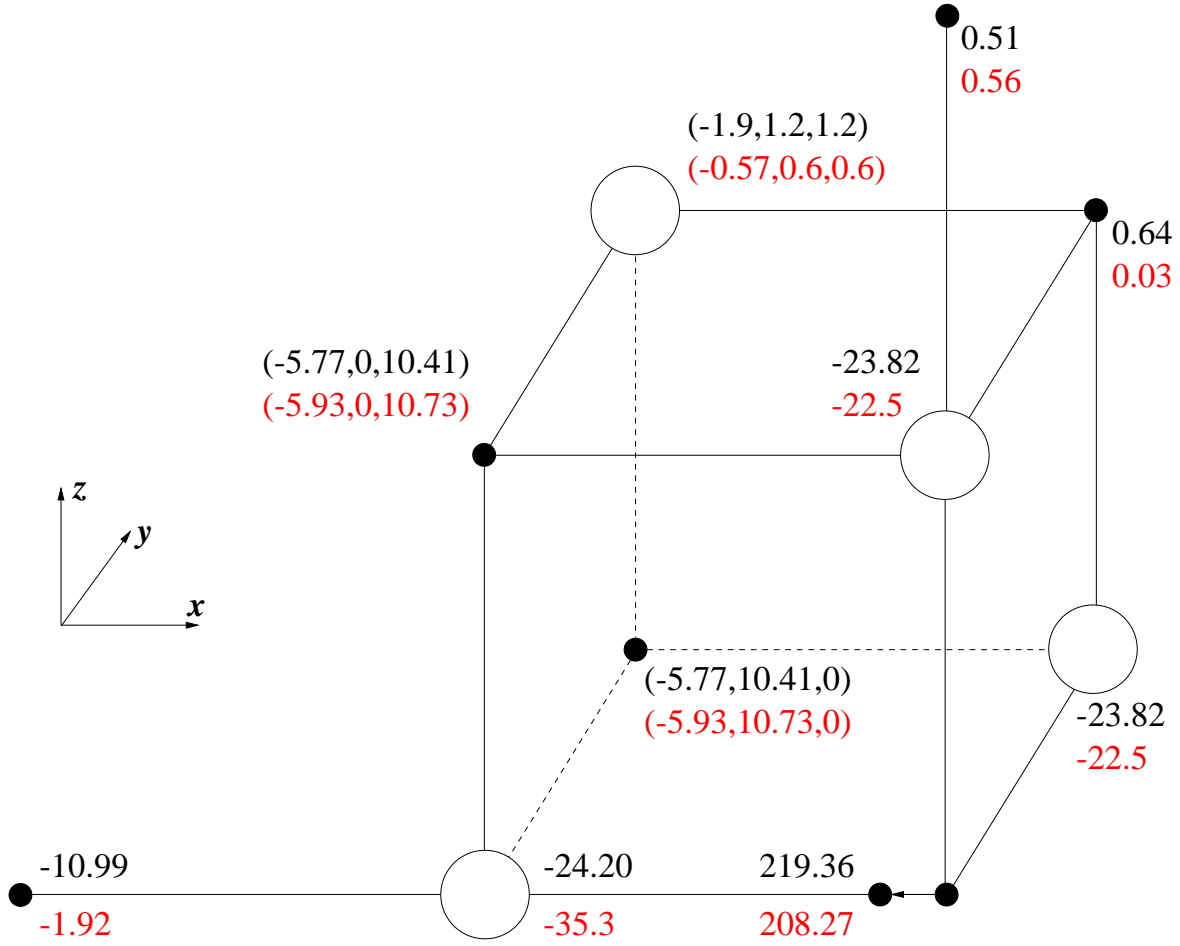


Figure 4-16: C atom force constants in ZrC in unit of N/m. Jochym *et al*'s GGA calculation results [201] are the numbers above, my results are the numbers below. Only the atoms that contribute significantly to the total “resistance” are shown, and some are omitted by symmetry.

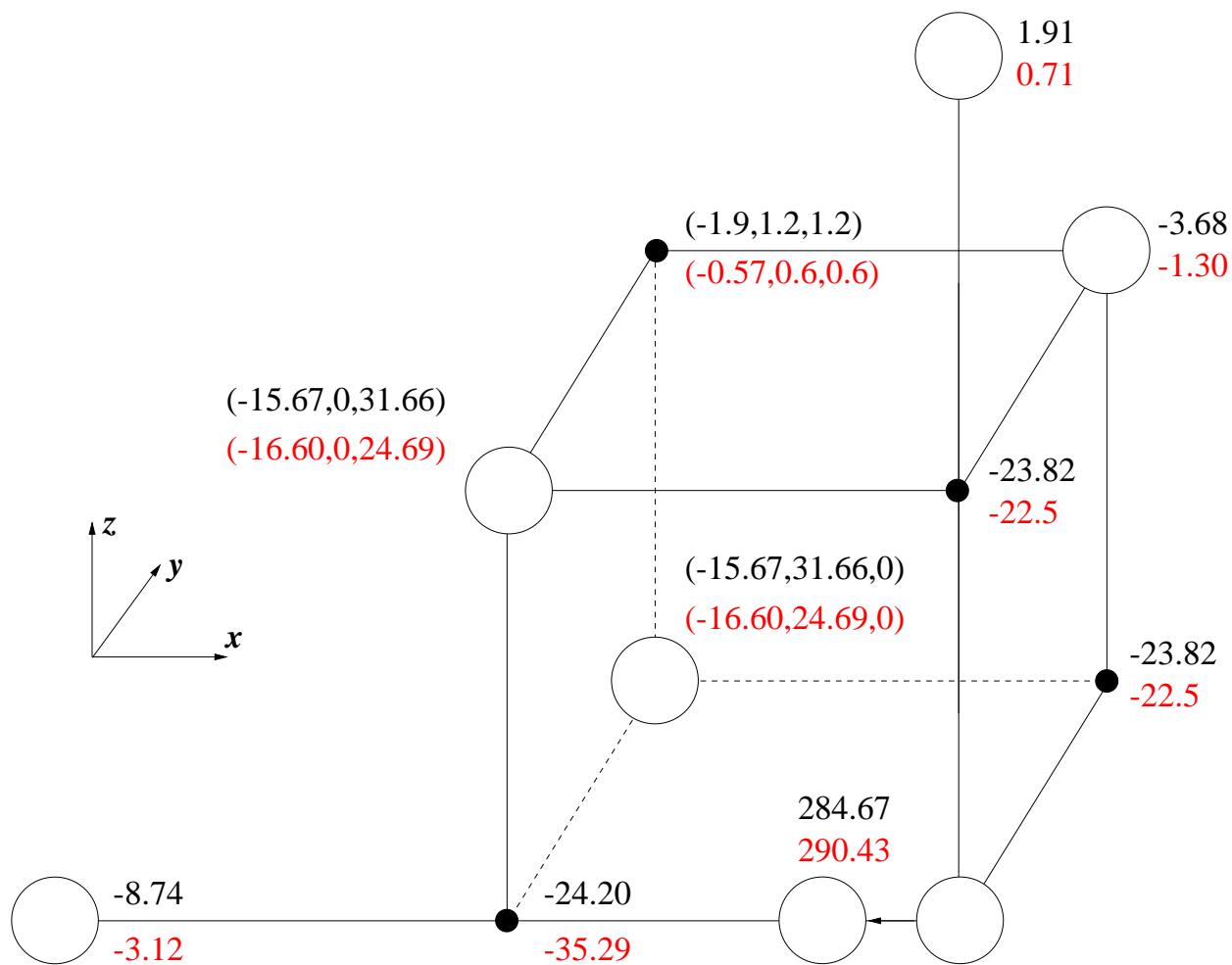


Figure 4-17: Zr atom force constants in ZrC in unit of N/m. Jochym *et al*'s GGA calculation results [201] are the numbers above, my results are the numbers below. Only the atoms that contribute significantly to the total “resistance” are shown, and some are omitted by symmetry.

in Fig. 4-17. Only the atoms that contribute significantly to the total “resistance” are shown, and some are omitted by symmetry. The agreement is seen to be quite good. Especially, note that in the GGA result, the four neighbors in the transverse plane of the displacement offer as much resistance per atom as the two neighbors directly opposite to or behind of the displacement. This, more than anything, supports our primary understanding about the nature of bonding in ZrC, which is the strong bond angle dependence. If one uses a pair potential, as I have tried using both the binary Lennard-Jones and Morse potentials, one can never capture this essential piece of physics, as the atom directly opposite to the displacement always offers > 3 times more resistance than the lateral atoms. In other words, as I have verified, even as the binary Lennard-Jones or the Morse potential are able to give satisfactory cohesive energy curves and C_{11} , $C_{12} = C_{44}$, they are still bound to fail catastrophically in terms of the atomic force constants. The atomic force constants provide unique microscopic insights otherwise covered up in the total energetics. They are highly sensitive reflections of the nature of bonding.

The phonon dispersion curve of ZrC is plotted in Fig. 4-18, along with experimental results [209] and results from Jochym *et al*’s GGA calculations [201]. The agreement is excellent for the acoustic branches, and is satisfactory for the optical branches as they do not contribute significantly to the lattice thermal conductivity. The overall quality of agreement in Fig. 4-18 is better than that of the Tersoff potential for SiC.

Phonon DOS and LDOS are shown in Fig. 4-19. They are in good agreement with the results of Jochym *et al* [201]. Especially, the Zr atom LDOS almost completely fills the acoustic band while the C atom LDOS almost completely fills the optical band. This “decoupled” behavior is somewhat unexpected since the Zr and C atoms interact strongly. My explanation to this is that there is a large *size* difference between Zr and C atoms. If one compares Fig. 4-16 with Fig. 4-17, one sees that the second nearest neighbor interaction between C-C is much weaker than the second nearest neighbor interaction between Zr-Zr, which supports the picture of packed spheres (Zr) but with interstices filled by tiny spheres (C), where the main

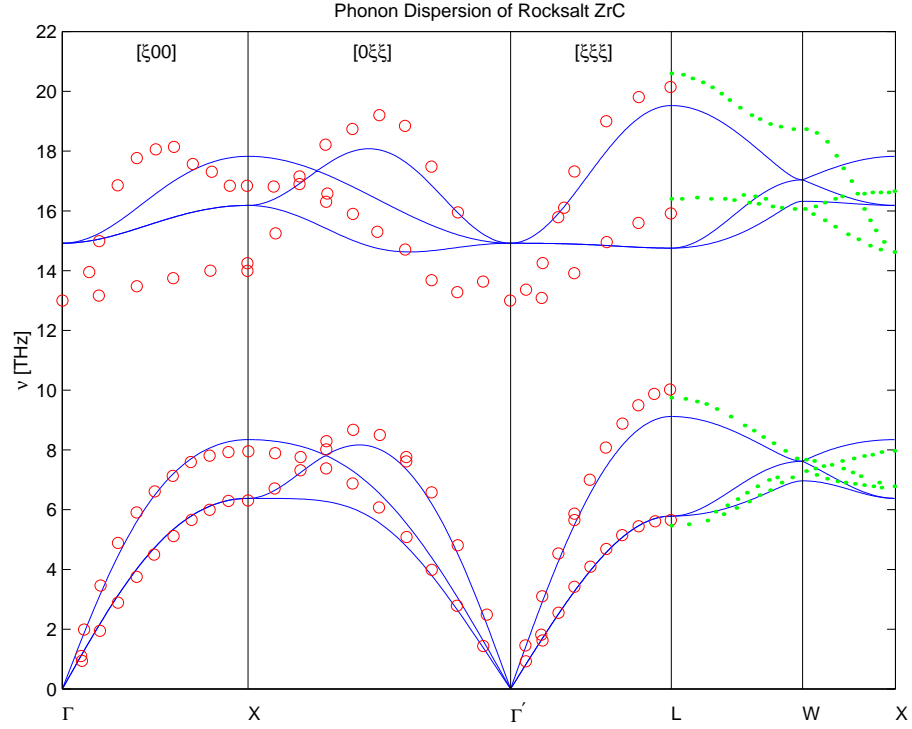


Figure 4-18: Phonon dispersion curve of ZrC: comparing my result (solid line) with experiment [209] (circles), and recent GGA calculations [201] (dots).

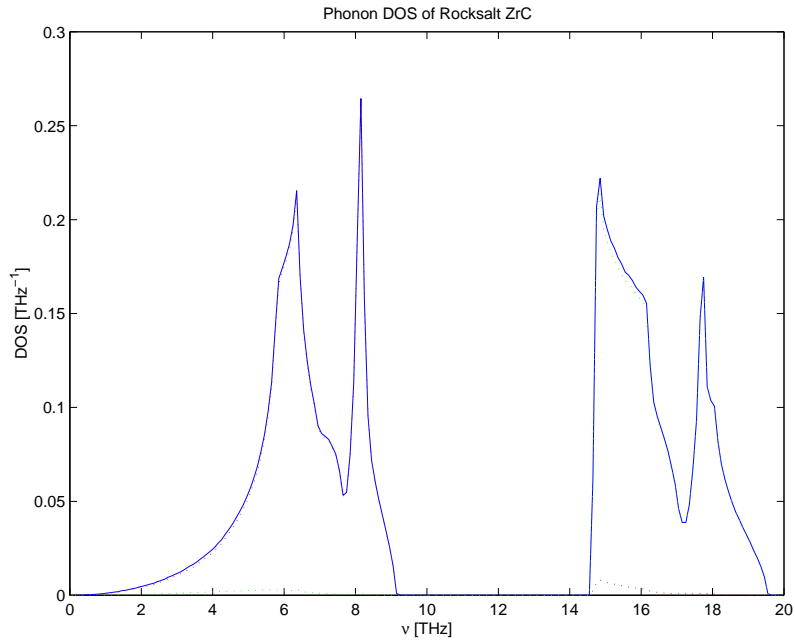


Figure 4-19: Phonon DOS (full line) and LDOS (dotted lines) in ZrC. Zr atom LDOS almost completely fills the acoustic band, while the C atom LDOS almost completely fills the optical band.

contacts (interactions) are between C-Zr and Zr-Zr, but there is not much C-C interaction. That means a C atom is quite isolated in a Zr-cage, and “rattles” with high frequency like a single-atom oscillator, whereas the Zr atoms “see” other Zr atoms and vibrate coherently as acoustic phonons. This suggests that, for Zr atoms, not much has changed from vibrations in the pure Zr lattice, except Zr-Zr now interact with “renormalized” strengths.

Heat of Formation

The heat of formation during ZrC synthesis,



is tabulated in Table 4.5. My result (2.47 eV/pair) is in good agreement with the experimental determination of Guillermet (2.14 eV/pair) [210].

	Exp’t[210]	New
eV/pair	2.14	2.47

Table 4.5: Heat of formation of ZrC.

The heat of formation reflects the strength of the chemical bond and is closely related to the thermal and chemical stability of the compound. The large value of ZrC makes it highly stable, and having one of the highest melting points known.

4.5 Predicted Properties

The following properties are not used in the fitting in any way, and are genuine predictions of this model.

Hexagonal WC Phase

The hexagonal WC-ZrC structure serves as a good test of the transferability of the potential since it only fits to the three cubic phases of ZrC (Fig. 4-15). The WC-structure is so named because it is the ground state of the tungsten/carbon system which replaces the NaCl structure as the ground state going from group IV to group VI transition metal carbides [212]. In WC-WC, $c/a = 0.976$, there are six nearest neighbors per atom, and the bond angles are 80.4° , 82.8° and 135.1° , respectively.

For WC-ZrC, the c/a and $E - E_{\text{NaCl}}$ results are tabulated in Table 4.6, in comparison to the full-potential linear muffin tin orbital (FPLMTO) calculation results of Price *et al* [212] which are believed to be accurate, and the tight-binding results of Tan *et al* [205]. My results are relatively superior to Tan *et al*'s results, whose 0.21 eV/atom lattice stability is very low, reflecting the weak bond angle dependence of the tight-binding model.

	c/a	$E - E_{\text{NaCl}}$
FPLMTO [212]	0.8596	0.78 eV/atom
TB [205]	0.67	0.21 eV/atom
New	0.9706	0.5574 eV/atom

Table 4.6: Comparison of equilibrium structure and lattice stability for the hexagonal WC phase. The FPLMTO results are believed to be the most accurate.

Carbon Vacancy Formation and Migration Energies

Carbon vacancy is the dominant microstructure in ZrC_X , which largely controls the thermomechanical and transport behavior of this material. It is extremely important for a potential model to reproduce its characteristics well.

To obtain the carbon vacancy formation energy, I carry out a procedure of creating a Zr-terminated kink on ZrC's (001) surface, pulling out a carbon atom from the bulk, and then sticking it to the surface kink. Since this procedure provides the initial and final states of an actual physical process of free surface acting as vacancy source, the

obtained energy difference is physically meaningful, and is interpreted as the carbon vacancy formation energy.

For the carbon vacancy migration energy, Harris and Bristowe [206] assumed a simple diagonal transition path and carried out constrained minimization as they move a neighboring carbon atom to the vacancy site, whose method I follow.

	formation [eV]	migration [eV]
TB [206]	1.50	2.66
New	1.91	4.86

Table 4.7: Carbon vacancy formation and migration energies in ZrC/TiC.

The results are shown in Table 4.7. There is significant discrepancy between mine and Harris and Bristowe’s results [206] with Tan *et al*’s tight-binding potential [205]. There are no comparable *ab initio* calculation determinations. On the other hand there are experiments, but whose results are subject to interpretation.

Using radioactive tracer technique, Sarian and Criscione [217] measured the bulk diffusion constant of carbon atoms in ZrC to be $1.62 \times 10^2 \exp(-113200/RT) \text{ cm}^2/\text{s}$, which converts to a thermal activation energy of $Q = 4.904 \text{ eV}$ for the carbon vacancy diffusion mechanism. Harris and Bristowe [206] argued that this [218] is in good agreement with their calculation results, since $1.50 + 2.66 = 4.16 \text{ eV}$.

But I think that interpretation is defective. Sarian has explicitly expressed [218, 219] that the activation energy for carbon vacancy diffusion should *be the migration energy only, since there is already ample amount of preexistent carbon vacancies in the lattice*, even at 0K. In the experiment above, the sample used was $\text{ZrC}_{0.965}$ [217]. It is inconceivable that at this very large (preexistent) vacancy density, thermal activation can still increase the vacancy density as a function of T as much as the Boltzmann factor $\exp(-E_f/k_B T)$ suggests.

If the thermal activation energy should be accounted for by the migration energy alone, then my migration energy result of 4.86 eV is in excellent agreement with the experiment. Harris *et al*’s small migration energy should be due to the persistent

problem with Tan *et al*'s potential [205] of weak shear resistance, since large bond angle distortion occurs on the migration path.

Metal Vacancy Formation and Migration Energies

I carry out similar calculations for Zr vacancy formation and migration energies, and the results are listed in Table 4.8.

	formation [eV]	migration [eV]	total [eV]
TB [206]	2.37	4.16	6.53
New	2.9196	5.4545	8.3741

Table 4.8: Metal vacancy formation and migration energies in ZrC/TiC.

Sarian [219] measured the diffusion constant of ^{44}Ti in TiC to be $4.36 \times 10^4 \exp(-176400 \pm 3600/RT) \text{ cm}^2/\text{s}$, which converts to an activation energy of $Q = 7.642 \pm 0.156 \text{ eV}$. Unlike the carbon vacancy problem, since there are no preexistent metal vacancies in the system, the thermal activation energy of metal atom diffusion should be the sum of formation and migration energies, in which case my results are comparable in quality with Harris and Bristowe's [206].

(001) Surface Relaxation

There had been controversy concerning the direction of the rumpled relaxation of TiC(001) surface [204, 213], but recently it has become clear that the correct direction should be carbon atoms relaxing *outward* and metal atoms relaxing *inward* [214, 215]. Both the tight-binding model [204] and my potential give the wrong relaxation direction (C in, metal out), but my magnitude is smaller. The results are tabulated in Table 4.9. As my potential has only 10 parameters in which I can only control 6, it misses this rather subtle effect that has to do with electric fields near the surface [213].

I have also computed the ZrC(001) surface energy to be $0.1012 \text{ eV}/\text{\AA}^2$, but have found no direct values in the literature to compare with. Maerky *et al* [216] measured

	FPLMTO [213]	Exp't [214]	TB [204]	New
$z_C - z_{\text{metal}}$	0.05 Å	0.076 Å	-0.07 Å	-0.0314 Å

Table 4.9: Rumped relaxation of ZrC/TiC(001) surface.

the room temperature fracture toughness of single crystal $\text{TiC}_{0.96}$ along (001) plane to be $1.5 \text{ MPa}\cdot\text{m}^{1/2}$, which converts to a critical strain energy release rate of 4.5 J/m^2 . If one assumes the Griffith law $G_{IC} = 2\gamma$ [234] to hold true, that converts to a surface energy of $0.1404 \text{ eV}/\text{\AA}^2$ for the TiC(001) surface, which is about 1/3 of the SiC(001) surface energy (section 3.3.1), and therefore ZrC/TiC should be more brittle than SiC.

Bond Shrinkage near Carbon Vacancy

Aside from the formation and migration energies, it is instructive to look at the local geometry near a carbon vacancy [205], as Moisy-Maurice *et al* had measured the relevant quantities in $\text{TiC}_{0.76}$ using elastic diffuse neutron scattering [220]. Fig. 4-20 illustrates the atomic arrangements near a carbon vacancy, and I am going to focus on the shrinkage of the nearest C-M bond pointing to the vacancy with relaxation direction indicated by the arrow. The results are shown in Table 4.10.

Shrinkage	TB [205]	New	Exp't [220]
[Å]	0.1	0.028	0.03
[%]	4.62%	1.2%	1.39%

Table 4.10: Shrinkage of the nearest C-Zr bond pointing to a carbon vacancy.

Again, my result is better than Tan *et al*'s [205] in view of the experiment [220]. The explanation is simple: in a sense the tight-binding model by Tan *et al* [205] is better suited for metal than for metal carbide, since $h_{\alpha\beta} = h_{\alpha\beta}(r)$, $C_{44} \ll C_{12}$, and the main resistance to a particle's displacement should come from the atom directly in front of the displacement. As Figs. 4-16, 4-17 indicate, this is not the case in ZrC,

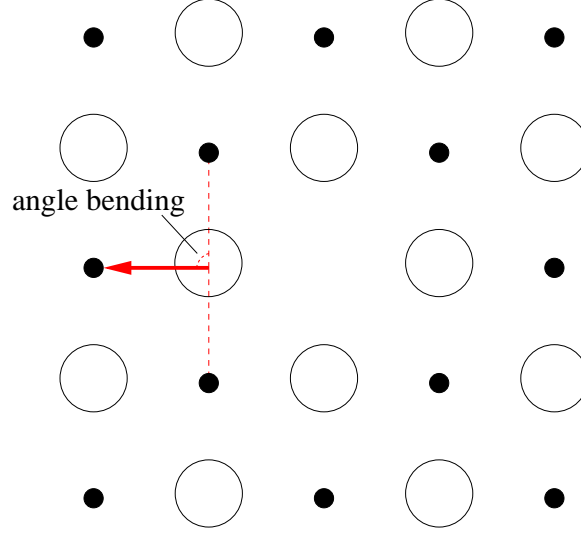


Figure 4-20: Illustration of the shrinkage of the nearest C-M bond pointing to a carbon vacancy.

where the main resistance comes from atoms *in the transverse plane*. Therefore the amount of bond shrinkage should mostly reflect *bond angle stiffness* than the bond stiffness itself, where my potential, though crude, consistently performs better, since it describes the orthogonality preference of $pd\sigma$ bonds in a minimal manner.

Grüneisen Parameter and Thermal Expansion Coefficient

I numerically evaluate the mode-specific Grüneisen parameter at 0K,

$$\gamma_k \equiv - \left(\frac{d \log \omega_k}{d \log \Omega} \right), \quad (4.37)$$

where ω_k is the frequency of a specific phonon mode k , and Ω is the cell volume. I then average γ_k with mode-specific heat capacity $c_v(k)$,

$$c_v(k) \equiv \frac{\hbar^2 \omega_k^2}{k_B T^2} \cdot \frac{e^{\hbar \omega_k / k_B T}}{(e^{\hbar \omega_k / k_B T} - 1)^2}, \quad (4.38)$$

to obtain the overall Grüneisen parameter $\gamma(T)$, plotted in Fig. 4-21. The high temperature limit agrees well with a recently published value of 1.33 for TiC by Wolf *et al* [221] using all-electron full-potential linearized augmented plane-wave method

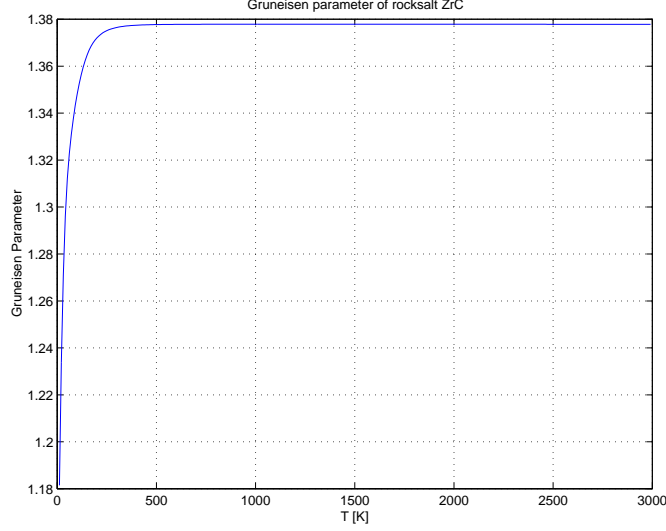


Figure 4-21: Average Grüneisen parameter of ZrC as a function of T using phonon frequencies at 0K.

(FLAPW).

The total $C_V(T)$ is obtained by summing (4.38). Then the thermal expansion coefficient under the 0K phonon frequencies approximation can be obtained from,

$$\alpha(T) \equiv \frac{1}{3} \cdot \left. \frac{\partial \log \Omega}{\partial T} \right|_{P=0} = \frac{C_V(T)\gamma(T)}{3B(T)}, \quad (4.39)$$

which is shown in Fig. 4-22, and it is in excellent agreement with the experimentally measured [145] $6.7 \times 10^{-6}/\text{K}$ in the high T limit.

$C_P(T)$ then can be calculated as [6],

$$C_P(T) = C_V(T) + 9\alpha(T)^2 B(T) T \Omega. \quad (4.40)$$

C_V , C_P , and the experimentally measured [145] C_P for $\text{ZrC}_{0.96}$ are shown in Fig. 4-23. The agreement is satisfactory up to 1500K, at which point the measured C_P starts to deviate significantly from the harmonic phonon C_P .

If I use the Debye function (section D.3) as an analytical approximation for $C_V(T)$ of Fig. 4-23, and align their values at 300K, the sole parameter of the Debye function is determined to be $T_D = 747\text{K}$. In my MD simulations for ZrC, I will use this Debye

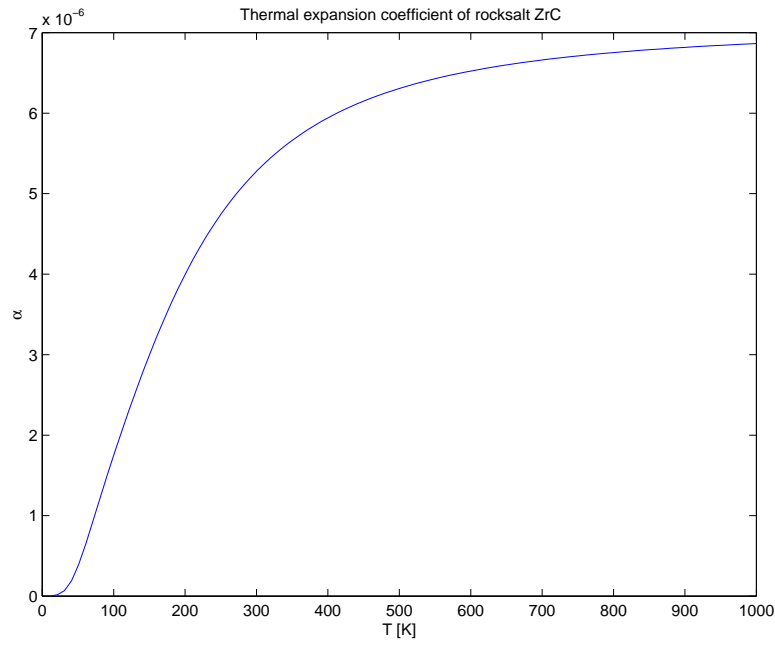


Figure 4-22: Thermal expansion coefficient derived from the overall 0K Grüneisen parameter.

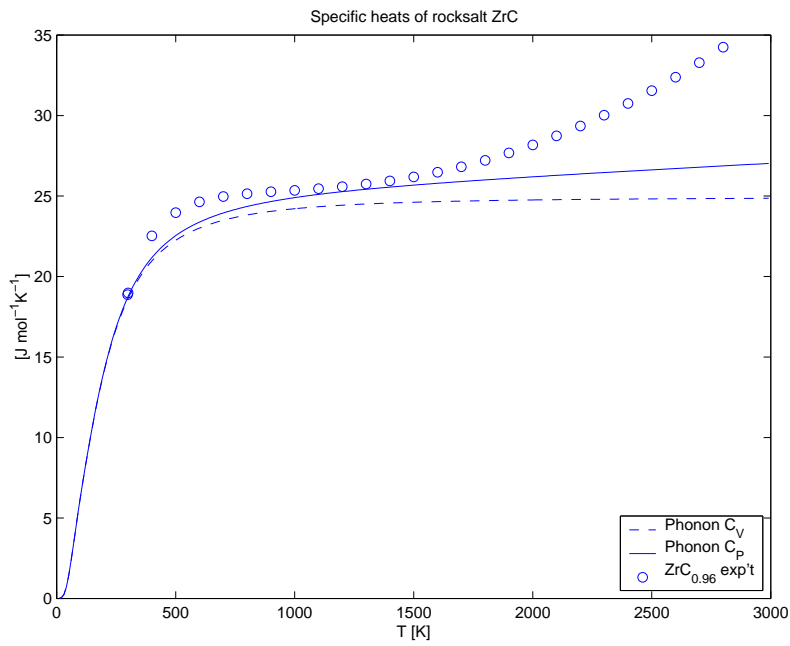


Figure 4-23: Calculated heat capacities of ZrC using phonon frequencies at 0K. The circles are experimentally measured C_P for $ZrC_{0.96}$ [145].

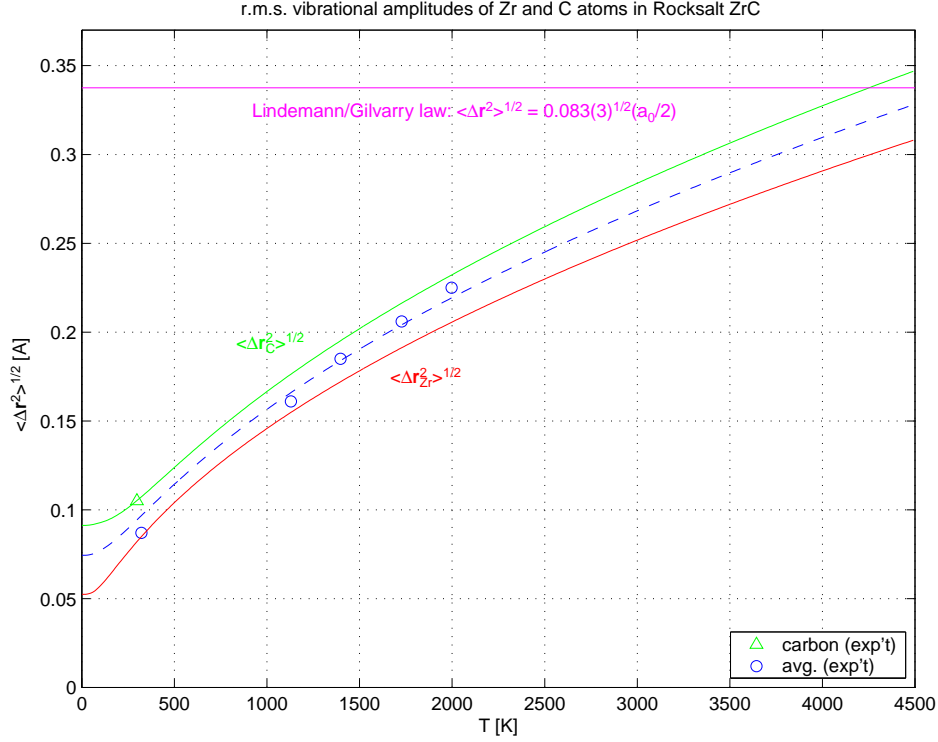


Figure 4-24: Vibrational amplitudes of Zr and C atoms in NaCl-ZrC (dash line is the average $\sqrt{0.5[\langle |\Delta \mathbf{r}_{\text{Zr}}|^2 \rangle + \langle |\Delta \mathbf{r}_{\text{C}}|^2 \rangle]}$), and Lindemann’s law’s prediction of the melting point. One experimental measurement of carbon atom’s vibrational amplitude at room temperature is shown in triangle, and five “averaged” experimental points at other temperatures are shown in circles [222].

function and associated zero-point energies as my temperature rescaling relation [149], with the benefits of smoothness and correct behaviors in both low and high T limits. Using this technique, I perform direct MD heating simulations in section 4.6.1 to study the real thermal expansion, as Fig. 4-22 of this section is yet based on harmonic phonon theory.

Vibrational Amplitudes and Melting

The vibrational amplitudes of Zr and C atoms are calculated separately using phonon theory. They are shown in Fig. 4-24, in comparison with the X-ray diffraction measurements by Houska [222].

By the Lindemann/Gilvarry law [224], a crystal melts when atoms’ vibrational amplitudes reach a certain empirical fraction of the nearest neighbor distance. Fig.

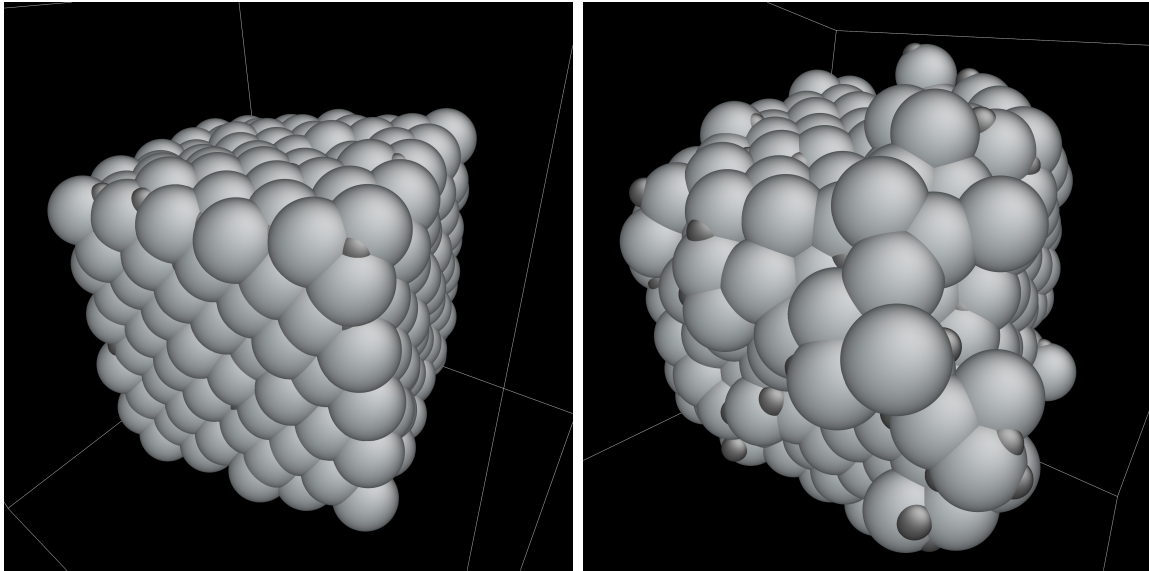


Figure 4-25: (a) Cluster configuration at 3500K. (b) Cluster configuration at 3650K.

4-24 suggests a very high melting point at around 4000K.

This prediction is independently verified in the following manner. I created a 1000-atom ZrC cubic crystallite that has six free surfaces, and gradually rise the temperature in the MD simulation. At high temperatures, there will be some disordering on the surfaces, but I do not consider it to have started melting as long as it maintains the overall cubic shape. Especially, the 8 cube vertices are monitored. When they all vanish, it is a sign that surface tension has taken control.

I find that the configuration is cubically stable in the simulation up to 3500K (Fig. 4-25a), but approaches a droplet shape when T is increased to 3650K (Fig. 4-25b). Therefore, the melting point should be around 3500K, in fair agreement with the experimental value of 3700K [145].

4.6 MD Calculation of Lattice Thermal Conductivity

By matching the phonon C_V of ZrC at 300K (Fig. 4-23) to the Debye function (section D.3), the Debye temperature T_D is determined to be 747.4K, in fair agreement with

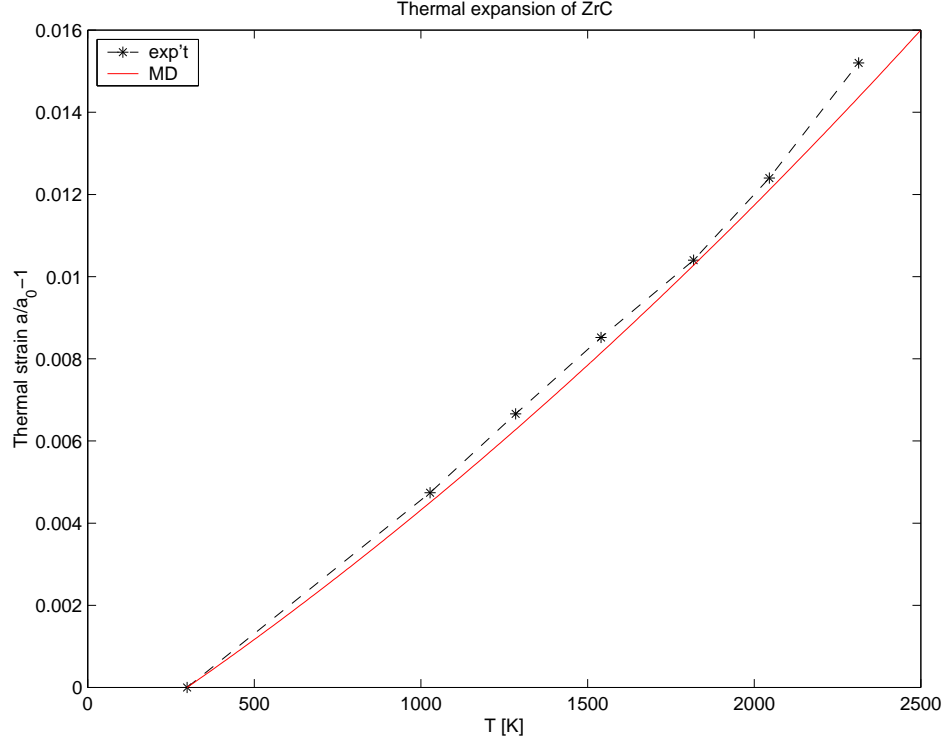


Figure 4-26: Thermal strain measured in experiment [222] and in a direct MD simulation.

the experimental determinations (each may use a different property to fit) [145].

4.6.1 MD Heating Experiment

A direct MD heating simulation is performed where T is slowly raised from 300K to 2500K. The temperature rescaling scheme [149] using the Debye model is implemented. Fig. 4-26 compares the experimentally measured thermal strains [222] with my results. The agreement is seen to be excellent.

4.6.2 Thermal Conductivity Calculation

Thermal conductivity calculations are performed on ZrC perfect crystal, $\text{ZrC}_{0.99}$, $\text{ZrC}_{0.98}$, $\text{ZrC}_{0.97}$, and $\text{ZrC}_{0.9}$. Appendices C, E and the SiC reference [80] already explain the methodology, so I will not dwell on that. However, I want to describe the differences between SiC and ZrC calculations.

In Fig. 4-27, a small piece ($\tau \sim 0$) of the heat current correlation function of

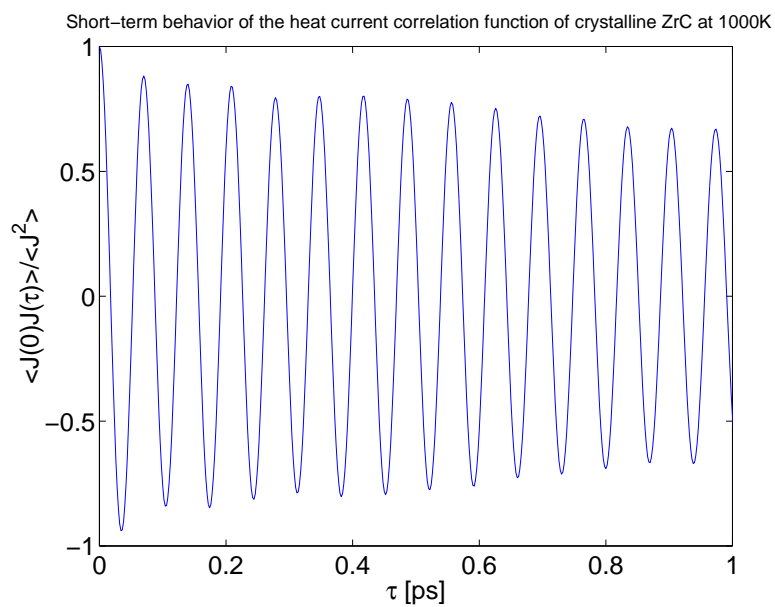


Figure 4-27: Short-term behavior of the heat current correlation function of crystalline ZrC at 1000K

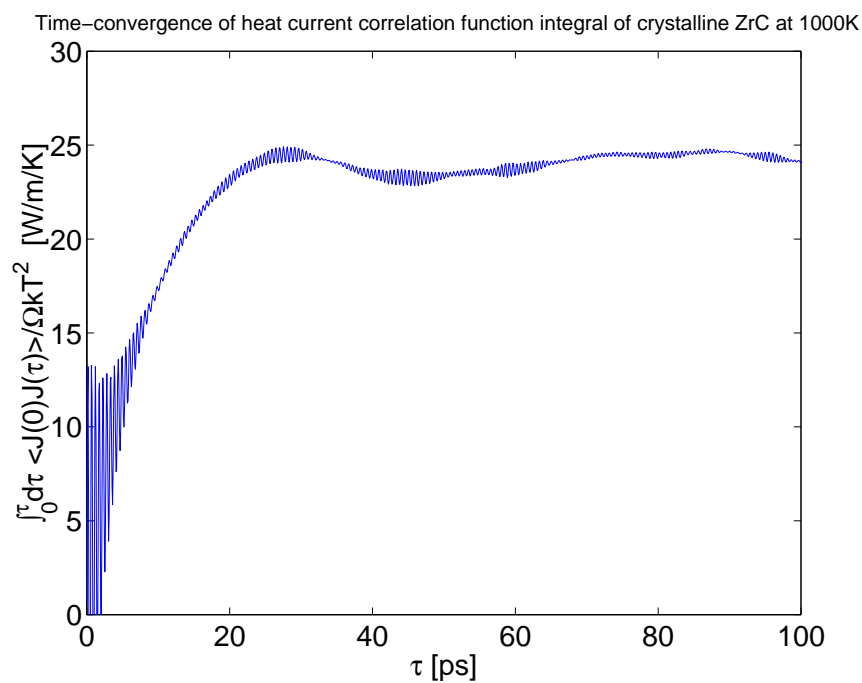


Figure 4-28: Time-convergence of the heat current correlation function integral of crystalline ZrC at 1000K.

crystalline ZrC at 1000K is shown, which is fast-oscillating and seems dramatically different from that of SiC. This could cause additional numerical convergence problems if the MD integration scheme is not accurate enough. But I have paid attention to that by using a high-order (10-value) predictor-corrector trajectory integration scheme, and the convergence, shown in Fig. 4-28, is seen to be satisfactory.

The fast oscillation of the heat current correlation function corresponds to the vibrations of the carbon atoms, which though is of large instantaneous magnitude, does not contribute significantly to the lattice thermal conductivity as the carbon atom vibrations mainly reside on the optical branch (Fig. 4-19) and have very small group velocities (more like a standing wave than a propagating wave) [57].

T	[K]	300	500	1000	1500	2000	2500	3000	3500
ZrC	[W/m/K]	87.0	65.0	24.6	10.8	5.45	4.06	3.57	2.51
ZrC _{0.99}	[W/m/K]	19.5	15.2	12.8	7.59	4.65	3.48	2.70	1.68
ZrC _{0.98}	[W/m/K]	N/A	10.0	7.0	4.54	4.63	3.09	2.28	1.95
ZrC _{0.97}	[W/m/K]	6.5	6.0	4.15	3.8	3.32	3.4	2.36	1.83
ZrC _{0.9}	[W/m/K]	N/A	2.44	2.84	2.17	2.10	1.50	1.29	1.02

Table 4.11: MD Simulation Results for the Lattice Thermal Conductivity of ZrC_X

In Table 4.11 the MD calculation results for the lattice thermal conductivities of ZrC_X are tabulated. Each data point comes from at least one 8-million-timestep simulation run in a 216 atom supercell, and I have paid full attention to the numerical convergence problem. These results, as the potential function itself, should be trusted with high confidence due to the demonstrated painstaking effort at testing and validation.

From Table 4.11, we see that even at $X = 0.99$, the calculated lattice thermal conductivities are still much smaller than the recommended total conductivities of Fig. 4-1 at $T > 1000\text{K}$. In practice, ZrC_X, as with the specimens used in the Fig. 4-1 measurements, seldom comes with $X > 0.98$, and therefore the results of Table 4.11 verify our suspicion that the electron contribution dominates the total thermal conductivity at $T > 1000\text{K}$ to a degree that *the lattice contribution can be safely*

neglected. This conclusion is in marked contrast to the recently published decomposition of the total conductivity (Fig. 4-5), which is based on the assumption that the normal Wiedemann-Franz law still holds in ZrC_X .

By reverse reasoning, we have obtained the first quantitative evidence ever that the normal Wiedemann-Franz law does not hold in refractory carbides, and its Lorenz number, even after taking into account of the residual electrical resistivity, should be $\sim 4 \times 10^{-8} \text{ volt}^2/\text{K}^2$ instead of the “universal” constant $2.45 \times 10^{-8} \text{ volt}^2/\text{K}^2$ in normal metals (Fig. 4-4). This in turn supports the theory of the existence of ambipolar diffusion heat carriers in ZrC_X which contributes to the transport of heat but not charge, causing the Lorenz number anomaly.

Chapter 5

Nano-Indentation of Cu

5.1 Calculation of General Properties

There exist many interatomic potentials for Cu. The so-called Effective Medium Theory (EMT) potential [186], which has a strong *ab initio* flavor, originally includes only nearest-neighbor interactions, but was extended by Hakkinen and Manninen [187] to include up to the third-nearest neighbor interactions. This version of the EMT potential, hence called EMT-HM, was applied to study edge dislocations [188] and thermal properties [189] of Cu and Al, and (110), (100), and (111) surfaces of Cu [190]. EMT-HM was also used by Heino *et al* to study strength of Cu with built-in defects [194], stacking-fault energies [195], and plastic deformation of nanocrystalline copper [121].

The original nearest-neighbor EMT model is computationally very inexpensive. Jacobsen *et al* gave a new set of parameterizations [191] in 1996, hence called EMT-96-NN. In the same paper, they also described a scheme for extending beyond the nearest neighbor interactions with a smooth cutoff ¹, hence called EMT-96-MN, but they did not give any details. It seems that EMT-96-NN cannot provide sufficient stacking-fault energies, so Rasmussen *et al* [196] imposed an additional small pair potential of Gaussian shape centered around the fifth-nearest neighbor, hence called

¹This is important because although EMT-HM seems to provide sound stacking-fault energies, the lack of a smooth cutoff causes problems as pointed out by Heino *et al* [195].

EMT-GP, so to reproduce reasonable stacking fault energies; but the authors did not provide any details. EMT-GP was then used to study cross slip of screw dislocations in copper [196, 197].

In another slightly different approach, Daw and Baskes developed the Embedded-Atom Method (EAM) [178, 179], which was extended by Voter and Chen [180] and recently by Mishin *et al* [181]. Baskes later generalized to the Modified Embedded-Atom Method (MEAM) that describes the weak angular dependence in fcc, bcc and hcp metals [182, 183], and even the strong angular dependence in covalent materials [184]. In my opinion, due to its relatively high cost, MEAM is not very suitable for large-scale simulations of mechanical deformation, but is very competitive for high-accuracy tasks such as surface relaxation [185].

Chantasiriwan and Milstein recently developed an EAM-type potential for 12 cubic metals that incorporates higher-order elastic moduli data [192]. They then used the potential to compute ideal strength [133].

Lastly, there is the Finnis-Sinclair form of EAM that is derived from the second-moment approximation, originally for transition metals [169], then extended to noble metals and nickel [170], and finally to Cu-Ag-Au alloys [171] whose point-defect properties were studied by Deng and Bacon [172]². The above potentials are short-ranged with smooth cutoffs. In a different development, Sutton and Chen modified the interactions to longer-range but simple power-law decay forms [173], which Belonoshko *et al* recently re-fitted for Cu [174] and Fe [177] (hence called BAJ potential) using a database that is 100% generated from FPLMTO *ab initio* calculations, and which also include liquid configurations. The BAJ re-parameterizations are found to improve significantly over the original Sutton-Chen parameterizations in liquid and melting properties while not significantly damaging the solid-state properties. Due to its very simple form (4 free parameters in all), I shall focus on using BAJ, and EMT-96-NN, for my calculations.

In Table 5.1, the calculated equilibrium properties using BAJ and EMT-96-NN

²Deng and Bacon also made small changes to the pure Cu parameterization of Ackland and Vitek [171] to improve the high-pressure behavior.

	a_0 [Å]	E_{coh} [eV/at.]	C_{11} [GPa]	C_{12} [GPa]	C_{44} [GPa]
BAJ [174]	3.520790	-3.960711	200.0	146.0	80.81
EMT-96-NN [191]	3.615445	-3.51	191.4	109.7	81.70
exp't [192, 193]	3.60	-3.50	176.2	124.9	81.77

Table 5.1: Comparison of calculated and experimental crystalline Cu equilibrium properties at 0K.

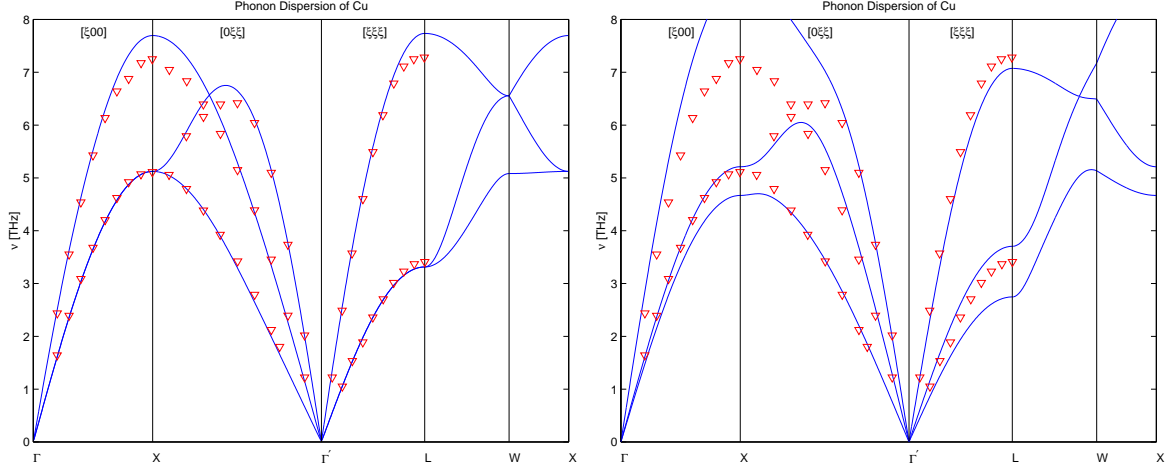


Figure 5-1: Comparison of Cu phonon dispersion at $P = 0$ using BAJ and EMT-96-NN potentials (solid line) with experimental measurements (triangles) [225].

potentials are compared with those from experiments. Notice that the experimental C_{12} is more than 50% larger than C_{44} , which suggests that a pair potential cannot adequately describe this system.

In Fig. 5-1, the phonon dispersion curves of BAJ and EMT-96-NN Cu at $P = 0$ are compared with experiment [225]. We see that overall, the BAJ potential has a better quality.

	γ	Θ_D [K]	E_V^f [eV]	Ω_V^f [Ω_0]
BAJ [174]	2.6	326.4	1.15	0.71
EMT-96-NN [191]	2.3	331.6	1.25	0.91
exp't	2.0 [224]	315 [6]	1.19 [170]	0.77 [170]

Table 5.2: Comparison of the average Gruneisen parameter, Debye temperature, vacancy formation energy and formation volume in crystalline Cu.

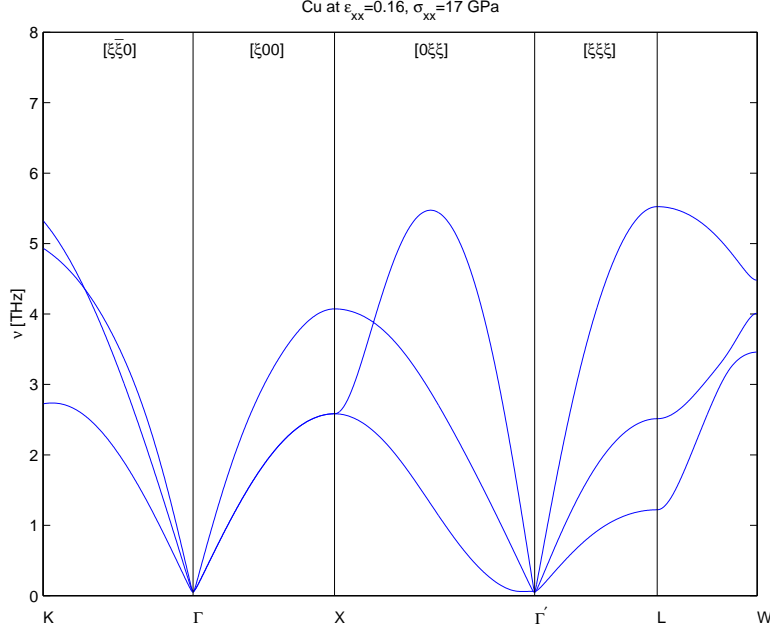


Figure 5-2: Phonon dispersion relation of Cu crystal under uniaxial tensile strain $\epsilon_{xx} = 0.16$, with $\sigma_{xx} = 17.3$ and $\sigma_{yy} = \sigma_{zz} = 12.2$ GPa, using the BAJ potential [174]. A label tracks only one of the original high-symmetry \mathbf{k} -points. Notice the Γ -point soft mode in the $[011]$ direction.

In Table 5.2, the average Gruneisen parameter, Debye temperature, vacancy formation energy and formation volume are listed.

5.2 Ideal Strength

In Fig. 5-2, the phonon dispersion relation of Cu crystal under uniaxial tensile strain $\epsilon_{xx} = 0.16$, with $\sigma_{xx} = 17.3$ GPa and $\sigma_{yy} = \sigma_{zz} = 12.2$ GPa, are shown. The soft-mode is of the long-wave type in the $[011]$ direction. Milstein and Chantasirivan performed uniaxial tension analysis [133] using their newly fitted potential and predicted that tensile instability occurs at $\sigma_{xx} = 9.82$ GPa. However their loading condition relaxes σ_{yy} and σ_{zz} which corresponds to the plane-stress condition, while my loading corresponds to the plane-strain condition – which in the fracture mechanics context is known to increase the yield stress in the main load direction. A different way to look at the results is that my system fails at von Mises shear stress $\sigma_s = 2.93$ GPa under dilational stress $\sigma_m = 13.9$ GPa, while their system fails at $\sigma_s = 5.67$ GPa

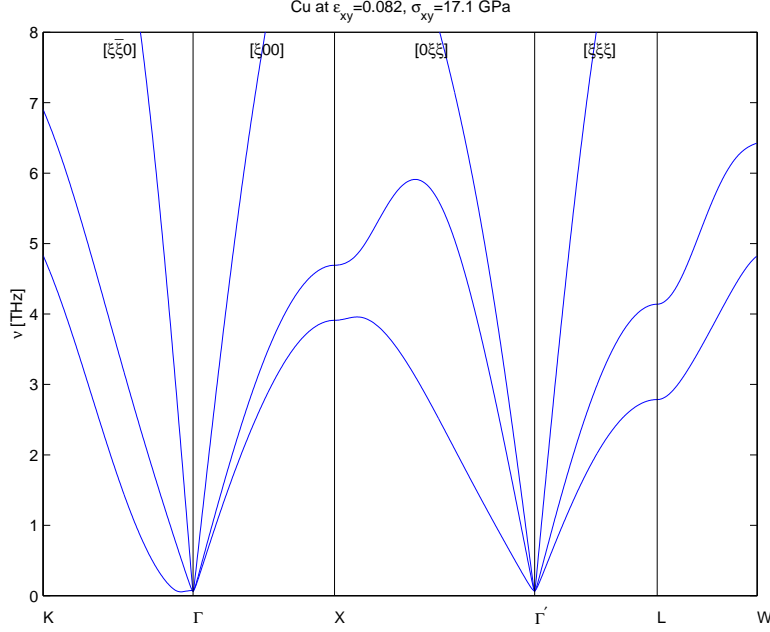


Figure 5-3: Phonon dispersion relation of Cu crystal under shear strain $\epsilon_{xy} = 0.082$, with $\sigma_{xy} = 17.1$, $\sigma_{xx} = \sigma_{yy} = -10.9$ and $\sigma_{zz} = -9.35$ GPa, using the BAJ potential [174]. A label tracks only one of the original high-symmetry \mathbf{k} -points. Notice the Γ -point soft mode in the $[1\bar{1}0]$ direction.

under $\sigma_m = 3.27$ GPa, so the results are consistent.

In Fig. 5-3, the phonon dispersion relation of Cu crystal under shear strain $\epsilon_{xy} = 0.082$, with $\sigma_{xy} = 17.1$ GPa and $\sigma_{xx} = \sigma_{yy} = -10.9$, $\sigma_{zz} = -9.35$ GPa is plotted using the BAJ potential [174]. The soft-mode is of the long-wave type in the $[1\bar{1}0]$ direction. Roundy *et al* [134, 135] found that the critical shear stress on the $[11\bar{2}](111)$ slip system is 4.0 GPa if the vertical stress is unrelaxed, and 2.65 GPa if relaxed. For my BAJ result, the traction resolved on the (111) plane is $[3.62, 3.62, -0.54]$ GPa, or 3.4 GPa component in the $[11\bar{2}]$ direction, under a vertical *tensile* stress of 3.9 GPa. Thus my result is not drastically different with Roundy *et al*'s although appearing to be so. Also note that $\sigma_m = -7.6$ GPa in my case, which although is still insufficient to cause vertical pressure on the (111) plane, does considerably compress this plane in the lateral directions, which should increase the resolved critical shear stress.

I reach the same stress analysis conclusions for the tensile case of Fig. 5-2. As with the Ar example of section 3.1.3, both tensile and shear instabilities in the $[100]$ system are controlled by $[11\bar{2}](111)$ slip, whose initial product ideally should be a

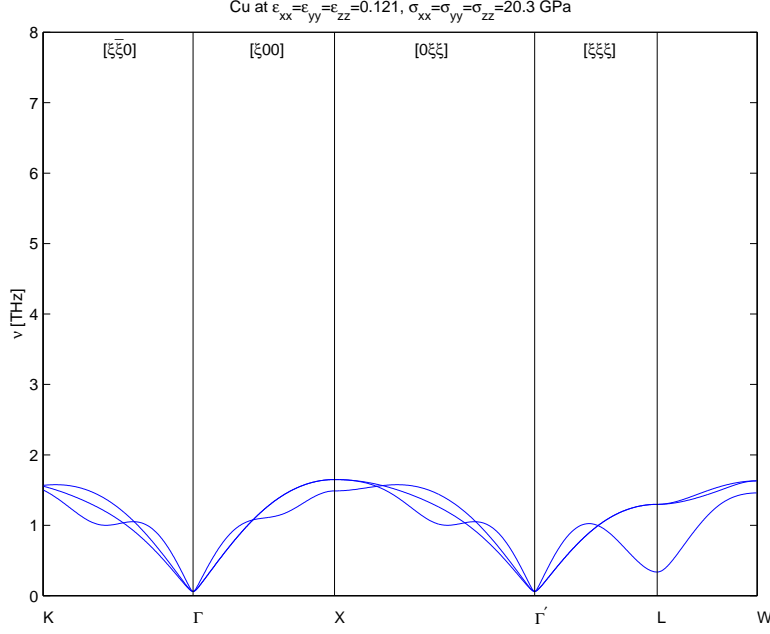


Figure 5-4: Phonon dispersion relation of Cu crystal under hydrostatic strain $\epsilon_{xx} = \epsilon_{yy} = \epsilon_{zz} = 0.121$, with $\sigma_{xx} = \sigma_{yy} = \sigma_{zz} = 20.3$ GPa, using the BAJ potential [174]. Notice the L-point finite \mathbf{k} soft mode.

stacking fault.

Different from the tensile and shear cases, hydrostatic failure of BAJ Cu occurs by a finite- \mathbf{k} soft mode, shown in Fig. 5-4. Also, the critical hydrostatic stress $\sigma_m^C = 20.3$ GPa puts a practical cutoff to the σ_s versus σ_m relation in the tensile and shear failures, which if compared with the actual results, appears to be reasonable.

The EMT-96-NN potential gives approximately the same critical strains and stresses under all three modes of deformation, shown in Fig. 5-5, 5-6 and 5-7. In terms of failure modes, however, the EMT-96-NN Cu fails by X -point finite \mathbf{k} soft mode (Fig. 5-5) under uniaxial tensile strain while BAJ Cu fails by Γ -point soft mode (Fig. 5-2). On the other hand, both EMT-96-NN and BAJ Cu fails by L -point finite \mathbf{k} soft mode under hydrostatic tension. Although these results might be due to artifacts of the empirical potentials, one cannot from principle exclude the possibility that such finite \mathbf{k} lattice instabilities do occur prior to elastic instabilities even in simple materials such as Cu, especially since the EMT potential has a strong *ab initio* nature. Therefore, current works on Cu ideal strength by Milstein and Chantasirawan

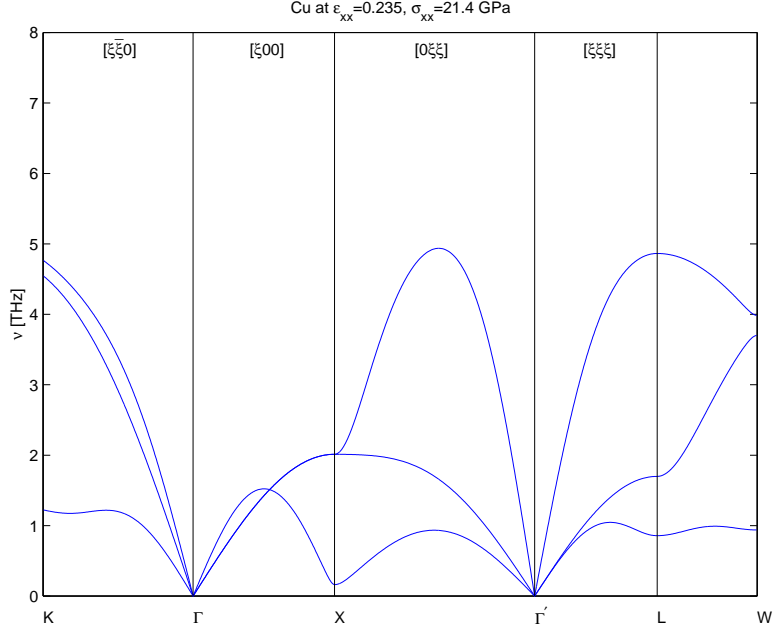


Figure 5-5: Phonon dispersion relation of Cu crystal under uniaxial tensile strain $\epsilon_{xx} = 0.235$, with $\sigma_{xx} = 21.4$ and $\sigma_{yy} = \sigma_{zz} = 11.4$ GPa, using the EMT-96-NN potential [191]. Notice the X-point finite \mathbf{k} soft mode.

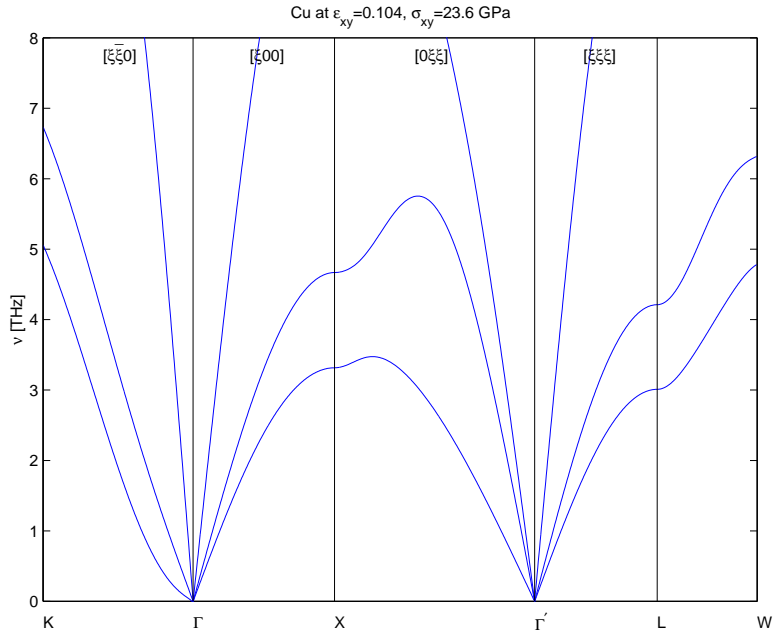


Figure 5-6: Phonon dispersion relation of Cu crystal under shear strain $\epsilon_{xy} = 0.104$, with $\sigma_{xy} = 23.6$, $\sigma_{xx} = \sigma_{yy} = -16.0$ and $\sigma_{zz} = -11.4$ GPa, using the EMT-96-NN potential [191]. Notice the Γ -point soft mode in the $[1\bar{1}0]$ direction.

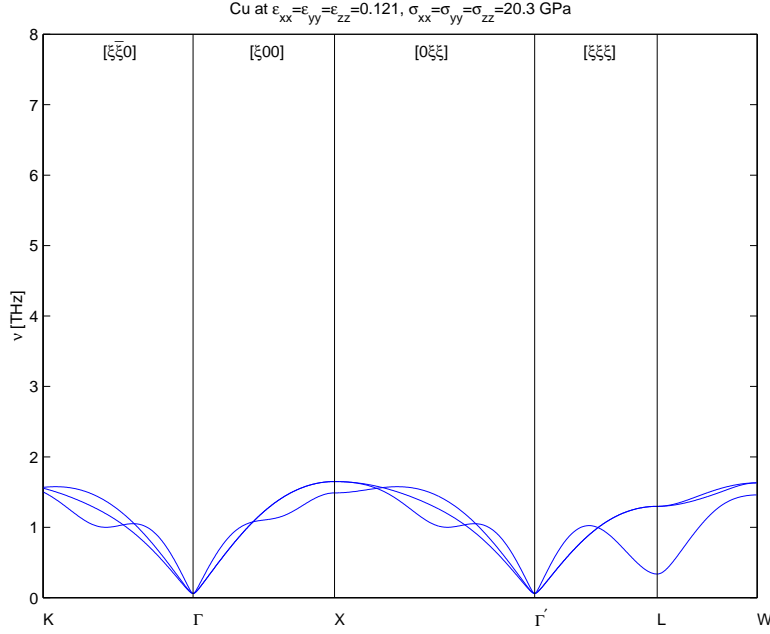


Figure 5-7: Phonon dispersion relation of Cu crystal under hydrostatic strain $\epsilon_{xx} = \epsilon_{yy} = \epsilon_{zz} = 0.0905$, with $\sigma_{xx} = \sigma_{yy} = \sigma_{zz} = 19.4$ GPa, using the the EMT-96-NN potential [191]. Notice the L-point finite \mathbf{k} soft mode.

[133], and by Roundy *et al* [134, 135] who use state-of-the-art *ab initio* total energy relaxation but with constrained degrees of freedom, although highly convincing, still needs to be confirmed by phonon calculations.

5.3 Nano-Indentation Simulation

MD simulation of nano-indentation of Cu is performed in a system consisting of 41,200 atoms of size $9.3 \times 7.0 \times 9.2$ nm, under periodic boundary conditions. The (111) surface of the system faces the indenter, which is a blunt cylinder 2.5 nm in diameter, composed of immobile Cu atoms, shown in Fig. 5-8. The simulation is carried out at $T = 0\text{K}$ and $T = 300\text{K}$. The EMT-96-NN potential is used, because it is about 7 times faster than the BAJ potential. These are very small calculations meant for getting preliminary results, yet one can already learn something from it.

In Fig. 5-9, the nominal pressure on the indenter is plotted against indentation depth at $T = 0\text{K}$ and 300K . The nominal pressure is defined to be the total force

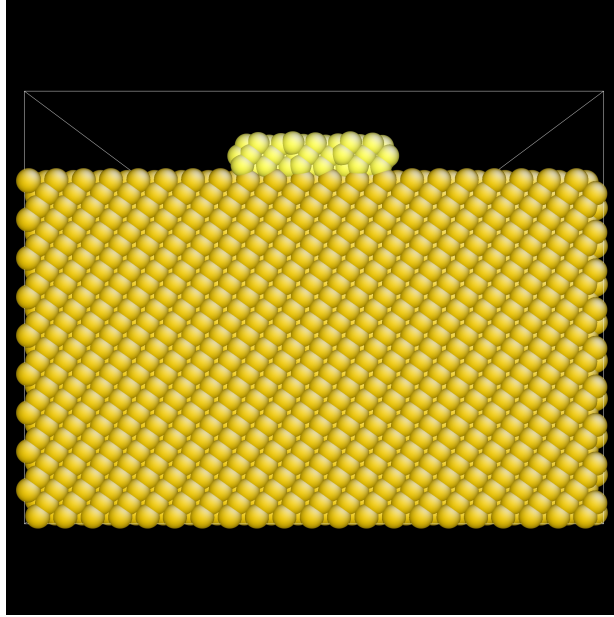


Figure 5-8: Nano-indentation simulation setup.

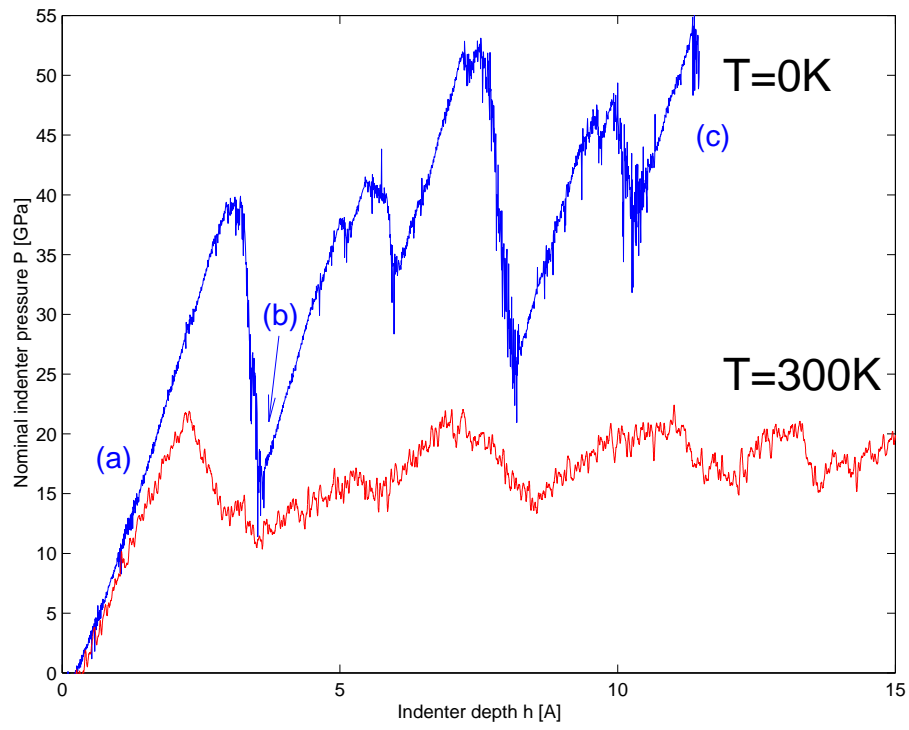


Figure 5-9: Indenter nominal pressure versus indentation depth at $T = 0K$ and $300K$.

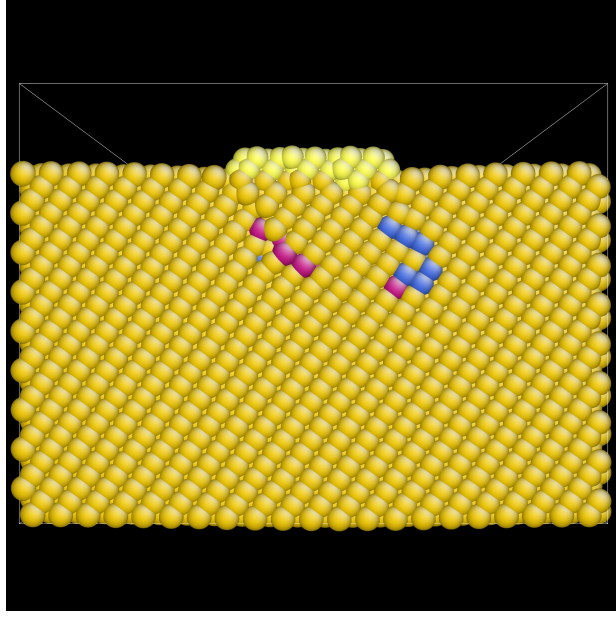


Figure 5-10: Configuration immediately after the first cusp (labeled as b) in Fig. 5-9, color-encoded by the atom coordination number, at $T = 0\text{K}$.

on the indenter's immobile atoms exerted on by all other (mobile) atoms, divided by the indenter's cross-section (about 5 nm^2). To compensate for the reaction force, the center of mass of all mobile atoms is fixed. Temperature rescaling is applied on the system at each step to absorb the heat generated.

We see that for the $T = 0\text{K}$ indentation, the first cusp in the nominal pressure versus indentation depth curve occurs at nominal pressure $\sim 40 \text{ GPa}$. The configuration immediately after the cusp is shown in Fig. 5-10. A dislocation loop is observed to have formed with an edge-type Burgers vector, which does not stay immediately under the indenter because the activated slip system is slanted with respect to the (111) surface.

Fig. 5-11 shows the final configuration after several cusps in Fig. 5-9. It is now harder to distinguish individual dislocation loops as they do move too far away from the indenter which causes a pile-up. This artifact is most probably due to the small system size used, and also the extremely fast “strain-rate”. But it is clear that the deformation is quite homogeneous now directionally, which means other slip systems are activated after (b).

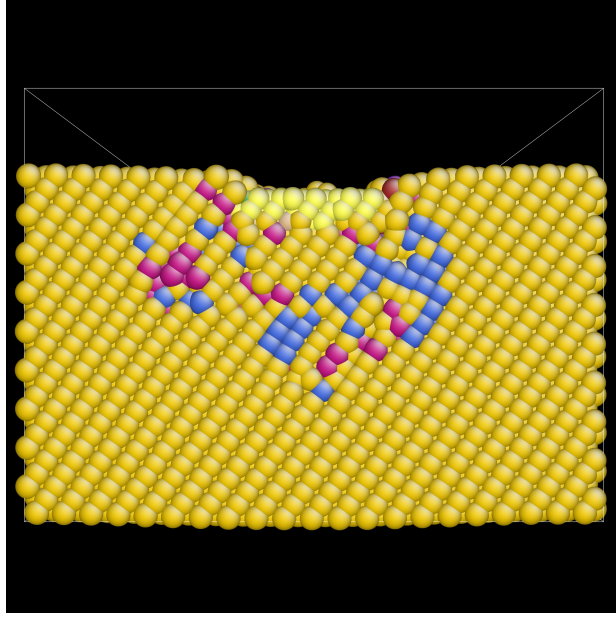
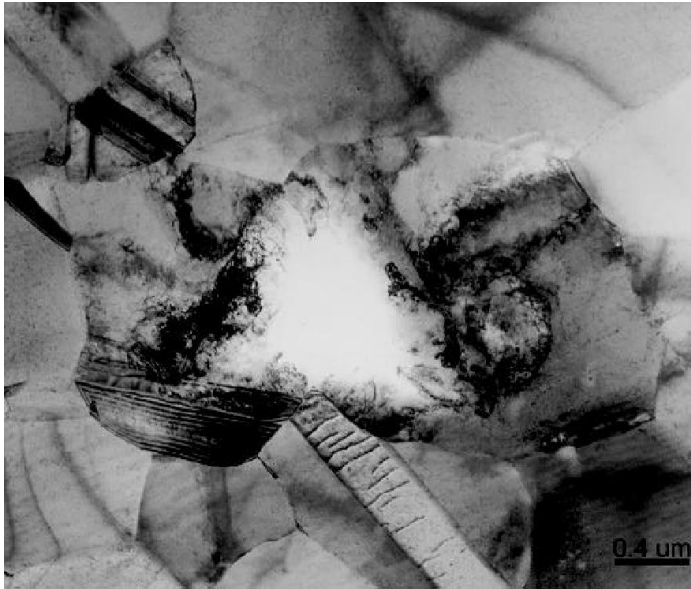


Figure 5-11: Configuration color-encoded by the atom coordination number after several cusps in Fig. 5-9 (labeled as c), at $T = 0\text{K}$.

In Fig. 5-9, we see an apparent “hardening” behavior for the $T = 0\text{K}$ indentation, but not for the $T = 300\text{K}$ indentation. I do not have a satisfactory explanation for this behavior yet, but it is possibly due to thermal annealing of local damages that impede the trailing dislocations.

5.4 Experimental Result

Fig. 5-12 shows the brief summary of a recent nano-indentation experiment on Cu thin films [142, 143].



A. Gouldstone, H.-J. Koh, K.-Y. Zeng,
A.E. Giannakopoulos, S. Suresh,
Acta Materialia 48, 29, (2000).

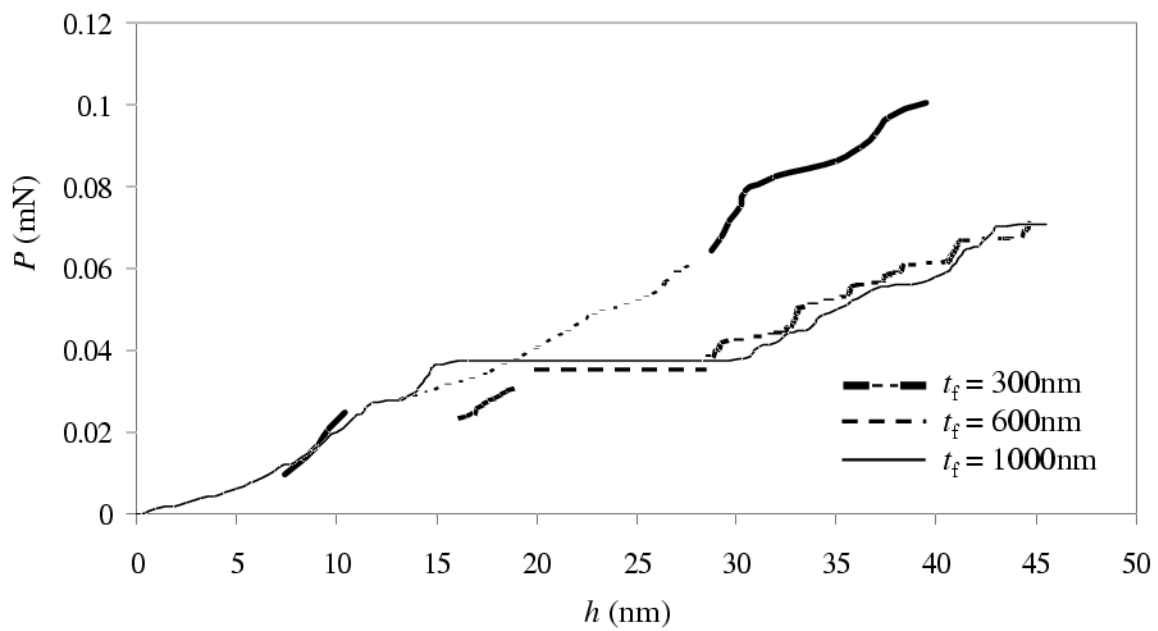
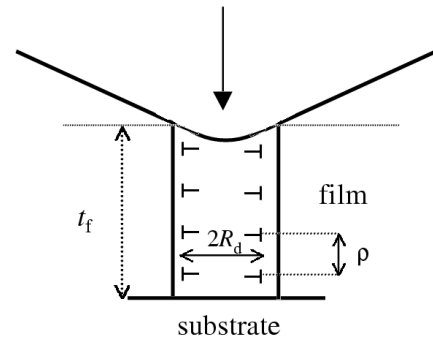


Figure 5-12: Brief summary of recent nano-indentation experiment on Cu thin films by Gouldstone *et al* [142, 143].

Chapter 6

Atomistic Measure of Thermodynamic Driving Force

6.1 Motivation

Atomistic simulation has already become an important tool for studying defect mobility [230] and mechanical behavior in general. Without it, one can still build extremely powerful models such as the Peierls-Nabarro solution for dislocation core “structure” and translation barrier [231], or the line tension model for the activation energies of kink pair processes, just to mention two, which can capture the generic features of the problem very well. Atomistic simulation complements rather than replaces the generic models: one is a high-level description that reveals the nature of the problem and one obtains valuable intuition, the other is a low-level description that fills in the missing atomistic details (not necessarily informative), is more quantitative, and hopefully can make direct connections with experiment. In a sense atomistic simulation is as close to experiment as to theory, since it plays the role of a miniature, in fact nanometer-scale *testing machine* for investigating mechanical properties. As with experiment, the raw information it provides does not automatically convert into physical insights or even useful parameters, and must be subjected to careful interpretation. The advantage of this “testing machine” over its real-world analog is that it has more controls and better visualization, with the complete set of details; the

disadvantage is that due to keeping all such details, it cannot be big. A one million atom Si simulation, which is the practical size limit for routine runs nowadays, is less than 30 nm across in a cubic cell.

This leads to the following question: at this small size, can atomistic simulation provide realistic information? If so, in what form should it be? This is the question I try to answer.

Small system size makes trouble in two ways: first is that we cannot directly simulate large microstructures such as normal-sized grains or an entire dislocation. We must “cut” a small piece, say a patch of GB or a segment of dislocation, put it in a well-characterized environment – in this case our simulation cell, compute its various behavior as we vary the environment, and collect the data so eventually we can parameterize the behavior of it and all the pieces, and then put together a bigger model. This is scientific reductionism which should work.

The real challenge here is how to characterize environments of such small length-scales – does such characterization exist? Note that since the cell is tiny, no matter what boundary conditions one uses (PBC or fixed), there are going to be image effects, which are equivalent to putting microstructures tens of nanometers away from the defect of interest, that tremendously complicates the characterization of the local environment if one were to use conventional stress field analysis approach. Such nanometer-scale separations between defects not only happen in simulation, but also in nature in important scenarios such as the mobility of dislocation near a crack-tip [232]. We would like to know to what minimal dislocation-tip separation do the dislocation react to its local environment, no matter how that is defined, rather than couple directly with the crack-tip so we have to model the two together. Is that lengthscale 1 nm, 10 nm, or 100 nm? Answering such questions is important both for physical insights and for expediency in modeling.

Historically, defect interactions were modeled in terms of stress fields. And the driving force on defect motion was also represented in terms of stress, with well-known results such as the Peach-Koehler formula [231]. Unfortunately, these results are the asymptotic field solutions valid in the limit of large defect separation, which might

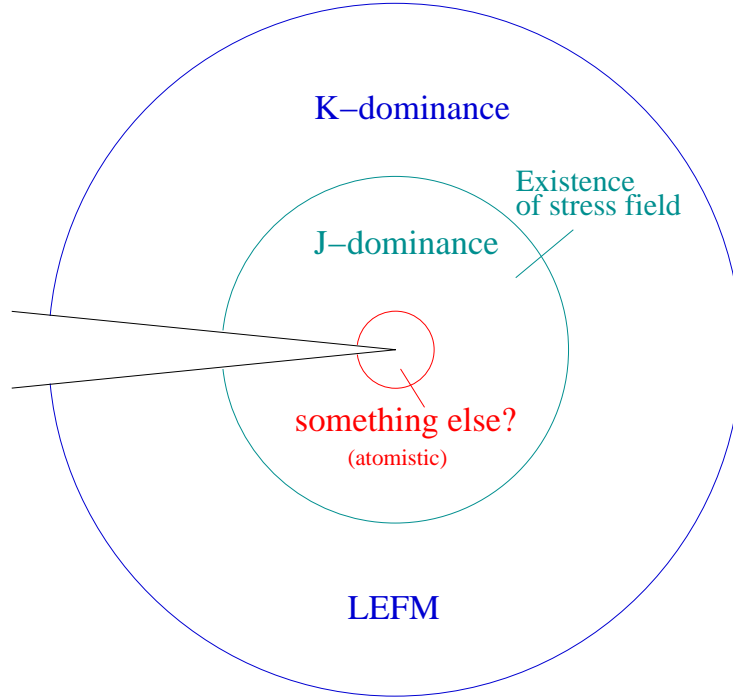


Figure 6-1: Illustration of how the validity of a theoretical description influences the applicable range of the corresponding invariant measure.

not be valid when the separations are only tens of nanometers. Even if they work all right, there are enormous difficulties in computing the local stress because it is a field concept alien to the discrete atom representation. In many cases the asymptotic stress fields of microstructures are not even known.

The nature of this problem is very similar to the standardization of fracture toughness [233, 234, 235]. A crack can be loaded in seemingly different environments with variations in specimen shape, loading points etc., but there is only one number, the fracture toughness, that controls whether the crack moves or not. That number is an intrinsic property of the material that does not vary with respect to the detailed loading environment. Successful atomistic simulations should be able to define and produce such invariant measure irrespective of the gory details of each simulation.

The reason that the condition of a crack, for instance, can be characterized by a single invariant measure, be it the stress intensity factor K or the strain energy release rate J , is that the crack-tip does not directly couple with the environment – whatever that may be, but only via a loading ring surrounding the tip (see Fig.

6-1). The state of the loading ring would solely depend on K or J if the specimen is large enough to accommodate the ring size required by the corresponding theoretical description. In the case of K , the theoretical description is Linear Elastic Fracture Mechanics (LEFM), which is valid only when the material is within the linear elastic strain, and therefore cannot be too close to the crack-tip, namely it has to be certain ratio away from the perimeter of the plastic zone (if there is one); when that prerequisite is satisfied, and if the specimen is large enough to accommodate such a ring, the stress field would be $\propto K/\sqrt{r}$ in the ring which encloses the crack-tip, and therefore the loading condition of the tip can be solely characterized by K . But what happens if the specimen is not large enough, so small in fact that one cannot draw a valid K -ring to carry the K/\sqrt{r} solution? Does that mean one can no longer find an invariant measure? The answer is no, as long as there is another theoretical description that does not require as big a ring as the K -invariant. The derivation of the J -integral and the corresponding HRR stress field solution [233] does not require the material to be within the linear elastic strain, and the description remains valid much closer to the plastic zone, so the ring can be much smaller, thus allowing one to define and *measure* this J -invariant with a much smaller specimen. The J -invariant in a sense is superior to the K -invariant because where the K -invariant is valid, the two are equivalent by $J = K^2/E$, but not the other way around.

Observe, however, that the J -invariant still requires a stress field. For reasons listed earlier this tends to be a false assumption, or is computationally infeasible in atomistic simulations. Naturally, one would look for even lower level descriptions than the J -invariant that do not use the stress field concept, hoping to shrink the ring to such small size that it would fit our atomistic “testing-machine”.

6.2 Derivation

Before going into the formal derivations, let me first give an overall picture. On top left of Fig. 6-2, a box on a floor with friction is under external force \mathbf{f} : one knows from experience that the box is *likely* to move right (and once it does, it won’t stop as

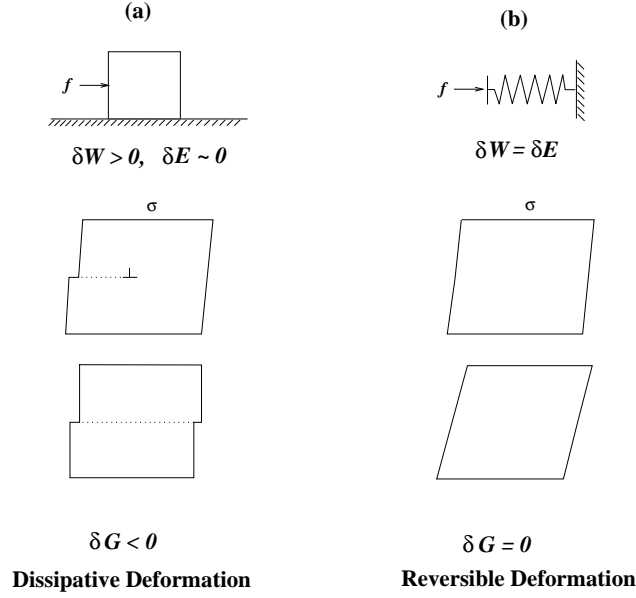


Figure 6-2: Illustration of reversal versus dissipative deformations.

long as \mathbf{f} persists). One way of understanding this is from the mechanical perspective of force balance¹. Another is the energy perspective: that *suppose* the box move by δx , the outside world would have done work $\delta W = f\delta x$. Thus the likeness of the box to move right under \mathbf{f} can be interpreted as its likeness to *let work be done upon it* from outside.

Consider another scenario (b): a spring is pressed by external force \mathbf{f} and have reached equilibrium. At that point, there is no propensity for the spring end to move right, nor left. However, suppose it moves to the right by δx , the outside world would still have done work $\delta W = f\delta x$. How come in *this* case the spring do not like to move right? Explanation from the energy perspective would be: yes, the spring still likes you to do work as *much* as before, but now if it moves δx to accommodate you, its *own* potential energy would be jacked up by certain amount δE . The spring does not like that: one never sees an automatically wrought-up spring. And given the chance, it would like to release whatever potential energy it has. Therefore, equilibrium is achieved when the two opposite desires of the spring is balanced: $\delta W = \delta E$. It likes you to do work, but it does not liked to have a worked-up potential energy.

¹The box will move if $\mathbf{f} > \mathbf{f}_s = \mu_s mg$ where \mathbf{f}_s is the static friction. Once it moves, the balance is from sliding friction that is a function of the box speed.

But there has to be energy balance. When $\delta W > \delta E$, the deficit has to become heat. In (a), it becomes heat that radiates out or propagates to the floor. The critical difference between (a) and (b) is that (b) has the intrinsic means - its configuration - to take in W or release E in an orderly fashion - much like a bank. Whereas (a) has no such means. At a closer look, one sees that (a) can *never* have such a means due to translational invariance. There is no difference between points x and $x + \delta x$ on the floor, no possible marker to even denote how much potential energy the box has, and therefore $E \equiv 0$. If the outside does work between x and $x + \delta x$, fine, the box will take it, and may even store it *temporarily* in its kinetic energy. But because there is no place for lossless storage, it's going to get spent eventually; and once gone, cannot be got back.

The two examples illustrate the two modes of deformation in a solid: elastic and plastic. Elastic deformation is like (b). A perfect crystal is willing to get strained under external stress σ , but its own potential energy gets jacked-up along the way more and more steeply, that once the point $\delta W = \delta E$ is reached, it is no longer willing to change. The process is reversible so long as the crystal remains perfect, a good indication of which is that each atom's coordination number is not altered. On the other hand, plastic deformation is like (a): work gets done, but potential energy of the system does not go up, or at least not nearly as much as it should. Much of this has to do with dislocation, a defect with *perfect translation*: for although the dislocation core is very disordered, it is enveloped by perfect crystal; and the place the dislocation core sweep by goes back into perfect crystal again as if nothing has happened. Without this property - imagine dislocation leave permanent damage behind its wake like a crack does, which increases system E , plastic deformation would not happen so easily in metals. To certain degree, the perfect translation of the dislocation is like the translational invariance of the box on floor, as both have no means *to store the work done* except transforming it to heat.

This can be illustrated in (a). Call the body's volume Ω with height h and depth d . After the dislocation passes though, the body obtains an equivalent shear strain of $\epsilon \sim b/h$ where b is the Burgers vector, and the external stress would have done work

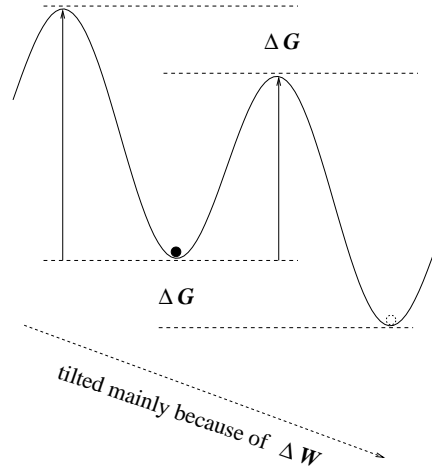


Figure 6-3: Illustration of free energy change as defect motion driving force, reflected by kinetic transition rates.

$\delta W \sim \Omega \sigma \epsilon$. If one asserts the same amount of strain ϵ to the perfect crystal in (b) to dole out the same amount of work δW , δW would have been converted completely into potential energy increase δE , often called the *strain energy*. But not so in (a). If one evaluates the potential energy of (a)'s final state, one finds that E has only increased by $2\gamma bd$, which accounts for the surface energy of the two ledges created – since, as we have noted, the place dislocation sweeps by goes back to perfect crystal again. Thus, compared to elastically straining the body to get that work δW done upon it, (a) is the more profitable way to go because it almost does not increase the potential energy: $\delta E \sim 0$.

Let us look closer to see how W is spent instead of being saved as potential energy. When the Peierls barrier is low like in Al, the dislocation moves rather continuously and the phonon drag, operating much like the floor friction in (a), radiates away the energy. When the Peierls barrier is high, the dislocation moves by kink mechanism and there is no steady motion. But kink migration, like any thermally activated barrier-crossing, is dissipative because there is no place to store the small energy profit between the downward and upward legs of the barrier-crossing, except converting it to local kinetic energy - which raises the local temperature and diffuses away via thermal conduction. The kinks, with their few atoms, do not *really* appreciate free energy, but they decreased it involuntarily anyway. The reason is because there is beautiful

consistency between thermodynamics and specific transition rates²: the kink region borrows from its environment a thermal fluctuation \mathcal{E} of relative likelihood $\exp(-\beta\mathcal{E})$ and use it *randomly* to cross *any* barrier, not just the one in the forward direction (see Fig. 6-3). But there is a slight difference in the barrier *heights* between the forward and the backward *peaks*, which, due to lattice periodicity, is actually equal to the energy difference between the two corresponding neighboring *valleys* – the free energy profit that we have mentioned. Thus, the forward-jump is $\exp(-\beta\Delta G)$ times more likely than the backward-jump, and it is not overstated that ΔG controls how hard the dislocation is driven to move forward.

As we have shown in Fig. 6-2, $\Delta G < 0$ in dislocation-assisted shear deformation consists predominantly of ΔW , compared to $\Delta E \sim 0$. Whether this remains true when the dislocation and/or other microstructural separations goes down to less than 100 atoms across remains to be checked. But for the moment let us consider how, in that scenario, δW can be evaluated. For people who do atomistic calculations, he does not need the concepts of stress and strain to evaluate δW , because he already has in his full command the interatomic forces.

Consider Fig. 6-4, where we have chosen a loop L that encloses an atomistic region of about ten atoms across. Imagine that it is only a small part of an atomistic calculation that may contain many other microstructures, may be under external loading, and may be under PBC. But by the merit of L we have partitioned the atoms into two sets: B - those labeled as inside, and A - everything else. One notice that B is very small indeed, but it nevertheless covers the dislocation core, so L passes through a highly strained yet perfectly coordination-numbered region which one can use to illustrate the Burgers circuit. When the atomistic configuration is relaxed, there is of course total force balance for each atom of B . But that total force consists of B - B and A - B contributions, that is, a B atom may feel force from another B atom,

²As an example, Einstein derived the black-body spectrum by studying photon rate equation. The specific form of the rate equation has to with purely quantum mechanical details such as the Fermi's golden rule and that the boson operators \hat{a}^+, \hat{a}^- lead to $\sqrt{n+1}, \sqrt{n}$ factors. Yet the equilibrium distribution he got agrees with the one based on elementary combinatorics without using the quantum rate equation at all.

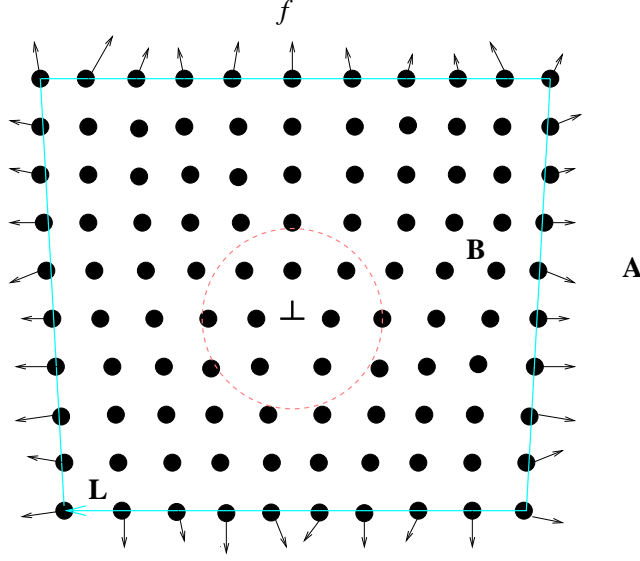


Figure 6-4: Illustration of virtual work by atomistic summation.

or from an A atom, which individually may not be zero³. One cannot help but think that, as far as the B region is concerned, \mathbf{f}_i^{A-B} is like an *external* force.

For a short-ranged pairwise interaction such as the Lennard-Jones potential, let me define

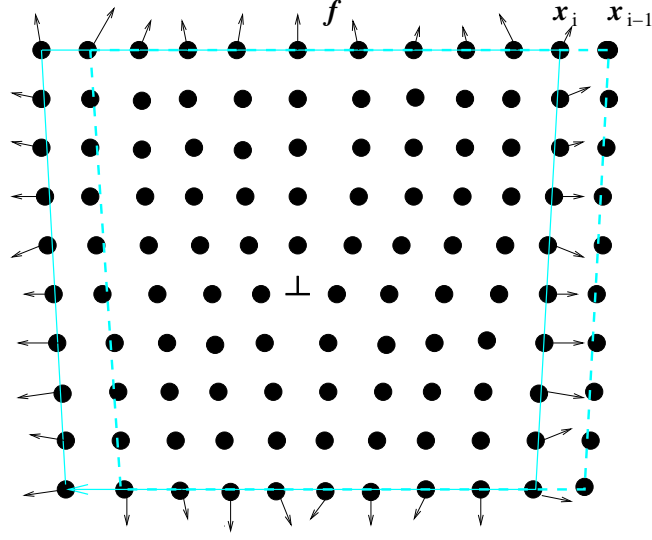
$$\mathbf{f}_i^e = \sum_{j \in A} \mathbf{f}_{ij}, \quad i \in B, \quad (6.1)$$

where \mathbf{f}_{ij} is the interaction force between atoms i and j . A useful feature of \mathbf{f}_i^e is that it is only nonzero for a thin *layer* of atoms in B which are close to A. Atoms buried deep in B, like those in the dislocation core, cannot feel any force from A atoms and therefore $\mathbf{f}_i^e = 0$. By intuition, the following virtual work expression is proposed:

$$\delta W \equiv \sum_{i \in B} \mathbf{f}_i^e \cdot \delta \mathbf{u}_i = \sum_{i \in L} \mathbf{f}_i^e \cdot \delta \mathbf{u}_i, \quad (6.2)$$

where $\delta \mathbf{u}_i$ is the displacement of a given B atom when the dislocation moves by one Burgers vector. Since $\mathbf{f}_i^e = 0$ for most of B atoms, the summation actually only runs over a band of atoms near A, which we idealized to be just L.

³This partition holds true for all empirical interatomic potentials except Coulomb interactions. For electronic structure calculations, it is theoretically feasible to do a cluster expansion to fit the Born-Oppenheimer surface, which due to screening should have a satisfactory short-ranged cutoff. Most empirical potentials are meant to such expansions anyway.



Due to lattice periodicity,

$$\delta \mathbf{u}_i \sim \mathbf{x}_{i-1} + \mathbf{b} - \mathbf{x}_i$$

$$\delta W \sim \sum_i (\mathbf{f}_{i-1} + \mathbf{f}_i) \cdot (\mathbf{x}_{i-1} + \mathbf{b} - \mathbf{x}_i) / 2$$

Figure 6-5: Illustration of further simplifications for defect translation.

$\delta \mathbf{u}_i$ can be directly evaluated for any loop-enclosed microstructure by obtaining two consecutive relaxed atomistic configurations. But in the case of a dislocation, which has *perfect translation*, a good approximation may exist whereby just the current atomistic configuration provides enough information.

See Fig. 6-5. Due to strong translational periodicity, it may be a good approximation for an atom five-lattice-spacing away from the core to assume that

$$\delta \mathbf{u}_i = \mathbf{x}_{i-1} + \mathbf{b} - \mathbf{x}_i, \quad (6.3)$$

in which \mathbf{x}_i and \mathbf{x}_{i-1} are the *current* atomic positions. (6.3) is well-defined for atoms on L (meaning each i has an $i-1$) because L only passes through perfectly coordination-numbered region, as in the Burgers circuit construction.

Therefore, the *external* driving potential for dislocation translation is simply

$$\delta W = \sum_{i \in L} \mathbf{f}_i^e \cdot (\mathbf{x}_{i-1} + \mathbf{b} - \mathbf{x}_i). \quad (6.4)$$

By referring to the analysis of Fig. 6-2, one may reasonably expect that the total driving potential δG is composed predominantly of δW with $\delta E \sim 0$, or at least δE is small compared to δW . This assumption may break down when the dislocation cores are so close that they begin to coalesce, or when the dislocation intersects other microstructures. In these situations, both δW and δE must be carefully evaluated within B.

(6.2) is called *microscopic* virtual work. Compared to the usual definitions of virtual work, it bypasses the concept of stress altogether, because after all - what is stress? In almost all contexts, stress means stress *field* - a continuous function dependent on continuous variables. If we think of one atom as one discrete sample of this function, then by common sense, we can hopefully reconstruct the continuous function out of discrete data if there are hundreds of them - and more importantly, there should be apparent order in the data. Such might be the case for a chunk of crystal 50 nm across, but the task of extrapolating a continuous function out of merely *ten* atoms seems hopeless. Yet ten-atom separations are not uncommon. They not only arise out of computational cost constraints in atomistic calculations, but also in nature, when microstructures are coming close together like crack-tip dislocation. To analyze their interactions as if via a *continuous stress field* when they are that close involves at best uncontrollable approximations. In those situations, one should evaluate δW using interatomic forces since they have the atomic resolution; or when the stress field formulas are practically too hard to implement due to image summation.

(6.2) is based on strong intuition but is not on very firm grounds, because no one can guarantee that thermodynamic principles is applicable locally down to less than 100 atoms. A formal derivation is given in the next section, which also works at finite T . Even before that, my intuition has staked the claim that except from changing \mathbf{f}_i^e to $\bar{\mathbf{f}}_i^e$ - the ensemble average of the external force, and $\delta \mathbf{u}_i$ to $\delta \bar{\mathbf{u}}_i$ - the ensemble average of atomic position shift after microstructural evolution, nothing should change in (6.2) at finite T .

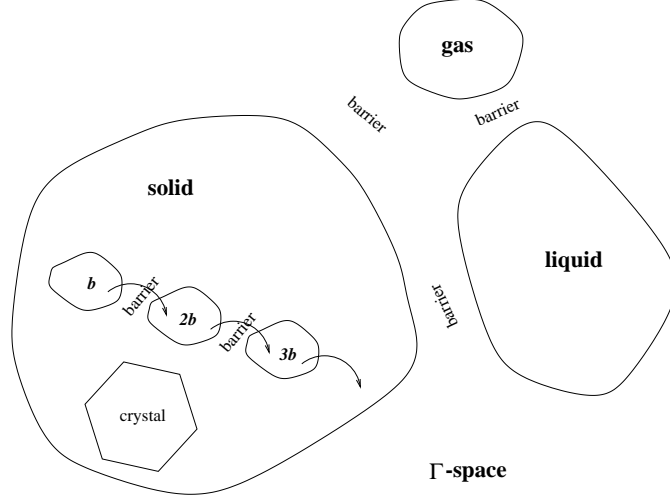


Figure 6-6: Illustration of the true meaning of free energy.

6.3 Microscopic Free Energies

The Helmholtz free energy

$$F = -k_B T \log(Z) \quad (6.5)$$

of an N -body system under constant T and shape/volume constraint Ω is the fertile ground of many theories, where Z is the partition function:

$$Z = \int \exp(-\beta \mathcal{H}(\mathbf{p}^N, \mathbf{q}^N)) \frac{d\mathbf{p}^N d\mathbf{q}^N}{N! h^{3N}}. \quad (6.6)$$

For our purpose let us integrate \mathbf{p}^N out and ignore the constants, to focus on the configurational integral

$$Z = \int \exp(-\beta V(\mathbf{q}^N)) d\mathbf{q}^N, \quad (6.7)$$

where $V(\mathbf{q}^N)$ is the total potential energy.

One often uses the thermodynamic law that an $NT\Omega$ system evolves in the direction of decreasing F . But that needs some clarification in light of (6.7), because if the $d\mathbf{q}^N$ integral in (6.7) covers the *entire* phase volume, then Z and F are constants which cannot be “decreased”. What the law actually means corresponds to the drawing in Fig. 6-6: the phase space is partitioned into well-defined “puddles” by high energy barriers, and F is only the Boltzmann-weighted phase volume *within each*

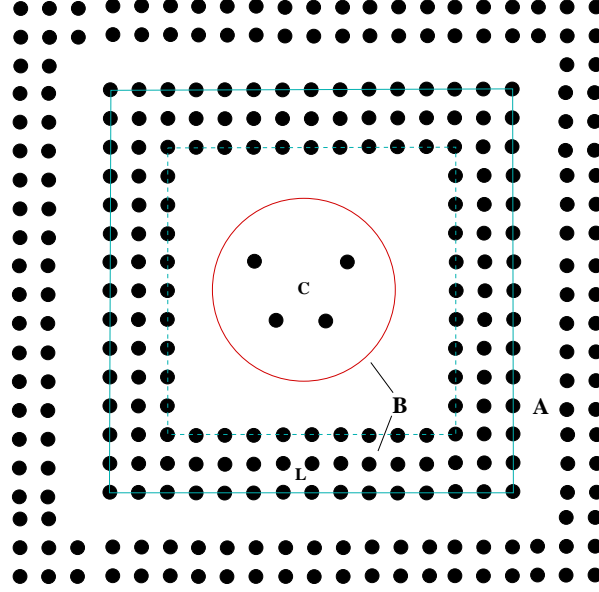


Figure 6-7: Domain decomposition that de-couples defect core with the outside environment by an atom layer of finite thickness.

puddle. A “puddle” should have distinct characters that is easily identified - such as the liquid and solid phases, and within the solid phase there are further partitions like the perfect crystal, a crystal with a dislocation at b , $2b$, $3b$, etc. Within each “puddle” a phase point moves around without difficulty (e.g., atom vibrations), but only infrequently does it traverse the barrier with the help of local energy fluctuations. The frequencies of barrier traversals favor the direction of decreasing F , as Fig. 6-3 illustrates. Free energy reduction for a dislocation mainly has to do with the *local loading* environment quantified as δW , because without δW to break the symmetry, b , $2b$, $3b$ are intrinsically equivalent positions for a dislocation. The thesis of this writeup is that elasticity theory expresses δW in terms of stress and strain, *field* concepts which are no longer *guaranteed* to be *well-defined* at the nano-meter scale, while microstructures sometime *do* get that close. In those situations this memo reminds people that δW can be directly evaluated using interatomic forces, bypassing the concept of stress altogether. The only assumption is that $V(\mathbf{q}^N)$, as far as mechanical properties are concerned, can be satisfactorily truncated as a finite summation of short-ranged interactions, a standard practice in almost all empirical interatomic potentials.

Consider Fig. 6-7. An atomistic domain is decomposed into A and B, where B covers the concerned defect that is about to change conformation. B is further divided into C – the core, where violent atomic rearrangements are to take place, and L – the loading loop, where no *rearrangements* occur even as C transforms. L, however, can be *highly strained*.

It is also required that L completely cuts off the interaction between atoms in A and C, in which case $V(\mathbf{q}^N)$ partly decouples:

$$V(\mathbf{q}^N) = V(\mathbf{q}^A) + V(\mathbf{q}^A, \mathbf{q}^L) + V(\mathbf{q}^L, \mathbf{q}^C) + V(\mathbf{q}^C), \quad (6.8)$$

where \mathbf{q}^A , \mathbf{q}^L , \mathbf{q}^C are coordinates of the three non-overlapping sets of atoms, respectively. This can always be done if the interatomic potential has a cutoff.

Because $d\mathbf{q}^N = d\mathbf{q}^A d\mathbf{q}^L d\mathbf{q}^C$, we have from (6.7),

$$Z = \int d\mathbf{q}^L \exp(-\beta(F_A(\mathbf{q}^L) + F_C(\mathbf{q}^L))), \quad (6.9)$$

$$F_A(\mathbf{q}^L) \equiv -k_B T \log \int d\mathbf{q}^A \exp(-\beta(V(\mathbf{q}^A, \mathbf{q}^L) + V(\mathbf{q}^A))), \quad (6.10)$$

$$F_C(\mathbf{q}^L) \equiv -k_B T \log \int d\mathbf{q}^C \exp(-\beta(V(\mathbf{q}^L, \mathbf{q}^C) + V(\mathbf{q}^C))). \quad (6.11)$$

Let me call $F_C(\mathbf{q}^L)$ the *microscopic* Helmholtz free energy of C. As free energies go, $F_C(\mathbf{q}^L)$ is a bit peculiar because,

1. It is for a tiny collection of atoms, maybe less than 100.
2. Its dependent variables, \mathbf{q}^L , are more numerous than the usual shape/volume constraint Ω .

One may think of (6.11) as purely a mathematical construct. However calling it a free energy is not too far-fetched because it corresponds to the physical situation of throwing away all atoms in A, impose a fixed atom boundary condition L, while allowing the C atoms to move and thermalize, which, since only a small number of atoms participate, can be quickly evaluated using any free-energy calculation method for a given defect conformation and \mathbf{q}^L . $F_A(\mathbf{q}^L)$ and $F_C(\mathbf{q}^L)$ are *regular* functions

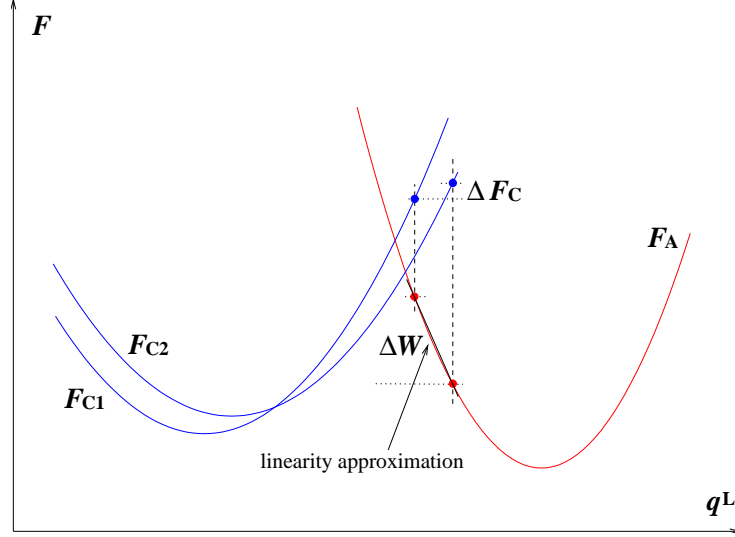


Figure 6-8: Illustration of what happens to the free energies when a defect moves.

of \mathbf{q}^L when it deviates slightly from the equilibrium position \mathbf{q}_0^L , which is in turn determined by the saddle point of the integral, (6.9),

$$\mathbf{q}_0^L : \left. \frac{\partial F_A}{\partial \mathbf{q}^L} \right|_{\mathbf{q}_0^L} + \left. \frac{\partial F_C}{\partial \mathbf{q}^L} \right|_{\mathbf{q}_0^L} \equiv 0. \quad (6.12)$$

\mathbf{q}_0^L is interpreted as the compromise between A-to-B loading and C's microscopic Helmholtz free energy. In Fig. 6-8, \mathbf{q}_0^L is indicated by the dash line at which point the slopes of $F_A(\mathbf{q}^L)$ and $F_C(\mathbf{q}^L)$ are exactly equal and opposite to each other.

Our concern is how much system free energy is decreased when the defect conformation in C transforms. How would that reflect in (6.9)? Recall that *not much* happens to an L atom even as C transforms. It means that besides small displacements $\Delta \mathbf{q}^L$, there is no change in their fundamental atomic environments. For example, the coordination number of an L atom would *not* change after the defect transforms, in comparison to some atoms in C. Same holds true beyond L, in A. Thus $F_A(\mathbf{q}^L)$ *stays* on the same *regular* branch of the free energy function before and after the C transformation. In comparison, the C transformation switches $F_C(\mathbf{q}^L)$ from $F_{C1}(\mathbf{q}^L)$ to $F_{C2}(\mathbf{q}^L)$ due to “puddle-jump” described in Fig. 6-6. The result is illustrated in Fig. 6-8.

Because $F_A(\mathbf{q}^L)$ stays regular, it can be treated by the usual techniques of pertur-

bation expansion, the lowest order of which is

$$F_A(\mathbf{q}^L) = F_A(\mathbf{q}_{0C1}^L) + \left. \frac{\partial F_A}{\partial \mathbf{q}^L} \right|_{\mathbf{q}_{0C1}^L} (\mathbf{q}^L - \mathbf{q}_{0C1}^L) + \dots, \quad (6.13)$$

where I have chosen the origin of the expansion to be

$$\mathbf{q}_{0C1}^L : \left. \frac{\partial F_A}{\partial \mathbf{q}^L} \right|_{\mathbf{q}_{0C1}^L} + \left. \frac{\partial F_{C1}}{\partial \mathbf{q}^L} \right|_{\mathbf{q}_{0C1}^L} \equiv 0, \quad (6.14)$$

which approximates the thermally averaged L position at C1. Furthermore, from (6.10),

$$\left. \frac{\partial F_A}{\partial \mathbf{q}^L} \right|_{\mathbf{q}_{0C1}^L} = \frac{\int d\mathbf{q}^A \exp(-\beta(V(\mathbf{q}^A, \mathbf{q}_{0C1}^L) + V(\mathbf{q}^A))) \left. \frac{\partial V(\mathbf{q}^A, \mathbf{q}^L)}{\partial \mathbf{q}^L} \right|_{\mathbf{q}_{0C1}^L}}{\int d\mathbf{q}^A \exp(-\beta(V(\mathbf{q}^A, \mathbf{q}_{0C1}^L) + V(\mathbf{q}^A)))}, \quad (6.15)$$

which is nothing other than the ensemble-averaged force of A on L – the “external” loading that we have mentioned:

$$\left. \frac{\partial F_A}{\partial \mathbf{q}^L} \right|_{\mathbf{q}_{0C1}^L} = \left\langle \frac{\partial V(\mathbf{q}^A, \mathbf{q}^L)}{\partial \mathbf{q}^L} \right\rangle_{C1} \equiv -\langle \mathbf{f}^e \rangle_{C1}. \quad (6.16)$$

By prior definition (6.15), $\langle \rangle_{C1}$ runs over $d\mathbf{q}^A$, while holding \mathbf{q}^L constant at \mathbf{q}_{0C1}^L . But to the first-order expansion accuracy of (6.13), $\langle \rangle_{C1}$ can simply be the ensemble average over $d\mathbf{q}^A d\mathbf{q}^L d\mathbf{q}^C$ when the defect is at conformation C1. Either way, $\langle \mathbf{f}^e \rangle_{C1}$ can be efficiently evaluated in an atomistic calculation.

Therefore, (6.9) is simplified as,

$$Z \approx \int d\mathbf{q}^L \exp(-\beta(F_C(\mathbf{q}^L) - \langle \mathbf{f}^e \rangle_{C1} \cdot (\mathbf{q}^L - \mathbf{q}_{0C1}^L))). \quad (6.17)$$

Let me define the *microscopic* Gibbs free energy of C as,

$$G_C \equiv -k_B T \log \int d\mathbf{q}^L \exp(-\beta(F_C(\mathbf{q}^L) - \langle \mathbf{f}^e \rangle_{C1} \cdot (\mathbf{q}^L - \mathbf{q}_{0C1}^L))). \quad (6.18)$$

(6.18) can be evaluated with the usual saddle-point integration method. Although

we are not at the thermodynamic limit, $\exp(-\beta\tilde{G}_C)$ should still be a quite narrow function. To the lowest order in β , there is,

$$G_C \approx F_C(\mathbf{q}_0^L) - \langle \mathbf{f}^e \rangle_{C1} \cdot (\mathbf{q}_0^L - \mathbf{q}_{0C1}^L). \quad (6.19)$$

As the thermally averaged L coordinates shift to

$$\mathbf{q}_{0C2}^L : \left. \frac{\partial F_A}{\partial \mathbf{q}^L} \right|_{\mathbf{q}_{0C2}^L} + \left. \frac{\partial F_{C2}}{\partial \mathbf{q}^L} \right|_{\mathbf{q}_{0C2}^L} \equiv 0, \quad (6.20)$$

after the C1→C2 transformation, let me define the *spatial relaxation* in L to be

$$\Delta \mathbf{q}_0^L = \mathbf{q}_{0C2}^L - \mathbf{q}_{0C1}^L. \quad (6.21)$$

There is then, finally,

$$\Delta F \approx \Delta G_C \approx [F_{C2}(\mathbf{q}_{0C2}^L) - F_{C1}(\mathbf{q}_{0C1}^L)] - \langle \mathbf{f}^e \rangle_{C1} \cdot \Delta \mathbf{q}_0^L \equiv \Delta F_C - \Delta W. \quad (6.22)$$

ΔG_C is the free energy profit illustrated in Fig. 6-3. It is more elegant than its starting point ΔF because it is a *local* variable defined for *every* defect in the system, each having a different ΔG_C . It is more suggestive than ΔF to describe the activation process, because after all, thermal activation happens locally – why is the value of *system free energy* F relevant to the few atoms participating in the activation? As we have seen, details of the other billions of atoms are indeed of *no interest* to the “few atoms”: the “few atoms” only care about their nearby \mathbf{f}_i^e ’s, the “external” loading that the environment exerts on L, because they, and only they, help or thwart the effort to cross the *local* energy barrier, which then influence the transition rates. ΔF to ΔG_C , therefore, is a *reduction* approach.

Both analytically and computationally, ΔG_C is more handy than ΔF , as we will see in the ensuing sections. The approximations used in going from ΔF to ΔG_C (starting from (6.13)), can be controlled via higher order expansions, as $F_A(\mathbf{q}^L)$ is a regular function. For example, if $\Delta \mathbf{q}_0^L$ is too large to render \mathbf{f}_0^e to be nearly a constant

during the transformation, using $(\langle \mathbf{f}^e \rangle_{C1} + \langle \mathbf{f}^e \rangle_{C2})/2$ instead of $\langle \mathbf{f}^e \rangle_{C1}$ should eliminate most of *that* error; but at the cost of doing two computations instead of one. Lastly, since ΔF can always be fully evaluated in an atomistic calculation at a greater cost, all ΔF to ΔG_C approximations can have exact error benchmarks.

6.4 Connection to Atomistic Local Stress

The Virial summation

$$\sigma = -\frac{1}{\Omega} \sum_{i>j}^N \langle \mathbf{f}_{ij} \mathbf{q}_{ij}^T \rangle, \quad (6.23)$$

is frequently used in atomistic calculations to evaluate the system-averaged stress tensor⁴. Derivation of (6.23) is based on the system’s total Helmholtz free energy $F(\Omega)$ differentiated against overall shape/volume constraint Ω . The equivalence between (6.23) and the mechanical definition of stress tensor (“traction per area”) can be proved for a microstructurally homogenized system under equilibrium[137].

Ω , however, is only well-defined for a PBC system. A small cluster of atoms embedded in the sea of other atoms has no rigorous definition of Ω . More importantly, affine transformation $\Omega' = \mathbf{J}\Omega$ does *not* describe all the ways the cluster’s boundary can move. Operationally, atomistic local stress is the artificial distribution of the (6.23) sum into tiny volumetric partitions, a sort of coarse-grained spatial average at the smallest scale. But its connection to first-principles is unclear.

The virtual work summation (6.2) provides an interpretation of the atomistic local stress. Let me first verify that when the boundary of an atom cluster – L of B in Fig. 6-7, undergoes a virtual and uniform *affine* transformation

$$\Omega' = \mathbf{J}\Omega, \quad \text{or} \quad \mathbf{q}'_i = \mathbf{J}\mathbf{q}_i, \quad \forall i \in L, \quad (6.24)$$

theorem (6.2) agrees with the *intuitive* answer based on stress concept. In other words, if σ_B is a valid definition of the atomistic local stress in B, then the virtual

⁴I have neglected the kinetic energy contribution in (6.23) and adopted a pairwise interatomic potential, in order to simplify the notation. Both are non-crucial simplifications.

work due to this deformation should be

$$\delta W = \Omega_B \text{Tr}(\sigma_B \mathbf{U}), \quad \mathbf{U} \equiv \mathbf{J} - \mathbf{I}, \quad (6.25)$$

as if we are using continuum elasticity.

Such a consistent definition of σ_B indeed exists: let me define

$$\Omega_B = \sum_i^B \Omega_i^V, \quad (6.26)$$

where Ω_i^V is the Voronoi volume of atom i . I stipulate that a term of (6.23) only contributes to σ_B if *both i and j belong to B*. Then,

$$\sigma_B = -\frac{1}{\Omega_B} \sum_{i>j}^B \langle \mathbf{f}_{ij} \mathbf{q}_{ij}^T \rangle. \quad (6.27)$$

On the other hand, because

$$\delta \mathbf{u}_i = \mathbf{q}'_i - \mathbf{q}_i = (\mathbf{J} - \mathbf{I}) \mathbf{q}_i = \mathbf{U} \mathbf{q}_i, \quad \forall i \in L, \quad (6.28)$$

there is, by plugging into theorem (6.2),

$$\delta W = \sum_{i \in L} \mathbf{f}_i^e \cdot \delta \mathbf{u}_i = \text{Tr} \left(\left(\sum_{i \in L} \mathbf{f}_i^e \mathbf{q}_i^T \right) \mathbf{U} \right). \quad (6.29)$$

Since B atoms are at total force equilibrium, and as a B atom either interacts with an A atom (which then contributes to \mathbf{f}_i^e) or another B atom, there is

$$\mathbf{f}_i^e + \sum_{j \in B} \mathbf{f}_{ij} = 0, \quad \forall i \in B. \quad (6.30)$$

Therefore, in (6.29),

$$\sum_{i \in L} \mathbf{f}_i^e \mathbf{q}_i^T = - \sum_{i \in L} \left(\sum_{j \in B} \mathbf{f}_{ij} \right) \mathbf{q}_i^T$$

$$\begin{aligned}
&= - \sum_{i \in B} \left(\sum_{j \in B} \mathbf{f}_{ij} \right) \mathbf{q}_i^T \\
&= - \sum_{i > j}^B \mathbf{f}_{ij} \mathbf{q}_{ij}^T,
\end{aligned} \tag{6.31}$$

where in step two I am free to extend the L summation to B summation because $\sum_{j \in B} \mathbf{f}_{ij} = 0$ for $i \in C$, and in step three I use the property that $\mathbf{f}_{ij} = -\mathbf{f}_{ji}$. Therefore, I have proved the *exact equivalence* between virtual work theorem (6.2) and atomistic local stress definition (6.27) for *uniform affine transformation*, (6.24).

When (6.24) is not true, there is no exact equivalence and no immediate interpretation of σ_B . But (6.24) can be a first-order *approximation*. In other words, given L atom coordinates $\{\mathbf{q}_i\}$ and their spatial relaxations $\{\delta \mathbf{u}_i\}$, one may wish to correlate the two sets of discrete data and construct an expansion of the type:

$$\delta \mathbf{u}_i = \mathbf{U} \mathbf{q}_i + \mathbf{W} : \mathbf{q}_i \mathbf{q}_i + \dots, \quad \forall i \in L, \tag{6.32}$$

where \mathbf{U} , or rather $\mathbf{U}/2 + \mathbf{U}^T/2 + \mathbf{U}^T \mathbf{U}$, takes on the interpretation of the *average strain increment* in B. There is no zeroth-order term in the expansion because

$$\sum_{i \in L} \mathbf{f}_i^e = 0, \tag{6.33}$$

and thus a net B translation does not reflect in the virtual work. (6.32) is in fact a *multipole* expansion of $\{\delta \mathbf{u}_i\}$, with \mathbf{U} being its *dipole moment*. In this sense σ_B plays the role of the average “electric field” in region B because it is exactly the energy conjugate to the dipole moment in δW , in (6.25).

How does one practically carry out the (6.32) expansion? A least-square fitting approach is recommended. Let us minimize the error

$$e = \sum_{i \in L} w_i |\delta \mathbf{u}_i - \mathbf{U} \mathbf{q}_i - \mathbf{W} : \mathbf{q}_i \mathbf{q}_i - \dots|^2, \tag{6.34}$$

against \mathbf{U} , \mathbf{W} , etc. for a given order of expansion, where w_i is the weight on each atom, which, if there is no better idea, can be taken to be 1. For the moment let us

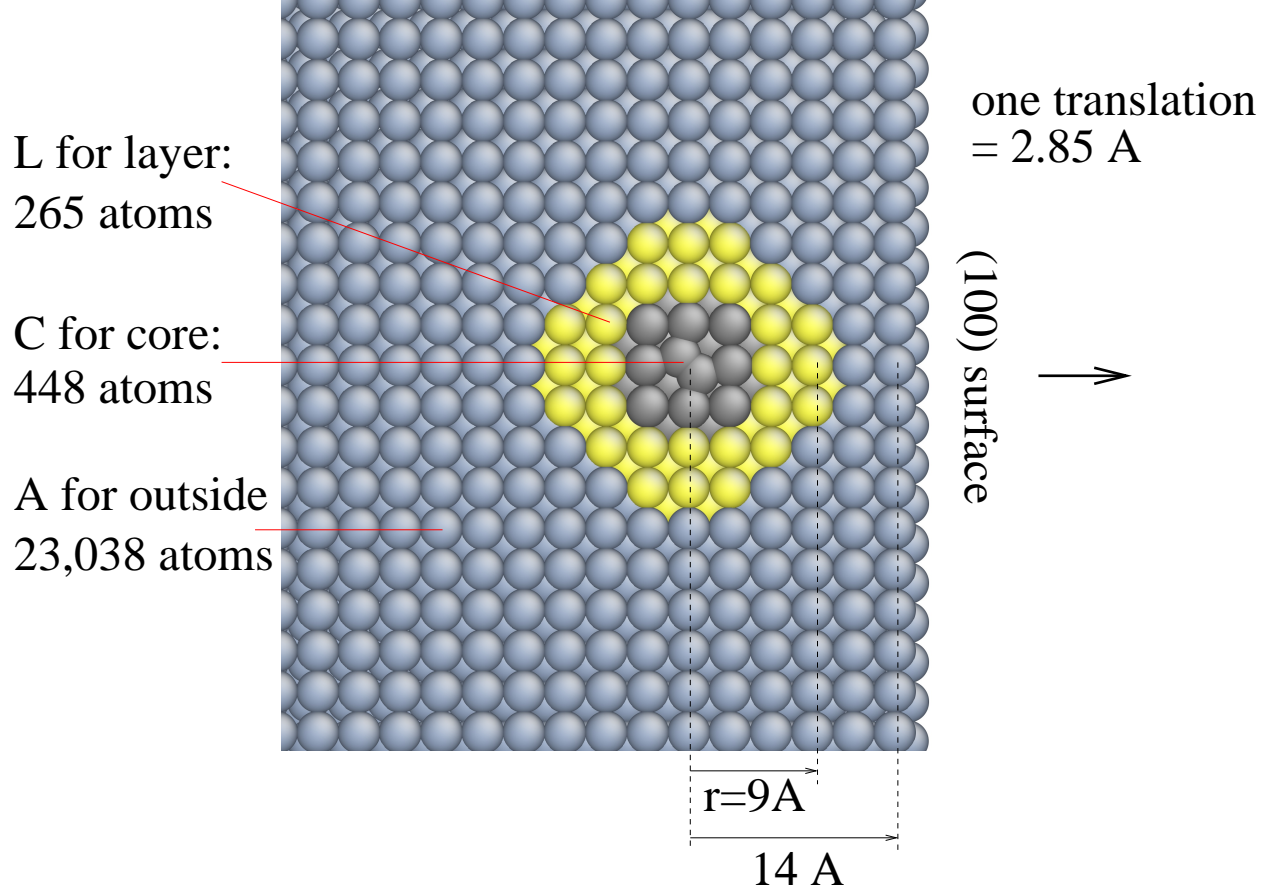


Figure 6-9: Diffusion near surface: invariant loop summation for $\langle 110 \rangle$ dumbbell self-interstitial in α -iron.

just do a first-order expansion. It is not difficult to show that

$$\mathbf{U} = \left(\sum_{i \in L} w_i \mathbf{q}_i \mathbf{q}_i^T \right)^{-1} \left(\sum_{i \in L} w_i \delta \mathbf{u}_i \mathbf{q}_i^T \right), \quad (6.35)$$

minimizes the error, where both $\{\delta \mathbf{u}_i\}$ and $\{\mathbf{q}_i\}$ in (6.35) had been subtracted off their weighted averages among L .

6.5 Self-Interstitial near Surface in α -Iron

I use the Finnis-Sinclair potential [169] to simulate α -iron. The formation energy of a single vacancy is found to 1.83 eV, and the formation energy of a $\langle 110 \rangle$ dumbbell self-interstitial, believed to be the lowest energy interstitial configuration in α -iron

[175], is 3.67 eV. No computation is done for the migration energies that may have complex pathways, but it is a general feature of such materials that the vacancy has a higher migration energy than the interstitial. Therefore an interstitial defect, once created, diffuses more quickly than the vacancy. I will use this as the first example to test the validity of invariant loop summations.

See Fig. 6-9. An interstitial defect is placed only 14 Å away from a (100) free surface. It is energetically favorable for the interstitial to drift toward the surface, which acts as source or sink to the defect. To increase the drive a bit, I put a 0.5% compression on the whole system. First, I compute the exact energy change before and after the defect moves one elementary distance (lattice constant) toward the surface, by doing two full relaxations on the entire system, which contains 24,000 atoms. The energy change is found to be extremely small: -0.00013921 eV. Thus this is a stringent test on the invariant loop summation method.

r [Å]	C atoms	2-Eval [eV]	1-Eval [eV]
8	170	-0.00022667	-0.00022573
9	265	-0.00012683	-0.00012654
10	338	-0.00013634	-0.00013679
11	506	-0.00014005	-0.00014068
12	610	-0.00013860	N/A
13	776	-0.00013856	N/A
14	952	-0.00013859	N/A
15	1240	-0.00013866	N/A

Table 6.1: Convergence of 2- and 1-evaluation invariant loop summations for the $\langle 110 \rangle$ dumbbell self-interstitial diffusion near (100) surface in α -iron. The exact energy change is -0.00013921 eV.

In Table 6.1, I list the convergence result for the 2-evaluation and 1-evaluation invariant loop summations. The first column is the loop radius (core radius), the second column is the number of atoms contained in the core. The 1-evaluation loop stops at $r = 12$ Å because by then the layer atoms would touch the surface, which destroys the translational invariance required by the 1-evaluation method. There are no such requirements for the 2-evaluation method, therefore the loop size can increase

indefinitely.

We see that the convergence is satisfactory, considering this is a very small energy change. Especially, both methods give acceptable results at $r = 10 \text{ \AA}$.

6.6 Crack-Tip Extension near Void in Si

Si is simulated using the Stillinger-Weber potential [157]. There are 17,548 atoms in the entire simulation cell. An atomically sharp crack is created (see Fig. 6-10) on the (111) cleavage plane (shuffle-set). There is a void to the right of the crack. The crack-tip to void distance is about 5 nm, or 10 rows of atoms. The simulation cell is strained in the y direction to keep the crack open, and as one increases ε_{yy} , the load on the crack increases, until at a certain critical ε_{yy}^c , the total energy change for an elementary crack extension switches from positive sign to negative sign, which is the turning point in the competition between strain energy release rate and surface energy, if Griffith's analysis is to be carried over. However, since the void is only 5 nm away from the crack-tip, one cannot expect to have a stress field near the tip, not to say the K -zone with $\propto K/\sqrt{r}$ dependence. Therefore conventional stress intensity factor analysis cannot be carried over to this tiny specimen. Such an analysis would not be easy anyway for a much larger system, due to the presence of the void and the periodic boundary condition. Therefore, besides full relaxation of the entire atomistic configuration (each takes about 20 minutes on a 450 MHz Intel Pentium computer), there is no way of evaluating the ΔE - ε_{yy} loading curve until the present, as I test the atomistic invariant loop summation.

The convergence result at $\varepsilon_{yy} = 0.04$ is shown in Table (6.6). The quality of convergence is much better than that of the interstitial diffusion in α -iron. Both methods converge to less than 0.5% relative error from the exact answer at $r = 1 \text{ nm}$.

The high quality of convergence at loop radius 1 nm maintains throughout the entire ΔE - ε_{yy} loading curve, as shown in Fig. 6-11. The predicted ε_{yy} transition point is at $\sim 5\%$, across which the crack theoretically becomes unstable. I am able to continue the static minimization somewhat into the negative ΔE zone because

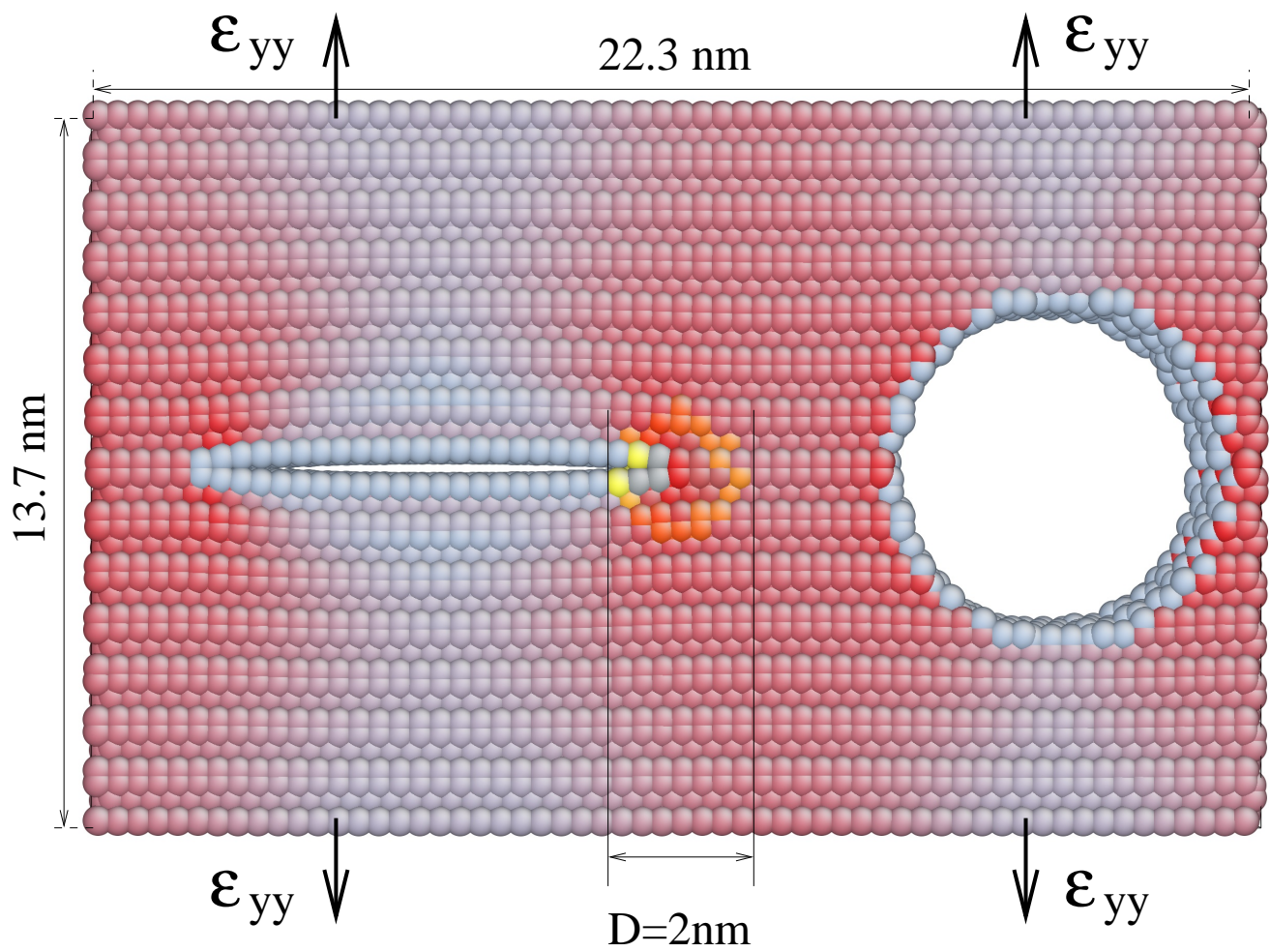


Figure 6-10: Crack-tip extension near a void: atoms are color-encoded by the atomistic local shear strain. The invariant loop of $r = 1\text{ nm}$ is also labeled.

r [Å]	C atoms	2-Eval [eV]	1-Eval [eV]
8	128	3.16652	3.17395
9	160	3.15973	3.16721
10	192	3.15909	3.16658
11	242	3.15841	3.16594
12	280	3.15794	3.16548
13	322	3.15765	3.16520
14	388	3.15733	3.16488
15	432	3.15715	3.16471
20	786	3.15664	3.16421
30	1778	3.15627	3.16391
40	3158	3.15614	3.16299
50	4844	3.15607	N/A

Table 6.2: Convergence of 2- and 1-evaluation invariant loop summations for crack tip extension near a void in Si at $\varepsilon_{yy} = 0.04$. The exact energy change is 3.15602 eV.

there still exists a barrier between the two configurational minima, and there is no thermal fluctuation. In a real crack at finite T , as soon as ΔE turns negative, there is incentive for thermally activated crack front propagation, and in a fixed-loading condition, if the crack elongates the stress intensity factor increases, so the front propagates even faster, until eventually we have catastrophic failure. Therefore the critical ε_{yy}^c computed here is physically significant for a real crack.

6.7 Peierls-Nabarro Stress of Perfect Screw Dislocation in Si

6.7.1 Slip Systems

Slip occurs on (111)-oriented planes in Si and Si-like materials such as GaAs and InP because those planes have the smallest Burgers vector. But unlike simple fcc, the diamond cubic structure has 2 atom per unit cell, so there is the further distinction between the *glide-set* plane and the *shuffle-set* plane, illustrated in Fig. 6-12. Both planes are parallel to [111], but one cuts three bonds, the other cuts one bond. There

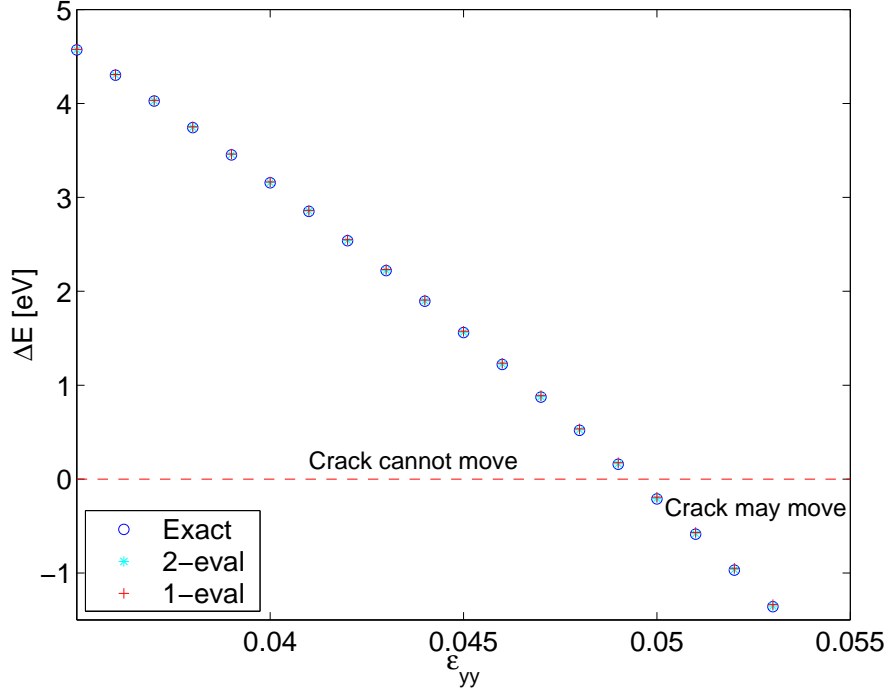


Figure 6-11: Crack-tip extension near a void: the entire loading curve.

always has been debates about which slip plane controls what deformation, but only recently do people begin seriously clarifying the situation via atomistic simulation [237, 238, 242, 243].

It is commonly accepted that the high- T plastic deformation of Si-like materials are controlled by dissociated dislocations on the glide-set plane, supported by direct TEM evidence for Si and Ge [236]. A basic feature of such motion is that it is quite impossible for the dissociated partials (separated by tens of nanometers) to first constrict and then cross-slip, so the two partials would remain the glide-set plane, and the resultant slip lines should be straight.

6.7.2 Low- T Plastic Deformation

In a series of very recent experiments [239, 240, 241], Suzuki *et al* were able to plastically deform GaAs, InP and InSb to T as low as 77K by applying pressure that suppresses fracture. They observed humps in the resolved yield stress versus T relation at $T = 300 - 420$ K, plotted in Fig. 6-13 in both $\tau - T$ and $\ln \tau - 1/T$ scales,

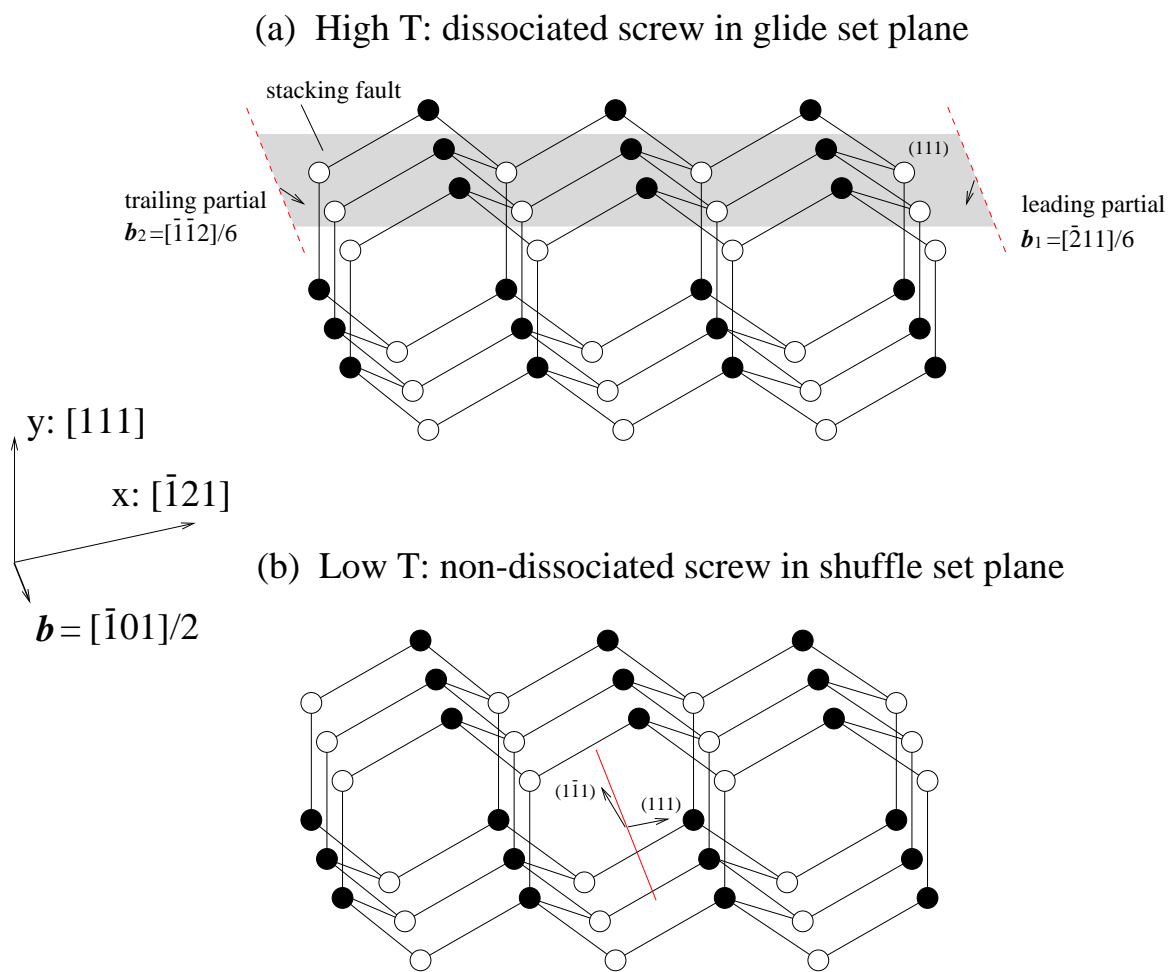
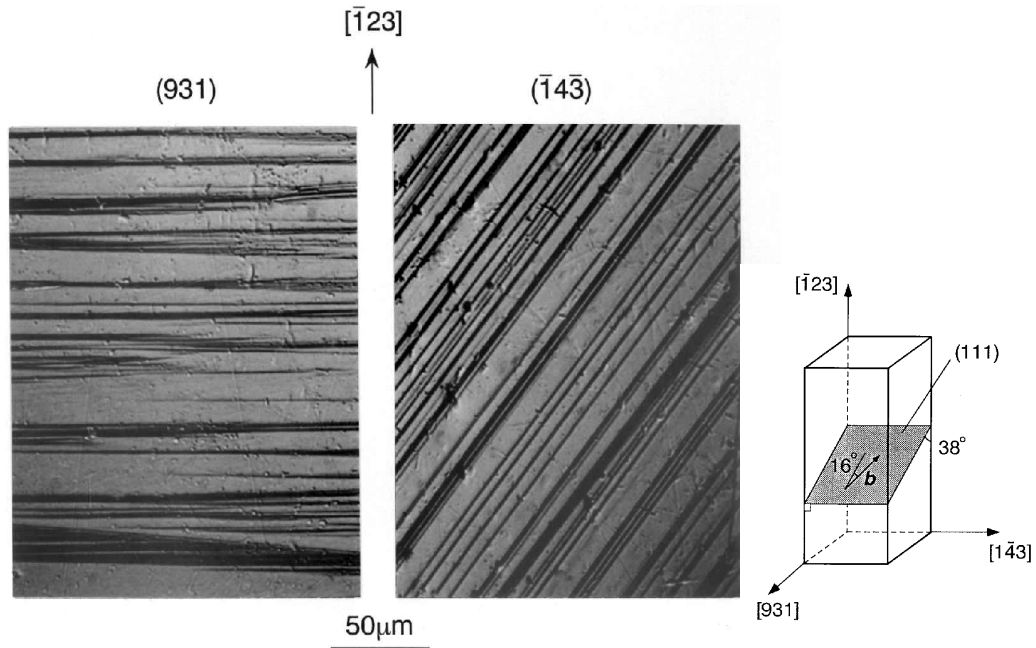


Figure 6-12: Slip system in Si-like materials.

T. Suzuki, T. Yasutomi, T. Tokuoka, I. Yonenaga,
 Phil. Mag. A 79, 2637, (1999).



Slip lines on the surfaces of InP deformed at 300 K. The slip traces indicate $\frac{1}{2}[101](111)$ slip with frequent cross-slip.

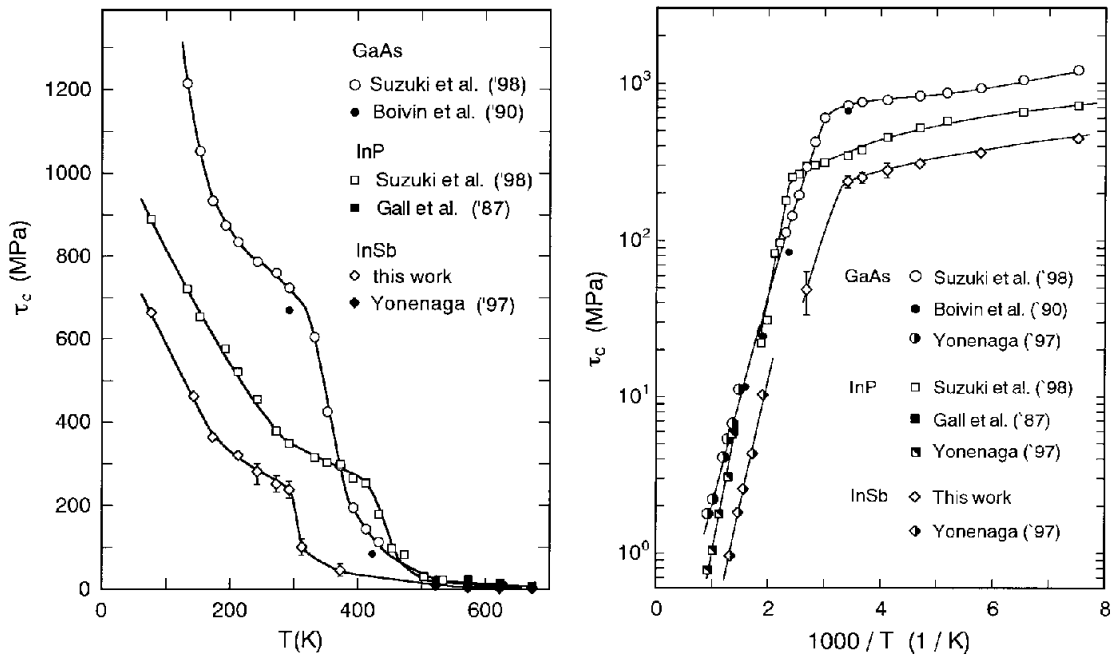


Figure 6-13: Recent experimental results by Suzuki *et al* [239, 240, 241].

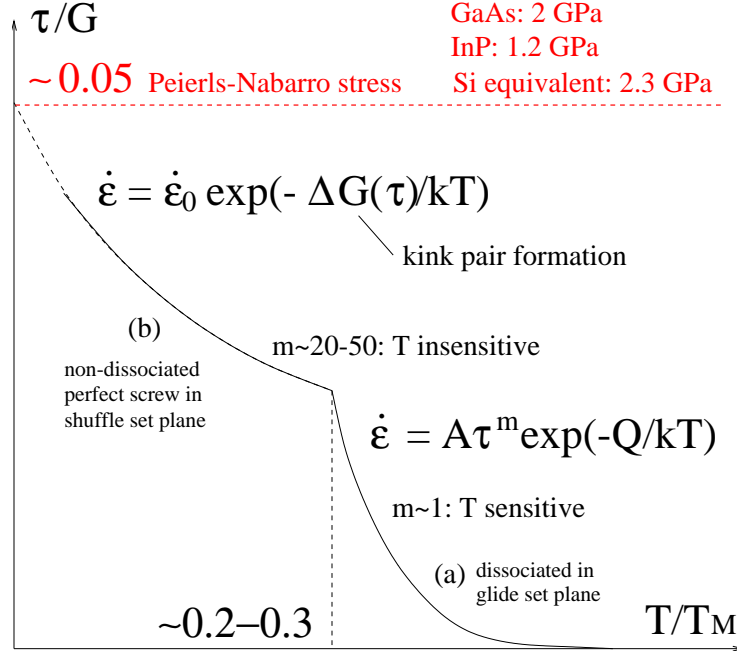


Figure 6-14: Proposed plastic deformation mechanisms for Si-like materials.

which indicates a cross-over in mechanism. The low- T mechanism is clearly much less T -sensitive than the high- T mechanism.

A study of the slip lines suggest that cross-slip happens frequently at low- T . Armed with this information, Suzuki *et al* suggests that the low- T behavior is controlled by perfect screw dislocations on the shuffle-set plane, illustrated as (b) in Fig. 6-12, which easily cross-slips.

One can scale the measured τ by the resolved shear modulus G of the material, and T by its melting point T_M , and pretty much collapse the measurements of different materials on one curve, shown in Fig. 6-14. At high T , the measured strain rate can be fit well by the empirical relation $\dot{\epsilon} \propto \tau^m \exp(-Q/kT)$ with $m \sim 1$, indicating a viscous behavior. At low T , one can still carry out the fitting with $\dot{\epsilon} \propto \tau^m \exp(-Q/kT)$, but m would be 20-50, and the quality of the fit is not good. On the other hand, with a different form, $\dot{\epsilon} \propto \exp(-\Delta G(\tau)/kT)$ with $\Delta G(\tau)$ taking on the interpretation of the activation energy of nucleating a kink pair across the Peierls barrier on the stressed perfect screw, one may get excellent fit. $\Delta G(\tau)$, in a simple line tension model for the process, has a form that can be parameterized with 1 or 2 calibrations, one of

which must be the Peierls-Nabarro stress τ_{PN} , which is the limit of τ as $T \rightarrow 0$. At $\tau = \tau_{\text{PN}}$, the lattice potential is so tilted by the external work that a barrier no longer exists between the two configurational minima, and only then can the dislocation spontaneous translate as a whole without the help of thermal activation to form a kink pair. As can be imagined, if we assume a simple form for the lattice potential such as sinusoidal, then knowing its maximal slope which corresponds to τ_{PN} would completely determine the lattice potential. Therefore τ_{PN} is an important number that is not only useful for $T = 0$, but also would help the parameterization of the entire $\Delta G(\tau)$ function which controls the low- T plastic behavior. It is thus important to be able to compute τ_{PN} in an atomistic calculation, which is the first step toward the eventual determination of $\Delta G(\tau)$.

Experimentally, by extrapolating the finite temperature results, Suzuki *et al* proposed a τ_{PN} of $\sim 0.05G$, which converts to 2.3 GPa for Si.

6.7.3 Status of Atomistic Calculations

	τ_{PN}	τ_{PN}/G	Size	Method
[238]	4.0 GPa	0.086	3,000-15,000 atoms	Fixed boundary
[242]	2.0 GPa	0.044	970-5,960 atom rows	Anisotropic elasticity
Me	2.9 GPa	0.063	<7,560 atoms	PBC, invariant loop

Table 6.3: Summary of the simulation results for τ_{PN} in Si.

Unfortunately, as shown in Table 6.7.3, the atomistic calculation results vary greatly from people to people, for the same Stillinger-Weber potential and the same defect: perfect screw on the shuffle set plane. The reason for such large discrepancies must be attributed to the different simulation setups. Ren *et al* [238] uses fixed boundary condition computed from elasticity solutions; the τ_{PN} he quotes are the system average Virial stress when the screw begin to move. Koizumi *et al* [242] also uses fixed boundary condition but with more sophisticated anisotropic elasticity solution. They do not explain the exact origin of their τ_{PN} but I guess it is in

conformance with the elasticity solution. My results are calculated in a PBC cell with the invariant loop methods which I will explain in detail in the next section.

I would refrain from commenting on whose number is correct because that would go into the details of each calculation, but would just like to comment on the root causes for such discrepancies which also happen frequently in other atomistic calculations of defect mobility. In my opinion, the root cause is the lack of a transferable standard for the driving force on defects, the well-characterized environment that I talked about at the beginning of the chapter. People tend to rely on elasticity solutions, but for such small systems ($\sim 10,000$ atoms in all three calculations), that is really a risky option full of perils.

I suggest that the true test of a correct answer is to demonstrate transferability, that is, since τ_{PN} is an intrinsic property of the defect, then no matter in what measure it is defined and how one computes it, that measure should be largely invariant when a different atomistic environment is used to drive the defect. That is, setups of the “testing-machine” should not influence the final result, which is supposed to be an intrinsic property.

6.7.4 Results

I create a screw-dipole configuration illustrated in Fig. 6-15, and a screw-notch configuration illustrated in Fig. 6-16, where the notch tip is only about 10 atomic rows from the screw dislocation, and therefore (a) and (b) can be regarded as completely different atomistic environments for the left screw that is being driven. Shear strain ϵ_{yz} is applied in both (a) and (b) until the screw spontaneously moves. Convergence of the 2- and 1-evaluation invariant loop against the exact answer for the energy change in the case of (a) at $\epsilon_{yz} = 0$ is shown in Table 6.4.

In Fig. 6-17, the average shear stress of the simulation cell is plotted as x , and ΔE , calculated by the exact, 2- and 1-evaluation invariant loops (at $r=1$ nm) are plotted as y . As we see the invariant loop summations still give satisfactory results for ΔE in comparison with the exact answer, and (a) and (b) both move at a critical ΔE that is less than 1% off for the two entirely different environments, which prove

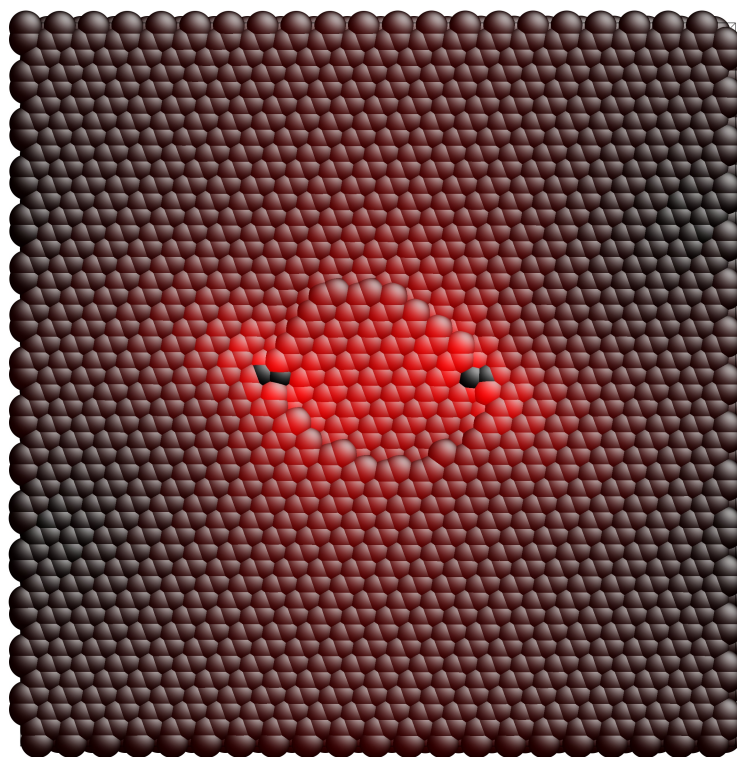


Figure 6-15: Environment (a): screw-screw configuration.

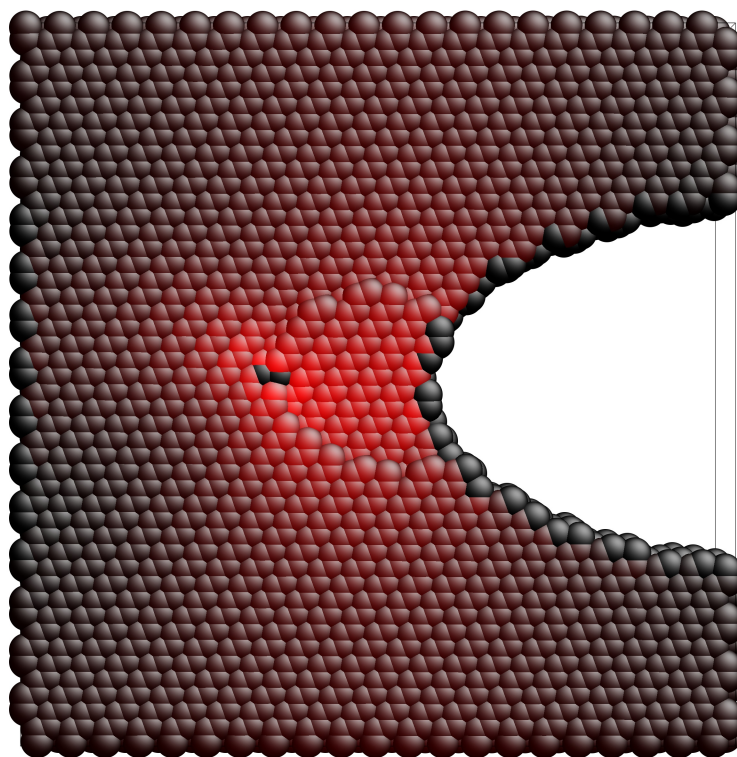


Figure 6-16: Environment (b): screw-notch configuration.

r [Å]	C atoms	2-Eval [eV]	1-Eval [eV]
6	42	1.101799	1.169171
7	62	1.013047	1.080053
8	80	1.044961	1.111075
9	96	1.051984	1.117816
10	122	1.052406	1.118232
15	268	1.053037	1.118950
20	490	1.053011	1.118987
25	740	1.052976	1.119009

Table 6.4: Convergence of the 2- and 1-evaluation invariant loop summations for the Si screw-dipole configuration (7560 atoms, supercell $(139.6821 \times 141.1002 \times 7.6805$ Å) has $21 \times 15 \times 2$ unit cells, $\epsilon_{yz} = 0$, dipole separation is 6 out of 21, or 39.91 Å). The exact energy change is 1.052396 eV.

that ΔE , with similar interpretation as J – the strain energy release rate, is a true characterization of the diving force.

On the other hand, we see that (a) and (b) move at very different simulation cell Virial stress averages (also different ϵ_{yz} ’s), which shows that the overall stress average, at least, is not a transferable standard. For (a), if we plug in the simulation cell Virial averages into the Peach-Koehler formula, we would get an naive ΔE prediction that is off from the true value by 1 eV, which translates to 20% error in the τ_{PN} prediction. But such setups are used by people all the time. When we do this for (b), it would be off by more.

Of course one may try to improve upon the result by image summations to get the so-called “local stress”, but for (b) at least, this is very hard because we are under PBC, and in general it is quite infeasible. Also, I doubt one can do very well in extrapolating a smooth stress field in a piece of material 10 atoms wide, to whose left there is a singular dislocation core, and to whose left there is an elliptical notch.

(b) actually is not a contrived example because it shows the behavior of a dislocation very close to a crack-tip. The result in Fig. 6-15 demonstrates that even when the dislocation is 10 atoms away from the crack-tip, it still behaves according to its own local environment, thus verifying the intuition of *strong locality*, that is, the screw

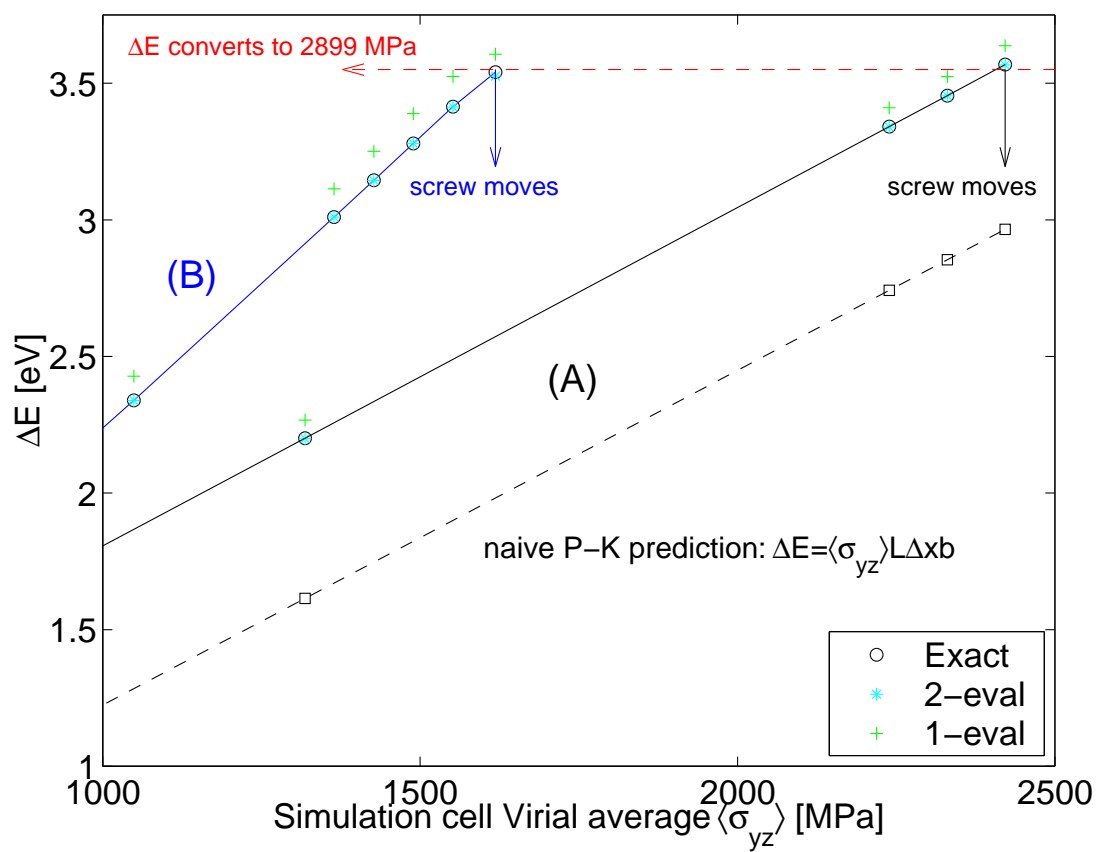


Figure 6-17: Comparison of results from environments (a) and (b).

is driven by atoms *immediately* surrounding it; it does not care about who “charges up” that small ring of atoms, but only about whether it is sufficiently “charged”. Furthermore, this very local characterization is quantifiable as the atomistic loop invariant, and is directly computable at essentially zero additional cost. We also see that a stress field description can never lead us this far and reveal this insight, since stress field simply does not exist so close to the core.

What is the minimal lengthscale of the strong locality? 1 nm , as it turned out for Si, which is minimal loop size one can take around the crack tip or the screw that will keep the result approximately invariant. If the loop size is still smaller, it would cut into the genuine defect core.

6.8 Conclusion and Insights

It is my opinion that people who do atomistic calculations, in order to produce meaningful result *vis-a-vis* experiments, **in principle** never *have to* resort to elasticity theory tools like image summation. Elasticity provides good guidance, can improve efficiency (e.g., finite-element/MD coupling) in the sense of cost, but should never be the *only* route to answer in terms of fundamental principles, for ones who already possess the most detailed atomistic information. Atomistic representation is self-sufficient in the production of data, and therefore should be self-sufficient in the analysis of data, too. For example, in order to resolve the actual driving force on a dislocation in an atomistic calculation with PBC, it is against the author’s intuition that one must out of necessity use the image stress formulas with parameters like μ, ν and continuum expressions like $\log r$. They are not native but alien to the discrete atom representation.

The similarity between this formulation and the real J -integral is striking despite the atomistic nature of the former: both characterize the deformation driving force the environment exerts on the microstructure *not* in terms of stress, but in terms of Gibbs free energy (release rate), because energy is the most robust concept in physics. In the case of fracture mechanics, the energy criterion outlives the K criterion –

essentially a stress criterion, in the J dominance zone where linear elastic fracture mechanics (LEFM) fails. Before the advent of J , fracture toughness was measured in K with units of $\text{Pa}\sqrt{\text{m}}$ following LEFM stress asymptotic form $\sigma \propto K/\sqrt{r}$, and in order to satisfy K dominance required by ASTM standards, the specimen in loading experiments sometimes must be as big as 10^3 kg. After the J formulation, ASTM rewrote standards in $\text{Pa}\cdot\text{m}$ and the same material can now be tested for fracture toughness with a specimen size of 10^1 kg, which greatly saved the cost. The moral of the story is that atomistic simulation can be viewed as a fantastic testing machine but with a severe size limitation: at its scale – the atom scale, the concept of stress field may often become obsolete or too unwieldy, but the concept of energy lives even down to the atomistic resolution. The theory proposed is nothing exotic but I hope that people develop and test practical techniques based on it, via which atomistic calculations could align with each other and with experiments.

Chapter 7

Summary

The problems tackled in this thesis are of great technological and scientific importance, as the study of mechanical behavior - strength, deformation, and toughness by means of atomistic simulation is believed to be on the threshold of significant fundamental progress. Simulation can provide valuable insights into mechanistic details of defect interactions and mobility, particularly under conditions of large deformation and elevated temperatures. In this thesis I take an integrated approach to modeling thermal and mechanical responses, tied together by their common dependence on the physics of bonding and their sensitive dependences on microstructures.

There are both conceptual and technical challenges to studying deformation and thermal resistances with an atomistic approach. One must overcome the intrinsic small length- and time-scale limitations and be able to focus on the controlling mechanisms. But on the other hand, physical laws valid at larger scales may become invalid when features reach the nano-scale, as now clearly seen in microelectronics research after 30 years of relentlessly shrinking the scales. In terms of mechanical response, conventional descriptions such as stress-field characterizations may be no longer applicable, and one must come up with new descriptions based on first-principles that would remain valid down to the nano-meter and nano-second scale. Here we are aided by the complete knowledge about the atoms in our simulation, and therefore do not have to use the asymptotic field theories out of necessity.

Another major challenge is the lack of reliable interatomic potentials to carry out

the simulation. Empirical potentials do not have to be highly accurate, but it is essential for them to be highly transferable, meaning being able to work reasonably well in many different atomistic environments. To achieve that requires an intimate knowledge of the nature of bonding, which can now be systematically revealed by highly accurate *ab initio* calculations. On the other hand, electronic structure methods cannot be used to directly model most mechanical and thermal transport properties, since “long” simulations at least on the order of nanoseconds are needed. Thus, my approach to solving the problem is an example of Multiscale Materials Modeling; and the fact that I can construct and verify a robust empirical potential using electronic structure information, model its lattice thermal conductivity with property-governing defects, and finally reach quantitative and mechanistic answer to this long-standing problem of practical significance *all from scratch*, is a demonstration of the power of MMM. In the long view, similar strategies can be carried over for predicting other properties and on different materials.

For the ideal strength problem, I have revealed its connection to slip and dislocation nucleation in Cu (Ar), which can now be directly probed by nano-indentation experiment. The insights gained here are important in other contexts as well, such as the Rice-Thomson model for crack-tip dislocation nucleation, which all belong to various manifestations of the lattice barrier. I have also shown that ideal strengths can be modeled by either lattice dynamical or molecular dynamics methods, each with its own advantages, and that finite \mathbf{k} instabilities are possible in both SiC and Cu. I have studied the influence of microstructures such as void and nano-grains on the athermal strength, and related that to the Hall-Petch relation. Clearly, more work needs to be done in this direction and much more are yet to be revealed.

Lastly, I would like to emphasize the importance of the invariant summation method. Atomistic calculations of defect mobility require knowing the local driving forces, which is a general bottleneck. The solution I proposed is much in the same spirit as the standardization of fracture toughness. The idea is to focus on the change in the local free energy rather than the local stress which is ambiguous at the nanometer level. This leads to the atom cluster invariant summation and the development

of efficient method for practical evaluations. By moving a dislocation in seemingly very different atomistic environments, I have shown that such an invariant measure indeed controls the behavior of the defect, thus confirming the principle of strong locality which literally holds down to 1 nm in lengthscale.

Appendix A

Nodal Dynamics Study of Precipitation Hardening

For the problem: dislocation motion impeded by a random distribution of point-like obstacles, it may be better to discretize the x -direction by regular, equally h -spaced mesh. However I am no longer assuming $\partial y/\partial x$ to be small, thus the canonical equation of motion (assuming no lattice barrier) for “nearly straight” dislocation[231, 139],

$$m \frac{\partial^2 y}{\partial t^2} = \epsilon \frac{\partial^2 y}{\partial x^2} - B \frac{\partial y}{\partial t} + \sigma b - F(x, y|c, a, K) \quad (\text{A.1})$$

is no longer good. I shall briefly explain the physical parameters appearing in (A.1), whose meanings hold true in general even when (A.1) does not.

- m is the dislocation “mass” density ([kg/m]), which is related to the kinetic energy by $dK = (ds)mv_n^2/2$, where ds is the differential line length ([m]) and v_n is its “apparent”, normal velocity ([m/s]). Of course, dislocation is not a *physical* object and does not have mass in the literal sense; it does, however, describes a peculiar arrangement of atoms near it which carries quanta of materials deformation and has far-field elastic stress/strain. Thus, if the dislocation moves, the stress/strain field is going to be time-dependent, thus the atoms are going to throb up and down just like a boat in wavy water. So dK is actually the kinetic energy of atoms surrounding the moving dislocation.

- ϵ is the dislocation line tension or energy ([J/m]), which is the sum of core energy and elastic energy outside the core. In a not-too-bad idealization called *constant line energy model*, $\epsilon = \mu b^2/2$ is a constant (does not depend on orientation), where μ is the shear modulus ([J/m³]) of the isotropic continuum and b is the Burger's vector ([m]) of the dislocation. Interestingly, one can derive for screw dislocation: $\epsilon = mv_s^2$, in close analogy with the special relativity formula $E = mc^2$, where c is replaced by the shear wave speed $v_s = \sqrt{\mu/\rho}$ ([m/s]), and ρ is mass density of the material ([kg/m³]). It is thus very convenient to use a reduced unit system in which the length unit is b , the velocity unit is v_s , and the energy unit is ϵb ; from which all other units (time [b/v_s], stress [ϵ/b^2], ..) can be defined. And this unit system $m = 1$, $b = 1$, $\epsilon = 1$ in (A.1).
- B is the phonon drag coefficient ([J·s/m³] or [$\epsilon/v_s b$]), which gives dissipation to the dislocation motion. It is similar in mechanism to the resistance a man feels when walking in the rain, who receives more raindrops at front than back. B can be shown to be on the order of $k_B T/v_s b^2$, where T is the material temperature.
- σ is the external stress ([J/m³] or [ϵ/b^2]). It makes the dislocation move normal to itself to increase the area swept by since the material can be deformed that way, and σ likes the material to be deformed because the total free-energy is reduced.
- $F(x, y|c, a, K)$ is the resistance force field due to impurities in the material. Here c is the volume ratio of the impurity, a is its average size (or force range) ([m] or [b]), and K is the maximum resistance the impurity offers ([J/m] or [ϵ]). There exist two opposite limits to F : one is $c \gg K/2\epsilon$, called “Mott statistics”, corresponding to weak but populous obstacles (*solute atom strengthening*). The theoretically predicted critical stress in this limit¹ is

$$\sigma_c = \frac{2}{3} \left(\frac{K}{2\epsilon} \right)^{4/3} c^{2/3} \mu, \quad (\text{A.2})$$

¹The theory was first proposed by Mott and Nabarro [246], and later was analyzed by Schwarz and Labusch [250]

above which the dislocation can move steadily *in spite of* the obstacles and the material can deform plastically. The other limit, $c \ll K/2\epsilon < 1$, is called “Friedel statistics”² (*precipitate-particle strengthening*), corresponding to fewer but stronger obstacles, which has a predicted flow stress of

$$\sigma_c = \frac{2\epsilon}{bL} \left(\frac{K}{2\epsilon} \right)^{3/2} = \frac{2\epsilon}{ba} \left(\frac{3c}{2\pi} \right)^{1/2} \left(\frac{K}{2\epsilon} \right)^{3/2} \quad (\text{A.3})$$

where L^2 is the average area an obstacle “owns” on the slip plane ($[m^2]$ or $[b^2]$), related to c and a . (A.3) is derived based on a geometrical argument by Friedel, who also predicts that at the critical point,

$$\lambda_c = L \left(\frac{K}{2\epsilon} \right)^{-1/2}, \quad (\text{A.4})$$

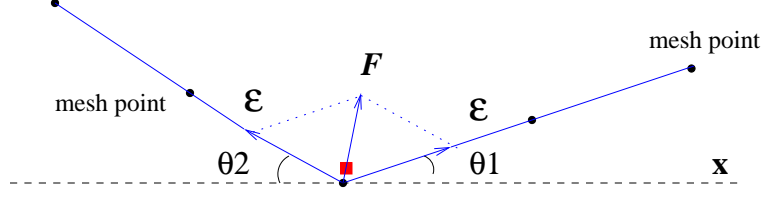
where λ is the average separation between two nearest obstacles impeding the same dislocation.

I will focus on $c \ll K/2\epsilon$ limit first, in testing my own numerical scheme, since (A.3) was well-confirmed by experiments and simulations and is also conceptually convincing; while the theoretical derivation of (A.2), to me, looks suspicious. The main significance of (A.3) is the scaling law

$$\sigma_c \propto c^{1/2}, \quad (\text{A.5})$$

which says that the plastic strength of an alloy does not scale *linearly* with the concentration of strengthening agents, thus by adding a small amount of agents one can greatly enhance its strength (making dislocation harder to move and so the flow stress is increased); also, from (A.3) one can show that *peak* strength can be obtained by controlling precipitate-particle size a (as K also depend on a), through a thermal process called “aging”.

²A theory neglecting mass and dissipation was first proposed by Friedel [247]. A review was given by Ardell [251].



Arrest: $\mathbf{F} < \mathbf{K}$

Free: Orowan loop formation

$\mathbf{F} > \mathbf{K}$

Thermal activation

Figure A-1: Dislocation impeded by the obstacle, forming a cusp.

Now returning to (A.1), which in the reduced unit system is

$$\frac{\partial^2 y}{\partial t^2} = \frac{\partial^2 y}{\partial x^2} - B \frac{\partial y}{\partial t} + \sigma - F(x, y|c, a, K) \quad (\text{A.6})$$

where actually everything is dimensionless in (A.6) but I am too lazy to add the \sim . Since the obstacles are now point-like, it makes sense to use its size a as the x -mesh size h . That is, I am going to neglect all details happening below a , effectively treating obstacle-dislocation interaction as a simple “arrest/free” rule, where a single mesh point (ih, y_i) is going to be detained at the obstacle position (x_k^o, y_k^o) , if it is found trying to cross y_k^o but the flanking angles on two sides are not enough to break through the obstacle, i.e.,

$$\theta_1 + \theta_2 < \frac{K}{\epsilon} \quad (\text{A.7})$$

in Fig. A-1.

So, a cusp is going to form at the obstacle position (x_k^o, y_k^o) , and may be released later if σ is large enough to make the flanks bow out beyond $K/2\epsilon$, or if the inertia is large enough to induce that. The accuracy and stability of the numerical scheme is of foremost concern here. Although I am going to adopt periodic boundary condition, using the spectral method is out of the question because it loses all its magic when

cusps exist in the solution. How about finite-difference schemes on a regular mesh? Surprisingly, the first thing I tried, an explicit, central-difference scheme, works well, for reasons I will explain later. The scheme is just

$$\frac{y_i^{n+1} - 2y_i^n + y_i^{n-1}}{\Delta t^2} = \frac{y_{i+1}^n - 2y_i^n + y_{i-1}^n}{\Delta x^2} - B \frac{y_i^{n+1} - y_i^{n-1}}{2\Delta t} + \sigma + \mathcal{O}(\Delta x^2) + \mathcal{O}(\Delta t^2), \quad (\text{A.8})$$

which leads to

$$y_i^{n+1} \approx \frac{(y_{i+1}^n - 2y_i^n + y_{i-1}^n)r^2 + \sigma\Delta t^2 - (1 - B\Delta t/2)y_i^{n-1} + 2y_i^n}{1 + B\Delta t/2} \quad (\text{A.9})$$

if node (ih, y_i^n) is free, and

$$y_i^{n+1} \equiv y_k^o \quad (\text{A.10})$$

if otherwise. That is, the arrest and release of the dislocation node (segment) by the obstacle is assumed to take on the *smallest* length/time scales, whose details are of no relevance to the overall behavior. Here

$$r = \frac{v_s \Delta t}{\Delta x} \quad (v_s = 1) \quad (\text{A.11})$$

should be less than 1, by the Courant-Friedrichs-Levy (CFL) convergence condition [252]. Fig. A-2 is a simulation of the evolution of an initially straight triangular cusp between $x = [0, 2\pi]$ (under PBC) from $t = 0$ to $t = 1$, with $B = \sigma = 0$, in comparison with the exact solution. One can see that (A.9) is stable and works quite well.

Why do I insist on using a regular x -mesh? Because it simplifies the computation of obstacle-dislocation interactions. Say there are M mesh-points and W obstacles, how can I determine which nodes are crossing which obstacle at a given time? If my nodes are specified by (x_i, y_i) , i.e., they have two degrees of freedom, the calculation may take $\mathcal{O}(MW)$ efforts per step. But, if I use a regular x -mesh, $x_i = ih$, and make a not-too-restricting assumption that all obstacles also lay on *integer* multiples of h , $x_k^o = n_k h$, then instead of letting the dislocation seek out obstacles, I can let the obstacles seek out the dislocation, i.e., check if the k th obstacle is crossed by node

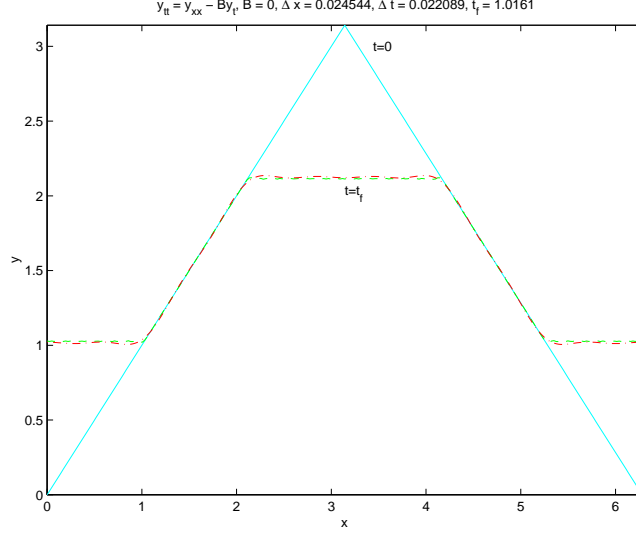


Figure A-2: Numerical solution of cusp evolution using finite difference scheme (A.9) with $r = 0.9$.

$i = x_k^o/h$ or not, which takes only $\mathcal{O}(W)$ effort to do per step.

Before moving on, let me add that there are two other ways a dislocation may overcome an obstacle in addition to “simple breaking through” indicated by (A.7). The first one is “Orowan loop formation”, which happens when the obstacles is impenetrable (*dispersal-particle strengthening*) by the dislocation, $K/2\epsilon > 1$, but the external stress σ is large enough to make θ_1 and θ_2 approach $\pi/2$; then the two flanks merge *ahead* of the obstacle – a new dislocation is formed and marches on, leaving a little dislocation loop behind surrounding the obstacle. The actual process is quite complicated because of dislocation self-interaction, which is ignored in our treatment; so I won’t lose much by simply stipulating that whenever $\theta_1 + \theta_2 > \pi/3$ during the simulation, the dislocation is freed by Orowan loop shedding. The other mechanism is thermal activation, which means that even if $K - F > 0$, there is still a finite probability that an arrested segment can spontaneously overcome the energy barrier

$$E \approx a \cdot (K - F) \quad (\text{A.12})$$

of the obstacle with the help of thermal fluctuation, much like tunneling in quantum mechanics. The rate of transition ν is on the order of

$$\nu \approx \frac{\nu_D}{n} \exp\left(-\frac{E}{k_B T}\right), \quad (\text{A.13})$$

where $\nu_D \approx v_s/b$ is the Debye (characteristic atomic vibration) frequency of the solid and n is the number of atoms involved in this collective transition, which is $\sim a/b$ in our case. Thus, even if $E > 0$ and the segment can not be freed by force, there is still probability $1 - e^{-\nu t}$ that the trapped segment could be released by thermal activation. These two features can be easily incorporated into the simulation.

The problem now is to generalize (A.1), which is only valid for “nearly straight” dislocations, to situations where $|\partial y/\partial x|$ is $\mathcal{O}(1)$. But I am still going to adopt a regular x -mesh with spacing h due to above-mentioned efficiency considerations, thus comes by the name “abacus model”. So long as $|\partial y/\partial x|$ does not approach ∞ , the abacus discretization *should* work fine as (A.9). But as I find out, it is not as easy to come up with a stable scheme. Some seemingly plausible schemes works fine for smooth $y(x, t)$, but is unable to cope with the cusp situation and the quickly becomes unstable. Some schemes may work fine but are implicit, requiring at least a tridiagonal linear system solver³. I am looking for a robust scheme that is explicit, has good physics in its form and does not *have* to provide too high accuracy because neglecting dislocation self-interaction is already a sin.

To incorporate the correct dynamics, we must know the Lagrangian

$$\mathcal{L} = K - V, \quad (\text{A.14})$$

and minimize the action

$$A = \int \mathcal{L}(t) dt. \quad (\text{A.15})$$

³It is worse than that: because the meshes wrap around (PBC), the matrix is actually tridiagonal plus two elements on the corners, which could be solved “quickly” by moving the two elements to RHS and do a self-consistent iteration.

\mathcal{L} is itself a line integral over ds , and it is more convenient to discretize it that way first, as a function of $\{y_i(t), i = 1..M\}$ where I stipulate that $(ih, y_i(t))$ is right *on* the dislocation at time t . Remember that $(ih, y_i(t))$ is not a real object but collectively they represent a curve, so it makes no sense to identify $(ih, y_i(t))$ as a physical object. Also, it makes no sense if the mesh point moves along the dislocation line because the curve they represent does not change.

In the constant line energy model, the elastic energy is simply

$$V_e = \int \epsilon ds = \int \epsilon \sqrt{dx^2 + dy^2}, \quad (\text{A.16})$$

which I discretize as

$$V_e \approx \sum_i \epsilon \sqrt{h^2 + (y_i - y_{i-1})^2} + \mathcal{O}(h^2). \quad (\text{A.17})$$

I tried to be clever once and discretized it as

$$V_e \approx \sum_i \epsilon \sqrt{h^2 + (y_{i+1} - y_{i-1})^2/4}, \quad (\text{A.18})$$

thinking it may provide better accuracy. But the resultant numerical scheme was found to have a “crumpling” instability for short-wavelength fluctuations, because (A.18) does not provide enough tension to straighten up the curve. The reason is because (A.17) is a physically-based discretization where we “sew” straight elastic strings between nodes, which though crude, provides real cohesion. But what physical model (A.18) represent, with its central difference look? Strings with detached ends? Clearly there exists modes which deform the nodes, such as $y_i = (-1)^i$, but which does not receives energy penalty from (A.18) at all, that is the cause of the “crumpling” instability.

The kinetic energy K is more complicated than V_e , which formally is

$$K = \int ds \cdot mv_n^2/2, \quad (\text{A.19})$$

where v_n is the normal, or “apparent” velocity of the dislocation. At the i th node, I approximate the normal vector \mathbf{n} as

$$\mathbf{n}_i \approx \frac{[(y_{i-1} - y_{i+1})/2, h]}{\sqrt{h^2 + (y_{i+1} - y_{i-1})^2/4}} = [-\frac{d_i}{s_i}, \frac{h}{s_i}], \quad (\text{A.20})$$

where I define

$$d_i \equiv \frac{y_{i+1} - y_{i-1}}{2}, \quad s_i \equiv \sqrt{h^2 + d_i^2}, \quad (\text{A.21})$$

thus

$$v_n(ih) = \mathbf{v}_i \cdot \mathbf{n}_i = (\dot{y}_i)(n_i^y) \approx (\dot{y}_i)(\frac{h}{s_i}). \quad (\text{A.22})$$

Also, let me approximate ds centered around node i to be

$$ds \approx s_i, \quad (\text{A.23})$$

so,

$$K \approx \sum_i m s_i (\frac{h}{s_i})^2 (\dot{y}_i)^2 / 2. \quad (\text{A.24})$$

How dare I use central difference here? I can fend off by mumbling: “energetics is zeroth-order, dynamics is first-order”, but it does not convince people. The actual reason is because it is quite difficult to make the effective mass go to zero in (A.24), but we can invent a mode in (A.18) to make things immediately go wrong ($dV_e \equiv 0$) without *any* initial resistance. With the correct (A.17) straightening out the curve, (A.24) is in fact a very good approximation. However, (A.24) is not *consistent* with the physical picture depicted by (A.17) of nodes linked by straight segments, whose kinetic energy *should be*

$$K = \sum_i \frac{m}{2} \frac{h^2 (\dot{y}_i/2 + \dot{y}_{i-1}/2)^2}{\sqrt{h^2 + (y_i - y_{i-1})^2}}. \quad (\text{A.25})$$

I am convinced that (A.25) would lead to a stable, and better scheme; but computationally it is a nightmare, which as I mentioned, is implicit and involves tridiagonal linear system and iterative relaxations. So I have to give it up and use (A.24) instead

– and let me note here that

$$\frac{\partial s_i}{\partial d_i} = \frac{d_i}{s_i}, \quad \frac{\partial s_{i-1}}{\partial y_i} = \frac{d_{i-1}}{2s_{i-1}}, \quad \frac{\partial s_{i+1}}{\partial y_i} = -\frac{d_{i+1}}{2s_{i+1}}, \quad (\text{A.26})$$

from (A.21).

So for an elastic curve with inertia, without dissipation, the equations of motion of “abacus” mesh points are

$$\frac{\partial}{\partial t} \left(\frac{\partial \mathcal{L}}{\partial \dot{y}_i} \right) = \frac{\partial \mathcal{L}}{\partial y_i}. \quad (\text{A.27})$$

Here

$$\frac{\partial \mathcal{L}}{\partial \dot{y}_i} = \frac{\partial \mathcal{K}}{\partial \dot{y}_i} = \frac{mh^2}{s_i} \dot{y}_i, \quad (\text{A.28})$$

and so

$$\frac{\partial}{\partial t} \left(\frac{\partial \mathcal{L}}{\partial \dot{y}_i} \right) = \frac{mh^2}{s_i} \ddot{y}_i - \frac{mh^2}{s_i^3} d_i \dot{y}_i. \quad (\text{A.29})$$

On the other hand,

$$\frac{\partial \mathcal{L}}{\partial y_i} = \frac{\partial K}{\partial y_i} - \frac{\partial V_e}{\partial y_i}, \quad (\text{A.30})$$

with

$$\frac{\partial K}{\partial y_i} = \frac{mh^2}{2} \left(\frac{\partial s_{i-1}^{-1}}{\partial y_i} (\dot{y}_{i-1})^2 + \frac{\partial s_{i+1}^{-1}}{\partial y_i} (\dot{y}_{i+1})^2 \right) = \frac{mh^2}{2} \left(\frac{d_{i+1}(\dot{y}_{i+1})^2}{2s_{i+1}^3} - \frac{d_{i-1}(\dot{y}_{i-1})^2}{2s_{i-1}^3} \right), \quad (\text{A.31})$$

and

$$\frac{\partial V_e}{\partial y_i} = \epsilon \left(\frac{y_i - y_{i-1}}{\sqrt{h^2 + (y_i - y_{i-1})^2}} + \frac{y_i - y_{i+1}}{\sqrt{h^2 + (y_i - y_{i+1})^2}} \right). \quad (\text{A.32})$$

What is the effect of external stress? Say y_i is increased by amount δy_i , then the area swept by the dislocation increases by $h\delta y_i$, so the external stress would have done work $\sigma b \cdot h\delta y_i$ – thus the RHS of (A.27) should include an external stress term $\sigma b h$.

What is the effect of phonon drag? Say that the line segment ds feels dragging force

$$d\mathbf{F} = -ds \cdot Bv_n \mathbf{n}, \quad (\text{A.33})$$

decomposed into the y -axis, that is

$$dF_y = -ds \cdot Bv_n n_y = -Bv_n h, \quad (\text{A.34})$$

thus, following (A.22), we should add a force term $-B(\dot{y}_i)(h/s_i)h$ to RHS of (A.27), which is very reasonable since, if the dislocation slope is large, $\partial y/\partial x \gg 1$, even if \dot{y}_i is quite big, there should not be a significant phonon drag.

So let me put all the pieces together and the equation now reads

$$\begin{aligned} \frac{mh^2}{s_i} \ddot{y}_i - \frac{mh^2}{s_i^3} d_i \dot{y}_i &= \frac{mh^2}{2} \left(\frac{d_{i+1}(\dot{y}_{i+1})^2}{2s_{i+1}^3} - \frac{d_{i-1}(\dot{y}_{i-1})^2}{2s_{i-1}^3} \right) + \\ \epsilon \left(\frac{y_{i-1} - y_i}{\sqrt{h^2 + (y_i - y_{i-1})^2}} + \frac{y_{i+1} - y_i}{\sqrt{h^2 + (y_i - y_{i+1})^2}} \right) &+ \sigma b h - B(\dot{y}_i) \left(\frac{h}{s_i} \right) h. \end{aligned} \quad (\text{A.35})$$

Dividing both sides by h^2/s_i , we have

$$\begin{aligned} m\ddot{y}_i - \frac{m}{s_i^2} d_i \dot{y}_i &= \frac{ms_i}{2} \left(\frac{d_{i+1}(\dot{y}_{i+1})^2}{2s_{i+1}^3} - \frac{d_{i-1}(\dot{y}_{i-1})^2}{2s_{i-1}^3} \right) + \\ \epsilon \frac{s_i}{h^2} \left(\frac{y_{i-1} - y_i}{\sqrt{h^2 + (y_i - y_{i-1})^2}} + \frac{y_{i+1} - y_i}{\sqrt{h^2 + (y_i - y_{i+1})^2}} \right) &+ \sigma b \cdot \frac{s_i}{h} - B\dot{y}_i. \end{aligned} \quad (\text{A.36})$$

Let me define

$$\sigma' b \equiv \sigma b \cdot \frac{s_i}{h} + \frac{ms_i}{2} \left(\frac{d_{i+1}(\dot{y}_{i+1})^2}{2s_{i+1}^3} - \frac{d_{i-1}(\dot{y}_{i-1})^2}{2s_{i-1}^3} \right), \quad (\text{A.37})$$

and

$$B' \equiv B - \frac{m}{s_i^2} d_i \dot{y}_i = B - \frac{md_i(\dot{y}_{i+1} - \dot{y}_{i-1})}{2s_i^2}, \quad (\text{A.38})$$

so now we have

$$m\ddot{y}_i = \epsilon \frac{s_i}{h^2} \left(\frac{y_{i-1} - y_i}{\sqrt{h^2 + (y_i - y_{i-1})^2}} + \frac{y_{i+1} - y_i}{\sqrt{h^2 + (y_i - y_{i+1})^2}} \right) + \sigma' b - B' \dot{y}_i, \quad (\text{A.39})$$

which, compared with (A.1), suggests a finite-difference scheme by just taking σ' as σ and B' as B in (A.9). Of course, σ' and B' are not constants here but depend on

i and t_n , and in evaluating (A.37), (A.38) we need to use $\dot{y}_{i\pm 1}(t_n)$ which, unless one enjoys doing full-blown Newton's iteration with lots of indices, can only be explicitly computed by forward difference approximation,

$$\dot{y}_{i\pm 1}(t_n) \approx \frac{y_{i\pm 1}^n - y_{i\pm 1}^{n-1}}{\Delta t} + \mathcal{O}(\Delta t), \quad (\text{A.40})$$

which ruin the second-order accuracy of (A.9) but match the first-order accuracy⁴ of (A.17). With cusps everywhere, self-interaction ignored and constant line energy model, this is probably as good as we deserve. (A.37)-(A.40), in combination with (A.9), and “arrest/free” rules (Orowan loop formation, simple breakaway, thermal activation), define the numerical scheme that I will use below to simulate precipitate-particle strengthening.

Before looking into the results, let me define a prototype system, which is Cu ($A=63.546$) strengthened by Co ($A=58.933$) or Fe ($A=55.845$) precipitate-particles of volume concentration $0.0001 - 0.05$ and $K/2\epsilon = 0.05 - 1$. The particles have size $5 - 50b$ and are coherent with the matrix, with size misfit on the order of 1%. At $T = 300\text{K}$, Cu has shear modulus $\mu = 48 \text{ GPa}$ and density $\rho = 8920 \text{ kg/m}^3$. ρ is taken to be independent of T , from which we infer that the Burger's vector $b = 2.56 \text{ \AA}$; but μ is in fact quite sensitive to the temperature. Using a rule of thumb that μ is reduced to half its $T = 0\text{K}$ value at the melting point (for Cu, $T_m = 1357.77\text{K}$), we assume that

$$\mu(T) = \mu(0) \left(1 - \frac{T}{2T_m}\right), \quad (\text{A.41})$$

with $\mu(0) = 54 \text{ GPa}$. The point is, our fundamental units ϵ and v_s depend on μ , and so they will depend on T . For numbers, at $T = 300\text{K}$, $\epsilon \approx 0.872 \text{ eV/\AA}$ and $v_s = 2187.8 \text{ m/s}$; and one reduced stress unit $= \mu(T)/2 \approx 24 \text{ GPa}$, etc.

The code is written in C. In order to visualize the simulation in real time I also programmed a threaded X Window 2D animator. Fig. A-3 shows an overall snapshot of the simulation with cell size $40960b \times 10240b$ ($10\mu\text{m} \times 2.4\mu\text{m}$). The precipitate-

⁴One may improve upon (A.17) though, by inferring curvature through interpolation, with special consideration to cusps.

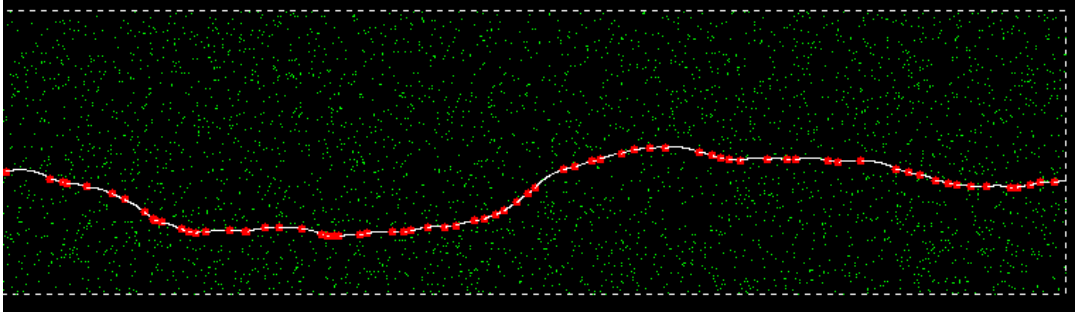


Figure A-3: Overall view of a simulation: dash rectangle shows the PBC cell; small green dots are the obstacles, which turns red/big if in contact with dislocation.

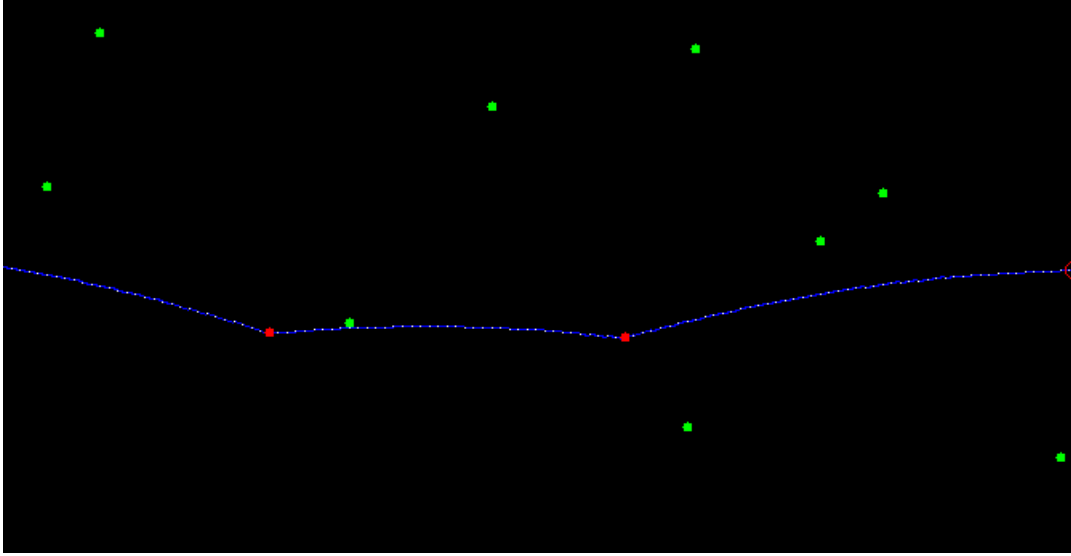


Figure A-4: Blowup of a tiny region: the white points are dislocation mesh points linked by blue lines to guide the eye. The green and red dots are obstacles.

particle size $a = 10b$, which is also the x -mesh size Δx , $c = 0.001$ and $K/2\epsilon = 0.2$. Fig. A-4 blows up a tiny region, where one can see the individual dislocation nodes.

To determine the critical flow stress σ_c^{sim} in my simulation, I calculate the dislocation average velocity $\langle v \rangle$ under different loading, and plot its ratio to the “full speed” $\sigma b/B$ – its speed if there were no obstacles. If the dislocation is hopelessly stuck during the simulation⁵, then $\langle v \rangle$ is taken to be 0. Fig. A-5 shows $\langle v \rangle / (\sigma b/B)$ at $T = 300K$, $a = 10b$, $c = 0.001$, $K/2\epsilon = 0.1$, versus external stress in $[\epsilon/b^2] = [\mu/2]$.

⁵As there is thermal activation, the dislocation will eventually be freed; but since E in (A.13) depends on loading, it takes very long; and soon after it is freed it will be trapped again. So the “stuck” behavior is quite easy to identify.

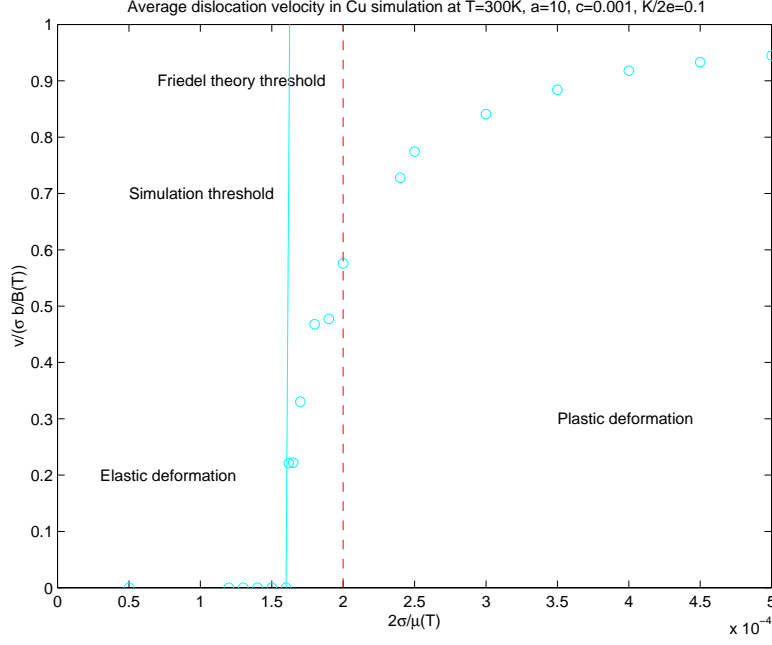


Figure A-5: Average dislocation velocity at $T = 300\text{K}$, $a = 10b$, $c = 0.001$, $K/2\epsilon = 0.1$.

We can clearly see a threshold behavior, with threshold stress $\sigma_c^{sim} \approx 0.8 \times 10^{-4}\mu$, which compares well with the theoretical threshold of $\sigma_c^{sim} = 1 \times 10^{-4}\mu$ of (A.3), predicted by Friedel. Fig. A-6 shows the behavior of λ , the average separation between nearest obstacles impeding the same dislocation, in comparison with the theoretical result (A.4). We see that again (A.4) is a highly accurate prediction; when λ/λ_c drops below 1, the dislocation loses its mobility.

Fig. A-7 verifies the $\sigma_c \propto (K/2\epsilon)^{3/2}$ scaling law for Cu at $T = 300\text{K}$ and $c = 0.001$. The agreement between theory and simulation is seen to be excellent. Fig. A-8 verifies the $\sigma_c \propto c^{1/2}$ scaling law for Cu at $T = 300\text{K}$ and $K/2\epsilon = 0.1$. The agreement is quite good for $c > 0.001$, but there seems to be a systematic deviation when c is very small. I attribute it to the inertia effect, since if the average separation between the obstacles is large, the dislocation can build up some momentum during its free flight to make the next jump easier. The Friedel theory is a static one, thus that effect is neglected. This deviation should be more pronounced at low T since $B \propto T$.

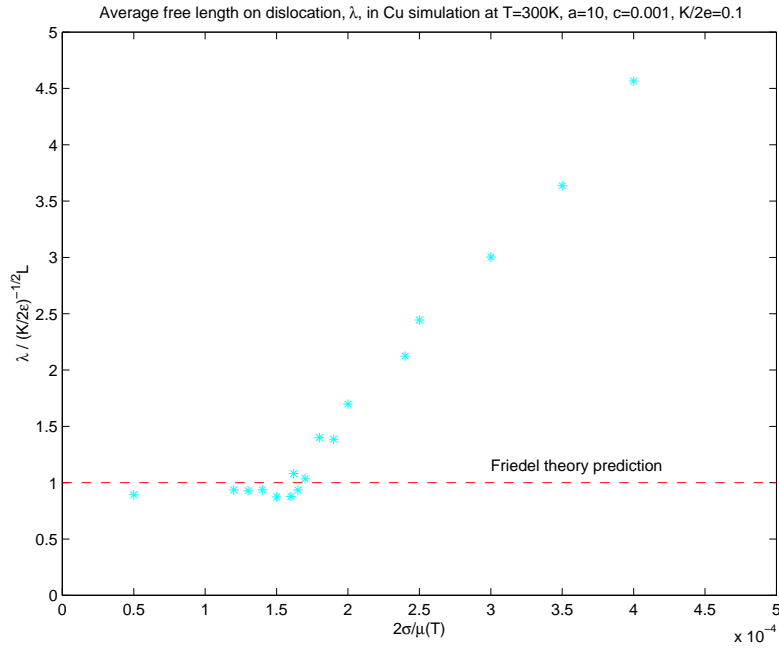


Figure A-6: Average separation of nearest obstacles impeding the dislocation λ , divided by theoretical threshold (A.4), λ_c .

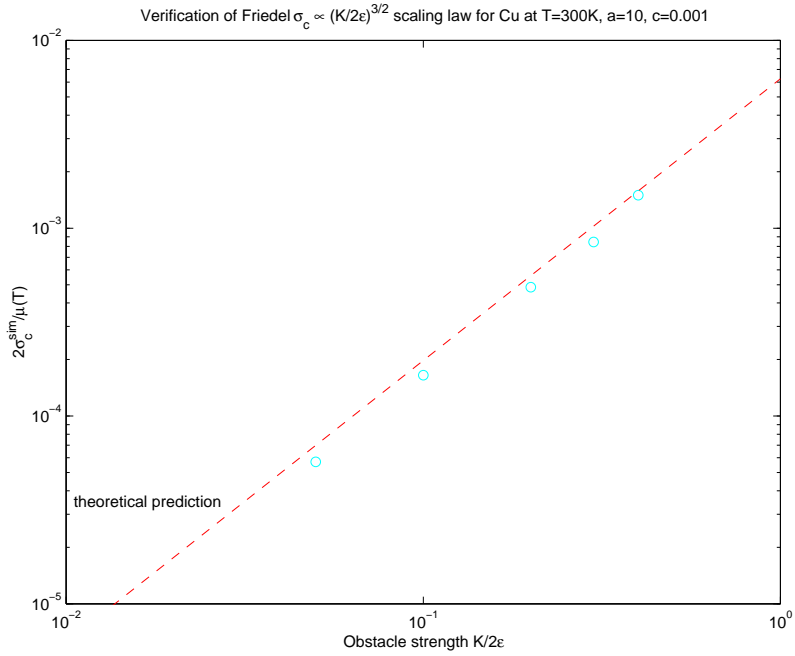


Figure A-7: Verification of the $\sigma_c \propto (K/2\epsilon)^{3/2}$ scaling law.

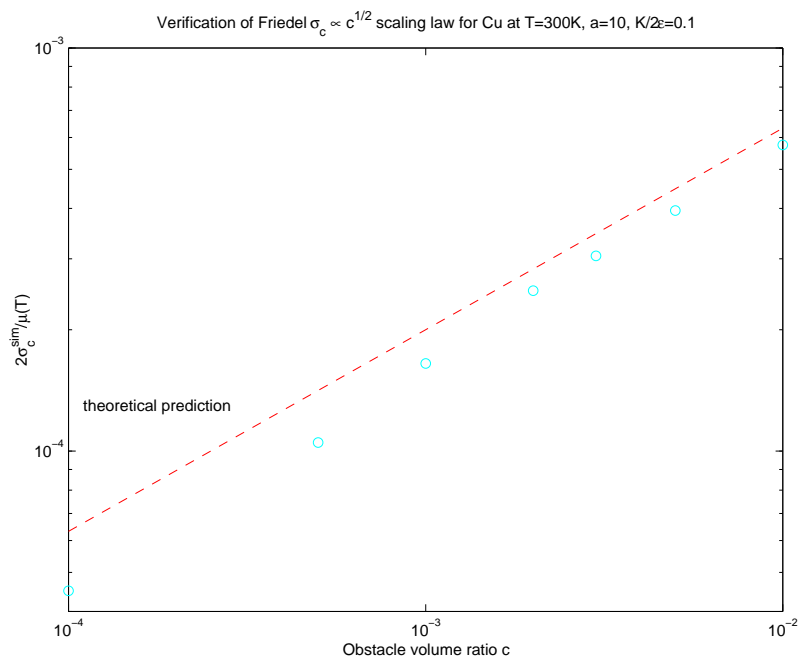


Figure A-8: Verification of the $\sigma_c \propto c^{1/2}$ scaling law.

Appendix B

Linear Response Theory of Transport

Following a review by Zwanzig [54], there are two kinds of transport coefficients: one kind, exemplified by electrical conductivity, corresponds to a real driving force - the electric field; the other kind, exemplified by thermal conductivity, corresponds to a thermodynamic driving force - the temperature gradient. The first driving force is easy to handle because it is a perturbation in the Hamiltonian, so it is amenable to straightforward quantum mechanical treatments, first shown by Kubo. The other is more difficult, and theoreticians had come up with as much as six different ways to derive the same results. The popular route is the so-called “indirect Kubo” method as summarized by Kadanoff and Martin [55]: the idea is that the overall form of macroscopic hydrodynamic equations, with empirical transport coefficients in them, can be derived purely by linearity and symmetry requirements, and is *independent* of the underlying microscopic physics. We can do a thought experiment¹, where one applies various fictitious test forces to atoms. Since the external force can now be expressed as a term in the Hamiltonian, one can investigate the system response due to this perturbation using the Kubo technique. On the other hand, such an external force adds an evident extra term in the hydrodynamic equations, and the system re-

¹Thought experiments are realizable on computers. In fact, there are several non-equilibrium MD algorithms to calculate the transport coefficients without using the Green-Kubo formula [64].

sponse will be parameterized by the transport coefficients, \mathbf{k} , ω , etc. Comparing the two responses which must agree asymptotically at small \mathbf{k} and ω , we arrive at microscopic expressions for the transport coefficients expressed in terms of time correlation functions of equilibrium fluctuations in a small sample.

An alternative is the following. Suppose we have an energy (temperature) wave of certain \mathbf{k} in a material under PBC – if one prepares the system at $t = 0$ and lets go, the wave amplitude will decay because the system wants to achieve maximum entropy. How *fast* it decays depends on material properties like the thermal conductivity κ , and \mathbf{k} – very often the time-dependence is *exponential*, with decay rate proportional to $|\mathbf{k}|^2$, as seen from the canonical heat conduction equation

$$c\dot{T} = \kappa \nabla^2 T. \quad (\text{B.1})$$

$T_{\mathbf{k}}$ in fact corresponds to an energy wave of the form

$$e_{\mathbf{k}} = \sum_i e_i e^{i\mathbf{k} \cdot \mathbf{r}_i}, \quad (\text{B.2})$$

based on some reasonable local division of the total energy, which is used here instead because $e_{\mathbf{k}}$ is a real operator. Thus, one uses

$$\dot{\bar{e}}_{\mathbf{k}} = -\bar{e}_{\mathbf{k}}/\tau_{\mathbf{k}}, \quad (\text{B.3})$$

to describe macroscopic transport, where $\bar{e}_{\mathbf{k}}$ is the coarse-grained energy density ², and $\tau_{\mathbf{k}}$ is macroscopic for \mathbf{k} 's that represent macroscopic gradients. Also, (B.3) is only valid for coarse-grained time because a finite system always has fluctuations.

In 1931, Onsager proposed a so-called “regression hypothesis”, which states that *equilibrium fluctuations*, which have very small amplitudes, obey the same rate law as (B.3), but only in the average sense. This average, denoted as $\langle \rangle_1$, in my understanding does not have to be unique, but for later derivations we select $\langle \rangle_1$ to be over

²In general, $\bar{A}_{\mathbf{k}}$ is unique in a certain context, but $A_{\mathbf{k}}$ may be not. As pointed out by [65], for a solid the $e^{i\mathbf{k} \cdot \mathbf{r}_i}$ factor in (B.2) can be replaced by $e^{i\mathbf{k} \cdot \mathbf{r}_i^0}$.

the sub-ensemble whose phase points satisfies $e_{\mathbf{k}}(0) = e_0$ at $t = 0$. Onsager proposed that

$$\langle \dot{e}_{\mathbf{k}}(t) \rangle_1 = -\langle e_{\mathbf{k}}(t) \rangle_1 / \tau_{\mathbf{k}}, \quad t > 0 \quad (\text{B.4})$$

just like (B.3), but with a provision: it is only correct for macroscopic t . That is out of necessity, because if (B.4) held true at $t = 0$ one would find that fluctuations are dying out. In fact, by a linearity argument³, there is

$$\langle \dot{e}_{\mathbf{k}}(t = 0) \rangle_1 \equiv 0, \quad (\text{B.5})$$

meaning that the long-term exponential decay is replaced by sort of Gaussian behavior at short t , even after sub-ensemble averaging, because the transport behavior is replaced by molecule free-flying behavior.

If equilibrium fluctuations on the average have the same relaxation law as their much larger, purposefully made cousins, then by studying how the fluctuations correlate we can learn about transport. Why does $e_{\mathbf{k}}$ operator, either due to equilibrium fluctuations or artificially prepared, behave this way? Let me make an analogy with human genetics: think $1/\tau_{\mathbf{k}}$ as the decay rate of inherited characteristics in a family. Since the number of genes in a person is fixed, the lost characteristics have to be replaced by something else which is mutation. The actual process of mutation is so complicated that it *appears* to be stochastic (think about “random numbers” on a computer). Let me be more specific: say certain animal on the average grows 50 blue hair among total of 100,000 black hair. Currently, some families grow more and some currently grow less. A microscopic period is something like one generation, where father with 70 bh may have a son that have 75 bh. A macroscopic period is like 10,000 years, during which the number of bh of a specific family must have gone through *lots* of changes. But, on average, in all families with 70 bh at year 0, the average bh at year 10,000 is still a steady 68, so bh is one of the slow “macroscopic” variables with $\tau_{\mathbf{k}} \sim 100,000$ years. However, aside from the expectation value of bh, there is

³Because e_0 is tiny, we can always expand $\langle \dot{e}_{\mathbf{k}}(t = 0) \rangle_1 = -\lambda \langle e_{\mathbf{k}}(t = 0) \rangle_1 + \dots$

practically *no* heritage that is left to the year 10,000 generation by the year 0 generation: the year 10,000 generation certainly would not be able to recall or deduce, for example, if the year 0 generation got a bh *increase* or not from father to son, because there are so many possibilities of ups and downs during the 10,000 years that makes inverse deduction impossible. This tells two things: 1) the correlation time of bh, a slow variable, is much longer than that of its actual time derivative, because a specific bh trajectory sustains high-frequency, “random” jolts, but the *average* of bh, due to underlying physics of the problem, decays slowly. 2) the fact that in macroscopic time it is bh that is important (persistent), not how it gets there, means that fluctuations have a Markoffian character and can be described by a Langevin-type equation.

Why is $e_{\mathbf{k}}$ a slow variable? Because there is the law of *conservation of energy* in the underlying microscopic dynamics, whose details are impossible to follow, so the conservation laws are the only rules of the game. Just put $\mathbf{k} = 0$ in (B.2), $e_{\mathbf{k}=0}$ is in fact conserved and thus never change. So $e_{\mathbf{k}}$ can be made very slow if we plug in a small \mathbf{k} . Such is also the case for the particle number, momentum and angular momentum.

Transport is the irreversible, macroscopic evolution of $e(\mathbf{r})$, $n(\mathbf{r})$, $\mathbf{p}(\mathbf{r})$. Because their integrals are conserved, and a single particle could not detect macroscopic gradients, the system is not in a hurry to zero them. So, the system is able to achieve a state of *local equilibrium* quickly given $e(\mathbf{r})$, $n(\mathbf{r})$, $\mathbf{p}(\mathbf{r})$, and then $e(\mathbf{r})$, $n(\mathbf{r})$, $\mathbf{p}(\mathbf{r})$ evolve at a more leisurely pace with everything else tracking them. This separation of time-scales is the basis of hydrodynamic equations⁴; the transport coefficients, though we do not know their values yet, must exist because $e(\mathbf{r})$, $n(\mathbf{r})$, $\mathbf{p}(\mathbf{r})$ are small, regular and slow. Also, $e(\mathbf{r})$, $n(\mathbf{r})$, $\mathbf{p}(\mathbf{r})$ can be used for labelling phase space volumes (non-equilibrium entropy) not immediately around the global equilibrium.

The statistical mechanics definition of the entropy of a system is how much phase

⁴For instance, the Navier-Stokes equation is the result of a perturbation expansion of the Boltzmann equation (Chapman-Enskog); the small parameter of the expansion is just the ratio of the two time-scales.

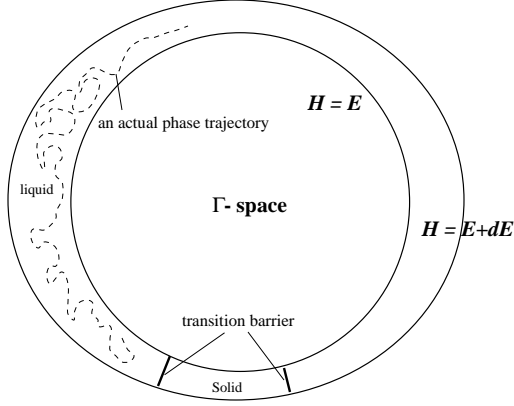


Figure B-1: Illustration of entropy increase.

volume is gained if one increases its energy from E to $E + dE$,

$$d\Gamma = e^{S/k} dE. \quad (\text{B.6})$$

Why does an isolated system tends to increase its entropy, so to speak? because there are phase space volumes that the system has the capacity to visit, but for some practical reasons hasn't visited yet. An example is a superheated solid which tends to melt to a liquid with the same E but hasn't yet. Why? because there are *transition barriers* to overcome, which, without nucleation sites (defects, surfaces), are so high that the *attainable* phase volume is separated into two isolated regions entirely: solid-like and liquid-like. Though theoretically one could add their volumes together to get the “total” entropy, practically if you are in the solid-like region, you are not able to transfer out; thus it makes sense to define a “solid entropy” that only includes the solid-like phase volume, which one calculates by phonon expansion at small T and perhaps more sophisticated methods at high T , but always assuming that the atoms do not drift away from their posts – which intrinsically they are able to do but hampered by the barrier. This is fine if the “solid entropy” (solid-like phase volume) is greater than the “liquid entropy” (liquid-like phase volume). But what happens if the reverse becomes true at large T ? The system becomes quite unhappy. Give it the chance, a nucleation site either by spontaneous fluctuation or externally created, a small valley is opened up in the barrier, and guess what – the

phase point would transit to the liquid-like region and never comes back again, since in the thermodynamic limit you either win big or lose big. A fish that transit from a pond to sea would not return to the pond by chance. This is just the law of increasing entropy for an isolated system.

Thus eventually a system will go to the largest patch of phase volume and *fluctuate* there, which is called *global equilibrium*. The global equilibrium of this universe is called *heat death*. Approaching global equilibrium by processes in subsystems is called *relaxation*, an *irreversible* process in the sense of the total entropy of this universe. Relaxation can be fast or slow; it can be controlled. An idealization of a very slow kind of relaxation is called “quasi-static” or “reversible” process⁵, by which things get done but the entropy of this universe practically does not increase. We can calculate the entropy of a subsystem by its definition (B.6), but that sometimes is infeasible; thus experimentally we *measure* the entropy, a potential function of its macroscopic state (which is N, E, V if it is homogeneous), by immersing it in a reservoir and quasi-statically changing it to another state through a reversible process, since the reservoir that the subsystem is in contact with loses entropy $dE/T, PdV/T, -\mu dN/T$, which by definition defines T, P, μ of the reservoir.

Clearly, if the subsystem is not isolated but is in contact with a reservoir, then we should not judge which direction the universe wants to go simply by seeing if the entropy of the subsystem (dS) would increase or not, because the entropy of the reservoir also changes as $dE/T, PdV/T, -\mu dN/T$. The reservoir and the subsystem in fact collude to increase the total entropy of the universe. It is not difficult to check that the total entropy of the universe increases as $-dF/T$ if the reservoir and the subsystem is able to exchange energy and particles, or $-dG/T$ if they are able to exchange energy and particles and volume. So the Helmholtz free energy $F = E - TS$ and the Gibbs free energy $G = E - TS + PV$ are the relevant potential for the two setups, which tend to decrease⁶. Note that although heat death hasn't been

⁵The reason that quasi-static process can exist, at least ideally, is that entropy generating rate may be quadratically dependent on the relaxation rate.

⁶An example is a fracture crack under constant loading: one can open and close the crack by δa *reversibly* if one puts a gadget in δa which stores some useful energy if δa were opened quasi-

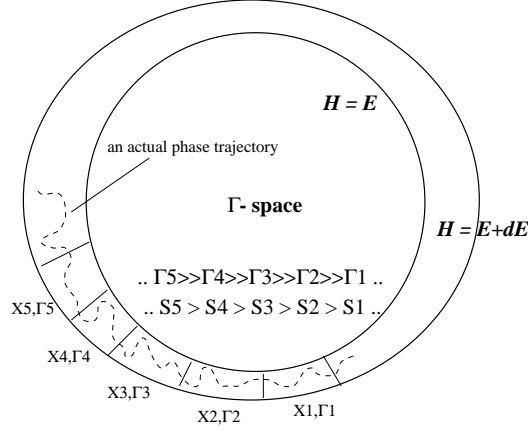


Figure B-2: Illustration of transport.

achieved yet, we do assume the subsystem to be in the state of local equilibrium so the phase volume it currently lives in can be labelled by a few macroscopic variables ($\Delta N, \Delta E, \Delta V$) or fields ($e(\mathbf{r}), n(\mathbf{r}), \mathbf{p}(\mathbf{r})$), instead of the full description; and that is OK because any other microstate relaxes to local equilibrium neighborhood in a matter of pico-seconds and they are “rare events” occupying insignificant phase volume anyway.

Thus, we now refine our definition of transport as the slow migration of a phase point from one local equilibrium neighborhood to another, as illustrated in Fig. B-2. The variables which we use to label the local equilibrium neighborhoods are called *gross variables*, X, Y etc., that are often $\mathbf{k} \neq 0$ components of conserved densities in continuous-space transport problems. For simplicity only X dependence is shown in Fig. B-2: X_1, X_2 etc. label the total phase space just like ‘solid’ and ‘liquid’ do in Fig. B-1, except that X is continuous. Also, let me use $X = Y = \dots = 0$ to label the global equilibrium. The phase volume is “by far” the largest there, so if the system *is* there, the total phase volume can be well-approximated by the volume of just that

statically. But in reality there is no gadget, there is nothing to contain this energy except inertia so it is turned into kinetic energy (or used to break up the material) which eventually becomes heat, and the reservoir blithely sucks that out. Using Hook’s law, one can show that of the W work done, only half can be absorbed into the strain energy when the transients stop; others are wasted. This example is what I call a *first-order* instability because finite free energy would be lost when δa is opened, which is used to judge if the system is stable ($f' < 0$). First-order instabilities are loading condition independent: the crack becomes unstable at the same state if constant displacement instead of constant traction condition is used. Another kind, second-order instability ($f' = 0, f'' < 0$), is loading condition dependent.

neighborhood, whereby the system is homogeneous and the equilibrium entropy S_E depends only on the total N, E, V . On the other hand, if the system is at a local, but not global, equilibrium, it is still possible to study S , the *non-equilibrium entropy*, which has *extra* dependencies on X, Y etc.; and S is crucial since the monotonic increase of neighborhood volume is *the* driving force of the gross variables' evolution. To quantify the above, we carve the total phase volume into

$$d\Gamma \equiv \frac{d\mathbf{p}^N d\mathbf{q}^N}{h^{3N}} \equiv \exp\left(\frac{S}{k_B}\right) \frac{dE}{g_E} \cdot \frac{dX}{g_X} \frac{dY}{g_Y} \dots \quad (\text{B.7})$$

where g_E, g_X etc. are the appropriate coarse-graining scales that are on the order of spontaneous fluctuations at global equilibrium (“neighborhood” size). Since we are interested not in the exact numerical value of $d\Gamma$ but its trend: with S on the order of J/K and $k = 1.380658 \times 10^{-23}$ J/K, the possible “exchange rates” of g_E, g_X etc. between different systems can be safely ignored. Thus one can show that S defined by (B.7) is actually consistent with the definition of equilibrium entropy S_E

$$d\Gamma \equiv \frac{d\mathbf{p}^N d\mathbf{q}^N}{h^{3N}} \equiv \exp\left(\frac{S_E}{k_B}\right) \frac{dE}{g_E}, \quad (\text{B.8})$$

and in this context, this is always

$$S_{total} = S_1 + S_2 \quad (\text{B.9})$$

for a weakly coupled system.

In a pedagogical example, two isolated systems 1 and 2 are connected by an unspecified weak link through which energy and particles can be exchanged. 1 and 2 have not reached homogeneity yet but are already homogeneous by themselves. The gross variables in this case are just $X = \Delta E$ and $Y = \Delta N$, where

$$E_1 \equiv E_1^G + \Delta E, \quad E_2 \equiv E_2^G - \Delta E; \quad N_1 \equiv N_1^G + \Delta N, \quad N_2 \equiv N_2^G - \Delta N, \quad (\text{B.10})$$

as the superscript G denote the values if global equilibrium is reached (but we are

not there yet). Then, the non-equilibrium entropy

$$S(X, Y | E = E_1^G + E_2^G, N = N_1^G + N_2^G) = S_1(E_1, N_1) + S_2(E_2, N_2), \quad (\text{B.11})$$

which at equilibrium: $X = Y = 0$,

$$S_E(E, N) = S(0, 0 | E, N), \quad (\text{B.12})$$

as S_E only depends on E and N instead of X, Y, E, N .

Now, one could see that

$$\delta S \equiv \frac{\partial S}{\partial X} \delta X + \frac{\partial S}{\partial Y} \delta Y = \left(\frac{1}{T_1} - \frac{1}{T_2} \right) \delta X + \left(-\frac{\mu_1}{T_1} + \frac{\mu_2}{T_2} \right) \delta Y. \quad (\text{B.13})$$

If one thinks S as a *potential*, then X and Y are the *displacements*, and

$$F_X \equiv \frac{\partial S}{\partial X} = \frac{1}{T_1} - \frac{1}{T_2}, \quad F_Y \equiv \frac{\partial S}{\partial Y} = -\frac{\mu_1}{T_1} + \frac{\mu_2}{T_2}, \quad (\text{B.14})$$

are the *forces*. Thus at global equilibrium there must be

$$F_X = F_Y = 0. \quad (\text{B.15})$$

This fixes the statics of the problem but not the dynamics. Can the dynamics be second-order like the Newton's equations? No, because the concept of “inertia” is absent here – look at the phase point trajectory in Fig. B-2: the frequent “jolts” there are enough to make a phase point forget where it was 100 ps ago. And if it cannot remember the past, inertia could not exist, and the overall trend of where the system is going is only dependent on the *current* position, a character of phase flow and first-order equations except that the number of variables is greatly reduced. Also, from day to day experience it is clear that transport does not have the oscillatory behavior that is a character of second-order equations. A fish that has swum from

pond to the sea is not going to swim back again⁷. Thus the dynamics is most probably first-order, as first proposed by Fourier, and indeed it is found to be such universally. With small X and Y , we are also entitled to do linear expansions: firstly in (B.14), and secondly in the dynamics, where quite generally we would have

$$\dot{X} \equiv L_{XX}F_X + L_{XY}F_Y, \quad \dot{Y} \equiv L_{YX}F_X + L_{YY}F_Y, \quad (\text{B.16})$$

and $L_{XX}, L_{XY}, L_{YX}, L_{YY}$ are called *transport coefficients* – equilibrium properties of the system. In general, for a system with n non-zero gross variables slightly deviated from global equilibrium, \mathbf{X} ,

$$F_i \equiv \frac{\partial S}{\partial X_i} \equiv - \sum_{j=1}^n S_{ij}X_j, \quad \dot{X}_i = \sum_{j=1}^n L_{ij}F_j. \quad (\text{B.17})$$

The Onsager regression hypothesis deals with a subtle point: if the gross variables \mathbf{X} are not only defined macroscopically but also have a real microscopic representation in terms of phase point coordination $(\mathbf{p}^N, \mathbf{q}^N)$, then we can study the time-evolution of \mathbf{X} 's fluctuations near the *global* equilibrium, which is not quite the same problem that the transport law (B.17) describes originally, since the \mathbf{X} there are artificially prepared and, though small, are macroscopically measurable. Here, the magnitude of \mathbf{X} is on the order of \sqrt{N} . Nevertheless, given a sub-ensemble at $t = 0$ *having* certain \mathbf{X}_0 in the global equilibrium neighborhood, how would the *average* of \mathbf{X} evolve? Conceivably, the bundle of \mathbf{X} will *diffuse*, and its average will *decay*, as the initial character of the sub-ensemble becomes more and more washed-out. It is quite possible that this “mini”-transport problem has the same rate law as the real transport problem, with the qualification that sufficient time (greater than the molecular correlation time) has elapsed since $t = 0$ that the sub-ensemble has achieved the same fluctuation spread in \mathbf{X} as the real transport problem⁸, which has a very small but non-zero mean.

⁷Well, not before the Poincaré recurrence time, that is. The Poincaré recurrence theorem serves no other purpose besides confusing people since the recurrence time is irrelevantly large - much larger than the heat death time of the universe.

⁸This is necessary from the view of Ito's calculus that is also used for modeling the stock market: if x is a Wiener's process $dx = \mu_x dt + \alpha \sigma_x \sqrt{dt}$ where α belongs to the standard normal distribution

If the above hypothesis is true, then as side-product of the derivations which we will do next, and by invoking time-inversion symmetry (essentially $\mathbf{p} \rightarrow -\mathbf{p}$ symmetry), Onsager proved his famous reciprocity theorem,

$$L_{ij} = L_{ji}, \quad i \neq j \quad (\text{B.18})$$

in the absence of magnetic field (which will interact with \mathbf{p} in the Hamiltonian). Thus \mathbf{L} is a symmetric matrix, and it must also be positive definite because the entropy generating rate \dot{S} , by (B.13) and (B.17), is

$$\dot{S} = \mathbf{f}^T \mathbf{L} \mathbf{f}. \quad (\text{B.19})$$

(B.17), (B.18) and (B.19) summarize the general laws of linear transport for systems not far from global equilibrium.

Returning to Onsager's hypothesis, if

$$\langle \dot{X}_i(t) \rangle_0 = \sum_{j=1}^n L_{ij} \langle F_j(t) \rangle_0 = - \sum_{j=1}^n L_{ij} \sum_{k=1}^n S_{jk} \langle X_k(t) \rangle_0 \quad \text{for } t \gg \tau_M \quad (\text{B.20})$$

where τ_M is the molecular correlation time (on the order of ps), and we pick a t such that

$$|(\mathbf{L}\mathbf{S})^{-1}| \gg t \gg \tau_M, \quad (\text{B.21})$$

which is always feasible since $|(\mathbf{L}\mathbf{S})^{-1}|$, like τ_k in (B.3), is macroscopic (on the order of seconds). We then multiply both sides by $X_l(0)$,

$$\langle \dot{X}_i(t) \rangle_0 X_l(0) = - \sum_{j=1}^n L_{ij} \sum_{k=1}^n S_{jk} \langle X_k(t) \rangle_0 X_l(0), \quad (\text{B.22})$$

and average over the distribution of initial $\mathbf{X}(0)$ generated from the the equilibrium

(operationally Wiener's process is defined by a random walk with the proper stepsize, bias, and frequency ν in the limit of $\nu dt \rightarrow \infty$ for a given time resolution dt), then locally $f(x)$ also follows a Wiener's process with $\sigma_f = f' \sigma_x$ and $\mu_f = f' \mu_x + f'' \sigma_x^2 / 2$, thus the *spread* of x does influence the *mean* rate of change of f .

ensemble,

$$\langle \langle \dot{X}_i(t) \rangle_0 X_l(0) \rangle_{\mathbf{X}(0)} = - \sum_{j=1}^n L_{ij} \sum_{k=1}^n S_{jk} \langle \langle X_k(t) \rangle_0 X_l(0) \rangle_{\mathbf{X}(0)}. \quad (\text{B.23})$$

Because $|(\mathbf{LS})^{-1}| \gg t$, the $\langle X_k(t) \rangle_0$ term on RHS is very close to $X_k(0)$ since $\langle X_k(0) \rangle_0 \equiv X_k(0)$, and $\langle \mathbf{X}(t) \rangle_0$ evolves with time constants that are macroscopic, so

$$\langle \langle X_k(t) \rangle_0 X_l(0) \rangle_{\mathbf{X}(0)} \approx \langle X_k(0) X_l(0) \rangle_{\mathbf{X}(0)}. \quad (\text{B.24})$$

As for the LHS, it is clear that for any properly defined sub-ensemble, there is

$$\langle \langle A(t) \rangle_0 B(0) \rangle_{B(0)} = \langle A(t) B(0) \rangle, \quad (\text{B.25})$$

where $\langle \rangle$ is the usual equilibrium ensemble average over $\mathbf{p}^N(0), \mathbf{q}^N(0)$,

$$\langle A(t) B(0) \rangle = \langle A(\mathbf{p}^N(t), \mathbf{q}^N(t) | \mathbf{p}^N(0), \mathbf{q}^N(0)) B(\mathbf{p}^N(0), \mathbf{q}^N(0)) \rangle. \quad (\text{B.26})$$

Thus (B.23) is transformed into

$$\langle \dot{X}_i(t) X_l(0) \rangle = \sum_{j=1}^n L_{ij} \sum_{k=1}^n S_{jk} \langle X_k(0) X_l(0) \rangle. \quad (\text{B.27})$$

However, since there is

$$d\Gamma \propto \exp\left(\frac{S}{k_B}\right) dE \cdot dX_1 dX_2 \dots dX_n,$$

for an isolated system by the definition (B.7), and because near equilibrium there is

$$S \approx S_E - \sum_{i=1}^n \sum_{j=1}^n S_{ij} X_i X_j / 2, \quad (\text{B.28})$$

by (B.17), the equilibrium fluctuations have amplitude

$$\langle X_k(0) X_l(0) \rangle = S_{kl}^{-1} k_B. \quad (\text{B.29})$$

And thus, RHS of (B.27) becomes

$$-\sum_{j=1}^n L_{ij} \sum_{k=1}^n S_{jk} S_{kl}^{-1} k_B = -\sum_{j=1}^n L_{ij} \delta_{jl} k_B = -k_B L_{il}. \quad (\text{B.30})$$

On the LHS, we notice that

$$\begin{aligned} \langle \dot{X}_i(t) X_l(0) \rangle &= \langle (\dot{X}_i(0) + \int_0^t d\tau \ddot{X}_i(\tau)) X_l(0) \rangle \\ &= \int_0^t d\tau \langle \ddot{X}_i(\tau) X_l(0) \rangle = - \int_0^t d\tau \langle \dot{X}_i(\tau) \dot{X}_l(0) \rangle, \end{aligned} \quad (\text{B.31})$$

where we use the lemma that in the presence of $\mathbf{p} \rightleftharpoons -\mathbf{p}$ symmetry,

$$\langle A(t) B(0) \rangle = \langle A(0) B(-t) \rangle = \langle A(0) B(t) \rangle \Rightarrow \langle \dot{A}(0) B(0) \rangle = \langle A(0) \dot{B}(0) \rangle, \quad (\text{B.32})$$

but because

$$0 = \left. \frac{d}{dt} \langle A(t) B(t) \rangle \right|_{t=0} = \langle \dot{A}(0) B(0) \rangle + \langle A(0) \dot{B}(0) \rangle, \quad (\text{B.33})$$

there must be

$$\langle \dot{A}(0) B(0) \rangle = 0. \quad (\text{B.34})$$

Combining (B.30) and (B.31), and by letting $t/\tau_M \rightarrow \infty$ while keeping $t \ll |(\mathbf{LS})^{-1}|$, we arrive at a general result

$$L_{ij} = \frac{1}{k_B} \int_0^\infty d\tau \langle \dot{X}_i(\tau) \dot{X}_j(0) \rangle, \quad (\text{B.35})$$

the Green-Kubo *fluctuation-dissipation theorem*. The assumptions of this derivation are

- The correlation time of a slow variable is much longer than the correlation time of its fluctuations⁹.

⁹This may sound paradoxical when the slow variables have the same amplitudes as fluctuations, and indeed are defined based on the fluctuations. But note that the *average* of a specific bundle of fluctuations is not a fluctuation.

- Onsager's hypothesis that linear transport holds at the smallest amplitudes.

And, based on the second assumption, Onsager proved his famous reciprocity theorem: $L_{ij} = L_{ji}$, which is plainly seen from (B.35). These are the core of present-day *non-equilibrium* statistical thermodynamics, which essentially is a perturbation theory about the global equilibrium. It seems to me in hindsight that a thorough understanding of the basic ideas behind equilibrium ensemble theory, starting from Gibbs and Boltzmann, leads naturally to these results.

Let me now return to the special case of thermal conduction, following prior discussions from (B.1) to (B.3). Due to the spatial homogeneity of the material on the large scale, only components with the same \mathbf{k} can couple to each other, so we can focus our attention on just one $e_{\mathbf{k}}$ describing a single sinusoidal internal energy wave in a periodic system. In many materials, stresses propagates much faster than the heat wave, so stresses will be fully relaxed inside the system and thus will be uniform. The non-equilibrium entropy, S , as in the simple pedagogical example, can be approximated by the sum of parts in local equilibrium, in this case an integral of specific entropy

$$S = \int d\mathbf{r} s(e(\mathbf{r}), v(\mathbf{r})), \quad (\text{B.36})$$

where $d\mathbf{r}$ runs over volume elements of a reference system in perfect equilibrium, and

$$e(\mathbf{r}) = e_0 + e_{\mathbf{k}} \cos(\mathbf{k} \cdot \mathbf{r}). \quad (\text{B.37})$$

Associated with $e(\mathbf{r})$ there is a change in the specific volume

$$v(\mathbf{r}) = v_0 + v_{\mathbf{k}} \cos(\mathbf{k} \cdot \mathbf{r}), \quad (\text{B.38})$$

which does not alter the total volume V of the periodic system. Without losing generality, we can assume that

$$v_{\mathbf{k}} = \alpha e_{\mathbf{k}} \quad (\text{B.39})$$

with parameter α to be optimized. We then expand (B.36) in terms of $e_{\mathbf{k}}$ and $v_{\mathbf{k}}$: it

is apparent that the first-order terms vanish after the integral and we are left with the second-order contributions,

$$S = S_E + \frac{V}{4} \left(s_{ee} e_{\mathbf{k}}^2 + 2s_{ev} e_{\mathbf{k}} v_{\mathbf{k}} + s_{vv} v_{\mathbf{k}}^2 \right), \quad (\text{B.40})$$

whose maximum is achieved by taking

$$\alpha = -\frac{s_{ev}}{s_{vv}}, \quad (\text{B.41})$$

and the maximal S (after relaxing the gross variable $v_{\mathbf{k}}$ instantaneously) is

$$S = S_E + \frac{V}{4} \cdot \frac{s_{ee}s_{vv} - s_{ev}^2}{s_{vv}} \cdot e_{\mathbf{k}}^2. \quad (\text{B.42})$$

The above seemingly complicated fraction, after being calculated in a homogeneous system, is simply (almost by definition)

$$S = S_E - \frac{V}{4} \frac{1}{c_P T^2} e_{\mathbf{k}}^2. \quad (\text{B.43})$$

And so, the thermodynamic driving force corresponding to $e_{\mathbf{k}}$ is

$$f_{\mathbf{k}} = -\frac{V}{2c_P T^2} e_{\mathbf{k}}, \quad (\text{B.44})$$

and the canonical transport equation is

$$\dot{e}_{\mathbf{k}} = L_{\mathbf{k}} f_{\mathbf{k}} = -L_{\mathbf{k}} \frac{V}{2c_P T^2} e_{\mathbf{k}}. \quad (\text{B.45})$$

Comparing with the empirical formula (B.1) and using (B.35), we see that

$$\kappa = \frac{V}{2|\mathbf{k}|^2 T^2} L_{\mathbf{k}} = \frac{V}{2|\mathbf{k}|^2 k_B T^2} \int_0^\infty d\tau \langle \dot{e}_{\mathbf{k}}(\tau) \dot{e}_{\mathbf{k}}(0) \rangle. \quad (\text{B.46})$$

Note that $e_{\mathbf{k}}$ defined by (B.37) differs from $e_{\mathbf{k}}$ defined in (B.2) in two ways: it is the coefficient of a cosine wave instead of $e^{i\mathbf{k}\cdot\mathbf{r}}$ wave, and it has been normalized

by volume. Thus, if we use the $e_{\mathbf{k}}$ of (B.2) which is more natural in dealing with particles¹⁰, the thermal conductivity would be

$$\kappa = \lim_{|\mathbf{k}| \rightarrow 0} \frac{1}{V k_B T^2 |\mathbf{k}|^2} \int_0^\infty d\tau \langle \dot{e}_{\mathbf{k}}(\tau) \dot{e}_{\mathbf{k}}^*(0) \rangle, \quad (\text{B.47})$$

where the $|\mathbf{k}| \rightarrow 0$ limit is taken in the scale of spatial correlation of molecular contributions to $\dot{e}_{\mathbf{k}}$.

Let us consider the \mathbf{k} -dependence more carefully, and focus on solid materials, so that

$$\dot{e}_{\mathbf{k}}(t) = \sum_{i=1}^N \dot{e}_i(t) \exp(i\mathbf{k} \cdot \mathbf{r}_i^0). \quad (\text{B.48})$$

In (B.48), $\dot{e}_i(t)$'s are spatially *correlated*. Why? because the energy is conserved – if one atom is losing energy, then its neighbors are gaining the equal amount. That energy will in turn spread and influence further-away atoms at some later time, so there is also temporal correlation. However, the correlation does *not* persist forever, spatially or temporally, since the original energy packet interact with other atoms' packets in complicated fashions and eventually gets *scattered*. Imagine that you receive a package from a stranger! It will almost look *stochastic* to you, and if you keep receiving such packages it will influence your ability to discern packages that were originally meant for you, and your ability to pass on packages. In phonon physics, the temporal correlation is characterized by the phonon mean free time τ_p and the spatial correlation is characterized by the phonon mean free path $l_p \sim |\mathbf{v}_G| \tau_p$, where \mathbf{v}_G is the phonon group velocity. Beyond τ_p and l_p the correlation decays exponentially, so τ_p and l_p are the maximal extent of *indirect* correlation¹¹.

Now, as engineers are interested in \mathbf{k} 's that satisfy $|\mathbf{k}| l_p \ll 1$, we can do the

¹⁰We see that for a solid, because (B.36) is defined in such a manner (Eulerian instead of Lagrangian description), it is more natural (and simpler) to define $e_{\mathbf{k}} \equiv \sum_i e_i \exp(i\mathbf{k} \cdot \mathbf{r}_i^0)$, first pointed out by W. Hoover.

¹¹Direct *interaction*, on the other hand, reaches no further than a few atomic spacing, which temporally corresponds to ν_D^{-1} where ν_D is the Debye frequency.

following:

$$\begin{aligned}
& \langle \dot{e}_{\mathbf{k}}(\tau) \dot{e}_{\mathbf{k}}^*(0) \rangle \\
= & \sum_{i=1}^N \sum_{j=1}^N \langle \dot{e}_i(\tau) \dot{e}_j(0) \rangle \exp(i\mathbf{k} \cdot \mathbf{r}_{ij}^0) \\
\approx & \sum_{i=1}^N \sum_{j=1}^N \langle \dot{e}_i(\tau) \dot{e}_j(0) \rangle (1 + i\mathbf{k} \cdot \mathbf{r}_{ij}^0 - |\mathbf{k} \cdot \mathbf{r}_{ij}^0|^2/2 + \dots), \tag{B.49}
\end{aligned}$$

as $\langle \dot{e}_i(\tau) \dot{e}_j(0) \rangle$ already vanishes when the $\exp(i\mathbf{k} \cdot \mathbf{r}_{ij}^0)$ expansion goes bad. Here \mathbf{r}_{ij}^0 is defined as

$$\mathbf{r}_{ij}^0 \equiv (\mathbf{r}_i^0 - \mathbf{r}_j^0) \bmod L, \quad V \equiv L^3, \tag{B.50}$$

i.e., \mathbf{r}_{ij}^0 is the *real* separation between atom i and j instead of the literal subtraction, that should always be much shorter than L – the system size. The two definitions are equivalent for $e^{i\mathbf{k} \cdot \mathbf{r}_{ij}^0}$, but only (B.50) can be used in its expansion since it requires $\mathbf{k} \cdot \mathbf{r}_{ij}^0 \ll 1$. Thus in (B.49), the zeroth order term does not contribute because

$$\sum_{i=1}^N \dot{e}_i(t) \equiv 0 \tag{B.51}$$

for this splendidly isolated system. The first order terms also does not contribute anything in a $\mathbf{p} \rightleftharpoons -\mathbf{p}$ system because

$$\langle \dot{e}_i(\tau) \dot{e}_j(0) \rangle = \langle \dot{e}_i(0) \dot{e}_j(-\tau) \rangle = \langle \dot{e}_i(0) \dot{e}_j(\tau) \rangle \tag{B.52}$$

is symmetric in $i \rightleftharpoons j$ but \mathbf{r}_{ij}^0 is anti-symmetric. This leaves us with the second-order terms; all ensuing orders give no contribution in the limit of $\mathbf{k}l_p \rightarrow 0$. For an isotropic system (in the sense of 3×3 tensor), we will have

$$\langle \dot{e}_{\mathbf{k}}(\tau) \dot{e}_{\mathbf{k}}^*(0) \rangle = -|\mathbf{k}|^2 \sum_{i=1}^N \sum_{j=1}^N \langle \dot{e}_i(\tau) \dot{e}_j(0) \rangle |\mathbf{r}_{ij}^0|^2/6. \tag{B.53}$$

So following (B.46) and (B.53), we arrive at

$$\kappa = \frac{-1}{6Vk_{\text{B}}T^2} \int_0^\infty d\tau \langle \sum_{i=1}^N \sum_{j=1}^N \dot{e}_i(\tau) \dot{e}_j(0) |\mathbf{r}_{ij}^0|^2 \rangle. \quad (\text{B.54})$$

What makes $\dot{e}_i(t) \neq 0$? Clearly, if the atoms do not interact, then e_i will be the particle's kinetic energy and $\dot{e}_i \equiv 0$. Thus, without losing generality, one could assume that

$$\dot{e}_i \equiv \sum_p \dot{e}_{ip}, \quad (\text{B.55})$$

where p counts *interactions*, for instance a certain pair interaction between i and k , a triplet interaction between ikk' , etc. An interaction modifies the kinetic energies of constituent atoms and their share of its potential energy, but a sum rule

$$\sum_i \dot{e}_{ip} \equiv 0 \quad (\text{B.56})$$

always holds for a specific p , which can be named *micro-conservation of energy*¹². One can also assign a geometrical location \mathbf{r}_p^0 to p , the details of which are not important except that \mathbf{r}_p^0 is close to its constituent atoms, and so atoms i and j in (B.54). Thus

$$\begin{aligned} & \sum_{i=1}^N \sum_{j=1}^N \dot{e}_i(\tau) \dot{e}_j(0) |\mathbf{r}_{ij}^0|^2 \\ = & \sum_{i=1}^N \sum_{j=1}^N \sum_p \dot{e}_i(\tau) \dot{e}_{jp}(0) |\mathbf{r}_{ip}^0 - \mathbf{r}_{jp}^0|^2 \\ = & \sum_{i=1}^N \sum_{j=1}^N \sum_p \dot{e}_i(\tau) \dot{e}_{jp}(0) (|\mathbf{r}_{ip}^0|^2 - 2\mathbf{r}_{ip}^0 \cdot \mathbf{r}_{jp}^0 + |\mathbf{r}_{jp}^0|^2) \\ = & \sum_{i=1}^N \sum_{j=1}^N \sum_p -2\dot{e}_i(\tau) \mathbf{r}_{ip}^0 \cdot \dot{e}_{jp}(0) \mathbf{r}_{jp}^0 \\ = & \sum_{i=1}^N \sum_{p'} \sum_{j=1}^N \sum_p -2\dot{e}_{ip'}(\tau) \mathbf{r}_{ip'}^0 \cdot \dot{e}_{jp}(0) \mathbf{r}_{jp}^0. \end{aligned} \quad (\text{B.57})$$

¹²One can always do a cluster expansion of the total potential energy surface $V = \sum_p V_p$. Since $\dot{e}_i = \mathbf{v}_i \cdot \mathbf{F}_i + \sum_{j=1}^N \mathbf{v}_j \cdot \partial V_i / \partial \mathbf{r}_j$, and both \mathbf{F}_i and V_i are some linear combination of p 's, $\dot{e}_i \equiv \sum_p \dot{e}_{ip}$. It is also easy to verify that a specific p gives zero contribution to $\sum_{i=1}^N \dot{e}_i$.

where we used (B.56) and (B.51). \mathbf{r}_{ip}^0 and \mathbf{r}_{jp}^0 are defined same as \mathbf{r}_{ij}^0 in (B.50), which for \mathbf{r}_p^0 near atoms i and j , satisfy the decomposition

$$\mathbf{r}_{ij}^0 = \mathbf{r}_{ip}^0 - \mathbf{r}_{jp}^0. \quad (\text{B.58})$$

And so by virtue of (B.54) and (B.57), we finally arrived at

$$\kappa = \frac{1}{3Vk_{\text{B}}T^2} \int_0^\infty d\tau \langle \sum_{i=1}^N \sum_{p'} \dot{e}_{ip'}(\tau) \mathbf{r}_{ip'}^0 \cdot \sum_{j=1}^N \sum_p \dot{e}_{jp}(0) \mathbf{r}_{jp}^0 \rangle, \quad (\text{B.59})$$

whereby if one defines the system total heat current \mathbf{J} as

$$\mathbf{J}(t) \equiv \sum_{i=1}^N \sum_p \dot{e}_{ip}(t) \mathbf{r}_{ip}^0, \quad (\text{B.60})$$

the well-known result is recovered. The point of using p in defining (B.60) is to remove the ambiguities in using periodic coordinates, a concern that disappears when one uses local origins of *interactions* instead of a single fixed origin. The reader should check that procedures from (B.47) to (B.59) are mathematically rigorous, but relying on physical assumptions of

- The system is macroscopic and isolated: $\sum_{i=1}^N \dot{e}_i(t) \equiv 0$.
- $L \sim |\mathbf{k}|^{-1} \gg l_p$.
- Linear partition of interatomic potential to local interactions.

The above derivation is theoretically in good standing for the imagined isolated macroscopic system in periodic boundary conditions. However it is not a viable MD scheme by itself because MD cannot reach the macroscopic lengthscale, and indeed is quite difficult to reach the l_p scale ($\sim 100 \text{ \AA}$ to $1 \text{ }\mu\text{m}$) of perfect crystals. One could not have derived (B.59) *starting from* such a tiny system. Instead, the hope is to directly relate to (B.59), study the size dependence of $\langle \mathbf{J}(\tau) \cdot \mathbf{J}(0) \rangle$ MD results, and hopefully demonstrate the *possibility* that that it has reached a plateau of some sort in size-dependence even at this tiny scale, and then extrapolate to infinity. If it

is a perfect crystal at low temperature, perhaps there is a systematic way to estimate the error of evaluating (B.59) in a small \mathbf{k} -mesh system by studying the phonon Boltzmann equation. But this size-dependence business is far from over.

Appendix C

N -body Microscopic Heat Current Expression

Suppose the Hamiltonian of a collection of particles is written as

$$\mathcal{H} = \sum_i K_i + \sum_{i < j} V_2(\mathbf{r}_i, \mathbf{r}_j) + \sum_{i < j < k} V_3(\mathbf{r}_i, \mathbf{r}_j, \mathbf{r}_k) + \dots + \sum_{i_1 < i_2 < \dots < i_n} V_n(\mathbf{r}_{i_1}, \mathbf{r}_{i_2}, \dots, \mathbf{r}_{i_n}) + \dots, \quad (\text{C.1})$$

where K_i is the kinetic energy of each particle:

$$K_i = \frac{1}{2} m_i |\mathbf{v}_i|^2, \quad (\text{C.2})$$

and the n -body potential $V_n(\mathbf{r}_{i_1}, \mathbf{r}_{i_2}, \dots, \mathbf{r}_{i_n})$ is invariant with respect to any permutation of particles,

$$\mathbf{r}_{i_\alpha} \rightleftharpoons \mathbf{r}_{i_\beta}, \quad 1 \leq \alpha, \beta \leq n, \quad (\text{C.3})$$

i.e., the functional form puts no extra emphasis on any specific particle, then the division of \mathcal{H}

$$\mathcal{H} = \sum_i E_i \quad (\text{C.4})$$

into “single particle energies” E_i is intuitively clear:

$$E_i = K_i + \sum_{pairs} V_2(\mathbf{r}_i, \mathbf{r}_j)/2 + \sum_{triplets} V_3(\mathbf{r}_i, \mathbf{r}_j, \mathbf{r}_k)/3 + .. + \sum_{n-lets} V_n(\mathbf{r}_i, \mathbf{r}_{i_2}, .., \mathbf{r}_{i_n})/n + .. \quad (C.5)$$

where “pairs”, “triplets” etc. refer to all interactions that this i th particle participates in, and it is reasonable to say that it “owns” $1/n$ of all the V_n interactions that it took parts in.

The net heat current of the system, \mathbf{J} , is defined as

$$\begin{aligned} \mathbf{J} &= \frac{d}{dt} \left(\sum_i E_i \mathbf{r}_i \right) \\ &= \sum_i E_i \mathbf{v}_i + \dot{E}_i \mathbf{r}_i \\ &= \sum_i E_i \mathbf{v}_i + \tilde{\mathbf{J}}. \end{aligned} \quad (C.6)$$

It is easy to show that $\tilde{\mathbf{J}}$ is *linearly superpositionable*, in the sense that the influence of any n -let interaction (via V_n) *directly adds* onto $\tilde{\mathbf{J}}$,

$$\tilde{\mathbf{J}} = \sum_{i < j} \tilde{\mathbf{J}}_{ij}^2 + \sum_{i < j < k} \tilde{\mathbf{J}}_{ijk}^3 + .. + \sum_{i_1 < i_2 < .. < i_n} \tilde{\mathbf{J}}_{i_1 i_2 .. i_n}^n + .. \quad (C.7)$$

which is true even if V_n does not have permutation symmetry. One underlying reason is that

$$\dot{K}_i = \mathbf{F}_i \cdot \mathbf{v}_i, \quad (C.8)$$

but \mathbf{F}_i is the linear sum of all interactions,

$$\mathbf{F}_i = \sum_{pairs} \mathbf{F}_{ij}^i + \sum_{triplets} \mathbf{F}_{ijk}^i + .. + \sum_{n-lets} \mathbf{F}_{i i_2 i_3 .. i_n}^i + .. \quad (C.9)$$

in which, for instance, \mathbf{F}_{ijk}^i is the force contribution of any ijk -triplet interaction to particle i .

So now we can focus on a specific n -let interaction, and simply add everything together in the end onto $\tilde{\mathbf{J}}$. Let me denote the particles involved $\mathbf{r}_1, \mathbf{r}_2, .., \mathbf{r}_n$, and

the part that this n -let interaction contributes to by Δ . Because of Eqn. (C.5), $\Delta\dot{E}_i$ contains two parts: a kinetic energy part and a potential energy part. With $\Delta\dot{K}_i = \Delta\mathbf{F}_i \cdot \mathbf{v}_i$ and

$$\Delta V = \Delta V(\mathbf{r}_1, \mathbf{r}_2, \dots, \mathbf{r}_n), \quad (\text{C.10})$$

there is

$$\begin{aligned} \Delta \left(\frac{\dot{V}}{n} \right) &= \frac{1}{n} \sum_{j=1}^n \frac{\partial \Delta V}{\partial \mathbf{r}_j} \cdot \mathbf{v}_j \\ &= -\frac{1}{n} \sum_{j=1}^n \Delta \mathbf{F}_j \cdot \mathbf{v}_j, \end{aligned} \quad (\text{C.11})$$

as by definition,

$$\Delta \mathbf{F}_j = -\frac{\partial \Delta V}{\partial \mathbf{r}_j}. \quad (\text{C.12})$$

So, there is

$$\begin{aligned} \Delta \tilde{\mathbf{J}} &= \sum_{i=1}^n (\Delta \dot{E}_i) \mathbf{r}_i \\ &= \sum_{i=1}^n \left(\Delta \mathbf{F}_i \cdot \mathbf{v}_i - \frac{1}{n} \sum_{j=1}^n \mathbf{F}_j \cdot \mathbf{v}_j \right) \mathbf{r}_i. \end{aligned} \quad (\text{C.13})$$

One can see from Eqn. (C.13) that $\Delta \tilde{\mathbf{J}}$ depends only on the relative separations of $\mathbf{r}_1, \mathbf{r}_2, \dots, \mathbf{r}_n$ and not on the origin of the coordinate frame, i.e., it is *frame-independent*, because for any uniform shift: $\mathbf{r}_i \rightarrow \mathbf{r}_i + \mathbf{a}$, where \mathbf{a} is a constant,

$$\begin{aligned} \Delta(\Delta \tilde{\mathbf{J}}) &= \sum_{i=1}^n \left(\Delta \mathbf{F}_i \cdot \mathbf{v}_i - \frac{1}{n} \sum_{j=1}^n \mathbf{F}_j \cdot \mathbf{v}_j \right) \mathbf{a} \\ &= \left(\sum_{i=1}^n \Delta \mathbf{F}_i \cdot \mathbf{v}_i - \frac{1}{n} \sum_{i=1}^n \sum_{j=1}^n \Delta \mathbf{F}_j \cdot \mathbf{v}_j \right) \mathbf{a} \\ &= 0. \end{aligned} \quad (\text{C.14})$$

Thus, in evaluating Eqn. (C.13), we are free to pick any coordinate origin that we like.

One further simplification is

$$\sum_{i=1}^n (\Delta \mathbf{F}_i) = 0, \quad (\text{C.15})$$

which can be derived from the translational invariance of V_n .

Two-body interaction

For any particle pair (i, j) that falls into the interaction range,

$$\Delta V = V_2(\mathbf{r}_i, \mathbf{r}_j), \quad (\text{C.16})$$

and there is

$$\Delta \mathbf{F}_i = -\Delta \mathbf{F}_j. \quad (\text{C.17})$$

Because I am free to choose any coordinate frame origin, I can let $\mathbf{r}_i = 0$, and so only one term in Eqn. (C.13) (the $n = j$ term) contributes,

$$\begin{aligned} \Delta \tilde{\mathbf{J}}_2 &= \left(\Delta \mathbf{F}_j \cdot \mathbf{v}_j - \frac{1}{2} (\Delta \mathbf{F}_i \cdot \mathbf{v}_i + \Delta \mathbf{F}_j \cdot \mathbf{v}_j) \right) \mathbf{r}_j \\ &= \frac{1}{2} (\Delta \mathbf{F}_j \cdot (\mathbf{v}_j + \mathbf{v}_i)) \mathbf{r}_j, \end{aligned} \quad (\text{C.18})$$

where we have made use of Eqn. (C.17). If one remembers that the present frame origin is on particle i , the expression must be

$$\Delta \tilde{\mathbf{J}} = \frac{1}{2} (\Delta \mathbf{F}_j \cdot (\mathbf{v}_j + \mathbf{v}_i)) (\mathbf{r}_j - \mathbf{r}_i) \quad (\text{C.19})$$

in other frames.

Three-body interaction

Now,

$$\Delta V = V_3(\mathbf{r}_i, \mathbf{r}_j, \mathbf{r}_k), \quad (\text{C.20})$$

and

$$\Delta \mathbf{F}_i = -\Delta \mathbf{F}_j - \Delta \mathbf{F}_k. \quad (\text{C.21})$$

I still can choose $\mathbf{r}_i = 0$, then

$$\begin{aligned} \Delta \tilde{\mathbf{J}}_3 &= \left(\Delta \mathbf{F}_j \cdot \mathbf{v}_j - \frac{1}{3}(\Delta \mathbf{F}_i \cdot \mathbf{v}_i + \Delta \mathbf{F}_j \cdot \mathbf{v}_j + \Delta \mathbf{F}_k \cdot \mathbf{v}_k) \right) \mathbf{r}_{ji} + \\ &\quad \left(\Delta \mathbf{F}_k \cdot \mathbf{v}_k - \frac{1}{3}(\Delta \mathbf{F}_i \cdot \mathbf{v}_i + \Delta \mathbf{F}_j \cdot \mathbf{v}_j + \Delta \mathbf{F}_k \cdot \mathbf{v}_k) \right) \mathbf{r}_{ki} \\ &= \frac{1}{3} \{ \quad (\Delta \mathbf{F}_j \cdot (2\mathbf{v}_j + \mathbf{v}_i) + \Delta \mathbf{F}_k \cdot (\mathbf{v}_i - \mathbf{v}_k)) \mathbf{r}_{ji} + \\ &\quad (\Delta \mathbf{F}_k \cdot (2\mathbf{v}_k + \mathbf{v}_i) + \Delta \mathbf{F}_j \cdot (\mathbf{v}_i - \mathbf{v}_j)) \mathbf{r}_{ki} \quad \}, \end{aligned} \quad (\text{C.22})$$

where

$$\mathbf{r}_{ji} = \mathbf{r}_j - \mathbf{r}_i, \quad \mathbf{r}_{ki} = \mathbf{r}_k - \mathbf{r}_i. \quad (\text{C.23})$$

Appendix D

Lattice Thermal Conductivity

The thermal conductivity of solids usually consists of two parts: those due to electrons and those due to the lattice. For insulators and semiconductors, the main contribution comes from lattice conduction, and the heat influx

$$\mathbf{J}^q = -\hat{\kappa}\nabla T \tag{D.1}$$

where we had assumed a spatially varying local temperature to be properly defined. κ is generally a 3×3 tensor, but for crystals with point symmetry higher than T_d , it's a scalar.

If a crystal is purely harmonic, κ should be $+\infty$: that's because a purely harmonic crystal cannot support local temperature variance, since all our normal coordinates in the Hamiltonian are of global character. If we heat up the atoms in part of the crystal and let it go, it will automatically do a normal coordinate analysis and the crystal will be homogeneously vibrating in no time, each normal coordinate independent of other. Thus, for a solid to have finite thermal conductivity/resistivity, there must be anharmonicity of some sort: either it's the higher-order term in the expansion, or defects. The exact solution of these problems are extremely difficult, so usually we treat the crystal as nearly harmonic and do perturbation theories on phonons states.

Another important concept is that of lattice wave packet. When the lattice is under a heat gradient, it can't be described by a single stationary state $|n_{k_1}, n_{k_2}, \dots, n_{k_{3rN}}\rangle$,

but should be the linear combination of many such states with time-dependent coefficients, to form a wave packet, localized in some spatial region. It's well known in wave mechanics that such packets will travel in the speed of group velocity,

$$\mathbf{v}_G = \frac{\partial w_j(\mathbf{q})}{\partial \mathbf{q}} \quad (\text{D.2})$$

and so is the energy it carries. Thus, the heat current is

$$\Omega \mathbf{J}^q = \sum_k n_k \hbar \omega_k \mathbf{v}_G \quad (\text{D.3})$$

This picture might work best for lattices with some anharmonicity or defects, so that the packet would be deflected to form a new one before it's too much widely spread. However when the anharmonicity is too much the formula will also break down.

D.1 Phonon Boltzmann Equation

There is Boltzmann's equation:

$$\frac{\partial f(k, r)}{\partial t} + \nabla_r \cdot (f(k, r) \mathbf{v}_G(k)) + \text{collision integral} = 0 \quad (\text{D.4})$$

where $f(k, r)$ is the local density distribution of phonon states. The 2nd term is due to the drift of phonons in varying spatial density, the collision integral comes from local transitions between different phonon states, which is the combination of a variety of phonon-defect, phonon-phonon scattering mechanisms.

For a steady state,

$$\frac{\partial f(k, r)}{\partial t} = 0 \quad (\text{D.5})$$

and

$$\nabla_r \cdot (f(k, r) \mathbf{v}_G(k)) = \frac{\partial f(k, r)}{\partial T} \mathbf{v}_G(k) \cdot \nabla_r T \quad (\text{D.6})$$

The exact solution of Eq(D.4) is fairly difficult, so people use variational methods to get approximate solutions. [57] Here it suffices to sketch the basics of the problem.

It is convenient to cast Eq(D.4) into a canonical form. Define

$$f(k) = f_0(k) - \Phi_k \frac{\partial f_0(k)}{\partial E_k} \quad (\text{D.7})$$

Since phonons are Boson with zero chemical potential, in thermal equilibrium there is

$$f_0(k, r) = \frac{1}{\exp(\beta E_k) - 1} \quad (\text{D.8})$$

and so

$$\frac{\partial f_0(k)}{\partial E_k} = -\frac{f_0(k)(1 + f_0(k))}{k_B T} \quad (\text{D.9})$$

Take elastic phonon-defect scattering for example. Here a phonon state k could be scattered into another state k' of the same energy by the defect, with positive transition rate $\mathcal{L}(k, k')$. From the principle of microscopic reversibility, and by verification, there should be

$$\mathcal{L}(k, k') = \mathcal{L}(k', k) \quad (\text{D.10})$$

Then obviously, for a steady state,

$$\begin{aligned} \frac{\partial f(k, r)}{\partial T} \mathbf{v}_G(k) \cdot \nabla_r T &= \text{--collision integral} \\ &= -\int (f(k) - f(k')) \mathcal{L}(k, k') dk' \\ &= -\frac{1}{k_B T} \int (\Phi_k - \Phi_{k'}) f_0(k)(1 + f_0(k)) \mathcal{L}(k, k') dk' \\ &= \frac{1}{k_B T} \int (\Phi_{k'} - \Phi_k) \mathcal{P}(k, k') dk' \end{aligned} \quad (\text{D.11})$$

where we have defined

$$\mathcal{P}(k, k') = f_0(k)(1 + f_0(k)) \mathcal{L}(k, k') \quad (\text{D.12})$$

and in the derivation we have use the fact that since $E_k = E_{k'}$, they have the same occupancy in equilibrium. This is the so called *canonical form* of the Boltzmann's equation.

This equation must be satisfied for all k 's. If we define X_k to be what's on the

left of Eq(D.11), it can be written as

$$X_k = P\Phi_k \quad (\text{D.13})$$

where P is a linear operator, and X_k is a known quantity, once the dispersion curve is known. Further examination will show that \mathcal{P} is a Hermitian operator too. Solution of the inhomogeneous integral equation Eq(D.75) can be sought by minimizing the functional

$$\frac{\langle \Phi_k, P\Phi_k \rangle}{\langle \Phi_k, X_k \rangle^2} \propto \frac{1}{\kappa} \quad (\text{D.14})$$

where we have defined the inner product

$$\langle A_k, B_k \rangle = \int A_k B_k dk \quad (\text{D.15})$$

The physical meaning of Eq(D.14) being that nature will facilitate heat conduction, thus maximizing the rate of entropy production, under the constraint of maintaining steady state.

Relaxation time approximation

One of the most common approximations we make to Eq(D.4) is the *collision time approximation*, where we approximate the collision integral by

$$\text{collision integral} = -\frac{f(k) - f_0(k)}{\tau(k)} = -\frac{\tilde{f}(k)}{\tau(k)} \quad (\text{D.16})$$

irrespective of the distribution of other phonon states. Then at steady state,

$$\frac{\partial f(k, r)}{\partial T} \mathbf{v}_G(k) \cdot \nabla_r T = -\frac{\tilde{f}(k)}{\tau(k)} \quad (\text{D.17})$$

So the heat current is

$$\mathbf{J}_k^q = \hbar \omega_k \tilde{f}(k) \mathbf{v}_G(k)$$

$$= \hbar\omega_k \left(-\tau(k) \frac{\partial f(k, r)}{\partial T} \mathbf{v}_G(k) \cdot \nabla_r T \right) \mathbf{v}_G(k) \quad (\text{D.18})$$

But since

$$\mathbf{J}^q = \sum_k \mathbf{J}_k^q = -\hat{\kappa} \nabla_r T$$

there is

$$\begin{aligned} \hat{\kappa} &= \sum_k \tau(k) \frac{\partial \hbar\omega_k f(k, r)}{\partial T} \mathbf{v}_G(k) \mathbf{v}_G(k) \\ &= \sum_k \tau(k) C_v(k) \mathbf{v}_G(k) \mathbf{v}_G(k) \end{aligned} \quad (\text{D.19})$$

where

$$C_v(k) = \frac{\hbar^2 \omega_k^2}{k_B T^2} f_0(k) (1 + f_0(k)) \quad (\text{D.20})$$

is the heat capacity of phonon-state k .

Isotope Scattering

Suppose an isotope with extra mass ΔM is situated at (LS) , then

$$\hat{\mathcal{H}} = \hat{\mathcal{H}}_0 + \hat{V} \quad (\text{D.21})$$

$$\hat{V} = \frac{\hat{p}_S^{(L)^2}}{2(M_S + \Delta M)} - \frac{\hat{p}_S^{(L)^2}}{2M_S} = \frac{-\Delta M}{2M_S^2} \hat{p}_S^{(L)^2} \quad (\text{D.22})$$

And so, from Eq(2.199), there is

$$\begin{aligned} \hat{V} &= -\frac{\Delta M}{2M_S^2} \left(\sum_k -i \sqrt{\frac{\hbar M_S \omega_k}{2N}} \mathbf{e}^k(S) \exp(i\mathbf{q} \cdot \mathbf{R}(L)) (\hat{a}_k - \hat{a}_{-k}^\dagger) \right) \\ &\quad \cdot \left(\sum_{k'} i \sqrt{\frac{\hbar M_S \omega_{k'}}{2N}} \mathbf{e}^{k'}(S)^* \exp(-i\mathbf{q}' \cdot \mathbf{R}(L)) (\hat{a}_{k'}^\dagger - \hat{a}_{-k'}) \right) \\ &= -\frac{\Delta M}{2M_S^2} \frac{\hbar M_S}{2N} \sum_{kk'} \mathbf{e}^k(S) \cdot \mathbf{e}^{k'}(S)^* \exp(i(\mathbf{q} - \mathbf{q}') \cdot \mathbf{R}(L)) \\ &\quad \sqrt{\omega_k \omega_{k'}} (\hat{a}_k \hat{a}_{k'}^\dagger - \hat{a}_k \hat{a}_{-k'} - \hat{a}_{-k}^\dagger \hat{a}_{k'}^\dagger + \hat{a}_{-k}^\dagger \hat{a}_{-k'}) \end{aligned} \quad (\text{D.23})$$

Since energy is conserved in 1st-order PT, the $\hat{a}_k \hat{a}_{-k'}, \hat{a}_{-k}^\dagger \hat{a}_{k'}^\dagger$ terms won't survive,

also there must be

$$\omega_k = \omega_{k'} \quad (\text{D.24})$$

So,

$$\begin{aligned} \hat{V} = - \sum_{kk'} \frac{\hbar \Delta M \omega_k}{4NM_S} & \{ \mathbf{e}^k(S) \cdot \mathbf{e}^{k'}(S)^* \exp(i(\mathbf{q} - \mathbf{q}') \cdot \mathbf{R}(L)) \hat{a}_k \hat{a}_{k'}^\dagger \\ & + \mathbf{e}^{k*}(S) \cdot \mathbf{e}^{k'}(S) \exp(-i(\mathbf{q} - \mathbf{q}') \cdot \mathbf{R}(L)) \hat{a}_k^\dagger \hat{a}_{k'} \} \end{aligned} \quad (\text{D.25})$$

Now, because we are mostly interested in the scattering by a random distribution of isotope defects, we are considering the problem,

$$\begin{aligned} \hat{V}_{tot} = - \sum_{kk'} & \left(\sum_i \mathbf{A}^k(S) \cdot \mathbf{A}^{k'}(S)^* \exp[i(\mathbf{q} - \mathbf{q}') \cdot \mathbf{R}(L_i)] \right) \hat{a}_k \hat{a}_{k'}^\dagger \\ & + \left(\sum_i \mathbf{A}^{k*}(S) \cdot \mathbf{A}^{k'}(S) \exp[-i(\mathbf{q} - \mathbf{q}') \cdot \mathbf{R}(L_i)] \right) \hat{a}_k^\dagger \hat{a}_{k'} \end{aligned} \quad (\text{D.26})$$

where

$$\mathbf{A}^k(S) = \sqrt{\frac{\hbar \Delta M \omega_k}{4NM_S}} \mathbf{e}^k(S) \quad (\text{D.27})$$

For a specific scattering process, say, a phonon $k \rightarrow k'$, the matrix element is

$$\begin{aligned} & \left| \langle n_k - 1, n_{k'} + 1 | \hat{V}_{tot} | n_k, n_{k'} \rangle \right|^2 \\ = & \left| 2 \sum_i \mathbf{A}^k(S) \cdot \mathbf{A}^{k'}(S)^* \exp(i(\mathbf{q} - \mathbf{q}') \cdot \mathbf{R}(L_i)) \right|^2 \\ & \left| \langle n_k - 1, n_{k'} + 1 | \hat{a}_k \hat{a}_{k'}^\dagger | n_k, n_{k'} \rangle \right|^2 \end{aligned} \quad (\text{D.28})$$

Here a factor of 2 appears in the module because of the possible interchange of k, k' in Eq(D.26). Since L_i , the position of isotopes, are uncorrelated, the average is

$$4D \left| \mathbf{A}^k(S) \cdot \mathbf{A}^{k'}(S)^* \right|^2 n_k (n_{k'} + 1)$$

where D is the total number of defects. So the transition probability from k to other

states is just, by Fermi's Golden rule,

$$W_{k,out} = \frac{2\pi}{\hbar} \sum_{k'} 4D \left| \mathbf{A}^k(S) \cdot \mathbf{A}^{k'}(S)^* \right|^2 n_k(n_{k'} + 1) \delta(\hbar\omega_k - \hbar\omega_{k'}) \quad (\text{D.29})$$

For materials with T_d or higher point symmetry there can be a nice simplification, because then all vectors (x, y, z) belong in whole to a single irreducible representation Γ_{vec} of the point group, and

$$\begin{aligned} & \sum_{k'} \left| \mathbf{A}^k(S) \cdot \mathbf{A}^{k'}(S)^* \right|^2 \\ = & \sum_{k', \alpha, \beta} A_\alpha^k(S) A_\alpha^{k'*}(S) A_\beta^{k*}(S) A_\beta^{k'}(S) \\ = & \sum_{k', \alpha, \beta} \frac{1}{h} \sum_{\{U\}} A_\alpha^k(S) A_\beta^{k*}(S) A_\alpha^{Uk'*}(S) A_\beta^{Uk'}(S) \\ = & \sum_{k', \alpha, \beta} A_\alpha^k(S) A_\beta^{k*}(S) \frac{1}{h} \left(\sum_{\{U\}} D_{\alpha\alpha'}^{*\Gamma_{vec}}(U) D_{\beta\beta'}^{\Gamma_{vec}}(U) \right) A_{\alpha'}^{k'*}(S) A_{\beta'}^{k'}(S) \\ = & \sum_{k', \alpha, \beta} A_\alpha^k(S) A_\beta^{k*}(S) \frac{1}{h} \frac{h}{d_{vec}} \delta_{\alpha\beta} \delta_{\alpha'\beta'} A_{\alpha'}^{k'*}(S) A_{\beta'}^{k'}(S) \\ = & \sum_{k'} \frac{1}{3} \left| \mathbf{A}^k(S) \right|^2 \left| \mathbf{A}^{k'}(S) \right|^2 \end{aligned} \quad (\text{D.30})$$

For monoatomic crystals, $\mathbf{e}^k(S)$ is a unit vector, so

$$\frac{1}{3} \left| \mathbf{A}^k(S) \right|^2 \left| \mathbf{A}^{k'}(S) \right|^2 = \frac{1}{3} \left(\frac{\hbar \Delta M \omega_k}{4NM_S} \right)^2 \quad (\text{D.31})$$

If it's not, we can approximate it by

$$\frac{1}{3r^2} \left(\frac{\hbar \Delta M \omega_k}{4NM_S} \right)^2$$

Exact Solution in Debye Model

Let us assume there is a monoatomic crystal with simple dispersion relations of isotropic elastic medium. Let the sound velocity of transverse and longitudinal wave

be c_t , c_l respectively, and the transverse branch is doubly degenerate. In this case,

$$\begin{aligned}
& \left. \frac{dn_k}{dt} \right)_{\text{colli}} \\
= & W_{k,in} - W_{k,out} \\
= & \frac{8\pi D}{3\hbar} \sum_{k'} \left(\frac{\hbar \Delta M \omega_k}{4NM_S} \right)^2 [n_{k'}(n_k + 1) - n_k(n_{k'} + 1)] \delta(\hbar\omega_k - \hbar\omega_{k'}) \\
= & \frac{8\pi D}{3\hbar} \left(\frac{\hbar \Delta M \omega_k}{4NM_S} \right)^2 (\bar{n}_k - n_k) \sum_{k'} \delta(\hbar\omega_k - \hbar\omega_{k'}) \tag{D.32}
\end{aligned}$$

In the last step we have replaced $n_{k'}$ by the average occupation number \bar{n}_k , which is like collision-time approximation where we ignore the possibility of “group deficiency”.

Inside the summation is just the density of states, which we can replace by integral

$$\begin{aligned}
& \sum_{k'} \delta(\hbar\omega_k - \hbar\omega_{k'}) \\
= & \sum_{\text{branches}} \int \frac{\Omega 4\pi k^2 dk}{8\pi^3} \delta(\hbar\omega_k - \hbar\omega_{k'}) \\
= & \frac{\Omega}{2\pi^2} \frac{1}{\hbar} \omega_k^2 \left(\frac{1}{c_l^3} + \frac{2}{c_t^3} \right) \tag{D.33}
\end{aligned}$$

Combining our results, we have

$$\begin{aligned}
& \left. \frac{dn_k}{dt} \right)_{\text{colli}} \\
= & \frac{8\pi D}{3\hbar} \left(\frac{\hbar \Delta M \omega_k}{4NM_S} \right)^2 \frac{\Omega}{2\pi^2} \frac{1}{\hbar} \omega_k^2 \left(\frac{1}{c_l^3} + \frac{2}{c_t^3} \right) (\bar{n}_k - n_k) \\
= & \frac{D\Omega(\Delta M)^2 w_k^4}{12N^2 M^2 \pi} \left(\frac{1}{c_l^3} + \frac{2}{c_t^3} \right) (\bar{n}_k - n_k) \tag{D.34}
\end{aligned}$$

It's not surprising that we recover the ubiquitous w^4 laws again, which conforms to the general long-wave *Rayleigh* scattering result of a ball ($ka \ll 1$) stuck in an infinite elastic medium, with higher density.

D.2 3-Phonon Process

In the expansion Eq(2.144) we have ignored the cubic term in harmonic approximation

$$\hat{V}_3 = \frac{1}{6} \Phi_{mm'm''} \hat{u}_m \hat{u}_{m'} \hat{u}_{m''} \quad (\text{D.35})$$

Express it fully in normal coordinates using Eq(2.198), it becomes

$$\begin{aligned} \hat{V}_3 &= \frac{1}{6} \left(\frac{\hbar}{2N} \right)^{\frac{3}{2}} \sum_{\{LS\alpha\}} \Phi_{\alpha\alpha'\alpha''} \binom{LL'L''}{SS'S''} (M_S M_{S'} M_{S''})^{-1/2} \sum_{kk'k''} \frac{e_{\alpha}^k(S) e_{\alpha'}^{k'}(S') e_{\alpha''}^{k''}(S'')}{(\omega_k \omega_{k'} \omega_{k''})^{1/2}} \\ &\quad \exp \left(i[\mathbf{q} \cdot \mathbf{R}(L) + \mathbf{q}' \cdot \mathbf{R}(L') + \mathbf{q}'' \cdot \mathbf{R}(L'')] \right) (\hat{a}_k + \hat{a}_{-k}^{\dagger}) (\hat{a}_{k'} + \hat{a}_{-k'}^{\dagger}) (\hat{a}_{k''} + \hat{a}_{-k''}^{\dagger}) \end{aligned} \quad (\text{D.36})$$

Since the summation is irrelevant with respect to the translation of $(LL'L'')$ as whole, it vanishes unless

$$\mathbf{q} + \mathbf{q}' + \mathbf{q}'' = 0 \quad (\text{D.37})$$

or

$$\mathbf{q} + \mathbf{q}' + \mathbf{q}'' = \mathbf{G} \quad (\text{D.38})$$

where \mathbf{G} is a reciprocal lattice vector. (D.37) is called *normal* or *N-process*, (D.38) is called *Umklapp* or *U-process*.

Multiplying out the terms in Eq(D.36), we have

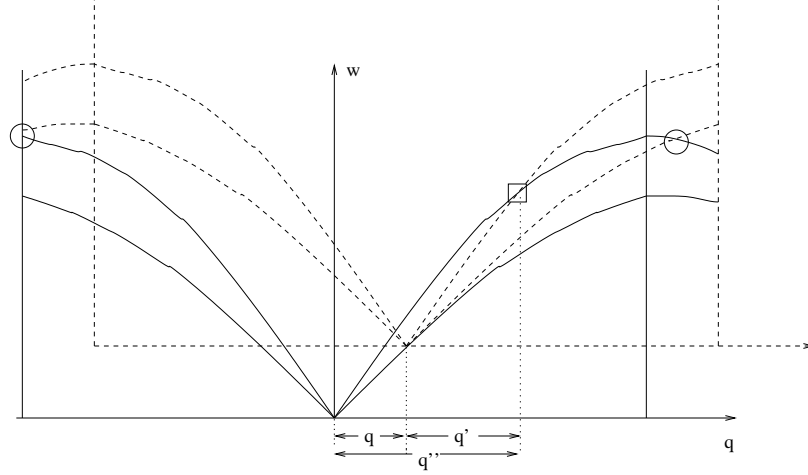
$$\begin{aligned} &\hat{a}_k \hat{a}_{k'} \hat{a}_{k''}^{[1]} + \hat{a}_{-k}^{\dagger} \hat{a}_{k'} \hat{a}_{k''}^{[2]} + \hat{a}_k \hat{a}_{-k'}^{\dagger} \hat{a}_{k''}^{[3]} + \hat{a}_{-k}^{\dagger} \hat{a}_{-k'}^{\dagger} \hat{a}_{k''}^{[4]} + \\ &\hat{a}_k \hat{a}_{k'} \hat{a}_{-k''}^{\dagger [5]} + \hat{a}_{-k}^{\dagger} \hat{a}_{k'} \hat{a}_{-k''}^{\dagger [6]} + \hat{a}_k \hat{a}_{-k'}^{\dagger} \hat{a}_{-k''}^{\dagger [7]} + \hat{a}_{-k}^{\dagger} \hat{a}_{-k'}^{\dagger} \hat{a}_{-k''}^{\dagger [8]} \end{aligned} \quad (\text{D.39})$$

If two of the \mathbf{q} 's are fixed, there is only one possible value for the third, either through (D.37) or (D.38). The conservation of energy further requires that

$$\pm \omega_k \pm \omega_{k'} \pm \omega_{k''} = 0 \quad (\text{D.40})$$

Due to this reason, the terms [1],[8] in Eq(D.39) are not possible in first order process.

The solutions of Eq(D.58) could be sought from the following graphical construc-



Construction for 3-phonon process.
circle: $t+t=l$. square: $t+l=l$

Figure D-1: Possible three-phonon processes.

tion: First we draw the dispersion curve. If we want to investigate possible interactions concerning (\mathbf{q}, ω) , we just translate the whole dispersion curve onto (\mathbf{q}, ω) , and search for its possible crossing with the old curve: the crossing point on the old coordinates would be (\mathbf{q}'', ω'') , on the new coordinate would be (\mathbf{q}', ω') . Note that the crossing point could be beyond 1st Brillouin zone: if it does, then it's *U-process*, otherwise it's *N-process*. By careful observations of these constructions on a simple Debye model, we arrive at only two possible types of processes:

$$\text{transverse} + \text{transverse} \rightarrow \text{longitudinal} \quad (\text{D.41})$$

$$\text{transverse} + \text{longitudinal} \rightarrow \text{longitudinal} \quad (\text{D.42})$$

For multi-atom systems, we would have $3r - 3$ optical branches. It's generally believed that optical phonons doesn't contribute much to the thermal conductivity because they have less group velocity. Also only one type of process is allowed for Debye model:

$$\text{acoustic} + \text{acoustic} \rightarrow \text{optical} \quad (\text{D.43})$$

3-phonon process constitute the main part of thermal resistivity in a perfect crys-

tal. It is also believed that the *Normal* process is the main part of it. However, if there are *only* N-processes in the system, the thermal resistivity will be infinite, since then the quantity

$$\mathbf{Q} = \sum_k \mathbf{q} f(k) \quad (\text{D.44})$$

would be conserved always. That means once we establish $\mathbf{Q} \neq 0$ in the system, it will continue to be so without the ability to recover true statistical equilibrium, thus having finite heat current (best seen in Debye model) without constant thermal gradient, which implies infinite thermal conductivity. It follows then, that the *Umklapp* process plays a vital role.

We can approximate the thermal conductivity at low temperatures ($T \ll \Theta$) by the following argument: in order for Eq(D.38) to hold, one of the phonon \mathbf{q} must exceed $\mathbf{G}/3$, while smaller than $\mathbf{G}/2$ in order to stay in the 1st B.Z. Since the Debye temperature Θ corresponds to \mathbf{G} , it follows that the probability of existence of such phonon excitation is proportional to

$$\exp(-\gamma\Theta/T) \quad (\text{D.45})$$

with γ between 1/3 and 2/3, for the *Umklapp* process to be possible. And thus the thermal conductivity holds the same scaling.

D.3 Debye Function for Temperature Rescaling

Debye proposed the following single-parameter spectrum density,

$$dP = d\left(\frac{\omega}{\omega_D}\right)^3, \quad \omega < \omega_D, \quad 0, \quad \omega \geq \omega_D, \quad (\text{D.46})$$

where the normalization is a single *degree of freedom*, which *should* possess $k_B T$ total energy under classical mechanics and harmonic approximation. In contrast, under

quantum mechanics, the total energy is

$$\langle E \rangle = \int_0^{\omega_D} d\left(\frac{\omega}{\omega_D}\right)^3 \left(\frac{1}{2} + \frac{1}{\exp\left(\frac{\hbar\omega}{k_B T}\right) - 1} \right) \hbar\omega. \quad (\text{D.47})$$

Let us define

$$k_B T_D \equiv \hbar\omega_D. \quad (\text{D.48})$$

We then have the quantum energy average,

$$\langle E \rangle = k_B T_D \int_0^{\omega_D} d\left(\frac{\omega}{\omega_D}\right)^3 \left(\frac{1}{2} + \frac{1}{\exp\left(\frac{T_D}{T} \cdot \frac{\omega}{\omega_D}\right) - 1} \right) \frac{\omega}{\omega_D}, \quad (\text{D.49})$$

which can be written as,

$$\langle E \rangle = k_B T_D \int_0^1 dy^3 \left(\frac{1}{2} + \frac{1}{\exp\left(\frac{T_D}{T} \cdot y\right) - 1} \right) y, \quad (\text{D.50})$$

or,

$$\langle E \rangle = k_B T_D \int_0^1 dy \left(\frac{1}{2} + \frac{1}{\exp\left(\frac{T_D}{T} \cdot y\right) - 1} \right) 3y^3. \quad (\text{D.51})$$

Alternatively, one can rewrite (D.51) as

$$\langle E \rangle = k_B T_D \left(\frac{T}{T_D} \right)^4 \int_0^{\frac{T_D}{T}} dy \left(\frac{1}{2} + \frac{1}{e^y - 1} \right) 3y^3. \quad (\text{D.52})$$

Therefore, if we require the classical system to have equal energy as the quantum system on average, we would demand

$$T_{\text{MD}} = T_D \left(\frac{T}{T_D} \right)^4 \int_0^{\frac{T_D}{T}} dy \left(\frac{1}{2} + \frac{1}{e^y - 1} \right) 3y^3. \quad (\text{D.53})$$

This form is more ready for numerical evaluation. We see that when $T \rightarrow 0$, $T_{\text{MD}} \rightarrow (3/8)T_D$, a nonzero value. But when $T \rightarrow \infty$, $T_{\text{MD}} = T + \mathcal{O}(1/T)$.

To get the heat capacity, or dT_{MD}/dT , it is easier to work on (D.51):

$$\frac{dT_{\text{MD}}}{dT} = \left(\frac{T_{\text{D}}}{T}\right)^2 \int_0^1 dy \frac{\exp\left(\frac{T_{\text{D}}}{T} \cdot y\right)}{\left(\exp\left(\frac{T_{\text{D}}}{T} \cdot y\right) - 1\right)^2} 3y^4, \quad (\text{D.54})$$

or alternatively,

$$\frac{dT_{\text{MD}}}{dT} = \left(\frac{T}{T_{\text{D}}}\right)^3 \int_0^{\frac{T_{\text{D}}}{T}} dy \frac{3y^4 e^y}{(e^y - 1)^2} \equiv D\left(\frac{T}{T_{\text{D}}}\right), \quad (\text{D.55})$$

where $D(x)$ is the well-known Debye function [6], with $D(x) \sim (4\pi^4/5)x^3$ as $x \sim 0$ and $D(x) \rightarrow 1$ as $x \rightarrow \infty$.

In practice, the phonon spectrum density or DOS is of course *not* in the same form as (D.46). Especially, multi-component systems have optical bands that are of entirely different structure than (D.46). Nevertheless, (D.53) and (D.55) provide good functional forms for $T_{\text{MD}}(T)$ representation, both numerically and physically. Let us consider the temperature rescaling procedure's physical effect on classical MD: it can be proved that the initial $\hbar\omega/2$ and the later flatter $T_{\text{MD}}(T)$ excitation in classical MD mimics the effect of quantum phonon Boltzmann equation, but with the unsatisfactory aspect that this correction is incorrectly smeared out throughout the entire spectrum (if one allows the classical system to equilibrate), so only an average correction effect remains. Given that, the question is suppose we have a wide spectrum which contains optical band that is far from the acoustic band, *which part should one sacrifice*, that is, *more* incorrectly smeared out? It is not hard to see that it should be the optical bands, since they do not contribute significantly to the thermal conductivity. Furthermore, one often worries more about the quantum effects on thermo-mechanical properties near room temperature, and less for when the temperature is high, say $T = 1000\text{K}$. The reason is not just because these properties might be less important at high temperature than at room temperature, but also because the quantum effects themselves are not significant enough to have a big influence at high temperature. If we think about it, it is common practice to do classical MD without *any* correction - but one is still expected to get sound result

at high temperature, so it must be all right if we apply correction but *which is not neatly fitted for high temperature*. Therefore, I think it is a good idea to fit (D.55) to the actual heat capacity at $T = 300\text{K}$, where only the acoustic band is likely to be activated.

D.4 Connection between Classical and Quantum Phonon Scattering

In the past years, we numerically calculate the lattice thermal conductivity of dielectric solids using the Green-Kubo fluctuation-dissipation formula and molecular dynamics simulation based on classical Newtonian dynamics using well-tested inter-atomic potential [80], with a crude temperature rescaling scheme due to Lee *et al* [149] to account for the quantum-mechanical heat capacities at low temperature. It is found that in the high temperature region ($T > T_D/2$) and for perfect crystal (Ar, Si and SiC), where κ follows $T^{-\alpha}$ behavior ($\alpha \sim 1$), the calculations yield reliable results as compared with experiments. It also provides a qualitatively correct picture of the drastic defect-induced reduction of thermal conductivity at high defect concentration. On the other hand, the simulation fails to produce the low-temperature thermal conductivity of these crystals, where κ has the form of $e^{\theta/T}$, while our model continues to give $T^{-\alpha}$ behavior and becomes much lower in absolute magnitude in comparison with the experiments. In view that the Debye temperature for Si is 550K and SiC $> 1000\text{K}$, this includes room temperature and is a severe drawback to the usefulness of our simulation.

At extremely low temperatures ($T < T_D/20 - T_D/10$), the experimental κ heads for a drastic decrease ($\kappa \propto T^3$) as the phonon mean free path becomes limited by the macroscopic sample size. Our model produce qualitatively the same result by coincidence.

To see why the simulation fails at low temperatures, we must concede that the conventional classical MD simulation describes a fictitious world where classical me-

chanics and statistical mechanics always hold true at any given temperature. Consider a spring with Hamiltonian,

$$\mathcal{H}(p, q) = \frac{p^2}{2} + \frac{1}{2}\omega^2 q^2, \quad (\text{D.56})$$

whose trajectories on pq -plane are closed ellipses with size dependent on its total energy E , and encloses area $A = 2\pi E/\omega$. In classical mechanics, all E 's are allowable, and so all ellipses could exist, which fills up the phase plane as a continuum. The density of states on the pq -plane is the continuous integral $\int dpdq$, and the partition function is

$$Z_{\text{classical}} = \int dpdq e^{-\mathcal{H}/k_B T}. \quad (\text{D.57})$$

In this world, the property averages are just Gaussian integrals and one can easily show that

$$\langle E \rangle = k_B T, \quad (\text{D.58})$$

independent of ω , which is the famous equi-partition theorem, provided that the classical Newtonian mechanics are followed.

But, in our real world, a quantum world, the energy is quantized instead of continuous. The only allowable E 's are

$$E_N = (N + 1/2)\hbar\omega. \quad (\text{D.59})$$

It is still helpful to consider the pq -plane, for a so-called semi-classical picture which is the same as the classical one except only a countable number of ellipses *can* exist, satisfying the Bohr-Sommerfeld quantization condition ¹

$$\oint pdq = 2\pi(N + 1/2)\hbar, \quad (\text{D.60})$$

which is seen to be equivalent to (D.59). So, in the quantum world, the density of

¹The original formulation for Hydrogen electron is without the $\frac{1}{2}$ factor.

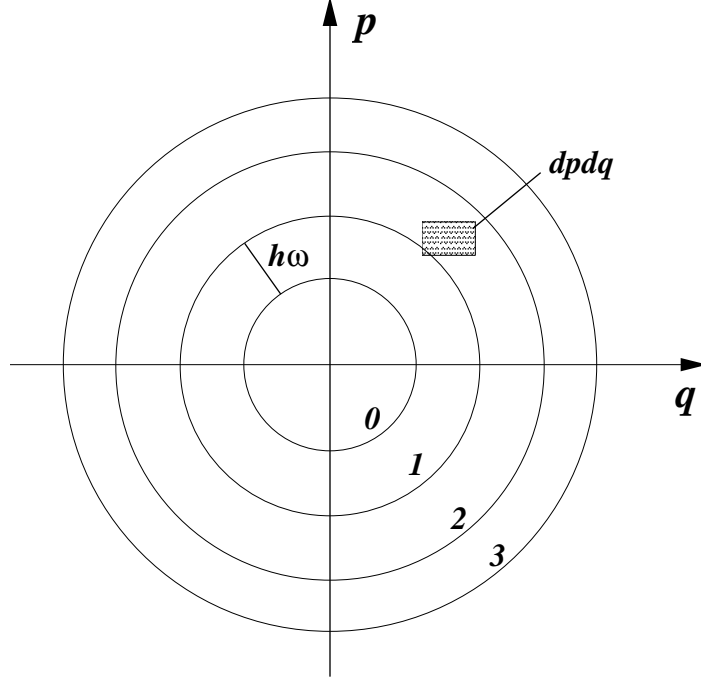


Figure D-2: Phase space trajectories of an harmonic oscillator and its quantization states is a discrete sum \sum_N instead of continuous integral $\int dpdq$,

$$Z_{\text{QM}} = \sum_N e^{-\mathcal{H}/k_B T}. \quad (\text{D.61})$$

(D.61) and (D.57) would not differ by much if the scale of available energy, $k_B T$, is much greater than the energy separation between two nearest ellipses, $\hbar\omega$; just like a man standing far away cannot distinguish the subtleties of a painting – which is the “approach to continuum” or “correspondence principle” between quantum and classical physics. But if the available energy is comparable to $\hbar\omega$, then the system can *distinguish* the discrete ellipses, which then could modify its behavior profoundly.

The most illustrious example worked out by Einstein is that of the “anomalous” heat capacity of solids at low temperature. From (D.61),

$$Z = e^{-\hbar\omega/2k_B T} + e^{-3\hbar\omega/2k_B T} + e^{-5\hbar\omega/2k_B T} + \dots = \frac{e^{-\hbar\omega/2k_B T}}{1 - e^{-\hbar\omega/k_B T}}, \quad (\text{D.62})$$

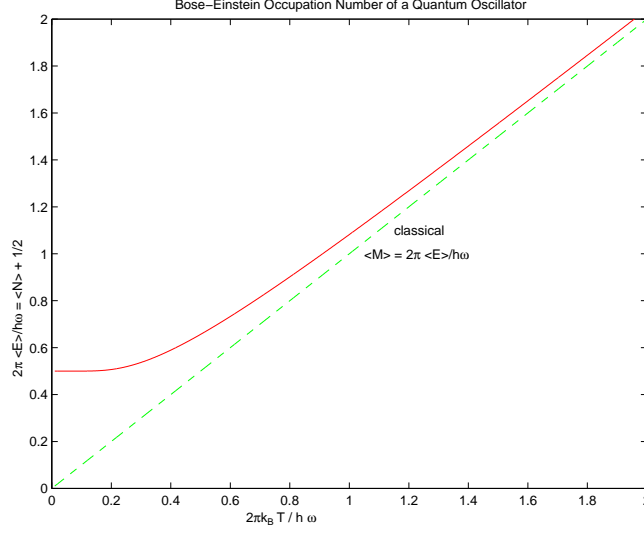


Figure D-3: Occupation number of a quantum oscillator as compared to a classical one (dash line).

and thus

$$\langle E \rangle = (\langle N \rangle + 1/2) \hbar \omega = -\frac{\partial \log Z}{\partial (1/k_B T)} = \left(\frac{1}{e^{\hbar \omega / k_B T} - 1} + 1/2 \right) \hbar \omega. \quad (\text{D.63})$$

Here

$$\langle N \rangle = \frac{1}{e^{\hbar \omega / k_B T} - 1}, \quad (\text{D.64})$$

is the Bose-Einstein distribution for boson. (D.63) can be shown to approach (D.58) asymptotically as $\mathcal{O}(1/T)$ when $T \rightarrow \infty$.

One can see that the heat capacity of a quantum oscillator (slope of Fig. D-3) – the derivative of average internal energy with respect to T , only approaches the constant k_B value predicted by the equi-partition theorem (D.58) at high enough temperatures. When $k_B T / \hbar \omega$ is on the order of unity, there is a severe discrepancy between the quantum and classical results. Same thing would happen for the thermal conductivity κ .

In a solid, there exist not just a single oscillator but a whole bunch (in fact, $3N$) of them, each with different ω 's. Labelling them can be difficult; but for a perfect crystal with translational symmetry, a great simplification happens (Bloch theorem) where one can label them by \mathbf{k} and branch number j 's. These vibrations with space-time

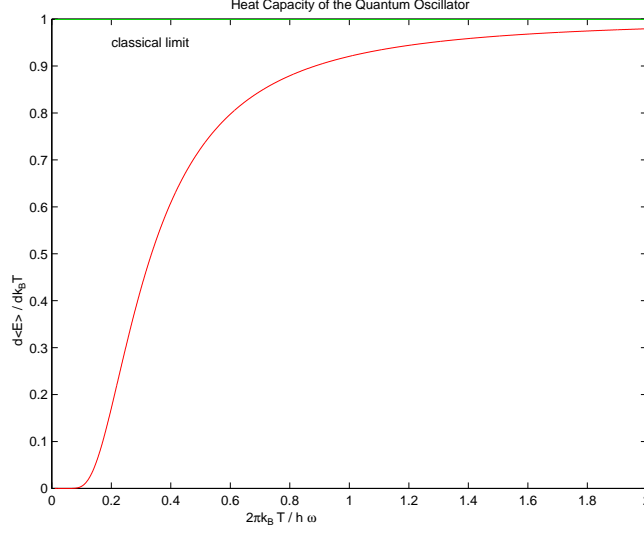


Figure D-4: Comparison of heat capacity between a quantum oscillator and a classical one (dash line).

periodicity $e^{i\mathbf{k}\cdot\mathbf{R}_n - i\omega_j(\mathbf{k})t}$ are called phonons; and $\omega_j(\mathbf{k})$ is called the phonon dispersion relation. When \mathbf{k} is small (long waves), there exist three j -branches that have almost linear dispersion: $\omega_j(\mathbf{k}) \simeq c_j|\mathbf{k}|$; they are nothing other than the sound and shear waves in a solid corresponding to macroscopic elastic deformations. They are special because only at small $|\mathbf{k}|$ do $\omega_j(\mathbf{k})$'s approach 0.

A continuum can support arbitrarily large \mathbf{k} ; but a discrete lattice can only support up to $2\pi/a$ where a is the lattice spacing of a pedagogical 1D lattice. It can be easily seen that $k + 2\pi/a$ and k represent the *same* wave on this lattice, which is called *aliasing*. Thus, $k + 2\pi/a$ and k are exactly the same label for vibrational eigenstates and so, we only need to label the eigenstates by $k \in (-\pi/a, \pi/a)$, which is called the first Brillouin Zone. If one traces the lowest ω of a given \mathbf{k} , it usually achieves maxima on $\pm\pi/a$, the BZ boundary; with maximum on the order of the so-called Debye frequency ω_D .

Depending on temperature, some phonons (grouped according to frequency) are more populous than others; the most populous is called *thermal phonon* frequency ω_T , which dominates the thermodynamics of the system. ω_T exists because there are more phonon states at large k ($\propto 4\pi k^2 dk$), but larger k also means larger ω which means smaller $\langle N \rangle$ in (D.64). The situation is thus divided into two scenarios:

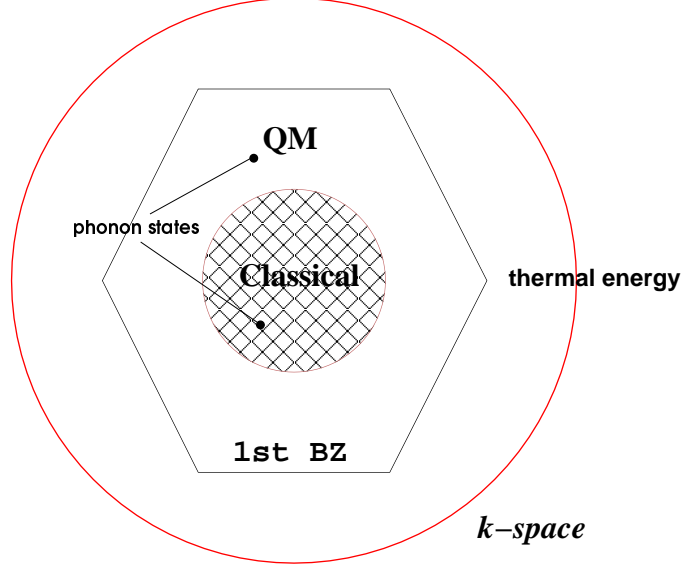


Figure D-5: Two scenarios in the activation of phonons. When $k_B T \gg \hbar \omega_D$, the thermal energy (large) circle encloses the entire BZ; so the classical equi-partition theorem is good for all phonons and thermal (representative) phonons are those on the BZ boundary. On the other hand, when $k_B T < \hbar \omega_D$, the activation circle is in BZ: inside the occupation is still classical, but outside the Bose-Einstein distribution must be used, which is exponentially small. The thermal phonons are those on the circle.

If $k_B T \gg \hbar \omega_D$, i.e., if the available thermal energy (signified by the big circle) is enough to excite even the highest available frequency, ω_D , at the BZ boundary, then $\omega_T = \omega_D$. In this case all phonon excitations can be well-approximated by the classical “effective” occupation number

$$M_{\mathbf{k}j} = k_B T / \hbar \omega_{\mathbf{k}j} \quad (\text{D.65})$$

and it is valid to study the entire system using classical mechanics. On the other hand, if the thermal energy is smaller than $\hbar \omega_D$ (small circle in BZ), then $\omega_T = k_B T / \hbar$; modes inside the circle are still excited according to classical equi-partition theorem, but those outside the circle ($\omega > \omega_T$) are not and (D.64) is essential. So it is inappropriate to describe such a system using classical mechanics without modification.

In the above we regard the phonon modes as perfect normal modes of the system, where the occupation number $N_{\mathbf{k}j}$, once assigned, has no reason to change. This

is not so once nonlinearities exists in the interaction potential, the leading order of which are the cubic terms, that can annihilate a phonon \mathbf{k}_1 and create two $(\mathbf{k}_2, \mathbf{k}_3)$, and vice versa, which makes the BZ look rather like a boiling pot of water. But, not any triplets of \mathbf{k} can scatter; energy must be conserved:

$$\omega_1 = \omega_2 + \omega_3, \quad (\text{D.66})$$

and so is the quasi-momentum

$$\mathbf{k}_1 = \mathbf{k}_2 + \mathbf{k}_3 (+\mathbf{G}), \quad (\text{D.67})$$

because, as we said, a discrete lattice can not support real momentum, so there is only a conservation law for the *quasi*-momentum. If the reciprocal vector \mathbf{G} in the bracket ($2\pi/a$ for the 1D lattice) is not involved, it is called a Normal or *N*-process; otherwise it is called Umklapp or *U*-process, which in German means “flip over”. One can see that in order to “flip over”, at least two of the three $|\mathbf{k}|$ ’s must be greater than $|\mathbf{G}|/2$, so at least two ω ’s involved are quite large. This means that the rate of Umklapp process will drop drastically in scenario II, because quite generally, it can be shown that the *rate* of a three-phonon process is proportional to

$$[N_1(+1)] \times [N_2(+1)] \times [N_3(+1)], \quad (\text{D.68})$$

where N_1, N_2, N_3 are the current occupation numbers of the phonons involved; since N is exponentially small if it lies outside the activation circle, one can see that the rate of Umklapp process becomes exponentially small ($\propto e^{-\theta/T}$) in the low temperature regime of $\omega_T \ll \omega_D$, when the rate of Normal process only decreases as algebraic powers of T . This is going to have important consequences on the crystal’s thermal conductivity.

Why do we have to distinguish between *N*- and *U*-processes? The reason lies in

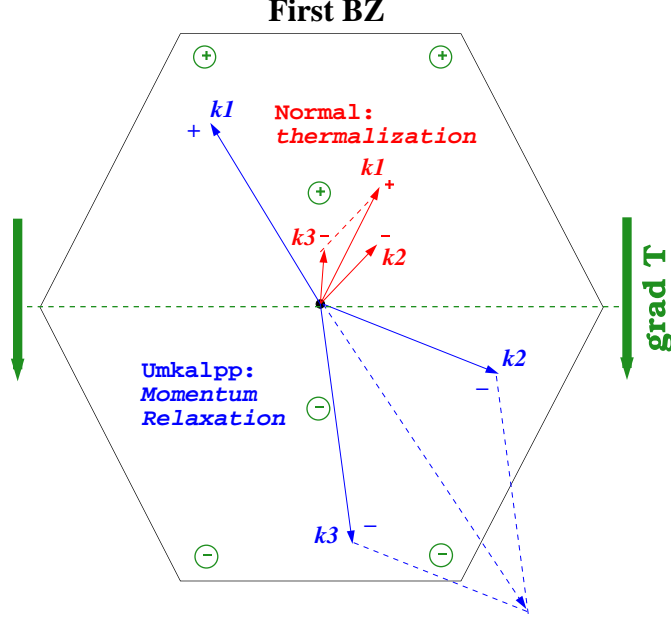


Figure D-6: Character of the streaming, Normal and Umklapp-collisional terms.

the form of the phonon transport equation (for details see the last reference),

$$\frac{\partial N_{\mathbf{k}j}}{\partial t} + \nabla \cdot (N_{\mathbf{k}j} \mathbf{v}_G) = \left. \frac{\partial N_{\mathbf{k}j}}{\partial t} \right|_{\text{collision}} = I_N[N] + I_U[N]. \quad (\text{D.69})$$

RHS of (D.69) describes the local phonon collisional processes that we mentioned above; it can be further categorized as N - and U - collision rate functionals $I_N[N]$ and $I_U[N]$. Note that their contributions to the rate of change in $N_{\mathbf{k}j}$ does not only depend on $N_{\mathbf{k}j}$ itself, but also on other phonon occupation numbers². $I_N[N]$ and $I_U[N]$ can further be shown to have the Bose-Einstein distribution $N_{BE}(\mathbf{k}j)$ as zero-modes, which means

$$I_N[N_{BE}] = I_U[N_{BE}] = 0; \quad N_{BE}(\mathbf{k}j) = \frac{1}{e^{\hbar\omega_{\mathbf{k}j}/k_B T} - 1}, \quad (\text{D.70})$$

so complete equilibrium is only achievable when T is constant everywhere.

The second term on LHS is the so-called *streaming* term, which for steady state ($\frac{\partial N_{\mathbf{k}j}}{\partial t} = 0$) heat flow, is the only input or inhomogeneous term of this integro-

²An effort to ignore that is the *relaxation time* approximation, which only makes sense in scenario I where $\tau_U \sim \tau_N$ and there is no clear distinction between mechanisms.

differential equation. It has the important feature that it carries net quasi-momentum [59] with it,

$$\sum_j \int \frac{d\mathbf{k}}{8\pi^3} \mathbf{k} \nabla \cdot (N_{\mathbf{k}j} \mathbf{v}_G) = S \nabla T \neq 0, \quad (\text{D.71})$$

where S is the entropy per volume of the crystal. By analogy, one can think of a 2D BZ phonon distribution as a pile of sand, whose height is the highest at zone center and lowest on zone boundaries. The streaming term is to such effect that the amount of sand is increased on one side (\mathbf{k} 's along the temperature gradient $-\nabla T$) and decreased on the opposite side. The overall result is that the center of mass of this sand dune is shifted toward $-\nabla T$.

Without counteractive processes, this shifting of center of mass will simply continue. Because each phonon mode carries certain amount of energy and propagates it by group velocity $\mathbf{v}_G = d\omega/d\mathbf{k}$ which is often along the \mathbf{k} -direction, the net effect is to induce a *macroscopic* heat current \mathbf{J}^q in the $-\nabla T$ direction; and in fact \mathbf{J}^q will just increase without bound. So without counteractive or scattering processes, the thermal conductivity will just be infinite.

Both Normal and Umklapp process are counteractive processes which tries to revoke whatever changes the streaming term causes to the phonon distribution. They cannot fully win, but they do strike a balance with it; so in the end the center of mass *is* displaced but is not growing, and a finite instead of infinite \mathbf{J}^q will be established.

We must distinguish between Normal and Umklapp processes because they play different roles in this struggle against the streaming term. To see this, we must understand that the Normal process cannot change the total quasi-momentum of the system, since by definition $\mathbf{k}_1 = \mathbf{k}_2 + \mathbf{k}_3$. So whatever the center of mass displacement the system currently has, Normal process cannot recover. The job, called *momentum relaxation*, has to be done by the Umklapp process, which catches anything that spills over the BZ and put it on the other side, in effect reducing the center of mass displacement of the system.

Then, what is the role of Normal process? Normal process induces *thermalization*, or approach to *local* equilibrium. This comes from the observation that not only

$N_{BE}(\omega)$, but also $N'_{BE}(\omega) = N_{BE}(\omega - \mathbf{k} \cdot \mathbf{V})$ for arbitrary \mathbf{V} having the dimensionality of velocity, are zero-modes of $I_N[N]$. $N'_{BE}(\omega)$ can be thought of as nothing other than a Bose-Einstein distribution with a displaced center of mass \mathbf{V} . Thus the Normal process is a mason with a good eye for details but cannot correct for the systematic deviation of the sand pile. It measures the average “center of mass” of the BZ at a given \mathbf{x} and then tries to re-shape the pile according to $N'_{BE}(\omega)$. If somewhere there is a notch (some \mathbf{k} -modes are under-excited), it can propagate the energy from surplus regions to this deficient region by many small Normal collisions. And, as we said, when $\omega_T \ll \omega_D$, such thermalization has a much shorter time scale (τ_N) than the momentum relaxation time scale (τ_U), since the rate of Umklapp process decreases exponentially with T while that of the Normal process only decreases algebraically. Thus the low-temperature crystalline thermal conductivity is controlled by Umklapp process rather than the Normal process, which is the *weaker* of the two in fighting against the streaming term. And at any given moment, the leading-order phonon distribution should have the form $N'_{BE}(\omega)$, as if relaxed instantaneously by I_N .

In exact analogy, a box of gas can only be at global equilibrium as $e^{-m|\mathbf{v}|^2/2k_B T}$, but a local equilibrium distribution $e^{-m|\mathbf{v} - \bar{\mathbf{v}}(\mathbf{r})|^2/2k_B T}$, which is also a zero mode of the gas collisional operator, can exist and persist for quite a while. Suppose one gives the gas an initial random distribution at $t = 0$, under suitable conditions (dense gas, namely) we will find that within a very short time τ_L , the system approaches local equilibrium; beyond τ_L , the macroscopic variable $\mathbf{v}(\mathbf{r})$ evolves with timescale τ_H with the leading order particle distribution $e^{-m|\mathbf{v} - \bar{\mathbf{v}}(\mathbf{r})|^2/2k_B T}$ co-moving³. The reduced equations (as a function of \mathbf{r} only) are called *hydrodynamics* equations, or fluid mechanics equations. The transition from kinetic to hydrodynamics theory relies critically on this separation of time-scales and the assumption of leading-order local equilibrium. By the same token, when $\omega_T \ll \omega_D$ and $\tau_N \ll \tau_U$, we can concentrate how $\mathbf{V}(\mathbf{r})$ evolves with time rather than the full $N_{\mathbf{k}j}$ description, which is appropriately named *phonon*

³There are, of course, next-order terms, without which there can be no shear stress or heat current; their relations to $\mathbf{v}(\mathbf{r})$ and its spatial gradients can be systematically calculated by the Chapman-Enskog expansion of the Boltzmann equation, which is essentially a τ_L/τ_H expansion.

hydrodynamics.

It should be quite clear now why classical MD cannot be used to study the low-temperature thermal conductivity without modification, since in that fictitious world the equi-partition theorem ordains that there should always be significant excitations for **all** phonon modes (think of $\hbar \rightarrow 0$ and the activation circle goes to infinity). So τ_U is always as big as τ_N , and there is no separation of timescale, no phonon hydrodynamics, and no $e^{\theta/T}$ like thermal conductivity rise.

Signer-Kirkwood \hbar -Expansion It can be shown that any two-point correlation function of the quantum world can be expanded in a power series of \hbar , the coefficients of which are classical n -point correlation functions. Besides being quite complicated analytically and numerically, I also doubt that a power series expansion can be useful in the deep quantum domain, as all previous applications were for liquids, where the quantum effect is indeed a small correction. Nevertheless, it is a trodden path and when we have nowhere to turn, we may try this.

Path-Integral MD PIMD seems to be something new that just appear recently in the simulation study of water⁴. The path integral MC is a rigorous way to sample quantum mechanical partition function, by linking many identical systems in a closed loop with springs $\propto \hbar/T$, and then do plain classical MC sampling. I am not sure that the extension of MC to MD yields the correct dynamics, although the quantum partition function *is* exactly reproduced. This method looks hopeful because it has a clear picture and is not hard to implement. Furthermore, I think the Wigner-Kirkwood expansion can be derived as a result of this approach.

Quasi-Momentum Relaxation Method One may think of our low-temperature trouble as a terrible complication; but the establishment of phonon hydrodynamics may also be a great simplification as in the theory of fluids, once we have means to deal with them in a fundamental way. For example, the following hydrodynamics

⁴There is a close analogy between a flexible water model and a quantum solid, and we have unfortunately met both.

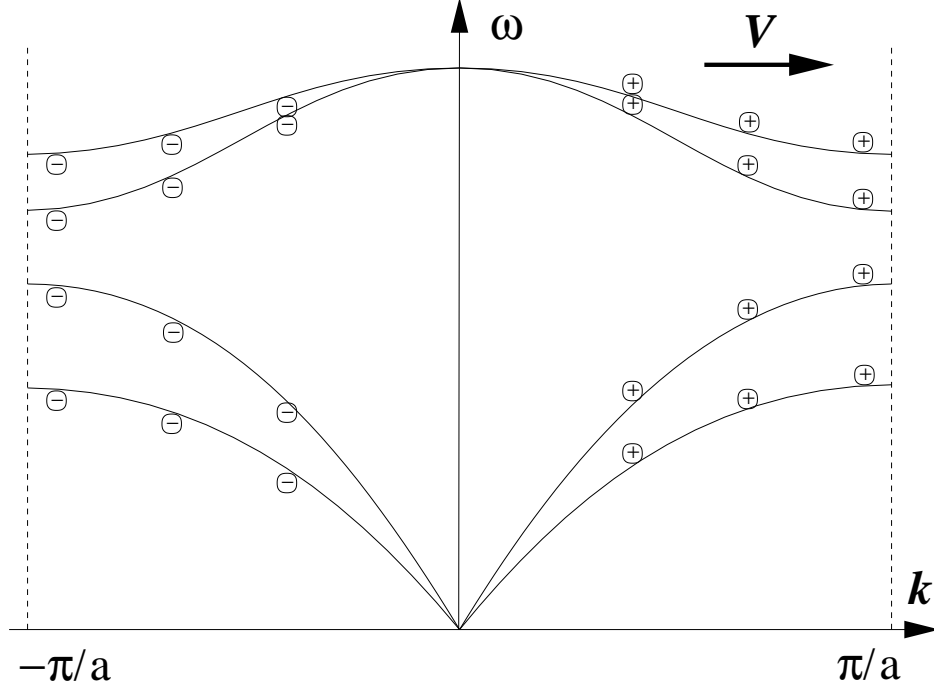


Figure D-7: Schematics of a collective deformation mode (D.73) in phonon occupation. \pm means increase or decrease from its global equilibrium distribution.

equation [59],

$$\frac{d\mathbf{P}}{dt} + \frac{TS^2}{\kappa p} \mathbf{P} = 0, \quad \mathbf{P} = p\mathbf{V}, \quad (\text{D.72})$$

for a spatially homogeneous system may be used to calculate κ directly, where S and p are the entropy and “mass density” of the phonon system, both of which have explicit expressions. What we need is a numerical “lab” in which $\mathbf{V}(0)$ can be assigned and $d\mathbf{V}/dt$ measured, and this lab must be quantum mechanical (at least for a short while), by which we mean the correct quantum mechanical evolution of \mathbf{V} must be reproduced. This is achievable by a simple equivalence rule and a specially conditioned *classical* MD system.

In above I described the critical differences between classical and quantized phonon *excitation amplitudes* at low temperatures, and why that leads to exponentially rare occurrence of the Umklapp processes and the establishment of local “drifted equilibrium”

$$N_{\mathbf{k}j} \approx N_{BE}(\omega - \mathbf{k} \cdot \mathbf{V}) \quad (+\Delta_2 N, \dots), \quad (\text{D.73})$$

by the more frequent Normal processes. One can derive, by τ_N/τ_U expansion, homologous to the Chapman-Enskog development, a set of phonon hydrodynamics equations ([59] pp. 138) which looks much simpler than the Boltzmann equation but are exact⁵. A simplified version is (D.72) ([59] pp.137), which describes the temporal relaxation of the total quasi-momentum, or “center of mass” of a spatially homogeneous phonon distribution, to zero due to U -processes. Its relaxation time τ_κ ($\sim \tau_U$) is thus directly related to the thermal conductivity by

$$\kappa = \frac{TS^2}{p}\tau_\kappa, \quad (\text{D.74})$$

where

$$S = \frac{k_B}{\Omega} \sum_{\mathbf{k}j} (N_{\mathbf{k}j} + 1) \log(N_{\mathbf{k}j} + 1) - N_{\mathbf{k}j} \log(N_{\mathbf{k}j}) \quad (\text{D.75})$$

is the entropy density, and

$$p = \frac{\hbar^2}{3\Omega k_B T} \sum_{\mathbf{k}j} |\mathbf{k}|^2 N_{\mathbf{k}j} (1 + N_{\mathbf{k}j}) \quad (\text{D.76})$$

is the “mass density” of the phonon system, relating \mathbf{V} to the total quasi-momentum density

$$\mathbf{P} = \sum_{\mathbf{k}j} \hbar \mathbf{k} N_{\mathbf{k}j} \quad (\text{D.77})$$

as

$$\mathbf{P} = p\mathbf{V} + \mathcal{O}(\mathbf{V}^2). \quad (\text{D.78})$$

Please note that this relation is exact as long as phonon hydrodynamics holds, unlike the well-used expression

$$\kappa = \sum_{\mathbf{k}j} C_V(\mathbf{k}j) |\mathbf{v}_G(\mathbf{k}j)|^2 \tau_{\mathbf{k}j} / 3, \quad (\text{D.79})$$

that comes by the single-relaxation time approximation, which represents a physical

⁵They are on the same footing as the Navier-Stokes equations, so as “exact” as the Navier-Stokes equations are “exact”.

picture of “broken rank” of the phonon system which is only valid at high temperatures. However, there is a close symmetry between the exact (D.74) and the empirical (D.79) which we shall heavily exploit later on.

The big surprise is that the crux of the matter: the relaxation of the total quasi-momentum by (D.72), whose origin is purely quantum physics, can be faithfully investigated by classical molecular dynamics.

The bridge is phonon Boltzmann equation, quantum and classical. It is my feeling that the full quantum *dynamics*, as described by the Schroedinger equation, cannot be simulated in a fool-proof manner as the classical world by MD, where if one needs something and computer is available, he can just blindly go through the procedure and get whatever he needs⁶. In this case, we have to learn about the specific problem, whose main theoretical tool is the quantum phonon Boltzmann equation, based on three-phonon scattering [61]. It is the unique symmetry of the phonon Boltzmann equation that leads to a simplified, “semi-classical” approach.

We are going to study the relaxation of \mathbf{V} in $N_{BE}(\omega - \mathbf{k} \cdot \mathbf{V})$ at low T due to phonon collisions, in the absence of spatial gradients such as ∇T , so there is no streaming term and the full equation reads

$$\begin{aligned}
\frac{\partial \langle N_{\mathbf{k}j} \rangle}{\partial t} &= \left. \frac{\partial \langle N_{\mathbf{k}j} \rangle}{\partial t} \right|_{\text{collision}} = I_N[N] + I_U[N] = \\
&\sum_{j'} \int \frac{d\mathbf{k}'}{8\pi^3} \left[\sum_{j''} \beta_{jj'j''}(\mathbf{k}, \mathbf{k}', -\mathbf{k}'') \delta(\omega'' - \omega - \omega') \right. \\
&\langle N''(N' + 1)(N + 1) - (N'' + 1)N'N \rangle + \\
&\frac{1}{2} \sum_{j'''} \beta_{jj'j'''}(\mathbf{k}', \mathbf{k}''', -\mathbf{k}) \delta(\omega - \omega' - \omega''') \\
&\left. \langle (N + 1)N'N''' - N(N' + 1)(N''' + 1) \rangle \right]. \tag{D.80}
\end{aligned}$$

⁶That is not true if complexity of the real problem is involved, but let me just naively call that a “computer time” problem.

following [59] pp. 55, (6.15), where

$$\beta_{j_1 j_2 j_3}(\mathbf{k}_1, \mathbf{k}_2, \mathbf{k}_3) = \frac{\pi \hbar}{4 \rho \omega_1 \omega_2 \omega_3 (\rho \Omega)^2} \times \left| \sum_{\mathbf{n}_1 \mathbf{n}_2 \mathbf{n}_3} \sum_{\gamma_1 \gamma_2 \gamma_3} B_{\gamma_1 \gamma_2 \gamma_3}^{\mathbf{n}_1 \mathbf{n}_2 \mathbf{n}_3} e_{\gamma_1}^{\mathbf{k}_1 j_1} e_{\gamma_2}^{\mathbf{k}_2 j_2} e_{\gamma_3}^{\mathbf{k}_3 j_3} \exp [i(\mathbf{k}_1 \cdot \mathbf{a}_{\mathbf{n}_1} + \mathbf{k}_2 \cdot \mathbf{a}_{\mathbf{n}_2} + \mathbf{k}_3 \cdot \mathbf{a}_{\mathbf{n}_3})] \right|^2 \quad (\text{D.81})$$

and $B_{\gamma_1 \gamma_2 \gamma_3}^{\mathbf{n}_1 \mathbf{n}_2 \mathbf{n}_3}$ are the cubic nonlinear coefficients of the potential,

$$\mathcal{U}_3 = \frac{1}{6} \sum_{\mathbf{n}_1 \mathbf{n}_2 \mathbf{n}_3} \sum_{\gamma_1 \gamma_2 \gamma_3} B_{\gamma_1 \gamma_2 \gamma_3}^{\mathbf{n}_1 \mathbf{n}_2 \mathbf{n}_3} u_{\mathbf{n}_1 \gamma_1} u_{\mathbf{n}_2 \gamma_2} u_{\mathbf{n}_3 \gamma_3}, \quad (\text{D.82})$$

as defined in [59] (6.3), (6.5) and (6.10).

The idea is that although we use (D.80) theoretically, practically we do not want to deal with $\beta_{jj'j''}(\mathbf{k}, \mathbf{k}', \mathbf{k}'')$'s, which are hard to calculate, hard to store, and RHS integral of (D.80) with δ -functions are hard to evaluate. The next order, quartic terms will be even more complicated. We want to realize (D.80) by doing a real MD simulation using the full interatomic potential, from which the $\beta_{jj'j''}(\mathbf{k}, \mathbf{k}', \mathbf{k}'')$'s are derived.

However, although the $\beta_{jj'j''}(\mathbf{k}, \mathbf{k}', \mathbf{k}'')$ coefficients in (D.80) are inherited exactly in a classical MD simulation, (D.80) itself, which is derived from Fermi's Golden Rule in quantum perturbation theory, does not. In fact the +1 factors after N' , N , etc. are the unique property of boson operators. How can that be inherited by a classical simulation?

To show the symmetry of (D.80), let me concentrate on the first term (second term follows identically) of the collisional integral and omit all inconsequential symbols, and write it as

$$\begin{aligned} \frac{\partial \langle N \rangle}{\partial t} &= \hbar \langle N''(N' + 1)(N + 1) - (N'' + 1)N'N \rangle \delta(\omega'' - \omega - \omega') + \dots \\ &= \hbar \langle N''N' + N''N + N'' - N'N \rangle \delta(\omega'' - \omega - \omega') + \dots \end{aligned} \quad (\text{D.83})$$

One can readily check that if

$$1 + N^{-1} = \exp(\text{const} \cdot \omega) \equiv \exp\left(\frac{\omega}{k_B T}\right) \quad (\text{D.84})$$

then RHS of (D.83) vanishes identically. So (D.84) is in fact the necessary and sufficient condition for the establishment of equilibrium Bose-Einstein distribution⁷.

The corresponding Boltzmann equation in a fictitious, classical lattice vibrational system can be derived purely based on classical mechanics. However a much simpler way is to let $\hbar \rightarrow 0$ in (D.80) while one keeps the energy E fixed,

$$\hbar \rightarrow 0, \quad N \rightarrow \infty, \quad N\hbar \rightarrow M \equiv \frac{E}{\omega} = \left(N + \frac{1}{2}\right)\hbar \text{ fixed.} \quad (\text{D.85})$$

Then (D.83) becomes, after multiplying both sides by \hbar ,

$$\frac{\partial \langle \hbar N \rangle}{\partial t} = \left\langle (\hbar N'')(\hbar N') + (\hbar N'')(\hbar N) + \hbar^2 N'' - (\hbar N')(\hbar N) \right\rangle \delta(\omega'' - \omega - \omega') + \dots \quad (\text{D.86})$$

Thus in the classical limit the third term $\hbar^2 N''$ vanishes and one obtains

$$\frac{\partial \langle M \rangle}{\partial t} = \langle M''M' + M''M - M'M \rangle \delta(\omega'' - \omega - \omega') + \dots, \quad (\text{D.87})$$

where $M \equiv E/\omega$ can be related to the classical vibrational amplitude. Eqn (D.87) is then the Boltzmann equation of a fictitious classical vibrational system, which MD simulation realizes in full. One can easily check that the necessary and sufficient condition for RHS of (D.87) to vanish is

$$E = \text{const} \equiv k_B T, \quad M = \frac{k_B T}{\omega}, \quad (\text{D.88})$$

re-confirming the classical equi-partition theorem.

⁷For the same reason, if only N -process is present, local equilibrium $N_{BE}(\omega - \mathbf{k} \cdot \mathbf{V})$ can be established because we have an additional conserved quantity \mathbf{k} for *every* Normal collision. This development is entirely analogous to the gas Boltzmann equation and $e^{-m|\mathbf{v} - \bar{\mathbf{v}}(\mathbf{r})|^2/2k_B T}$. In a sense, the U -process is the only thing new, as a crystal is discrete while space-time is continuous.

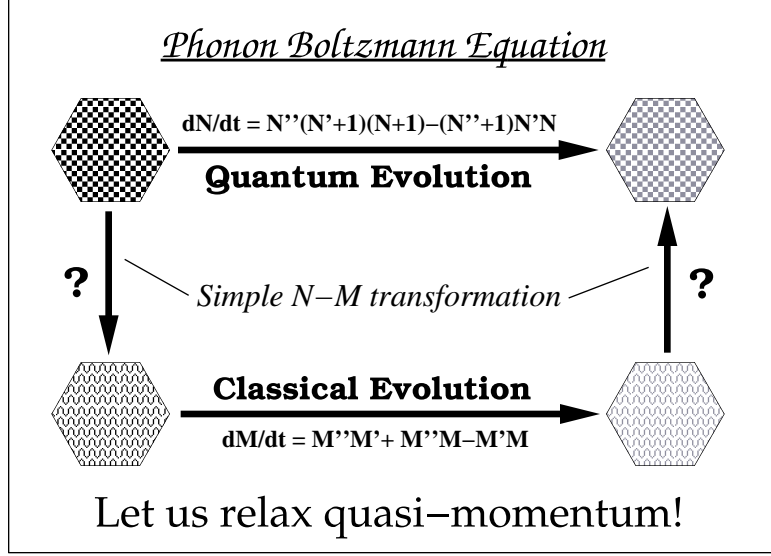


Figure D-8: Schematics of quantum \leftrightarrow classical partial equivalence transformation.

Since we have (D.87) at our **full** disposal (through MD), can we learn something about the **real** equation (D.80) by studying a fictitious classical MD system? More specifically, we need an equivalence transformation between N and M that guarantees the evolution of certain properties, in this case \mathbf{V} , is exactly reproduced by a classical simulation, at least *for a short while*. The idea is sketched in Fig. D-8.

Despite their seemingly small differences, (D.83) and (D.87) are in fact quite different, because N at low temperatures is exponentially *small*. As a consequence of keeping the third term N'' , the quantum (D.83) has

$$N_{\mathbf{k}j} = \frac{1}{e^{\hbar\omega_{\mathbf{k}j}/k_B T} - 1} \quad (\text{D.89})$$

as its zero-mode, while the classical (D.87) has

$$M_{\mathbf{k}j} = \frac{k_B T}{\omega} \quad (\text{D.90})$$

as its zero-mode (see Fig. D-3). A complete one-to-one mapping between (D.83) evolution and (D.87) evolution seems impossible.

However, let us just think about what it would take to get there anyway, keeping in

mind the physical picture of phonon scattering. Phonons scatter because of potential nonlinearities. How much potential nonlinearity an atom sees clearly depend on how far it leaves its origin, or $\langle \Delta x^2 \rangle$, which both *classically* and *quantum mechanically* can be shown to be related to the total vibrational energy as

$$\langle \Delta x^2 \rangle = \frac{E}{m\omega^2}. \quad (\text{D.91})$$

The harmonic approximation would be very good if $\langle \Delta x^2 \rangle$ is very small, hence phonons collide less frequently and the thermal conductivity is high, or vice versa. That is why $T \downarrow, \kappa \uparrow$. However, there is a clear distinction between quantum phonon total energy and classical phonon total energy at a given T , as shown in Fig. D-3. The most extreme case is $T = 0\text{K}$: a classical vibrational system would just sit at the potential well bottom, and any infinitesimal excitation leads to purely harmonic oscillations; but a quantum phonon at $T = 0\text{K}$ still has $k_B T/2$ total energy, *still* has a non-negligible $\langle \Delta x^2 \rangle$, and so is *still* sampling potential nonlinearities. Thus we see that the only chance we have to mimic the quantum behavior is to let the classical phonons having the same total energy as its corresponding quantum phonon; otherwise a quantum phonon will be sampling parts of the interatomic potential where the classical phonon does not have enough energy to access; and then how could it reproduce the thermal conductivity correctly!

This is not a brand-new idea. Lee *et al*'s temperature re-scaling scheme is an attempt to treat the above problem. However, they equate the total energy of a phonon *system* instead of individual phonons, with the equi-partition theorem still holding internally in the MD simulation. One can understand that this definitely will lead to wrong thermal conductivity at low T , as indeed we discovered. The entire fact about the role of U -process and the existence of phonon hydrodynamics depends on the highly unequal distribution of “wealth” in the BZ “population”, not the “total wealth”.

But, we just showed that the zero-mode of (D.87) can only be $E = k_B T$, so one cannot have $(N_{BE}(\omega) + 1/2)\hbar\omega$ as the *equilibrium* energy distribution in *any* classical

simulation. Does it mean that we have met the dead-end?

The answer is no: it is OK to use a non-equilibrium distribution as the *initial condition* of a classical MD simulation as long as one is concerned with the correct properties, and only for a short time. Fortunately I can prove that for \mathbf{V} using (D.83) and (D.87).

Let the NM partial-equivalence transformation be

$$M = \alpha(\tilde{N} + \frac{1}{2})\hbar, \quad (\text{D.92})$$

where \hbar is the Planck constant of our quantum world and α is a constant. Plug this into (D.87), we get, after dividing both sides by $\alpha^2\hbar$,

$$\begin{aligned} & \frac{\partial \langle \tilde{N} \rangle}{\partial(\alpha t)} \\ = & \hbar \left\langle (\tilde{N}'' + \frac{1}{2})(\tilde{N}' + \frac{1}{2}) + (\tilde{N}'' + \frac{1}{2})(\tilde{N} + \frac{1}{2}) - (\tilde{N}' + \frac{1}{2})(\tilde{N} + \frac{1}{2}) \right\rangle \delta(\omega'' - \omega - \omega') \\ & + \dots \\ = & \hbar \left\langle \tilde{N}''\tilde{N}' + \frac{\tilde{N}''}{2} + \frac{\tilde{N}'}{2} + \frac{1}{4} + \tilde{N}''\tilde{N} + \frac{\tilde{N}''}{2} + \frac{\tilde{N}}{2} + \frac{1}{4} - \tilde{N}'\tilde{N} - \frac{\tilde{N}'}{2} - \frac{\tilde{N}}{2} - \frac{1}{4} \right\rangle \\ & + \dots \\ = & \hbar \left\langle \tilde{N}''\tilde{N}' + \tilde{N}''\tilde{N} + \tilde{N}'' - \tilde{N}'\tilde{N} + \frac{1}{4} \right\rangle \delta(\omega'' - \omega - \omega') + \dots \end{aligned} \quad (\text{D.93})$$

For the moment let $\alpha = 1$. Comparing (D.93) with (D.83), we see that we recover back the lost N'' term, which is the critical difference between the classical (D.87) and quantum (D.83), and N is much greater than the N^2 terms at low temperatures! But we also get an additional $1/4$ factor; so we cannot achieve complete victory in this mapping, since \tilde{N} still have a different time-evolution than N in (D.87).

However since it is a constant, the $1/4$ term does not contribute to the evolution of \mathbf{V} in the short time-window when $\tilde{N} \approx N$, because \mathbf{V} is an odd moment of the occupation distribution. The way to see it is to imagine $\tilde{N} = 0$ for all \mathbf{k} 's in (D.93), meaning initially in a classical simulation we only give each vibrational mode its zero-point energy $\hbar\omega/2$. Then only the $1/4$ term operates in (D.93); but clearly the “center

of mass” of the distribution will not change with time but stays at $\mathbf{V} = 0$!⁸ What does happen due to the $1/4$ term is that the quantum zero-point energy distribution $E_{\mathbf{k}j} = \hbar\omega_{\mathbf{k}j}/2$ will be transformed into a classical profile $E_{\mathbf{k}j} = k_B T'$ as the simulation is carried out for a long enough time, i.e., the shape of E will change from a bowl to a flat surface, but the “center of mass” will not change because of it. What does relax the “center of mass” is the Umklapp part of the $\tilde{N}''\tilde{N}' + \tilde{N}''\tilde{N} + \tilde{N}'' - \tilde{N}'\tilde{N}$ terms in (D.93), whose rate the classical simulation reproduces exactly, as long as \tilde{N} stays close to N ; in this case N is of the known form $N_{BE}(\omega - \mathbf{k} \cdot \mathbf{V})$, due to the *simplifications* of phonon hydrodynamics.

Thus, eqns. (D.72), (D.75), (D.76), (D.77) and

$$E_{\mathbf{k}j}(0) = (N_{BE}(\omega_{\mathbf{k}j} - \mathbf{k} \cdot \mathbf{V}) + 1/2) \hbar\omega_{\mathbf{k}j} \quad (\text{D.94})$$

specifies an MD scheme to calculate the low-temperature lattice thermal conductivity. Detailed prescriptions are,

1. Evaluate the force constants numerically or analytically at the equilibrium volume of the crystal structure at a given temperature.
2. Choose an MD simulation box with PBC and find out the \mathbf{k} -points of the unit cell that are compatible with the supercell PBC. Identify those on the BZ boundary which needs special treatment.
3. Assemble the dynamical matrix $\mathbf{D}(\mathbf{k})$ for all \mathbf{k} 's and diagonalize them. Save $\omega_{\mathbf{k}j}$ and eigenvectors $\mathbf{e}_{\mathbf{k}j}$. Calculate the group velocities \mathbf{v}_G using Hellman-Feymann theorem.
4. Calculate S and p using (D.75) and (D.76). Also, calculate the total zero-point energy, Debye-Waller factor $\langle \Delta x^2 \rangle$, C_V . Estimate the sound speeds; infer the Debye temperature and shear/bulk moduli.

⁸This can be shown rigorously using the time-reversal symmetry of $\beta_{jj'j''}(\mathbf{k}, \mathbf{k}', \mathbf{k}'')$, but it suffices here to just see the picture.

5. Choose an initial $\mathbf{V}(0)$, usually a small percentage of the sound speed. Its direction can be random if κ is isotropic.
6. Assign particle $\{\mathbf{x}_i, \mathbf{p}_i\}$ in the supercell all vibrational modes with energy (D.94) and random phases. BZ boundary \mathbf{k} -points are treated as $1/2 \mathbf{k}$ and $1/2 -\mathbf{k}$.
7. Do *NEV* MD simulation on the particle system, in essence letting the phonons collide according to (D.93), and \mathbf{V} is relaxed by the U -processes among them.
8. At intervals, do normal mode analysis on $\{\mathbf{x}_i, \mathbf{p}_i\}$ to get $N_{\mathbf{k}j}(t)$. Calculate $\mathbf{P}(t)$ using (D.77).
9. Monitor $\langle N_{\mathbf{k}j}(t) \rangle$. When they change *significantly* from the assigned distribution, stop the MD simulation. Choose a new $\mathbf{V}(0)$ and repeat the experiment. The lower T is, the shorter time-window one has, and the more experiments one needs to do in order to get rid of the fluctuations⁹.
10. Least-square fit $\langle \mathbf{P}(t) \rangle$ to determine the quasi-momentum relaxation time constant τ_κ and its statistical error. Use hydrodynamic formula (D.74) to evaluate κ .

Now, let us consider $\alpha \neq 1$ in (D.92), which seems devoid of any “physical” meaning. But the algebra carries through and one can easily show that, instead of (D.72),

$$\frac{d\mathbf{P}}{d(\alpha t)} + \frac{TS^2}{\kappa p} \mathbf{P} = 0, \quad (\text{D.95})$$

i.e., the relaxation of \mathbf{P} in the classical system is *accelerated* by a factor of α in comparison with the quantum system, since we pump more energy into it. α can be thought of as the scaling factor between “quantum time” and “classical time”, which exploits the x^3 scaling of the leading cubic nonlinearity. This reminds us the fictitious nature of our MD “lab”, whose only connection with the quantum reality at low T is through the phonon Boltzmann equation. The partial-equivalence transformation

⁹After all, the Boltzmann equation is a coarse-grained description, and is for $\langle N_{\mathbf{k}j}(t) \rangle$ instead of $N_{\mathbf{k}j}(t)$.

(D.92), $\alpha = 1$ or not, is only a physically inspired **algebraic** transformation, which should not be attached too much meaning or to be used to predict other properties.

Depending on whether there is “too little” or “too much” nonlinearity in the system at a given temperature, $\alpha > 1$ or $\alpha < 1$ can be used to enhance the computational efficiency, leveraging between quantum real time and classical simulation time.

As one can see, the scheme is already of considerable complexity; yet compared with explicitly tabulating $\beta_{jj'j''}(\mathbf{k}, \mathbf{k}', \mathbf{k}'')$'s and solving the integral equation (D.80), it is still much simpler, both conceptually and computationally. As long as it can yield satisfactory results with the same order of computational cost as a) the explicit Boltzmann equation solver, b) the Green-Kubo method, this technique could prove superior since it can be fully automated. The current program only requires the user to provide interatomic force routine.

Successful Extension to High Temperature

At high temperature, the N -process no longer dominates over the U -process, and one can not expect the steady-state phonon distribution to be in drifted equilibrium form, (D.73). The phonons behave more “individualistically”, each is scattered more “independently” or “stochastically” rather than as a collective whole specified by a single parameter \mathbf{V} . This is the basis of the relaxation time approximation

$$\left. \frac{\partial \langle N_{\mathbf{k}j} \rangle}{\partial t} \right|_{\text{collision}} = I_N[N] + I_U[N] \approx -\frac{\Delta N_{\mathbf{k}j}}{\tau_{\mathbf{k}j}}, \quad (\text{D.96})$$

from which the well-known formula

$$\kappa = \sum_{\mathbf{k}j} C_V(\mathbf{k}j) |\mathbf{v}_G(\mathbf{k}j)|^2 \tau_{\mathbf{k}j} / 3 \quad (\text{D.97})$$

is derived.

Let me rewrite (D.97) as

$$\kappa = W \bar{\tau}, \quad (\text{D.98})$$

where

$$W \equiv \sum_{\mathbf{k}j} C_V(\mathbf{k}j) |\mathbf{v}_G(\mathbf{k}j)|^2 / 3, \quad (\text{D.99})$$

and

$$\bar{\tau} \equiv \left(\sum_{\mathbf{k}j} C_V(\mathbf{k}j) |\mathbf{v}_G(\mathbf{k}j)|^2 \tau_{\mathbf{k}j} \right) / \left(\sum_{\mathbf{k}j} C_V(\mathbf{k}j) |\mathbf{v}_G(\mathbf{k}j)|^2 \right) \quad (\text{D.100})$$

is a “properly averaged” relaxation time. Although (D.98) is essentially a high temperature formula, it is nevertheless interesting to compare with (D.74), since they are quite alike in that both are some prefactor multiplied by a relaxation time. As TS^2/p must have the same dimension as W , how do they compare with each other in magnitude at high and low T ?

Consider the entropy density S first. Since

$$C_V \equiv T \frac{\partial S}{\partial T}, \quad (\text{D.101})$$

and it is well-known that

$$C_V \propto T^3 \text{ as } T \rightarrow 0, \quad (\text{D.102})$$

there must be

$$S \rightarrow \frac{C_V}{3} \text{ at } T \rightarrow 0. \quad (\text{D.103})$$

Also, since C_V approaches a constant at high T , there is

$$S \sim \log T \text{ at } T \rightarrow \infty. \quad (\text{D.104})$$

How about the phonon “mass density” p ? For systems with isotropic κ ,

$$p \equiv \frac{\hbar^2}{3\Omega k_B T} \sum_{\mathbf{k}j} |\mathbf{k}|^2 N_{\mathbf{k}j} (1 + N_{\mathbf{k}j}).$$

At low enough T , $N_{\mathbf{k}j}$ for finite $|\mathbf{k}|$ is exponentially small, as illustrated in Fig. D-5, and only those modes within the “thermal activation circle” are excited. They are long-wave acoustic phonons in the limit, which then have approximately linear

dispersion with \mathbf{k}^{10} ,

$$\omega_{\mathbf{k}j} \simeq c|\mathbf{k}|, \quad |\mathbf{v}_G| \equiv \left| \frac{d\omega_{\mathbf{k}j}}{d\mathbf{k}} \right| \simeq c, \quad (\text{D.105})$$

and they are the main contributors to p . Thus

$$p \simeq \frac{\hbar^2}{3\Omega k_B T c^2} \sum_{\mathbf{k}j} \omega_{\mathbf{k}j}^2 N_{\mathbf{k}j} (1 + N_{\mathbf{k}j}). \quad (\text{D.106})$$

But RHS of (D.106) is proportional to C_V ! In fact,

$$C_V \equiv \frac{1}{\Omega} \sum_{\mathbf{k}j} \frac{\exp(\frac{\hbar\omega_{\mathbf{k}j}}{k_B T}) \frac{\hbar^2 \omega_{\mathbf{k}j}^2}{k_B T^2}}{\left(\exp(\frac{\hbar\omega_{\mathbf{k}j}}{k_B T}) - 1 \right)^2} = \frac{\hbar^2}{\Omega k_B T^2} \sum_{\mathbf{k}j} \omega_{\mathbf{k}j}^2 N_{\mathbf{k}j} (1 + N_{\mathbf{k}j}). \quad (\text{D.107})$$

So,

$$p \simeq \frac{TC_V}{3c^2} \quad (\text{D.108})$$

in the low temperature limit, which, combined with (D.103), gives

$$\frac{TS^2}{p} \rightarrow \frac{T(C_V/3)^2}{(TC_V/3c^2)} = \frac{C_V c^2}{3} \simeq W, \quad \text{as } T \rightarrow 0, \quad (\text{D.109})$$

without missing a single coefficient!

So there is a remarkable symmetry between (D.74) and (D.98) in that the prefactors before the relaxation time, TS^2/p and W , approach each other asymptotically at low T . This prediction had been explicitly verified using the definitions of TS^2/p and W , and the numerically calculated $\omega_{\mathbf{k}j}$ and $\mathbf{v}_G(\mathbf{k}j)$'s of Si perfect crystal with $11 \times 11 \times 11$ \mathbf{k} -sampling (2662 atom MD supercell), and the agreement is within 10% below 70K.

Now let us think about why and how we should extend the previous methodology to high temperature. It comes rather as a necessity than as an additional improvement, since TS^2/p rises too quickly even at a moderate T . As I found out, the ideal phonon hydrodynamics regime is possibly below 100K for Si, which is too narrow

¹⁰Actually c should be a matrix, with $\det |\omega^2 \mathbf{I} - \mathbf{k} \underline{\underline{c}}^2 \mathbf{k}| = 0$, but that subtlety has a negligible effect.

for our method to be practically useful. The vast intermediate region between 100 and 400K are of mixed character, neither purely low T (hydrodynamics) or high T (classical) behavior. There, the prefactor TS^2/p is already too large for (D.74) to be correct, and even the temperature dependence becomes wrong. One can show that TS^2/p blows up as $(\log T)^2$ while W approaches a constant at $T \rightarrow \infty$, though they agree with each other asymptotically at low T , as T^3 . This information, combined with the fact that (D.98) is a high temperature formula, suggest that we use a modified formula

$$\kappa = W\tau_\kappa, \quad (\text{D.110})$$

that is of considerable validity in both low and high temperature regime and smoothly link the two behaviors. Here τ_κ is the quasi-momentum relaxation time constant defined by (D.72) in an MD relaxation experiment, except now we *also* do it at high temperature. (D.110) is equivalent to (D.74) at low T since W agrees with TS^2/p then, but it also makes sense at high T because

$$\tau_\kappa \sim \tau_U \simeq \tau_N \simeq \bar{\tau} \text{ at high } T, \quad (\text{D.111})$$

where $\bar{\tau}$ is the “properly averaged” phonon relaxation time in (D.100). The rationale at high temperature is that since individual phonon relaxation times $\tau_{\mathbf{k}j}$ are probably too many to be calculable, and we only need a “proper average” of them anyway, why don’t we just pick a collective mode whose relaxation rate at high T reflects the average rate of phonon relaxations? And what collective mode is simpler than a displaced center of mass? That is, we acknowledge the $\mathbf{V}(t)$ relaxation suffers a mechanism change from low T to high T , where at low T $N_{\mathbf{k}j}$ stays close to drifted-equilibrium form (D.73) and $\mathbf{V}(t)$ relaxation is a real physical process described by phonon hydrodynamics; but at high T everything is chaotic and $\mathbf{V}(t)$ relaxation does not even describe a real process because the steady-state $N_{\mathbf{k}j}$ distribution is no longer (D.73), we nevertheless pick a deformation mode of the equilibrium distribution which is the most straightforward and do a fictitious relaxation of it in an MD simulation. It is like in order to determine the “average” crawl speed of ants, we put 10,000 of

them in a bucket, left side slightly more than the right, and measure how the surface levels off. Because (D.97) is itself only an approximation, and $\tau_N \sim \tau_U$, (D.110) does not do gross injustice to (D.97), and we expect it to provide a good estimate at high T . In fact it works perfectly for Si perfect crystal up to 1200K, using the Tersoff potential.

Once we have both limits right, the intermediate temperature region should be satisfactory because (D.110) is smooth.

Appendix E

Spectral Method in Thermal Conductivity Calculation

Introduction

We have calculated the thermal conductivity tensor $\underline{\kappa}$ of solid SiC with and without defects [80] using the Green-Kubo formula [50, 51, 52]

$$\underline{\kappa} = \frac{1}{k_{\text{B}}T^2\Omega} \int_0^\infty d\tau \langle \mathbf{J}^q(0) \mathbf{J}^q(\tau) \rangle, \quad (\text{E.1})$$

where \mathbf{J}^q is the instantaneous heat current of the system, provided by a molecular dynamics simulation run [65, 149, 66, 67]. Details about the interatomic potential model, simulation method and results for this material can be found at the above reference. Our main concern in this paper is one technical aspect which is often not fully treated by various literatures, that is how one evaluates $\underline{\kappa}$ once the MD simulation finishes and a finite length of the $\mathbf{J}^q(t)$ data has been recorded.

The problem is not critical for thermal conductivity calculations in liquids and non-crystalline solids simply because the heat current correlation function

$$\underline{g}(\tau) = \frac{1}{k_{\text{B}}T^2\Omega} \langle \mathbf{J}^q(0) \mathbf{J}^q(\tau) \rangle \quad (\text{E.2})$$

has a rather short correlation time, as the heat carriers quickly get scattered. Thus it is a relatively quick calculation which does not require very long simulation runs to get convergent results, and the correlation function can even be evaluated on the fly. However, a perfect crystalline solid material usually has a much longer correlation time (by one or two decades), and thus a much higher thermal conductivity ¹.

In the case of crystalline β -SiC, even at the high temperature of 1500K, to get a barely convergent result of the correlation integral requires a MD run longer than 2 million timesteps (800 *ps*). Further taking into the account that

1. To get realistic results, an interatomic potential of some sophistication, in our case the Tersoff three-body potential [162, 163], must be used for this industrial material.
2. The calculation of thermal conductivity depends sensitively on the simulation cell size, due to the intrinsic mechanism of three-phonon scattering. In our work we find that a 216-particle cell is the minimum, while 512 or 1000 particle cells are recommended.
3. At low temperatures, longer simulation runs need to be taken because the correlation time gets even longer. For instance, at 500K a minimally convergent run is 8 million timesteps, or approximately 4000 *ps*.
4. We find that the result of a simulation run is sensitively dependent on the *initial* particle velocity (phonon density) distribution of the run, because when the crystal has a high thermal conductivity the existent phonons are not easily scattered; the system will retain memory of the initial condition for a long time, staying in a limited region of phase space and the ergotic hypothesis not fully coming into effect at least for reasonable run lengths. For this reason, we need to do several independent runs starting from different initial conditions, and average over the respective correlation functions.

¹ $\underline{\underline{g}}(0)$ can be thought of as a static thermodynamic susceptibility which is usually not as sensitively dependent on the material state.

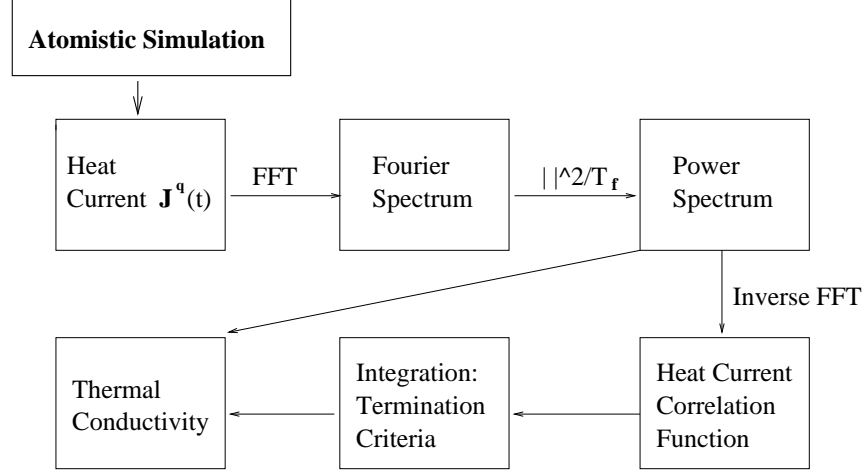


Figure E-1: Flowchart of the spectral method to calculate the thermal conductivity.

the necessary computational effort is quite formidable. Kitagawa *et al* [66] have reported similar constraints in calculating the thermal conductivity of AlN. Because of this, the treatment and analysis of the raw data, which sometimes is barely sufficient, becomes an important issue.

The computation of $\underline{g}(\tau)$ itself can be quite expensive. For instance, in the above case at $T = 1500\text{K}$ and $N = 2 \times 10^6$ timesteps “minimal-run”, the correlation in $\underline{g}(\tau)$ persists for $\tau < 20\text{ ps}$, which corresponds to $K = 60,000$ timesteps. If one tries to directly compute $\underline{g}(\tau)$ by brute force averaging, he faces multiplication operations on the order of $NK = 10^{11}$, which means evaluating all tensorial components will take more than 2 hours if the subroutine runs at 100 Mflop/s. One can of course down-sample the data or decrease the number of time origins, but getting the raw data is even a more expensive process that one certainly does not want to waste any information here. Furthermore, one is not sure what the correlation time is beforehand, and wants to see the entire $\underline{g}(\tau)$.

The spectral method delivers more and is faster, by taking advantage of the Fast Fourier Transform algorithm [253]. The number of operations is $\mathcal{O}(N \log N)$ with a small prefactor on the order of 10. Because $\log N$ is always much smaller than K , it is faster than the brute force method. It does not waste any information residing in the raw data; and it also provides frequency space information.

A flowchart of the procedure is shown in Fig. E-1. Basically one takes the FFT

of the $\mathbf{J}^q(0 < t < T_f)$ data to get $\mathbf{J}^q(\omega)$, square it and divide by T_f to get the power spectrum $\underline{g}(\omega)$, and do an inverse FFT to get $\underline{g}(\tau)$. One can either directly read off the thermal conductivity by taking a limit of the power spectra

$$\underline{\kappa} = \lim_{\omega \rightarrow 0} \frac{1}{k_B T^2 \Omega} \frac{\mathbf{J}^q(\omega) \mathbf{J}^{q*}(\omega)}{2T_f},$$

or take the more cautious route of integrating $\underline{g}(\tau)$, whereas a termination of the integration is needed sooner or later due to finite data length. We shall propose two termination criteria which works for solid SiC, that minimizes human intervention, yet giving reasonable results.

A simple, analytically solvable model

$$a_i = a_{i-1} e^{-\frac{1}{L}} + R_i$$

is proposed, which illustrates most of the above issues and can be used to test the code, hopefully providing a handle for beginners.

Spectral Analysis

Consider a truncated function $f(t)$ which is finite from $t = 0$ to T_f , and 0 elsewhere, so it is absolutely integrable. Then

$$f(\omega) = \int_{-\infty}^{+\infty} f(t) \exp(i\omega t) dt, \quad (\text{E.3})$$

$$f(t) = \frac{1}{2\pi} \int_{-\infty}^{+\infty} f(\omega) \exp(-i\omega t) d\omega. \quad (\text{E.4})$$

Notice that the artificial truncation of $f(t)$ will come to affect $f(\omega)$ statistically only when ωT_f is comparable to unity. In order to rule out the arbitrariness and make sure that the information we get is intrinsic to the signal, we should take care not to use the spectrum between $0 < |\omega| < \pi/T_f$, which is of course a very small region because T_f is large, and will vanish as $T \rightarrow \infty$. Nevertheless, we cannot use $f(\omega)$ at ω equals absolute zero, because all our applications have finite T_f . We can only

use ω 's which are much greater than π/T_f but are still very small, as the limiting behavior of $w \rightarrow 0$.

The correlation function of $f(t)$ can be defined to be

$$g(\tau) = \frac{1}{T_f} \int_{-\infty}^{+\infty} f^*(t) f(t + \tau) dt. \quad (\text{E.5})$$

For $g(\tau)$ to behave well, there should be $\tau \ll T_f$. Let's define a maximum correlation length τ_{\max} above which $g(\tau)$ is negligible; thus $\tau_{\max} \ll T_f$.

From Eq. (E.4), (E.5), there is

$$\begin{aligned} g(\tau) &= \frac{1}{4\pi^2 T_f} \int_{-\infty}^{+\infty} d\omega \int_{-\infty}^{+\infty} d\omega' f^*(\omega) f(\omega') \exp(-i\omega' \tau) \\ &\quad \cdot \int_{-\infty}^{+\infty} \exp(i(\omega - \omega')t) dt \\ &= \frac{1}{4\pi^2 T_f} \int_{-\infty}^{+\infty} d\omega \int_{-\infty}^{+\infty} d\omega' f^*(\omega) f(\omega') \exp(-i\omega' \tau) \\ &\quad \cdot 2\pi \delta(\omega - \omega') \\ &= \frac{1}{2\pi T_f} \int_{-\infty}^{+\infty} d\omega |f(\omega)|^2 \exp(-i\omega \tau) \end{aligned} \quad (\text{E.6})$$

which means that the Fourier spectrum of $g(\tau)$ is just the *power spectrum* of the signal $f(t)$.

There is a frequently quoted result that the integral of $g(\tau)$ from 0 to $+\infty$ is just the power spectrum $|f(\omega)|^2/T_f$ taken at $\omega = 0$ and divided by 2 [149]. This needs some clarification, because if we put $\omega = 0$ in Eq. (E.3) directly, then

$$f(\omega = 0) = \int_{-\infty}^{+\infty} f(t) dt = \int_0^{T_f} f(t) dt, \quad (\text{E.7})$$

which is a random number of no physical significance.

This is not what we expect. To see what is wrong, let

$$A = \int_{-\tau_{\max}}^{\tau_{\max}} g(\tau) d\tau, \quad (\text{E.8})$$

then by Eq. (E.6),

$$\begin{aligned}
A &= \frac{1}{2\pi T_f} \int_{-\infty}^{+\infty} d\omega |f(\omega)|^2 \int_{-\tau_{\max}}^{\tau_{\max}} \exp(-i\omega\tau) d\tau \\
&= \frac{1}{2\pi T_f} \int_{-\infty}^{+\infty} d\omega |f(\omega)|^2 \frac{2 \sin(\omega\tau_{\max})}{\omega}.
\end{aligned} \tag{E.9}$$

Since T_f can be very large as we do long simulation runs, τ can also be allowed to be very large, *provided that* $\tau \ll T_f$. Thus

$$\frac{2 \sin(\omega\tau_{\max})}{\omega} \rightarrow 2\pi\delta(\omega) \tag{E.10}$$

as $\tau_{\max} \rightarrow +\infty$. Note that however, as we said before, we cannot really use the *absolute* $\omega = 0$ value of $f(\omega)$, but only its limit well above $1/T_f$, so the system is able to demonstrate its intrinsic behavior in Eq. (E.3) through several oscillations. Also, notice that the main peak of Eq. (E.10) vanishes at π/τ_{\max} , so we should pick

$$\frac{\pi}{T_f} \ll |\omega_0| < \frac{\pi}{\tau_{\max}} \tag{E.11}$$

such that $\omega_0 T_f \gg 1$, yet $\omega_0 \tau_{\max} < \pi$, and so

$$A \approx \frac{1}{T_f} \langle |f(\omega_0)|^2 \rangle \tag{E.12}$$

by Eq. (E.9), (E.10), where $\langle \rangle$ is taking the proper average over ω_0 's that satisfy Eq. (E.11). As both T_f and τ_{\max} goes to infinity, $\omega_0 \rightarrow 0$, which is the true meaning of “taking $\omega = 0$ ” in $|f(\omega)|^2/T_f$.

For equilibrium systems, $g(-\tau) = g^*(\tau)$. If the signal is real, then $g(\tau)$ is also real, and we can write

$$\int_0^{\tau_{\max}} g(\tau) d\tau \approx \frac{1}{2T_f} \langle |f(\omega_0)|^2 \rangle. \tag{E.13}$$

Discrete Implementation

Fast Fourier Transform is the discrete implementation of Eq. (E.3) and (E.4). Let

$$f_k = f((k-1)\Delta), \Delta = \frac{T_f}{N}, k = 1..N, \quad (\text{E.14})$$

then

$$\begin{aligned} F_n &= \sum_{k=1}^N f_k \exp\left(i \frac{2\pi(n-1)(k-1)}{N}\right), \\ f_k &= \frac{1}{N} \sum_{n=1}^N F_n \exp\left(-i \frac{2\pi(n-1)(k-1)}{N}\right). \end{aligned} \quad (\text{E.15})$$

Obviously, F_n corresponds to $\frac{1}{\Delta} f\left(\omega = \frac{2\pi(n-1)}{N\Delta}\right)$ when $\omega\Delta \ll 1$, i.e., when the sample frequency is much bigger than the frequency of interest. As a convention, F_0 is always set to zero after the Fast Fourier Transform by us, because it represents the heat current average during the simulation, which should be subtracted off from the signal.

Let us define

$$g_j = \frac{1}{N} \sum_{k=1}^N f_k^* f_{k+j-1}, \quad j = 1..N, \quad (\text{E.16})$$

where $f_{k+j-1 > N}$ is interpreted as $f_{k+j-1-N}$, and

$$\begin{aligned} G_n &= \sum_{j=1}^N g_j \exp\left(i \frac{2\pi(n-1)(j-1)}{N}\right) \\ &= \frac{1}{N} \sum_{j,k=1}^N f_k^* f_{k+j-1} \exp\left(i \frac{2\pi(n-1)(j-1)}{N}\right) \\ &= \frac{1}{N} |F_n|^2. \end{aligned} \quad (\text{E.17})$$

And so,

$$g_j = \frac{1}{N} \sum_{n=1}^N G_n \exp\left(-i \frac{2\pi(n-1)(j-1)}{N}\right). \quad (\text{E.18})$$

The idea is that we can calculate the correlation function by first FFT the original signal f_k , take the square module of it and divide by N , than inverse FFT back.

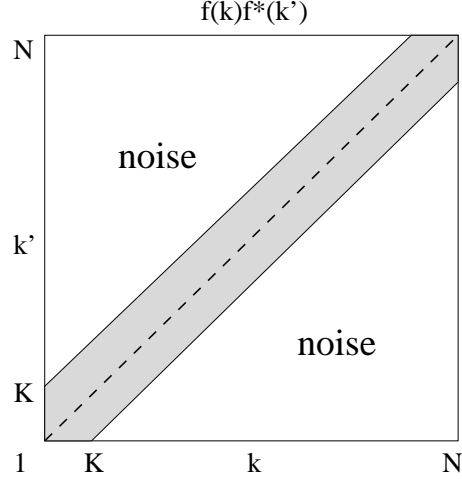


Figure E-2: Discrete power spectrum summation.

The discrete power spectrum summation

$$\frac{|F_n|^2}{N} = \frac{1}{N} \sum_{k,k'=1}^N f_k f_{k'}^* \exp \left(i \frac{2\pi(n-1)(k' - k)}{N} \right) \quad (\text{E.19})$$

is represented graphically in Fig. E-2. The discretized maximum correlation length is $K = N\tau_{\text{max}}/T_f$. The shaded region lies between $|k - k'| < K$, so $f_k, f_{k'}$ are correlated within. Outside the shaded region their products can be regarded as random noise, so passing through a wave with enough many oscillations in the range would filter them out, which then requires

$$\frac{2\pi n}{N} N = 2\pi n \gg 2\pi. \quad (\text{E.20})$$

We may also want to sum up the correlation $f_k f_{k'}^*$ inside the shaded region, which requires the phase factor $\exp(i2\pi(n-1)(k' - k)/N)$ in Eq. (E.19) to be approximately unity for $|k - k'| < K$. Thus if

$$\frac{2\pi n}{N} K \ll \frac{\pi}{2}, \quad (\text{E.21})$$

or combined with Eq. (E.20),

$$1 \ll n \ll N/4K, \quad (\text{E.22})$$

we would have

$$\frac{|F_n|^2}{N} \approx 2 \langle \sum_{j=1}^K f_1 f_j \rangle. \quad (\text{E.23})$$

It is easy to see that finding such an n is equivalent to choosing ω_0 in the case of continuous variables.

Correlation Integral Termination

From now we will properly redefine $\mathbf{J}^q(t)$ such that the $1/k_B T^2 \Omega$ factor in Eq. (E.1) vanishes. Also, τ will take the unit of ps and $\underline{\kappa}$ will take the unit of $W/m/K$. The spectral analysis of $f(t)$ can be easily generalized to vector $\mathbf{J}^q(t)$ whereas we define

$$g_{ij}(\tau) = \langle J_i^q(0) J_j^q(\tau) \rangle, \quad (\text{E.24})$$

so there is

$$\kappa_{ij} = \int_0^\infty d\tau g_{ij}(\tau). \quad (\text{E.25})$$

$\mathbf{J}^q(t)$ and $g_{ij}(\tau)$ are real, and $g_{ij}(\tau) = g_{ji}(-\tau)$. Furthermore, by time-reversal invariance of physical systems, $g_{ij}(\tau) = g_{ij}(-\tau)$. So we should have

$$\begin{aligned} & g_{ij}(\tau) \\ = & \frac{1}{2\pi T_f} \int_{-\infty}^{+\infty} d\omega \langle J_i^*(\omega) J_j(\omega) \rangle \exp(-i\omega\tau) \\ = & \frac{1}{2\pi T_f} \int_{-\infty}^{+\infty} d\omega \text{Re}[\langle J_i^*(\omega) J_j(\omega) \rangle] \exp(-i\omega\tau). \end{aligned} \quad (\text{E.26})$$

For crystals with point symmetry higher than T_d , such as β -SiC, $\underline{\kappa}$ is a scalar matrix: $\kappa_{ij} = \kappa \delta_{ij}$, and we can use this symmetry by defining $|J(\omega)|^2 = (|J_{xx}^q(\omega)|^2 + |J_{yy}^q(\omega)|^2 + |J_{zz}^q(\omega)|^2)/3$ and $g(\tau) = (g_{xx} + g_{yy} + g_{zz})/3$, from the data of a single MD

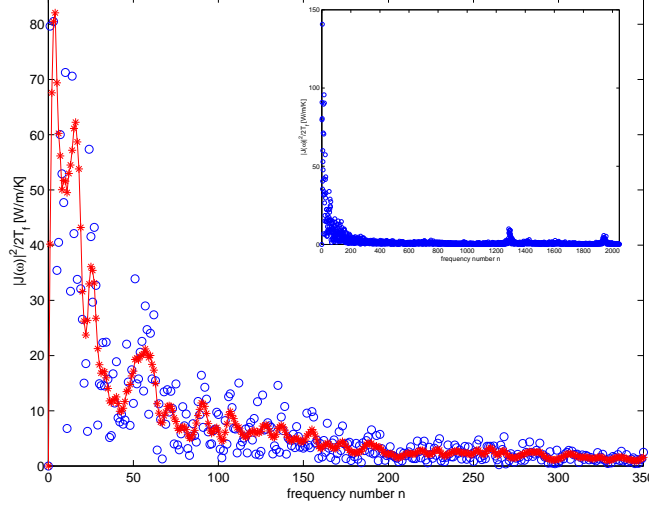


Figure E-3: Power spectrum (plotted in circles and properly normalized to the unit of W/m/K) versus frequency number n , of the heat current data from a 747 *ps* MD simulation of β -SiC crystal at $T = 1500\text{K}$ in a 512-particle cell. The stars are results after 4-point smoothing, with solid line to guide the eye.

run. So $\kappa = (\kappa_{xx} + \kappa_{yy} + \kappa_{zz})/3$.

Theoretically the power spectrum $|J(\omega)|^2/2T_f$ provides full information about the thermal conductivity, because

$$\kappa = \int_0^{+\infty} g(\tau) d\tau = \lim_{\omega_0 \rightarrow 0} \frac{1}{2T_f} |J(\omega_0)|^2. \quad (\text{E.27})$$

In practice however, it is not a straightforward implementation because $|J(\omega)|^2/2T_f$ from a single MD run is usually a “cloud” of points which requires smoothing. Fig. E-3 shows such a power spectrum from a 2 million timestep MD simulation of a β -SiC crystal in a 512-particle cell at 1500K. The x -axis is the frequency number n after FFT. The y -axis is properly scaled to the thermal conductivity unit W/m/K. The raw values are plotted in empty circles, while results after properly smoothing are shown in stars with solid line to guide the eye. As we show in the last section, taking ω_0 to zero in Eq. (E.27) is equivalent to choosing an n on the discrete grid such that $1 \ll n \ll N/4K$. We shall see in Fig. E-4 that the correlation $\langle J(0)J(\tau) \rangle$ is significant for $\tau < \tau_{\max} \approx 20 \text{ ps}$, which corresponds to $K = 60,000$. So n should satisfy $1 \ll n \ll 10$, say $n = 6$ (in this case because $|J(\omega)|^2$ is the average of three

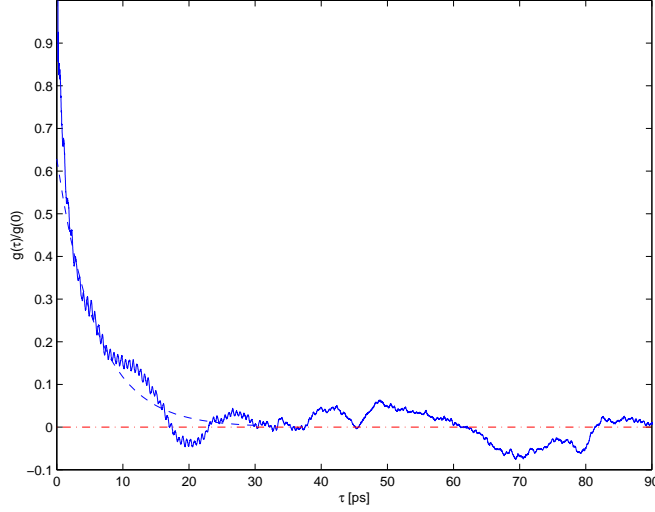


Figure E-4: Normalized heat current correlation function $g(\tau)/g(0)$ from a single MD run ($g(0) = 17.3 \text{ W/m/K/ps}$), for perfect β -SiC at 1500K. The dashed line is the fit to exponential decay in the range 1 to 9 ps.

independent directions, the bounds are not so strict), which roughly corresponds on Fig. E-3 to a thermal conductivity value of $70 \pm 15 \text{ W/m/K}$, in reasonably good agreement with the experimental value of 62.6 W/m/K . However, this is probably the most we can do from the power spectrum; the indeterminate nature of this inference procedure forces us to find better, or at least more automatic, ways of finding out the simulation thermal conductivity result.

Notice that the requirement Eq. (E.22) is only barely satisfied in the above example due to the smallness of $N/4K$, which is the reason we call this a *minimal run*. As we shall demonstrate later, the error bar of one's result is largely determined by the ratio $N/4K$. By doing longer simulation runs at the same temperature, one increases $N/4K$ and thus improves the quality of his result.

As a brief digression, we note (see inset graph of Fig. E-3) that the power spectra sometimes show small peaks at finite frequencies. Besides roughening up $g(\tau)$ a bit, this will have little influence on the calculated thermal conductivity. Nevertheless, the nature of these peaks, whether to be something physical or as a simulation artifact such as finite cell size effect, remains unknown.

We now turn to the correlation function picture by inverse Fourier transforming $|J(\omega)|^2$ using Eq. (E.18). Fig. E-4 shows in solid line the normalized correlation

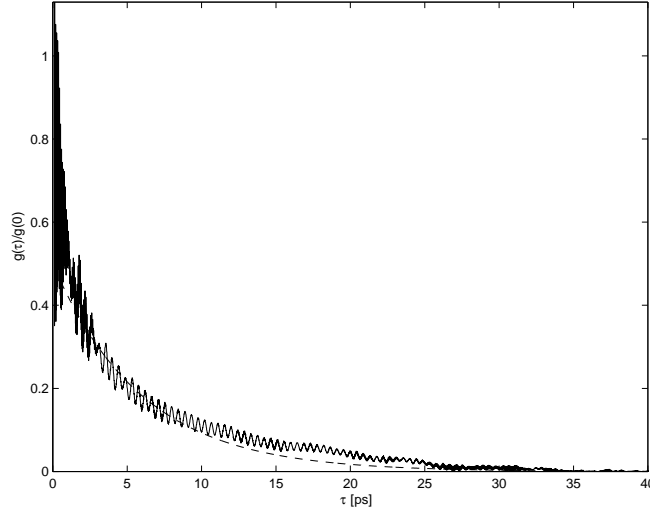


Figure E-5: Well converged normalized heat current correlation function $g(\tau)/g(0)$ for perfect β -SiC at 1700K ($g(0) = 22.0$ W/m/K/ps). The dashed line is the fit to exponential decay in the range 1 to 9 ps.

function $g(\tau)/g(0)$ after proper local smoothing. Only the first 1/8 portion of entire data is plotted in the graph (total run length = 747 ps) because it appears to be completely random fluctuations after that. Clearly, we need a termination rule if somehow we want to retrieve the $\kappa = \int_0^{+\infty} g(\tau)d\tau$ information. Fig. E-4 represents the typical outcome of a minimal run, which provides a test example for the termination criterion.

One observation is that in the case of β -SiC, especially at high temperatures, the *actual* shape of $g(\tau)$ closely resembles that of an exponential decay with somewhat faster relaxation in the first few pico-seconds and a slight flattening of the tail. This observation are confirmed by simulation results after multiple runs are done and better statistics are collected (see Fig. E-5, E-6, E-7). It induces us to propose the following exponential fitting or EF criterion: we can do a least square fit of $g(\tau)$ to an exponential decay form $ae^{-(\tau-\tau_f)/b}$ in the time range $[\tau_i, \tau_f]$, where simulation accuracy is still believed to be good, in order to determine the best coefficients $\{a, b\}$. We then numerically integrate $g(\tau)$ up to τ_f , and add with the analytically estimated tail contribution ab . This termination rule only requires two parameters to be chosen beforehand, τ_i and τ_f , depending on simulation run length, correlation time and

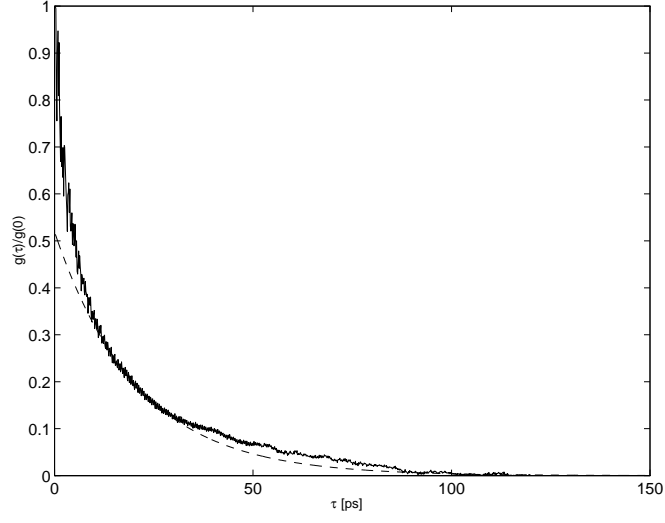


Figure E-6: Well converged normalized heat current correlation function $g(\tau)/g(0)$ for perfect β -SiC at 760K ($g(0) = 15.5$ W/m/K/ps). The dashed line is the fit to exponential decay in the range 5 to 25 ps.

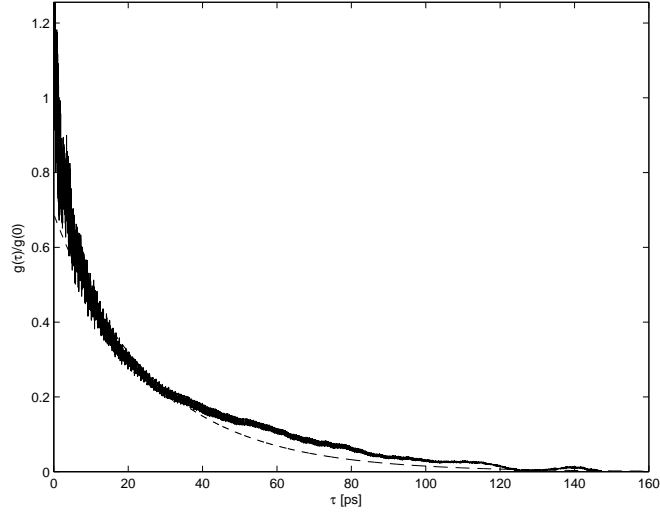


Figure E-7: Well converged normalized heat current correlation function $g(\tau)/g(0)$ for perfect β -SiC at 284K ($g(0) = 7.8$ W/m/K/ps). The dashed line is the fit to exponential decay in the range 5 to 35 ps.

Table E.1: Recommended Parameters for Perfect Crystal β -SiC Thermal Conductivity Calculation

T (K)	Steps	Timestep (fs)	Runs	EF $\tau_i(ps)$	EF $\tau_f(ps)$
250 – 500	8×10^6	0.30-0.35	6-10	5.0	35.0
500 – 1000	4×10^6	0.30-0.35	4-6	3.5	21.0
1000 – 1500	4×10^6	0.25-0.30	3-4	1.0	9.0
> 1500	2×10^6	< 0.25	3-4	1.0	9.0

number of runs being averaged. The recommended values for β -SiC are given in Table E.1, along with other simulation parameters.

Another more straightforward way is to postulate that the actual heat current correlation function $g(\tau)$ *never* turns negative. We know that certain self-correlation functions such as the velocity autocorrelation function in liquids can have negative parts sometimes, but the occurrence is rare and it is very unlikely that it happens in solid SiC. If this is the case, then at the point where the calculated correlation curve first turns negative, one can argue that the calculated curve must be finally corrupted by random fluctuations, and data from now on can not be trusted. One can then estimate the thermal conductivity by numerically integrating the raw data up to the point where the “first dip” happens, and this is called the first-dip or FD rule.

Usually $g(\tau)$ from a long simulation run with a large $N/4K$ ratio or the average of multiple runs will give FD and EF results that are close to each other, especially at high temperatures; and large difference occurs for those runs that are not well-converged (small $N/4K$) and can be seen to be rather irregular. We list several examples down below:

- 2 million step run, $T = 1500K$, 512-particle cell (see Fig. E-3, E-4). EF result: 71.2 W/m/K; FD result: 67.8 W/m/K; Exp’t: 62.6 W/m/K.
- 2 million step run, $T = 1055K$, 216-particle cell. EF result: 88.6 W/m/K; FD result: 89.3 W/m/K; Exp’t: 95.7 W/m/K.
- 2 million step run, $T = 790K$, 216-particle cell. EF result: 172.6 W/m/K; FD result: 229.7 W/m/K; Exp’t: 162.4 W/m/K.

- Average of 4×4 million step runs (see Fig. E-5), $T = 1700\text{K}$, 216-particle cell.
EF result: 69.2 W/m/K; FD result: 77.5 W/m/K; Exp't: 51.9 W/m/K.
- Average of 4×4 million step runs (see Fig. E-6), $T = 760\text{K}$, 216-particle cell.
EF result: 152.2 W/m/K; FD result: 162.7 W/m/K; Exp't: 138.5 W/m/K.
- Average of 12×8 million step runs (see Fig. E-7), $T = 284\text{K}$, 216-particle cell.
EF result: 146.2 W/m/K; FD result: 161.3 W/m/K; Exp't: 318.6 W/m/K.

Just by looking at the above reports and comparing with experiments, one cannot clearly distinguish between the error due to the *model*, such as inexact interatomic potential or the negligence of quantum effects which is quite damaging at low temperatures [80], and the error due to the *implementation*, such as the termination criteria. They can only be distinguished after doing many identical runs with different random seeds, and accumulating enough data so that we can claim certain result to be the *true* simulation result, and then benchmark the quality of a specific implementation giving it only part of the information. This procedure would be very time-consuming. By experience, we think that for a single minimal run, the EF result may be more accurate because it acts like a filter; but when one can manage to do long simulation runs, and many of them, the FD rule may yield better results because one then know the tail part to be real. Table E.1 lists the parameters which we think are appropriate for β -SiC crystal at various temperatures.

Finally, we note that the difficulty in benchmarking implementations does not exist if we know the exact correlation function. This is done in Section E where we propose a simple analytically solvable model.

Simple Solvable Model

Consider discrete series

$$a_0 = 0, \quad a_i = a_{i-1}e^{-1/L} + R_i, \quad (\text{E.28})$$

where R_i is an independent random number uniformly distributed on $(-0.5, 0.5)$, and L is an arbitrary constant signifying the characteristic correlation length. The series can be shown to have a simple correlation function:

$$\begin{aligned}
g_k &= \langle a_i a_{i+k-1} \rangle \\
&= \langle a_i a_{i+k-2} e^{-1/L} + a_i R_{i+k-1} \rangle \\
&= \langle a_i a_{i+k-2} \rangle e^{-1/L},
\end{aligned} \tag{E.29}$$

because R_{i+k-1} is not correlated with a_i . And so

$$g_k = \langle a_i a_i \rangle e^{-(k-1)/L}. \tag{E.30}$$

Now,

$$\begin{aligned}
a_i &= R_i + a_{i-1} e^{-1/L} \\
&= R_i + R_{i-1} e^{-1/L} + R_{i-2} e^{-2/L} + \dots
\end{aligned} \tag{E.31}$$

so

$$\begin{aligned}
\langle a_i a_i \rangle &= \langle R_i^2 \rangle + \langle R_{i-1}^2 \rangle e^{-2/L} + \langle R_{i-2}^2 \rangle e^{-4/L} + \dots \\
&= \frac{\langle R^2 \rangle}{1 - e^{-\frac{2}{L}}}.
\end{aligned} \tag{E.32}$$

Because

$$\langle R^2 \rangle = \int_{-0.5}^{0.5} x^2 dx = \frac{1}{12},$$

there is

$$\langle a_i^2 \rangle = \frac{1}{12(1 - e^{-\frac{2}{L}})}, \tag{E.33}$$

and

$$g_k = \frac{e^{-(k-1)/L}}{12(1 - e^{-\frac{2}{L}})}. \tag{E.34}$$

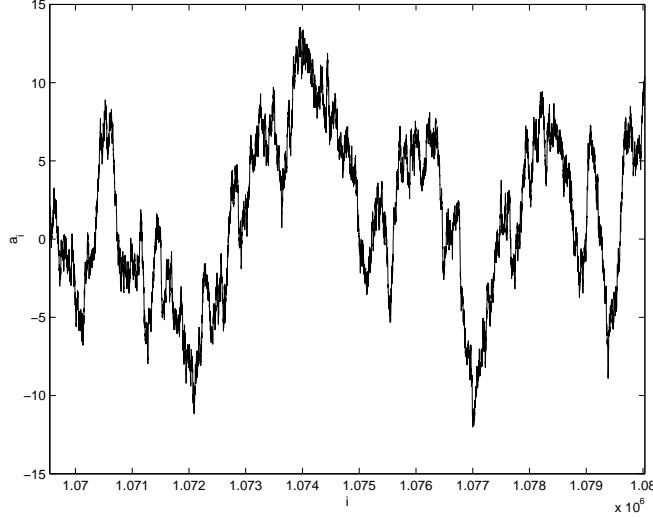


Figure E-8: A small portion of the random signal a_i in case A, with $N = 2^{21}$ and $N/L = 1000$.

The theoretical thermal conductivity is then

$$\kappa \equiv \sum_{k=1}^{+\infty} g_k = \frac{1}{12(1 - e^{-\frac{2}{L}})(1 - e^{-\frac{1}{L}})}. \quad (\text{E.35})$$

Using this known result we can check our codes by directly plugging in the series, and see if after the procedure in Fig. E-1, we indeed get a correlation function of the correct form and a correct “thermal conductivity” value. This is the best way to ensure that all the coefficients are made right.

Let us illustrate the issues discussed in this paper by numerically studying three examples of Eq. (E.28), following the steps outlined in Fig. E-1:

- Case A: $N = 2^{21}$, $N/L = 1000$, representing a well-converged MD run. The theoretical thermal conductivity is $\kappa_A = 1.834 \times 10^5$.
- Case B: $N = 2^{21}$, $N/L = 100$, representing a minimal MD run ². The theoretical thermal conductivity should be $\kappa_B = 1.833 \times 10^7$.

²There is some numerical difference between K in Eq. (E.22) and L in Eq. (E.28): K signifies the *maximum* correlation length, above which correlation can be neglected, while L is the characteristic period by which correlation decays by e^{-1} . If we consider $e^{-3} \approx 0.05$ to be “negligibly small”, then $K \approx 3L$. For instance, in the $T = 1500\text{K}$ β -SiC example in Section E, the fitted EF decay time is 5.95 ps (L), while we consider correlation to be significant up to 20 ps (K) by looking at Fig. E-4. So there should be $1 \ll n \ll N/4K \approx N/12L$.

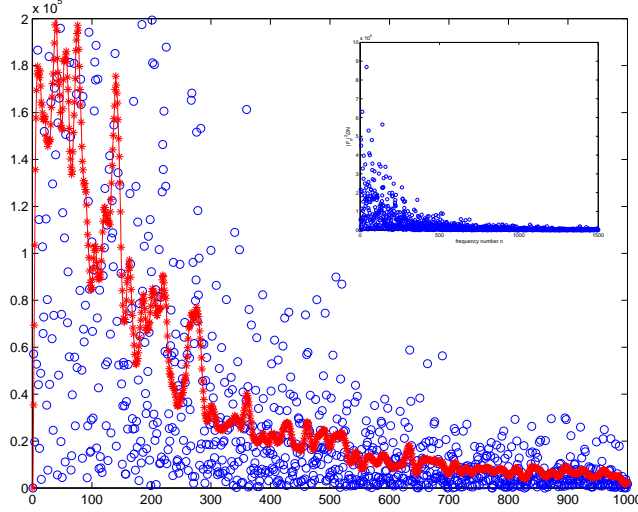


Figure E-9: Power spectrum $|F_n|^2/2N$ versus frequency number n in case A. The empty circles are the raw data, while the stars (with solid line to guide the eye) are the smoothed results after passing through a zero-phase filter of nearby 10 points. The inset graph shows the raw data on a larger scale.

- Case C: Identical to case B but with a different random number seed.

where we take care to let the sequence iterate $N/8$ steps to “equilibrate” before collecting the N data points. Fig. E-8 shows a small portion of the signal in case A for $5L \approx 10,000$ steps.

Fig. E-9 plots the power spectrum $|F_n|^2/2N$ of case A (the inset shows the raw data on a larger scale) versus the frequency number n between $[1, N/L]$, which are the only relevant ones to thermal conductivity as we demonstrated in Section E. The empty circles are the raw values, while the stars are the smoothed result after passing through a zero-phase filter of nearby 10 points (Matlab *filtfilt*), with solid line to guide the eye. We can see that the raw data is still a “cloud” of points, very much like that of Fig. E-3, but after smoothing it becomes more regular, with discernible leveling off as $n \rightarrow 0$, which is related to the fact that as $L \gg 1$ $|F_n|^2/2N$ becomes a Lorentzian. The $n \rightarrow 0$ limit, as we can see, corresponds to a thermal conductivity value of about $(1.7 \pm 0.3) \times 10^5$ at frequency number n around $N/25L$. This verifies Eq. (E.23) and Eq. (E.22) and the agreement is actually pretty good, for this “well-converged run” with $N/L = 1000$.

We then inverse FFT the power spectrum to get g_k . The numerical result is

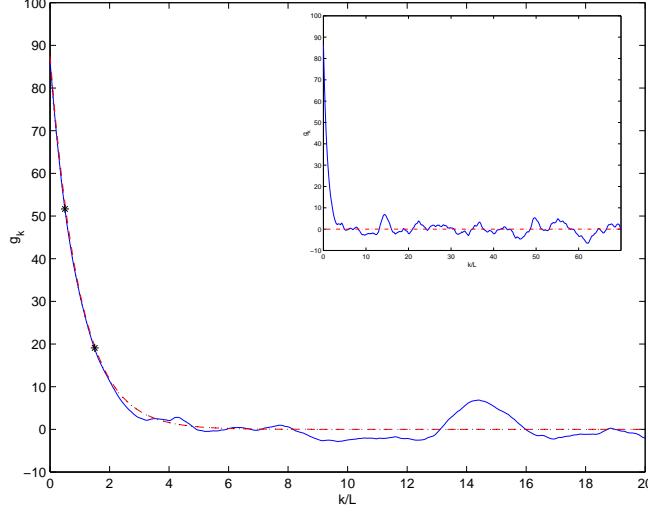


Figure E-10: Correlation function g_k versus k/L in case A. The solid line is the numerical result; the dashed line is the theoretical prediction of Eq. (E.34). The dotted line (indistinguishable from the theoretical curve in this case) is the EF fit to numerical result in the region $0.5 \leq k/L \leq 1.5$, indicated by the two stars. The inset graph shows the numerical result on a larger scale.

plotted in Fig. E-10 in solid line, against the theoretical prediction of Eq. (E.34) in dashed line. Since the only timescale in this problem is L , the x -axis is scaled as k/L . The numerical result is also shown in the inset on a larger scale. We can clearly discern a region ($5 < k/L < 8$) in the numerical result where $g_k \approx 0$ and is almost flat and parallel to the x -axis, to the left of which g_k is regular and well-converged, and to the right it begins to randomly fluctuate. Due to the existence of this region, the thermal conductivity result we get using g_k (versus the power spectrum method) is bound to be very good, no matter which termination rule is invoked. And this is what actually happens in defect-state SiC thermal conductivity calculations.

We then apply our EF rule to the data: the region of fitting ($[\tau_i, \tau_f]$ in last section) is chosen to be $k/L = [0.5, 1.5]$ (indicated by the two stars) which roughly corresponds to same position in β -SiC. The resultant exponential curve is plotted in dotted lines, which because it *has* the correct functional dependence, is almost indistinguishable from the theoretical curve. The inferred characteristic decay time is $L'/L = 1.0043$, and the inferred thermal conductivity is $\kappa_A^{\text{EF}}/\kappa_A = 0.979$.

If we apply the FD rule to the same data, we find that the first dip occurs at

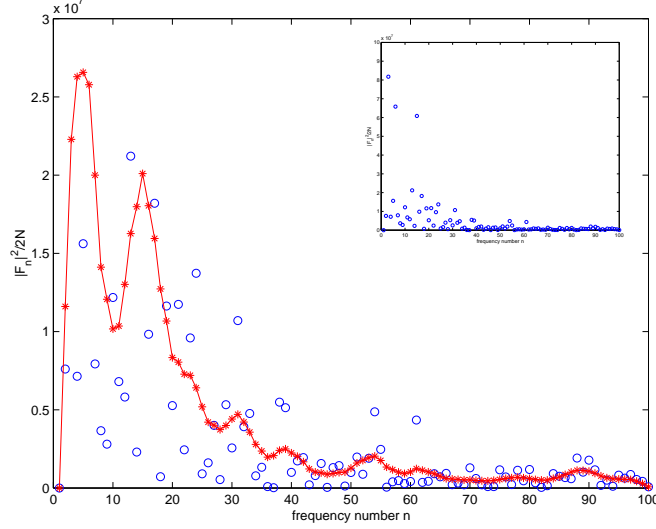


Figure E-11: Power spectrum $|F_n|^2/2N$ versus frequency number n in case B. The empty circles are the raw data, while the stars (with solid line to guide the eye) are the smoothed results after passing through a zero-phase filter of nearby 5 points. The inset graph shows the raw data on a larger scale.

$k_{\text{dip}}/L = 4.918$, which of course is completely random, and the FD estimation gives a thermal conductivity value of $\kappa_A^{\text{FD}}/\kappa_A = 0.962$.

The entire procedure for case A registers 2.75×10^8 flops on Matlab, while the brute force method requires computations on the order of $NL = 4.40 \times 10^9$ flops, thus demonstrating the efficiency of this approach. The comparison of cost will go even more favorably for the spectral method in case B and C, which represents more realistic scenarios. Furthermore, the spectral method loses no information about the original data; and one can gain extra knowledge about the power spectrum.

Now let us do case B. The meaning of symbols in the figures will be the same as those in case A. Fig. E-11 shows the power spectrum, where the stars are the smoothed result of nearby 5 points. Because N/L is small, we have much less relevant frequency numbers than those in Fig. E-11. The $n \rightarrow 0$ limit gives a thermal conductivity value of $(2 \pm 0.6) \times 10^7$ around $n = 7$, which agrees well with the theoretical value of $\kappa_B = 1.833 \times 10^7$, considering this is a minimal run.

Fig. E-12 shows the correlation function g_k versus k/L . We still fit the numerical result to an exponential form in the region $0.5 \leq k/L \leq 1.5$. The inferred characteristic decay time is $L'/L = 1.280$, and the inferred thermal conductivity is

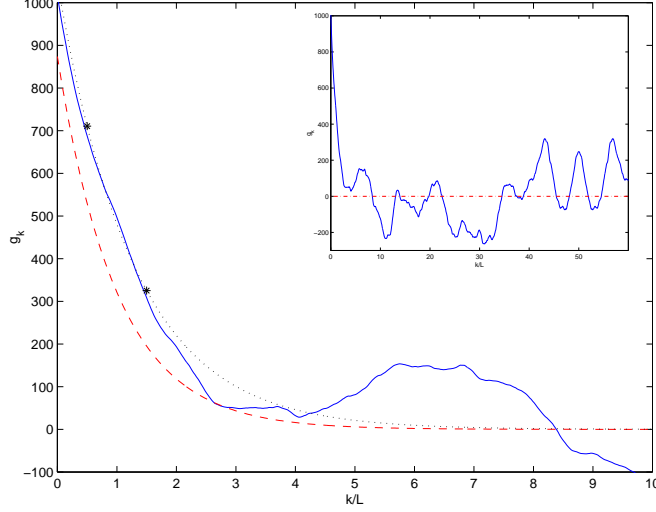


Figure E-12: Correlation function g_k versus k/L in case B. The solid line is the numerical result; the dashed line is the theoretical prediction of Eq. (E.34). The dotted line is the EF fit to numerical result in the region $0.5 \leq k/L \leq 1.5$, indicated by the two stars. The inset graph shows the numerical result on a larger scale.

$\kappa_B^{\text{EF}}/\kappa_B = 1.518$. The fitted exponential curve is shown in dotted lines, where the region of fitting is between the two stars. We can see that neither the original data nor the EF curve agrees well with the theoretical curve, due to small N/L , i.e., insufficient data. However, the EF curve is able to filter out the fictitious bulge between $4 < k/L < 8$.

If we apply the FD rule to the same data, we find that in this case the first dip happens at $k_{\text{dip}}/L = 8.385$, and the FD estimation of the thermal conductivity value is $\kappa_A^{\text{FD}}/\kappa_A = 1.854$.

Neither of these results are good, but it is the kind of accuracy we should expect from a single minimal run. The power spectrum estimation in fact does better than the g_k estimations in this case, but as we said, the procedure depends more heavily on human, which is usually not a good idea.

Now let us turn to case C, whose conditions are completely identical with case B except changing the initial random number generator seed to have a different sequence. The goal is to find out how minimal runs differ from case to case. As it turns out, their difference can be quite large. Fig. E-13 shows the power spectrum of case C, which does not seem very different from Fig. E-11. The $n \rightarrow 0$ limit

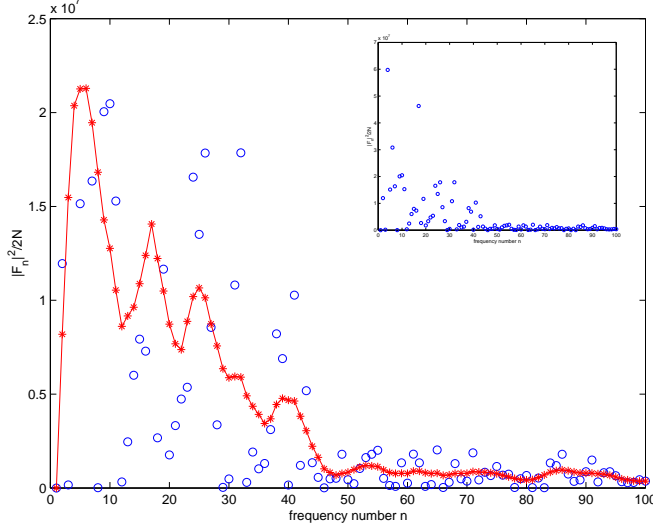


Figure E-13: Power spectrum $|F_n|^2/2N$ versus frequency number n in case C. The empty circles are the raw data, while the stars (with solid line to guide the eye) are the smoothed results after passing through a zero-phase filter of nearby 5 points. The inset graph shows the raw data on a larger scale.

gives a thermal conductivity value of $(1.7 \pm 0.4) \times 10^7$ at about $n = 8$. However, the correlation function (Fig. E-14) behaves much better at small k/L than case B. Applying the EF rule between $0.5 \leq k/L \leq 1.5$, we find that $L'/L = 0.778$, and the inferred thermal conductivity value is $\kappa_C^{\text{EF}}/\kappa_C = 0.972$. If we apply the FD rule, the first-dip in correlation function happens at $k_{\text{dip}}/L = 5.786$, and the FD estimation gives $\kappa_A^{\text{FD}}/\kappa_A = 1.123$. So in this case both results are better than the power spectrum estimation. This might be due to the fact the power spectrum in case C happens to fluctuate less at small frequency numbers (compare inset graphs of Fig. E-13 with Fig. E-11).

Now we had a glimpse of the subtleties involved in calculating the thermal conductivity from minimal runs, which currently are often the only things one can afford to do for realistic crystalline solids ($N/K \sim 30$ or $N/L \sim 100$). On the one hand, one expects the error to be big, say 50%, and often biased to the positive side. On the other hand, some minimal runs may happen to hit right on target. In general the difference from run to run is large. The difficulty is that unlike in this case where one knows the exact answer, one cannot tell for sure whose error is smaller. It is true that certain correlation curves “look” better than others, such as Fig. E-14 than Fig.

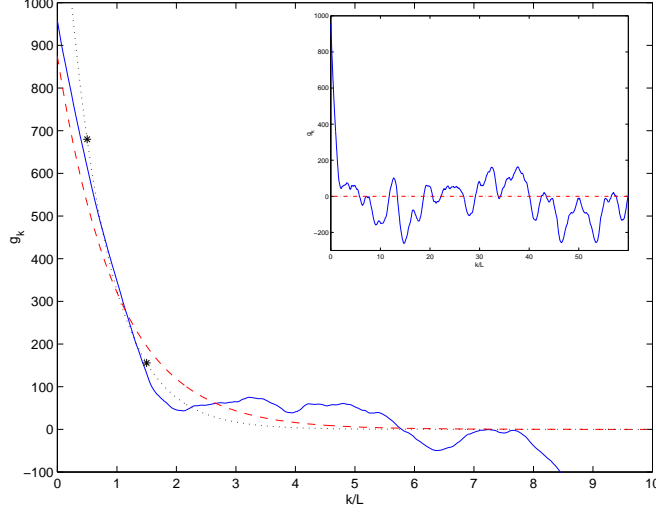


Figure E-14: Correlation function g_k versus k/L in case C. The solid line is the numerical result; the dashed line is the theoretical prediction of Eq. (E.34). The dotted line is the EF fit to numerical result in the region $0.5 \leq k/L \leq 1.5$, indicated by the two stars. The inset graph shows the numerical result on a larger scale.

E-12, so one may assign bigger weights to these results, but it is a complicated issue.

In the case of β -SiC, by making the assumption that the correlation function follows an exponential decay form, or that it never turns negative, we devise the EF and the FD termination rules. As we said in Section E, those curves which give similar EF and FD values are often found to be closer to the correct (well-averaged) result. This is also found to be the case for our simple solvable model (compare case B and C); and it may also be helpful for other system calculations.

Notice that the EF results in case A, B and C are always better than the FD results, which we think is because the true correlation function *is* exponentially decaying. In general, we believe that the EF rule is more reliable for the data from a single minimal run, while the FD rule is better for well-converged or well-averaged data.

Should people do minimal-run simulations? Sometimes they are forced to: a minimal run for β -SiC at $T = 500\text{K}$ is 216 particles running 8 million steps under the Tersoff potential, which takes 50 processor hours on the high-end computer of SGI Origin 2000. The memory requirement to analyze the data afterwards is also demanding. But even if one can do very long simulations, he should investigate

before doing so. As we saw, case A has a much better convergence than case B and C, but it takes (relatively) 10 times longer to run. We think that if one does 10 minimal runs ($N = 2^{21}/10$) and average over the correlation functions, he will get comparable accuracy as case A. In reality one may benefit more from the latter route because he has taken a better ensemble average, by starting from different initial conditions (see discussion in Section E).

Appendix F

Four Heat Currents in a Crystal

Let us consider an isolated system of monoatomic perfect crystal in periodic boundary conditions, with atoms interacting via a pair-potential,

$$V(\mathbf{r}^N) = \sum_{pairs} V_{ij}(\mathbf{r}_{ij}). \quad (\text{F.1})$$

One encounters four different heat current¹ expressions for such a system[65]. The first expression, which we called the *canonical form*, is

$$\mathbf{J}_1 \equiv \frac{1}{2} \sum_{pairs} [\mathbf{F}_{ij} \cdot (\mathbf{v}_i + \mathbf{v}_j) \mathbf{r}_{ij} + V_{ij}(\mathbf{v}_i + \mathbf{v}_j)] + \frac{1}{2} \sum_{i=1}^N m |\mathbf{v}_i|^2 \mathbf{v}_i, \quad (\text{F.2})$$

where \mathbf{r}_{ij} 's are defined in the sense of (B.50). (F.2) can be derived by nominally taking the time-derivative of the internal energy “dipole” of this system,

$$\mathbf{D} \equiv \sum_{i=1}^N e_i \mathbf{r}_i, \quad (\text{F.3})$$

using a sensible partition of the total internal energy,

$$e_i = \frac{1}{2} m |\mathbf{v}_i|^2 + \sum_{i \in pairs} V_{ij}/2. \quad (\text{F.4})$$

¹Define \mathbf{J} to be the total heat current of a system with volume Ω , and $\mathbf{j} \equiv \mathbf{J}/\Omega$, the heat current density.

One can check that (F.2) gives the correct heat current macroscopically, since for any material in steady-state heat conduction, one could identify a small volume element Ω and claim that its internal energy dipole,

$$\mathbf{D} = \int_{\Omega} e(\mathbf{r}) \mathbf{r} dV = \sum_{\mathbf{r}_i \in \Omega} e_i \mathbf{r}_i, \quad (\text{F.5})$$

is a constant of time (in the coarse-grained sense). But, by definition, the outside world dumps energy to the skin of the sample with rate $-\mathbf{j} \cdot \mathbf{n}$, so its contribution to \mathbf{D} is

$$\dot{\mathbf{D}}_{ext} = - \int_{\partial\Omega} (\mathbf{j} \cdot \mathbf{n}) \mathbf{r} dS. \quad (\text{F.6})$$

Since \mathbf{j} varies little in such a small sample, one could treat \mathbf{j} as a constant, and the above integral turns out to be

$$\dot{\mathbf{D}}_{ext} = - \int_{\Omega} \partial_i (j_i \mathbf{r}) dV = -\mathbf{j} \Omega \equiv -\mathbf{J}. \quad (\text{F.7})$$

However because the system is in steady-state heat conduction,

$$0 \equiv \dot{\mathbf{D}} = \dot{\mathbf{D}}_{ext} + \dot{\mathbf{D}}_{int}, \quad (\text{F.8})$$

where $\dot{\mathbf{D}}_{int}$ is the change of \mathbf{D} *through internal mechanisms* operating in the bulk of Ω , such as lattice vibrations, which work against any established \mathbf{D} . Or put it another way, internal mechanisms are any *ij*-interactions that does not cross the surface of Ω but contributing to $\dot{\mathbf{D}}$. From (F.7) and (F.8), it is clear that the “heat current” in engineers’ notion could be

$$\mathbf{J} = \dot{\mathbf{D}}_{int} = \frac{d}{dt} \left(\sum_{i \in \Omega} e_i \mathbf{r}_i \right) \Big|_{int. \text{ mech.}}. \quad (\text{F.9})$$

And so comes the canonical definition² of \mathbf{J} , (F.2), which is most frequently used. Because there is no external heat source in a global equilibrium simulation with periodic

²The development from (F.5) to (F.9) is parallel to the derivation of Virial’s theorem for microscopic pressure and stress.

boundary conditions, we are only observing the internal heat currents (fluctuations, for that matter) due to $\dot{\mathbf{D}}_{int}$.

However, in a solid there is nothing preventing us from defining \mathbf{D} to be

$$\mathbf{D} \equiv \sum_{\mathbf{r}_i^0 \in \Omega} e_i \mathbf{r}_i^0, \quad (\text{F.10})$$

where \mathbf{r}_i^0 is the time-averaged position of atom i , which is time-independent. It is intuitively obvious that for a material under finite temperature gradient, both (F.5) and (F.10) gives the same dipole for a sample Ω with macroscopical size. Indeed, it *would* be more natural to tag atoms inside Ω at $t = 0$ and follow them than to track atoms coming in and out of Ω , so long as the tagged atoms do not drift away indefinitely. So, by taking the time-derivative of (F.10), we arrive at the second heat current expression,

$$\mathbf{J}_2 \equiv \frac{1}{2} \sum_{pairs} \mathbf{F}_{ij} \cdot (\mathbf{v}_i + \mathbf{v}_j) \mathbf{r}_{ij}^0, \quad (\text{F.11})$$

which can be called the *simplified canonical form*. We use (F.11) to derive the Green-Kubo formula in Appendix B, because it is easier for analysis. But using (F.2) and (F.11) gives exactly the same κ result in the $\mathbf{k} \rightarrow 0$ limit, because the material must have a unique *macroscopic* thermal conductivity, whose operations do not care about the exact *microscopic* definition of the internal energy distribution. On the other hand, $\langle \mathbf{J}_1(\tau) \mathbf{J}_1(0) \rangle$ and $\langle \mathbf{J}_2(\tau) \mathbf{J}_2(0) \rangle$ do have different shapes, and their “finite- \mathbf{k} thermal conductivities” have no reason to be equal. In other words, we can use the discrepancies between the two calculated “thermal conductivities” of a simulation to estimate the small cell-size error which is mentioned at the end of Appendix B. Also, (F.2) works for liquids unlike other expressions, since it takes into account the particle *convection* contribution to \mathbf{J} which is non-existent in solids.

Note that as $T \rightarrow 0$, (F.2) approaches (F.11) since in a harmonic expansion,

$$\mathbf{u}_i \equiv \mathbf{r}_i - \mathbf{r}_i^0, \quad \mathbf{v}_i \equiv \dot{\mathbf{u}}_i, \quad (\text{F.12})$$

are of linear order ($\propto \sqrt{T}$), while constant orders of \mathbf{F}_{ij} ’s and constant and linear

orders of V_{ij} 's turn out not to contribute in a perfect crystal³. One then finds that the leading order expansion of (F.2) and (F.11) are *quadratic* and *equal*, which we define to be \mathbf{J}_3 , the *harmonic heat current*⁴,

$$\mathbf{J}_3 \equiv \frac{1}{2} \sum_{pairs} \sum_{\alpha=1}^D \sum_{\beta=1}^D (u_{i\alpha} - u_{j\alpha}) \Phi_{\alpha\beta}^{ij} (v_{i\beta} + v_{j\beta}) \mathbf{r}_{ij}^0, \quad (\text{F.13})$$

where D is the dimensionality of the system, and $\Phi_{\alpha\beta}^{ij}$'s are the specific interactions' force constants, relating displacement $j\beta$ to the negative force on $i\alpha$,

$$\Phi_{\alpha\beta}^{ij} \equiv \left. \frac{\partial^2 V_{ij}}{\partial r_{i\alpha} \partial r_{j\beta}} \right|_0 = (2\delta_{ij} - 1) \left. \frac{\partial^2 V_{ij}(|\mathbf{r}|)}{\partial r_\alpha \partial r_\beta} \right|_0 = (2\delta_{ij} - 1) \left[\frac{V'}{r} \delta_{\alpha\beta} + (V'' - \frac{V'}{r}) \frac{r_\alpha r_\beta}{r^2} \right], \quad (\text{F.14})$$

and one can easily show from (F.2), (F.11) that

$$\mathbf{J}_1 = \mathbf{J}_3 + \mathcal{O}(T^{\frac{3}{2}}), \quad \mathbf{J}_2 = \mathbf{J}_3 + \mathcal{O}(T^{\frac{3}{2}}), \quad \text{as } T \rightarrow 0. \quad (\text{F.15})$$

We would like to study the properties of \mathbf{J}_3 , but it is much more convenient in a perfect crystal to transform it first to phonon coordinates. Let us remind ourselves that for a monoatomic perfect crystal of atom mass m , the $D \times D$ dynamical matrix $\mathbf{D}(\mathbf{k})$ is

$$D_{\alpha\beta}(\mathbf{k}) = \frac{1}{m} \sum_{j=1}^N \Phi_{\alpha\beta}^{ij} e^{-i\mathbf{k} \cdot \mathbf{r}_{ij}^0}, \quad \text{for any } i, \quad (\text{F.16})$$

whose eigenvalue problem

$$\sum_{\beta=1}^D D_{\alpha\beta}(\mathbf{k}) e_\mu^\beta(\mathbf{k}) = \omega_\mu(\mathbf{k})^2 e_\mu^\alpha(\mathbf{k}), \quad \omega_\mu(\mathbf{k}) > 0, \quad \mu = 1..D, \quad (\text{F.17})$$

produces the phonon mode \mathbf{k} with branch number μ . By the orthogonality and

³The ij interaction repeats itself in a perfect crystal, and $\sum_{i=1}^N \mathbf{v}_i \equiv 0$.

⁴I suspect that \mathbf{J}_3 also works for defected crystals. A defect carries a small “cloud” of energy surplus with it, so the instantaneous \mathbf{J}_1 might be $\propto \sqrt{T}$. However, one can add and subtract a constant off the surplus and show that its contribution to κ is proportional to the defect self-diffusion coefficient, which is negligible.

completeness of Hermitian matrix basis, there are

$$\sum_{\alpha=1}^D e_{\mu}^{\alpha*}(\mathbf{k}) e_{\nu}^{\alpha}(\mathbf{k}) = \delta_{\mu\nu}, \quad \sum_{\mu=1}^D e_{\mu}^{\alpha}(\mathbf{k}) e_{\mu}^{\beta*}(\mathbf{k}) = \delta_{\alpha\beta}. \quad (\text{F.18})$$

To calculate the group velocity $\mathbf{v}_G^{\mu}(\mathbf{k})$ of phonon branch μ at \mathbf{k} , differentiate both (F.17) and (F.18) with respect to \mathbf{k} , and one would arrive at

$$\mathbf{v}_G^{\mu}(\mathbf{k}) = \frac{d\omega_{\mu}(\mathbf{k})}{d\mathbf{k}} = \frac{1}{2\omega_{\mu}(\mathbf{k})} \sum_{\alpha=1}^D \sum_{\beta=1}^D e_{\mu}^{\alpha*}(\mathbf{k}) \frac{dD_{\alpha\beta}(\mathbf{k})}{d\mathbf{k}} e_{\mu}^{\beta}(\mathbf{k}), \quad (\text{F.19})$$

which is an application of the well-known Hellmann-Feymann theorem. Using (F.16), one could evaluate the above explicitly as

$$\mathbf{v}_G^{\mu}(\mathbf{k}) = \frac{-i}{2m\omega_{\mu}(\mathbf{k})} \sum_{j=1}^N \sum_{\alpha=1}^D \sum_{\beta=1}^D e_{\mu}^{\alpha*}(\mathbf{k}) e_{\mu}^{\beta}(\mathbf{k}) \Phi_{\alpha\beta}^{ij} e^{-i\mathbf{k} \cdot \mathbf{r}_{ij}^0} \mathbf{r}_{ij}^0, \quad \text{for any } i. \quad (\text{F.20})$$

After obtaining the normal modes, atom displacements can be expressed as

$$u_{i\alpha} = \frac{1}{\sqrt{2m}} \sum_{\mathbf{k}} \sum_{\mu=1}^D \left\{ Q_{\mu}(\mathbf{k}) \frac{e^{i\mathbf{k} \cdot \mathbf{r}_i^0 - i\omega_{\mu}(\mathbf{k})t} e_{\mu}^{\alpha}(\mathbf{k})}{\sqrt{N}} + c.c. \right\}, \quad (\text{F.21})$$

within the harmonic approximation, and their velocities are simply

$$v_{i\alpha} = \frac{1}{\sqrt{2m}} \sum_{\mathbf{k}} \sum_{\mu=1}^D \left\{ -i\omega_{\mu}(\mathbf{k}) Q_{\mu}(\mathbf{k}) \frac{e^{i\mathbf{k} \cdot \mathbf{r}_i^0 - i\omega_{\mu}(\mathbf{k})t} e_{\mu}^{\alpha}(\mathbf{k})}{\sqrt{N}} + c.c. \right\}, \quad (\text{F.22})$$

where though $Q_{\mu}(\mathbf{k})$ and $Q_{\mu}(-\mathbf{k})$ *could* have coupled in the system Hamiltonian,

$$\mathcal{H} = \sum_{i=1}^N \sum_{\alpha=1}^D \frac{mv_{i\alpha}^2}{2} + \sum_{i=1}^N \sum_{\alpha=1}^D \sum_{j=1}^N \sum_{\beta=1}^D \frac{u_{i\alpha} \Phi_{\alpha\beta}^{ij} u_{j\beta}}{2} + \mathcal{O}(T^{\frac{3}{2}}), \quad (\text{F.23})$$

they turn out *not* to, and one can show by using (F.21), (F.22) and (F.17), (F.18) that

$$\mathcal{H} = \sum_{\mathbf{k}} \sum_{\mu=1}^D \omega_{\mu}(\mathbf{k})^2 |Q_{\mu}(\mathbf{k})|^2 + \mathcal{O}(T^{\frac{3}{2}}), \quad (\text{F.24})$$

so $Q_{\mu}(\mathbf{k})$'s are slowly varying and nearly independent for all \mathbf{k}, μ .

Let us convert (F.13), the harmonic heat current, into phonon coordinates. Before doing it, notice that

$$\Phi_{\alpha\beta}^{ij} = \Phi_{\alpha\beta}^{ji} = \Phi_{\beta\alpha}^{ji}, \quad (\text{F.25})$$

since $i \rightleftharpoons j \equiv \mathbf{r} \rightarrow -\mathbf{r}$ for a pair potential (see (F.14)). Thus we can rewrite (F.13) as

$$\mathbf{J}_3 = \frac{1}{4} \sum_{i=1}^N \sum_{j=1}^N \sum_{\alpha=1}^D \sum_{\beta=1}^D \Phi_{\alpha\beta}^{ij} (u_{i\alpha} v_{i\beta} + u_{i\alpha} v_{j\beta} - u_{j\alpha} v_{i\beta} - u_{j\alpha} v_{j\beta}) \mathbf{r}_{ij}^0. \quad (\text{F.26})$$

But sums involving $u_{i\alpha} v_{i\beta}$ and $u_{j\alpha} v_{j\beta}$ go to zero, since a monoatomic perfect crystal *always* has inversion symmetry, so $\Phi_{\alpha\beta}^{ij} u_{i\alpha} v_{i\beta} \mathbf{r}_{ij}^0$ vanishes after summing over all j 's. On the other hand, because $u_{i\alpha} v_{j\beta} - u_{j\alpha} v_{i\beta}$ and \mathbf{r}_{ij}^0 are both anti-symmetric with respect to $i \rightleftharpoons j$, the harmonic heat current can be further reduced to

$$\mathbf{J}_3 = \frac{1}{2} \sum_{i=1}^N \sum_{j=1}^N \sum_{\alpha=1}^D \sum_{\beta=1}^D \Phi_{\alpha\beta}^{ij} u_{i\alpha} v_{j\beta} \mathbf{r}_{ij}^0. \quad (\text{F.27})$$

We can now plug (F.21) and (F.22) in (F.27), but clearly components other than $\pm \mathbf{k}$ do not mix after summing over i and j 's, so we can save some trouble by feigning that $u_{i\alpha}$ only comes from $\mu = 1..D$ branches of $\pm \mathbf{k}$,

$$u_{i\alpha} = \frac{1}{\sqrt{2mN}} \sum_{\mu=1}^D \left[Q_{\mu}(\mathbf{k}) e^{i\mathbf{k} \cdot \mathbf{r}_i^0 - i\omega_{\mu}(\mathbf{k})t} e_{\mu}^{\alpha}(\mathbf{k}) + Q_{\mu}^*(\mathbf{k}) e^{-i\mathbf{k} \cdot \mathbf{r}_i^0 + i\omega_{\mu}(\mathbf{k})t} e_{\mu}^{\alpha*}(\mathbf{k}) \right. \\ \left. + Q_{\mu}(-\mathbf{k}) e^{-i\mathbf{k} \cdot \mathbf{r}_i^0 - i\omega_{\mu}(\mathbf{k})t} e_{\mu}^{\alpha*}(\mathbf{k}) + Q_{\mu}^*(-\mathbf{k}) e^{i\mathbf{k} \cdot \mathbf{r}_i^0 + i\omega_{\mu}(\mathbf{k})t} e_{\mu}^{\alpha}(\mathbf{k}) \right] \quad (\text{F.28})$$

where we invoke the properties $e_{\mu}^{\alpha}(-\mathbf{k}) = e_{\mu}^{\alpha*}(\mathbf{k})$, $\omega_{\mu}(-\mathbf{k}) = \omega_{\mu}(\mathbf{k}) > 0$. Similarly,

$$v_{j\beta} = \frac{1}{\sqrt{2mN}} \sum_{\nu=1}^D \left[-i\omega_{\nu}(\mathbf{k}) Q_{\nu}(\mathbf{k}) e^{i\mathbf{k} \cdot \mathbf{r}_j^0 - i\omega_{\nu}(\mathbf{k})t} e_{\nu}^{\beta}(\mathbf{k}) \right. \\ \left. + i\omega_{\nu}(\mathbf{k}) Q_{\nu}^*(\mathbf{k}) e^{-i\mathbf{k} \cdot \mathbf{r}_j^0 + i\omega_{\nu}(\mathbf{k})t} e_{\nu}^{\beta*}(\mathbf{k}) \right. \\ \left. - i\omega_{\nu}(\mathbf{k}) Q_{\nu}(-\mathbf{k}) e^{-i\mathbf{k} \cdot \mathbf{r}_j^0 - i\omega_{\nu}(\mathbf{k})t} e_{\nu}^{\beta*}(\mathbf{k}) \right. \\ \left. + i\omega_{\nu}(\mathbf{k}) Q_{\nu}^*(-\mathbf{k}) e^{i\mathbf{k} \cdot \mathbf{r}_j^0 + i\omega_{\nu}(\mathbf{k})t} e_{\nu}^{\beta}(\mathbf{k}) \right]. \quad (\text{F.29})$$

Apparently, the $e^{i\mathbf{k} \cdot \mathbf{r}}$ terms in (F.28) are only going to couple with the $e^{-i\mathbf{k} \cdot \mathbf{r}}$ terms

in (F.29) and vice versa in (F.27). And two kinds of contributions are going to be generated from this product: $\mathbf{J}_3^+(\mathbf{k})$ from $Q_\mu(\mathbf{k})$, $Q_\nu(\mathbf{k})$ coupling, and $\mathbf{J}_3^-(\mathbf{k})$ from $Q_\mu(\mathbf{k})$, $Q_\nu(-\mathbf{k})$ coupling,

$$\Delta \mathbf{J}_3 \equiv \mathbf{J}_3^+(\mathbf{k}) + \mathbf{J}_3^+(-\mathbf{k}) + \mathbf{J}_3^-(\mathbf{k}), \quad (\text{F.30})$$

where

$$\begin{aligned} \mathbf{J}_3^+(\mathbf{k}) \equiv & \sum_{j=1}^N \sum_{\alpha=1}^D \sum_{\beta=1}^D \sum_{\mu=1}^D \sum_{\nu=1}^D \frac{i\omega_\nu(\mathbf{k})Q_\mu(\mathbf{k})Q_\nu^*(\mathbf{k})e^{-i\omega_{\mu\nu}(\mathbf{k})t}}{4m} e_\mu^\alpha(\mathbf{k})e_\nu^{\beta*}(\mathbf{k})\Phi_{\alpha\beta}^{ij}e^{i\mathbf{k}\cdot\mathbf{r}_{ij}^0}\mathbf{r}_{ij}^0 \\ & - \frac{i\omega_\nu(\mathbf{k})Q_\mu^*(\mathbf{k})Q_\nu(\mathbf{k})e^{i\omega_{\mu\nu}(\mathbf{k})t}}{4m} e_\mu^{\alpha*}(\mathbf{k})e_\nu^\beta(\mathbf{k})\Phi_{\alpha\beta}^{ij}e^{-i\mathbf{k}\cdot\mathbf{r}_{ij}^0}\mathbf{r}_{ij}^0, \quad (\text{F.31}) \end{aligned}$$

and

$$\begin{aligned} \mathbf{J}_3^-(\mathbf{k}) \equiv & \sum_{j=1}^N \sum_{\alpha=1}^D \sum_{\beta=1}^D \sum_{\mu=1}^D \sum_{\nu=1}^D \frac{-i\omega_\nu(\mathbf{k})Q_\mu(\mathbf{k})Q_\nu(-\mathbf{k})e^{-i\Omega_{\mu\nu}(\mathbf{k})t}}{4m} e_\mu^\alpha(\mathbf{k})e_\nu^{\beta*}(\mathbf{k})\Phi_{\alpha\beta}^{ij}e^{i\mathbf{k}\cdot\mathbf{r}_{ij}^0}\mathbf{r}_{ij}^0 \\ & + \frac{i\omega_\nu(\mathbf{k})Q_\mu^*(\mathbf{k})Q_\nu^*(-\mathbf{k})e^{i\Omega_{\mu\nu}(\mathbf{k})t}}{4m} e_\mu^{\alpha*}(\mathbf{k})e_\nu^\beta(\mathbf{k})\Phi_{\alpha\beta}^{ij}e^{-i\mathbf{k}\cdot\mathbf{r}_{ij}^0}\mathbf{r}_{ij}^0 \\ & - \frac{i\omega_\nu(\mathbf{k})Q_\mu(-\mathbf{k})Q_\nu(\mathbf{k})e^{-i\Omega_{\mu\nu}(\mathbf{k})t}}{4m} e_\mu^{\alpha*}(\mathbf{k})e_\nu^\beta(\mathbf{k})\Phi_{\alpha\beta}^{ij}e^{-i\mathbf{k}\cdot\mathbf{r}_{ij}^0}\mathbf{r}_{ij}^0 \\ & + \frac{i\omega_\nu(\mathbf{k})Q_\mu^*(-\mathbf{k})Q_\nu^*(\mathbf{k})e^{i\Omega_{\mu\nu}(\mathbf{k})t}}{4m} e_\mu^\alpha(\mathbf{k})e_\nu^{\beta*}(\mathbf{k})\Phi_{\alpha\beta}^{ij}e^{i\mathbf{k}\cdot\mathbf{r}_{ij}^0}\mathbf{r}_{ij}^0, \quad (\text{F.32}) \end{aligned}$$

where the *differential* and *combined* frequencies are

$$\omega_{\mu\nu}(\mathbf{k}) \equiv \omega_\mu(\mathbf{k}) - \omega_\nu(\mathbf{k}), \quad \Omega_{\mu\nu}(\mathbf{k}) \equiv \omega_\mu(\mathbf{k}) + \omega_\nu(\mathbf{k}) > 0. \quad (\text{F.33})$$

Comparing (F.31) with the group velocity formula (F.20), we see that some simplification is at foot. Let us separate the $\sum_{\mu=1}^D \sum_{\nu=1}^D$ summation in (F.31) into two parts, *diagonal* $\sum_{\mu=\nu}^D$, and *off-diagonal* $\sum_{\mu \neq \nu}^D$,

$$\mathbf{J}_3^+(\mathbf{k}) \equiv J_3^D(\mathbf{k}) + J_3^F(\mathbf{k}), \quad (\text{F.34})$$

where it can be easily checked against (F.20) that

$$\begin{aligned}\mathbf{J}_3^D(\mathbf{k}) &\equiv \sum_{j=1}^N \sum_{\alpha=1}^D \sum_{\beta=1}^D \sum_{\mu=1}^D \text{Im} \frac{\omega_\mu(\mathbf{k}) Q_\mu^*(\mathbf{k}) Q_\mu(\mathbf{k}) e_\mu^{\alpha*}(\mathbf{k}) e_\mu^\beta(\mathbf{k}) e^{-i\mathbf{k} \cdot \mathbf{r}_{ij}^0}}{2m} \Phi_{\alpha\beta}^{ij} \mathbf{r}_{ij}^0 \\ &= \sum_{\mu=1}^D \omega_\mu(\mathbf{k})^2 |Q_\mu(\mathbf{k})|^2 \mathbf{v}_G^\mu(\mathbf{k}),\end{aligned}\tag{F.35}$$

using the fact that $\mathbf{v}_G^\mu(\mathbf{k})$ is real. And the off-diagonal heat current $J_3^F(\mathbf{k})$, after some manipulations, is found to be

$$\mathbf{J}_3^F(\mathbf{k}) \equiv \sum_{j=1}^N \sum_{\alpha=1}^D \sum_{\beta=1}^D \sum_{\mu>\nu}^D \text{Im} \frac{\Omega_{\mu\nu}(\mathbf{k}) Q_\mu^*(\mathbf{k}) Q_\nu(\mathbf{k}) e^{i\omega_{\mu\nu}(\mathbf{k})t - i\mathbf{k} \cdot \mathbf{r}_{ij}^0} e_\mu^{\alpha*}(\mathbf{k}) e_\nu^\beta(\mathbf{k})}{2m} \Phi_{\alpha\beta}^{ij} \mathbf{r}_{ij}^0,\tag{F.36}$$

where we used the inversion symmetry of the crystal.

In the same spirit, $\mathbf{J}_3^-(\mathbf{k})$ in (F.32) can be simplified as

$$\begin{aligned}&\sum_{j=1}^N \sum_{\alpha=1}^D \sum_{\beta=1}^D \sum_{\mu=1}^D \sum_{\nu=1}^D \text{Im} \frac{\omega_\nu(\mathbf{k}) Q_\mu(\mathbf{k}) Q_\nu(-\mathbf{k}) e^{-i\Omega_{\mu\nu}(\mathbf{k})t}}{2m} e_\mu^\alpha(\mathbf{k}) e_\nu^{\beta*}(\mathbf{k}) \Phi_{\alpha\beta}^{ij} e^{i\mathbf{k} \cdot \mathbf{r}_{ij}^0} \mathbf{r}_{ij}^0 \\ &\quad + \text{Im} \frac{\omega_\nu(\mathbf{k}) Q_\mu(-\mathbf{k}) Q_\nu(\mathbf{k}) e^{-i\Omega_{\mu\nu}(\mathbf{k})t}}{2m} e_\mu^{\alpha*}(\mathbf{k}) e_\nu^\beta(\mathbf{k}) \Phi_{\alpha\beta}^{ij} e^{-i\mathbf{k} \cdot \mathbf{r}_{ij}^0} \mathbf{r}_{ij}^0 \\ &= \sum_{j=1}^N \sum_{\alpha=1}^D \sum_{\beta=1}^D \sum_{\mu>\nu}^D \text{Im} \frac{\omega_\nu(\mathbf{k}) Q_\mu(\mathbf{k}) Q_\nu(-\mathbf{k}) e^{-i\Omega_{\mu\nu}(\mathbf{k})t}}{2m} e_\mu^\alpha(\mathbf{k}) e_\nu^{\beta*}(\mathbf{k}) \Phi_{\alpha\beta}^{ij} e^{i\mathbf{k} \cdot \mathbf{r}_{ij}^0} \mathbf{r}_{ij}^0 \\ &\quad + \text{Im} \frac{\omega_\nu(\mathbf{k}) Q_\mu(-\mathbf{k}) Q_\nu(\mathbf{k}) e^{-i\Omega_{\mu\nu}(\mathbf{k})t}}{2m} e_\mu^{\alpha*}(\mathbf{k}) e_\nu^\beta(\mathbf{k}) \Phi_{\alpha\beta}^{ij} e^{-i\mathbf{k} \cdot \mathbf{r}_{ij}^0} \mathbf{r}_{ij}^0 \\ &\quad + \text{Im} \frac{\omega_\mu(\mathbf{k}) Q_\nu(\mathbf{k}) Q_\mu(-\mathbf{k}) e^{-i\Omega_{\mu\nu}(\mathbf{k})t}}{2m} e_\nu^\alpha(\mathbf{k}) e_\mu^{\beta*}(\mathbf{k}) \Phi_{\alpha\beta}^{ij} e^{i\mathbf{k} \cdot \mathbf{r}_{ij}^0} \mathbf{r}_{ij}^0 \\ &\quad + \text{Im} \frac{\omega_\mu(\mathbf{k}) Q_\nu(-\mathbf{k}) Q_\mu(\mathbf{k}) e^{-i\Omega_{\mu\nu}(\mathbf{k})t}}{2m} e_\nu^{\alpha*}(\mathbf{k}) e_\mu^\beta(\mathbf{k}) \Phi_{\alpha\beta}^{ij} e^{-i\mathbf{k} \cdot \mathbf{r}_{ij}^0} \mathbf{r}_{ij}^0 \\ &= \sum_{j=1}^N \sum_{\alpha=1}^D \sum_{\beta=1}^D \sum_{\mu>\nu}^D \text{Im} \frac{\omega_{\mu\nu}(\mathbf{k}) Q_\nu(\mathbf{k}) Q_\mu(-\mathbf{k}) e^{-i\Omega_{\mu\nu}(\mathbf{k})t}}{2m} e_\nu^\alpha(\mathbf{k}) e_\mu^{\beta*}(\mathbf{k}) \Phi_{\alpha\beta}^{ij} e^{i\mathbf{k} \cdot \mathbf{r}_{ij}^0} \mathbf{r}_{ij}^0 \\ &\quad + \text{Im} \frac{\omega_{\mu\nu}(\mathbf{k}) Q_\nu(-\mathbf{k}) Q_\mu(\mathbf{k}) e^{-i\Omega_{\mu\nu}(\mathbf{k})t}}{2m} e_\nu^{\alpha*}(\mathbf{k}) e_\mu^\beta(\mathbf{k}) \Phi_{\alpha\beta}^{ij} e^{-i\mathbf{k} \cdot \mathbf{r}_{ij}^0} \mathbf{r}_{ij}^0\end{aligned}\tag{F.37}$$

where again we used the inversion symmetry of the crystal to make the diagonal terms vanish and to combine off-diagonal terms.

The sum of $\mathbf{J}_3^D(\mathbf{k})$ with \mathbf{k} 's turns out to be the canonical *phonon heat current*,

$$\mathbf{J}_4 \equiv \sum_{\mathbf{k}} \mathbf{J}_3^D(\mathbf{k}) = \sum_{\mathbf{k}} \sum_{\mu=1}^D \omega_{\mu}(\mathbf{k})^2 |Q_{\mu}(\mathbf{k})|^2 \mathbf{v}_G^{\mu}(\mathbf{k}) = \sum_{\mathbf{k}} \sum_{\mu=1}^D E_{\mu}(\mathbf{k}) \mathbf{v}_G^{\mu}(\mathbf{k}), \quad (\text{F.38})$$

where $E_{\mu}(\mathbf{k})$ is the total energy of a specific phonon (see (F.24)). It has the intuitive interpretation of a phonon *wave-pack* with central frequency $\omega_{\mu}(\mathbf{k})$ and slight $\Delta\omega$ dispersion, traveling with velocity $\mathbf{v}_G^{\mu}(\mathbf{k})$ and carrying with it its own energy. Since Peierls first proposed the (F.38) form in 1929, it is almost always taken as exact at the start of a phonon-theoretical calculation for κ . Even the most careful textbooks [57, 59] lack a quantitative derivation of where it comes from, and an estimation of its range of validity. The potential problems with (F.38), as I see it, are

- It is not clear that the phonon wave-pack picture is literally correct in a conducting lattice, which says that any $\mathbf{k}\omega$ vibration is more or less localized in space like particles. How does that come about? Do the vibrations have tendency to form wave-packs? How does a wave-pack contain its dispersion – the increase of $\Delta\omega$ with time? If the above picture is not literally correct, that the actual lattice is a jiggling web with more or less *uniform* activities everywhere, then how should one justify (F.38)?
- In using (F.38) with phonon perturbation theories such as the phonon Boltzmann's equation, we can at best do the lowest-order perturbation accurately since the heat current expression itself is only accurate to the lowest order, as seen by (F.15), and the fact that harmonic approximation is used ((F.21),(F.22)) in deriving \mathbf{J}_4 from \mathbf{J}_3 .

(F.38) is a simplified description which does not *necessarily* give the complete inventory of heat carriers by atomic vibrations. What might be left out, in a significant way, are the anharmonic and *non-coherent* carriers, which we shall call the *atomistic heat carriers*, that have lifetimes on the order of ν_D^{-1} and “mean free paths” on the order of a few atomic spacing, which should play an increasingly important role at high T . Their existence is suggested by the atomistic simulation of Ladd *et al*, where

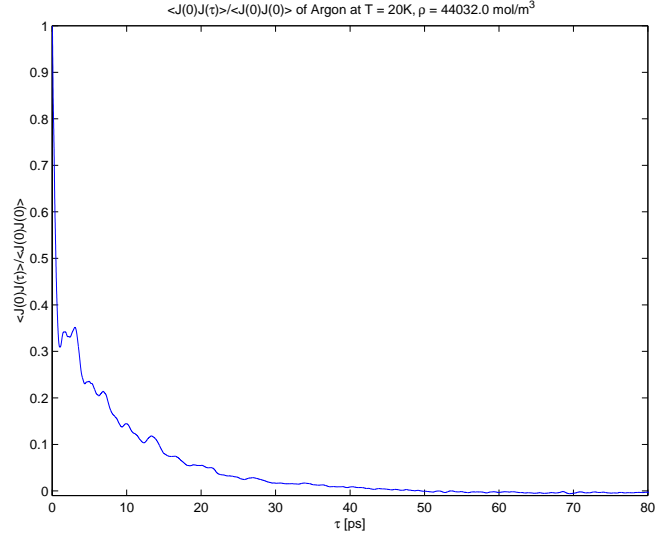


Figure F-1: Normalized $\langle \mathbf{J}_1(\tau) \cdot \mathbf{J}_1(0) \rangle$ of solid Ar (500 particles) at 20K, using Woon's pair potential[71]. The calculated $\kappa = 1.56 \text{ W/M/K}$.

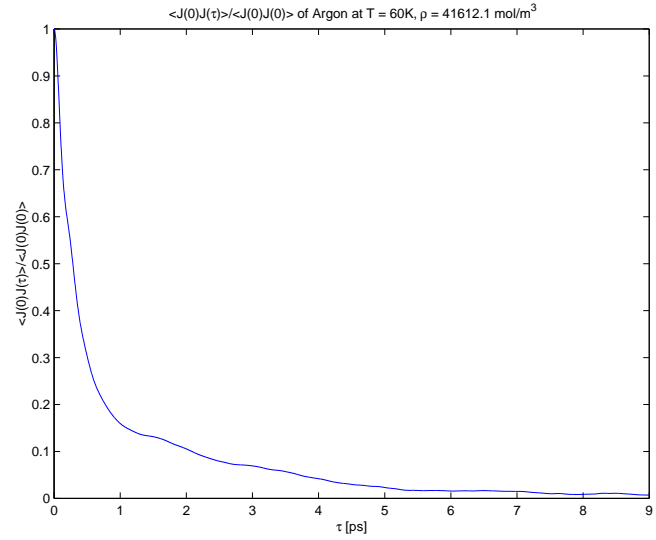


Figure F-2: Normalized $\langle \mathbf{J}_1(\tau) \cdot \mathbf{J}_1(0) \rangle$ of solid Ar (500 particles) at 60K, using Woon's pair potential. The calculated $\kappa = 0.334 \text{ W/M/K}$.

the “phonon contribution” $\langle \mathbf{J}_4(\tau) \cdot \mathbf{J}_4(0) \rangle$ accounts for only 60% of the material’s κ at half of the melting temperature⁵ (see their Table I). Associated with this enlarging discrepancy in κ at high T is a significant “zeroth-stage” in the correlation function $\langle \mathbf{J}_2(\tau) \cdot \mathbf{J}_2(0) \rangle$ (see their Fig. 1, and our Fig. F-1, F-2), which has a much bigger $\tau = 0$ value than $\langle \mathbf{J}_4(\tau) \cdot \mathbf{J}_4(0) \rangle$, but decays fast ($\sim \nu_D^{-1}$) and is then replaced by a second, much slower ($\sim \tau_p$) “phonon stage”. This two-stage behavior could not be derived based on (F.38), and was first discovered in the atomistic simulation of Ladd *et al.* Is it merely a peculiarity of us choosing to use the atomistic heat currents \mathbf{J}_1 or \mathbf{J}_2 , or does it suggest that some real physical mechanisms are at work? At this moment we are not sure yet, but the fact that there is a significant discrepancy in calculated κ at high T seems to suggest the latter. Also, taking the view that there exists a distinct sort of “atomistic heat carriers” may help us better understand κ of amorphous and other defect-saturated materials, since the phonon picture and the slow “phonon stage” in $\langle \mathbf{J}_2(\tau) \cdot \mathbf{J}_2(0) \rangle$ are *non-existent* there, leaving one with only the non-coherent carriers that have mean free times ν_D^{-1} and mean free paths of a few atomic spacing, and just the “zeroth-stage”. It is our hope that through the atomistic heat currents \mathbf{J}_1 and \mathbf{J}_2 , one could relate the thermal conductivity of the amorphous phase to that of the perfect crystal, which is not possible in the picture of coherent phonon carriers⁶.

On the other hand, it is not easy to directly analyze \mathbf{J}_1 or \mathbf{J}_2 since they are fully nonlinear expressions. But by empirical evidence (see Fig. 1 in Ladd *et al.*’s paper), it is likely that the zeroth-stage of $\langle \mathbf{J}_3(\tau) \cdot \mathbf{J}_3(0) \rangle$ *closely approximates* that of $\langle \mathbf{J}_2(\tau) \cdot \mathbf{J}_2(0) \rangle$, with better $\tau = 0$ value and nearly the same decay rate. Thus it *might* do us some service by looking at the terms which we drop when going from \mathbf{J}_3 to \mathbf{J}_4 , namely, \mathbf{J}_3^- and \mathbf{J}_3^F , which are *harmonic* (they also come from \mathbf{J}_3), but are also *non-coherent*, meaning that they are not steady in \mathbf{k} and slowly-varying as the

⁵And this is only by the difference between \mathbf{J}_4 and \mathbf{J}_2 – the trajectory is still fully atomistic in evaluating $\langle \mathbf{J}_4(\tau) \cdot \mathbf{J}_4(0) \rangle$! It is thus hard to imagine that an accurate phonon theory can afford to dismiss higher-order nonlinearities, and in that respect using the expression (F.38), without appropriate justifications.

⁶Or rather, in that paradigm of thought, what I said is like talking from a psychiatric ward.

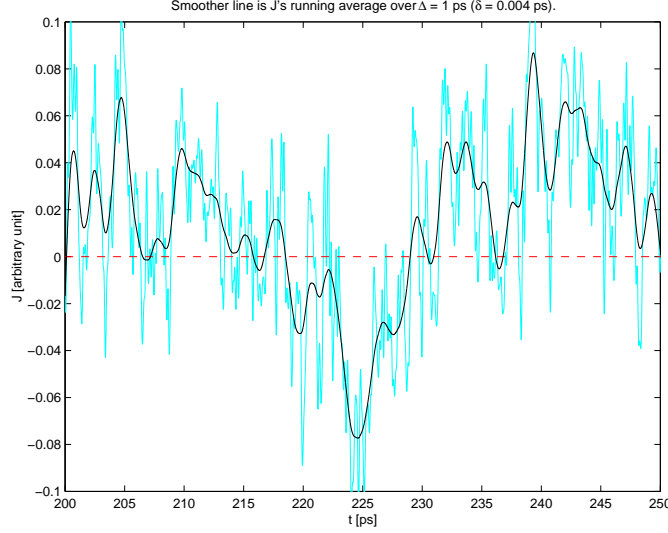


Figure F-3: A length of J_{1x} heat current in an atomistic simulation of solid Ar at 20K using Woon’s pair potential. The smoothed curve will be shown to mainly come from the phonon heat current \mathbf{J}_4 , while the high-frequency “fluctuations” mainly come from \mathbf{J}_3^- and \mathbf{J}_3^F .

coherent \mathbf{J}_3^D , but are instead Langevin-type “random” fluctuations which nonetheless carry some heat.

The reason that \mathbf{J}_3^F and \mathbf{J}_3^- behave like fluctuations is that the phonon amplitude $Q_\mu(\mathbf{k})$ is *almost*⁷ independent of $Q_{\nu'}(-\mathbf{k})$ and $Q_{\nu \neq \mu}(\mathbf{k})$ ’s, since Q ’s with different \mathbf{k} or μ do not couple in the system Hamiltonian (F.24). So as products of nearly independent variables (see (F.36), (F.37)), $\mathbf{J}_3^F(\mathbf{k})$ and $\mathbf{J}_3^-(\mathbf{k})$ could either be positive or negative at a given moment; which happens is completely random. Also, given that $\mathbf{J}_3^F(\mathbf{k})$ has a certain sign at t , it will be reversed in a matter of $2\pi\omega_{\mu\nu}^{-1}(\mathbf{k})$ seconds because of the $e^{i\omega_{\mu\nu}(\mathbf{k})t}$ factor in (F.36). Same thing happens for $\mathbf{J}_3^-(\mathbf{k})$, defined in (F.37), except that it is even quicker, in a matter of $2\pi\Omega_{\mu\nu}^{-1}(\mathbf{k}) \sim \nu_D^{-1}$ seconds. This means that $\mathbf{J}_3^-(\mathbf{k})$ and $\mathbf{J}_3^F(\mathbf{k})$ vary much more quickly compared to the steadier $\mathbf{J}_3^D(\mathbf{k})$, which also varies but with time-constant $\sim \tau_p$, the phonon mean free time, because $|Q_\mu(\mathbf{k})|^2$, the phonon occupation number, evolves with that timescale. Thus, correlation in \mathbf{J}_4 decays as $\sim \tau_p$, while correlation in \mathbf{J}_3^- decays as $\sim 2\pi\Omega_{\mu\nu}^{-1}(\mathbf{k})^{-1}$ and correlation in \mathbf{J}_3^F decays as $\sim 2\pi\omega_{\mu\nu}^{-1}(\mathbf{k})$, slower than \mathbf{J}_3^- but nonetheless fluctuation-like. This

⁷Almost, because the harmonic approximation is only an approximation, with error $\sim T^{3/2}$.

explains the two-stage (or three-stage) behavior of $\langle \mathbf{J}_3(\tau) \cdot \mathbf{J}_3(0) \rangle$, with the estimated time-constants agreeing with simulation results. For instance, the Debye temperature of perfect Ar crystal is about 80K, which corresponds to a typical atomic oscillation period of

$$\nu_D^{-1} = \frac{h}{k_B T_D} = \frac{6.6260755 \times 10^{-34} \text{J} \cdot \text{s}}{1.380658 \times 10^{-23} \text{J/K} \times 80 \text{K}} = 0.6 \text{ ps}, \quad (\text{F.39})$$

which compares well with the cease-times of the “zeroth-stage” in Fig. F-1, F-2.

Our last task is to estimate the contribution of \mathbf{J}_3^F and \mathbf{J}_3^- to $\langle \mathbf{J}_3(0) \cdot \mathbf{J}_3(0) \rangle$. Note that there is no cross-coupling between \mathbf{J}_3^F , \mathbf{J}_3^- , and \mathbf{J}_4 in $\langle |\mathbf{J}_3|^2 \rangle$, because a single Q is always left out inside the contraction, which averages to zero on a complex circle. Since

$$\mathbf{J}_4 = \sum_{\mathbf{k}} \sum_{\mu=1}^D E_{\mu}(\mathbf{k}) \mathbf{v}_G^{\mu}(\mathbf{k}) = \sum_{\mathbf{k}} \sum_{\mu=1}^D \delta E_{\mu}(\mathbf{k}) \mathbf{v}_G^{\mu}(\mathbf{k}), \quad (\text{F.40})$$

where $\delta E_{\mu}(\mathbf{k})$ is the instantaneous deviation in phonon occupation,

$$\delta E_{\mu}(\mathbf{k}) \equiv E_{\mu}(\mathbf{k}) - \langle E_{\mu}(\mathbf{k}) \rangle. \quad (\text{F.41})$$

And, we will later benefit from the following property,

$$\langle \delta E_{\mu}(\mathbf{k})^2 \rangle = \langle E_{\mu}(\mathbf{k}) \rangle^2, \quad (\text{F.42})$$

which happens to be exactly correct for the equilibrium Boltzmann distribution,

$$dP \propto \exp \left(-\frac{E_{\mu}(\mathbf{k})}{k_B T} \right) dE_{\mu}(\mathbf{k}), \quad E_{\mu}(\mathbf{k}) > 0, \quad (\text{F.43})$$

that enables us to use $\langle |\mathbf{J}_4|^2 \rangle$ as a benchmark, against which $\langle |\mathbf{J}_3^F|^2 \rangle$, $\langle |\mathbf{J}_3^-|^2 \rangle$ are compared. In the end we simply add everything together to obtain the *total harmonic fluctuation*,

$$\langle |\mathbf{J}_3|^2 \rangle = \langle |\mathbf{J}_4|^2 \rangle + \langle |\mathbf{J}_3^F|^2 \rangle + \langle |\mathbf{J}_3^-|^2 \rangle. \quad (\text{F.44})$$

We note that the $\mathbf{J}_3^F(\mathbf{k})$ expression (F.36), which has $D(D-1)/2$ terms, is similar to $\mathbf{J}_3^D(\mathbf{k})$ in (F.35) before it is simplified, which has D terms, except that $\Omega_{\mu\nu}(\mathbf{k})$

now takes the place of $\omega_\mu(\mathbf{k})$, and an off-diagonal matrix element constant $\mathbf{W}_{\mu\nu}$ now takes the place of the group velocity $\mathbf{v}_G^\mu \equiv \mathbf{W}_{\mu\mu}$. Let us assume that, on the average, $\Omega_{\mu\nu}(\mathbf{k})$ can be taken as $2\omega_\mu(\mathbf{k})$, and the $\mu\nu$ transition strength on the average is

$$|\overline{\mathbf{W}_{\mu\nu}}|^2 \approx \Gamma |\overline{\mathbf{W}_{\mu\mu}}|^2, \quad \mu \neq \nu, \quad (\text{F.45})$$

where the Γ factor is clearly potential-model dependent⁸ and could be anywhere between 1/3 and 1/2. Also, the phase of $Q_\mu^*(\mathbf{k})Q_\nu(\mathbf{k})e^{i\omega_{\mu\nu}(\mathbf{k})t}$ is indeterminate, making $|\text{Im}|^2$ shrink by a factor of 2 on the time average. We thus expect that on the average,

$$\frac{\langle |\mathbf{J}_3^F|^2 \rangle}{\langle |\mathbf{J}_4|^2 \rangle} \sim \frac{D(D-1)}{2} \times \frac{1}{D} \times 2^2 \times \Gamma \times \frac{1}{2} = (D-1)\Gamma. \quad (\text{F.46})$$

As for \mathbf{J}_3^- , let me assume that $|\omega_{\mu\nu}(\mathbf{k})|$ can be approximated by $\lambda\omega_\mu(\mathbf{k})$, with a sensible choice⁹ of λ perhaps between 1/4 and 1/3. We also see that the final expression (F.37) is actually composed of a $Q_\nu(\mathbf{k})Q_\mu(-\mathbf{k})$ part and a $Q_\nu(-\mathbf{k})Q_\mu(\mathbf{k})$ part with $\mu > \nu$, which do *not* couple with each other in $\langle |\mathbf{J}_3|^2 \rangle$. Thus, following the same arguments for \mathbf{J}_3^F ,

$$\frac{\langle |\mathbf{J}_3^-|^2 \rangle}{\langle |\mathbf{J}_4|^2 \rangle} \sim \frac{D(D-1)}{2} \times \frac{1}{D} \times \lambda^2 \times \Gamma \times \frac{1}{2} = \frac{\lambda^2}{4}(D-1)\Gamma, \quad (\text{F.47})$$

which is actually quite small compared with $\langle |\mathbf{J}_3^F|^2 \rangle$ contribution.

Thus, the total harmonic fluctuation $\langle |\mathbf{J}_3|^2 \rangle$ is enhanced from the phonon contribution $\langle |\mathbf{J}_4|^2 \rangle$ by a factor of

$$F_3(T) \equiv \frac{\langle |\mathbf{J}_3|^2 \rangle}{\langle |\mathbf{J}_4|^2 \rangle} \sim 1 + (D-1)\Gamma \left(1 + \frac{\lambda^2}{4} \right). \quad (\text{F.48})$$

So if we take reasonable parameters $\Gamma = 1/2$, $\lambda = 1/3$ at $D = 3$, $F_3(T)$ will be slightly bigger than 2, which compares well with Ladd *et al's* Fig. 1.

⁸For instance, if one assumes that $|V''| \gg |V'/r|$ in (F.14), then it can be shown that $\Gamma = 1/3$ if the orientations of $\mathbf{e}_\mu(\mathbf{k})$, $\mathbf{e}_\nu(\mathbf{k})$ are spherically “random”, but which of course is not true.

⁹To evaluate λ of an monoatomic crystal, we should calculate the average $|\Delta\omega(\mathbf{k})|$ between one longitudinal branch and two transverse branches, and between the two transverse branches.

Formally, one could always define

$$F_1(T) \equiv \frac{\langle |\mathbf{J}_1|^2 \rangle}{\langle |\mathbf{J}_4|^2 \rangle}, \quad F_2(T) \equiv \frac{\langle |\mathbf{J}_2|^2 \rangle}{\langle |\mathbf{J}_4|^2 \rangle}. \quad (\text{F.49})$$

At low temperature the harmonic approximation is very good, so

$$\mathbf{J}_1(t) \approx \mathbf{J}_2(t) \approx \mathbf{J}_3(t), \quad F_1(T) \approx F_2(T) \approx F_3(T). \quad (\text{F.50})$$

At higher temperatures the harmonic approximation starts to break down, so one can no longer use $F_3(T)$ to track $F_1(T)$ and $F_2(T)$ in an accurate manner. In doing so, we would have made two errors: 1) the nonlinear *terms* that we drop in going from \mathbf{J}_1 or \mathbf{J}_2 to \mathbf{J}_3 . 2) in deriving \mathbf{J}_3^F , \mathbf{J}_3^- and \mathbf{J}_3^D , we made use of (F.21) and (F.22), which come from the harmonic approximation of particle *dynamics*. One needs a genuine nonlinear theory to account for $F_1(T)$ and $F_2(T)$, and for that matter, $F_3(T)$ itself, at higher T , instead of the harmonic analysis above.

From the simulation results of solid Ar we find that $F_1(T)$ is quite stationary, ranging from 2.5 at 10K to about 3.0 at 60K. It might be correct that $F_1(T)$ and $F_2(T)$ are *always greater* than $F_3(T)$, as suggested by Ladd *et al*'s Fig. 1 (which is at 1/4 of the melting temperature), due to extra contributions from the nonlinear terms. It is also an observed property that the transition from the zeroth-stage to the phonon stage happens at about 1 *ps*, despite of the quite large temperature and κ variations. The “extra area” enclosed by the zeroth-stage in $\langle \mathbf{J}_1(\tau) \cdot \mathbf{J}_1(0) \rangle$ is found to be about 0.1 – 0.2 W/M/K for Ar.

We also see from (F.36) and (F.37) that a 1D chain with one degree of motion has

$$\mathbf{J}_3^F(\mathbf{k}) = \mathbf{J}_3^-(\mathbf{k}) = 0, \quad (\text{F.51})$$

so its $\langle \mathbf{J}_3(\tau) \cdot \mathbf{J}_3(0) \rangle$ has no zeroth-stage, and the harmonic heat current \mathbf{J}_3 , unlike that of Ar in Fig. F-3, is smooth and slowly-varying. This rather strange behavior corroborates with the fact that such 1D chain has $\kappa = +\infty$ in the lowest-order phonon perturbation theory, since in no way can $\mathbf{k}_1 \pm \mathbf{k}_2 \pm \mathbf{k}_3 = 0$ and $\omega(\mathbf{k}_1) \pm \omega(\mathbf{k}_2) \pm \omega(\mathbf{k}_3) = 0$

be simultaneously satisfied. So we cannot learn much from 1D chain in this regard¹⁰. I mention it because the 1D chain system is the simplest to simulate, and to evaluate (F.38), which uses FFT in only one dimension. Higher-dimensional systems require diagonalizing the dynamical matrix and storing all the eigenvectors, but it seems to be the only way one can proceed to get physically meaningful results.

¹⁰Does this remain true when higher-order nonlinearities or defects are included? I do not know.

Appendix G

Truncation Schemes for Pair Potential

Consider the single-element LJ6-12 potential,

$$V(r) = 4\varepsilon \left[\left(\frac{\sigma}{r} \right)^{12} - \left(\frac{\sigma}{r} \right)^6 \right]. \quad (\text{G.1})$$

Practically we can only carry out the potential summation up to a certain radius cutoff¹. There are many ways to truncate, the simplest of which is to modify the interaction as

$$V_0(r) = \begin{cases} V(r) - V(r_c), & r < r_c \\ 0, & r \geq r_c \end{cases}. \quad (\text{G.2})$$

However, $V_0(r)$ is discontinuous in the 1st derivative at $r = r_c$, which causes large error in motion integration (especially in high-order algorithms such as the predictor-corrector method) if an atom crosses r_c , and is very detrimental to calculating long correlation functions. Another commonly used scheme

$$V_1(r) = \begin{cases} V(r) - V(r_c) - V'(r_c)(r - r_c), & r < r_c \\ 0, & r \geq r_c \end{cases} \quad (\text{G.3})$$

¹It is also physically impossible to maintain r^{-6} asymptote in condensed matter because of exponential screening.

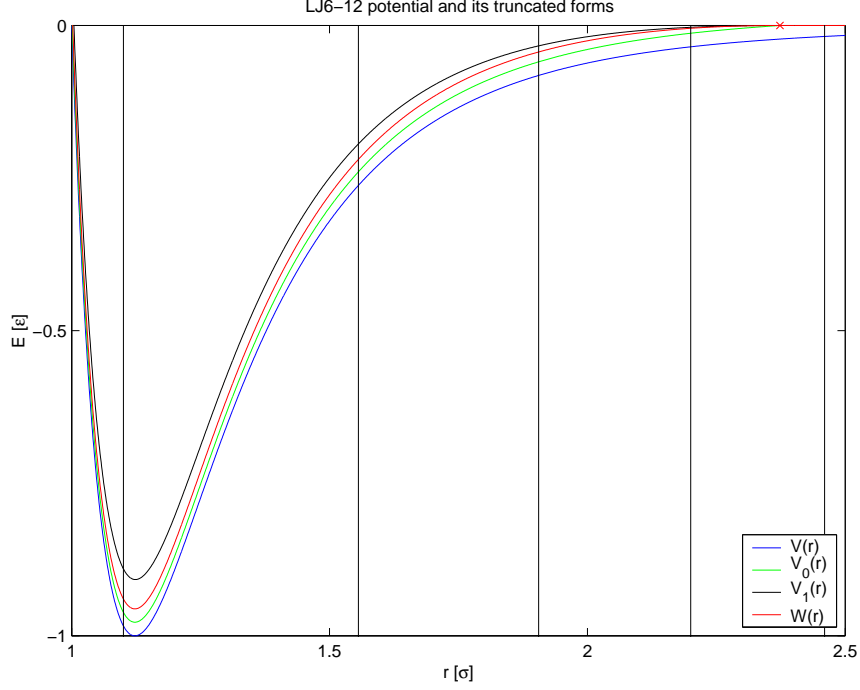


Figure G-1: Lennard Jones potential and its modified forms with cutoff $r_c = 2.37343 \sigma$. Black lines indicate positions of neighbors in a single-element fcc crystal at 0K.

makes the force continuous at $r = r_c$, but also makes the potential well too shallow (see Fig. G-1), and is more expensive computationally because we have to take the square root for each neighbor.

I recommend using the following truncation scheme,

$$W(r) = \begin{cases} 4\epsilon \left[\left(\frac{\sigma}{r}\right)^{12} - \left(\frac{\sigma}{r}\right)^6 + \left(2\left(\frac{\sigma}{r_c}\right)^{18} - \left(\frac{\sigma}{r_c}\right)^{12}\right) \left(\frac{r}{\sigma}\right)^6 - 3\left(\frac{\sigma}{r_c}\right)^{12} + 2\left(\frac{\sigma}{r_c}\right)^6 \right], & r < r_c, \\ 0, & r \geq r_c. \end{cases} \quad (\text{G.4})$$

$W(r)$, $V(r)$, $V_0(r)$ and $V_1(r)$ are all plotted in Fig. G-1 for comparison. r_c is chosen to be 2.37343077641σ , which falls exactly at the 2/3 interval between the 4th and 5th neighbors at equilibrated fcc lattice of 0K.

There is clearly a tradeoff in picking r_c . If r_c is large, the effect of the artificial truncation is small. And since an atom interacts with more neighbors, it supposedly reflects more physics. On the other hand, maintaining and summing over a large neighbor list costs more. For a properly implemented $\mathcal{O}(N)$ MD code, that neighbor

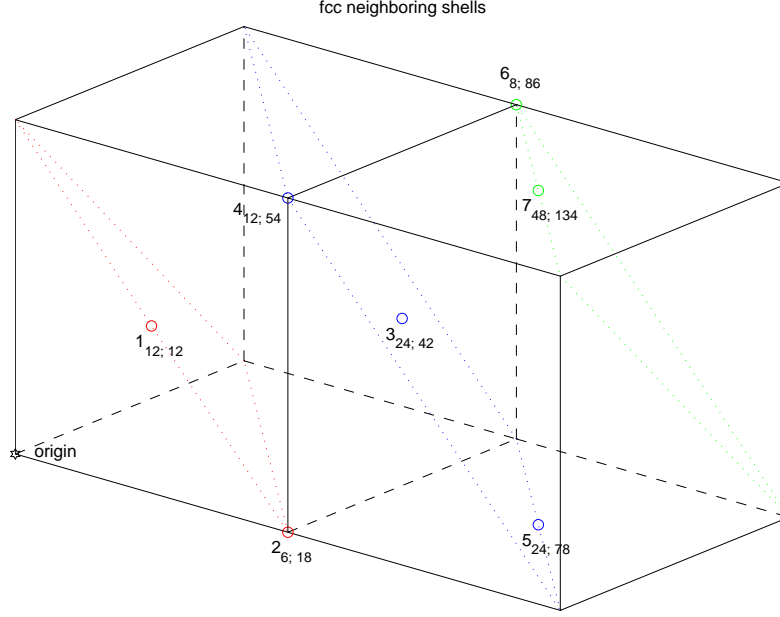


Figure G-2: fcc neighboring shells. For example, label “6_{8; 86}” means there are eight 6th-nearest neighbors of the type shown in figure, which adds up to 86 neighbors in all if included. The ABC stacking planes are also shown in the figure.

number *vs* cost relation is almost linear.

Let us see what is the minimal r_c for a fcc solid. Fig. G-2 shows the neighboring atom shells and their duplicity. Also drawn are the three glide planes. With (G.4), once the number of interacting neighbor shells are determined, we can evaluate the equilibrium volume and bulk modulus of the crystal in closed form. The potential energy of the i th atom is

$$e_i = \frac{1}{2} \sum_{j \neq i}^{r_{ij} < r_c} W(r_{ij}). \quad (\text{G.5})$$

For fcc crystal, we can extract scale-independent coefficients from the above summation and differentiate with only to the lattice constant a – the minima of which yields the equilibrium lattice constant a_0 . If we demand r_c to fall into an exact position between the highest included shell and the lowest excluded shell, we can iterate the process until mutual consistency is achieved. We then plug a_0 into (G.5) to calculate the binding energy per atom, e_0 ; the atomic volume

$$\Omega_0 = \frac{a_0^3}{4}, \quad (\text{G.6})$$

Table G.1: FCC neighboring shells included in Eqn (G.4)

n	N	$r_c[\sigma]$	$a_0[\sigma]$	$\Omega_0[\sigma^3]$	$e_0[\varepsilon]$	$B[\varepsilon\sigma^{-3}]$
1	12	1.44262944953	1.59871357076	1.02153204121	-2.03039845846	39.39360127902
2	18	1.81318453769	1.57691543349	0.98031403353	-4.95151157088	52.02448553061
3	42	2.11067974132	1.56224291246	0.95320365252	-6.12016548816	58.94148705580
4	54	2.37343077641	1.55584092331	0.94153307381	-6.84316556834	64.19738627468
5	78	2.61027143673	1.55211914976	0.93479241591	-7.27254778301	66.65093979162
6	86	2.82850677530	1.55023249772	0.93138774467	-7.55413237921	68.53093399765
7	134	3.03017270367	1.54842162594	0.92812761235	-7.74344974981	69.33961787572
8	140	3.21969263257	1.54727436382	0.92606612556	-7.88758411490	70.63452119577
9	176	3.39877500485	1.54643096926	0.92455259927	-7.99488847415	71.18713376234
10	200	3.56892997792	1.54577565469	0.92337773387	-8.07848627384	71.76659559499

and the bulk modulus

$$B = \left. \frac{dP}{d \log \Omega} \right|_{\Omega_0} = \frac{4}{9a_0} \left. \frac{d^2 e}{da^2} \right|_{a_0}. \quad (\text{G.7})$$

The self-consistent results for r_c ratio $2/3$ are shown in Table G.1. That is, r_c is exactly at $2/3$ the distance between the n th interacting shell and the $(n+1)$ th non-interacting shell. The reason for $2/3 > 1/2$ is that we expect more tension tests than compression tests, and there is thermal expansion at finite temperature.

Appendix H

Improving the Efficiency of Stillinger-Weber Potential

The Stillinger-Weber potential[157, 156] has a three-body site energy of the form,

$$V_{3i} = \lambda \sum_{j < k} \exp \left(\frac{\gamma}{r_{ij} - a} + \frac{\gamma}{r_{ik} - a} \right) \left(\cos \theta_{jik} + \frac{1}{3} \right)^2, \quad r_{ij}, r_{ik} < a, \quad (\text{H.1})$$

that seems to require double looping over neighbors. By converting it to a single summation in a tensorial EAM type, one can reduce the computational time and memory requirement to about 1/3 of the original, which is advantageous for large scale molecular dynamics simulations. Two side benefits are improved numerical accuracy, and smaller and faster neighborlist, since one can now count pairs instead of neighbors.

Consider the following re-summations,

$$\begin{aligned} & \sum_{j < k} g(r_{ij})g(r_{ik}) \\ = & \frac{1}{2} \left[\sum_{j,k} g(r_{ij})g(r_{ik}) - \sum_j g(r_{ij})^2 \right] \\ = & \frac{1}{2} \left[\left(\sum_j g(r_{ij}) \right)^2 - \sum_j g(r_{ij})^2 \right], \end{aligned} \quad (\text{H.2})$$

$$\begin{aligned}
& \sum_{j < k} g(r_{ij})g(r_{ik}) \cos(\theta_{jik}) \\
&= \frac{1}{2} \left[\sum_{j,k} g(r_{ij})g(r_{ik}) \cos(\theta_{jik}) - \sum_j g(r_{ij})^2 \right] \\
&= \frac{1}{2} \left[\sum_{j,k} g(r_{ij})g(r_{ik}) \sum_{\alpha=1}^3 \hat{r}_{ij}^\alpha \hat{r}_{ik}^\alpha - \sum_j g(r_{ij})^2 \right] \\
&= \frac{1}{2} \left[\sum_{\alpha=1}^3 \left(\sum_j g(r_{ij}) \hat{r}_{ij}^\alpha \right)^2 - \sum_j g(r_{ij})^2 \right], \tag{H.3}
\end{aligned}$$

$$\begin{aligned}
& \sum_{j < k} g(r_{ij})g(r_{ik}) \cos^2(\theta_{jik}) \\
&= \frac{1}{2} \left[\sum_{j,k} g(r_{ij})g(r_{ik}) \cos^2(\theta_{jik}) - \sum_j g(r_{ij})^2 \right] \\
&= \frac{1}{2} \left[\sum_{j,k} g(r_{ij})g(r_{ik}) \sum_{\alpha=1}^3 \sum_{\beta=1}^3 \hat{r}_{ij}^\alpha \hat{r}_{ik}^\alpha \hat{r}_{ij}^\beta \hat{r}_{ik}^\beta - \sum_j g(r_{ij})^2 \right] \\
&= \frac{1}{2} \left[\sum_{\alpha=1}^3 \sum_{\beta=1}^3 \left(\sum_j g(r_{ij}) \hat{r}_{ij}^\alpha \hat{r}_{ij}^\beta \right)^2 - \sum_j g(r_{ij})^2 \right]. \tag{H.4}
\end{aligned}$$

Therefore, in the case of Stillinger-Weber potential,

$$\begin{aligned}
& \sum_{j < k} g(r_{ij})g(r_{ik}) \left(\cos(\theta_{jik}) + \frac{1}{3} \right)^2 \\
&= \sum_{j < k} g(r_{ij})g(r_{ik}) \left(\cos^2(\theta_{jik}) + \frac{2}{3} \cos(\theta_{jik}) + \frac{1}{9} \right) \\
&= \frac{1}{2} \left(\left[\sum_{\alpha=1}^3 \sum_{\beta=1}^3 \left(\sum_j g(r_{ij}) \hat{r}_{ij}^\alpha \hat{r}_{ij}^\beta \right)^2 - \sum_j g(r_{ij})^2 \right] + \right. \\
& \quad \left. \frac{2}{3} \left[\sum_{\alpha=1}^3 \left(\sum_j g(r_{ij}) \hat{r}_{ij}^\alpha \right)^2 - \sum_j g(r_{ij})^2 \right] + \frac{1}{9} \left[\left(\sum_j g(r_{ij}) \right)^2 - \sum_j g(r_{ij})^2 \right] \right) \\
&= \frac{1}{2} \sum_{\alpha=1}^3 \sum_{\beta=1}^3 \left(\sum_j g(r_{ij}) \hat{r}_{ij}^\alpha \hat{r}_{ij}^\beta \right)^2 + \frac{1}{3} \sum_{\alpha=1}^3 \left(\sum_j g(r_{ij}) \hat{r}_{ij}^\alpha \right)^2 + \\
& \quad \frac{1}{18} \left(\sum_j g(r_{ij}) \right)^2 - \frac{8}{9} \sum_j g(r_{ij})^2. \tag{H.5}
\end{aligned}$$

One can reach (H.5) faster by extending \hat{r}_{ij} to 4-D. Define vector

$$\tilde{r}_{ij} \equiv \left(\hat{r}_{ij}, \frac{1}{\sqrt{3}} \right), \quad (\text{H.6})$$

with constant fourth component $1/\sqrt{3}$. It is easily seen that (H.5) is equivalent to

$$\sum_{j < k} g(r_{ij})g(r_{ik}) \sum_{\alpha=1}^4 \sum_{\beta=1}^4 \tilde{r}_{ij}^{\alpha} \tilde{r}_{ik}^{\alpha} \tilde{r}_{ij}^{\beta} \tilde{r}_{ik}^{\beta} = \frac{1}{2} \sum_{\alpha=1}^4 \sum_{\beta=1}^4 \left(\sum_j g(r_{ij}) \tilde{r}_{ij}^{\alpha} \tilde{r}_{ij}^{\beta} \right)^2 - \frac{8}{9} \sum_j g(r_{ij})^2 \quad (\text{H.7})$$

Both (H.5) and (H.7) indicates that the Stillinger-Weber three-body potential is a tensorial extension of the embedded atom formalism with embedding exponent 2.

To obtain the force on atom j due to site energy of atom i , let us define 4×4 “charge density matrix” at atom i ,

$$\mathbf{M}_i : \quad M_i^{\alpha\beta} = \sum_j g(r_{ij}) \tilde{r}_{ij}^{\alpha} \tilde{r}_{ij}^{\beta}, \quad \alpha, \beta = 1..4. \quad (\text{H.8})$$

We then have

$$V_{3i} = \frac{1}{2} \text{Tr} \mathbf{M}^2 - \frac{8}{9} \sum_j g(r_{ij})^2. \quad (\text{H.9})$$

The second part is in ordinary pair potential form with force contributions,

$$\Delta F_j^{\mu} = -\Delta F_i^{\mu} = \frac{16}{9} g(r_{ij}) g'(r_{ij}) \hat{r}_{ij}^{\mu}, \quad \mu = 1..3. \quad (\text{H.10})$$

The first part is more interesting because it must give angular (bond-bending) forces.

If atom j is displaced by dx_j^{μ} , $\mu = 1..3$, there would be,

$$dr_{ij}^{\mu} = dx_j^{\mu} \rightarrow d\tilde{r}_{ij}^{\nu} = d\hat{r}_{ij}^{\nu} = d \left(\frac{r_{ij}^{\nu}}{r_{ij}} \right) = \sum_{\mu=1}^3 \frac{\delta^{\nu\mu} - \hat{r}_{ij}^{\nu} \hat{r}_{ij}^{\mu}}{r_{ij}} dx_j^{\mu}, \quad \nu = 1..3; \quad d\tilde{r}_{ij}^4 = 0.$$

And so there is,

$$dM_i^{\alpha\beta} = \sum_{\mu=1}^3 \left[g'(r_{ij}) \hat{r}_{ij}^{\mu} \tilde{r}_{ij}^{\alpha} \tilde{r}_{ij}^{\beta} + g(r_{ij}) \frac{(\delta^{\alpha\mu} - \hat{r}_{ij}^{\alpha} \hat{r}_{ij}^{\mu}) \tilde{r}_{ij}^{\beta} + \tilde{r}_{ij}^{\alpha} (\delta^{\beta\mu} - \hat{r}_{ij}^{\beta} \hat{r}_{ij}^{\mu})}{r_{ij}} \right] dx_j^{\mu}$$

$$\begin{aligned}
= & \sum_{\mu=1}^3 \left[\left(g'(r_{ij}) \tilde{r}_{ij}^\alpha \tilde{r}_{ij}^\beta - \frac{g(r_{ij})}{r_{ij}} \hat{r}_{ij}^\alpha \tilde{r}_{ij}^\beta - \frac{g(r_{ij})}{r_{ij}} \tilde{r}_{ij}^\alpha \hat{r}_{ij}^\beta \right) \hat{r}_{ij}^\mu + \right. \\
& \left. g(r_{ij}) \frac{\delta^{\alpha\mu} \tilde{r}_{ij}^\beta + \tilde{r}_{ij}^\alpha \delta^{\beta\mu}}{r_{ij}} \right] dx_j^\mu, \tag{H.11}
\end{aligned}$$

where we achieve consistency in notation by defining $\hat{r}_{ij}^4 \equiv 0$.

Plugging (H.11) into (H.9), the force contribution is

$$\Delta F_j^\mu = -\Delta F_i^\mu = - \sum_{\alpha=1}^4 \sum_{\beta=1}^4 M_i^{\alpha\beta} \frac{\partial M_i^{\alpha\beta}}{\partial x_j^\mu}. \tag{H.12}$$

We find that the first part of (H.11) still gives a pair potential like contribution, with

$$\Delta F_j^\mu = -\Delta F_i^\mu = \left(\sum_{\alpha=1}^4 \sum_{\beta=1}^4 M_i^{\alpha\beta} \left[\frac{g(r_{ij})}{r_{ij}} \hat{r}_{ij}^\alpha \tilde{r}_{ij}^\beta + \frac{g(r_{ij})}{r_{ij}} \tilde{r}_{ij}^\alpha \hat{r}_{ij}^\beta - g'(r_{ij}) \tilde{r}_{ij}^\alpha \tilde{r}_{ij}^\beta \right] \right) \hat{r}_{ij}^\mu,$$

for $\mu = 1..3$, in which be aware of the distinction that $\hat{r}_{ij}^4 = 0$ but $\tilde{r}_{ij}^4 = 1/\sqrt{3}$.

The second part of (H.11) gives

$$\Delta F_j^\mu = -\Delta F_i^\mu = - \sum_{\alpha=1}^4 \sum_{\beta=1}^4 M_i^{\alpha\beta} g(r_{ij}) \frac{\delta^{\alpha\mu} \tilde{r}_{ij}^\beta + \tilde{r}_{ij}^\alpha \delta^{\beta\mu}}{r_{ij}} = -2 \frac{g(r_{ij})}{r_{ij}} \sum_{\alpha=1}^4 M_i^{\mu\alpha} \tilde{r}_{ij}^\alpha,$$

for $\mu = 1..3$, which is the sole contributor to the angular forces. We see that it has a very simple spatial dependence of the form

$$\Delta \mathbf{F} \propto \frac{g(r)}{r} \left(\underline{\underline{M}}^{3 \times 3} \hat{\mathbf{r}} + \frac{\mathbf{M}_4}{\sqrt{3}} \right),$$

despite the fact that before the re-summation it looks quite intractable. One further notices that the second term is nothing other than a concerted effort to move i to the weighted center of j 's, and the first term has three mutually orthogonal eigen-directions along which there are only radial forces.

The above derivation can be generalized to any triplet potential of the form

$$\sum_{j < k} g(r_{ij}) g(r_{ik}) f(\theta_{jik})$$

as one can always expand $f(\theta)$ in polynomial of $\cos \theta$. It is easily seen that if $(\cos \theta)^n$ is included, then the angular force expression would have $n - 1$ \tilde{r}_{ij}^α 's contracting with a local rank- n tensor. However, computational efficiency suggests that $n \leq 2$ is the only worthwhile case for the re-summation technique.

Bibliography

- [1] I.S. Sokolnikoff, *Tensor Analysis, Theory and Applications to Geometry and Mechanics of Continua* (Wiley, New York, 1964).
- [2] S.C. Hunter, *Mechanics of Continuous Media*, 2nd edition (Halsted Press, New York, 1983).
- [3] L.D. Landau and E.M. Lifshitz, *Theory of Elasticity*, 2nd English edition, revised and enlarged (Pergamon Press, Oxford, New York, 1970).
- [4] D.C. Wallace, *Thermodynamics of Crystals*, (Wiley, New York 1972).
- [5] K. Huang, *Statistical Mechanics* (Wiley, New York, 1987).
- [6] D.A. McQuarrie, *Statistical Mechanics* (Harper Collins Publishers, New York, 1976).
- [7] M.P. Allen and D.J. Tildesley, *Computer Simulation of Liquids* (Clarendon, New York, 1987).
- [8] J.M. Haile, *Molecular Dynamics Simulation: Elementary Methods* (Wiley, New York, 1997).
- [9] E.M. Pearson, T. Halicioglu, W.A. Tiller, “Laplace-transform technique for deriving thermodynamic equations from the classical microcanonical ensemble”, *Phys. Rev. A* **32**, 3030-3039 (1985).
- [10] T. Cargin, J.R. Ray, “Fundamental treatment of molecular-dynamics ensembles”, *Phys. Rev. A* **37**, 247-251 (1988).
- [11] J.R. Ray, “Correct microcanonical ensemble in molecular dynamics”, *Phys. Rev. E* **59**, 4781-4785 (1999).
- [12] C.W. Gear, *Numerical Initial Value Problems in Ordinary Differential Equation* (Prentice-Hall, Englewood Cliffs, N.J., 1971).
- [13] L. Verlet, “Computer Experiments on Classical Fluids. I. Thermodynamical Properties of Lennard-Jones Molecules”, *Phys. Rev.* **159**, 98 (1967).

- [14] R.D. Ruth, "A Canonical Integration Technique", *IEEE Trans. Nucl. Sci.* **30**, 2669 (1983).
- [15] H. Yoshida, "Construction of higher order symplectic integrators", *Phys. Lett. A* **150**, 262 (1990).
- [16] Ch. Tsitouras, "A tenth order symplectic Runge-Kutta-Nystrom method", *Celestial Mechanics* **74**, 223-230 (1999).
- [17] J.M. Sanz-Serna, M.P. Calvo, *Numerical Hamiltonian Problems* (Chapman & Hall, London, 1994).
- [18] Ch. Schlier and A. Seiter, "Symplectic Integration of Classical Trajectories: A Case Study", *J. Phys. Chem. A* **102**, 9399-9404 (1998).
- [19] Ch. Schlier and A. Seiter, "High-Order Symplectic Integration: An Assessment", *Computer Physics Communications* **130**, 176-189 (2000).
- [20] H.J.C. Berendsen, J.P.M. Postma, W.F. van Gunsteren, A. DiNola, J.R. Haak, "Molecular dynamics with coupling to an external bath", *J. Chem. Phys.* **81**, 3684-3690 (1984).
- [21] S. Nose, "A unified formulation of the constant temperature molecular dynamics method", *J. Chem. Phys.* **81**, 511 (1984).
- [22] W.G. Hoover, "Canonical dynamics: Equilibrium phase-space distributions", *Phys. Rev. A* **31**, 1695 (1985).
- [23] T. Cargin, J.R. Ray, "Isothermal molecular-dynamics ensembles", *Phys. Rev. A* **37**, 4510-4513 (1988).
- [24] S. Nose, "Constant temperature molecular dynamics methods", *Prog. Theor. Phys. Suppl.* **103**, 1-46 (1991).
- [25] K. Cho, J.D. Joannopoulos, "Ergodicity and dynamical properties of constant-temperature molecular dynamics", *Phys. Rev. A* **45**, 7089 (1992).
- [26] K. Cho, J.D. Joannopoulos, L. Kleinman, "Constant-temperature molecular dynamics with momentum conservation", *Phys. Rev. E* **47** 3145-3151 (1993).
- [27] G.J. Martyna, M.E. Tuckerman, "Symplectic reversible integrators - predictor corrector methods", *J. Chem. Phys.* **102**, 8071-8077 (1995).
- [28] G.J. Martyna, M.E. Tuckerman, D.J. Tobias, M.L. Klein, "Explicit reversible integrators for extended systems dynamics", *Molecular Physics* **87**, 1117-1157 (1996).
- [29] M.E. Tuckerman, G.J. Martyna, "Understanding modern molecular dynamics: Techniques and applications", *J. Phys. Chem. B* **104**, 159-178 (2000).

- [30] J.R. Ray, "Elastic constants and statistical ensembles in molecular dynamics", *Computer Physics Reports* **8**, 109 (1988).
- [31] J.F. Lutsko, "Stress and Elastic Constants in Anisotropic Solids - Molecular Dynamics Techniques", *J. Appl. Phys.* **64**, 1152 (1988).
- [32] J.F. Lutsko, "Generalized Expressions for the Calculation of Elastic Constants by Computer Simulation", *J. Appl. Phys.* **65**, 2991 (1989).
- [33] H.C. Anderson, "Molecular dynamics at constant pressure and/or temperature", *J. Chem. Phys.* **72**, 2384-2393 (1980).
- [34] M. Parrinello and A. Rahman, "Polymorphic transitions in single crystals: A new molecular dynamics method", *J. Appl. Phys.* **52**, 7182-7190 (1981).
- [35] R.M. Wentzcovitch, "Invariant Molecular Dynamics Approach to Structural Phase Transitions", *Phys. Rev. B* **44**, 2358-2361 (1991).
- [36] G.J. Martyna, D.J. Tobias, M.L. Klein, "Constant pressure molecular dynamics algorithms", *J. Chem. Phys.* **101**, 4177-4189 (1994).
- [37] J.H. Wang, "Atomistic Study of Stress-Induced Unstable Structural Responses of Crystals at Finite Temperatures", Ph. D. Thesis supervised by S. Yip, Massachusetts Institute of Technology, Department of Nuclear Engineering (1993).
- [38] J. Wang, S. Yip, S. Phillpot, D. Wolf, "Crystal Instabilities at Finite Strain", *Phys. Rev. Lett.* **71**, 4182 (1993).
- [39] M. Tang and S. Yip, "Lattice Instability in β -SiC and Simulation of Brittle Fracture", *J. Appl. Phys.* **76**, 2719-2725 (1994).
- [40] M. Tang, "Elastic Instabilities and Structural Responses of β -SiC under Stress", Ph. D. Thesis supervised by S. Yip, Massachusetts Institute of Technology, Department of Nuclear Engineering (1995).
- [41] J. Wang, J. Li, S. Yip, S. Phillpot, D. Wolf, "Mechanical Instabilities of Homogeneous Crystals", *Phys. Rev. B* **52**, 12627-35 (1995).
- [42] J. Wang, J. Li, S. Yip, S. Phillpot, D. Wolf, "Unifying two criteria of Born: Elastic instability and melting of homogeneous crystals", *Physica A* **240**, 396 (1997).
- [43] M.A. El Khakani, M. Chaker, A. Jean, S. Boily, J.C. Kieffer, M.E. Ohern, M.F. Ravet, F. Rousseaux, "Hardness and Young's modulus of amorphous a-SiC thin films determined by nanoindentation and bulge tests", *Journal of Materials Research* **9**, 96-103 (1994).

- [44] M.A. El Khakani, D. Guay, and M. Chaker, X.H. Feng, “Composition and thermal-annealing-induced short-range ordering changes in amorphous hydrogenated silicon carbide films as investigated by extended x-ray-absorption fine structure and infrared absorption”, *Phys. Rev. B* **51**, 4903-4914 (1995).
- [45] G. Galli, F. Gygi, A. Catellani, “Quantum Mechanical Simulations of Microfracture in a Complex Material”, *Phys. Rev. Lett.* **82**, 3476-9 (1999).
- [46] M. Born and K. Huang, *Dynamical Theory of Crystal Lattices* (Clarendon, Oxford, 1956).
- [47] J.W. Martin, “Many-body forces in solids and the Brugger elastic constants. II. Inner elastic constants”, *Journal of Physics C: Solid State Physics* **8**, 2858 (1975).
- [48] I. Alber, J.L. Bassani, M. Khantha, V. Vitek and G.J. Wang, “Grain boundaries as heterogeneous systems: Atomic and continuum elastic properties”, *Philosophical Transactions of the Royal Society of London A* **339**, 555 (1992).
- [49] J.L. Bassani, V. Vitek, I. Alber, “Atomic-level elastic properties of interfaces and their relation to continua”, *Acta Metallurgica et Materialia* **40**, S307 (1992).
- [50] M.S. Green, “Markoff Random Processes and the Statistical Mechanics of Time-Dependent Phenomena. II. Irreversible Processes in Fluids”, *J. Chem. Phys.* **22**, 398 (1954).
- [51] R. Kubo, *J. Phys. Soc. Japan* **12**, 570 (1957); R. Kubo, M. Yokota and S. Nakajima, “Statistical-Mechanical Theory of Irreversible Processes. II. Response to Thermal Disturbance”, *ibid* **12**, 1203 (1957).
- [52] R. Kubo, “The fluctuation-dissipation theorem”, *Rep. Prog. Phys.* **29**, 255-84 (1966).
- [53] H. Mori, *Phys. Rev.* **112**, 1829-42 (1958).
- [54] R. Zwanzig, “Time-Correlation Functions and Transport Coefficients in Statistical Mechanics”, in *Ann. Rev. Phys. Chem.* **16**, edited by H. Eyring, 67 (1965).
- [55] L.P. Kadanoff and P.C. Martin, “Hydrodynamic equations and correlation functions”, *Annals of Physics, N.Y.* **24**, 419 (1963).
- [56] J.-P. Boon, S. Yip, *Molecular Hydrodynamics*, (McGraw-Hill, New York, 1980).
- [57] J.M. Ziman, *Electrons and Phonons; the Theory of Transport Phenomena in Solids* (Clarendon Press, Oxford, 1960).
- [58] A.A. Maradudin, E.W. Montroll and G.H. Weiss, *Theory of Lattice Dynamics in the Harmonic Approximation*, second edition (Academic Press, New York, 1971).

- [59] V.L. Gurevich, *Transport in Phonon Systems*, (Elsevier, Amsterdam, 1986).
- [60] G.P. Srivastava, *The Physics of Phonons*, (A. Hilger, Bristol, 1990).
- [61] M. Omini, A. Sparavigna, “Beyond the isotropic-model approximation in the theory of thermal conductivity”, *Phys. Rev. B* **53**, 9064-9073 (1996).
- [62] M. Omini, A. Sparavigna, “Heat transport in dielectric solids with diamond structure”, *Nuovo Cimento D* **19**, 1537-1563 (1997).
- [63] M. Omini, A. Sparavigna, “Role of grain boundaries as phonon diffraction gratings in the theory of thermal conductivity”, *Phys. Rev. B* **61**, 6677-6688 (2000).
- [64] M.J. Gillan and M. Dixon, “The calculation of thermal conductivities by perturbed molecular dynamics simulation”, *J. Phys. C* **16**, 869-878 (1983).
- [65] A. Ladd, B. Moran, W.G. Hoover, “Lattice thermal conductivity: A comparison of molecular dynamics and anharmonic lattice dynamics”, *Phys. Rev. B* **34** 5058 (1986).
- [66] H. Kitagawa, Y. Shibutani, S. Ogata, “Ab-initio simulation of thermal properties of AlN ceramics”, *Modell. Simul. Mater. Sci. Eng.* **3**, 521-531 (1995).
- [67] H. Kaburaki, J. Li, S. Yip, to be published.
- [68] I.N. Krupskii, V.G. Manzhelii, “Multiphonon interactions and the thermal conductivity of crystal argon, krypton and xenon”, *Zhurnal Eksperimentalnoi i Teoreticheskoi Fiziki* **55**, 2075-82 (1968). English translation: *Soviet Physics - JETP* **28**, 1097 (1969).
- [69] D.K. Christen, G.L. Pollack, “Thermal conductivity of solid argon”, *Phys. Rev. B* **12**, 3380-91, (1975).
- [70] J. Li, S. Yip, “Order-N Method to Calculate the Local Density of States”, *Phys. Rev. B* **56**, 3524 (1997).
- [71] D.E. Woon, “Accurate modeling of intermolecular forces - a systematic Moller-Plesset study of the argon dimer using correlation consistent basis-sets”, *Chemical Physics Letters* **204**, 29-35 (1993).
- [72] E. Kaxiras, S. Yip, “Modelling and simulation of solids - editorial overview”, *Current Opinion in Solid State and Materials Science* **3**, 523-525 (1998).
- [73] E. Ermakova, J. Solca, H. Huber, M. Welker, “Argon in condensed phase: Quantitative calculations of structural, thermodynamic, and transport properties from pure theory”, *J. Chem. Phys.* **102**, 4942-4951 (1995).
- [74] Melting curve for argon calculated from pure theory J. Solca, A.J. Dyson, G. Steinebrunner, B. Kirchner, H. Huber, *Chemical Physics* **224**, 253-261 (1997).

- [75] Y. Fujii, N.A. Lurie, R. Pynn, G. Shirane, “Inelastic neutron scattering from solid ^{36}Ar ”, *Phys. Rev. B* **10**, 3647-59 (1974).
- [76] M.L. Klein, J.A. Venables, *Rare Gas Solids* (Academic Press, London, 1976-77).
- [77] J.M. Ziman, *Models of Disorder: The Theoretical Physics of Homogeneously Disordered Systems* (Cambridge University Press, Cambridge, 1979).
- [78] N. Cusack, *The physics of structurally disordered matter: An introduction* (A. Hilger, Bristol, 1987).
- [79] L.J. Porter, J. Li, S. Yip, “Atomistic modeling of finite-temperature properties of β -SiC: I. Lattice vibrations, heat capacity, and thermal expansion”, *Journal of Nuclear Materials* **246**, 53 (1997).
- [80] J. Li, L. J. Porter, S. Yip, “Atomistic modeling of finite-temperature properties of crystalline β -SiC: II. Thermal conductivity and effects of point defects”, *Journal of Nuclear Materials* **255**, 139-152 (1998).
- [81] P.J.D. Lindan, M.J. Gillan, “A molecular dynamics study of the thermal conductivity of CaF_2 and UO_2 ”, *J. Phys.: Condens. Matter* **3**, 3929-3939 (1991).
- [82] K. Takase, I. Akiyama, N. Ohtori, “Thermal conductivity of silica glass at high temperature by molecular dynamics simulation”, *Materials Transactions JIM*, **40**, 1258-1261 (1999).
- [83] P.B. Allen, J.L. Feldman, J. Fabian, F. Wooten, “Diffusons, locons and propagons: Character of atomic vibrations in amorphous Si”, *Phil. Mag. B* **79**, 1715-1731 (1999).
- [84] J.R. Lukes, X.G. Liang, C.L. Tien, “Molecular Dynamics Study of Solid Thin-Film Thermal Conductivity”, *Proceedings of the ASME Heat Transfer Division* **361-4**, 229-240 (1998), presented at the 1998 ASME International Mechanical Engineering Congress and Exposition, November 15-20, 1998, Anaheim, California.
- [85] C.L. Tien, J.R. Lukes, F.C. Chou, “Molecular dynamics simulation of thermal transport in solids”, *Microscale Thermophysical Engineering* **2**, 133-137 (1998).
- [86] S.G. Volz, G. Chen, “Molecular dynamics simulation of thermal conductivity of silicon nanowires”, *Applied Physics Letters* **75**, 2056-2058 (1999).
- [87] S.G. Volz, G. Chen, “Molecular-dynamics simulation of thermal conductivity of silicon crystals”, *Phys. Rev. B* **61**, 2651-2656 (2000).
- [88] J.C.M. Li, “Hall-Petch Relation and Grain Boundary Sources”, *Transactions of the Metallurgical Society of AIME* **227**, 239-247 (1963).
- [89] I.M. Lifshitz, “On the theory of diffusion-viscous flow of polycrystalline bodies”, *Soviet Physics JETP* **17**, 909 (1963).

- [90] L.G. Orlov, "Generation of Dislocations on External and Internal Surfaces of Crystals", *Soviet Physics - Solid State* **9**, 1836 (1968).
- [91] R.L. Bell, T.G. Langdon, "Grain-boundary Sliding", in *Review papers and abstracts of research papers: Interfaces Conference 1969, Melbourne*, pp. 115-137, edited by R.C. Gifkins, (Australian Institute of Metals, 1969).
- [92] R. Raj, M.F. Ashby, "On Grain Boundary Sliding and Diffusional Creep", *Metallurgical Transactions* **2**, 1113 (1971).
- [93] A.H. Chokshi, A. Rosen, J. Karch, H. Gleiter, "On the validity of the Hall-Petch relationship in nanocrystalline materials", *Scripta Metallurgica* **23**, 1679-84 (1989).
- [94] H. Gleiter, "Nanocrystalline Materials", *Prog. Mater. Sci.* **33**, 223-315 (1989).
- [95] J.H. Schneibel, P.M. Hazzledine, "Diffusion-accommodated sliding of irregularly shaped grain boundaries", *Journal of Materials Research* **5**, 563-9, (1990).
- [96] R.Z. Valiev, V.G. Khairullin, A.D. Sheikh-Ali, "Phenomenology and Mechanisms of Grain Boundary Sliding", *Soviet Physics Journal* **34**, 253 (1991).
- [97] T.G. Nieh, J. Wadsworth, "Hall-Petch relation in nanocrystalline solids", *Scripta Metallurgica et Materialia* **25**, 955-8 (1991).
- [98] V.V. Astanin, O.A. Kaibyshev, S.N. Faizova, "Cooperative Grain Boundary Sliding under Superplastic Flow", *Scripta Metallurgica et Materialia* **25**, 2663-8 (1991).
- [99] R.D. Nixon, R.F. Davis, "Diffusion-accommodated grain boundary sliding and dislocation glide in the creep of sintered alpha silicon carbide", *Journal of the American Ceramic Society* **75**, 1786-95 (1992).
- [100] M.G. Zelin, A.K. Mukherjee, "Analysis of the cooperative grain boundary sliding in terms of cellular dislocations", *Phil. Mag. A* **68**, 1183-93 (1993).
- [101] M.G. Zelin, A.K. Mukherjee, "On the macroscopic character of cooperative grain boundary sliding", *Journal of Materials Science Letters* **13**, 1258-60 (1994).
- [102] R. Monzen, M. Futakuchi, T. Suzuki, "Misorientation dependence of nanometer grain boundary sliding of (011) twist boundaries in copper", *Scripta Metallurgica et Materialia* **32**, 1277-82 (1995).
- [103] A.D. Sheikh-Ali, "On the influence of intragranular slip on grain boundary sliding in bicrystals", *Scripta Metallurgica et Materialia* **33**, 795-801 (1995).
- [104] T.G. Langdon, "The significance of grain boundaries in the flow of polycrystalline materials", *Materials Science Forum* **189-190**, 31-42 (1995).

- [105] C. Molteni, G.P. Francis, M.C. Payne, V. Heine, "First Principles Simulation of Grain Boundary Sliding", *Phys. Rev. Lett.* **76**, 1284-7 (1996).
- [106] K.A. Padmanabhan, J. Schlipf, "Model for grain boundary sliding and its relevance to optimal structural superplasticity. 1. Theory", *Materials Science and Technology* **12**, 391-9 (1996).
- [107] V.V. Astanin, S.N. Faizova, K.A. Padmanabhan, "Model for grain boundary sliding and its relevance to optimal structural superplasticity. 2. Evidence for cooperative grain/interphase boundary sliding and plane interface formation", *Materials Science and Technology* **12**, 489-94 (1996).
- [108] V.V. Astanin, K.A. Padmanabhan, S.S. Bhattacharya, "Model for grain boundary sliding and its relevance to optimal structural superplasticity. 3. Effect of flow localisation and specimen thickness on superplasticity in alloy Supral 100", *Materials Science and Technology* **12**, 545-50 (1996).
- [109] T.A. Venkatesh, S.S. Bhattacharya, K.A. Padmanabhan, J. Schlipf, "Model for grain boundary sliding and its relevance to optimal structural superplasticity. 4. Experimental verification", *Materials Science and Technology* **12**, 635-43 (1996).
- [110] C. Suryanarayana, J. Singh, F.H. Froes, eds., "Processing and properties of nanocrystalline materials", (Minerals, Metals & Materials Society, Warrendale, PA, 1996).
- [111] C. Molteni, N. Marzari, M.C. Payne, V. Heine, "Sliding mechanisms in aluminum grain boundaries", *Phys. Rev. Lett.* **79**, 869-72 (1997).
- [112] R.J. DiMelfi, "Grain boundary sliding and its relation to ductility and fracture in fine-grained polycrystalline materials with a particular focus on γ -TiAl", *Materials Science and Engineering A* **237**, 141-9 (1997).
- [113] Z.L. Wang, "Structural analysis of self-assembling nanocrystal superlattices", *Advanced Materials* **10**, 13-30 (1998).
- [114] L.Q. Xing, C. Bertrand, J.-P. Dallas, M. Cornet, "Nanocrystal evolution in bulk amorphous $\text{Zr}_{57}\text{Cu}_{20}\text{Al}_{10}\text{Ni}_8\text{Ti}_5$ alloy and its mechanical properties", *Materials Science and Engineering A* **241**, 216-25 (1998).
- [115] S.R. Agnew, B.R. Elliot, C.J. Youngdahl, K.J. Hemker, J.R. Weertman, "Structure and Mechanical Properties of Nanocrystalline Metals – With Opportunities for Modeling", in *Modelling of Structure and Mechanics of Materials from Microscale to Product: Proceedings of the 19th Riso International Symposium on Materials Science*, 7-11 September 1998, edited by J.V. Carstensen.
- [116] H. Dai, "Geometrically-necessary dislocation density in continuum plasticity theory, FEM implementation and applications", Ph. D. Thesis supervised by

- D.M. Parks, Massachusetts Institute of Technology, Department of Mechanical Engineering (1997).
- [117] J. Schiotz, F.D. Di Tolla, K.W. Jacobsen, "Softening of nanocrystalline metals at very small grain sizes", *Nature* **391**, 561-563 (1998).
 - [118] H. Van Swygenhoven, M. Spaczer, A. Caro, "Microscopic description of plasticity in computer generated metallic nanophase samples: A comparison between Cu and Ni", *Acta Materialia* **47**, 3117-3126 (1999).
 - [119] H. Van Swygenhoven, D. Farkas, A. Caro, "Grain-boundary structures in polycrystalline metals at the nanoscale", *Phys. Rev. B* **62**, 831-838 (2000).
 - [120] S. Yip, "Nanocrystals - the strongest size", *Nature* **391**, 532-533 (1998).
 - [121] P. Heino, P. Holloway, E. Ristolainen, "Strength of nanoscale copper under shear", *Journal of Vacuum Science and Technology A* **18**, 1202-1206 (2000).
 - [122] M.J. Slavin and G.D. Quinn, "Mechanical Property Evaluation at Elevated Temperature of Sintered β -Silicon Carbide", *International Journal of High Technology Ceramics* **2**, 47-63 (1986).
 - [123] M.D. Sacks, "Effect of composition and heat treatment conditions on the tensile strength and creep resistance of SiC-based fibers", *Journal of the European Ceramic Society* **19**, 2305-15 (1999).
 - [124] Y.-M. Chiang, D.P. Birnie, W.D. Kingery, *Physical Ceramics: Principles for Ceramic Science and Engineering*, (J. Wiley, New York, 1997).
 - [125] B.S. Bokshtein, S.Z. Bokshtein, A.A. Zhukhovitskii, *Thermodynamics and Kinetics of Diffusion in Solids* (Amerind Publishing Co., 1985).
 - [126] J. Pilling and N. Ridley, *Superplasticity in Crystalline Solids* (Institute of Metals, London, 1989).
 - [127] R.M. Nedderman, *Statics and Kinematics of Granular Materials* (Cambridge University Press, Cambridge, 1992).
 - [128] M.A. Nastasi, D.M. Parkin, H. Gleiter, *Mechanical Properties and Deformation Behavior of Materials having Ultra-fine Microstructures*, proceedings of the NATO Advanced Study Institute on Mechanical Properties and Deformation Behavior of Materials Having Ultra-Fine Microstructures, Porto Novo, Portugal (Kluwer Academic, Dordrecht, 1993).
 - [129] R.W. Evans, B. Wilshire, *Introduction to Creep* (Institute of Materials, London, 1993).
 - [130] M.A. Ootoni, R.W. Armstrong, N.J. Grant, K. Ishizaki, *Grain Size and Mechanical Properties: Fundamentals and Applications* (Materials Research Society, Pittsburgh, 1995).

- [131] D. Bideau, J. Dodds, *Physics of Granular Media* (Nova Science Publishers, Commack, 1991).
- [132] B. Cambou, *Behaviour of Granular Materials* (Springer, Wien, 1998).
- [133] F. Milstein and S. Chantasiriwan, "Theoretical study of the response of 12 cubic metals to uniaxial loading", *Phys. Rev. B* **58**, 6006-6018 (1998).
- [134] D. Roundy, C.R. Krenn, M.L. Cohen, J.W. Morris, "Ideal shear strengths of fcc aluminum and copper", *Phys. Rev. Lett.* **82**, 2713 (1999).
- [135] J.W. Morris, C.R. Krenn, D. Roundy, M.L. Cohen, "Elastic stability and the limit of strength", in *Phase Transformations and Evolution in Materials*, Proceedings: 2000 Hume-Rothery Symposium in honor of A.G. Khachaturyan, edited by P.E. Turchi and A. Gonis (TMS, Warrendale, Pa., 2000).
- [136] K. Yashiro, T. Kitamura, R. Ohtani, "Criterion of Dislocation Nucleation in terms of Local Instability", to be published.
- [137] J. Li, S. Yip, to be published.
- [138] F.A. McClintock, A.S. Argon, *Mechanical Behavior of Materials* (Addison-Wesley, Reading, 1966).
- [139] U.F. Kocks, A.S. Argon, M.F. Ashby, *Thermodynamics and Kinetics of Slip* (Pergamon Press, Oxford, 1975).
- [140] R.W. Cahn, P. Haasen, *Physical Metallurgy*, fourth, revised and enhanced edition (North-Holland, Amsterdam, 1996).
- [141] R.W. Cahn, P. Haasen, E.J. Kramer, *Materials Science and Technology: A Comprehensive Treatment*, volume 6, *Plastic Deformation and Fracture Mechanics* (VCH Publishing, Weinheim, 1993).
- [142] S. Suresh, T.-G. Nieh, B.W. Choi, "Nano-indentation of Copper Thin Films on Silicon Substrates", *Scripta Materialia* **41**, 951 (1999).
- [143] A. Gouldstone, H.-J. Koh, K.-Y. Zeng, A.E. Giannakopoulos, and S. Suresh, "Discrete and Continuous Deformation During Nanoindentation of Thin Films", *Acta Materialia* **48**, 2277-2295 (2000).
- [144] V.B. Shenoy, R. Phillips, E.B. Tadmor, "Nucleation of dislocations beneath a plane strain indenter", *Journal of the Mechanics and Physics of Solids* **48**, 649-73 (2000).
- [145] L.E. Toth, *Transition Metal Carbides and Nitrides* (Academic Press, New York, 1971).
- [146] J.F. Shackelford, W. Alexander and J.S. Park, *CRC Materials Science and Engineering Handbook*, 2nd edition, pp. 279-280 (CRC Press, 1994).

- [147] Y.S. Touloukian, R.W. Powell, C.Y. Ho and P.G. Klemens, *Thermophysical Properties of Matter*, volume 2 (IFI/Plenum, New York, 1970).
- [148] W.S. Williams, “The Thermal Conductivity of Metallic Ceramics”, *JOM - Journal of the Minerals Metals & Materials Society* **50**, 62 (1998).
- [149] Y.H. Lee, R. Biswas, C.M. Soukoulis, C.Z. Wang, C.T. Chan, and K.M. Ho, “Molecular Dynamics Simulation of Thermal Conductivity in Amorphous Silicon”, *Phys. Rev. B* **43**, 6573 (1991).
- [150] W. Jones and N.H. March, *Theoretical Solid State Physics* (Wiley-Interscience, London, 1973).
- [151] J.C. Slater, “Atomic Radii in Crystals”, *J. Chem. Phys.* **41**, 3199 (1964). See also J.C. Slater, *Quantum Theory of Molecules and Solids*, volume 2, table 3-1 (McGraw-Hill, New York, 1963-74).
- [152] Z.-W. Lu, D. Singh, H. Krakauer, “Equilibrium properties of hcp titanium and zirconium”, *Phys. Rev. B* **36**, 7335 (1987).
- [153] W.A. Harrison, *Electronic Structure and the Properties of Solids: The Physics of the Chemical Bond* (W.H. Freeman and Company, San Francisco, 1980).
- [154] R. Car and M. Parrinello, “Unified Approach for Molecular Dynamics and Density Functional Theory”, *Phys. Rev. Lett.* **55**, 2471 (1985).
- [155] A.P. Sutton, *Electronic Structure of Materials* (Oxford University Press, Oxford, 1993).
- [156] H. Balamane, T. Halicioglu, W.A. Tiller, “Comparative Study of Silicon Empirical Interatomic Potentials”, *Phys. Rev. B* **46**, 2250-2279 (1992).
- [157] F.H. Stillinger, T.A. Weber, “Computer Simulation of Local Order in Condensed Phases of Silicon”, *Phys. Rev. B* **31**, 5262 (1985).
- [158] J. Tersoff, “New Empirical Model for the Structural Properties of Silicon”, *Phys. Rev. Lett.* **56**, 632 (1986).
- [159] J. Tersoff, “New Empirical Approach for the Structure and Energy of Covalent Systems”, *Phys. Rev. B* **37**, 6991 (1988).
- [160] J. Tersoff, “Empirical Interatomic Potential for Silicon with Improved Elastic Properties”, *Phys. Rev. B* **38**, 9902 (1988).
- [161] J. Tersoff, “Modeling solid-state chemistry: Interatomic potentials for multi-component systems”, *Phys. Rev. B* **39**, 5566 (1989).
- [162] J. Tersoff, “Carbon defects and defect reactions in silicon”, *Phys. Rev. Lett.* **64**, 1757 (1990).

- [163] J. Tersoff, “Chemical order in amorphous silicon carbide”, *Phys. Rev. B* **49**, 16349 (1994).
- [164] D.W. Brenner, “Empirical potential for hydrocarbons for use in simulating the chemical vapor deposition of diamond films”, *Phys. Rev. B* **42**, 9458 (1990).
- [165] B. Pailthorpe, P. Mahon, “Molecular Dynamics Simulations of Thin Film Diamond”, *Thin Solid Films* **193**, 34 (1990).
- [166] E.G. Gerstner, B.A. Pailthorpe, “Molecular Dynamics Simulation of Thin Film Amorphous Carbon Growth”, *Journal of Non-Crystalline Solids* **189**, 258 (1995).
- [167] B.A. Pailthorpe, D. Mitchell, N.S. Bordes, “Thermal Diffusion in Molecular Dynamics Simulations of Thin Film Diamond Deposition”, *Thin Solid Films* **332**, 109 (1998).
- [168] M.S. Tang, C.Z. Wang, C.T. Chan, K.M. Ho, “Environment-dependent tight-binding potential model”, *Phys. Rev. B* **53**, 979 (1996).
- [169] M.W. Finnis and J.E. Sinclair, “A simple empirical N-body potential for transition metals”, *Phil. Mag. A* **50**, 45 (1984); erratum, *ibid* **53**, 161 (1986).
- [170] G.J. Ackland, G. Tichy, V. Vitek, M.W. Finnis, “Simple N-body potentials for the noble metals and nickel”, *Phil. Mag. A* **56**, 735-56 (1987). See also, G.J. Ackland, “Theoretical study of the effect of point defects on the elastic constants of copper”, *Journal of Nuclear Materials* **152**, 53-63 (1988).
- [171] G.J. Ackland and V. Vitek, “Many-body potentials and atomic-scale relaxations in noble-metal alloys”, *Phys. Rev. B* **41**, 10324-10333 (1990).
- [172] H.-F. Deng, D.J. Bacon, “Simulation of point defects and threshold displacements in pure Cu and a dilute Cu-Au alloy”, *Phys. Rev. B* **48**, 10022-30 (1993).
- [173] A.P. Sutton and J. Chen, “Long-range Finnis-Sinclair potentials”, *Phil. Mag. Lett.* **61**, 139-146 (1990).
- [174] A.B. Belonoshko, R. Ahuja, O. Eriksson, and B. Johansson, “Quasi ab initio molecular dynamic study of Cu melting”, *Phys. Rev. B* **61**, 3838-3844 (2000).
- [175] A.F. Calder, D.J. Bacon, “A molecular dynamics study of displacement cascades in α -iron”, *Journal of Nuclear Materials* **207**, 25 (1993).
- [176] G.J. Ackland, D.J. Bacon, A.F. Calder, T. Harry, “Computer simulation of point defect properties in dilute Fe-Cu alloy using a many-body interatomic potential”, *Phil. Mag. A* **75**, 713-732 (1997).
- [177] A.B. Belonoshko, R. Ahuja, B. Johansson, “Quasi ab initio molecular dynamic study of Fe melting”, *Phys. Rev. Lett.* **84**, 3638-3641 (2000).

- [178] M.S. Daw and M.I. Baskes, “Embedded-atom method: derivation and application to impurities, surfaces, and other defects in metals”, *Phys. Rev. B* **29**, 6443-53 (1984).
- [179] M.S. Daw, S.M. Foiles, M.I. Baskes, “The Embedded-Atom Method - A Review of Theory and Applications”, *Materials Science Reports* **9**, 251 (1993).
- [180] A.F. Voter and S.P. Chen, in *High Temperature Ordered Inter-Metallic Alloys*, edited by R.W. Siegel, J.R. Weertman, and R. Sundan, MRS Symposia Proceedings No. 82 Materials Research Society, Pittsburgh, 1987, p. 175.
- [181] Y. Mishin, D. Farkas, M.J. Mehl, D.A. Papaconstantopoulos, “Interatomic potentials for monoatomic metals from experimental data and ab initio calculations”, *Phys. Rev. B* **59**, 3393-3407 (1999).
- [182] M.I. Baskes, “Modified Embedded-Atom Potentials for Cubic Materials and Impurities”, *Phys. Rev. B* **46**, 2727 (1992).
- [183] M.I. Baskes and R.A. Johnson, “Modified Embedded-Atom Potentials for HCP Metals”, *Modelling and Simulation in Materials Science and Engineering* **2**, 147 (1994).
- [184] H.C. Huang, N.M. Ghoniem, J.K. Wong, M.I. Baskes, “Molecular dynamics determination of defect energetics in β -SiC using 3 representative empirical potentials”, *Modelling and Simulation in Materials Science and Engineering* **3**, 615-627 (1995).
- [185] J. Wan, Y.L. Fan, D.W. Gong, S.G. Shen, X.Q. Fan, “Surface relaxation and stress of fcc metals: Cu, Ag, Au, Ni, Pd, Pt, Al and Pb”, *Modelling and Simulation in Materials Science and Engineering* **7**, 189-206 (1999).
- [186] Interatomic interactions in the effective-medium theory, K.W. Jacobsen, J.K. Norskov, M.J. Puska, *Phys. Rev. B* **35**, 7423 (1987).
- [187] H. Hakkinen, M. Manninen, “The effective-medium theory beyond the nearest-neighbour interaction”, *Journal of Physics - Condensed Matter* **1**, 9765-9777 (1989). Also see, H. Hakkinen, in *Many-Atom Interactions in Solids*, pp.168-75, edited by R.M. Nieminen, M.J. Puska and M.J. Manninen (Springer-Verlag, Berlin, 1990).
- [188] H. Hakkinen, S. Makinen, M. Manninen, “Edge dislocations in fcc metals: Microscopic calculations of core structure and positron states in Al and Cu”, *Phys. Rev. B* **41**, 12441-12453 (1990).
- [189] H. Hakkinen and M. Manninen, “Molecular dynamics of metals with many-atom interactions”, *Physica Scripta T* **33**, 210-215 (1990).
- [190] H. Hakkinen and M. Manninen, “Computer simulation of disordering and pre-melting of low-index faces of copper”, *Phys. Rev. B* **46**, 1725-1742 (1992).

- [191] K.W. Jacobsen, P. Stoltze, J.K. Norskov, “A semi-empirical effective medium theory for metals and alloys”, *Surface Science* **366**, 394 (1996).
- [192] S. Chantasiriwan, F. Milstein, “Embedded-atom models of 12 cubic metals incorporating second- and third-order elastic-moduli data”, *Phys. Rev. B* **58**, 5996-6005 (1998).
- [193] G. Simmons and H. Wang, *Single Crystal Elastic Constants and Calculated Aggregate Properties: A Handbook*, second edition (M.I.T. Press, Cambridge, 1971).
- [194] P. Heino, H. Hakkinen, K. Kaski, “Molecular dynamics study of copper with defects under strain”, *Phys. Rev. B* **58**, 641-652 (1998).
- [195] P. Heino, L. Perondi, K. Kaski, E. Ristolainen, “Stacking-fault energy of copper from molecular-dynamics simulations”, *Phys. Rev. B* **60**, 14625-14631 (1999).
- [196] T. Rasmussen, K.W. Jacobsen, T. Leffers, O.B. Pedersen, “Simulations of the atomic structure, energetics, and cross slip of screw dislocations in copper”, *Phys. Rev. B* **56**, 2977-2990 (1997). See also, T. Rasmussen, K.W. Jacobsen, T. Leffers, O.B. Pedersen, S.G. Srinivasan, H. Jonsson, “Atomistic determination of cross-slip pathway and energetics”, *Phys. Rev. Lett.* **79**, 3676-3679 (1997).
- [197] T. Rasmussen, T. Vegge, T. Leffers, O.B. Pedersen, K.W. Jacobsen, “Simulation of structure and annihilation of screw dislocation dipoles”, *Phil. Mag. A* **80**, 1273-1290 (2000).
- [198] F. Willaime and C. Massobrio, “Temperature-Induced hcp-bcc Phase Transformation in Zirconium: A Lattice and Molecular-Dynamics Study Based on an N -Body Potential”, *Phys. Rev. Lett.* **63**, 2244 (1989).
- [199] F. Willaime and C. Massobrio, “Development of an N -body interatomic potential for hcp and bcc-zirconium”, *Phys. Rev. B* **43**, 11653 (1991).
- [200] M.G. Fernandes, “Fast impurity diffusion in hcp Zr”, Ph. D. Thesis supervised by S. Yip and K. Russell, Massachusetts Institute of Technology, Department of Materials Science and Engineering (1996).
- [201] P.T. Jochym, K. Parlinski, “Ab initio lattice dynamics and elastic constants of ZrC”, *Eur. Phys. J. B* **15**, 265 (2000).
- [202] A.H. Cottrell, *Chemical Bonding in Transition Metal Carbides* (Institute of Materials, London, 1995).
- [203] F. Cyrot-Lackmann, *J. Phys. Chem. Solids* **29**, 1235 (1968).
- [204] K.E. Tan, A.P. Horsfield, D. Nguyen-Manh, D.G. Pettifor, A.P. Sutton, “Theory for the (1x1) Rumbled Relaxation at TiC(001) and TaC(001) Surfaces”, *Phys. Rev. Lett.* **76**, 90 (1996).

- [205] K.E. Tan, A.M. Bratkovsky, R.M. Harris, A.P. Horsfield, D. Nguyen-Manh, D.G. Pettifor, A.P. Sutton, "Carbon vacancies in titanium carbide", *Modelling and Simulation in Materials Science and Engineering* **5**, 187-198 (1997); errata: *ibid* **6**, 335 (1998).
- [206] R.M. Harris and P.D. Bristowe, "Computer modeling of slip in TiC", *Phil. Mag. A* **79**, 705 (1999).
- [207] S.-H. Jhi and J. Ihm, "Electronic structure and structural stability of $\text{TiC}_x\text{N}_{1-x}$ alloys", *Phys. Rev. B* **56**, 13826 (1997).
- [208] Electronic mechanism of hardness enhancement of transition metal carbonitrides, Seung-Hoon Jhi, J. Ihm, S. G. Louie, M. L. Cohen, *Nature* **399**, 132 (1999).
- [209] H.G. Smith, N. Wakabayashi, and M. Mostoller, in *Phonon anomalies in transition metals, alloys and compounds, Superconductivity in d- and f-band metals, Second Rochester Conference*, edited by D.H. Douglas, pp. 223 (Plenum Press, New York, 1976).
- [210] A.F. Guillermet, "Analysis of thermochemical properties and phase stability in the zirconium carbon system", *Journal of Alloys and Compounds* **217**, 69-89 (1995).
- [211] T. Inui, Y. Tanabe, Y. Onodera, *Group Theory and its Applications in Physics*, second edition (Springer-Verlag, New York, 1996).
- [212] D.L. Price and B.R. Cooper, "Total energies and bonding for crystallographic structures in titanium-carbon and tungsten-carbon systems", *Phys. Rev. B* **39**, 4945 (1989).
- [213] D.L. Price, J.M. Wills and B.R. Cooper, "TiC(001) Surface Relaxation", *Phys. Rev. Lett.* **77**, 3375-3378 (1996).
- [214] Y. Kido, T. Nishimura, Y. Hoshino, S. Otani, R. Souda, "Rumpled relaxation of TiC(001) and TaC(001) determined by high-resolution medium-energy ion scattering spectroscopy", *Phys. Rev. B* **61**, 1748-1751 (2000).
- [215] K. Kobayashi, "First-principles study of the surface electronic structures of transition metal carbides", *Japanese Journal of Applied Physics*, Part 1, **39**, 4311-4314 (2000).
- [216] C. Maerky, M.O. Guillou, J.L. Henshall, R.M. Hooper, "Indentation Hardness and Fracture Toughness in Single Crystal $\text{TiC}_{0.96}$ ", *Materials Science and Engineering A* **209**, 329-336 (1996).
- [217] S. Sarian and J.M. Criscione, "Diffusion of Carbon through Zirconium Monocarbide", *J. Appl. Phys.* **38**, 1794 (1967).

- [218] S. Sarian, “Diffusion of Carbon in TiC”, *J. Appl. Phys.* **39**, 3305 (1968).
- [219] S. Sarian, “Diffusion of ^{44}Ti in TiC_x ”, *J. Appl. Phys.* **40**, 3515 (1969).
- [220] V. Moisy-Maurice, C.H. de Novion, A.N. Christensen and W. Just, “Elastic diffuse neutron scattering study of the defect structure of $\text{TiC}_{0.76}$ and $\text{NbC}_{0.73}$ ”, *Solid State Communications* **39**, 661 (1981).
- [221] W. Wolf, R. Podloucky, T. Antretter, F.D. Fisher, “First-principles study of elastic and thermal properties of refractory carbides and nitrides”, *Phil. Mag. B* **79**, 839-858 (1999).
- [222] C.R. Houska, “Thermal Expansion and Atomic Vibration Amplitudes for TiC, TiN, ZrC, ZrN, and pure Tungsten”, *J. Phys. Chem. Solids* **25**, 359-366 (1964).
- [223] L.J. Porter, S. Yip, M. Yamaguchi, H. Kaburaki, M.J. Tang, “Empirical bond-order potential description of thermodynamic properties of crystalline silicon”, *J. Appl. Phys.* **81**, 96 (1997).
- [224] J.J. Gilvarry, “The Lindemann and Gruneisen Laws”, *Phys. Rev.* **102**, 308 (1956).
- [225] K.-H. Hellwege and J.L. Olsen, *Metals: Phonon States, Electron States and Fermi Surfaces, Landolt-Bornstein* volume III/13 (Springer-Verlag, Berlin, 1981).
- [226] *American Institute of Physics Handbook*, third edition, edited by D.E. Gray (McGraw-Hill, New York, 1972).
- [227] T.A. Hahn, “Thermal expansion of copper from 20 to 800 K - standard reference material 736”, *J. Appl. Phys.* **41**, 5096-101 (1970).
- [228] J.W. Harrison, “The use of divergent beam interferometry in the measurement of small displacements: an application to the measurement of the thermal expansion of copper up to 1200K”, *Journal of Physics E* **9**, 545-8 (1976).
- [229] R. Berman, *Thermal Conduction in Solids* (Clarendon Press, Oxford, 1976).
- [230] V.V. Bulatov, S. Yip, A.S. Argon, “Atomic Modes of Dislocation Mobility in Silicon”, *Phil. Mag. A* **72**, 453 (1995).
- [231] J.P. Hirth, J. Lothe, *Theory of Dislocations*, second edition (Wiley, New York, 1982).
- [232] K.S. Cheung, “Atomistic study of dislocation nucleation at a crack tip”, Ph. D. Thesis supervised by S. Yip, Massachusetts Institute of Technology, Department of Nuclear Engineering (1990).
- [233] M.F. Kanninen, *Advanced Fracture Mechanics* (Oxford University Press, New York, 1985).

- [234] T.L. Anderson, *Fracture Mechanics: Fundamentals and Applications*, second edition (CRC Press, Boca Raton, 1995).
- [235] S. Suresh, *Fatigue of Materials*, second edition (Cambridge University Press, 1998).
- [236] H. Alexander, “Dislocations in Covalent Crystals”, in *Dislocations in Solids*, volume 7, pp. 113-234, edited by F.R.N. Nabarro (North-Holland, Amsterdam, 1986).
- [237] E. Kaxiras and M.S. Duesbery, “Free energies of generalized stacking faults in Si and implications for the brittle-ductile transition”, in *Phys. Rev. Lett.* **70**, 3752 (1993).
- [238] Q. Ren, B. Joos, M.S. Duesbery, “Test of the Peierls-Nabarro model for dislocations in silicon”, *Phys. Rev. B* **52**, 13223 (1995).
- [239] T. Suzuki, T. Nishisako, T. Taru, T. Yasutomi, “Plastic deformation of InP at temperatures between 77 and 500 K”, *Phil. Mag. Lett.* **77**, 173 (1998).
- [240] T. Suzuki, T. Yasutomi, T. Tokuoka, I. Yonenaga, “Plasticity of III-V compounds at low temperatures”, *Physica Status Solidi A* **171**, 47 (1999).
- [241] T. Suzuki, T. Yasutomi, T. Tokuoka, I. Yonenaga, “Plastic deformation of GaAs at low temperatures”, *Phil. Mag. A* **79**, 2637 (1999).
- [242] H. Koizumi, Y. Kamimura, T. Suzuki, “Core structure of a screw dislocation in a diamond-like structure”, *Phil. Mag. A* **80**, 609 (2000).
- [243] J.F. Justo, M. de Koning, W. Cai, V.V. Bulatov, “Vacancy interaction with dislocations in silicon: The shuffle-glide competition”, *Phys. Rev. Lett.* **84**, 2172 (2000).
- [244] V.V. Bulatov, A.S. Argon, “A stochastic-model for continuum elasto-plastic behavior: I. Numerical approach and strain localization, II. A study of the glass-transition and structural relaxation, III. Plasticity in ordered versus disordered solids”, *Modelling and Simulation in Materials Science and Engineering* **2**, 167-222 (1994).
- [245] A.S. Argon, V.V. Bulatov, P.H. Mott, U.W. Suter, “Plastic deformation in glassy polymers by atomistic and mesoscopic simulations”, *Journal of Rheology* **39**, 377-399 (1995).
- [246] N.F. Mott, F.R.N. Nabarro, “Dislocation Theory and Transient Creep”, in *Report of a Conference on Strength of Solids*, held at the H.H. Wills Physical Laboratory, University of Bristol (Physical Society, London, 1948).
- [247] J. Friedel, in *Electron Microscopy and Strength of Crystals*, pp. 605, edited by G. Thomas and J. Washburn (Interscience Publishers, New York, 1962).

- [248] R.L. Fleischer and W.R. Hibbard, in *The Relation between the Structure and Mechanical Properties of Metals*, pp. 261 (H. M. Stationery Office, London, 1963).
- [249] R. Labusch, “A statistical theory of solid solution hardening”, *Physica Status Solidi A* **41**, 659-71 (1970).
- [250] R.B. Schwarz, R. Labusch, “Dynamic simulation of solution hardening”, *J. Appl. Phys.* **49**, 5174-87 (1978).
- [251] A.J. Ardell, “Precipitation Hardening”, *Metallurgical Transactions A* **16A**, 2131-65 (1985).
- [252] A. Iserles, *A First Course in the Numerical Analysis of Differential Equations* (Cambridge University Press, 1996).
- [253] W.H. Press, S.A. Teukolsky, W.T. Vetterling, B.P. Flannery, *Numerical Recipes in C – the Art of Scientific Computing* (Cambridge University Press, Cambridge, 1992).